

ZAŠTITA MATERIJALA

Godina LXV

Beograd, 2024.

Broj 4

Editor in Chief

Prof. dr **Časlav Lačnjevac**, University of Belgrade, Faculty of Agriculture, Belgrade, Serbia

Co - editors

Dr **Nebojša Nikolić**, University of Belgrade, Serbia

Dr **Vladimir Panić**, University of Belgrade, Serbia

Prof. dr **Abd El-Aziz S. Fouda**, El-Mansoura University, Egypt

Prof. dr **Branimir Grgur**, University of Belgrade, Serbia

Prof. dr **Susai Rajendran**, Department of Chemistry, Thamarapady, India

Prof. dr **Iveta Vaskova**, Teknikal University of Kosice, Slovakia

Prof. dr.habil. **Marian Jaskula**, Jagiellonian University, Poland

Prof. dr **Leonid Dvorkin**, National University of Water and Environmental Engineering, Ukraine

Prof. dr **Vaso Manojlović**, University of Belgrade, TMF, Belgrade, Serbia

Dr **Marija Ercegović**, Institute ITMNS, Serbia

Editorial Board

Prof. dr **Benedetto Bozzini**, Italy

Prof. dr **J. G. Gonzalez-Rodriguez**, México

Prof. dr **Heiner Jakob Gores**, Germany

Prof. dr **Tor Henning Hemmingsen**, Norway

Dr **Mirjana Stojanovic**, Serbia

Prof. dr **K. F. Khaled**, Egypt

Prof. dr **Miomir G. Pavlović**, Serbia

Prof. dr **Liudmila Tsygankova**, Russian Federation

Dr **Andrzej Kowal**, Poland

Prof.dr **Dragica Chamovska**, R.N.Macedonia

Prof. dr **Svetlana Kaluzhina**, Russian Federation

Prof. dr **Srdjan Roncevic**, Serbia

Prof. dr **Refik Zejnilović**, Montenegro

Dr **Ronald Latanision**, USA

Prof. dr **Miodrag Maksimović**, Serbia

Prof. dr **Vesna Mišković-Stanković**, Serbia

Dr **Dorothy Rajendran**, India

Prof. dr **Milan Jaić**, Serbia

Prof. dr **Kozeta Vaso**, Albania

Prof. dr **A. S. Sarac**, Turkey

Prof.dr **Milorad Tomić**, BiH

Prof.dr **Jelena Bajat**, Serbia

Dr **Aleksandra Daković**, Serbia

Prof. dr **Ladislav Vrsalović**, Croacia

Prof.dr **Darko Vuksanović**, Montenegro

Prof.dr **Deana Wahyuningrum**, Indonesia

Dr **Nebojsa Marinkovic**, USA

Dr **Slavko Bernik**, Slovenia

Prof.dr **Milica Gvozdenovic**, Serbia

Dr **Tsvetina Dobrovoljska**, Bulgaria

Prof.dr **Oguike Raphael Shadai**, Nigeria

Dr **Miroslav Sokic**, Serbia

Prof.dr **Djendji Vaštag**, Serbia

Prof. dr **Maria Joany Rajendran**, India

Prof.dr **Regina Fuchs Godec**, Slovenia

Prof. dr **Aurel Nuro**, Albania

Dr **Muhammed Ernur Akiner**, Turkey

Dr **Branimir Jugovic**, Serbia

Dr **Petar Ljumovic**, Croacia

Prof. dr **Manjeet Singh Goyat**, India

Prof. dr **Aleksandar Kostic**, Serbia

Prof. dr **Borko Matijević**, Serbia

Dr **Miroslav Pavlovic**, Serbia

Prof. dr **Blažo Laličić**, Serbia

Izdavački savet – Publisher board

Dr **Sreco Pavlin**, predsednik, R. Slovenia

Mr **Ivan Burić**, Montenegro

Zoran Ivljanin, Serbia

Gordana Miljević, Serbia

Dr **Ilija Nasev**, R. S. Macedonia

Dr **Zoran Avramović**, Serbia

Momir Ilić, Serbia

Dosadašnji glavni i odgovorni urednici

Prof. dr **Sreten Mladenović** (1967–2001)

Prof. dr **Miodrag Maksimović** (2002 – 2005)

Prof. dr **Milan Antonijević** (2006-2012)

Technical editor: **Slavka Vukašinić**

Za izdavača – For publisher

Prof. dr **Časlav Lačnjevac**, predsednik

Izdavač- Publisher:

INŽENJERSKO DRUŠTVO ZA KOROZIJU, Beograd, Kneza Miloša 9/I,

Tel/fax (011) 3860 - 867 i (011) 3230–028,

E-mail:editor@idk.org.rs; idk@idk.org.rs, www.idk.org.rs, E-mail:caslav.lacnjevac@gmail.com

EVROPSKA FEDERACIJA ZA KOROZIJU (EFC) SMATRA OVAJ ČASOPIS ZVANIČNOM PUBLIKACIJOM ZA OBJAVLJIVANJE IZVEŠTAJA I INFORMACIJA

EUROPEAN FEDERATION OF CORROSION (EFC) CONSIDERES THIS JOURNAL TO BE THE OFFICIAL PUBLICATION FOR PUBLISHING THE REPORTS AND INFORMATION

SADRŽAJ – CONTENT

Sarap Krishnaprasad, Mohammed Shareefuddin, Siddey Laxmi Srinivasa Rao, Gokarakonda Ramadevudu Structural Investigation and Physical Properties of RO-ZnO-Li₂B₄O₇-K₂B₄O₇ (RO= SrO and BaO) Glasses....	561
https://doi.org/10.62638/ZasMat1147	
Mansi Sharma, Priyanka Mahajan Nature's prescription: decoding the power of biopolymers in medical and pharmaceutical applications.....	578
https://doi.org/10.62638/ZasMat1205	
Priya Agarwal, SatyaPrakash, GauravSaini, Ikhwan Syafiq Mohd Noor Recent Advances in Research from Plastic Materials to Microplastics	595
https://doi.org/10.62638/ZasMat1176	
Parvaiz Ahmad Dar, MuhdZuAzhanYahya, Serguei V. Savilov, SharadAgrawal Bacillus amyloliquefaciens strain NSB4 bacteria for treating wastewater for fuel cell application.....	612
https://doi.org/10.62638/ZasMat1194	
Marija Mitrović, Milena Milovanović, Nebojša Vasiljević, Milorad Tomić The Effect of Anodization and Subsequent Treatments on Corrosion Resistance of Aluminium.....	623
https://doi.org/10.62638/ZasMat1174	
Bashir Abdu Muzakkari, Amina Salihi Bayero, Musalbrahim Mohammed, Pramod Kumar Singh, Umar Muhammad Jibreel Waste Tyres Pyrolysis Oil (WTPO) as an Alternative Source of Fuel and Chemicals: A Review.....	634
https://doi.org/10.62638/ZasMat1153	
Esraa Razaq, Shaymaa Abbas Abdulsada Effect of Corrosion Inhibitors on Internal Corrosion in Oil Pipelines: A Brief Review	645
https://doi.org/10.62638/ZasMat1161	
Bui Xuan Vuong Hydrothermal synthesis of bioactive calcium silicate glass	653
https://doi.org/10.62638/ZasMat1049	
Etuk Sunday Edet, Robert Ubong Williams, Agbasi, Okechukwu Ebuka, Inyang Namdie Joseph Influence Of Rice Husk Ash Inclusion On Electrical Characteristics Of Dry Cement Mortar	660
https://doi.org/10.62638/ZasMat1051	
Leonid Dvorkin, Vitalii Marchuk, Mykola Kuzlo Influence of Adhesive Additives on the Properties of Bitumen and Asphalt Mixtures	668
https://doi.org/10.62638/ZasMat1170	
Lyudmila Nyrkova, Vitaliy Knysh, Sergiy Solovey, Svetlana Osadchuk Influence of Different Methods of Surface Treatment on Corrosion Resistance of Low-Alloy Steel.....	680
https://doi.org/10.62638/ZasMat1052	
Monika Srivastava, Ikhwan Syafiq Mohd Noor, Muhd Zu Azhan Yahya, R. C. Singh Synthesis and scalable process for fabrication of Perovskite Solar Cells using organic and inorganic hole transport materials	690
https://doi.org/10.62638/ZasMat1257	
Sushant Kumar, Manoj K. Singh, Muhd Zu Azhan Yahya, Ikhwan Syafiq Mohd Noor, Pramod K. Singh Structural, Electrochemical, and Dielectric Studies of Phytigel and 1-ethyl-3-methylimidazolium Tricyanomethanide-based Bio-polymer Electrolytes	703
https://doi.org/10.62638/ZasMat1050	
Liubov Melnyk, Lev Chernyak, Valentin Svidersky, Ludmila Vovchenko, Viktoria Yevpak Comparative Study of Various Volcanic Materials as Fillers in Polymer Composites	712
https://doi.org/10.62638/ZasMat1171	
Sirisha Korrai, B. Vinay Sagar, Madhavi Earle, Sangeetha Sankhyayani Achanta, Hemanshu Mediboyana Evaluating the water quality of a Kondakarla Ava Lake for Agricultural Endeavours in Visakhapatnam, India.....	724
https://doi.org/10.62638/ZasMat1172	
Rawnaq Jima'a, Naser Shaalan, Muna Bufaroosha, Gamal A. El-Hiti, Benson M. Kariuki, Dina S. Ahmed, Emad Yousif Synthesis and Properties of New Metal Complexes Containing Heterocyclic Moieties and Investigation of the Role of the Metal in Carbon Dioxide Gas Capture	734
https://doi.org/10.62638/ZasMat1045	
Amina Salihi Bayero, Nura Alhaji Yaro, Musa Ibrahim Mohammed, Pramod Kumar Singh, Bashir Abdu Muzakkari, Umar Muhammad Jibreel Pyrolysis Char from Waste Tyres its Characteristics, Upgrading and Application.....	748
https://doi.org/10.62638/ZasMat1046	
Anna Stepashkin*, Khurram Shehzad Examining the Impact of Anisotropic Particle Orientation in a Polymer Matrix on the Electrical Properties of Composite Materials	756
https://doi.org/10.62638/ZasMat1110	

Thangarajan Umamathi, Venkatachalam Prathipa, Arockiam Roslin, Arockiaraj Little Jewelcy, Micheal Velankanni Jeevithe Clara, Nilavan Anitha, Mohamed Ibrahim Nasrin Sahana, Suai Rajendran, Arjunan Krishnaveni Influence of sodium chloride on corrosion resistance of silver vessels in the presence of curd rice.....765 https://doi.org/10.62638/ZasMat1173	
Paulcy Rani Palayyan Raja Bai, Sivakala Sarojam, Anju Krishna Salimkumar Shailaja, Anu Mini Aravind, Xavier Thankappan Suryabai The Electrochemical Performance of Perovskite LaMnO₃.....778 https://doi.org/10.62638/ZasMat1175	
Sonia Yadav, Nadeem Sharma Cerium(III) Phosphotungstate: an Efficient Catalyst in Esterification of Fatty Acids786 https://doi.org/10.62638/ZasMat1067	
Vladimir D. Jović The long time performance of catalysts usually used in the literature797 https://doi.org/10.62638/ZasMat1308	

SUIZDAVAČI

**INSTITUT ZA TEHNOLOGJU NUKLEARNIH I DRUGIH MINERALNIH SIROVINA, BEOGRAD
UDRUŽENJE INŽENJERA SRBIJE ZA KOROZIJU I ZAŠTITU MATERIJALA
CRNOGORSKO DRUŠTVO ZA ZAŠTITU MATERIJALA**

DONATORI

JP ELEKTROMREŽA SRBIJE, BEOGRAD	PITURA", NOVI BEOGRAD
JKP DRUGI-OKTOBAR, VRŠAC	UNIPROMET, ČAČAK
"NIS - FAM", KRUŠEVAC	FAKULTET ZAŠTITE NA RADU, NIŠ
GALFOS, BEOGRAD	INSTITUT ZA VODOPRIVREDU
PD DRINSKO LIMSKE ELEKTRANE,	„JAROSLAV ČERNI“, BEOGRAD
BAJINA BAŠTA	„GALVA“, KRAGUJEVAC
INSTITUT ZA PREVENTIVU, NOVI SAD	PERIĆ & PERIĆ, POŽAREVAC
MAŠINSKI FAKULTET, BEOGRAD	HORIZONT PRES, BEOGRAD
TEHNOLOŠKO-METALURŠKI FAKULTET, BEOGRAD	VISOKA TEHNOLOŠKA ŠKOLA STRUKOVNIH STUDIJA,
TEHNIČKI FAKULTET, BOR	NOVI BEOGRAD
TEHNOLOŠKI FAKULTET, LESKOVAC	VISOKA STRUKOVNA ŠKOLA, NIŠ
ALFA PLAM ad, VRANJE	VISOKA TEH. SKOLA STRUK. STUDIJA, NOVI SAD
„HELIOS“, DOMŽALE	INSTITUT ZA PUTEVE, BEOGRAD
ŠUMARSKI FAKULTET, BEOGRAD	IMPOL SEVAL, UŽICE
AGRONOMSKI FAKULTET, ČAČAK	ALFATERM, ČAČAK
GRAĐEVINSKO-ARHITEKTONSKI FAKULTET, NIŠ	METALAC A.D., GORNJI MILANOVAC
TEHNOSAM, SUBOTICA	SINVOZ DOO, ZRENJANIN

U finansiranju izdavanja časopisa "ZAŠTITA MATERIJALA" učestvuju:



MINISTARSTVO NAUKE, TEHNOLOŠKOG RAZVOJA I INOVACIJA REPUBLIKE SRBIJE



INŽENJERSKA KOMORA SRBIJE

CIP - Katalogizacija u publikaciji
Narodna biblioteka Srbije, Beograd

620.1

ZAŠTITA MATERIJALA = Materials Protection / Glavni urednik (Časlav Lačnjevac),
[Štampano izd.] - God. 1, br. 1 (1953)-god. 22, br. 3/4 (1974) ; god. 23, br. 1 (1982)-. - Beograd: Inženjersko
društvo za koroziju, 1953-1974; 1982- (Zemun : Akademska izdanja). - 29 cm
Dostupno i na: <https://www.zastita-materijala.org> - Tromesečno. - Drugo izdanje na drugom medijumu:
Zaštita materijala (Online) = ISSN 2466-2585
ISSN 0351-9465 = Zaštita materijala
COBISS.SR-ID 4506626

Redakcija: Beograd, Kneza Miloša 9/I, Tel/fax (011) 3860 - 867, i (011) 3230 - 028, E-mail: iddk@iddk.org.rs;
E-mail: editor@iddk.org.rs, www.idk.org.rs; www.zastita-materijala.org/index.php/home/issuse
Tekući račun: 205 - 24967 – 71, Komercijalna banka, Beograd; Časopis izlazi četiri puta godišnje
Rukopisi se ne vraćaju; Štampa: Akademska izdanja, Zemun

ISTORIJAT INŽENJERSKOG DRUŠTVA ZA KOROZIJU

Inženjersko društvo za koroziju, koji je pravni naslednik Saveza inženjera i tehničara za zaštitu materijala Srbije i Crne Gore, je društveno stručna organizacija koja je član Saveza inženjera i tehničara Srbije. Savez inženjera i tehničara za zaštitu materijala Jugoslavije, kako se prvobitno zvalo Inženjersko društvo za koroziju, početke svog delovanja je imao još 1952. godine preko Komisije za zaštitu od korozije. Ova komisija je postojala u okviru Društva hemičara i tehnologa DIT-a, mada se neki koreni iz zaštite od korozije pominju i pre drugog svetskog rata. Inicijatori za oformljenje ove Komisije bili su dr.inž Frano Podbrežnik, prof.dr Blažon, prof.dr Milan Pajević i Sveta Živanović. Komisija je imala 15 aktivnih članova i radila je u tri potkomisije.

Januara 1953. godine ova Komisija prerasta u Centar za zaštitu od korozije sa osnovnim zadatkom da radi na antikorozijskoj zaštiti svih materijala, uređaja, opreme i instalacija. Već u prvoj godini postojanja ovaj Centar je obrazovao svoju servisnu radionicu za fosfatiranje i pristupio izdavanju svojih stručnih publikacija.

Dalji rad Centra, do svog prerastanja u Društvo a kasnije u Savez, odvijao se u komisijama i servisnim radionicama preko kojih se intenzivno radilo na održavanju raznih kurseva i predavanja iz oblasti korozije materijala i zaštite od nje a, takođe, i na izradi projekata za korozionu zaštitu raznih objekata i opreme za mnoga preduzeća.

PREDSEDNIŠTVO IDK: Predsednik IDK prof.dr Časlav Lačnjevac Potpredsednik IDK Zoran Ivljanin, dipl.inž.tehn. Članovi Upravnog odbora – Srećko Stefanović, dipl.inž.tehn. – Dragan Petrović, dipl.elek.inž. – Momir Đurović, dipl.inž.tehn. Članovi Nadzornog odbora – Ljupče Milosavljević, dipl.inž.tehn. – Miodrag Jovanović, dipl.građ.inž. – Mirko Bačilović, dipl.ecc. Tehnički sekretar IDK – Srbislav Nešić, dipl.maš.inž.

Delatnost strukovnih udruženja (udruživanje u okviru profesije i tehničkih oblasti, uključujući i udruženja specijalista angažovanih u naučnoj delatnosti); – Obrazovanje odraslih (obrazovanje na seminarima, naučno-stručnim skupovima, specijalističkim kursovima i sl.); – Istraživanje procesa korozije i zaštite od korozije; – Izrada tehničke dokumentacije, ekspertiza i vršenje nadzora iz oblasti hidroizolacije, antikorozijske zaštite i protivpožarne zaštite.

Inženjersko društvo za koroziju Republike Srbije je izdavač časopisa Zaštita materijala, počelo je sa radom daleke 1953. godine, kao deo Centra za zaštitu od korozije u okviru Saveza inženjera i tehničara za zaštitu materijala Jugoslavije. Iste godine Društvo je pokrenulo časopis Zaštita materijala, koji i danas aktivno izlazi. Pridružite se bezbrojnim čitaocima koji su imali koristi od njegovog zanimljivog naučnog sadržaja.



Otvaranje naučnog skupa

Zaštita materijala je recenzirani časopis koji sadrži radove o originalnom eksperimentalnom ili teorijskom istraživanju i značajno unapređuju razumevanje u oblastima korozije i zaštite materijala, zaštite životne sredine, ekološkog inženjerstva i tehnologija, inženjerstva materijala (keramika, polimeri, kompoziti; biomaterijali, materijali za skladištenje i konverziju energije, itd.); nanomaterijala i nanotehnologija; hemijskog i biohemijskog inženjerstva, primenjene hemije, upravljanja tehnologijom, i obrazovanja o održivom razvoju. Časopis prihvata radove koji prikazuju eksperimentalne i teorijske naučne i inženjerske rezultate na osnovu dostavljenih podataka.

Naučni radovi za ZM moraju biti dostavljeni na engleskom jeziku i treba da sadrže rezime na engleskom i srpskom jeziku. Za autore van srpskog govornog područja, izdavač će obezbediti rezimee i naslove tabela i slika na srpskom jeziku. Časopis izlazi 4 puta godišnje.

Časopis je indeksiran u Scopus, DOAJ, International Scientific Indexing (ISI), Journalspedia (JPSA), Sherpa Romeo itd.

Digitalne kopije časopisa su arhivirane u repozitorijumu.

Sarap Krishnaprasad^{1,2}, Mohammed Shareefuddin¹, Siddey Laxmi Srinivasa Rao³, Gokarakonda Ramadevudu⁴*

¹Department of Physics, Osmania University, Telangana, Hyderabad, India;

²SRR Government Arts & Science College (A), Karimnagar, Telangana, India; ³Department of Physics, Government City College (A), Hyderabad;

⁴Department of Physics, Vasavi College of Engineering (A), Telangana, Hyderabad, India

Scientific Paper

ISSN 0351-9465, E-ISSN 2466-2585

<https://doi.org/10.62638/ZasMat1147>



Zastita Materijala 65 (4)
561 – 577 (2024)

Structural Investigation and Physical Properties of RO-ZnO-Li₂B₄O₇-K₂B₄O₇ (RO= SrO and BaO) Glasses

ABSTRACT

Glass samples 10RO-30ZnO-xLi₂B₄O₇-(60-x) K₂B₄O₇ (RO=SrO and BaO) with alkali tetra borates varying from 0 to 60 mol% were produced by traditional quenching procedure. Peak free broad X-ray diffraction patterns established the amorphous feature of glass samples. FTIR and Raman spectroscopic analysis showed the existence of BO₃ and BO₄ structural groups and other borate units. The BO₃ ⇌ BO₄ conversion rate was not much affected by variation in one of the alkali-tetra borates. EPR spectra of copper doped glasses confirmed the ground state of Cu²⁺ ions as ²B_{1g}. Physical and optical properties namely density, molar volume, refractive index, molar refractivity, optical band gap and Urbach energy values were found to be composition dependent. The inflections observed in density, and other optical properties around equal mol.% of alkali oxides in the glass system were attributed to structural modifications and mixed alkali effect. These results exposed the structural variations caused by competitiveness between the two different alkali and alkaline oxides in occupying the geometrical positions of the borate glass network.

Keywords: mixed alkali effect (MAE), alkaline earth-oxide glasses, optical bandgap, electron paramagnetic resonance, FTIR and Raman spectroscopy

1. INTRODUCTION

Mixed alkali and alkaline earth oxide borate glasses containing various dopants got popularity due to their utilization in various sectors including solid state ionics, bio-active glasses, host materials for lasers, radiation shielding, memory applications, electronic devices, acoustics, solar cells, energy storage, sensors, laser, and infrared detection etc. [1-6]. The oxides Li₂O, Na₂O, K₂O, MgO, CaO, SrO, BaO, ZnO, PbO etc., are extensively used as glass modifiers or additional formers (depending on their mol%) added in conjunction with B₂O₃. The glass modifiers are used to improve the physical, electrical, mechanical, and optical properties of oxide glasses. Borate glasses consisting of different alka-

li and alkaline earth oxides can be prepared below 1200°C temperature with ease by quenching.

Addition of ZnO into borate glass network particularly improves optical properties and stability. The role of ZnO changes from glass modifier to glass former if its composition is greater than 45 mol % [7]. The alkaline earth oxides SrO and BaO in general extend the glass producing ability as network modifiers or formers depending on their mol% in the glass matrix. These two oxides improve the chemical durability of the glass. It was reported by researchers that these oxides act as glass modifiers at low concentration (below 30%) and formers when their content is high [8-10].

Borate glasses with rich alkali content display boron anomaly namely "Mixed Alkali Effect" (MAE) when two or more than two alkali oxides are present in the glass matrix. Similarly mixed alkaline oxides also exhibit a similar phenomenon namely "Mixed Alkaline Effect". The MAE induces significant

* Corresponding author: Gokarakonda Ramadevudu

E-mail: dr.ramdev@gmail.com

Paper received: 31.1.2024.

Paper accepted: 11.04.2024.

changes in many physical, electrical, and optical properties of glasses when one alkali/alkaline oxide is replaced by the other alkali/alkaline oxide. The observed changes might result in due to the competitive role of occupation of different structural positions by the alkali/alkaline oxide ions. The varying content of alkali oxides favours sudden or gradual changes in various properties and exhibits positive or negative inflections around equal mole percentage of the two alkali oxides in the glass composition [11-13].

The mixed effect of glass formers or glass modifiers such as SrO and BaO results in significant variation of glass properties, in addition to effect the glass formation. It was observed that presence of two glass modifier oxides SrO and BaO reduces the diffusion because of the competition between them. The heavy oxide BaO in general disrupts the glass network by forming non-bridging oxygens (NBO) and thereby causes change in structure as well as physical and optical properties [14-16]. Glasses containing mixed alkaline oxides show interesting properties such as increased thermal stability and decreasing mechanical properties. Ternary borate glasses containing SrO have shown improved bioactivity [17,18].

There are a few studies on structural and physical properties in the literature on glasses containing double tetraborates. The studies on the role of alkaline oxides in tetraborate glasses scarcely found. The present work investigates the effect of alkali tetraborate oxides on the structural units of the glass, spectroscopic parameters, physical and optical properties of 10RO-30ZnO-xLi₂B₄O₇-(60-x)K₂B₄O₇ (RO=SrO and BaO) glass system. This paper analyzes the role of RO and ZnO as glass modifiers. The role played by alkali ions in occupying various structural locations was also discussed. In the base glass, copper oxide (CuO) is added to undertake electron paramagnetic resonance studies and to know the nature of ligand field in the surroundings of the spin probe Cu²⁺ ion. By estimating Hamiltonian parameters and the bonding coefficients the ground state of Cu²⁺ ion is determined.

2. EXPERIMENTAL TECHNIQUES

10RO-30ZnO-xLi₂B₄O₇-(60-x)K₂B₄O₇ (RO=SrO, BaO) were made by quenching process. The present glass composition contained ZnO at fixed 30 mol% and alkaline earth oxide content retained

constant at 10 mol%. The alkali tetraborate oxides were gradually swapped in the glass matrix from 0 to 60 mol%. The base glass composition was doped with 1 mol% of CuO to make fresh glasses 10RO-30ZnO-xLi₂B₄O₇-(59-x)K₂B₄O₇-1CuO (RO=SrO, BaO) for EPR and optical absorption analysis. Li₂B₄O₇ (Sigma-Aldrich), K₂B₄O₇ (Sigma-Aldrich), SrO (Sigma-Aldrich), BaO (Sigma-Aldrich), ZnO (SD-fine), and CuO (SDfine) were the starting chemical ingredients in mol%. These chemicals were mixed thoroughly in appropriate amounts in a mortar and pestle. Then the mixtures taken in porcelain crucibles were melted at around 1100°C temperature for half-an-hour.

The uniform and homogenous vitreous melts were instantly poured onto a stainless steel plate held around 200°C. The melts were immediately flattened with another steel plate. The prepared glass samples were annealed at 200°C for nearly 2 hour to relieve the leftover internal mechanical stresses and brought them to room temperature gradually. In the present study, the annealing temperature was chosen from the literature corresponding to alkali-alkaline borate glasses and accordingly annealing was done at 200°C. The glasses thus made were very clear, transparent and prepared in disc and rod shapes for characterization.

The X-ray patterns were taken on Bruker D8 Advance machine. The optical measurements were carried on samples of average thickness 0.5mm. Smaller the thickness of the sample better will be the approximation in the optical bandgap energy measurements. The optical absorption spectra were scanned on Agilent technologies-Carry 5000 with UMA spectrophotometer (wavelength range 200-1100 nm). FTIR spectra were recorded on SHIMADZU-8400S spectrometer (wavenumber range 400-4000cm⁻¹). LAB RAM HR Horiba France with 532 nm Nd-YAG laser 100 mW Raman Spectrometer was used to get Raman spectra (wavenumber range 200-2000 cm⁻¹). The electron paramagnetic resonance spectra of Cu²⁺ ions were recorded on JES - FA200 ESR Spectrometer in X-band (8.75-9.65 GHz) frequencies keeping the a field modulation of 100 KHz. The magnetic field was varied between 250mT and 400 mT. All the above measurement were made at room temperature. The refractive index values of the glass samples were determined from the optical bandgap (E_{opt}) values. The glass codes and compositions of the prepared glass samples were given in **Table.1**.

3. RESULTLS AND DISCUSSION

3.1. X-ray diffraction

Fig.1 represents x-ray diffraction shapes of 10RO-30ZnO-xLi₂B₄O₇-(60-x) K₂B₄O₇ (RO= SrO, BaO) glasses. The broad x-ray diffractograms with no sharp peaks indicated amorphous nature of the present glass samples.

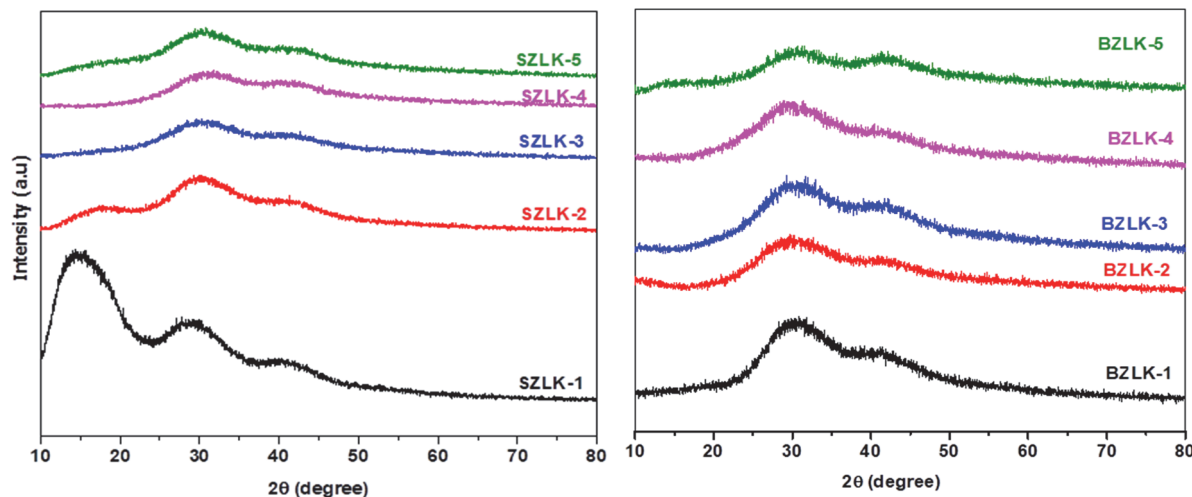


Figure 1. X-ray diffraction patterns of 10RO-30ZnO-xLi₂B₄O₇-(60-x)K₂B₄O₇ (RO= SrO and BaO) glasses

3.2. Structural characterization

3.2.1. Fourier Transform Infrared (FTIR) studies:

Fig.2 illustrates Fourier Transform Infrared (FTIR) spectra of SZLK1 to SZLK5 and BZLK1 to BZLK5 glasses. The characteristics fingerprint peak positions (400 to 1600 cm⁻¹) of borate glasses are clearly visible in **Fig.2**. It is well established fact that the infrared active bands of several borate glasses appear in three categories specifying bending vibrations between 600cm⁻¹ and 800cm⁻¹, stretching vibrations of BO₄ units (800-1200 cm⁻¹) and BO₃ units (1200 –1600 cm⁻¹) stretching vibrations. The band position between 2200 to 4000 cm⁻¹ corresponds to H-O-H and OH⁻ groups vibrations. These three primary vibrations are detected in the FTIR spectra of the glass samples. In addition to the borate vibrational bands, there are bands about 440 cm⁻¹ due to the presence of cations like Zn²⁺ ions.

Various infrared peaks observed between 400 to 4000 cm⁻¹ and their assignments are provided in **Table.2**. From **Fig.2** it is apparent that both SZLK and BZLK glasses contained similar IR bands with a slight shift in wave numbers. The observed shifts are as expected due to the difference in the molar

masses of SrO (103.62 g/mol) and BaO (153.33 g/mol). The IR bands at lower wave numbers between 440 and 480cm⁻¹ in SZLK and BZLK glasses respectively correspond to existence of Zn²⁺ metal cations and Zn-O bond vibration from ZnO₄ tetrahedral units [19,20]. These vibrational frequencies indicated formation of Zn-O bonds in the glass network. The structures also contain Sr²⁺ cations in SZLK glasses and Ba²⁺ cations in BZLK glass matrix.

Table.1 Composition and codes of 10RO-30ZnO-xLi₂B₄O₇-(60-x) K₂B₄O₇ Glass Systems

Glass code	pure samples (SZLK/BZLK) (mol%)				
	SrO	BaO	ZnO	Li ₂ B ₄ O ₇	K ₂ B ₄ O ₇
SZLK1	10	-	30	0	60
SZLK2	10	-	30	15	45
SZLK3	10	-	30	30	30
SZLK4	10	-	30	45	15
SZLK5	10	-	30	60	0
BZLK1	-	10	30	0	60
BZLK2	-	10	30	15	45
BZLK3	-	10	30	30	30
BZLK4	-	10	30	45	15
BZLK5	-	10	30	60	0

Various infrared peaks observed between 200 to 4000 cm⁻¹ and their assignments are provided in **Table.2**. From **Fig.2** it is apparent that both SZLK and BZLK glasses contained similar IR bands with a slight shift in wave numbers. The IR bands at lower wave numbers between 440 and 480cm⁻¹ in SZLK and BZLK glasses respectively correspond to existence of Zn²⁺ metal cations and Zn-O bond vibration from ZnO₄ tetrahedral units. These vibrational frequencies indicated formation of Zn-O bonds in the glass network.

The characteristic boroxol ring vibrations (806 cm⁻¹) [21] are absent in the present glass samples. Infrared peaks of small intensity detected in the range 600-800 cm⁻¹ are attributed to bending of B-O linkages. The bands occurring in 900-1200 cm⁻¹ region are arising from asymmetric stretching vibration of BO₄ units. Peaks around 1230–1630 cm⁻¹ are as-

signed to stretching of BO₃⁻ units belonging to meta, pyro and ortho borate networks. Ali and Rammah et al also observed borate group vibrations in the range 800-1200 cm⁻¹ and attributed them to stretching vibrations of B-O units present in BO₄ groups [22]. The concentration of BO₃ (i.e. N₃) and BO₄ (i.e. N₄) units is found to vary in a non-linear manner with Li₂B₄O₇ composition. Therefore, exchange of bridging oxygens to non-bridging oxygens or BO₃ ⇌ BO₄ transformation with Li₂B₄O₇ mole % in the glass matrix can be assumed to be trivial. Accordingly, the present glasses contain a complex structure having blend of (BO₃), (BO₄) with bridging and non-bridging oxygens, >B-O- end groups and zinc-borate groups. Although Zinc oxide may not have played major role in the transformation of BO₃ units into BO₄ units but efficient to form zinc-borate complexes such as ZnO₄ [10, 23].

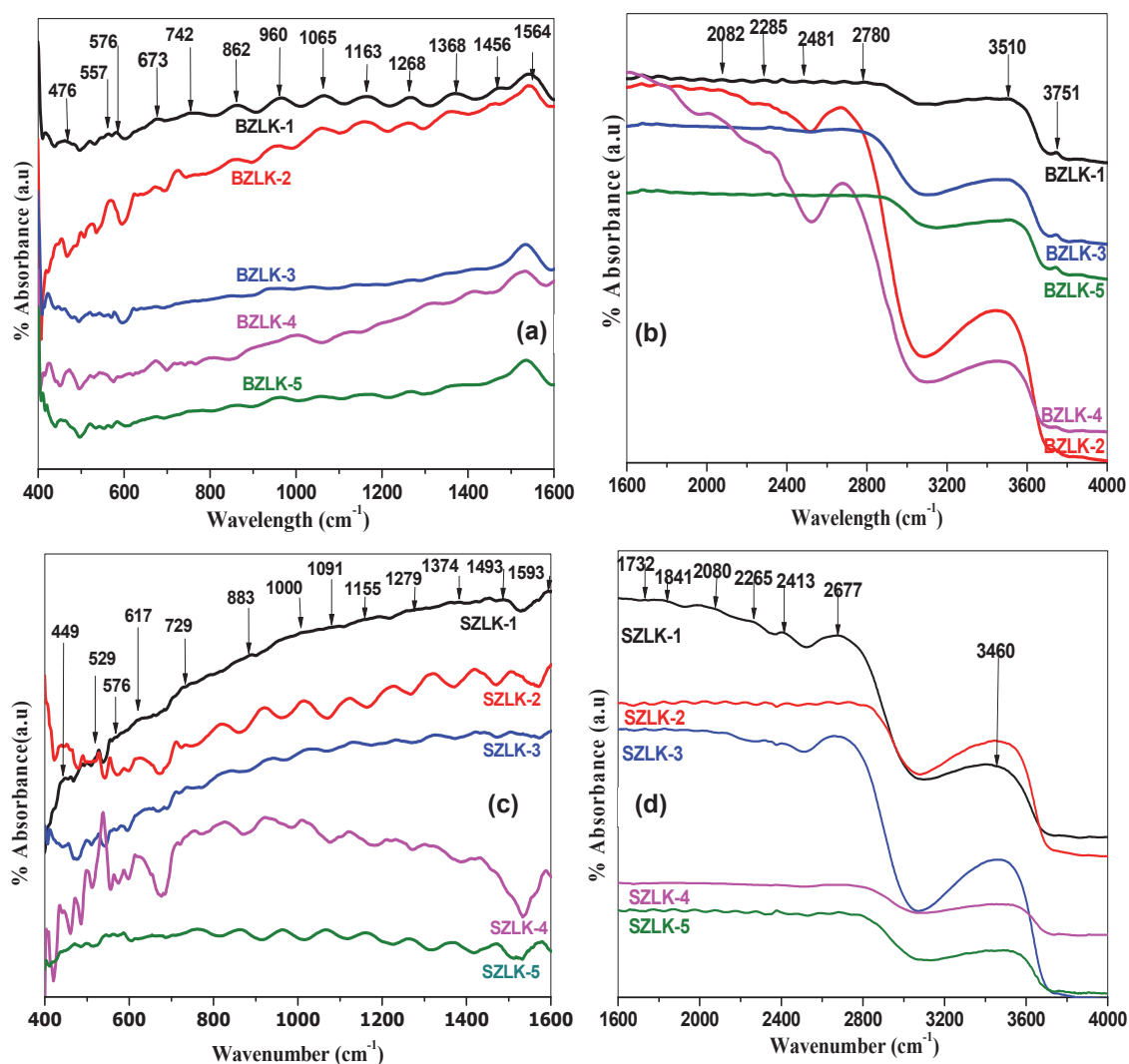


Figure 2. FTIR spectra: a) BZLK 400-1600 cm⁻¹ b) BZLK 1600-4000 cm⁻¹ c) SZLK 400-1600 cm⁻¹ and d) SZLK 1600-4000cm⁻¹.

It can be concluded from FTIR studies that both SZLK and BZLK glasses did not exhibit vibrational peak at 806 cm⁻¹ corresponding to boroxol rings in their glass structure [21]. Zinc oxide and alkaline earth oxides could have gradually converted boroxol rings into diborate, triborate, tetra and penta borate units of BO₃ and BO₄ groups. Ultimately the present glass structural landscape consists of BO₃ and BO₄ groups which in turn are interconnected in the random glass network. These structural units are not uniformly distributed and randomized with progressive substitution of Li₂B₄O₇ [23,24]. In addition, metal cations Li⁺ and K⁺ vibrations are also observed due to the presence of infrared peaks between 530 and 560 cm⁻¹ [25].

3.2.2. Raman Spectroscopic studies

Fig.3 depicts Raman spectra of SZLK and BZLK glasses. The Raman bands involved are clearly identified by using deconvolution spectra. Some of the Raman peaks are not resolved clearly. For better identification of Raman peak locations deconvolution spectra is used. The deconvoluted spectra of SZLK-1 and BZLK-1 are given in **Fig.4**. A similar approach of deconvolution is used for the other samples of the present study. Raman band assignments are presented in **Table.3**.

Table.2 FTIR band assignments of SZLK and BZLK glass samples

FTIR peak positions Wavenumber (cm ⁻¹)					Band Assignments
SZLK1	SZLK2	SZLK3	SZLK4	SZLK5	
449	443	449	443	462	Zn ²⁺ metal cation vibrations and Zn-O bonds vibrations from ZnO ₄ tetrahedral [19,20]
529	531	533	538	542	Li ⁺ and K ⁺ metal cations vibrations [25]
576	588	588	588	590	Sr-O vibrations and Zn-O bending vibrations [26]
617-737	636-724	649-737	600-718	649-774	B-O-B bending vibrations in BO ₃ units [26,27]
883-1155	919-1211	926-1155	921-1180	965-1155	B—O stretching vibrations of tri, tetra, penta and diborate units of BO ₄ groups [26]
1279-1593	1227-1636	1230-1630	1230-1593	1268-1580	B-O asymmetric stretching vibrations of [BO ₃] trigonal units in meta-, pyro-and orthoborate units [26]
		2200–3000			H—O—H bending vibrations (hydrogen bonds) [27]
		3200–3600			Hydroxyl/ water groups stretching vibration [27]
BZLK1	BZLK2	BZLK3	BZLK4	BZLK5	
476	483	470	483	456	Zn ²⁺ metal cation vibrations and Zn-O bonds vibrations from ZnO ₄ tetrahedral units [19,20]
551	560	549	551	553	Li ⁺ and K ⁺ metal cations vibrations [25]
576	569	572	576	581	Ba-O vibrations and Zn-O bending vibrations [26]
673-862	667-854	667-854	673-824	660-856	B-O-B bending vibrations in BO ₃ units [26,27]
960-1163	966-1161	945-1170	980-1194	987-1177	B—O stretching vibrations of tri, tetra, penta and diborate units of BO ₄ groups [26]
1272-1564	1265-1564	1299-1545	1286-1537	1380-1681	B-O asymmetric stretching vibrations of [BO ₃] trigonal units in meta-, pyro-and orthoborate units [26]
		2200–3000			H—O—H bending vibrations (hydrogen bonds) [27]
		3200–3600			Hydroxyl/water groups stretching vibration [27]

From the Raman and FTIR spectroscopic analysis the structural groups present in the glass samples are diborate, triborate, tetra and penta borate units of BO₃ and BO₄ groups. The structure has meta borates and pyroborate groupings. Eventually the structure of both SZLK and BZLK consists of interconnected random glass network of several structural units [33-37].

Both the glass systems under investigation have shown Raman bands almost at the same peak positions with slight shift. From the deconvolution spectra, it is inferred that with varying Li₂B₄O₇ mole %, the Raman band intensities varied non-uniformly. The observed non-linear changes can be assigned to mixed alkali effect. Similar results also had been reported by Padmaja et al. [26,27].

Fong et al attributed bands below 300 cm⁻¹ to metal ion vibrations [28]. Existence of Sr²⁺ and Ba²⁺ ions respectively in SZLK and BZLK glasses and Zn-O stretching and bending vibrations of O-Zn-O of ZnO₄ tetrahedra are noted from the Raman bands around 277 cm⁻¹ Raman Peaks and shoulders around 430-500 cm⁻¹ corresponds to diborate groups vibrat-

ing in isolation and such Raman bands were also reported by Anghel et al [29]. The bands in the range 679 to 774 cm⁻¹ corresponds to six-membered borate rings breathing vibrations of BO₃ and BO₄ units. A high intense peak around 770cm⁻¹ depicts the existence of symmetric breathing vibration of six-membered rings with one BO₄ tetrahedron i.e., triborate, tetraborate or penta-borate units. Maniu et al also seen strong band at ~770 cm⁻¹ in potassium borate glasses holding TiO₂ [30]. Raman bands that appeared at wavenumbers 940 and ~1070 cm⁻¹ proved the formation and existence of metaborates induced in the network due to alkaline earth oxides SrO/BaO. Tetsuji Yano et al ascribed Raman bands in the range 1100- 1600cm⁻¹ to vibration modes of BO₂O- triangles connected with other borate triangular units and short-range structures of BO₃ [31]. The broad region of bands between 1320–1600 cm⁻¹ are associated with B-O bond stretching vibrations connected with triangular borate units [32]. The intensity of vibrational bands corresponding to [BO₄] units slightly decreased while intensity of [BO₃] bands slightly increased and broadened, but substantial change in the intensity of the peaks is not seen.

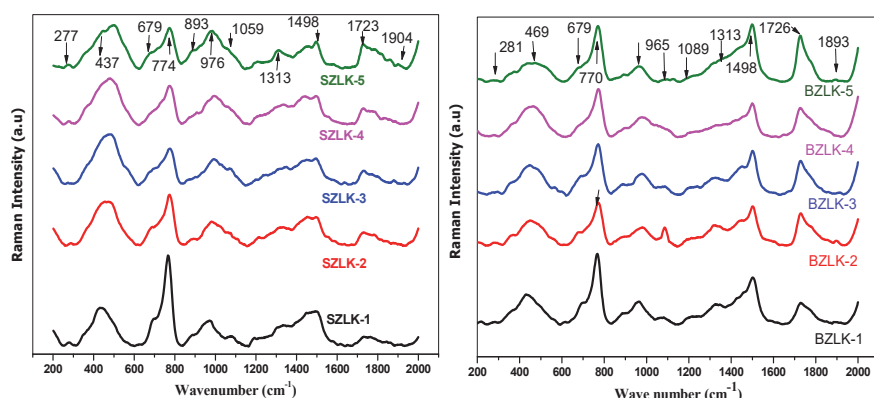


Figure 3. Raman spectra of 10RO-30ZnO-xLi₂B₄O₇-(60-x)K₂B₄O₇ (RO= SrO and BaO) glass systems

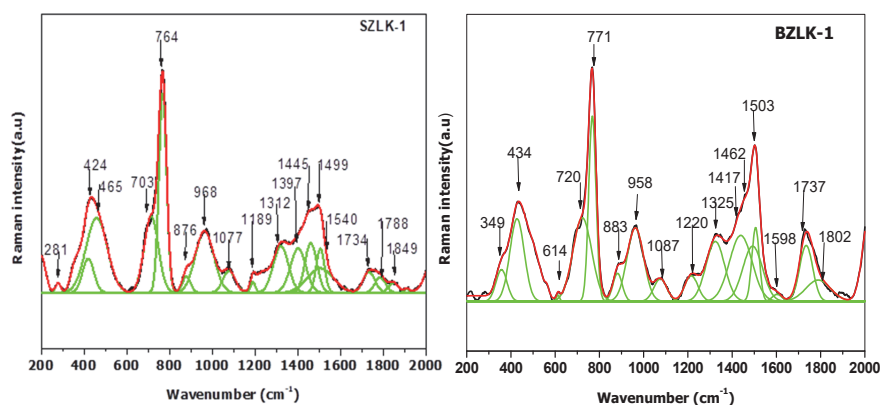


Figure 4. Deconvoluted Raman spectra of SZLK-1 and BZLK-1 glass systems

Table.3 Raman band assignments of SZLK and BZLK glass samples

Raman bands Wavenumber (cm ⁻¹)					Band Assignments
SZLK1	SZLK2	SZLK3	SZLK4	SZLK5	
277	288	277	274	277	vibrations of Sr ²⁺ ions. Zn-O stretching vibrations and bending vibrations of O-Zn-O of ZnO ₄ tetrahedra [28]
498	480	476	473	437	Vibrations of ring angle bending (B-O-B) of borate units or isolated diborate units [29,30]
701	690	694	683	679	bending modes of metaborate chains [20,37].
766	777	777	777	774	Symmetric breathing vibration of six-membered rings with BO ₄ tetrahedron i.e., tri-, tetra- or penta borate units [30]
973	984	991	994	976	asymmetric stretching modes of tetrahedral borate BO ₄ groups [32,33]
1081	1071	1071	1059	1059	
1321	1335	1342	1335	1313	Stretching vibrations of B-O bonds of large number of borate groups [27, 31]
1498	1502	1498	1502	1498	B-O ⁻ bond stretching vibrations and vibrations of BO ₂ O ⁻ triangles connected with other borate triangular units and vibration modes of short-range structures of BO ₃ [31]
1740	1733	1730	1730	1723	
1853	1850	1882	1889	1904	BO stretching vibrations in BO ₃ triangular units [27]
BZLK1	BZLK2	BZLK3	BZLK4	BZLK5	
277	284	288	277	281	vibrations of Ba ²⁺ ions. Zn-O stretching vibrations and bending vibrations of O-Zn-O of ZnO ₄ tetrahedra [28]
434	444	451	448	485	Vibrations of ring angle bending (B-O-B) of borate units or isolated diborate units [29,30]
694	679	694	686	679	bending modes of metaborate chains [20,37].
774	774	770	774	770	Symmetric breathing vibration of six-membered rings with BO ₄ tetrahedron i.e., tri, tetra or penta borate units [30].
965	980	980	980	965	asymmetric stretching modes of tetrahedral borate BO ₄ groups [32, 33].
1078	1092	1089	1103	1089	
1324	1321	1321	1321	1313	Stretching vibrations of B-O bonds of large number of borate groups [27, 31]
1502	1502	1502	1502	1498	B-O ⁻ bond stretching vibrations and vibrations of BO ₂ O ⁻ triangles connected with other borate triangular units and vibration modes of short-range structures of BO ₃ [31]
1730	1730	1730	1726	1726	
1893	1900	1911	1867	1893	BO stretching vibrations in BO ₃ triangular units [27]

3.2.3. EPR and Optical absorption of Cu²⁺ ions:

Fresh glass sample-s of 10RO-30ZnO-xLi₂B₄O₇-(59-x)K₂B₄O₇-1CuO made (SZLKC and BZLKC glasses) to investigate EPR splittings. EPR spectra of Cu²⁺ ion in the SZLK and BZLK glasses are given in **Fig.5** and **Fig.6** depicts Cu²⁺ ion optical absorption spectra of SZLKC and BZLKC glass samples. The errors in the evaluation of g and A values respectively are about ±0.001 and ±2×10⁻⁴ cm⁻¹.

In general, EPR spectrum of Cu²⁺ ion consists of four parallel and four perpendicular hyperfine components. But only three parallel components in the low magnetic field side are clearly observed. The perpendicular components are not resolved. Similar observations have been reported by several authors [38,39]. Here the fourth parallel component is supposed to overlap with perpendicular components. The EPR spectrum was analyzed with the help of axial spin Hamiltonian [39]:

$$\mathcal{H} = \beta[g_{\parallel}H_zS_z + g_{\perp}(H_xS_x + H_yS_y)] + A_{\parallel}I_zS_z + A_{\perp}(I_xS_x + I_yS_y) \quad (1)$$

The parallel (g_{\parallel}) and perpendicular (g_{\perp}) components of g-tensor and parallel (A_{\parallel}) and perpendicular (A_{\perp}) components of A-tensor are obtained from the EPR spectra of present glasses doped with the Cu²⁺ ions. The optical absorption maxima of Cu²⁺ are designated to the ²B_{1g} → ²B_{2g} transition. The spin-Hamiltonian, bond parameters and covalency values are listed in **Table.4**. The various parameters are evaluated using the equations given below with different terms having usual meanings [40,41].

$$h\nu = g_{\parallel}\beta H + mA_{\parallel} + \left(\frac{15}{4} - m^2\right) \frac{A_{\perp}^2}{2\beta H g_{\parallel}} \quad (2)$$

$$h\nu = g_{\perp}\beta H + mA_{\perp} + \left(\frac{15}{4} - m^2\right) \frac{A_{\perp}^2 + A_{\parallel}^2}{4\beta H g_{\parallel}} \quad (3)$$

$$\Delta E_{xy,yz} = \frac{1656K^2}{g_{\perp} - 2.0023} \quad (4)$$

$$\alpha^2 = -\left(\frac{A_{\parallel}}{p}\right) + (g_{\parallel} - 2) + \frac{3}{7}(g_{\perp} - 2) + 0.04 \quad (5)$$

$$\beta^2 = \left(\frac{g_{\perp}}{g_e} - 1\right) \frac{\Delta E_{xy,yz}}{828\alpha^2} \quad (6)$$

$$\beta_1^2 = \left(\frac{g_{\parallel}}{g_e} - 1\right) \frac{\Delta E_{xy}}{3312\alpha^2} \quad (7)$$

$$\tau_{\sigma} = \frac{200(1-S)(1-\alpha^2)}{1-2S} \% \quad (8)$$

$$\tau_{\pi} = 200(1 - \beta_1^2) \% \quad (9)$$

Here S is the overlap integral and S_{oxy} has a value of 0.076.

The estimated g_{\parallel} values of present glasses are noted to be higher than g_{\perp} values and A_{\parallel} values are larger than A_{\perp} values. This type of conduct reveals Cu²⁺ ions inhabiting in stretched octahedral sites ($g_{\parallel} > g_{\perp} > g_e = 2.0023$) in the glass. The ground state of Cu²⁺ ion is attributed to d_{x²-y²}. From the EPR spectra, it is observed that peak intensity in SZLKC glass samples increased from SZLKC1 to SZLKC5 indicating a greater number of Cu²⁺ ions participating in the resonance. In BZLKC glass system peak intensity increased from BZLKC1 to BZLKC4, while BZLKC5 peak intensity decreased indicating non-linear variation of Cu²⁺ ion concentration in the glass samples.

Fig.7 reveals that g_{\parallel} and A_{\parallel} values varied non-linearly with Li₂B₄O₇ mole %. Many alkali/alkaline earth oxide containing borate glasses display such type of behaviour [25,32,38]. When an alkali tetra borate (K₂B₄O₇) is substituted by another alkali tetra borate (Li₂B₄O₇) in the glass composition, there occurs a race between the two alkali ions in occupying sites in the glass network and hence the variation of g_{\parallel} and A_{\parallel} is non-linear which can be attributed to mixed alkali effect (MAE) which caused due to structural adjustments. The mixed alkali effect is known for improving glass properties and its applications in various areas including bioactive glasses [42].

The bonding coefficients α^2 , β^2 , and β_1^2 respectively corresponds to in-plane σ - and π - bondings and out-of-plane π bonding of Cu(II) complex. These values (**Table.4**) are close to unity. Hence the bonding coefficients signifies moderate ionic character of the glasses under study.

The incorporation of copper ions into the glass matrix breaks down some of B-O-B bonds and thereby responsible for formation of other borate structural units such as creation of Non-Bridging Oxygens (NBOs) or conversion of BO₃ units into BO₄ units occurs. However, in the present glass system no significant structural changes are observed due to doping of copper as the mole percent of CuO is kept constant at a low value of 1 mol%.

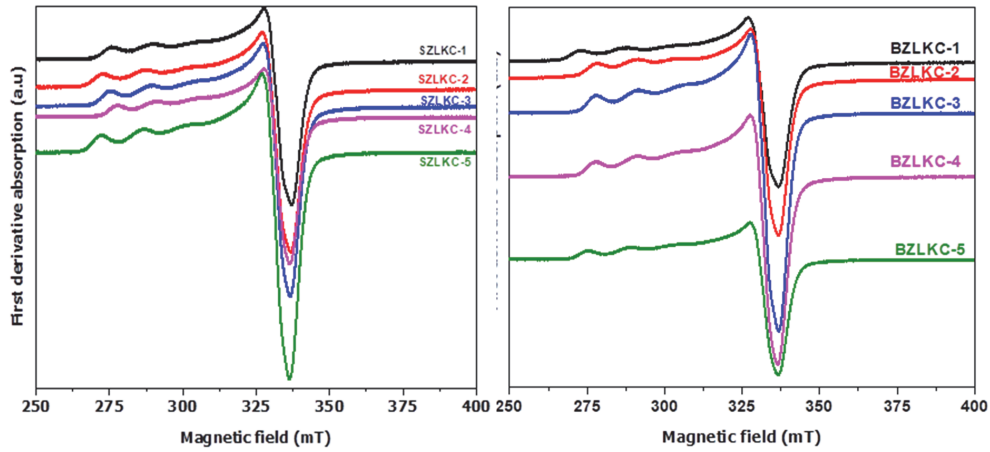


Figure 5. EPR spectra of copper ions in SZLKC and BZLKC glass systems

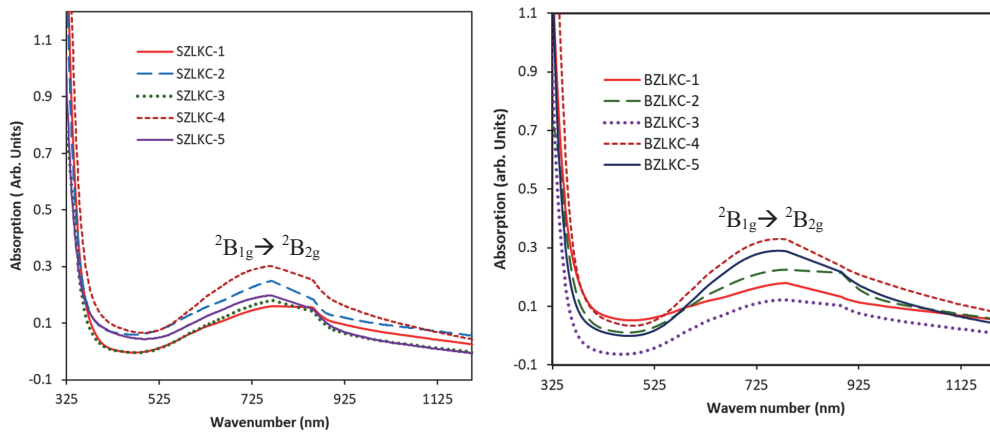


Figure 6. Optical absorption spectra of SZLK and BZLK glass systems

Table.4 EPR Parameters of SZLKC and BZLKC glass samples

Glass Code	$g_{ }$	g_{\perp}	$A_{ } \times 10^{-4}$ (cm^{-1})	$A_{\perp} \times 10^{-4}$ (cm^{-1})	ΔE_{xy} (cm^{-1})	$\Delta E_{xy,yz}$ (cm^{-1})	α^2	β^2	β_1^2	τ_{σ} %	τ_{π} %
SZLKC1	2.284	2.036	138	31	12630	29134	0.722	0.820	0.741	60.58	51.80
SZLKC2	2.297	2.039	147	33	12640	26716	0.762	0.777	0.737	51.87	52.60
SZLKC3	2.284	2.038	141	30	12630	27477	0.732	0.809	0.732	58.40	53.60
SZLKC4	2.271	2.038	135	29	12890	27395	0.703	0.843	0.744	64.72	51.20
SZLKC5	2.302	2.041	147	32	12920	25973	0.767	0.772	0.76	50.78	48.00
BZLKC1	2.299	2.039	144	33	12706	26814	0.756	0.783	0.753	53.17	49.40
BZLKC2	2.266	2.037	138	30	12787	28476	0.707	0.838	0.719	63.85	56.20
BZLKC3	2.376	2.036	138	30	12987	28890	0.815	0.727	0.898	40.32	20.40
BZLKC4	2.276	2.038	130	30	13037	27099	0.693	0.854	0.775	66.90	45.00
BZLKC5	2.289	2.038	135	29	12953	27481	0.720	0.822	0.777	61.02	44.60

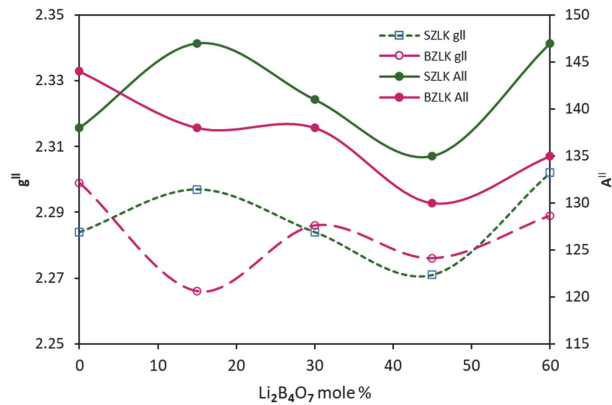


Figure 7. Variaton of $g_{||}$ and $A_{||}$ values with $Li_2B_4O_7$ mol% in SZLKC and BZLKC glass systems

4. PHYSICAL AND OPTICAL PROPERTIES

4.1. Density and Molar Volume:

Using Archimedes liquid immersion process the densities (ρ) of glass samples are measured at room temperature with Xylene ($\rho = 0.86 \text{ g/cm}^3$) as immersion liquid. Three iterations were performed to calculate the density of every sample using the formula [43].

$$\rho = \left(\frac{A}{A-B} \right) * \rho_{\text{xylene}} \quad (10)$$

Here A and B are respectively weight of the sample in in xylene and in air. The error in the estimation of density is around $\pm 0.01 \text{ g/cc}$. From the density values molar volume (V_m) of the glass samples are computed by the below given formula with usual notation [43],

$$V_m = \frac{\sum x_i M_i}{\rho} \text{ cm}^3/\text{mol} \quad (11)$$

The density and molar volume values are recorded in **Table.5**. The changes of densities and molar volumes with $Li_2B_4O_7$ mole % are shown in **Fig.8**.

As expected like many other alkali and alkaline earth borate glasses, the present glass samples also have shown opposing trend [39,43]. The density and molar volume normally offer information on the structure units since these parameters are closely depend on distribution of fundamental structural units that makes the glass network.

SZLK glasses have low density values compared to BZLK glasses. The molar volume values of SZLK glasses are higher than that of BZLK glasses. It is observed that both densities and molar volumes within each glass series varied in a non-linear

maner. The density values increased with increasing content of $Li_2B_4O_7$ (x mol%) in the glass network and except showing a minimum value when $Li_2B_4O_7$ mol% equals to $K_2B_4O_7$ 30 mole % in the glass composition. The higher densities of BZLK systems compared to SZLK glasses are due to high molecular weight of BaO compared to SrO. The molar volume of SZLK and BZLK samples almost decreased linearly with $Li_2B_4O_7$ mol% in the glass matrix showing an inflection at 30 mol%.

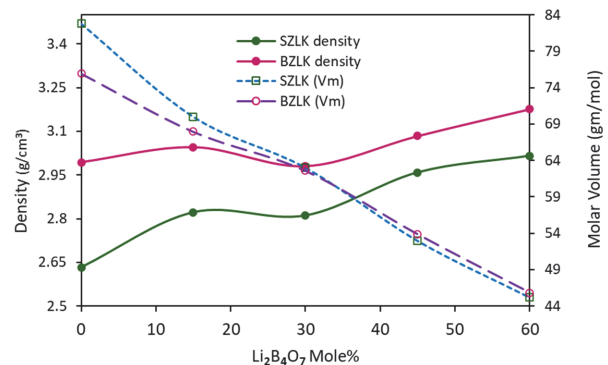


Figure 8. Variation of density and molar volume with $Li_2B_4O_7$ mol%.

The non-linear changes might be assigned to the ionic sizes of the alkali and alkaline ions. The sizes of Li^+ ion (0.076nm), K^+ (0.138 nm), Mg^{2+} (0.072nm), Zn^{2+} (0.060nm four coordinated) ions indicate that smaller metal ions like Mg^{2+} and Zn^{2+} might have taken interstitial or void locations. Hence there is competition between ions present in the glass network to occupy various structural locations. Therefore the changes in density and molar volumes could be attributed to ionic sizes that might have caused the so called mixed alkali effect (MAE) in particular or mixed oxide effect (MOE) in general.

4.2. Optical band gap and Urbach Energy

The power law region is clearly shown in optical absorption spectra. The optical absorption followed Beer-Lambert- Bouguer law. The absorption coefficient $\alpha(\omega)$ of a glass sample having thickness 't' is arrived from the expression [44]. According to Tauc, Mott and Davis power law, amorphous materials like glasses obey Tauc's rule [44]

$$\alpha(\omega) = \frac{A}{\hbar\omega} \cdot (\hbar\omega - E_{opt})^r \quad (12)$$

Here 'A' is a constant, $\hbar\omega$ is the incident optical energy, 'r' can have $\frac{1}{3}$, $\frac{1}{2}$, 2, 3 values that represents respectively direct forbidden, direct allowed,

indirect allowed, indirect forbidden transitions. Using above relation the optical energy band gap E_{opt} is evaluated. For the present glass systems the best fit is achieved when $r=2$. The Tauc plot drawn between $(\alpha h\nu)^{1/2}$ and $(h\nu)$ and are shown in **Fig.9**. If the fundamental absorption energy (ω) edge is in low energy range (10^2 to 10^4 cm⁻¹), then $\alpha(\omega)$ follows Urbach law [44]:

$$\alpha(\omega) = B \cdot e^{(h\omega/\Delta E)} \quad (13)$$

where B is a constant and ΔE is the Urbach's energy. ΔE values are obtained from slopes of the linear portions of the graph shown in **Fig.9**. Urbach energies are estimated from **Fig.10**. The arrived values of optical band gap energies (E_{opt}) and Urbach energy (ΔE) are reported in **Table.5**

The calculated values E_{opt} and ΔE of SZLK and BZLK glasses are in comparison with similar glasses

reported in the literature [43-46]. The errors in the calculation of E_{opt} and ΔE respectively about ± 0.05 eV and ± 0.005 eV. E_{opt} and Urbach energies have shown varied differently with Li₂B₄O₇ mol% in the glass (**Fig.11**). Optical band gap energies and Urbach have shown a marked change when the two alkali tetraborates are equal.

Glasses show static and dynamic disorders. But static disorder caused by structural changes is predominant in glasses. This structural disorder indicates the amount of band tails of electron density states [47]. SZLK system have shown slightly lower Urbach energies than that of BZLK system. The higher Urbach energies of BZLK glasses may be due to replacement of BaO (Ba²⁺ ionic radius is 1.35Å⁰) in place of SrO (Sr²⁺ ionic radius is 1.18Å⁰).

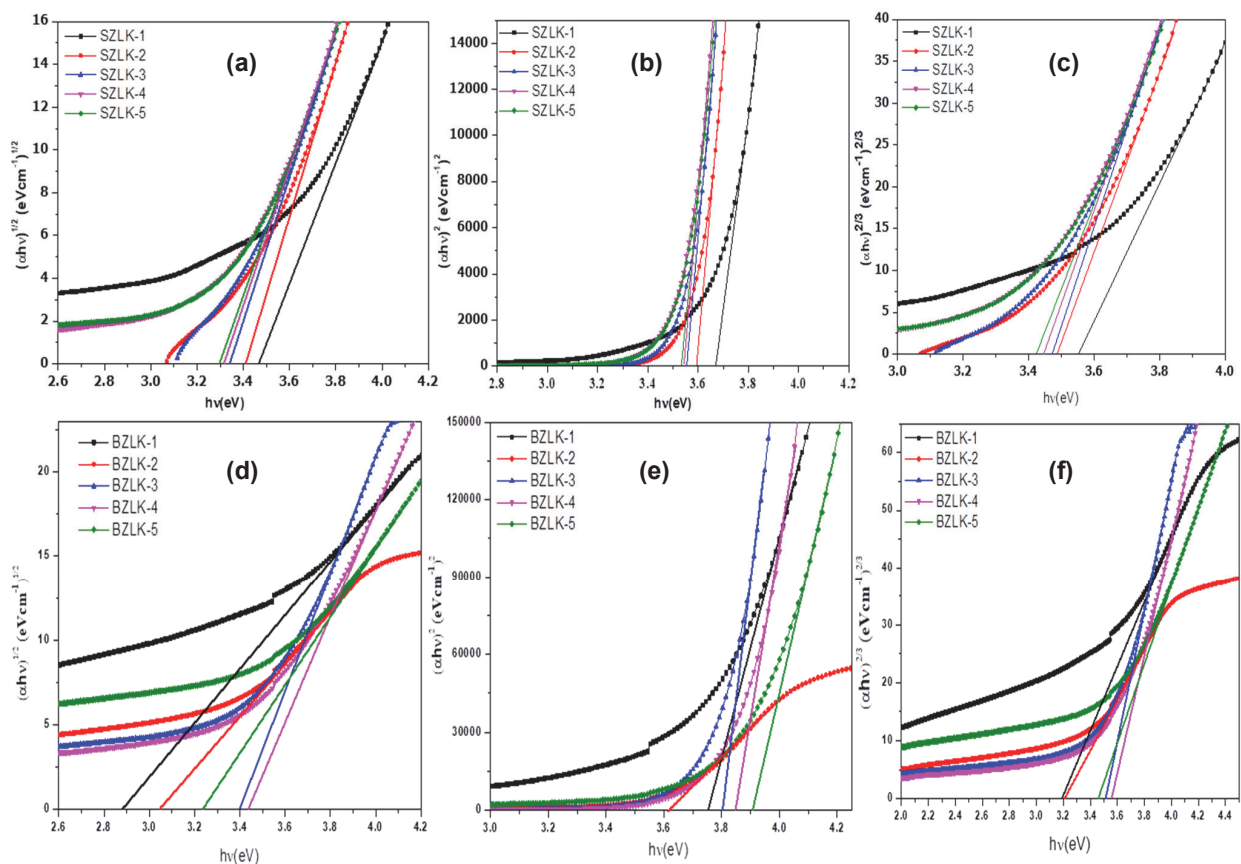


Figure 9. Tauc plots of SZLK glasses: a) indirect, b) direct allowed; c) indirect allowed and BZLK glasses: d) indirect, e) direct allowed; f) indirect allowed.

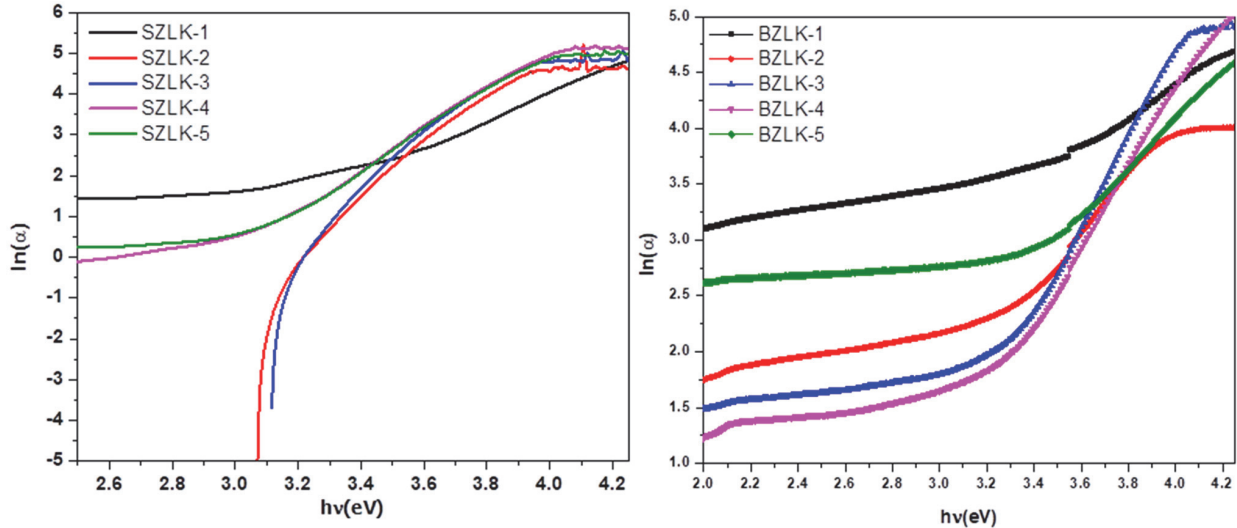


Figure 10. Estimation of Urbach energies from $\ln(\alpha)$ versus hu plots

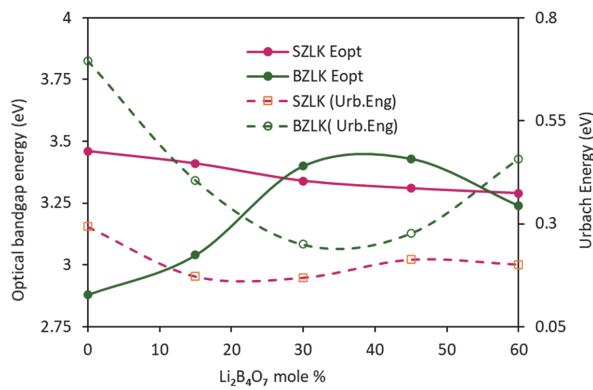


Fig.11 Variation of optical bandgap energy and Urbach energy with $\text{Li}_2\text{B}_4\text{O}_7$ mole %

4.3 Refractive Index, Electronic Polarizability and Optical Basicity

Refractive indices (n) of the samples are calculated by the following expression [48,49] and are given in **Table.5**

$$\frac{n^2-1}{n^2+2} = 1 - \sqrt{\frac{E_{opt}}{20}} \quad (14)$$

The refractive indices values of SZLK glass systems and BZLK glass systems are almost in the same range. The variation in ' n ' with $\text{Li}_2\text{B}_4\text{O}_7$ content in the glass has shown a small inflection at 30 mol% of $\text{Li}_2\text{B}_4\text{O}_7$ (= 30 mol% $\text{K}_2\text{B}_4\text{O}_7$). The change in the refractive indices values can be attributed to changes in density and dielectric constant in each glass system. The average molar refraction (R_m -cm³/mol) is evaluated using the Lorentz- Lorentz equation [44].

$$R_m = \frac{n^2-1}{n^2+2} * V_m \quad (15)$$

The molar electronic polarizability (α_m in 0⁻²⁴ cm³) is evaluated using R_m values in Clausius-Mosotti relation.

$$\alpha_m = \left(\frac{3}{4\pi N_A} \right) * R_m \quad (16)$$

The electronic polarizability of oxide ions α_o^{2-} (E_{opt}) are estimated using Dimitrov and Sakka relation [49].

$$\alpha_o^{2-}(E_{opt}) = \left[\left(\frac{V_m}{2.52} \right) \left(1 - \sqrt{\frac{E_{opt}}{20}} \right) - \Sigma \alpha_i \right] (N_o^{2-})^{-1} \quad (17)$$

Here, $[(n^2-1)/(n^2+2)]$ is reflection loss, V_m is molar volume, N_A is the Avogadro's number, $\Sigma \alpha_i$ is molar cation polarizability and N_o^{2-} is the number of oxide ions in the chemical formula. The molar Polarizability of cation (α_i) values are taken from the literature [44, 49]. The variation of refractive index and molar refraction (R_m) with x mol% are shown in **Fig.12**.

The metallization criterion M is used to determine metallic or insulating of glasses. The metallization parameter M values of glass samples vary around 0.40 indicating semiconducting type and perhaps have good ionic conductivity due to Li^+ ion or K^+ ion migration in the glass network.

The electronic polarizability (α_m), molar refraction (R_m), Metallization Criterion (M), refractive index (n) and dielectric constant (ϵ) of the glass samples are provided in **Table.5**. The non-linearity shown by the glass samples in some of the parameters might have caused by the progressive augmentation of Li atoms in place of K atoms. This substitution of atoms might caused more stress due to the insertion of Li atoms. The overall stress faced by K and Li atoms should

have reached optimum when the content of Li atoms equals the content of K atoms [50]. The observed non-linear variation and inflection with substitution of Li₂B₄O₇ progressively cause significant structural changes and is attributed to mixed alkali effect.

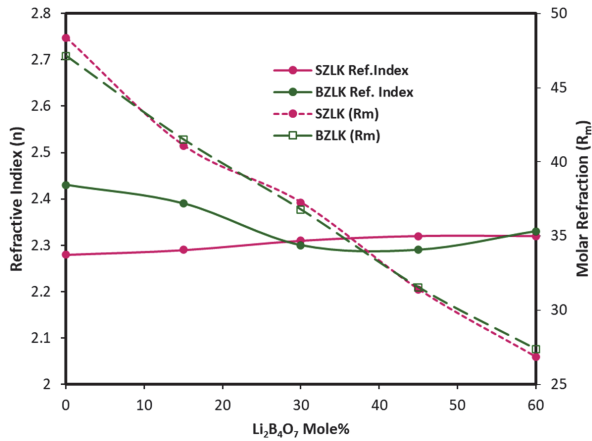


Figure 12. Variation of refractive index and molar refraction with Li₂B₄O₇ mole %.

4.4 Optical Basicity and oxygen packing density (OPD)

The electron donating capability of oxygen atom is measured by acidity or basicity of an oxide glass.

Table .5 density (ρ), molar volume (V_m), Urbach energy (ΔE), Molar refraction (R_m), oxygen packing density (OPD), theoretical basicity (Λ_{th}), experimental basicity (Λ_{exp}), electronic polarizability (α_m), electronic polarizability of oxide ion ($\alpha_{O^{2-}}$), metallization criteria (M), $\Sigma\alpha_{cation}$, refractive index (n), dielectric constant (ϵ), reflection loss (R), No. of oxygen atoms ($N_{O^{2-}}$), Optical energy band gaps (E_{opt}), No of BO₃ and BO₄ units of the glasses

Parameters	Glass code									
	SZLK1	SZLK2	SZLK3	SZLK4	SZLK5	BZLK1	BZLK2	BZLK3	BZLK4	BZLK5
ρ (g/cm ³)	2.63	2.82	2.81	2.96	3.02	2.99	3.05	2.98	3.08	3.18
V_m (cm ³ /mol)	82.80	70.01	63.01	52.95	45.17	75.95	67.95	62.58	53.86	45.82
ΔE (eV)	0.293	0.172	0.169	0.213	0.201	0.696	0.406	0.250	0.277	0.450
R_m (cm ⁻³)	48.36	41.10	37.26	31.41	26.85	47.13	41.5	36.78	31.55	27.38
OPD (mole/l)	55.55	65.70	73.00	86.87	101.83	60.56	67.69	73.50	85.41	100.38
Λ_{th}	1.767	1.707	1.647	1.587	1.527	1.772	1.712	1.652	1.592	1.532
Λ_{exp}	1.255	1.182	1.134	1.037	0.935	1.242	1.184	1.124	1.036	0.944
α_m ($\times 10^{-24}$ cm ³)	19.17	16.29	14.77	12.45	10.64	18.68	16.43	14.58	12.51	10.85
$\alpha_{O^{2-}}$	4.03	3.43	3.12	2.64	2.27	3.90	3.44	3.06	2.64	2.30
M	0.415	0.412	0.408	0.406	0.405	0.379	0.389	0.412	0.414	0.402
$\Sigma\alpha_{cation}$	0.666	0.550	0.434	0.318	0.202	0.739	0.623	0.507	0.391	0.275
n	2.28	2.29	2.31	2.32	2.32	2.43	2.39	2.30	2.29	2.33
ϵ	5.21	5.26	5.34	5.37	5.39	5.90	5.69	5.28	5.24	5.45
R	0.152	0.154	0.156	0.157	0.158	0.173	0.167	0.154	0.153	0.160
$N_{O^{2-}}$	4.6	4.6	4.6	4.6	4.6	4.6	4.6	4.6	4.6	4.6
E_{opt} (eV)										
indirect allowed	3.46	3.41	3.34	3.31	3.29	2.88	3.04	3.4	3.43	3.24
Direct allowed	3.67	3.59	3.55	3.54	3.53	3.75	3.62	3.8	3.84	3.90
Direct forbidden	3.55	3.48	3.47	3.44	3.42	3.19	3.21	3.51	3.55	3.46
Indirect forbidden	3.24	3.21	3.19	3.17	3.15	2.16	2.66	3.16	3.12	2.71
N_3 (BO ₃)	0.488	0.495	0.487	0.502	0.503	0.492	0.491	0.495	0.482	0.497
N_4 (BO ₄)	0.512	0.505	0.513	0.498	0.497	0.508	0.509	0.505	0.518	0.503

The basicity of a glass is generally expressed optical basicity [12, 51]. In the calculation of theoretical optical basicity (Λ_{th}), optical basicity values of individual oxides are taken from the literature [38]. Optical basicity and oxide ion polarizability ($\alpha_{O^{2-}}$) are related by [52]

$$\Lambda_{Exp} = 1.67 \left(1 - \frac{1}{\alpha_{O^{2-}}} \right) \quad (18)$$

The values of Λ_{exp} and Λ_{th} are mentioned **Table.5**. The values of two glass systems SZLK and BZLK declined with an increase of Li₂B₄O₇ mol%. The minimal changes of optical basicity values are accompanied by the slight modification of charge on the oxygen ions in network.

The oxygen packing density (OPD) of the samples is arrived from density (ρ) values by the formula:

$$OPD = \frac{\rho}{M} x O_n \quad (19)$$

Here M represents molecular weight of the glass in mole fraction and O_n is the number of oxygen atoms per formula unit. The values of OPD are provided in **Table.5**. The higher OPD values with Li₂B₄O₇ content in the glass signifies greater compactness of the glass systems.

5. CONCLUSIONS

Alkaline earth oxide containing two alkali tetraborate glass systems namely 10RO-30ZnO-xLi₂B₄O₇-(60-x)K₂B₄O₇ (R=SrO, BaO) were prepared by conventional melt quenching process. The peakless x-ray diffraction patterns indicated non-crystalline characteristics of prepared glass samples. The following inferences were drawn from the present studies:

- The structural landscaping investigations by FTIR and Raman spectroscopy unveiled that the glass samples contain various structural groups like diborate, triborate, tetra and penta borate units of BO₃ and BO₄ groups. The basic tetra borate structure was ruptured by the alkaline earth oxide and ZnO. Eventually the structural landscape of SZLK and BZLK glasses consisted interconnected random glass network of various BO₃ and BO₄ units.

- The existence of Sr²⁺ and Ba²⁺ ions and Zn-O stretching and bending vibrations of O-Zn-O of ZnO₄ tetrahedra were confirmed by Raman and FTIR studies.

- The observed structural changes were attributed to mixed alkali effect (MAE).

- From EPR and optical absorption spectroscopic analysis of glasses doped with copper, g_{||} and A_{||} values changed non-linearly with composition. There was a possibility of competition between Cu²⁺ ions and oxide cations Sr²⁺, Ba²⁺ and Zn²⁺ to attract oxygen ions nearest to them. Hence non-linear changes in spin-Hamiltonians, bonding coefficients and normalised covalencies were attributed to structural fluctuations.

- As one alkali tetra borate (K₂B₄O₇) was replaced by another (Li₂B₄O₇) in the glass matrix, The overall stress faced by K and Li atoms should have reached optimum when the content of Li atoms equals the content of K atoms and thereby various properties of glass samples had exhibited inflections. The structural changes were random and conversion of BO₃ triangles into BO₄ tetrahedra are not considerable since N₃ and N₄ values remained almost constant.

- The physical and optical properties such as density, molar volume, optical energy band gap, Urbach energy, molar refractivity, optical basicity and oxygen packing density have shown an inflections. The two alkalis had competition between them to take up various structural locations in the glass network causing the so called mixed alkali effect (MAE). These glasses are good media for ion conduction

and hence suitable as ion conductors to prepare solid state batteries.

ACKNOWLEDGEMENTS

The authors thank Sophisticated Analytical Instrument Facility (SAIF-IIT-Mumbai) for the recording of Electron Spin Resonance spectra, Central Sophisticated Instrumentation Facility (CSIF)-BITS-Goa for x-ray diffractograms and Raman spectra recording, Head, Department of Physics, Osmania University, Hyderabad for providing FTIR spectroscopy, and Principal, Vasavi College of Engineering (Autonomous), Hyderabad for providing sample preparation facilities.

REFERENCES

1. H. Aljawhara H. Almuqrin, Ashok Kumar, J.F.M. Jecong, Nuha Al-Harbi, E. Hannachi, M.I. Sayyed (2021) Li₂O-K₂O-B₂O₃-PbO glass system: Optical and gamma-ray shielding investigations, *Optik*, 247,167792. doi: 10.1016/j.ijleo.2021.167792.
2. V. Arunkumar, V. Banagar, M. Prashant Kumar, S. Sunanda, N. Nagaraja (2021) Mixed Alkali Effect in Structural and Electrical Conductivity Properties of V₂O₅-, K₂O- and Na₂O-Containing Borate Glasses, *J. of Elec Mater.*, 50, 4924–4932. doi: 10.1007/s11664-021-09000-9.
3. M. Fernandes Graça, M. Valente (2017) Ferroelectric glass-ceramics, *Matter. Res.Sci. Bulletin*, 42(3) 213-219. doi: 10.1557/mrs.2017.32.
4. K. Pradeesh, C.J. Oton, V.K. Agotiya, M. Raghavendra, G. Vijaya Prakash (2008) Optical properties of Er³⁺ doped alkali chlorophosphate glasses for optical amplifiers, *Optical Materials*,31(2),155-160. doi: 10.1016/j.optmat.2008.02.007.
5. V.T. Adamiv, Y.V. Burak, D.J. Wooten, J. McClory, J. Petrosky, I. Ketsman, Jie Xiao, Y.B. Losovyj, Peter A. Dowben (2010) The Electronic Structure and Secondary Pyroelectric Properties of Lithium Tetraborate, *Materials (Basel)*, 3(9), 4550–4579. doi: 10.3390/ma3094550.
6. A. Murali, R.P.S. Chakradhar, J. Lakshmana Rao (2005) Allowed and forbidden hyperfine structure of Mn²⁺ ions in sodium tetraborate glasses-an EPR and optical study, *Physica B Condensed Matter*, 358 (1-4), 19–26. doi: 10.1016/j.physb.2004.12.021.
7. N.M. Bobkova, S.A. Khot'ko (2005) Zinc Oxide in Borate Glass-Forming Systems, *Glass and Ceramics*, 62, 167–170. doi: 10.1007/s10717-005-0064-7.
8. V.C. Veeranna Gowda, R.V. Anvekar (2004) Elastic properties and spectroscopic studies of lithium lead borate glasses, *Ionics*, 10, 103-108. doi: 10.1007/BF02410315.
9. Y.B. Saddeek, K.A. Aly, Safaa A Bashier (2010) Optical study of lead borosilicate glasses, *Physica B Con-*

- densed Matter, 405(10), 2407-2412. doi: 10.1016/j.physb.2010.02.055.
10. Y.B. Saddeek, E. R. Shaaban, El Sayed Moustafa, Hesham, M. Moustafa (2008) Spectroscopic properties, electronic polarizability and optical basicity of Bi₂O₃-Li₂O-B₂O₃ glasses, *Physica B: Condensed Matter*, 403 (13-16), 2399-2407. doi: 10.1016/j.physb.2007.12.027.
 11. F. Lodesani, M. C. Menziani, H. Hijiya, Y. Takato, S. Urata, A. Pedone (2020) Structural origins of the Mixed Alkali Effect in Alkali Aluminosilicate Glasses: Molecular Dynamics Study and its Assessment, *Scientific Reports*, 10, 2906. doi:10.1038/s41598-020-59875-7.
 12. H. Othman, H. Elkholi, M. R. Cicconi, D. Palles, D. de Ligny, E. I. Kaisos, D. Möncke (2020) Spectroscopic study of the role of alkaline earth oxides in mixed borate glasses-site basicity, polarizability and glass structure, *J. Non-Cryst. Solids*, 533, 119892. doi: 10.1016/j.jnoncrysol.2020.119892.
 13. A. Atila, Y. Ouldhnini, S. Ouaskit, A. Hasnaoui (2002) Atomistic insights into the mixed-alkali effect in phosphor-silicate glasses, *Phys. Rev. B*, 105, 134101. doi: 10.1103/PhysRevB.105.134101.
 14. M. Kavgacı, H. Yaykaşlı, H. Eskalen, E. K. Perişanoğlu, S. Kalecik, R. Yılmaz, H. Tunç (2024) An experimental analysis of the effects of SrO on the mechanical, structural, optical, and nuclear radiation shielding properties of barium borate glasses, *Optical Materials*, 149, 114975. doi: 10.1016/j.optmat.2024.114975.
 15. S. Biradar, A. Dinkar, Manjunatha, A.S. Bennal, G.B. Devidas, B.T. Hareesh, M.K. Siri, K.N. Nandan, M.I. Sayyed, H. Es-soufi, M.N. Chandrashekara (2024) Comprehensive investigation of borate-based glasses doped with BaO: An assessment of physical, structural, thermal, optical, and radiation shielding properties, *Optical Materials*, 150, 115176. doi: 10.1016/j.optmat.2024.115176.
 16. T. Liu, Bin Duan, Y. Q. Li, C. Chun Ding (2023) The role of different alkaline earth oxide composition in copper borate glasses: Structure and optical properties, *J. Non-Cryst. Solids*, 604, 122134. doi: 10.1016/j.jnoncrysol.2023.122134.
 17. T. Walia, K. Singh (2021) Mixed alkaline earth modifiers effect on thermal, optical and structural properties of SrO-BaO-SiO₂-B₂O₃-ZrO₂ glass sealants, *J. of Non-Cryst. Solids*, 564, 120812. doi: 10.1016/j.jnoncrysol.2021.120812.
 18. A. Shearer, M. Molinaro, M. Montazerian, J. J. Sly, M. Miola, F. Bairo, J. C. Mauro (2024) The unexplored role of alkali and alkaline earth elements (ALAEs) on the structure, processing, and biological effects of bioactive glasses, *Biomaterials Science*, 12, 2521-2560. doi: 10.1039/D3BM01338C.
 19. A. AEI-Daly, M.A. Abdo, H.A. Bakr, M.S. Sadeq (2022) Structure, stability and optical parameters of cobalt zinc borate glasses, *Ceramics International*, 47(22), 31470-31475. doi: 10.1016/j.ceramint.2021.08.024.
 20. L. Heuser, M. Nofz (2022) Alkali and alkaline earth zinc and lead borate glasses: Structure and properties, *J. Non-Cryst. Solids: X*, 15, 100109. doi: 10.1016/j.nocx.2022.100109.
 21. S.G. Motke, S.P. Yawale, S.S. Yawale S (2002), Infrared spectra of zinc doped lead borate glasses, *Bull. Mater. Sci.*, 25(1), 75-78. doi: 10.1007/BF02704599.
 22. A.A. Ali, Y.S. Rammah, M.H. Shaaban (2019) The influence of TiO₂ on structural, physical and optical properties of B₂O₃-TeO₂-Na₂O-CaO glasses, *J. Non-Cryst. Solids*, 514(15), 52-59. doi: 10.1016/j.jnoncrysol.2019.03.030.
 23. Ao Li, M. Wang, Mei Li, Z. Liu, Y. Hu, X. Zhang (2018) The effect of mixed alkali on structural changes and ionic migration characteristics in zinc borate glasses, *Materials Chemistry and Physics*, 217, 519-526, doi: 10.1016/j.matchemphys.2018.07.013.
 24. R. A. Elsad, M. Ahmed, Abdel-Aziz, Emad M. Ahmed, Y.S. Rammah, F.I. El-Agawany, M.S. Shams (2021) FTIR, ultrasonic and dielectric characteristics of neodymium (III)/ erbium (III) lead-borate glasses: experimental studies, *J. Matter. Res. and Tech.*, 13, 1363-1373. doi: 10.1016/j.jmrt.2021.05.029.
 25. B. Tirumala Rao, B. R. Venkateswara Rao, K. Venkata Rao, S. Ravi Kumar, Ch. Rajyalakshmi, G.V.L. Kanth, G. Rama Swamy, S. Cole (2022) XRD, EPR and FT-IR Studies of Zinc Aluminium Lithium Borate (ZALB) Glasses Doped with Cu²⁺ Ions, *Phys. Chem. Res.*, 10(4), 455-460. doi:10.22036/pcr.2022.315242.1987.
 26. G. Padmaja, P. Kistaiah (2009) Infrared and Raman Spectroscopic Studies on Alkali Borate Glasses: Evidence of Mixed Alkali Effect, *J. of Phys. Chem A*, 113(11), 2397-2404. doi: 10.1021/jp809318e.
 27. C. Gautam, A. K. Yadav, A. K. Singh (2012) A Review on Infrared Spectroscopy of Borate Glasses with Effects of Different Additives, *International Scholarly Research Notices* 2012, 1-17. doi:10.5402/2012/428497.
 28. W.L Fong, Kh. A. Bashar, S.O.Baki, M.H.M. Zaid, B.T. Goh, M.A. Mahdi (2021) Thermal, structural and optical properties of Bi₂O₃-Na₂O-TiO₂-ZnO-TeO₂ glass system, *J. Non-Cryst. Solids*, 555, 120621. doi: 10.1016/j.jnoncrysol.2020.120621.
 29. E. M Anghel, M. Zaharescu, S. Zuca, E. Pavlatou (1999) Structure and phase diagram of the Na₂B₄O₇-Na₃AlF₆ system, *J. Mater. Sci.*, 34, 3923-3929, doi: 0.1023/A:1004635109184.
 30. D. Maniu, I. Ardelean, T. Iliescu, S. Crînta, V. Nagel, W. Kiefer (1999) Raman spectroscopic investigations on oxide glass system (1-x) [3B₂O₃·K₂O]·xTiO₂, *J. Molecular Structure* 480-481, 657-659. doi:10.1016/S0022-2860(98)00831-X.
 31. T. Yano, N. Kunimine, S. Shibata, M. Yamane (2003) Structural investigation of sodium borate glasses and melts by Raman spectroscopy: I Quantitative evaluation of structural units, *J. Non-Cryst. Solids*, 321(3), 137-146. doi: 10.1016/S0022-3093(03)00158-3.
 32. B. Topper, D. Möncke, R. E. Youngman, C. Valvi, E. I. Kamitsos, C. P.E. Varsamis (2023) Zinc borate

- glasses: properties, structure and modelling of the composition-dependence of borate speciation, *Phys. Chem. Chem. Phys.*, 25,5967-5988. doi: 10.1039/D2CP05517A.
33. Z. Shan, Y. Zhang, S. Liu, H. Tao, Y. Z. Yue (2020) Mixed-alkali effect on hardness and indentation-loading behavior of a borate glass system, *J. Non-Cryst. Solids*, 548,120314. Doi: 10.1016/j.jnoncrsol.2020.120314.
 34. M. Subhadra, P. Kistaiah (2012) Infrared and Raman spectroscopic studies of alkali bismuth borate glasses: Evidence of mixed alkali effect, *Vibrational Spectroscopy*, 62, 23-27. doi: 10.1016/j.vibspec.2012.07.001.
 35. Y.D. Yannopoulos, G.D. Chryssikos, E. I. Kamitsos (2001) Structure and properties of alkaline earth borate glasses, *Phys. Chem. Glasses*, 42(3), 164-72.
 36. H.M.H. Zakaly, S.A.M. Issa, H.O. Tekin, Ali Badawi, H.A. Saudi, A.M.A. Henaish, Y.S. Rammah (2022) An experimental evaluation of CdO/PbO-B₂O₃ glasses containing neodymium oxide: Structure, electrical conductivity and gamma-ray resistance, *Materials Research Bulletin*, 151,111828. doi: 10.1016/j.materresbull.2022.111828.
 37. A. A. Osipov, L. M. Osipova (2013) Raman scattering study of barium borate glasses and melts, *J. Phys. and Chem. of Solids*, 74(7), 971-978. doi: 10.1016/j.jpcs.2013.02.014.
 38. J. L. Rao, G. Sivaramaiah, N.O. Gopal (2004) EPR and optical absorption spectral studies of Cu²⁺ ions doped in alkali lead tetraborate glasses. *Physica B Condensed Matter*, 349(1-4), 206-213, doi:10.1016/j.physb.2004.03.089.
 39. B. Srinivas, B. Ashok, P. Naresh, Abdul Hameed, M. Narasimha Chary, Md. Shareefuddin (2022) Effect of SrO and TeO₂ on the physical and spectral properties of strontium tellurite boro-titanate glasses doped with Cu²⁺ ions, *J. Non-Cryst. Solids*, 575, 21218. doi: 10.1016/j.jnoncrsol.2021.121218.
 40. S. Vedavyas, K.C. Sekhar, S. Ahammed, G. Ramadevudu, M. Narasimha Chary, Md. Shareefuddin (2021) Physical and structural studies of cadmium lead boro-tellurite glasses doped with Cu²⁺ ions. *J Mater Sci: Mater Electron* 32, 3083-3091. doi: 10.1007/s10854-020-05058-z.
 41. C.Maalegoundla, K.C. Sekhar, A. Hameed, B. Srinivas, Md. Shareefuddin (2022) Physical and spectroscopic studies of CaF₂-Al₂O₃-Bi₂O₃-B₂O₃-CuO glasses, *J Aust Ceram Soc.*, 58, 1137-1146. doi:10.1007/s41779-022-00737-y.
 42. M. D. Ingram (2001) Amorphous Materials: Mixed Alkali Effect, *Encyclopedia of Materials: Science and Technology*, 220-223. doi :10.1016/b0-08-043152-6/00047-4.
 43. J. Bhemarajam, P. Syam Prasad, M. Mohan Babu, M. Özcan, M. Prasad (2021) Investigations on Structural and Optical Properties of Various Modifier Oxides (MO = ZnO, CdO, BaO, and PbO) Containing Bismuth Borate Lithium Glasses. *J. Compos. Sci.* 5(12), 308. doi: 10.3390/jcs5120308.
 44. S. L. Srinivasa Rao, G. Ramadevudu, Md. Shareefuddin, Abdul Hameed, M. Narasimha Chary, M. Lakshminipathi Rao (2012) Optical properties of alkaline earth borate glasses, *Int. J Engg, Sci. and Tech*, 4(4), 25-35. doi: 10.4314/ijest.v4i4.3.
 45. G. Srinivas, B. Ramesh, J. Siva Kumar, Md. Shareefuddin, M.N.Chary, R. Sayanna (2016) Mixed alkali effect in the physical and optical properties of xK₂O-(25-x) Na₂O-12.5MgO-12.5BaO-50B₂O₃ glasses, *J. Taibah University for Science*, 10(3), 442-449. doi: 10.1016/j.jtusc.2015.09.002.
 46. R.P. S. Chakradhar, G. Sivaramaiah, J. L. Rao, N.O. Gopal (2005) EPR and optical investigations of manganese ions in alkali lead tetraborate glasses, *Spectro Chimica Acta Part A: Molecular and Biomolecular Spectroscopy*,62(4-5), 761-768. doi: 10.1016/j.saa.2005.02.045.
 47. I.A Weinstein, A.F Zatssepina, V.S Kortov (2001) Effects of structural disorder and Urbach's rule in binary lead silicate glasses, *J. Non-Cryst. Solids*, 279(1),77-87. doi:10.1016/S0022-3093(00)00396-3.
 48. B. Eraiah (2006) Optical properties of samarium doped zinc-tellurite glasses, *Bull. Mater. Sci.*, 29(4), 375-378. doi:10.1007/BF02704138.
 49. V. Dimitrov, S. Sakka (1996) Electronic oxide polarizability and optical basicity of simple oxides-I, *J. Appl. Phy*, 79(3),1736-40. doi:10.1063/1.360962.
 50. Y. Yu, J. C. Mauro, M. Bauchy (2017) Stretched Exponential Relaxation of Glasses: Origin of the Mixed Alkali Effect, *American Ceramic Society Bulletin* 96(4),34-36. doi:10.48550/arXiv.1801.01969.
 51. V. Dimitrov, T. Komatsu (1999), Electronic polarizability, optical basicity and non-linear optical properties of oxide glasses, *J. Non-Cryst. Solids*, 249(2-3),160-179. doi:10.1016/S0022-
 52. H. Doweidar, Y. B. Saddeek (2009) FTIR and ultrasonic investigations on modified bismuth borate glasses, *J. Non-Cryst. Solids*,355(6),348-354. doi: 10.1016/j.jnoncrsol.2008.12.008.

IZVOD

ISTRAŽIVANJE STRUKTURA I FIZIČKIH SVOJSTAVA RO-ZNO-LI₂B₄O₇-K₂B₄O₇ (RO= SRO I BAO) STAKLA

Uzorcima stakla 10RO-30ZnO-kLi₂B₄O₇-(60-k) K₂B₄O₇ (RO=SrO i BaO) sa alkalnim tetra boratima u rasponu od 0 do 60 mol% proizvedeni su tradicionalnim postupkom gašenja. Široki rendgenski difrakcijski obrasci bez vrha utvrdili su amorfnu osobinu uzoraka stakla. FTIR i Raman spektroskopska analiza je pokazala postojanje strukturnih grupa BO₃ i BO₄ zajedno sa drugim jedinicama borata. Na stopu konverzije BO₃ ↔ BO₄ nije mnogo uticala varijacija jednog od alkalnih tetraborata. EPR spektri stakla dopiranih bakrom potvrdili su osnovno stanje Cu²⁺ jona kao 2B1g. Utvrđeno je da fizička i optička svojstva, odnosno gustina, molarna zapremina, indeks prelamanja, molarna refrakcija, optički pojas i Urbahova energija zavise od sastava. Pregibi uočeni u gustini i drugim optičkim svojstvima oko jednakih mol% alkalnih oksida u sistemu stakla pripisani su strukturnim modifikacijama i mešovitom alkalnom efektu. Ovi rezultati su razotkrili strukturne varijacije uzrokovane konkurentnošću između dva različita alkalna i alkalna oksida u zauzimanju geometrijskih pozicija mreže boratnog stakla.

Ključne reči: mešani alkalni efekat (MAE), zemnoalkalna stakla, optički pojas, elektronska paramagnetna rezonanca, FTIR i Ramanova spektroskopija

Naučni rad

Rad primljen: 11.04.2024.

Rad korigovan: 31.05.2024.

Rad prihvaćen: 9.06.2024.-

The ORCID Ids of all the authors are as follows:

Sarap Krishnaprasad: <https://orcid.org/0009-0008-2979-1316>

Mohammed Shareefuddin: <https://orcid.org/0000-0003-3747-1917>

Siddey Laxmi Srinivasa Rao: <https://orcid.org/0009-0006-5635-1557>

Gokarakonda Ramadevudu: <https://orcid.org/0000-0002-9931-1778>

Mansi Sharma^{1*}, Priyanka Mahajan²

¹Department of Environmental Sciences, Sharda School of Basic Sciences and Research, Sharda University, Greater Noida, UP-201310, India, ²University Centre for Research and Development, Chandigarh University, Mohali, Punjab, India

Scientific paper

ISSN 0351-9465, E-ISSN 2466-2585

<https://doi.org/10.62638/ZasMat.1205>



Zastita Materijala 65 (4)
578 - 594 (2024)

Nature's prescription: decoding the power of biopolymers in medical and pharmaceutical applications

ABSTRACT

Over the past few years, the utilization of several biopolymers of natural, synthetic or microbial origin has witnessed a peak in various medical and pharmaceutical applications, like drug delivery, drug formulation, tissue engineering scaffolds, medical implants (e.g., prosthetics, stents), wound healing and dressing materials, and biosensing. This is mainly attributed to their ease of processing, biodegradability, high bioactivity, and biocompatibility compared to synthetic polymers. Moreover, a surge in the development of bio-/nanocomposites has emerged, with an aim to enhance the inherent properties of raw biopolymers derived from natural/microbial sources. This review is mainly focused on the different types of biopolymers or their composites utilized in medicinal or pharmaceutical industries and sheds light on the key advantages and limitations associated with their synthesis or use. Furthermore, the article presents a list of commercialized biopolymer composites with a discussion on the future scope of using these "gifts of nature" in medical field.

Keywords: biopolymers; biosensing; drug delivery; surgical implants; tissue engineering

1. INTRODUCTION

Petroleum-based synthetic plastics have become ingrained in everyday life by offering a convenient way to substitute for conventional materials in various applications. However, due to environmental concerns, this has fuelled a rapid move to phase out these synthetic plastics and embrace their natural counterparts [1]. Driven by the need for eco-friendly alternatives to synthetic polymers, there is burgeoning interest in the production of biopolymers from sustainable resources, like biowaste and biomass. Concurrent research efforts are also dedicated to the crafting of novel biocomposites and nanobiocomposites from natural fibres and biomass, offering high biodegradability and biocompatibility [2]. The remarkable ease of handling, reliability, and inherent chemical structure of these biopolymers or composites paves the way for their diverse applications across food, biomedical, and pharmaceutical industries [3]. Despite gaining commercial success in food and pharmaceutical sectors, biopolymers struggle with

high cost and inefficiencies stemming from their synthesis, development, and post-processing steps [4]. The three main categories of natural polymers on the basis of their chemical structure include: (a) polysaccharides, (b) proteins, and (c) polyesters. Some protein-based polymers, including legumin, albumin, and gelatin, have garnered significant attention in medicine as nanodrug carriers, owing to their small size, increased stability, biodegradability, and non-toxicity [5]. Co-polymerization of specific polysaccharides (e.g., chitosan, cellulose, starch) with other polymers allows the engineering of biomaterials with tailored bioactivity, especially useful in biomedical applications [6].

Due to their excellent unique properties, natural biopolymers or their composites are weaving their magic in a plethora of medical applications, such as bone tissue engineering, targeted drug delivery systems, prosthetics, hydrogels, and drug formulations (Fig. 1). The use of a specific biopolymer for particular medical purpose is dictated by its fundamental characteristics, like molecular weight, mechanical properties, and degradation profile [5]. Biopolymers are mainly used in prosthetics and implantable devices with targeted molecule delivery, because of their non-toxicity, high selectivity, and biocompatibility [7]. Several biopolymer composites are used in surgeries across different medical fields, including cardiology and

*Corresponding author: Mansi Sharma

E-mail: mansi.sharma@sharda.ac.in

Paper received: 02. 03. 2024.

Paper accepted: 05.04. 2024.

ophthalmology. Synthetic polymers can also be combined with other natural polymers for the designing of advanced skin scaffolds [8]. Biopolymers are extensively used in the fabrication of gels, films, and wound dressing materials that carry therapeutic agents for faster wound healing. For instance, chitosan is a biopolymer that can promote skin cell proliferation, making it a perfect choice for skin regeneration [9]. This review delves into the fascinating world of biopolymers or their composites for biomedical and

pharmaceutical applications, with a special mention of the most commonly used biopolymers. The major research objective of this article is to discuss the various kinds of biopolymers or bio/nanocomposites utilized across areas like tissue engineering and regeneration, surgical implants and devices, drug delivery, and biosensing. The review concludes with an understanding of the potential limitations, challenges, and intricacies in biopolymer design, alongside a glimpse into their exciting future perspectives in medicine.

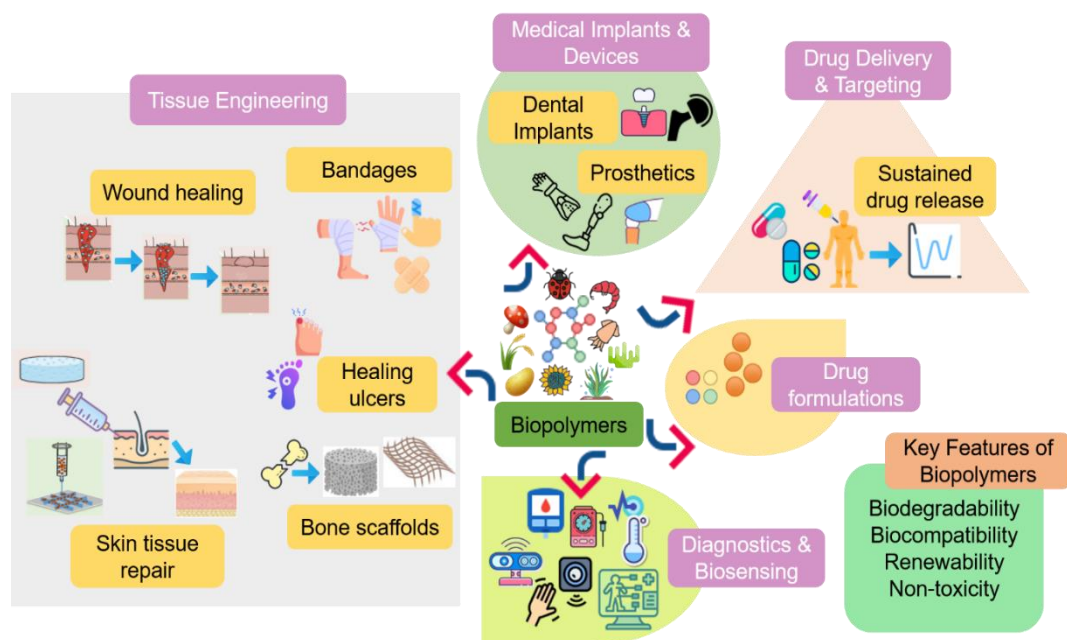


Figure 1. Applications of biopolymers in medicinal and pharmaceutical sectors

2. TYPES OF BIOPOLYMERS IN MEDICAL AND PHARMACEUTICAL APPLICATIONS

Biopolymers can be largely classified into two types: biodegradable or non-biodegradable, based on their nature of decomposition. Another major category of biopolymer grouping is based on their source of raw material, i.e., natural (e.g., plants and animals), synthetic (e.g., renewable sources and fossil fuels), and microbial (synthesized by microorganisms) biopolymers. Spanning from medical devices to environment-friendly packaging, these biopolymers possess functionalities suitable for applications across various sectors, including medicine, agriculture, agro-industries, sustainable packaging, and environmental remediation [10]. The different types of biopolymers utilized for medical and pharmaceutical purposes are explained below under separate headings.

Natural Biopolymers

Naturally derived biopolymers extracted from plant or animal biomass are either protein-based or

derived from polysaccharides. Some of the well-known plant/animal-derived protein biopolymers include collagen, gelatin, elastin, keratin, fibrinogen, zein, soy protein, egg protein, milk protein, whey protein, and wheat gluten. Similarly, the carbohydrate-derived polymers come from diverse polysaccharide sources, such as agar, pectin, cellulose, galactan, carrageenan, chitosan, alginate, hyaluronic acid, gums, and starch. These biopolymers are well-suited for a wide range of medical applications, thanks to their biodegradability, biocompatibility, non-toxicity, and ability to bind bioactive molecules for healing and therapy [11]. Polysaccharides, composed of monosaccharide units connected via glycosidic linkages, are promising candidates for applications in tissue engineering and regenerative medicine [12]. Proteins, composed of amino acid chains, exhibit a diverse range of functionalities, such as motility, stabilization, elasticity, and scaffolding. Their ability to protect cells and tissues makes them ideal candidates for drug delivery and tissue engineering scaffolds [13].

Polysaccharide-based Biopolymers

Common polysaccharides used in medical applications include hyaluronic acid, chitin, chitosan, alginate, and starch. Hyaluronic acid is a non-sulfated, linear polysaccharide composed of glucuronic acid and N-acetylglucosamine units linked by β -1,4 and β -1,3 glycosidic bonds. It has a high molecular mass and unique polymeric and polyelectrolyte characteristics that contribute to its remarkable viscoelastic properties. High molecular weight hyaluronic acid also exhibits muco-adherent and anti-inflammatory properties. Hyaluronic acid, found in the extracellular matrix of cartilage, skin, and vitreous humor, has been used in a variety of medical applications [14]. The 1970s saw the first hyaluronic acid-based medical product approved by U.S. Food and Drug Administration, revolutionizing corneal transplants [15]. Chitin, a polysaccharide made up of 2-acetamido-2-deoxy-D-glucose residues linked by β -1,4 glycosidic bonds, is hydrophobic and insoluble in water and organic solvents. Chitin can be transformed into chitosan through deacetylation to increase its solubility in aqueous acids. Chitin and chitosan, characterized by their highly basic nature owing to the presence of high nitrogen content as compared to synthetic cellulose, are commercially attractive biomaterials for diverse applications. The multifaceted properties of chitosan, such as water sorptivity, biodegradability, oxygen permeability, hemostatic capacity, and ability to induce cytokine expression, qualify it as a versatile component for scaffolding materials [16]. Alginates are linear polysaccharides made up of copolymers from 1,4-glycosidically linked β -D-mannuronic acid (M-blocks) and α -L-guluronic acid (G-blocks) monomers. They are used for countless biomedical applications, such as cell transplantation and drug delivery, thanks to their biocompatibility, minimal side effects, and cost-friendliness. Starch is a polysaccharide distinguished into amylose and amylopectin, where the former is made up of glucose units joined by α -(1,4) bonds, and the latter is a branched molecule linked by both α -(1,4) and α -(1,6) glycosidic linkages. Starch-based biopolymers have carved a niche in diverse biomedical applications, like replacing and fixing bones, scaffolds for tissue engineering, and drug delivery [12].

Protein-based Biopolymers

Many protein-based biopolymers have shown immense potential in biomedicine sector. For instance, collagen's exceptional biocompatibility, biodegradability, low immune response, robust mechanical properties, and cross-linking ability, makes it perfect for tissue engineering and delivery of bioactive molecules. Cross-linking enables the fabrication of collagen into intricate 3D networks,

-serving as ideal scaffolds for tissue engineering [17]. The thermoreversible gelation behaviour of gelatin, combined with its excellent biodegradability and biocompatibility within physiological environments, renders it a preferred gelling agent for biomedical and pharmaceutical applications. Chemical cross-linking of either acidic or basic gelatin using glutaraldehyde or carbodiimide can improve the mechanical properties of gelatin scaffolds [18]. Silk protein can be processed into diverse formats, such as nanofibers, films, scaffolds, gels, and powders, making it ideal for applications like barrier membrane and drug delivery [19].

Synthetic Biopolymers

Chemically synthesized synthetic polymers can be obtained from biomass (poly lactic acid [PLA]) or are petroleum-based (e.g., polystyrene, polyethylene, polyamides, poly glutamic acid [PGA], polycaprolactone [PCL], and polyvinyl alcohol [PVA]) [20]. Lactic acid, the precursor in PLA synthesis, is made up of a carbon atom with two different configurations (L-/D-isomers). PLA is a hydrophobic semi-crystalline polymer with unique characteristics, like glass transition temperature = 40–70 °C, melting temperature = 130–180 °C, tensile strength = 44–59 MPa, and degradation time = 18–24 months. Owing to their outstanding biocompatibility and mechanical properties, PLA and its copolymers have been employed in a wide range of biomedical uses, including implants, sutures, stent matrices, tissue engineering, and drug delivery [21]. PGA is an exceptional anionic polypeptide made up of D- and/or L-glutamic acid units polymerized via γ -amide linkages between α -amino and γ -carboxylic acid groups. The fabrication of PGA scaffolds through gamma-irradiation or chemical cross-linking using hexamethylene diisocyanate or physical blending with poly(ethylene imine) is useful for achieving desirable scaffold properties [22].

Microbial Biopolymers

A diverse array of biopolymers produced from microbes include polyhydroxybutyrate (PHB), polyhydroxyalkanoates (PHA), and poly(3-hydroxybutyrate-co-3-hydroxyvalerate) (PHBV), gellan, dextran, curdlan, levan, and bacterial cellulose. Besides, a variety of microbial polysaccharides, including xanthan, exopolysaccharides, and capsular polysaccharides, are used for biopolymer synthesis. Precise genetic manipulation of microbes produces custom-made biopolymers perfect for cutting-edge medical applications, including drug delivery and tissue engineering. Moreover, medium and large-scale fermentation processes have paved the way for commercialization of many bacterial polymers [23]. PHAs, mainly synthesized by PHA synthase enzyme, can accumulate within

cells as insoluble spherical inclusions having a core composed of polyester and a surrounding protein-rich phospholipid layer. They possess a unique combination of desirable properties, e.g., biodegradability, biocompatibility, and thermoplasticity, crucial for medical devices and tissue engineering applications [24]. Lower crystallinity of PHB translates to its increased flexibility and ease of processing, making it ideally suitable for cell support matrix in tissue engineering [25]. Dextrans, characterized by their high density of accessible hydroxyl groups, cost-effectiveness, reduced immunogenicity, and clinical safety, are highly attractive materials for drug/protein delivery [26].

Biopolymer Composites

Biocomposites are a blend of biopolymer resin (outer layer) and natural fibres (as fillers), weaved together into mechanically strong and eco-friendly materials. A diverse range of methodologies have been adopted to shape these composites, like electrospinning, solvent casting, extrusion, phase separation, intercalation, laser printing, etc. [27]. Bionanocomposites synthesized using appropriate plasticizers and solvents exhibit improved thermal stability, mechanical strength, rigidity, and matrix elastic modulus. There are two categories of biocomposites: (a) matrix-reinforced fibres (e.g., PHA, cellulose, PVA) and (b) natural fibres (e.g., sisal, hemp, jute), on the basis of dominant material and its role in composite's properties [28]. Some naturally occurring biocomposites, classified according to the content of wood fibre as either wood or non-wood fibres, are abundantly rich in cellulose and lignin, thus exhibit high tensile strength and crystallinity. Biopolymer composites are superior over their counterparts (i.e., pure biopolymers) due to improved dimensional stability provided by hydroxyl groups in their chemical structure [29]. For example, polymers obtained from natural resources have attracted significant attention due to their biodegradable and environment-friendly properties. Moreover, surface modification of biocomposites allows fine-tuning of their unique properties, opening doors for their potential competition with conventional materials in various industries [30].

3. APPLICATIONS OF BIOPOLYMERS AND BIOPOLYMER COMPOSITES IN VARIOUS MEDICAL FIELDS

Tissue Engineering and Regenerative Medicine

Biocomposites are a valuable tool for supporting cell seeding, proliferation, and tissue formation, key steps in tissue engineering. Their effectiveness has been demonstrated in human skin fibroblast-based nerve regeneration models. Common biopolymers, including chitosan, collagen, and hyaluronic acid are vital tools in dermis and skin regeneration, cartilage repair, vascular engine-

ering, and soft tissue repair. Biopolymer/ceramic composites exhibit remarkable flexibility, bioactivity, and mechanical strength, useful for scaffold construction in bone tissue engineering [22]. PLA, PCL, PGA, and PLGA are commonly employed biopolymers in building scaffolds for organs and tissues, which can mimic *in vitro* biological functions and promote cell growth and tissue regeneration [31]. Biopolymer nanocomposites are opening avenues for 3D-printing of organs, tissues, and body parts. This can create personalized scaffolds, mimicking intricate internal structures based on individual patient scans. Using this technology, nanomaterials such as nanotubes, nanofibers, and nano-structured particles can also be replicated [32]. Chitosan-based composites are used as bone graft substitutes in orthopaedic tissue engineering, owing to their strength, porosity, and osteoconductive properties. Moreover, excellent antibacterial and binding properties of chitosan composites render them as promising candidates for scaffolds in cartilage, bone, and disc tissue engineering [33]. Gelatin-chitosan-hyaluron scaffolds are effective in both soft and hard tissue regeneration, particularly in orthopaedics [8]. Chitosan incorporated single-walled carbon nanotubes are used for the fabrication of 3D films through laser printing [34]. Engineered polymer scaffolds made from materials such as hyaluronic acid, gelatin, collagen, elastin, and fibroin are used to regenerate a variety of tissues (adipose, ligament, blood vessels) and organs (liver, cartilage, bone, pancreas, spinal cord) [35].

A multitude of studies in the past have demonstrated the effectiveness of various biopolymers or their composites in tissue engineering. For instance, Pan et al. [36] created a hydrogel by combining oxidized dextran and modified gelatin for use in cartilage tissue engineering. The ability of this hydrogel to support cell viability was tested by using mesenchymal cells from the synovium, which have the potential to become chondrocytes. The hydrogel was loaded with mesenchymal cells and TGF- β 3 (a growth factor) for use in an animal testing model. The results were impressive and the hydrogel not only supported cell growth, but also allowed for the differentiation of mesenchymal cells. A study by Dong et al. [37] explored the benefits of incorporating a chitosan hydrogel into a 3D-printed poly(ϵ -caprolactone) scaffold. The chitosan-containing scaffold promoted better cell retention, proliferation, and good mechanical strength in a rabbit testing model using bone mesenchymal cells and a growth factor. Silvestro et al. [38] investigated the ideal conditions for cross-linking chitosan with TPP (tripolyphosphate anion) and the effect of these conditions on resulting scaffolds' physical and chemical characteristics. Among the various concentrations (1 and 2%; w/v for chitosan and TPP) and cross-linking reaction times (2, 4, and

8 h), the best formulation was identified to be 1% chitosan and 2% TPP due to high uniformity in the pore size (80 – 100 μm) of these scaffolds. Moreover, the scaffolds made with 1% chitosan, 2% TPP, and 8 h reaction time exhibited good cell viability. A hydrogel film was also prepared using chemically modified gelatin (gelatin-DTPH) and hyaluronic acid (HA-DTPH). The addition of HA-DTPH to this film offered two key advantages for effective tissue engineering process: (a) decrease in enzymatic degradation of gelatin-DTPH and (b) improvement in cell attachment to film surface [39]. Likewise, a hydrogel combining the properties of gelatin, hyaluronic acid, and hydroxyethyl acrylate was used in bone tissue engineering as an injectable material or a 3D-printed scaffold [40]. Gelatin nanofibers have also shown promise for tissue engineering retina and cornea in the eye. For example, a study by Xiang et al. [41] designed

a biocompatible scaffold from gelatin, silk fibroin, and polycaprolactone that mimics Bruch's membrane (a layer that supports retinal pigment epithelial [RPE] cells to prevent blindness). The scaffold exhibited long-term growth of RPE cells and supported their functionalization. Incorporation of collagen or agarose into sodium alginate-based ink greatly improved its mechanical strength for 3D bioprinting cartilage tissue engineering [42]. Salehi et al. [43] created a hydrogel combining alginate and chitosan and loaded it with olfactory ectomesenchymal cells for promoting nerve growth. *In vivo* testing of this hydrogel in a rat model confirmed better cell survival and function along with increased sciatic nerve regeneration abilities. Some commercially available biopolymer composites for tissue engineering and repair are listed in Table 1.

Table 1. Examples of biopolymer composites commercialized for tissue engineering processes

Product	Product information	Target tissue/organ	Purpose	Ref.
NeuroMatrix®	Type I collagen mesh Flexible tube	Nerve	Repair and regrowth	[44]
NeuroFlex®	Type I collagen mesh Flexible tube, kink-resistant	Nerve	Repair and regrowth	[44]
NeuroMend®	Type I collagen mesh Can wrap injured nerves for a range of injuries	Nerve	Repair and regrowth	[44]
Dynamatrix®	Acellular graft containing type I/II/VI collagen, glycosaminoglycans (hyaluronic acid, chondroitin sulfate A/B, heparin, heparin sulfate), proteoglycans, growth factors, and fibronectin	Skin	Wound healing, reconstruction of soft tissue	[45]
TachoSil®	Fibrin sealant (Human fibrinogen and thrombin on the surface of an equine collagen patch)	Heart	Sealant for cardiac wounds	[46]
Xelma	Blend of extracellular matrix proteins with propylene glycol and alginate	Skin	Healing of ulcer wounds	[47]
Dermagraft®	Cellular material (Human neonatal fibroblasts impregnated on bioabsorbable polyglactin mesh scaffold)	Skin	Healing of ulcers and other wounds	[48, 49]
Apligraf®	Cellular material (Foreskin-derived neonatal fibroblasts cultured <i>in vitro</i> , mixed with bovine type I collagen coated in cultured neonatal keratinocytes)	Skin	Healing of ulcers and other wounds	[50, 51]
BioDesign® Grafts	Water sealant (Acellular scaffold, non-cross-linked, non-dermis-based graft)	Brain, Abdomen, Heart, Skin	Brain surgery, abdominal reconstruction, wound healing, and heart surgery	[52]
INFUSE®	Absorbable collagen sponge in a metal Releases recombinant bone morphogenetic protein-2	Bone	Repair	[53]
DIABECCELL®	Alginate-based porcine-derived islet of Langerhans cell product	Blood	Treatment of Type I Diabetes	[54]
NTCELL®	Alginate-based choroid plexus cell product	Brain	Treatment of Parkinson's disease	[54, 55]
HCE	Permeable polycarbonate substrate incorporated with immortalized human corneal epithelial cells	Eye	Repair of corneal epithelium	[56]

Drug Delivery and Targeting

Biopolymers make perfect drug carriers, thanks to their structural diversity, physiological compatibility, low toxicity, durability, renewability, and biodegradability (Fig. 2). Moreover, they are revolutionizing the pharmaceutical sector by aiding in drug formulation through protecting drugs and guiding their controlled delivery to the target. Different types of polysaccharides (structural, protective, and reserve) are primarily used in pharmaceuticals because they can form conjugates with cell wall lipids and proteins. For example, biopolymers like cellulose, starch, gelatin, collagen, fibroin, and chitosan can be readily formulated into suspensions for the transport of variable size molecules. Supercritical fluid extraction, microemulsion, freeze drying, and electrospraying are some of the techniques used to deliver molecules at ocular, nasal, and dental systems [57]. The *in vivo* stability of biopolymeric nanoparticles was studied through their enzymatic degradation ability under different pH. Protein-based biopolymers were also explored for their potential applications via studying the relationship between their method of preparation and mechanism of drug release. These polymers with improved pharmacokinetic profiles ensured target-specific controlled drug delivery [58]. Temperature-responsive elastin-like polypeptides (ELPs) allow

for precise and sustained drug release in intra-articular regions. ELPs possess self-clearance properties from the joint space, making them ideal partners for protein drugs and elucidating their effectiveness as “fusion proteins” at tumour sites [59]. Albumin microspheres were chemically modified with amino acid addition and cationization to target specific tissues. Efficient bioactive encapsulation and controlled drug release profiles can be achieved by employing certain techniques that harden these drug carriers [60]. Bacterial nanocellulose is an ideal drug delivery material that can carry albumin protein with its integrity and activity remaining intact. This paves the way for exciting applications of bacterial nanocellulose in target-oriented drug delivery systems due to their hydrophilic and biocompatible nature together with controlled release kinetics [61]. Natural biopolymers can be crafted into hydrogels or nanogels using methods like precipitation, self-assembly, spray drying, extrusion, and complexation. Dextrin is one such biopolymer that can be modified into hydrogels that are mechanically strong, highly stable, and facilitate controlled drug release. Further, nanogels prepared from dextrin find use in *in vivo* cancer treatment, thanks to their biocompatibility and low immunogenicity [62].

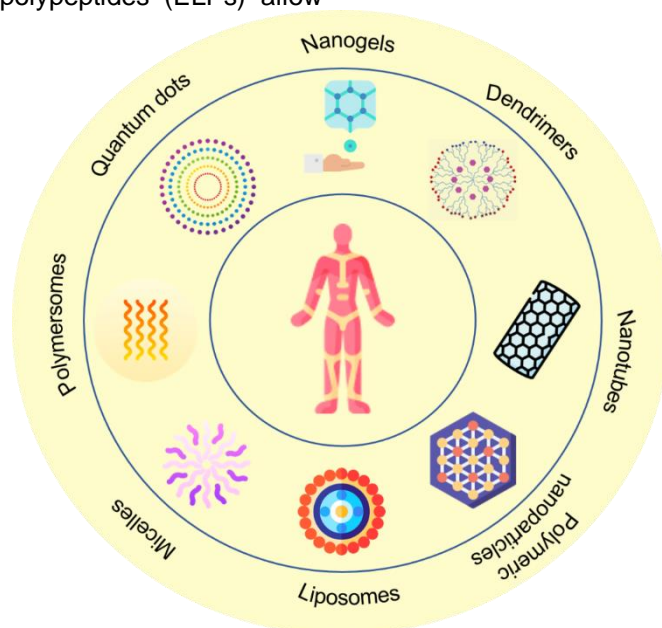


Figure 2. Types of biopolymeric drug carriers in drug delivery systems

Chitosan finds multifaceted applications in oral, nasal, ophthalmic, transdermal, and vaginal drug delivery systems. For example, in a study by Ren et al. [63], cinnamyl-chitosan was used as a potential material for formulating compressed tablets containing microcrystalline cellulose, magnesium stearate, and acetaminophen as binder, lubricant, and drug substance, respectively.

Cinnamyl-chitosan offered several advantages owing to its larger particle size, excellent release of acetaminophen, improved mechanical strength, increased antibacterial and antioxidant activities, making it a popular excipient choice for manufacturing direct compression tablets. Hybrid microgels prepared using modified chitosan and silicon dioxide nanoparticles exhibited a smaller

hydrodynamic diameter and two-stage release profile for the entrapped vitamin B12, i.e., an initial burst release of high dose for rapid pain relief and slower, sustained release for the healing process over time. This is particularly useful for the treatment of gastric wounds using oral drug delivery systems [64]. Dexamethasone was topically delivered to the eye using self-assembled particles made from chitosan and cholesterol. These submicron particles with hydrodynamic diameters within 700 – 900 nm and zeta potential > 30 mV were non-toxic, had cell membrane protecting abilities, and long-term anti-inflammatory effects [65]. Chitosan-coated niosomes prepared using a modified thin-film hydration technique were able to improve the bioavailability of azithromycin for treating bacterial conjunctivitis. The niosomes facilitated sustained release of the drug at three times higher rate than the commercially available drops in rabbit's eyes [66]. In a study by Rosch et al. [67], chitosan-alginate nanoparticles were loaded with doxorubicin using a water-in-oil emulsification procedure. The particles were rapidly taken up by 4T1 murine breast cancer cells *in vitro*. In another work, Nalini et al. [68] investigated the effects of quercetin-loaded chitosan-alginate nanoparticles at varying pH, alginate-chitosan ratio, and quercetin concentration using ionic gelation method. The optimum conditions were identified to be: (i) 1:2 alginate-chitosan ratio, (ii) pH = 7.4, and (iii) quercetin concentration = 7.5 mg/mL, for the initial drug release (4%) for 1 h and sustained release (78%) over the next 24 h. A hydrogel incorporating an antifungal drug, i.e., clotrimazole, Eudragit® RS100 nanocapsules, pullulan, and polyacrylic acid (Pemulen® TR1) was created for treating vulvovaginal candidiasis. Slow and sustained release (20.14 µg/cm² in 8 h) of the drug along with its reduced penetration into the bloodstream (14 µg/cm²) of cow vaginal tissue was achieved using this hydrogel [69]. Jackson et al. [70] developed cetyl trimethylammonium bromide (CTAB) surface-coated nanocrystalline cellulose for the delivery of anticancer drugs. The drugs, like paclitaxel, docetaxel, and etoposide could be delivered in a controlled manner for 2 days due to the effective uptake of these nanocrystals by KU-7 bladder cancer cells.

Surgical Implants and Devices

Several biopolymers, such as PLA and chitosan, naturally compatible and biodegradable, find diverse applications in pharmaceutical industries as implantable medical devices. Chitosan's versatility extends to various fields, like cardiology (e.g., heart valves), ophthalmology (e.g., contact lenses), and surgeries (e.g., regeneration of nerve) as medical implants [71]. Collagen serves as a supportive framework for bone, bone marrow and cardiovascular implants. PHAs can be used as implants in oesophagus, nerves, and vascular

cartilage. Gelatin has profound applications across medical fields as bone replacements in surgeries, grafts in cardiology, and 3D skin models in dermatology. Chitosan composites are used to prepare bone scaffolds, bio-livers, and in bone and peripheral nerve regeneration. Likewise, hyaluronic acid implants can be used to build new vocal folds and cartilages in otolaryngology. PHBs can be fabricated to produce surgical implants and scaffolds for cell culture [8]. Biopolymers obtained from sources like proteins, polysaccharides, microbes, and their composites were synthesized using various techniques, including 3D bioprinting, freeze drying, casting, and electrospinning. They are versatile materials for manufacturing stents, barrier membranes, and as cargo to deliver medicines, cells, genes, or growth factors [22]. For example, a type I porcine collagen-based injectable medical device (Dental SKIN BioRegulation) was investigated for its effects on human gingival fibroblast cells. The cells grown on collagen exhibited higher viability and wound healing properties, promising the potential of this device as a suitable mechanical bio-scaffold [72]. A collagen bone void filler (CBVF) was also developed using collagen, chitosan, and modified single-walled carbon nanotubes. This injectable device exhibited improved mechanical strength and bioactivity [73]. Li et al. [74] evaluated the effectiveness of collagen scaffolds incorporating human umbilical cord-derived stem cells for the treatment of spontaneous brain bleeding. Patients receiving the scaffold had better think abilities, improved day-to-day activities, reduced spots of brain damage, and enhanced healing rate. A biodegradable urethral stent developed from gelatin and alginate exhibited good mechanical properties. When placed in the ureters of a female pig, the stent maintained normal urine flow, displayed no symptoms of inflammation, and remained intact for 3 days and degraded completely [75]. Likewise, an ab interno gelatin stent (XEN 45 gel stent) was developed as a glaucoma surgery device by Grover et al. [76]. The patients receiving the implanted device reported a decrease in intra-ocular pressure by ≥20% at 12 months with no signs of intraoperative complications. Hasan and Al-Ghaban [77] investigated the effectiveness of hyaluronic acid (0.1 mL gel) for bone healing around implants by measuring the levels of tumor necrosis factor (TNF-α). The increased expression of TNF-α around the implant indicated early post-surgical healing response as a result of enhanced bonding of bone with the hyaluronic acid. In another study, hyaluronic acid hydrogel prepared using microbeads (diameter = 140 µm and swelling rate = 800 – 1200%) retained ~95% of its size even after 12 weeks of injection in rabbits. The hydrogel significantly subsided the inflammation after 8 weeks, leading to no fibrous capsule development or sub-chronic systemic toxicity in the rabbits [78].

Table 2. List of common biopolymers or their composites, showcasing their diverse applications, forms of use, and preparation technique in pharmaceutical industry

Biopolymer/ Biocomposite	Type of Biopolymer	Preparation Technique	Uses	Ref.
Biopolymers				
Albumin	Protein-based	Precipitation	Delivery of drug Ibuprofen	[91]
		Desolvation	Delivery of drug Irinotecan	[92]
Alginate	Polysaccharide-based	Dissolution	Delivery of drug Doxorubicin-loaded liposomes	[93]
		Precipitation	Delivery of drug Zidovudine	[94]
Bacterial cellulose	Microbial biopolymer	Gelation, cross-linking	Regeneration of muscle, vascular, and corneal tissues	[35]
Cellulose	Polysaccharide-based	Precipitation	Delivery of drug Betulinic acid	[95]
		Solvent evaporation	Delivery of drug Felodipine	[96]
Chitosan	Polysaccharide-based	Dissolution	Delivery of drug Quercetin	[97]
		Freeze-drying	Delivery of drug Curcumin	[98]
Collagen	Protein-based	Desolvation	Delivery of drug Fludarabine	[99]
		Electrospinning	Cardiovascular implants	[100]
		Freeze-drying	Delivery of drug Chloramphenicol	[101]
Elastin	Protein-based	Chemical synthesis/Acid solubilization/ Recombinant technology	Tissue scaffolds	[102]
Gelatin	Protein-based	Grafting, Electrospinning	Tissue scaffolds, Drug delivery	[103]
Hyaluronic acid	Polysaccharide-based	Chemical synthesis, cross-linking	Vocal fold implants, Tissue scaffolds	[35, 104]
Poly Lactic acid (PLA)	Synthetic biopolymer	Extrusion, Injection, Compression moulding	Drug delivery, tissue engineering, cell carriers, sutures	[105, 106]
Poly hydroxybutyrate (PHB)	Microbial biopolymer	Graft copolymerization, Solvent casting	Nerve tissue engineering, Bone implants	[107, 108]
Starch	Polysaccharide-based	Dissolution	Delivery of drug Doxorubicin	[109]
		Prototyping	Tissue engineering (e.g., bone scaffolds)	[110]
Biopolymer composites				
Alginate/ agarose/ gelatin	Polysaccharide/ Protein-based	Gelation, cross-linking	Regeneration of cartilage tissue	[35]
Cellulose/ collagen	Polysaccharide/ Protein-based	Gelation, cross-linking	Regeneration of cartilage tissue	[35]
Chitosan-alginate scaffold	Polysaccharide-based	Coacervation	Regeneration of ligament and tendon tissues, Bone scaffolds	[111]
Chitosan/chitin/ gelatin composite	Polysaccharide/ Protein-based	Blending	Nerve grafts	[112]
Chitosan/collagen/ heparin scaffold	Polysaccharide/ Protein-based	Blending	Artificial liver	[113]
Gelatin/Polyethylene glycol (PEG)	Protein/Synthetic polymer	3D printing	Administering cells to cutaneous wounds	[114]
PHB/PGA	Microbial/Synthetic biopolymer	Blending	Heart valve implant (in lambs)	[115]
Silk fibroin/gelatin	Protein-based	Moulding	Regeneration of ligament tissue	[35]

Diagnosics and Biosensing

A biosensor is an instrument used to translate biochemical information into electronic signals through an in-built transducer that can recognize the structures of different molecules. The device employs bioactive materials and turns molecular clues into precise quantifiable data, providing great opportunities in healthcare systems [79]. Biosensors have been used in wound dressing materials for monitoring a variety of parameters, like temperature, moisture, pH, and exudate release [80]. These built-in sensors can watch vital signs, such as moisture, pathogens, and necrotic tissues, guiding doctors to real-time intel for faster wound healing. This approach, especially crucial for stubborn wounds, including ulcers, diabetic foot, and bedsores, minimizes unnecessary bandage changes, provides barrier protection, and speeds up healing process [81]. Biopolymeric xerogels are cutting-edge tools in the realm of biosensing, relevant for studying important medical parameters (e.g., glucose level, cholesterol, uric acid, etc.). This is mainly attributed to their inherent properties, such as high porosity and surface area, making them perfect candidates for advanced biosensors [82]. Glycopolymer-based biosensors have been utilized for monitoring glucose levels, diagnosis of virus (e.g., influenza virus hemagglutinins), detection of antibodies in serum of diseased patients, neurotransmitter levels (e.g., dopamine), and measuring the protein concentration [83]. Cellulose acts as a robust and biocompatible substrate in anchoring the biological elements, like antibodies, enzymes, aptamers, etc. for optical biosensors. For example, a fibre-optic glucose biosensor was designed using glucose oxidase enzyme and carbon quantum dots impregnated within a cellulose acetate film. The biosensor was highly promising due to its high sensitivity, reusability, and ability to detect even low glucose levels [84]. Cellulose-based biosensors have also found exciting applications as diagnostic devices for elastase enzyme and used as a biomarker for various inflammatory diseases [85]. pH-sensitive hydrogels made from chitosan biopolymer have been used for treating asthma. Likewise, polyethylene glycol dimethacrylate-based hydrogel demonstrated *in vivo* efficacy against cancer by encapsulating the chemotherapy drug (doxorubicin) and gradually releasing it with response to change in pH around tumour sites [86]. Alharthi et al. [87] developed a specially designed nanocellulose acetate xerogel for the precise detection of urea. The gel contained two key components: (a) a urease enzyme (as catalyst) and (b) triarylmethane (for the determination of color change in presence of urea). Lee et al. [88] developed an amperometric biosensor using a xerogel-modified PtCr/C microelectrode for detecting carbon monoxide deposited on the surface of kidney. A glucose

biosensor was also developed from a metal-organic framework (zeolitic imidazolate framework-8; ZIF-8) supported with cellulose acetate nanofibers and encapsulated with enzymes, i.e., glucose oxidase and lactose operon. The sensor was highly effective at detecting glucose and remained stable up to 15 h [89]. In another study by Ranjbar and Shahrokhian [90], an electrochemical aptasensor was developed using a nanocomposite made up of carbon/gold nanoparticles and cellulose nanofibers for the detection of *Staphylococcus aureus* infection in human serum. The sensor could detect the bacterial infection with a high detection limit of 1 CFU/mL. Table 2 provides an overview of the various applications of biopolymers or their composites in different forms within the pharmaceutical sector.

4. ADVANTAGES AND LIMITATIONS OF USING BIOPOLYMERS IN MEDICINE

Advantages

(i) Biopolymers are natural polymers that possess an array of advantages compared to synthetic polymers in terms of their cost-effectiveness, eco-friendliness, biocompatibility, non-toxicity, and safety [116].

(ii) The similarity of naturally occurring polymers with the macromolecules present in human body increases their biocompatibility with different body tissues/organs. Biopolymers, being non-toxic, do not lead to allergic reactions or severe inflammation, as their properties are identical to extracellular fluids [22,116].

(iii) Biodegradable biopolymers are highly suitable for drug delivery systems, as they do not require surgical removal after drug gets released to the target site and are excreted naturally from the body [11].

(iv) Biopolymer-based drug delivery system is highly suitable for systematic and standardized administration of drugs to a specified cell or tissue, prolonging their therapeutic response [117].

(v) Biopolymers allow sustained drug release, i.e., the drug is released slowly to the target site via degradation of polymer matrix in which the drug is embedded [118]. Biopolymers are highly desirable for this purpose, as they can be tailor-made into properties suited for medical applications, such as drug deciphering kinematics, degradation speed, and mechanical strength [119].

(vi) Biopolymers play a significant role in stimuli-responsive drug delivery matrices, which could be briefed as the ability of biopolymer-based drug delivery system to respond quickly to external factors (e.g., temperature, enzymes, and pH) and facilitate the delivery of drug at appropriate time and desired location [120].

(vii) Biopolymers are cutting-edge tools over their synthetic counterparts in the preparation of surgical materials, owing to their biocompatibility, safety, and unique characteristics at the target site [121].

(viii) Scientists and surgeons are capable of modifying and developing new materials with advanced structure and properties from pre-existing biopolymers by altering their response to

external stimuli, gelling capacity, and vulnerability to chemical amendments. Therefore, architectural alteration of biopolymers can diversify the production of surgical materials, hence they seem to be the future of surgical industries [121].

(ix) Various biopolymers used in synthesis of biomedical materials due to their superior hygiene are given in Table 3.

Table 3. List of biopolymers utilized for the construction of biomedical materials (modified from [122])

Biomedical Materials	Applied Polymer	Probable Biopolymer
Surgical Sutures	Poly (amide), poly (propylene), poly (vinylidene fluoride)	PLA, PGA, PLGA
Wound dressing	Poly (vinyl alcohol), cotton	PGA, PLA
Tubing or blood or urine bags	Poly (vinyl chloride)	PBAT, PHB
Medical Catheters	High-density polyethylene (PE), Poly (dimethylsiloxane), polyether ether ketone, poly (propylene)	PLA, PGA, PLGA, TPS, PCL
Plasters	Toluene 3, 4 diisocyanate and polyethylene glycols (lycra fibers)	PLA, TPS
Surgical gowns	Cotton, polyesters, polypropylene (PP), PE	Bio-based (PET, PBT)
Caps, masks, and gowns	Polyethylene terephthalate, cotton	PLA, TPS
Surgical hosiery	PET, cotton, PP, PE	Bio-based PET
Pillow covers	Polyesters	PLA, TPS
Hospital Uniforms	Polyesters	Bio-based PET, TPS, PLA
Baby diapers	Polyacrylic acid, poly vinyl alcohol co-polymers	TPS

Abbreviations: PLA: Polylactic acid; PGA: Polyglycolic acid; PLGA: Poly (lactic-co-glycolic acid); PBAT: Polybutyrate adipate terephthalate; PHB: Polyhydroxybutyrate; TPS: Thermoplastic Starch; PCL: Polycaprolactone

Limitations

Although the unique properties of biopolymers have revolutionized the world of pharmaceuticals and medicine, yet their expeditious usage is impeded by diverse factors.

(i) Of late, most of the research in this field has been carried out *in vitro*, which compromises its precision and actual outcomes practically. Hence, biopolymer products should be validated at pilot-scale level, before introducing them to actual world. Therefore, *in vivo* as well as clinical trials are required at large scale, in order to evidence the health advantages of biopolymers, particularly assessing their biocompatibility as an encapsulation material during drug delivery. Moreover, extensive studies are required to evaluate their disease treating capacity either alone or in combination for attaining suitable outcomes, when administered at highly specific and therapeutically admissible levels [123].

(ii) The other constraint being faced in using biopolymers for medical applications includes the problem of developing the material possessing

properties superior or equivalent to artificial products by improving the inherent mechanical, thermal, barrier, kinetics, and release properties. This may overcome the issue of fast degradation, inferior mechanical solidity, and neutralizing the water absorption ability, especially during unfavourable conditions, interfering with the capacity of biopolymers in medical applications [124].

(iii) Another limitation in obtaining natural biopolymers from plants is linked with their production rate and chemical constituents, which depend upon the climate, season, place of origin, and species, which can affect water content of the biomaterial [125].

5. CONCLUSIONS

The quest for sustainable environmental solutions has turned its focus to developing "green" materials. With their environment-friendliness and impressive properties, biopolymers and their composites are being greatly valued as promising alternatives to synthetic polymers. Biopolymers are highly biodegradable, biocompatible, and non-toxic in nature. Their tailored properties find exciting applications in a variety of industries, especially biomedicine and pharmaceuticals, where they are increasingly being used as implantable devices, tissue engineering scaffolds, wound dressing

materials, and drug delivery systems. The biopolymer market is booming due to increasing societal interest spurred by their sustainability appeal. However, high costs incurred with biopolymer synthesis hinder their widespread adoption, necessitating the need for developing affordable biomass substrates for large-scale production. Bridging the performance gap between biopolymers and their synthetic counterparts also presents a critical challenge. Upgrading the quality and performance of biopolymers via modification or combination with other components is an innovative strategy for overcoming these barriers and achieving a biopolymer commercialized future. To sum up, the positive impacts of biopolymers in different medical and pharmaceutical applications has sparked a lot of interest lately, raising the call for a complete phase out of synthetic polymers in future.

Future Prospects

(i) Biopolymeric drugs and gene delivery hold immense potential in shaping the future of medicine. They can be employed as targeted and customized carriers of drugs and genes to specific cell or tissue in living beings. This will aid in efficacious and prompt disease eradication with minimal side-effects.

(ii) Biopolymeric drug delivery systems require more focused research and efforts on gaining the stability and accessibility of drugs, especially for drugs with poor absorption rates and low solubility. This could add to promising and effective therapies of biopolymeric drugs in managing diseases.

(iii) Merging various smart technologies and materials with biopolymeric drug delivery systems can further revolutionize the world of medicine. In this context, nanotechnology, plasma technology,

3D printing, electrospinning, and cryogenic technologies could be a great asset in facilitating controlled release of drug and its absorption in the body. Hence, anticipated and explicit outcomes could be achieved (Fig. 3).

(iv) In order to upgrade the controlled and targeted aspects of biopolymer-based drug delivery systems, more precise and efficacious biopolymer processing techniques should be prioritized due to their indispensable role in vital processes.

(v) Synergistic therapies involving delivery of multitude drugs or genes concurrently targeting different parameters of disease or multiple medical conditions, is another important aspect of medicine that can be achieved through biopolymeric drugs.

(vi) In future, the biopolymeric drug delivery system can be upgraded by designing a high-tech system, which allows long-lasting and non-invasive drug delivery. Hence, recurrent administration of drugs can be overcome, improving the patient's docility and mental acceptance towards the treatment.

(vii) Rigorous research on the surface properties and functionalities of biopolymers is the need of the hour for breakthrough achievements in biomedical field, because surface and functional alterations can vigorously modify the material-cell interaction ability.

(viii) Further research should emphasize on developing hybrid biopolymers by combining different polymers and traversing their potential application in blended form.

(ix) Last but not the least, with advancement in biopolymeric drug delivery systems, authorities have to face the regulatory and commercialization issues. Hence, system has to prepare itself to address these challenges.

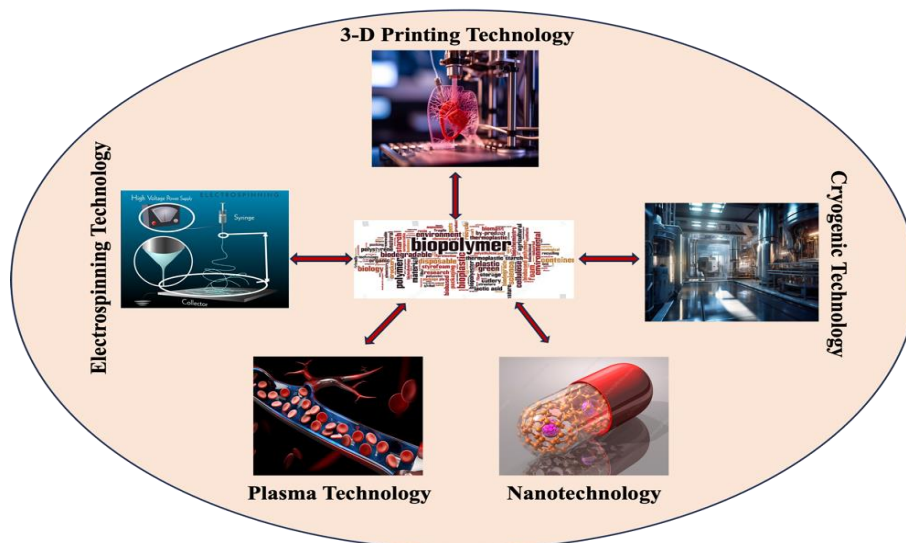


Figure 3. A diagrammatic representation of the networking of various smart technologies with biopolymers for effective drug delivery

Acknowledgements

The authors deeply acknowledge the support from Sharda University, Greater Noida, India during the entire process of writing this article.

6. REFERENCES

- [1] T.D.Moshood, G. Nawanir, F.Mahmud, F.Mohamad, M.H.Ahmad, A.AbdulGhani (2022) Sustainability of biodegradable plastics: new problem or solution to solve the global plastic pollution?, *Curr. Res. Green Sustain. Chem.*, 5, 100273. <https://doi.org/10.1016/j.crgsc.2022.100273>
- [2] A.Lotfi, H.Li, D.V.Dao, G.Prusty (2021) Natural fiber-reinforced composites: a review on material, manufacturing, and machinability, *J. Thermoplast. Compos. Mater.*, 34, 238-284. <https://doi.org/10.1177/0892705719844546>
- [3] M.Hassan, J.Bai, D.Q.Dou (2019) Biopolymers; definition, classification and applications, *Egypt. J. Chem.*, 62, 1725-1737. <https://doi.org/10.21608/ejchem.2019.6967.1580>
- [4] M.G.Rao, P.Bharathi, R.M.Akila (2014) A comprehensive review on biopolymers, *Sci. Rev. Chem. Commun.*, 4, 61-68.
- [5] A.Aravamudhan, D.M.Ramos, A.A.Nada, S.G.Kumbar (2014) Natural polymers: Polysaccharides and their derivatives for biomedical applications, book *Natural and Synthetic Biomedical Polymers*, Elsevier, Amsterdam, The Netherlands, p. 67-89.
- [6] S.Y.Rong, N.M.Mubarak, F.A.Tanjung (2017) Structure-property relationship of cellulose nanowhiskers reinforced chitosan biocomposite films, *J. Environ. Chem. Eng.*, 5, 6132-6136. <https://doi.org/10.1016/j.jece.2017.11.054>
- [7] L.M.Madikizela, L.Chimuka (2016) Synthesis, adsorption and selectivity studies of a polymer imprinted with naproxen, ibuprofen and diclofenac, *J. Environ. Chem. Eng.*, 4, 4029-4037. <https://doi.org/10.1016/j.jece.2016.09.012>
- [8] R.Bhatt, M.Jaffe (2015) Biopolymers in medical implants, book *Excipient applications in formulation design and drug delivery*, Springer, Cham, p. 311-348.
- [9] I.Bano, M.Arshad, T.Yasin, M.A.Ghauri, M.Younus (2017) Chitosan: a potential biopolymer for wound management, *Int. J. Biol. Macromol.*, 102, 380-383. <https://doi.org/10.1016/j.ijbiomac.2017.04.047>
- [10] A.George, M.R.Sanjay, R.Srisuk, J.Parameswaranpillai, S.Siengchin (2020) A comprehensive review on chemical properties and applications of biopolymers and their composites, *Int. J. Biol. Macromol.*, 154, 329-338. <https://doi.org/10.1016/j.ijbiomac.2020.03.120>
- [11] J.Baranwal, B.Barse, A.Fais, G.L.Delogu, A.Kumar (2022) Biopolymer: a sustainable material for food and medical applications, *Polymers*, 14, 983. <https://doi.org/10.3390/polym14050983>
- [12] N.Jabeen, M.Atif (2023) Polysaccharides based biopolymers for biomedical applications: a review, *Polym. Adv. Technol.*, 35, e6203. <https://doi.org/10.1002/pat.6203>
- [13] P.Gupta, K.K.Nayak (2015) Characteristics of protein-based biopolymer and its application, *Polym. Eng. Sci.*, 55, 485-498. <https://doi.org/10.1002/pen.23928>
- [14] P.Snetkov, K.Zakharova, S.Morozkina, R.Olekhovich, M.Uspenskaya (2020) Hyaluronic acid: the influence of molecular weight on structural, physical, physico-chemical, and degradable properties of biopolymer, *Polymers*, 12, 1800. <https://doi.org/10.3390/polym12081800>
- [15] S.L.Spurlock, G.H.Spurlock, S.Bernstad, P.Michanek, S.T.Chester (1999) Treatment of acute superficial flexor tendon injuries in performance horses with high molecular weight sodium hyaluronate, *J. Equine Vet. Sci.*, 19, 338-344. [https://doi.org/10.1016/S0737-0806\(06\)82052-6](https://doi.org/10.1016/S0737-0806(06)82052-6)
- [16] F.Tao, Y.Cheng, X.Shi, H.Zheng, Y.Du, W.Xiang, H.Deng (2020) Applications of chitin and chitosan nanofibers in bone regenerative engineering, *Carbohydr. Polym.*, 230, 115658. <https://doi.org/10.1016/j.carbpol.2019.115658>
- [17] N.F.Huang, T.S.Zaitseva, M.V.Paukshto (2023) Biomedical applications of collagen, *Bioengineering*, 10, 90. <https://doi.org/10.3390/bioengineering10010090>
- [18] C.E.Campiglio, N.Contessi Negrini, S.Farè, L.Draghi (2019) Cross-linking strategies for electrospun gelatin scaffolds, *Materials*, 12, 2476. <https://doi.org/10.3390/ma12152476>
- [19] C.Gonzalez-Obeso, E.J.Hartzell, R.A.Scheel, D.L.Kaplan (2023) Delivering on the promise of recombinant silk-inspired proteins for drug delivery, *Adv. Drug Deliv. Rev.*, 192, 114622. <https://doi.org/10.1016/j.addr.2022.114622>
- [20] E.Chaabouni, F.Gassara, S.K.Brar (2014) Biopolymers synthesis and application, book *Biotransformation Waste Biomass into High Value Biochem*, Springer, New York, USA, p. 415-443.
- [21] F.Ebrahimi, H.Ramezani Dana (2022) Poly lactic acid (PLA) polymers: from properties to biomedical application, *Int. J. Polym. Mater.*, 71, 1117-1130. <https://doi.org/10.1080/00914037.2021.1944140>
- [22] S.B.Park, E.Lih, K.S.Park, Y.K.Joung, D.K.Han (2017) Biopolymer-based functional composites for medical applications, *Prog. Polym. Sci.*, 68, 77-105. <https://doi.org/10.1016/j.progpolymsci.2016.12.003>
- [23] P.R.F.Marcelino, F.Gonçalves, N.S.Aizawa, H.P.Pereira, T.M.Lacerda, S.S.da Silva (2021) Microbial biopolymers and their derivatives as nanotechnological tools for medicine: applications, advantages, toxicity, and safety, book *Nanotechnology in medicine: toxicity and safety*, Wiley-Blackwell, New Jersey, USA, p. 29-46.
- [24] D.A.Gregory, C.S.Taylor, A.T.Fricker, E.Asare, S.S.Tetali, J.W.Haycock, I.Roy (2022) Polyhydroxyalkanoates and their advances for biomedical applications, *Trends Mol. Med.*, 28, 331-342. <https://doi.org/10.1016/j.molmed.2022.01.007>
- [25] S.Mohapatra, D.Mohanty, S.Sharma, S.Dikshit, I.Kohli, D.P.Samantaray, M.Kathpalia (2021) Biomedical application of polymeric biomaterial: polyhydroxybutyrate, book *Bioresource utilization*

- and management: applications in therapeutics, biofuels, agriculture, and environmental science, CRC Press, USA, p. 111-124.
- [26] Q.Hu, Y.Lu, Y.Luo (2021) Recent advances in dextran-based drug delivery systems: from fabrication strategies to applications, *Carbohydr. Polym.*, 264, 117999. <https://doi.org/10.1016/j.carbpol.2021.117999>
- [27] A.M.Díez-Pascual (2019) Synthesis and applications of biopolymer composites, *Int. J. Mol. Sci.*, 20, 2321. <https://doi.org/10.3390/ijms20092321>
- [28] R.Payal (2019) Reliable natural-fibre augmented biodegraded polymer composites, book *Sustainable polymer composites and nanocomposites*, Springer, Cham, p. 961-975.
- [29] B.Aaliya, K.V.Sunooj, M.Lackner (2021) Biopolymer composites: a review, *Int. J. Biobased Plast.*, 3, 40-84. <https://doi.org/10.1080/24759651.2021.1881214>
- [30] T.Gurunathan, S.Mohanty, S.K.Nayak (2015) A review of the recent developments in biocomposites based on natural fibres and their application perspectives, *Compos. Part A Appl. Sci. Manuf.*, 77, 1-25. <https://doi.org/10.1016/j.compositesa.2015.06.007>
- [31] M.Okamoto, B.John (2013) Synthetic biopolymer nanocomposites for tissue engineering scaffolds, *Prog. Polym. Sci.*, 38, 1487-1503. <https://doi.org/10.1016/j.progpolymsci.2013.06.001>
- [32] X.Li, R.Cui, L.Sun, K.E.Aifantis, Y.Fan, Q.Feng, F.Cui, F.Watari (2014) 3D-printed biopolymers for tissue engineering application, *Int. J. Polym. Sci.*, 2014, 829145. <https://doi.org/10.1155/2014/829145>
- [33] J.Tian, G.Yang, H.Huang, M.Liu, L.Liu, X.Zhang, Y.We (2020) Recent progress and development for the fabrication of antibacterial materials through mussel inspired chemistry, *J. Environ. Chem. Eng.*, 8, 104383. <https://doi.org/10.1016/j.jece.2020.104383>
- [34] M.S.Savelyev, A.Y.Gerasimenko, P.N.Vasilevsky, Y.O.Fedorova, T.Groth, G.N.Ten, D.V.Telyshev (2020) Spectral analysis combined with nonlinear optical measurement of laser printed biopolymer composites comprising chitosan/SWCNT, *Anal. Biochem.*, 598, 113710. <https://doi.org/10.1016/j.ab.2020.113710>
- [35] S.Van Vlierberghe, P.Dubruel, E.Schacht (2011) Biopolymer-based hydrogels as scaffolds for tissue engineering applications: a review, *Biomacromolecules*, 12, 1387-1408. <https://doi.org/10.1021/bm200083n>
- [36] J.F.Pan, L.Yuan, C.A.Guo, X.H.Geng, T.Fei, W.S.Fan, S.Li, H.F.Yuan, Z.Q.Yan, X.M.Mo (2014) Fabrication of modified dextran-gelatin in situ forming hydrogel and application in cartilage tissue engineering, *J.Mater.Chem. B*, 2, 8346-8360. <https://doi.org/10.1039/C4TB01221F>
- [37] L.Dong, S.J.Wang, X.R.Zhao, Y.F.Zhu, J.K.Yu (2017) 3D-printed poly (ϵ -caprolactone) scaffold integrated with cell-laden chitosan hydrogels for bone tissue engineering, *Sci. Rep.*, 7, 13412. <https://doi.org/10.1038/s41598-017-13838-7>
- [38] I.Silvestro, I.Francolini, V.DiLisio, A.Martinelli, L.Pietrelli, A.Scottod'Abusco, A.Scoppio, A.Piozzi (2020) Preparation and characterization of TPP-chitosan crosslinked scaffolds for tissue engineering, *Materials*, 13, 3577. <https://doi.org/10.3390/ma13163577>
- [39] X.Z.Shu, Y.Liu, F.Palumbo, G.D.Prestwich (2003) Disulfide-crosslinked hyaluronan-gelatin hydrogel films: a covalent mimic of the extracellular matrix for in vitro cell growth, *Biomaterials*, 24, 3825-3834. [https://doi.org/10.1016/S0142-9612\(03\)00267-9](https://doi.org/10.1016/S0142-9612(03)00267-9)
- [40] I.Noh, N.Kim, H.N.Tran, J.Lee, C.Lee (2019) 3D printable hyaluronic acid-based hydrogel for its potential application as a bioink in tissue engineering, *Biomater. Res.*, 23, 1-9. <https://doi.org/10.1186/s40824-018-0152-8>
- [41] P.Xiang, K.C.Wu, Y.Zhu, L.Xiang, C.Li, D.L.Chen, F.Chen, G.Xu, A.Wang, M.Li, Z.B.Jin (2014) A novel Bruch's membrane-mimetic electrospun substrate scaffold for human retinal pigment epithelium cells, *Biomaterials*, 35, 9777-9788. <https://doi.org/10.1016/j.biomaterials.2014.08.040>
- [42] X.Yang, Z.Lu, H.Wu, W.Li, L.Zheng, J.Zhao (2018) Collagen-alginate as bioink for three-dimensional (3D) cell printing based cartilage tissue engineering, *Mater. Sci. Eng. C*, 83, 195-201. <https://doi.org/10.1016/j.msec.2017.09.002>
- [43] M.Salehi, Z.Bagher, S.K.Kamrava, A.Ehterami, R.Alizadeh, M.Farhadi, M.Falah, A.Komeili (2019) Alginate/chitosan hydrogel containing olfactory ectomesenchymal stem cells for sciatic nerve tissue engineering, *J. Cell. Physiol.*, 234, 15357-15368. <https://doi.org/10.1002/jcp.28183>
- [44] S.Kehoe, X.F.Zhang, D.Boyd (2012) FDA approved guidance conduits and wraps for peripheral nerve injury: a review of materials and efficacy, *Injury*, 43, 553-572. <https://doi.org/10.1016/j.injury.2010.12.030>
- [45] M.Nevins, M.L.Nevins, M.Camelo, J.M.Camelo, P.Schubach, D.M.Kim (2010) The clinical efficacy of dynamatrix extracellular membrane in augmenting keratinized tissue, *Int. J. Periodontics Restor. Dent.*, 30, 151-161.
- [46] M.A.Erb, T.Claus, M.Hartrumpf, S.Bachmann, J.M.Albes (2009) The use of tachosil surgical patch or fibrin glue in coronary artery surgery does not affect quality of anastomosis or provoke postoperative adhesions in pigs, *Eur. J. Cardiothorac. Surg.*, 36, 703-707. <https://doi.org/10.1016/j.ejcts.2009.04.028>
- [47] M.Young, E.Bond, G.Bowen, P.Chadwick, J.McCardle, A.McInnes, D.Stang, L.Watret (2010) Consensus statement on the use of xelma in diabetic foot ulcers, *The Diabetic Foot*, 13, 148-151.
- [48] A.A.Omar, A.I.D.Mavor, A.M.Jones, S.Homer-Vanniasinkam (2004) Treatment of venous leg ulcers with dermagraft®, *Eur. J. Vasc. Endovasc. Surg.*, 27, 666-672. <https://doi.org/10.1016/j.ejvs.2004.03.001>
- [49] C.E.Hart, A.Loewen-Rodriguez, J.Lessem (2012) Dermagraft: use in the treatment of chronic wounds, *Adv. Wound Care*, 1, 138-141. <https://doi.org/10.1089/wound.2011.0282>
- [50] D.Fivenson, L.Scherschun (2003) Clinical and economic impact of apligraf® for the treatment of

- non-healing venous leg ulcers, *Int. J. Dermatol.*, 42, 960-965.
<https://doi.org/10.1111/j.1365-4632.2003.02039.x>
- [51] S.Hu, R.S.Kirsner, V.Falanga, T.Phillips, W.H.Eaglstein (2006) Evaluation of apligraf® persistence and basement membrane restoration in donor site wounds: a pilot study, *Wound Repair Regen.*, 14, 427-433.
<https://doi.org/10.1111/j.1743-6109.2006.00148.x>
- [52] C.N.Ellis (2010) Outcomes with the use of bioprosthetic grafts to reinforce the ligation of the intersphincteric fistula tract (biolift procedure) for the management of complex anal fistulas, *Dis. Colon Rectum*, 53, 1361-1364.
<https://doi.org/10.1007/DCR.0b013e3181ec4470>
- [53] R.D.Guyer, S.G.Tromanhauser, J.J.Regan (2007) An economic model of one-level lumbar arthroplasty versus fusion, *Spine J. Off. J. N. Am. Spine Soc.*, 7, 558-562.
<https://doi.org/10.1016/j.spinee.2006.09.006>
- [54] P.L.J.Tan (2010) Company profile: tissue regeneration for diabetes and neurological diseases at living cell technologies, *Regen.Med.*, 5, 181-187.<https://doi.org/10.2217/rme.10.4>
- [55] A.K.Wise, J.B.Fallon, A.J.Neil, L.N.Pettingill, M.S.Geaney, S.J.Skinner, R.K.Shepherd (2011) Combining cell-based therapies and neural prostheses to promote neural survival, *Neurotherapeutics*, 8, 774-787.
<https://doi.org/10.1007/s13311-011-0070-0>
- [56] F.E.Van Goethem, N.Adriaens, F.Alepee, B. Straube, M.De Wever, S.Cappadoro, E.Catoire, E. Hansen, A.Wolf, P.Vanparys (2006) Prevalidation of a new *in vitro* reconstituted human cornea model to assess the eye irritating potential of chemicals, *Toxicol. In Vitro*, 20, 1-17.
<https://doi.org/10.1016/j.tiv.2005.05.002>
- [57] J.Jacob, J.T.Haponiuk, S.Thomas, S.Gopi (2018) Biopolymer based nanomaterials in drug delivery systems: a review, *Mater. Today Chem.*, 9, 43-55.<https://doi.org/10.1016/j.mtchem.2018.05.002>
- [58] S.Gopi, A.Amalraj, N.P.Sukumaran, J.T.Haponiuk, S.Thomas (2018) Biopolymers and their composites for drug delivery: a brief review, *Macromol. Symp.*, 380, 1800114.
<https://doi.org/10.1002/masy.201800114>
- [59] H.Betre, W.Liu, M.R.Zalutsky, A.Chilkoti, V.B. Kraus, L.A.Setton (2006) A thermally responsive biopolymer for intra-articular drug delivery, *J.Control.Release*, 115, 175-182.
<https://doi.org/10.1016/j.jconrel.2006.07.022>
- [60] G.V.Patil (2003) Biopolymer albumin for diagnosis and in drug delivery, *Drug Dev. Res.*, 58, 219-247.<https://doi.org/10.1002/ddr.10157>
- [61] A.Müller, Z.Ni, N.Hessler, F.Wesarg, F.A.Müller, D.Kralisch, D.Fischer (2013) The biopolymer bacterial nanocellulose as drug delivery system: investigation of drug loading and release using the model protein albumin, *J. Pharm. Sci.*, 102, 579-592.<https://doi.org/10.1002/jps.23385>
- [62] D.Das, S.Pal (2015) Modified biopolymer-dextrin based crosslinked hydrogels: application in controlled drug delivery, *RSC Adv.*, 5, 25014-25050. <https://doi.org/10.1039/C4RA16103C>
- [63] G.Ren, C.Clancy, T.M.Tamer, B.Schaller, G.M.Walker, M.N.Collins (2019) Cinnamyl O-amine functionalized chitosan as a new excipient in direct compressed tablets with improved drug delivery, *Int. J. Biol. Macromol.*, 141, 936-946.
<https://doi.org/10.1016/j.ijbiomac.2019.08.265>
- [64] M.C.G.Pellá, A.R.Simão, M.K.Lima-Tenório, E.Tenório-Neto, D.B.Scariot, C.V.Nakamura, A.F. Rubira (2020) Chitosan hybrid microgels for oral drug delivery, *Carbohydr. Polym.*, 239, 116236.
<https://doi.org/10.1016/j.carbpol.2020.116236>
- [65] N.V.Dubashynskaya, A.S.Golovkin, I.V.Kudryavtsev, S.S.Prikhodko, A.S.Trulioff, A.N.Bokatyi, D.N.Poshina, S.V.Raik, Y.A.Skorik (2020) Mucoadhesive cholesterol-chitosan self-assembled particles for topical ocular delivery of dexamethasone, *Int. J. Biol. Macromol.*, 158, 811-818.
<https://doi.org/10.1016/j.ijbiomac.2020.04.251>
- [66] H.M.Eid, I.A.Naguib, R.I.Alsantali, I.Alsalahat, A.M.Hegazy (2021) Novel chitosan-coated niosomal formulation for improved management of bacterial conjunctivitis: a highly permeable and efficient ocular nanocarrier for azithromycin, *J. Pharm. Sci.*, 110, 3027-3036.
<https://doi.org/10.1016/j.xphs.2021.04.020>
- [67] J.G.Rosch, H.Winter, A.N.DuRoss, G.Sahay, C.Sun (2019) Inverse-micelle synthesis of doxorubicin-loaded alginate/chitosan nanoparticles and *in vitro* assessment of breast cancer cytotoxicity, *Colloids Interface Sci. Commun.*, 28, 69-74.<https://doi.org/10.1016/j.colcom.2018.12.002>
- [68] T.Nalini, S.K.Basha, A.M.M.Sadiq, V.S.Kumari, K.Kaviyarasu (2019) Development and characterization of alginate/chitosan nanoparticulate system for hydrophobic drug encapsulation, *J. Drug Deliv. Sci. Technol.*, 52, 65-72.<https://doi.org/10.1016/j.jddst.2019.04.002>
- [69] J.A.deLima, T.C.Paines, M.H.Motta, W.B.Weber, S.S.DosSantos, L.Cruz, C.D.B.daSilva (2017) Novel pemulen/pullulan blended hydrogel containing clotrimazole-loaded cationic nanocapsules: evaluation of mucoadhesion and vaginal permeation, *Mater. Sci. Eng. C*, 79, 886-893.<https://doi.org/10.1016/j.msec.2017.05.030>
- [70] J.K.Jackson, K.Letchford, B.Z.Wasserman, L.Ye, W.Y.Hamad, H.M.Burt (2011) The use of nanocrystalline cellulose for the binding and controlled release of drugs, *Int. J. Nanomed.*, 6, 321-330.<https://doi.org/10.2147/IJN.S16749>
- [71] R.Rebelo, M.Fernandes, R.Fangueiro (2017) Biopolymers in medical implants: a brief review, *Procedia Eng.*, 200, 236-243.
<https://doi.org/10.1016/j.proeng.2017.07.034>
- [72] T.Romasco, P.M.Mandrillo, E.Morsut, M.Tumedei, D.Mandatori, M.Petrini, M.C.Curia, F.DeAngelis, C.D'Arcangelo, A.Piattelli, N.DiPietro (2023) Morpho-functional effect of a new collagen-based medical device on human gingival fibroblasts: an *in vitro* study, *Biomedicines*, 11, 786.
<https://doi.org/10.3390/biomedicines11030786>
- [73] K.Kaur, S.Sa'Paiva, D.Caffrey, B.L.Cavanagh, C.M.Murphy (2021) Injectable chitosan/collagen hydrogels nano-engineered with functionalized single wall carbon nanotubes for minimally invasive

- applications in bone, *Mater. Sci. Eng. C*, 128, 112340. <https://doi.org/10.1016/j.msec.2021.112340>
- [74] X.Y.Li, W.S.Deng, Z.Q.Wang, Z.C.Li, S.L.Chen, Z.Song, Q.Zhang, J.Liang, X.Y.Chen (2023) Injectable collagen scaffold with human umbilical cord-derived mesenchymal stem cells promotes functional recovery in patients with spontaneous intracerebral hemorrhage: phase I clinical trial, *Neural Regen. Res.*, 18, 1999-2004. <https://doi.org/10.4103/1673-5374.366489>
- [75] A.A.Barros, C.Oliveira, E.Lima, A.R.C.Duarte, R.L.Reis (2016) Gelatin-based biodegradable ureteral stents with enhanced mechanical properties, *Appl. Mater. Today*, 5, 9-18. <https://doi.org/10.1016/j.apmt.2016.07.006>
- [76] D.S.Grover, W.J.Flynn, K.P.Bashford, R.A.Lewis, Y.J.Duh, R.S.Nangia, B.Nicksch (2017) Performance and safety of a new ab interno gelatin stent in refractory glaucoma at 12 months, *Am. J. Ophthalmol.*, 183, 25-36. <https://doi.org/10.1016/j.ajo.2017.07.023>
- [77] M.Hasan, N.Al-Ghaban (2017) The effects of hyaluronic acid on bone-implant interface in RABBITS (immunohistochemical study for TNF- α), *Int. J. Adv. Biotech. Res.*, 7, 733-738.
- [78] [78] J.T.Kim, D.Y.Lee, E.J.Kim, J.W.Jang, N.I.Cho (2014) Tissue response to implants of hyaluronic acid hydrogel prepared by microbeads, *J. Tissue Eng. Regen. Med.*, 11, 32-38. <https://doi.org/10.1007/s13770-013-1106-9>
- [79] H.A.Alhadrami (2018) Biosensors: classifications, medical applications, and future prospective, *Biotechnol. Appl. Biochem.*, 65, 497-508. <https://doi.org/10.1002/bab.1621>
- [80] A.Bruinink (2018) Biosensor-bearing wound dressings for continuous monitoring of hard-to-heal wounds: now and next, *J. Biosens. Bioelectron.*, 2018, 1-19. <https://doi.org/10.29011/BBOA-117.100017>
- [81] S.H.Lu, M.Samandari, C.Li, H.Li, D.Song, Y.Zhang, A.Tamayol, X.Wang (2022) Multimodal sensing and therapeutic systems for wound healing and management: a review, *Sens. Actuators Rep.*, 4, 100075. <https://doi.org/10.1016/j.snr.2022.100075>
- [82] T.A.Khattab, S.Dacrory, H.Abou-Yousef, S.Kamel (2019) Development of microporous cellulose-based smart xerogel reversible sensor via freeze drying for naked-eye detection of ammonia gas, *Carbohydr. Polym.*, 210, 196-203. <https://doi.org/10.1016/j.carbpol.2019.01.067>
- [83] M.R.Thalji, A.A.Ibrahim, K.F.Chong, A.V.Soldatov, G.A.Ali (2022) Glycopolymers-based materials: synthesis, properties, and biosensing applications, *Top. Curr. Chem.*, 380, 45. <https://doi.org/10.1007/s41061-022-00395-5>
- [84] S.Yu, L.Ding, H.Lin, W.Wu, J.Huang (2019) A novel optical fiber glucose biosensor based on carbon quantum dots-glucose oxidase/cellulose acetate complex sensitive film, *Biosens. Bioelectron.*, 146, 111760. <https://doi.org/10.1016/j.bios.2019.111760>
- [85] J.V.Edwards, N.T.Prevoost, A.D.French, M.Concha, B.D.Condon (2015) Kinetic and structural analysis of fluorescent peptides on cotton cellulose nanocrystals as elastase sensors, *Carbohydr. Polym.*, 116, 278-285. <https://doi.org/10.1016/j.carbpol.2014.04.067>
- [86] L.Madej-Kielbik, K.Gzyra-Jagiela, J.Jóźwik-Pruska, R.Dziuba, A.Bednarowicz (2022) Biopolymer composites with sensors for environmental and medical applications, *Materials*, 15, 7493. <https://doi.org/10.3390/ma15217493>
- [87] S.Alharthi, M.E.El-Naggar, M.A.Abu-Saied, T.A.Khattab, D.I.Saleh (2022) Preparation of biosensor based on triarylmethane loaded cellulose acetate xerogel for the detection of urea, *Mater. Chem. Phys.*, 276, 125377. <https://doi.org/10.1016/j.matchemphys.2021.125377>
- [88] S.Lee, K.Gwon, H.Kim, B.J.Park, J.H.Shin (2022) High-performance amperometric carbon monoxide sensor based on a xerogel-modified PtCr/C microelectrode, *Sens. Actuator B Chem.*, 369, 132275. <https://doi.org/10.1016/j.snb.2022.132275>
- [89] X.Li, Q.Feng, K.Lu, J.Huang, Y.Zhang, Y.Hou, H.Qiao, D.Li, Q.Wei (2021) Encapsulating enzyme into metal-organic framework during in-situ growth on cellulose acetate nanofibers as self-powered glucose biosensor, *Biosens. Bioelectron.*, 171, 112690. <https://doi.org/10.1016/j.bios.2020.112690>
- [90] S.Ranjbar, S.Shahrokhian (2018) Design and fabrication of an electrochemical aptasensor using Au nanoparticles/carbon nanoparticles/cellulose nanofibers nanocomposite for rapid and sensitive detection of *Staphylococcus aureus*, *Bioelectrochem.*, 123, 70-76. <https://doi.org/10.1016/j.bioelechem.2018.04.018>
- [91] M.Benkő, N.Varga, D.Seböck, G.Bohus, Á.Juhász, I.Dékány (2015) Bovine serum albumin-sodium alkyl sulfates bioconjugates as drug delivery systems, *Colloids Surf. B Biointerfaces*, 130, 126-132. <https://doi.org/10.1016/j.colsurfb.2015.04.018>
- [92] N.Taneja, K.K.Singh (2018) Rational design of polysorbate 80 stabilized human serum albumin nanoparticles tailored for high drug loading and entrapment of irinotecan, *Int. J. Pharm.*, 536, 82-94. <https://doi.org/10.1016/j.ijpharm.2017.11.024>
- [93] Y.Shtenberg, M.Goldfeder, H.Prinz, J.Shainsky, Y.Ghantous, I.A.El-Naaj, A.Schroeder, H.Bianco-Peled (2018) Mucoadhesive alginate pastes with embedded liposomes for local oral drug delivery, *Int. J. Biol. Macromol.*, 111, 62-69. <https://doi.org/10.1016/j.ijbiomac.2017.12.137>
- [94] K.S.Joshy, M.A.Susan, S.Snigdha, K.Nandakumar, A.P.Laly, T.Sabu (2018) Encapsulation of zidovudine in PF-68 coated alginate conjugate nanoparticles for anti-HIV drug delivery, *Int. J. Biol. Macromol.*, 107, 929-937. <https://doi.org/10.1016/j.ijbiomac.2017.09.078>
- [95] L.Dai, C.L.Si (2017) Cellulose-graft-poly (methyl methacrylate) nanoparticles with high biocompatibility for hydrophobic anti-cancer drug delivery, *Mater. Lett.*, 207, 213-216. <https://doi.org/10.1016/j.matlet.2017.07.090>
- [96] A.Solanki, S.Thakore (2015) Cellulose crosslinked pH-responsive polyurethanes for drug delivery: α -hydroxy acids as drug release modifiers, *Int. J. Biol. Macromol.*, 80, 683-691. <https://doi.org/10.1016/j.ijbiomac.2015.07.003>

- [97] R.de Oliveira Pedro, F.M.Goycoolea, S.Pereira, C.C.Schmitt, M.G.Neumann (2018) Synergistic effect of quercetin and pH-responsive DEAE-chitosan carriers as drug delivery system for breast cancer treatment, *Int. J. Biol. Macromol.*, 106, 579-586. <https://doi.org/10.1016/j.ijbiomac.2017.08.056>
- [98] K.M.Rao, A.Kumar, M.Suneetha, S.S.Han (2018) pH and near-infrared active; chitosan-coated halloysite nanotubes loaded with curcumin-Au hybrid nanoparticles for cancer drug delivery, *Int. J. Biol. Macromol.*, 112, 119-125. <https://doi.org/10.1016/j.ijbiomac.2018.01.163>
- [99] G.Voicu, R.E.Geanaliu-Nicolae, A.A.Pîrvan, E. Andronescu, F.Iordache (2016) Synthesis, characterization and bioevaluation of drug-collagen hybrid materials for biomedical applications, *Int. J. Pharm.*, 510, 474-484. <https://doi.org/10.1016/j.ijpharm.2015.11.054>
- [100] [100] A.Y.Lee, N.Mahler, C.Best, Y.U.Lee, C.K.Breuer (2014) Regenerative implants for cardiovascular tissue engineering, *Transl. Res.*, 163, 321-341. <https://doi.org/10.1016/j.trsl.2014.01.014>
- [101] [101] G.T.Tihan, C.Ungureanu, R.C.Barbaresso, R.G.Zgârian, I.Rău, A.Meghea, M.G.Albu, M.V.Ghica (2015) Chloramphenicol collagen sponges for local drug delivery in dentistry, *Comptes Rendus Chimie*, 18, 986-992. <https://doi.org/10.1016/j.crci.2015.06.004>
- [102] N.Mizutani, S.Kageyama, M.Yamada, M.Hasegawa, K.Miyamoto, T.Horiuchi (2014) The behavior of ligament cells cultured on elastin and collagen scaffolds, *J. Artif. Organs*, 17, 50-59. <https://doi.org/10.1007/s10047-013-0736-y>
- [103] A.Rogina (2014) Electrospinning process: Versatile preparation method for biodegradable and natural polymers and biocomposite systems applied in tissue engineering and drug delivery, *Appl. Surf. Sci.*, 296, 221-230. <https://doi.org/10.1016/j.apsusc.2014.01.098>
- [104] P.D.Ward, S.L.Thibeault, S.D.Gray (2002) Hyaluronic acid: its role in voice, *J. Voice*, 16, 303-309. [https://doi.org/10.1016/S0892-1997\(02\)00101-7](https://doi.org/10.1016/S0892-1997(02)00101-7)
- [105] A.J.R.Lasprilla, G.A.R.Martinez, B.H.Lunelli, A.L.Jardini, R.M.Filho (2012) Polylactic acid synthesis for application in biomedical devices—a review, *Biotechnol. Adv.*, 30, 321-328. <https://doi.org/10.1016/j.biotechadv.2011.06.019>
- [106] B.Tyler, D.Gullotti, A.Mangraviti, T.Utsuki, H.Brem (2016) Polylactic acid (PLA) controlled delivery carriers for biomedical applications, *Adv. Drug Deliv. Rev.*, 107, 163-175. <https://doi.org/10.1016/j.addr.2016.06.018>
- [107] M.T.Khorasani, S.A.Mirmohammadi, S.Irani (2011) Polyhydroxybutyrate (PHB) scaffolds as a model for nerve tissue engineering application: fabrication and *in vitro* assay, *Int. J. Polym. Mater.*, 60, 562-575. <https://doi.org/10.1080/00914037.2010.531809>
- [108] G.Uzun, D.Aydemir (2017) Biocomposites from polyhydroxybutyrate and bio-fillers by solvent casting method, *Bull. Mater. Sci.*, 40, 383-393. <https://doi.org/10.1007/s12034-017-1371-7>
- [109] H.Xiao, T.Yang, Q.Lin, G.Q.Liu, L.Zhang, F.Yu, Y.Chen (2016) Acetylated starch nanocrystals: preparation and antitumor drug delivery study, *Int. J. Biol. Macromol.*, 89, 456-464. <https://doi.org/10.1016/j.ijbiomac.2016.04.037>
- [110] D.LeCorre, J.Bras, A.Dufresne (2010) Starch nanoparticles: a review, *Biomacromolecules*, 11, 1139-1153. <https://doi.org/10.1021/bm901428y>
- [111] Z.Li, H.R.Ramay, K.D.Hauch, D.Xiao, M.Zhang (2005) Chitosan–alginate hybrid scaffolds for bone tissue engineering, *Biomaterials*, 26, 3919-3928. <https://doi.org/10.1016/j.biomaterials.2004.09.062>
- [112] Y.C.Kuo, C.C.Lin (2013) Accelerated nerve regeneration using induced pluripotent stem cells in chitin–chitosan–gelatin scaffolds with inverted colloidal crystal geometry, *Colloids Surf. B Biointerfaces*, 103, 595-600. <https://doi.org/10.1016/j.colsurfb.2012.11.001>
- [113] X.Yu, A.Bichtelen, X.Wang, Y.Yan, F.Lin, Z.Xiong, R.Wu, R.Zhang, Q.Lu (2005) Collagen/chitosan/heparin complex with improved biocompatibility for hepatic tissue engineering, *J. Bioact. Compat. Polym.*, 20, 15-28. <https://doi.org/10.1177/0883911505049653>
- [114] K.Xu, D.A.Cantu, Y.Fu, J.Kim, X.Zheng, P.Hematti, W.J.Kao (2013) Thiol-ene Michael-type formation of gelatin/poly (ethylene glycol) biomatrices for three-dimensional mesenchymal stromal/stem cell administration to cutaneous wounds, *Acta Biomater.*, 9, 8802-8814. <https://doi.org/10.1016/j.actbio.2013.06.021>
- [115] S.P.Hoerstrup, R.Sodian, S.Daebritz, J.Wang, E.A.Bacha, D.P.Martin, A.M.Moran, K.J.Guleserian, J.S.Sperling, S.Kaushal, J.P.Vacanti, F.J.Schoen, J.E.Mayer (2000) Functional living trileaflet heart valves grown *in vitro*, *Circulation*, 102, III-44-III-49. https://doi.org/10.1161/circ.102.suppl_3.III-44
- [116] S.Kulkarni Vishakha, D.Butte Kishor, S.Rathod Sudha (2012) Natural polymers, a comprehensive review, *Int. J. Res. Pharm. Biomed. Sci.*, 3, 1597-1613.
- [117] X.Tong, W.Pan, T.Su, M.Zhang, W.Dong, X.Qi (2020) Recent advances in natural polymer-based drug delivery systems, *React. Funct. Polym.*, 148, 104501. <https://doi.org/10.1016/j.reactfunctpolym.2020.104501>
- [118] E.Güncüm, N.Icsiklan, C.Anlacs, N.Ünal, E.Bulut, T.Bakirel (2018) Development and characterization of polymeric-based nanoparticles for sustained release of amoxicillin—an antimicrobial drug, *Artif. Cells Nanomed. Biotechnol.*, 46, 964-973. <https://doi.org/10.1080/21691401.2018.1476371>
- [119] K.C.Panigrahi, C.N.Patra, G.K.Jena, D.Ghose, J.Jena, S.K.Panda, M.Sahu (2018) Gelucire: a versatile polymer for modified release drug delivery system, *Future J. Pharm. Sci.*, 4, 102-108. <https://doi.org/10.1016/j.fjps.2017.11.001>
- [120] B.A.Lodhi, M.A.Hussain, M.Sher, M.T.Haseeb, M.U.Ashraf, S.Z.Hussain, I.Hussain, S.N.A.Bukhari (2019) Polysaccharide-based super-porous, superabsorbent, and stimuli responsive hydrogel from sweet basil: a novel material for sustained drug release, *Adv. Polym. Technol.*, 2019, 1-11. <https://doi.org/10.1155/2019/9583516>

- [121] T.Bibire, O.Yilmaz, C.M.Ghiciuc, N.Bibire, R.Dănilă (2022) Biopolymers for surgical applications, *Coatings*, 12, 211. <https://doi.org/10.3390/coatings12020211>
- [122] M.C.Biswas, B.Jony, P.K.Nandy, R.Chowdhury, S.Halder, D.Kumar, S.Ramakrishna, M.Hassan, M.A.Ahsan, M.E.Hoque, M.A.Imam (2022) Recent advancement of biopolymers and their potential biomedical applications, *J. Polym. Environ.*, 30, 51-74. <https://doi.org/10.1007/s10924-021-02199-y>
- [123] N.Zabihollahi, A.Alizadeh, H.Almasi, S.Hanifian, H.Hamishakar (2020) Development and characterization of carboxymethyl cellulose based probiotic nanocomposite film containing cellulose nanofiber and inulin for chicken fillet shelf life extension, *Int.J.Biol.Macromol.*, 160, 409-417. <https://doi.org/10.1016/j.ijbiomac.2020.05.066>
- [124] R.Gheorghita, L.Anchidin-Norocel, R.Filip, M.Dimian, M.Covasa (2021) Applications of biopolymers for drugs and probiotics delivery, *Polymers*, 13, 2729. <https://doi.org/10.3390/polym13162729>
- [125] P.C.Pires, F.Mascarenhas-Melo, K.Pedrosa, D.Lopes, J.Lopes, A.M.M.Soaes, D.Peixoto, P.Giram, F.J.B.Veiga, A.C.Paiva-Santos (2023) Polymer-based biomaterials for pharmaceutical and biomedical applications: a focus on topical drug administration, *Eur. Polym. J.*, 18, 111868. <https://doi.org/10.1016/j.eurpolymj.2023.111868>

IZVOD

PREPIS PRIRODE: DEKODIRANJE MOĆI BIOPOLIMERA U MEDICINSKIM I FARMACEUTSKIM PRIMENAMA

Tokom proteklih nekoliko godina, upotreba nekoliko biopolimera prirodnog, sintetičkog ili mikrobnog porekla doživela je vrhunac u različitim medicinskim i farmaceutskim primenama, kao što su isporuka lekova, formulacija lekova, skele za inženjering tkiva, medicinski implantati (npr. protetika, stentovi), materijali za zarastanje rana i zavoje i biosenzivanje. Ovo se uglavnom pripisuje njihovoj lakoći obrade, biorazgradivosti, visokoj bioaktivnosti i biokompatibilnosti u poređenju sa sintetičkim polimerima. Štaviše, pojavio se porast u razvoju bio-/nanokompozita, sa ciljem da se poboljšaju inherentna svojstva sirovih biopolimera dobijenih iz prirodnih/mikrobnih izvora. Ovaj pregled je uglavnom fokusiran na različite tipove biopolimera ili njihovih kompozita koji se koriste u medicinskoj ili farmaceutskoj industriji i baca svetlo na ključne prednosti i ograničenja povezana sa njihovom sintezom ili upotrebom. Nadalje, u članku je predstavljena lista komercijalizovanih biopolimernih kompozita sa diskusijom o budućem obimu korišćenja ovih „darova prirode“ u oblasti medicine.

Ključne reči: biopolimeri; biosensing; isporuka lekova; hirurški implantati; inženjering tkiva

Naučni rad

Rad primljen: 02.03.2024.

Rad prihvaćen 05.04.2024.

Rad je dostupan na sajtu: www.idk.org.rs/casopis

Mansi Sharma <https://orcid.org/0000-0001-6536-1075>

Priyanka Mahajan <https://orcid.org/0000-0002-6307-7975>

Priya Agarwal¹, Satya Prakash^{1*}, Gaurav Saini², Ikhwan Syafiq Mohd Noor³

¹ Department of Civil Engineering, Sharda University, Greater Noida, Uttar Pradesh, India; ² Department of Civil Engineering, Netaji Subhas University of Technology, Delhi, India; ³ Physics Division, Centre of Foundation Studies for Agricultural Science, Universiti Putra Malaysia, Selangor Darul Ehsan, Malaysia

Review paper

ISSN 0351-9465, E-ISSN 2466-2585

<https://doi.org/10.62638/ZasMat1176>



Zastita Materijala 65 (4)
595 – 611 (2024)

Recent Advances in Research from Plastic Materials to Microplastics

ABSTRACT

Plastics have become ubiquitous in our lives. Due to the ever-increasing population, rapid urbanization, and industrial advancement, the use of plastics has increased manifold. These plastic materials often disintegrate into microplastics (MPs) which are less than 5mm in size. MPs mostly enter aquatic habitats through improper waste management, illegal dumping, and unavoidable and unintentional discharges that take place during construction, manufacturing, farming, domestic consumption, and recreational activities. This review centers on exploring the origin, occurrence, and possible adverse effects of MPs on human well-being. Of the 485 literature reviewed for the study between 2014-2023, 105 were found to be related to the MPs which were spread over 10 themes. The maximum number of papers were on sources of MPs, followed by MPs in freshwater ecosystems and waste management. The least number of literature was from the themes, transport of MPs and MPs in the soil environment. The literature was published mostly in China, India, Europe, and the Americas. Other countries like Australia, Latin America, Africa, and the Middle East contribute very little. The literature scan reveals that only 9% of all the generated plastic waste material is recycled, 12% is burned, and 79% of plastic litter is dumped in landfills and oceans. The dumped plastic settles and pollutes a variety of environmental matrices. MPs are intentionally manufactured to be added to personal care products that are washed down the drains through sewage or industrial wastewater. These MPs vary in density and colour, subject to the polymer type, and are present in varying sizes and concentrations in aquatic environments. The characterization of MPs originating from different types of polymer materials, in the reviewed literature, was performed based on the data obtained from Scanning Electron Microscopy Energy Dispersive Spectroscopy (SEM-EDS), Attenuated Total Reflection Fourier Transform Infra-Red spectroscopy (ATR-FTIR), Raman spectroscopy, and Atomic Force Microscopy (AFM). MPs have the potential to absorb harmful hydrophobic pollutants from the surroundings resulting in an indirect transfer of contaminants into the food web. Such MPs enter and affect humans, causing problems with the reproductive system, body weight, sex ratio, and live births. MPs pose a serious threat to organisms when ingested since they can obstruct the digestive tract, leading to oxidative and pathological stress, slowing down growth, and interfering with reproduction. Apart from the above, a comprehensive analysis of MP pollution, as well as its effect on human beings and the environment, has been discussed in terms of source identification and abundance. Also, has been discussed is a detailed review of the existing waste material recycled into new materials or reused without alteration or degradation to produce new energy sources. In the end, integrated strategies have been proposed to prevent the input of plastic waste material into the environment, by source control, improved plastic waste management, and techniques for degradation and conversion of MPs.

Keywords: Microplastics; landfill; health impacts; aquatic environment; management; eco-friendly

* Corresponding author: Satya Prakash

E-mail: satya.prakash@sharda.ac.in

Paper received: 6.03.2024.

Paper accepted: 14.05.2024.

Papir is available on the website: www.idk.org.rs/journal

1. INTRODUCTION

Plastics are an important part of human daily life activities. They are flexible, lightweight, portable, and easy to transport and hence are omnipresent in our daily lives. Plastic materials have made significant contributions to food packaging, drug delivery, protection against infectious illness, roads, and pavements [1]. The increase in global plastic production is evident, with the output reaching 390 million tons in 2021 but is estimated to double in the next 20 years [2]. Only 9% of the produced plastic waste material is recycled, 12% is incinerated, and 79% of plastic litter is dumped in landfills and oceans. The dumped plastic settles and pollutes a variety of environmental matrices [3]. According to the United Nations Environment Programme, an estimated 9-14 million tons of plastic waste material found its way to the aquatic environment in 2016 which is expected to increase and may reach between 23 and 37 million tons per year by 2040 unless corrective actions are taken [4]. This is due to improper management, illegal dumping, and unavoidable and unintentional discharges of plastic waste causing severe ecological problems [5]. It is almost impossible to remove plastic from the environment, as the burning of plastics causes air pollution by emitting nitrogen oxides, dioxins, and dioxin-related chemicals into the atmosphere [6]. Once in the environment, plastic undergoes mechanical (erosion, abrasion), chemical (photo-oxidation, temperature), and biological (degradation by micro-organisms) actions [7]. All these degradation processes lead to their breakdown into microplastics (MPs) [8].

The term "microplastics" was introduced in 2004 by Richard Thompson [9]. The International Organization for Standardization (2020) has Technical Committee 61 (ISO/TC 61) focused on plastics and a Sub-committee 14 (SC 14) that deals with environmental aspect and defines MPs as solid plastic particles of a specific size range (1 μm to 1000 μm) [10]. Recently, researchers defined MPs as particles that are less than 5 mm in size [8]. MPs have been recognized as emerging pollutants (EPs) with potentially detrimental effects on river health and freshwater ecosystems. Harmful chemicals, including phthalates or polybrominated diphenyl ethers, have been found in MPs [11]. MPs are ubiquitous and have been detected in different sizes, concentrations, and chemical compositions in diverse environments, including marine environments [12] rivers and lakes [13], air [14], and soil [15].

There are various routes through which MPs enter freshwater environments [16]. These pathways highlight the pervasive nature of MP pollution and the diverse sources contributing to its presence in rivers and other water bodies. It includes run-off from various sources based on land, such as sewage sludge, agricultural plastic, garbage, road marking paint, tyre-wear debris, household dust, and artificial turf [17]. It is also released through wastewater such as washing synthetic clothes [18]; cosmetic microbeads [16]; and fragments of sanitary pads and wet wipes when flushed down the toilet. Sadia et al. [19] listed different types of MPs detected in wastewater treatment plants (WWTPs) viz., polypropylene (PP), polyethylene (PE), polycarbonate (PC), polyurethane (PU), polystyrene (PS), polyethylene terephthalate (PET), polyester (PES), and polyvinyl chloride (PVC). These MPs originate every day, enter WWTPs primarily through domestic wastewater, and make it a challenge to effectively capture and completely remove them due to their small size. The effluents from WWTP are transported from land via rivers to the oceans, contributing to MP pollution in marine ecosystems [20]. It is estimated that the global input of plastic debris being carried by rivers into the sea ranges between 0.41 to 4 $\times 10^6$ t/y [21]. The aquatic organisms ingest these MPs which can lead to various health issues, including internal blockages and damage to the gastrointestinal tract in fish, resulting in decreased appetite and mortality. These MPs have the potential to contaminate the sources of drinking water, migrate up the food chain, and emit toxic compounds that may be hazardous to human health and cause cancer. Furthermore, exposure to MPs can cause oxidative stress, metabolic dysfunction, immunological responses, neurotoxicity, and impacts on developing and reproductive systems [22].

Due to the rising level of demand for plastic products, there is an increase in production rates, which poses a significant challenge in the fight against MP pollution. As plastic production continues to grow, likely, MPs pollution will also increase, unless significant measures are taken to address its sources and impacts. Therefore, policies and laws are required to be implemented for plastic use, management, and disposal. Governments around the world have taken steps to address this issue by implementing measures to curb the usage of disposable plastic products in India [23], cosmetic products containing plastic microbeads in the U.K., U.S. and Canada, plastic bags in India, Australia, Bangladesh, Rwanda, South Africa and China [24], and non-biodegradable table-

ware in France [25]. Besides banning and limiting the use of plastics, Sweden has initiated the concept of home garbage collection and attained zero waste and sustainable energy by recycling 99% of household waste [26]. These regulations and bans are significant steps toward reducing the environmental impact of plastic pollution [25]. It will not only reduce the use of plastics but may also lead to the development of an alternative eco-friendly material to encourage a shift towards more sustainable practices. Considering the severity of the effects of MPs on humans, the environment, land, and aquatic animals, this study is a comprehensive review to assess the present state of the art about the characterization of MPs, the origin and abundance of MPs in rivers and identify toxicological effects on the environment and the human health. Additionally, it aims to identify the awareness gaps and take note of policy initiatives to minimize MPs in rivers and their management.

2. SCIENTOMETRIC ANALYSIS

2.1 Literature Search

For a better understanding of subject areas of interest related to MPs, the published papers were analyzed from 2004, when the term microplastics was first introduced by Thompson et al., [9] in 2004 to 2023. As per the Google Scholar database, the number of articles published on MPs vis-à-vis year is as,

2004-2008: 1520
 2009-2013: 2880
 2014-2018: 14,300 and
 2019-2023: 31,500

Since most of the articles were published after 2014, this paper focuses on the articles for the period between 2014 and 2023.

The online databases used to search for the papers were, Web of Science (<https://www.webofscience.com/>), Scopus (<https://www.scopus.com/>), and Science Direct (<http://www.sciencedirect.com>). “Microplastics”, “aquatic environment”, “rivers”, “environmental impacts”, “human health” and “management” are the search keywords used resulting in 485 articles. After eliminating irrelevant literature and then removing duplication of literature in databases, 105 articles, related to the topic, were selected for the study. The selected articles were classified according to the publication year, publication area, and the characterization techniques used in the study.

2.2 Overview of selected literature

The literature obtained from keyword search is shown in Table 1 as the initial number of articles indexed in different databases. After filtering the articles related to the title and removing the duplicates, the final number of articles viz., 105 were finalized for study.

Table 1. Literature search results

Database journal	Initial number of articles	Final number of articles
Web of Science (ESCI)	60	26
SCI	36	19
SCIE	70	40
Scopus	155	89
Pubmed	63	38
Pubmed Central	31	11
Medline	46	29
Others (Book chapter/conferences/facts /thesis)	24	13
Total	485	105 (excluding duplication)

The selected literature was **classified into 10 themes** viz., plastic waste and its additives, MPs pollution and its challenges, sources, and transport of MPs, MPs in soil environment, freshwater ecosystem, and aquatic system, toxicity of MPs in environ-

ment, impacts on human health, waste management and removal/treatment of plastics and MPs as depicted in Figure 1, where the numbers in parentheses are the number of articles found under the respective class, out of the total 105.

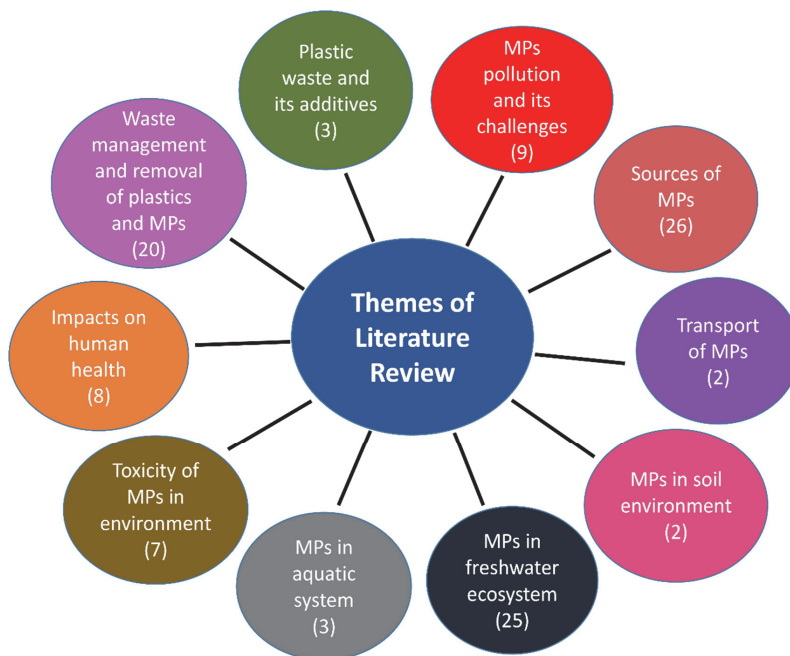


Figure 1. Themes of literature review

The **year-wise distribution** of the articles (Figure 2) shows an increase in the number of publications with each passing year since 2014, however, in the initial years, till 2016 the numbers were very less. Since 2017, the numbers started increasing and most of the publications came out after 2018, which peaked at 21 in 2021 and since then it has

decreased to 19 in 2023. The changing trend in the number of publications shows that MP distribution has become a highly researched topic, attracting a significant number of academic research. The number of publications slightly dropped in 2022, as the focus is more on developing more innovative and efficient methods for controlling MPs.

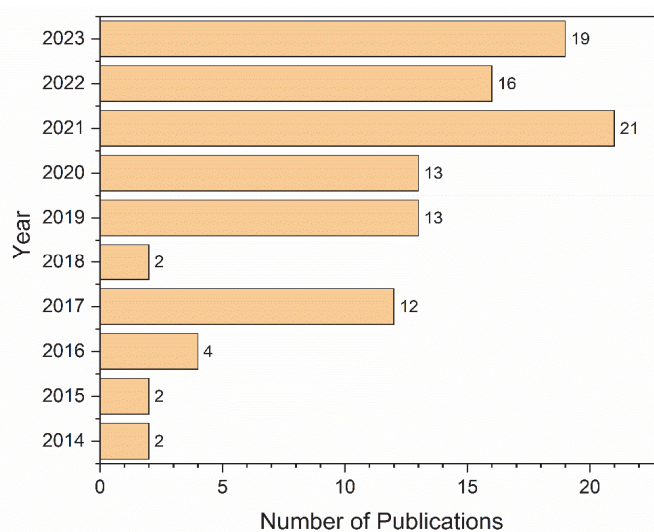


Figure 2. Number of papers published over the last 10 years

The **spatial spread** of the publications revealed that most of the research was carried out in countries such as China, India, the UK, and North America, as depicted in Figure 3. Latin American, African,

and Middle Eastern countries conducted very limited studies. The least number of publications (only one) is from Turkey, Finland, Sri Lanka, and Brazil.

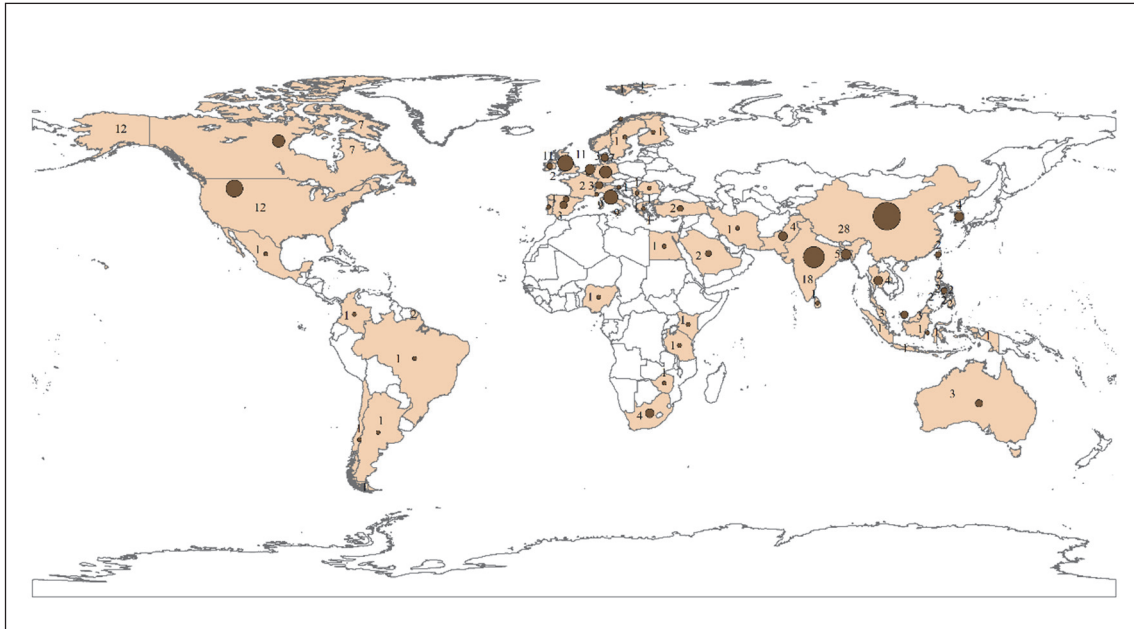


Figure 3. Publications' country distribution

The **main characterization factors** of the MPs were also studied and five factors were considered, viz., Size, Shape, Colour, Surface, and polymeric

composition (Figure 4). Further, how these factors were determined using which methodology(ies) were also studied.

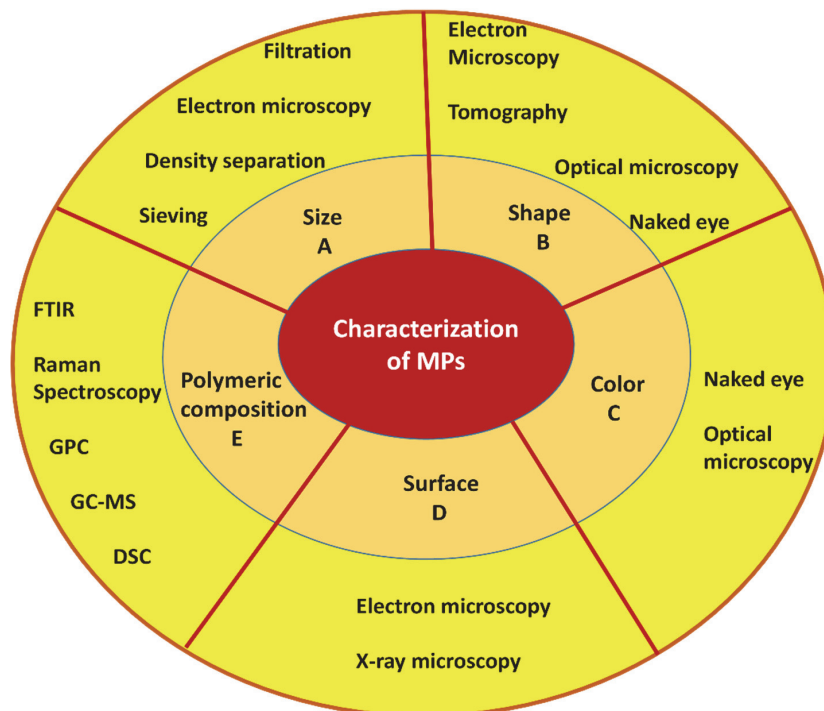


Figure 4. Summary of the characterization of MPs with the analytical methods

The current research on the characterization techniques of MPs includes ATR-FTIR, SEM-EDS, Raman spectroscopy, and AFM (Table S1).

To summarise, this paper is an attempt to present an up-to-date assessment of recent and advanced research about microplastics, their origin and occurrence, identification and removal methods, and proposes integrated strategies to prevent the input of plastic waste material into the environment, by source control, improved plastic waste management and techniques for degradation and conversion of MPs.

3. ORIGIN OF MPS

The origin of MPs in aquatic systems is multifaceted, with various sources contributing to their presence. MPs are found to exhibit a broad range of characteristics, including variations in size ($> 1 \mu\text{m}$ to $< 5 \text{mm}$) [8], shape (fibers, films, foams, and fragments) [15], colour (blue, white, green, black, brown, pink, and grey) [27], chemical composition (varying with the type of polymer) [28], and specific density (ranging from 0.89g/cm^3 to 1.58g/cm^3) [29]. These differences are the result of its diverse sources and processes. MPs are commonly categorized as primary and secondary sources. Primary MPs are designed for commercial use to be added intentionally to personal care products such as cleansers, shampoos, toothpaste, and cosmetics. Although primary MPs constitute just a fraction of the total MPs discovered (from $1 \mu\text{m}$ to 5mm) [30], sewage and wastewater are recognized as significant sources of MP pollution because these can easily pass through the filtration units and end up in aquatic environments [19]. Secondary MPs originate after large plastics breakdown on exposure to UV radiation, thermal degradation, biodegradation, hydrolysis, and mechanical abrasion [30]. Various materials, such as plastic shopping bags, containers, sewage and industrial waste, textiles, fishing gear, and tyres, might act as secondary pollutants.

The land-based point source of MPs is the direct inflow of wastewater effluents from coastal cities into the nearby coastal waters. In past studies, MPs have been detected in drinking groundwater [31], bottled water [32], and commercial food-grade sea salt [33]. Table S2 in supplementary information enumerates the different sources with their concentration such as PCPs, textiles, food packaging containers, etc that discharge MPs into the environment.

Among the various sources of MP pollution, a significant contribution is from textiles and single-use plastics. Fabrics made of polymers like nylon, polyes-

ter, and acrylic shed millions of microfibers with every wash. The composition of the textile, cleaning conditions, and detergent types all influence the release of these microfibers [18]. A study in Sweden provides insights into the staggering volume of MPs released from household laundry (8–950 tonnes of MP production per year) [34]. In a study [35], the quantities of fiber fragments released were 137,951 (65% polyester/35% cotton) and 728,789 (100% polyacrylonitrile (PAN)) while washing 6 kg of clothing. Direct washing of clothes in rivers, especially in underdeveloped and developing countries is another practice that directly introduces MPs into aquatic ecosystems [36]. Apart from textiles and single-use plastics, food packaging, straws, and cups are other significant contributors to plastic pollution. Plastic-coated paper cups, which contain polymers like PE, PP, and PS on the inside of the cup, can release 675-5984, 781-4951, and 838-5215 MPs/L respectively into beverages [37], consumed by humans. These MPs have harmful effects on human beings and after passing through the wastewater treatment plant (WWTP), end up in rivers and oceans.

4. OCCURRENCE OF MPS

Microplastic pollution varies significantly based on geographical locations. Different regions experience varying levels of pollution. Its distribution, quantity, and movement are influenced by complex factors including human activities (such as plastic usage and disposal), population density (which correlates with plastic consumption and waste generation), meteorological conditions (dispersion of plastic), and hydrological processes (which influence movement within water bodies) [38]. Studies conducted globally [39,40, 41], highlight the existence of MPs in riverine environments worldwide. MPs can enter rivers through surface runoff from roads and urban areas, wind dispersal, atmospheric deposition, and WWTP effluents [13]. Rivers are sources of MPs as it is consumed by the biota that inhabits river systems and wastewater sinks for untreated water discharged from the industry [39]. The sources of MPs have been identified by Horton et al. [42] in the river Thames basin (UK), which includes MPs from markings on the road surface from sewage and discharged input.

MPs of different sizes ($50 \mu\text{m}$ to 5mm) have been reported in rivers globally viz., the Ergene, Turkey [40]; Karnafull, Bangladesh [43]; Ganga, India [44]; Haihe, China [13]; Lawaye, Philippines [45] among many others. Table 2 lists the rivers across the diverse regions with the data on the concentration and particle size of the MPs.

Table 2. Abundance of MPs in rivers around the world

River	Country	Concentration	Particle size	References
		(MPs/ m ³)	(mm)	
Haihe River	China	0.69 to 74.95	0.333-5	[13]
Netravathi River	India	288	0.3-5	[39]
Ergene River	Turkey	(4.65 ± 2.06) x 10 ³ (May)	> 0.045	[40]
		(6.90 ± 5.16) x 10 ³ (Sept)		
Kosasthalaiyar River	India	(4.94 ± 8.98) x 10 ³	> 0.5	[41]
Karnafull River	Bangladesh	(0.57 ± 0.07 - 6.63 ± 0.52) x 10 ³		[43]
Ganga River	India	0.38–0.684	2.5–5	[44]
Lawaye River	Philippines	3333	0.363-5	[45]
Chao Phraya River	Thailand	21 ± 16	0.335- 5.15	[47]
Adyar River	India	0.33 x 10 ³	0.335 - 5	[48]
Kosasthalaiyar River	India	0.67 x 10 ³	0.335- 5	[48]
Multhirappuzhayar River	India	0.20 x 10 ³	0.335-5	[48]
Tapi-Phumduang River	Thailand	(0.136–0.562) x 10 ³	-	[49]
Rivers in Sungai Dungun	Malaysia	22.8–300.8	-	[50]
Nakdong River	South Korea	293 ± 83 (upstream)	0.050–0.150	[46]
		4760 ± 5242 (downstream)		
		210-15,560 (rainy season)	0.05-0.33	[51]
		260-1410 (dry season)		

For instance, the Ergene River in Turkey exhibits seasonal concentrations varying from $(4.65 \pm 2.06) \times 10^3$ in May to $(6.90 \pm 5.16) \times 10^3$ MPs/m³ in September, with particles exceeding 45 µm [40]. The Ganga River in India reported a concentration between 0.38 and 0.684 MPs/m³, with particle sizes ranging from 2.5 to 5 mm [44]. Other rivers in India including Netravathi, Kosasthalaiyar, Adyar, and Multhirappuzhayar also present varying concentrations and particle sizes [39, 41, 48]. The MP concentration of rivers from different countries including Bangladesh, Thailand, China, Malaysia, Philippines, and South Korea [13, 43, 45, 46, 47, 50] have varying concentrations with different sizes.

In South Korea, MPs abundance in the Nakdong River shows seasonal variations, with higher quantities observed during the rainy season (210 to 15,560 items/m³) as compared to the dry season (260 to 1410 items/m³). This variation may be influenced by factors such as increased surface runoff during heavy rainfall, carrying more MPs into the river [51]. Lebreton et al. [52] reported that 1.05×10^5 tons of plastic waste materials are dumped into the Indian Ocean annually by the Ganges in India, one of the rivers that carry millions of tons of plastic waste to the seas. According to Napper et al. [53], the

Ganges, along with the Brahmaputra and Meghna (GBM), release up to 1–3 billion MPs into the Indian Ocean daily. These inputs have severe implications for marine ecosystems and organisms, emphasizing the urgency of addressing plastic pollution at its source.

5. MPS EXPOSURE ROUTES AND THEIR EFFECTS ON THE ENVIRONMENT AND HUMAN

MPs have hydrophobic surfaces with a high surface area-to-volume ratio to adsorb organic chemicals from the surrounding environment thus increasing the toxicity [54]. The toxicity is influenced by factors such as size, shape, weathering process, surface charge, adsorption, etc. [55]. The type and concentrations of additives contained in plastics are the crucial factors, some of which may be toxic. When these plastics break down into MPs, their additives are released into the environment and subsequently absorbed and accumulated by living organisms. Phthalate plasticizers, bisphenol A (BPA), brominated flame retardants, triclosan, nonylphenol, and organotin chemicals are among the additives in plastics [56]. Therefore, interactions between MP and phytoplankton, zooplankton, and algae disrupt the marine carbon cycle and have an impact on carbon fixation,

which in turn affects climate change and global warming [57]. MPs pose a potential threat to human health due to their common existence in the environment. It has also been reported that these compounds may accumulate in humans because of biological processes. The risk of human exposure increases with

the movement of MPs. According to Cimmino et al. [58], BPA inhibits thyroid hormone, reduces pancreatic beta cell function, and worsens obesity and cardiovascular issues. Also, the usage of phthalates, a different addition, has been linked to cancer, abnormal sexual behavior, and birth defects [59].

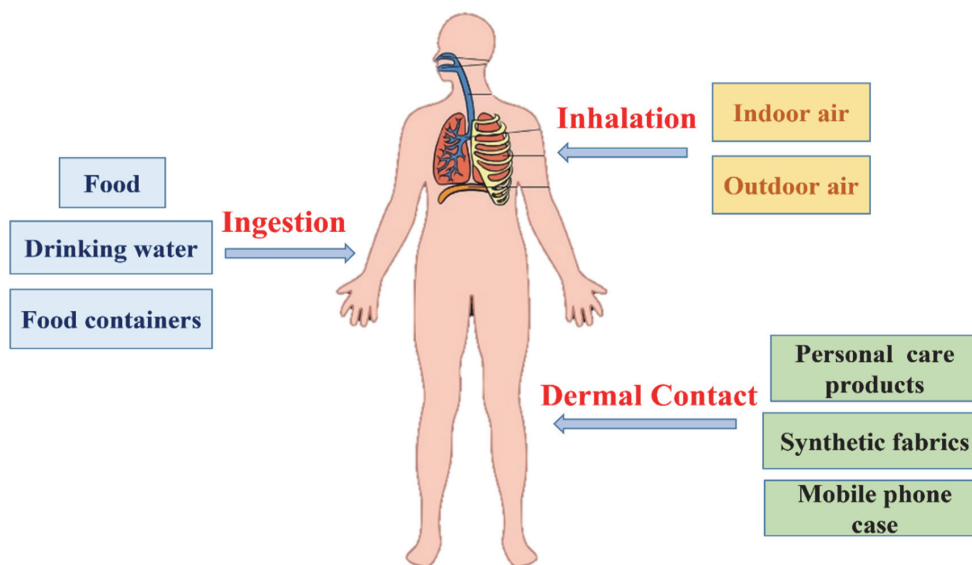


Figure 5. Pathways of human exposure to MPs

Humans are exposed to MPs through different routes: the ingestion of water or food, the inhalation of both indoor and outdoor air, and dermal contact through personal care products, clothing, and objects like cell phone cases (Figure 5). MPs are readily ingested by a variety of marine organisms, entering the food chain at its lowest levels. When these contaminated organisms, in the form of seafood, are consumed by humans, the MPs are transferred to the human body. These MPs affect humans causing problems with the reproductive system, body weight, sex ratio, and live births [60]. Common takeaway food containers are typically made of polypropylene (PP), polystyrene (PS), polyethylene (PE), and polyethylene terephthalate (PET) which become MPs contaminated on exposure to plastic products and goods that leach BPA [61]. A person who eats in takeaway containers 4–7 times a week consumes 12–203 pieces of MPs [62].

MPs act as vectors for pollutants in the environment, harmful diseases, and chemical parasites. MPs remain suspended in the atmosphere because of their small size and low density, making them inhalable. This ability of MPs to enter the respiratory system raises concerns about their potential health

effects on human beings [63]. When MPs are inhaled, they can potentially damage the human lungs and the gastrointestinal tract (GIT) followed by endocytosis [64]. Once MPs are inhaled, these particles can interact in various ways with the pulmonary epithelium, through active cellular uptake, direct cellular penetration, or diffusion. In Paris, MP contamination is not only limited to outdoor air (5.4 fibers/m³) but also to indoor air (0.9 fibers/m³) [65]. The average concentration of MPs reported in Shanghai is 1.42 particles/m³ in the outdoor air within the size range of 23 to 5000 μm [66]. According to Tursi et al. [67] the main sources of MPs in the air, both indoors and outdoors, include landfills, synthetic textiles, building materials, waste, and the degradation processes of plastic.

The application of cosmetics such as face creams or facial cleansers to the skin, increases the exposure risk of MPs. This damage causes localized inflammation and cytotoxicity which harm the skin [68]. The MPs are also transferred to human hands during the use of protective mobile phone cases (PMPCs) [69]. Table 3 indicates plastic components and their associated health and environmental effects.

Table 3. Health effects associated with the type of plastic polymer

Type of polymer	Health effects	Environmental effects	References
Polyethylene terephthalate (PETE)	Necrosis, erythema, pulmonary edema and coughing	Precursors of ozone in atmospheric environments	[70]
Poly Vinyl Chloride (PVC)	Liver damage, anemia, weakness, kidney and brain damage, carcinogenic, and effects on the central nervous system	Deteriorate air and drinking water quality	[71]
Polycarbonate (PC)	liver function alternation, insulin resistance changes, brain damage	Impacts the emission of greenhouse gases	[72]
Low-Density Polyethylene (LDPE)	Irritated throat, eyes, breathing shortness, mood swings, blurred vision, memory loss, nausea, headache and vomiting	Greenhouse gas emissions that contribute to climate change	[73]
High-Density Polyethylene (HDPE)	Brain function is limited by irritation to the eyes, skin, and respiratory system	Upon exposure to room temperature air, undergoes autoxidation to generate benzoic acid	[74]

It has also been reported in Table 3 that there are varying health and environmental effects for different polymers. For instance, exposure to PETE may result in necrosis and pulmonary complications, in addition to its involvement in the generation of ozone [70]. The utilization of PVC carries the potential of inducing liver injury and central nervous system impacts, while simultaneously contributing to the degradation of air and water quality [71]. PC and LDPE instigate a range of health issues and the emission of greenhouse gases [72,73]. Furthermore, HDPE can irritate the eyes and respiratory tract, and it undergoes autoxidation leading to the production of benzoic acid [74].

6. MANAGEMENT OF MPS

Although plastics have become ubiquitous in our lives, to minimize the effect of MPs on our health, a sustainable approach to the production and consumption of plastic products is highly desirable to protect the environment, human health, and the global economy. The marine pollution reduces the economic opportunities by damaging the marine industries (fishing and tourism) which will ultimately result in income loss among the fishermen [75]. Effective management strategies could involve a combination of research, policy-making, public engagement, and international collaboration. Authors

recommend government reduce the problem of MPs through environmental awareness campaigns to educate localities [76]. The fundamental strategies to address MP pollution should concentrate on (i) source control, through the implementation and enforcement of laws and regulations, and (ii) remediation and clean up, including removing MPs that are already present in water bodies [77].

6.1 MPs control at source

Controlling the sources of MP pollution is crucial in mitigating its impact on the environment. This can be achieved through the regulations that restrict the amount, and use of MPs, particularly in personal care and cosmetic products, thus, reducing the amount of MPs entering the aquatic environment. Additionally, the efforts to reduce disposable plastic materials by prohibiting water bottles, shopping bags, straws, and cutlery [78]. The Ministry of Environment, Forests, and Climate Change in India has made significant efforts to lessen the pollution caused by disposable plastic waste materials. Items prohibited under the Plastic Waste Management (Amendment) Rules, 2021 include stirrers, earbuds with plastic sticks, balloons with plastic sticks, plastic flags, candy sticks, ice-cream sticks, and decorative polystyrene (Thermocol) [79]. The strategies recommended for consumers, producers, and government to control MPs at source are mentioned in Table 4.

Table 4. Control strategies for MPs at the source

Sources	Responsibility	Strategies
Laundry	Consumer	Changing washing habits
		Buy textiles that release less fiber
	Producer	Setting filter in the washing machine
PCPs	Consumer	Buy plastic-free cosmetics
	Producer	Stop using plastic microbeads
	Government	Ban on plastic microbeads in PCCPs
Plastics bags	Consumer	Bringing a reusable carry bag for shopping (preferably a paper bag)
	Producer	Reduce unnecessary packaging
	Government	Ban, tax, or levy heavy fees on plastic bags/ heavy fines on usage
Bottled water	Consumer	Use of boiling water
		Use of reverse osmosis filters
	Producer	Reusable water bottle material
Government	Ban on Single-use plastics	
Tyre wear	Consumer	Change in way of operating vehicle (driving habits)
Wastewater	WWTP facility	Advanced treatment technologies

Clothes are one of the main causes of MP pollution in the world. Polyester or other types of MPs are undoubtedly present in the majority of clothing. These articles of clothing contain MP fiber that is released into the water while washing. The release of MPs can be reduced by adding a filter to washing machines which can trap these fibers [80]. Another way to reduce MPs is the use of public transit or carpooling which shall reduce tyre wear and, consequently, the release of MPs from degraded rubber [81]. It is advisable to avoid the use of products that contain MP beads including toothpaste and face washes by checking the ingredients label (It should be made mandatory for the producers to indicate the amount of MPs present/added to the product). These beads can get through filtration systems, travel long distances, and even get into the water supply. Choosing to avoid single-use plastics such as straws, glasses, plates, and takeaway containers can have a significant positive impact on reducing the plastic waste entering the environment hence reducing the production and release of MPs. Further, initiatives such as promoting the use of biodegradable alternatives, implementing recycling programs, raising public awareness about plastic pollution, encouraging businesses to adopt sustainable practices, and supporting research into innovative solutions are some of the other solutions that

when implemented may result in less production of MPs and its release in the environment.

6.2 Remediation and clean-up

The removal of MPs that are already present in water bodies is essential to prevent further contamination and minimize their impact on aquatic life. Authors have suggested that governments need to improve garbage collection systems and enhance recycling rates to prevent waste from leaking into the ecosystem between the trash can and the landfill. Additionally, strategies and initiatives to encourage businesses and users to promote the Refuse-Reduce-Reuse-Repair-Recycle circular economy would lessen the flow of MPs that end up in the environment [82]. There is a need for innovative technologies such as robotic devices to clean up MPs in aquatic environments. Moreover, designing and employing drones or autonomous vehicles equipped with sensors to find and remove MPs. The removal of MPs becomes challenging due to their small size and potential for increased ecological toxicity. Therefore, plastics can be collected and recycled into new materials, mixed with other materials, and reused by incorporating them into specific products or processes without alteration or degradation to produce new energy sources [83]. Table 5 provides details of different recycling practices for plastic waste into valuable products across different countries [84-88].

Table 5. Plastic waste into useful products

Plastic waste	Recycled product	Country	References
PET	Used to modify bitumen production which turns out to be durable and long-lasting	India	[84]
PET	Electrocatalytic upcycling into valuable commodity chemicals, potassium formate terephthalic acid, and H ₂ fuel.	China	[85]
PET powder and expanded polystyrene (EPS)	Incorporating waste foam into a bio-matrix Open-cell material for use as both acoustic and thermal insulation for industrial, civil, and maritime applications.	Italy	[86]
PVC	Used in pavement construction increases resistance to permanent deformation in terms of rutting	India	[87]
PP	Converted into oil (olefins, paraffins, cyclists, and aromatics) using supercritical water	US	[83]
PET	Used as a modifier in asphalt mixtures, tends to reduce the penetration and increase the softening point of the modified asphalt binder.	Egypt	[88]

India modifies bitumen production by adding up to 12% PET waste to achieve stronger binding between binder and aggregate for sustainable infrastructure production [84]. In China, PET is used for electrocatalytic upcycling, demonstrating the strategy for plastic waste management [85]. In Egypt, the addition of 12% PET waste material to asphalt binder upgraded the pavement service life by 2.81 times and saved around 20% of asphalt layer thickness [88]. The innovative use of PET and EPS in Italy for creating bio-matrix open-cell material capable of acting as an acoustic and thermal insulator signifies a sustainable and eco-friendly approach to recycling marine MP waste [86].

In another study, MP waste found in the ocean and soil is used as a source of liquid fuel. Here, Ni-Pd/TNPs nanocatalyst catalyst is designed for two specific reactions: catalytic cracking of MPs-phenol and steam reforming. These reactions result in the generation of valuable liquid products such as trimethyl-(2-trimethylsilylphenyl)silane, cyclohexane-1,3-dione, 2-allylaminomethylene-5,5-dimethyl-, bis(2-ethylhexyl)phthalate (BEHP), etc. and hydrogen fuel. It indicates the potential for converting MP pollution into value-added fuels and reducing threats to marine life. This approach promotes the management of MP waste through the use of sustainable materials in various industries [89].

7. CONCLUSIONS

MPs are abundant, ubiquitous, and persistent. These tiny plastic particles, often invisible to the naked eye, have permeated various ecosystems, from

the depths of oceans to the air we breathe. MPs represent a global environmental challenge with far-reaching implications. Comprehending the origins, occurrence, and health effects of MPs is vital for addressing this complex issue. The management of MPs is not only an environmental imperative but also a concern for public health and long-term sustainability. As the global community continues to address the sources, occurrence, and health effects of MPs, a multi-faceted approach involving research, regulation, education, and innovation is essential to mitigate this growing threat to our planet. It is also important to raise awareness of the impacts of MP and plastic waste mismanagement on the environment. Strict policies are required at local, national, regional, and international levels to reduce the use and consumption of plastics.

REFERENCES

- [1] R.Kumar, A.Verma, A.Shome, R.Sinha, S.Sinha, P.K. Jha, R.Kumar, P.Kumar, Shubham, S.Das, P.Sharma, P.V.Vara Prasad (2021) Impacts of plastic pollution on ecosystem services, sustainable development goals, and need to focus on circular economy and policy interventions. *Sustainability*, 13, 9963, <https://doi.org/10.3390/su13179963>
- [2] Plastics Europe Plastics – The Facts 2022 an analysis of European plastics production, demand and waste data. *Plastics Europe, Plastics the Fact 2022, Belgium*. https://plasticseurope.org/wp-content/uploads/2022/10/PE-PLASTICS-THE-FACTS_V7-Tue_19-10-1.pdf.
- [3] 3. A.A.Okunola, O.A.Kehinde, A.E.Olufiropo (2019) Public and environmental health effects of

- plastic wastes disposal: A review. *Journal of Toxicology and Risk Assessment*, 5, 76-86. <https://doi.org/10.23937/2572-4061.1510021>
- [4] UNEP (2021). *From Pollution to Solution*, p. 10.1016, [https://doi.org/S0262-4079\(18\)30486-X](https://doi.org/S0262-4079(18)30486-X),
- [5] A.Ashrafy, A.A.Liza, M.N.Islam, M.M.Billah, S.T.Arafat, M.M.Rahman, S.M.Rahman (2023) Microplastics pollution: A brief review of its source and abundance in different aquatic ecosystems. *Journal of Hazardous Materials Advances*, 9, 100215. <https://doi.org/10.1016/j.hazadv.2022.100215>
- [6] J.Ru, Y.Huo, Y.Yang (2020) Microbial degradation and valorization of plastic wastes. *Frontiers in Microbiology*, 11, 442, <https://doi.org/10.3389/FMICB.2020.00442>
- [7] F.Julienne, N.Delorme, F.Lagarde (2019) From macroplastics to microplastics: Role of water in the fragmentation of polyethylene. *Chemosphere*, 236, 124409, <http://doi.org/10.1016/j.chemosphere.2019.124409>
- [8] A.I.Osman, M.Hosny, A.S.Eltaweil, S.Omar, A.M.El-garhy, M.Farghali, P.S.Yap, Y.S.Wu, S.Nagandran, K.Batumalaie, S.C.B.Gopinath, O.D.John, M.Sekar, T.Saikia, P.Karunanithi, M.H.M.Hatta, K.A.Akinyede (2023) Microplastic sources, formation, toxicity and remediation: A review. *Environmental Chemistry Letters*, 21, 1–41, <http://doi.org/10.1007/s10311-023-01593-3>
- [9] R.C. Thompson, Y.Olsen, R.P.Mitchell, A.Davis, S. J.Rowland, A.W.G. John, D.McGonigle, A.E.Russell (2004) Lost at sea: Where is all the plastic? *Science*, 304, 838, <https://doi.org/10.1126/science.1094559>
- [10] ISO (2020). *Plastics-Environmental Aspects – State of Knowledge and Methodologies*, p. 41.
- [11] A.Parsaeimehr, C.M.Miller, G.Ozbyay (2023) Microplastics and their interactions with microbiota. *Heliyon*, 9, e15104, <https://doi.org/10.1016/j.heliyon.2023.e15104>
- [12] J.Wang, Z.Tan, J.Peng, Q.Qiu, M.Li (2016) The behaviors of microplastics in the marine environment. *Marine Environmental Research*, 113, 7–17, <https://doi.org/10.1016/j.marenvres.2015.10.014>
- [13] Y.Liu, J.Zhang, C.Cai, Y.He, L.Chen, X.Xiong, H.Huang, S.Tao, W.Liu (2020) Occurrence and characteristics of microplastics in the Haihe River: An investigation of a seagoing river flowing through a megacity in northern China. *Environmental Pollution*, 262, 114261, <https://doi.org/10.1016/j.envpol.2020.114261>
- [14] J.C.Prata (2018) Airborne microplastics: Consequences to human health? *Environmental Pollution*, 234, 115–126, <https://doi.org/10.1016/j.envpol.2017.11.043>
- [15] Y.M.Lozano, T.Lehnert, L.T.Linck, A.Lehmann, M.C.Rillig (2021) Microplastic shape, polymer type, and concentration affect soil properties and plant biomass. *Frontiers in Plant Science*, 12, 616645, <http://doi.org/10.3389/fpls.2021.616645>
- [16] G. Kalčíková, B. Alič, T. Skalar, M. Bundschuh, and A. Ž. Gotvajn (2017) Wastewater treatment plant effluents as source of cosmetic polyethylene microbeads to freshwater. *Chemosphere*, 188, 25–31, <https://doi.org/10.1016/j.chemosphere.2017.08.131>
- [17] J.Boucher, D.Friot (2017) Primary microplastics in the oceans: A global evaluation of sources. In: *Primary Microplastics in the Oceans: A Global Evaluation of Sources*, <https://doi.org/10.2305/iucn.ch.2017.01.en>
- [18] A.P.Periyasamy, A.Tehrani-Bagha (2022) A review on microplastic emission from textile materials and its reduction techniques. *Polymer Degradation and Stability*, 199, 109901, <https://doi.org/10.1016/j.polymdegradstab.2022.109901>
- [19] M.Sadia, A.Mahmood, M.Ibrahim, M.K.Irshad, A.H.A.Quddusi, A.Bokhari, M.Mubashir, L.F.Chuah, P.L.Show (2022) Microplastics pollution from wastewater treatment plants: A critical review on challenges, detection, sustainable removal techniques and circular economy. *Environmental Technology and Innovation*, 28, 102946, <https://doi.org/10.1016/j.eti.2022.102946>
- [20] I.E.Napper, A.Bakir, S.J.Rowland, R.C.Thompson (2015) Characterisation, quantity and sorptive properties of microplastics extracted from cosmetics. *Marine Pollution Bulletin*, 99, 178–185, <https://doi.org/10.1016/j.marpolbul.2015.07.029>
- [21] C.Schmidt, T.Krauth, S.Wagner (2017) Export of plastic debris by rivers into the sea. *Environmental Science and Technology*, 51, 12246–12253, <https://doi.org/10.1021/acs.est.7b02368>
- [22] Z.Yuan, R.Nag, E.Cummins (2022) Human health concerns regarding microplastics in the aquatic environment – From marine to food systems. *Science of the Total Environment*, 823, 153730, <https://doi.org/10.1016/j.scitotenv.2022.153730>
- [23] The gazette of India, extraordinary, Part II, Section 3; li. *Extraordinary. Ministry of the Environment, Forest and Climate Change*. <https://cpcb.nic.in/uploads/plasticwaste/Notification-12-08-2021.pdf>, Subsection (I).
- [24] D.Xanthos T.R.Walker (2017) International policies to reduce plastic marine pollution from single-use plastics (plastic bags and microbeads): A review. *Marine Pollution Bulletin*, 118, 17–26, <https://doi.org/10.1016/j.marpolbul.2017.02.048>
- [25] J.P.McDevitt, C.S.Criddle, M.Morse, R.C.Hale, C.B.Bott, C.M.Rochman (2017) Addressing the issue of microplastics in the wake of the microbead-free waters act—A new standard can facilitate improved policy. *Environmental Science and Technology*, 51, 6611–6617, <https://doi.org/10.1021/acs.est.6b05812>
- [26] G.Bakshi H.Does (2016) Sweden recycle 99% of its household waste? *Global Citizen*. Melbourne.
- [27] D.Saad, M.Ndlovu, G.Ramaremsa, H.Tutu, M.Sillanpää (2023) Characteristics of microplastics in sediment of the Vaal River, South Africa: Implications on bioavailability and toxicity. *International Journal of Environmental Science and Technology (Tehran)*, <http://doi.org/10.1007/s13762-023-05168-1>

- [28] S.Sarkar, H.Diab, J.Thompson (2023) Microplastic pollution: Chemical characterization and impact on wildlife. *International Journal of Environmental Research and Public Health*, 20, 1745, <http://doi.org/10.3390/ijerph20031745>
- [29] T.Dalu, T.Banda, T.Mutshekwa, L.F.Munyai, R.N.Cuthbert (2021) Effects of urbanisation and a wastewater treatment plant on microplastic densities along a subtropical river system. *Environmental Science and Pollution Research*, 28, 36102–36111, <https://doi.org/10.1007/s11356-021-13185-1>
- [30] M.N.Issac, B.Kandasubramanian (2021) Effect of microplastics in water and aquatic systems. *Environmental Science and Pollution Research*, 28, 19544–19562, <https://doi.org/10.1007/s11356-021-13184-2>
- [31] A.A.Koelmans, N.H.Mohamed Nor, E.Hermsen, M.Kooi, S.M.Mintenig, J.DeFrance (2019) Microplastics in freshwaters and drinking water: Critical review and assessment of data quality. *Water Research*, 155, 410–422, <https://doi.org/10.1016/j.watres.2019.02.054>
- [32] I.Gambino, F.Bagordo, T.Grassi, A.Panico, A.DeDonno (2022) Occurrence of microplastics in tap and bottled water: Current knowledge. *International Journal of Environmental Research and Public Health*, 19, 5283, <https://doi.org/10.3390/ijerph19095283>
- [33] F.Parvin, J.Nath, T.Hannan, S.M.Tareq (2022) Proliferation of microplastics in commercial sea salts from the world longest sea beach of Bangladesh. *Environmental Advances*, 7, 100173, <https://doi.org/10.1016/j.envadv.2022.100173>
- [34] K.Magnusson, K.Eliasson, A.Fråne, K.Haikonen, J.Hultén, M.Mikael Olshammar, J.Stadmark, A.Voisin, I.V.L.Svenska (2016) *Swedish Sources and Pathways for Microplastics to the Marine Environment. Report- C183* Swedish Environmental Research Institute, Stockholm.
- [35] I.E.Napper, R.C.Thompson (2016) Release of synthetic microplastic plastic fibres from domestic washing machines: Effects of fabric type and washing conditions. *Marine Pollution Bulletin*, 112, 39–45, <https://doi.org/10.1016/j.marpolbul.2016.09.025>
- [36] F.C.Alam, E.Sembing, B.S.Muntalif, V.Suendo (2019) Microplastic distribution in surface water and sediment river around slum and industrial area (case study: Ciwalengke River, Majalaya district, Indonesia). *Chemosphere*, 224, 637–645, <http://doi.org/10.1016/j.chemosphere.2019.02.188>
- [37] H.Chen, L.Xu, K.Yu, F.Weil, M.Zhang (2023) Release of microplastics from disposable cups in daily use. *Science of the Total Environment*, 854, 158606, <https://doi.org/10.1016/j.scitotenv.2022.158606>
- [38] R.A.Rojas-Luna, L.Oquendo-Ruiz, C.A.García-Alzate, V.A.Arana, R.García-Alzate, J.Trilleras (2023) Identification, abundance, and distribution of microplastics in surface water collected from Luruaco Lake, low basin Magdalena River, Colombia. *Water*, 15, 344, <https://doi.org/10.3390/w15020344>
- [39] K.Amrutha, A.K.Warrier (2020) The first report on the source-to-sink characterization of microplastic pollution from a riverine environment in tropical India. *Science of the Total Environment*, 739, 140377, <https://doi.org/10.1016/j.scitotenv.2020.140377>
- [40] Z.Akdogan, B.Guven, A.E.Kideys (2023) Microplastic distribution in the surface water and sediment of the Ergene River. *Environmental Research*, 234, (116500), <https://doi.org/10.1016/j.envres.2023.116500>
- [41] G.B.Priyanka, B.Govindarajulu (2023) Transportation of microplastics from the rural area into the urban area of the Kosasthalaiyar River in the metropolitan city of Chennai. *Regional Studies in Marine Science*, 66, (103151), <https://doi.org/10.1016/j.rsma.2023.103151>.
- [42] A.A.Horton, C.Svendsen, R.J.Williams, D.J.Spurgeon, E.Lahive (2017) Large microplastic particles in sediments of tributaries of the River Thames, UK – Abundance, sources and methods for effective quantification. *Marine Pollution Bulletin*, 114, 218–226, <http://doi.org/10.1016/j.marpolbul.2016.09.004>.
- [43] M.J.Hossain, S.AftabUddin, F.Akhter, N.Nusrat, A.Rahaman, M.N.A.Sikder, M.M.Monwar, M.S.N.Chowdhury, S.Jiang, H.Shi, J.Zhang (2022) Surface water, sediment, and biota: The first multi-compartment analysis of microplastics in the Karnafully river, Bangladesh. *Marine Pollution Bulletin*, 180, 113820, <https://doi.org/10.1016/j.marpolbul.2022.113820>
- [44] R.Singh, G.S.Singh (2020) Integrated management of the Ganga River: An ecohydrological approach. *Ecohydrology and Hydrobiology*, 20, 153–174, <https://doi.org/10.1016/j.ecohyd.2019.10.007>
- [45] E.Q.Espiritu, S.A.S.Dayrit, A.S.O.Coronel, N.S.C.Paz, P.I.L.Ronquillo, V.C.G.Castillo, E.P.Enriquez (2019) Assessment of quantity and quality of microplastics in the sediments, Waters, Oysters and Selected Fish Species in Key Sites Along the Bombong Estuary and the Coastal Waters of Ticalan in San Juan, Batangas. *Philippine Journal of Science*, 148 (4), 789–801.
- [46] S.Eo, S.H.Hong, Y.K.Song, G.M.Han, W.J.Shim (2019) Spatiotemporal distribution and annual load of microplastics in the Nakdong River, South Korea. *Water Research*, 160, 228–237, <https://doi.org/10.1016/j.watres.2019.05.053>
- [47] K.Ounjai, S.K.Boontanon, P.Piyaviriyakul, S.Tanaka, S.Fujii (2022) Assessment of microplastic contamination in the urban lower Chao Phraya River of Bangkok city, Thailand. *Journal of Water and Health*, 20, 1243–1254, <https://doi.org/10.2166/wh.2022.130>
- [48] S.Lechthaler, K.Waldschläger, C.G.Sandhani, S.A.Sannasiraj, V.Sundar, J.Schwarzbauer, H.Schütttrumpf (2021) Baseline study on microplastics in Indian rivers under different anthropogenic influences. *Water*, 13, 1648, <https://doi.org/10.3390/w13121648>
- [49] N.Chinfak, P.Sompongchaiyakul, C.Charoenpong, H.Shi, T.Yeemin, J.Zhang (2021) Abundance, composition, and fate of microplastics in water, sediment,

- and shellfish in the Tapi-Phumduang River system and Bandon Bay, Thailand. *Science of the Total Environment*, 781, 146700, <https://doi.org/10.1016/j.scitotenv.2021.146700>
- [50] Y.H.Tee, Y.S.Ibrahim, W.M.A.WanMohdKhalik (2020) Microplastic abundance, distribution, and composition in sungai dungun, Terengganu, Malaysia. *Sains Malaysiana*, 49, 1479–1490, <https://doi.org/10.17576/jsm-2020-4907-01>
- [51] J.H.Kang, O.Y.Kwon, K.W.Lee, Y.K.Song, W.J.Shim (2015) Marine neustonic microplastics around the southeastern coast of Korea. *Marine Pollution Bulletin*, 96, 304–312, <https://doi.org/10.1016/j.marpolbul.2015.04.054>
- [52] L. C. M. Lebreton, J. Van Der Zwet, J. W. Damsteeg, B. Slat, A. Andrady, and J. Reisser (2017) River plastic emissions to the world's oceans. *Nature Communications*, 8, 15611, <https://doi.org/10.1038/ncomms15611>
- [53] I.E. Napper, A. Baroth, A. C. Barrett, S. Bhola, G. W. Chowdhury, B. F. R. Davies, E.M.Duncan, S.Kumar, S.E.Nelms, M.N.HasanNiloy, B.Nishat, T.Maddalene, R.C.Thompson, H.Koldewey, H. (2021) The abundance and characteristics of microplastics in surface water in the trans-boundary Ganges River. *Environmental Pollution*, 274, 116348, <https://doi.org/10.1016/j.envpol.2020.116348>
- [54] T. Pelamatti, L. R. Cardelli, and L. M. Rios-Mendoza (2022) The role of microplastics in bioaccumulation of pollutants. In: *Handbook of Microplastics in the Environment*. Springer International Publishing: Cham, Germany, pp. 667–696.
- [55] X.Shi, Z.Chen, W.Weil, J.Chen, B.-J.Ni (2023) Toxicity of micro/nanoplastics in the environment: Roles of plastisphere and eco-corona. *Soil and Environmental Health*, 1, 100002, <http://doi.org/10.1016/j.seh.2023.100002>
- [56] P.J.Landrigan, H.Raps, M.Cropper, C.Bald, M.Brunner, E.M.Canonizado, D.Charles, T.C.Chiles, M.J.Donohue, J.Enck, P.Fenichel, L.E.Fleming, C.Ferrier-Pages, R.Fordham, A.Gozt, C.Griffin, M.E.Hahn, B.Haryanto, R.Hixson, H.Ianelli, B.D.James, P.Kumar, A.Laborde, K.L.Law, K.Martin, J.Mu, Y.Mulders, A.Mustapha, J. Niu, S.Pahl, Y.Park, M.Pedrotti, J.A.Pitt, M.Ruchirawat, B.J.Seewoo, M.Spring, J.J.Stegeman, W.Suk, C.Symeonides, H.Takada, R.C.Thompson, A.Vicini, Z.Wang, E.Whitman, D.Wirth, M.Wolff, A.K.Yousuf, S.Dunlop (2023) The minderoo-Monaco commission on plastics and human health. *Annals of Global Health*, 89, <https://doi.org/10.5334/aogh.4056>
- [57] M.Shen, S.Ye, G.Zeng, Y.Zhang, L.Xing, W.Tang, X.Wen, S.Liu (2020) Can microplastics pose a threat to ocean carbon sequestration? *Marine Pollution Bulletin*, 150, 110712, <https://doi.org/10.1016/j.marpolbul.2019.110712>
- [58] I.Cimmino, F.Fiory, G.Perruolo, C.Miele, F.Beguinet, P.Formisano, F.Oriente (2020) Potential mechanisms of bisphenol A (BPA) contributing to human disease. *International Journal of Molecular Sciences*, 21, 5761 <https://doi.org/10.3390/ijms21165761>
- [59] Y.Wang, H.Qian (2021) Phthalates and their impacts on human health. *Healthcare*, 9, 603, <https://doi.org/10.3390/healthcare9050603>
- [60] I.Dubey, S.Khan, S.Kushwaha (2022) Developmental and reproductive toxic effects of exposure to microplastics: A review of associated signaling pathways. *Frontiers in Toxicology*, 4, 901798, <https://doi.org/10.3389/ftox.2022.901798>
- [61] M.F.Manzoor, T.Tariq, B.Fatima, A.Sahar, F.Tariq, S.Munir, S.Khan, M.M.A.NawazRanjha, A.Sameen, X.A.Zeng, S.A.Ibrahim (2022) An insight into bisphenol A, food exposure and its adverse effects on health: A review. *Frontiers in Nutrition*, 9, 1047827, <https://doi.org/10.3389/fnut.2022.1047827>
- [62] F.Du, H.Cai, Q.Zhang, Q.Chen, H.Shi (2020) Microplastics in take-out food containers. *Journal of Hazardous Materials*, 399, 122969, <https://doi.org/10.1016/j.jhazmat.2020.122969>,
- [63] C. Pironti, M. Ricciardi, O. Motta, Y. Miele, A. Proto, and L. Montano (2021) Microplastics in the environment: Intake through the food web, human exposure and toxicological effects. *Toxics*, 9, 224, <https://doi.org/10.3390/toxics9090224>
- [64] T.K.Dey, M.E.Uddin, M.Jamal (2021) Detection and removal of microplastics in wastewater: Evolution and impact. *Environmental Science and Pollution Research*, 28, 16925–16947, <https://doi.org/10.1007/s11356-021-12943-5>,
- [65] R.Dris, J.Gasper, C.Mirande, C.Mandin, M.Guerrouache, V.Langlois, B.Tassin (2017) A first overview of textile fibers, including microplastics, in indoor and outdoor environments. *Environmental Pollution*, 221, 453–458, <https://doi.org/10.1016/j.envpol.2016.12.013>
- [66] K.Liu, X.Wang, T.Fang, P.Xu, L.Zhu, D.Li (2019) Source and potential risk assessment of suspended atmospheric microplastics in shanghai. *Science of the Total Environment*, 675, 462–471, <https://doi.org/10.1016/j.scitotenv.2019.04.110>
- [67] A.Tursi, M.Baratta, T.Easton, E.Chatzisymeon, F.Chidichimo, M.De Biase, G.De Filpo (2022) Microplastics in aquatic systems, a comprehensive review: Origination, accumulation, impact, and removal technologies. *RSC Advances*, 12, 28318–28340, <https://doi.org/10.1039/d2ra04713f>
- [68] L.M.Hernandez, N.Yousefi, N.Tufenkji, A.T.Nanoplastics (2017) Are There Nanoplastics in Your personal care products? *Environmental Science and Technology Letters*, 4, 280–285, <https://doi.org/10.1021/acs.estlett.7b00187>.
- [69] Q.L.Li, M.Yuan, Y. Chen, X.J.Jin, J.F.Shangguan, J.L.Cui, S.Chang, M.Guo, Y.Wang (2023) The neglected potential source of microplastics from daily necessities: A study on protective mobile phone cases. *Journal of Hazardous Materials*, 441, 129911, <https://doi.org/10.1016/j.jhazmat.2022.129911>

- [70] H.Zhang, Y.Xu, L.Jia, M.Xu (2021) Smog chamber study on the ozone formation potential of acetaldehyde. *Advances in Atmospheric Sciences*, 38, 1238–1251, <https://doi.org/10.1007/s00376-021-0407-5>
- [71] D.Boyle, A.I.Catarino, N.J.Clark, T.B.Henry (2020) Polyvinyl chloride (PVC) plastic fragments release Pb additives that are bioavailable in zebrafish. *Environmental Pollution*, 263, 114422, <https://doi.org/10.1016/j.envpol.2020.114422>
- [72] M.Shen, W.Huang, M.Chen, B.Song, G.Zeng, Y.Zhang (2020) plastic crisis: Un-ignorable contribution to global greenhouse gas emissions and climate change. *Journal of Cleaner Production*, 254, 120138, <https://doi.org/10.1016/J.JCLEPRO.2020.120138>
- [73] T.Lomonaco, E.Manco, A.Corti, J.LaNasa, S.Ghimenti, D.Biagini, F.DiFrancesco, F.Modugno, A.Ceccarini, R.Fuoco, V.Castelvetto (2020) Release of harmful volatile organic compounds (VOCs) from photo-degraded plastic debris: A neglected source of environmental pollution. *Journal of Hazardous Materials*, 394, 122596, <https://doi.org/10.1016/j.jhazmat.2020.122596>
- [74] M.Sankar, E.Nowicka, E.Carter, D.M.Murphy, D.W.Knight, D.Bethell, G.J.Hutchings (2014) The benzaldehyde oxidation paradox explained by the interception of peroxy radical by benzyl alcohol. *Nature Communications*, 5, 3332, <https://doi.org/10.1038/ncomms4332>
- [75] J.Kramm, C.Völker (2018) Understanding the risks of microplastics: A social-ecological risk perspective. In: *Handbook of Environmental Chemistry*. Springer International Publishing: Cham, Germany, 223–237.
- [76] A.Jakovcevic, L.Steg, N.Mazzeo, R.Caballero, P.Franco, N.Putrino, J.Favara (2014) Charges for plastic bags: Motivational and behavioral effects. *Journal of Environmental Psychology*, 40, 372–380, <http://doi.org/10.1016/j.jenvp.2014.09.004>
- [77] A.O.C.Iroegbu, S.S.Ray, V.Mbarane, J.C.Bordado, J.P.Sardinha (2021) Plastic pollution: A perspective on matters arising: Challenges and opportunities. *ACS Omega*, 6, 19343–19355, <https://doi.org/10.1021/acsomega.1c02760>
- [78] R.Geyer, J.R.Jambeck, K.L.Law (2017) Production, use, and fate of all plastics ever made. *Science Advances*, 3, e1700782, <https://doi.org/10.1126/sciadv.1700782>
- [79] E.Nøklebye, H.N.Adam, A.Roy-Basu, G.K.Bharat, E.H.Steindal (2023) Plastic bans in India – Addressing the socio-economic and environmental complexities. *Environmental Science and Policy*, 139, 219–227, <https://doi.org/10.1016/j.envsci.2022.11.005>
- [80] L.M.Erdle, D.NouriParto, D.Sweetnam, C.M.Rochman (2021) Washing machine filters reduce microfiber emissions: Evidence from a community-scale pilot in Parry Sound, Ontario. *Frontiers in Marine Science*, 8, <https://doi.org/10.3389/fmars.2021.777865>
- [81] I.SkumlienFuruset, E.StøhleRødland (2020) *Reducing the Release of Microplastic from Tire Wear: Nordic Efforts*. Nordic Council of Ministers.
- [82] C.F.Chien, K.Aviso, M.L.Tseng, M.Fujii, M.K.Lim (2023) Solid waste management in emerging economies: Opportunities and challenges for reuse and recycling. *Resources, Conservation and Recycling*, 188, 106635, <https://doi.org/10.1016/j.resconrec.2022.106635>
- [83] W.-T.Chen, K.Jin, N.-H.Linda Wang (2019) Use of supercritical water for the liquefaction of polypropylene into oil. *ACS Sustainable Chemistry and Engineering*, 7, 3749–3758, <http://doi.org/10.1021/acssuschemeng.8b03841>.
- [84] M.S.Ahmad, S.A.Ahmad (2022) The impact of polyethylene terephthalate waste on different bituminous designs. *Journal of Engineering and Applied Science*, 69, <http://doi.org/10.1186/s44147-022-00104-5>
- [85] H.Zhou, Y.Ren, Z.Li, M.Xu, Y.Wang, R.Ge, X. Kong, L.Zheng, H.Duan (2021) Electrocatalytic upcycling of polyethylene terephthalate to commodity chemicals and H₂ fuel. *Nature Communications*, 12, 4679, <https://doi.org/10.1038/s41467-021-25048-x>,
- [86] M.Caniato, L.Cozzarini, C.Schmid, A. Gasparella (2021) Acoustic and thermal characterization of a novel sustainable material incorporating recycled microplastic waste. *Sustainable Materials and Technologies*, 28, (e00274, <https://doi.org/10.1016/j.susmat.2021.e00274>
- [87] P.Chandrasekaran, K.Nirmalkumar, R.Uthra, K.S.VihashKumar, R.Vishnu (2021) Study on construction of roads using PVC wastes-review. *IOP Conference Series: Materials Science and Engineering*, 1145, 012105, <http://doi.org/10.1088/1757-899X/1145/1/012105>
- [88] I.A.El-Naga, M.Ragab (2019) Benefits of utilization the Recycle polyethylene terephthalate waste plastic materials as a modifier to asphalt mixtures. *Construction and Building Materials*, 219, 81–90, <https://doi.org/10.1016/j.conbuildmat.2019.05.172>
- [89] W. Nabgan, B. Nabgan, T. A. Tuan Abdullah, M. Ikram, A. H. Jadhav, M. W. Ali, A. A. Jalil (2022) Hydrogen and value-added liquid fuel generation from pyrolysis-catalytic steam reforming conditions of microplastics waste dissolved in phenol over bifunctional Ni-Pt supported on Ti-Al nanocatalysts. *Catalysis Today*, 400–401, 35–48, <https://doi.org/10.1016/j.cattod.2021.11.026>

IZVOD

NEDAVNI NAPREDAK U ISTRAŽIVANJU OD PLASTIČNIH MATERIJALA DO MIKROPLASTIKE

Plastika je postala sve prisutnija u našim životima. Zbog sve većeg broja stanovnika, brze urbanizacije i industrijskog napretka, upotreba plastike se višestruko povećala. Ovi plastični materijali se često raspadaju u mikroplastiku (MP) koja je manja od 5 mm. Mikroplastika uglavnom ulazi u vodena staništa nepravilnim upravljanjem otpadom, nelegalnim odlaganjem i neizbežnim i nenamernim ispuštanjima koja se dešavaju tokom izgradnje, proizvodnje, poljoprivrede, potrošnje i rekreativnih aktivnosti. Ovaj pregled se fokusira na istraživanje porekla, pojave i mogućih štetnih efekata mikroplastike na ljudsko blagostanje. Od 485 literature pregledane za studiju između 2014-2023, utvrđeno je da je 105 povezano sa mikroplastikom koji su bili raspoređeni na 10 tema. Najveći broj radova bio je o izvorima MP, zatim o mikroplastici iz slatkovodnih ekosistema i upravljanja otpadom. Najmanje literature je bilo iz tematike transporta mikroplastike i mikroplastike u zemljištu. Literatura je objavljena uglavnom u Kini, Indiji, Evropi i Americi. Druge zemlje poput Australije, Latinske Amerike, Afrike i Bliskog istoka doprinose vrlo malo. Skeniranje literature otkriva da se samo 9% celokupnog proizvedenog plastičnog otpada reciklira, 12% se spaljuje, a 79% plastičnog otpada se baca na deponije i okeane. Bačena plastika se taloži i zagađuje različite matrice životne sredine. MP su namerno proizvedeni da se dodaju proizvodima za ličnu negu koji se ispiru u kanalizaciju kroz kanalizacijske ili industrijske otpadne vode. Ovi MP se razlikuju po gustini i boji, zavisno od vrste polimera, i prisutni su u različitim veličinama i koncentracijama u vodenim sredinama. Karakterizacija MPs koji potiču od različitih tipova polimernih materijala, u recenziranoj literaturi, izvršena je na osnovu podataka dobijenih iz Skenirajuće elektronske mikroskopije, Energi Dispersive Spectroscopi (SEM-EDS), Attenuated Total Reflection, Fourier Transform Infra-Red spektroskopije (ATR-FTIR), Ramanova spektroskopija i mikroskopija atomske sile (AFM). Mikroplastike imaju potencijal da apsorbiraju štetne hidrofobne zagađivače iz okoline što dovodi do indirektnog prenosa zagađivača u mrežu hrane. Takvi MP ulaze i utiču na ljude, uzrokujući probleme sa reproduktivnim sistemom, telesnom težinom, odnosom polova i živorođenim. MP predstavljaju ozbiljnu pretnju organizmima kada se progutaju jer mogu da opstruiraju digestivni trakt, što dovodi do oksidativnog i patološkog stresa, usporavanja rasta i ometanja reprodukcije. Pored navedenog, razmatrana je i sveobuhvatna analiza zagađenja MP, kao i njegovog uticaja na ljude i životnu sredinu u smislu identifikacije izvora i rasprostranjenosti. Takođe, razmatran je detaljan pregled postojećeg otpadnog materijala koji se reciklira u nove materijale ili se ponovo koristi bez izmena ili degradacije za proizvodnju novih izvora energije. Na kraju, predložene su integrisane strategije za sprečavanje unošenja plastičnog otpadnog materijala u životnu sredinu, kontrolom izvora, poboljšanim upravljanjem plastičnim otpadom i tehnikama za degradaciju i konverziju MP.

Cljučne reči: mikroplastika; deponija; uticaji na zdravlje; vodena sredina; menadžment; ekološki

Pregledni rad

Rad poslat: 6.03.2024.

Rad revidiran: 24.04.2024.

Rad prihvaćen: 14.05.2024.

The ORCID Ids of all the authors are as follows:

1. Ikhwan Syafiq Mohd Noor: <https://orcid.org/0000-0003-0983-782X>
2. Gaurav Saini: <https://orcid.org/0000-0002-3975-346X>
3. Priya Agarwal: <https://orcid.org/0000-0003-4252-8172>
4. Satya Prakash: <https://orcid.org/0000-0001-6633-7480>

Parvaiz Ahmad Dar¹, Muhd Zu Azhan Yahya²,
Serguei V. Savilov³, Sharad Agrawal^{1*}

¹Centre for Development of Biomaterials and Department of Life Sciences, School of Basic Sciences and Research, Sharda University, Greater Noida, 201310, India, ²Faculty of Defence Science and Technology, Universiti Pertahanan Nasional Malaysia (UPNM), 57000 Kuala Lumpur, Malaysia, ³Department of Chemistry, Lomonosov Moscow State University, 1-3 Lenninskiye Gory 119991 Moscow

Scientific paper

ISSN 0351-9465, E-ISSN 2466-2585

<https://doi.org/10.62638/ZasMat1194>



Zastita Materijala 65 (4)
612 – 622 (2024)

***Bacillus amyloliquefaciens* strain NSB4 bacteria for treating wastewater for fuel cell application**

ABSTRACT

Pollutants in water bodies come from a variety of sources, including but not limited to domestic, industrial, municipal etc. Water contamination and energy shortages are global problems that require significant attention. Therefore, it is essential to synthesize sustainable energy and transport waste-free water to the water reception points. Concerns about energy shortages and water contamination have prompted the development of microbial fuel cell technology. Microorganisms are used by electrochemical cell nature of MFCs to anaerobically digest the organic wastes and produce energy. Focusing on a single-chambered mediator-less MFCs operating in batch mode, this study assesses the efficacy of a novel bacterial strain *Bacillus amyloliquefaciens* NSB4, as an exoelectrogen in terms of electricity yield and waste elimination. Results from the strain's electrochemical characterisation showed a maximum current density of 0.4804 A/m² and a power density of 41.281 mW/m². Additionally, the coulombic efficiency (72%) and COD reduction efficiency (90.46%) was also remarkably high. Growth of the anodic biofilm during the MFC process displayed the crucial performance of the exoelectrogen used. SEM images of the biofilm are also presented in the study.

Keywords: Microbial fuel cells, Mediator-free MFC, Separator, Biofilm, Waste-water treatment

1. INTRODUCTION

Human activities as well as rainwater runoff generate wastes in waterbodies and thus create a global challenge with respect to the water pollution. Wastewater can be typically categorised by the source of its generation such as domestic, industrial, municipal wastewater etc. [1]. In 2004 waste water, used as a feed for microbes in Microbial Fuel Cell (MFC) technology, possessed the advantage towards the treatment of sludge and energy savings from wastewater aeration [2,3]. Microbial fuel cell technology is an emerging environment friendly, eco-efficient and sustainable method to treat wastewater besides generating electricity from the organic and inorganic waste substances[4,5].

Electrochemical cell nature of MFC engages the microbes to anaerobically digest the organic wastes, thereby generates electricity. The energy transformation from chemical to electrical, by virtue of electrochemically active bacteria and the extracellular electron transfer mechanism along with simultaneous wastewater treatment largely escalates the interest towards the use of MFCs[6-8]. In the MFC system, the coherence of wastewater treatment as well as electricity production depends upon various factors viz. Electrochemically active microorganisms (exoelectrogens), architecture of microbial fuel cells (type of MFC, electrode material etc.), substrate used in the MFC, pH, temperature, and inoculum size [9]. One of the most significant factors mentioned above, is the electrochemically active bacteria (EAB), which acts as a biocatalyst, by transferring the electrons, generated during the degradation of pollutants present in the wastewater, to an extracellular electron acceptor and in doing so, it produces electrical energy and thus, affects the overall MFC performance[10,11]. These bio-catalytically active EABs passes on the electrons, generated during

*Corresponding author: Sharad Agrawal

E-mail: sharadagrawal39@gmail.com

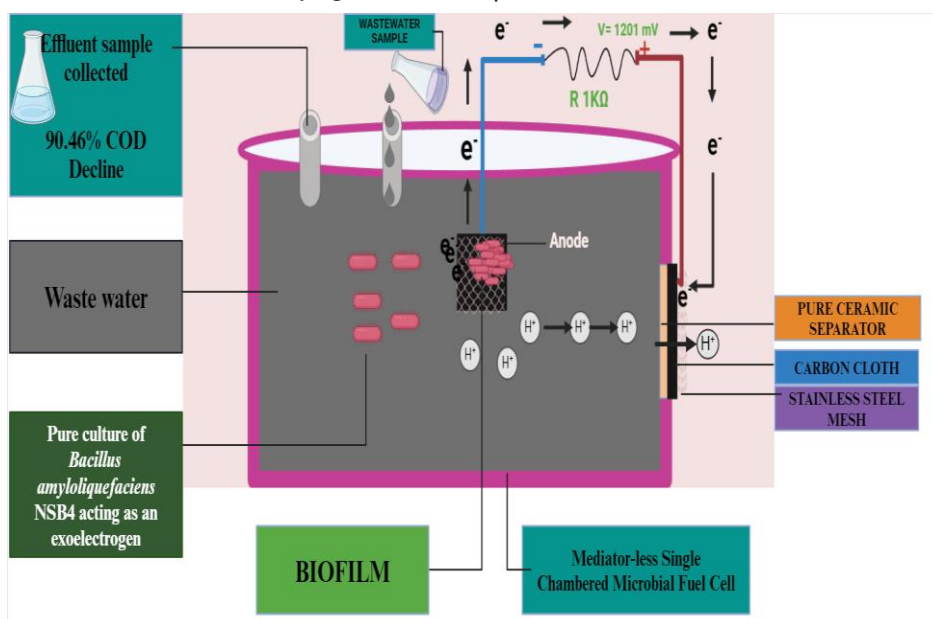
Paper received: 06. 03. 2024.

Paper corrected: 29. 04. 2024.

Paper accepted: 22. 05. 2024.

the metabolic processes, towards the anode surface and thus, makes the MFCs, mediator less. Some bacteria in MFC can boost the power generation while other plays an elemental role in eliminating the pollutants from the wastewater[12]. A huge variety of EABs have been isolated till date, from cow dung, soil, aerobically or anaerobically digested sludge, and/or anaerobically decomposed compost[13-15], the most studied genus acting as an exoelectrogen belong to *Shewanella*, *Proteobacter*, and *Pseudomonas* bacteria[16]. The current research is focussed on the role of an electrochemically active pure culture *Bacillus amyloliquefaciens* NSB4 in electricity generation

and removal of pollutants from domestic wastewater using batch MFC system. The robust treatment was evaluated through power production in mW/m^2 , decrement in COD value and achievement of high columbic efficiency. Although, several researchers have reported the involvement of mixed microbial cultures in MFCs, for the treatment of wastewater, the employment of a pure culture strain as an exoelectrogen has not been reported till date and hence, **this is the first report to explore the capability of using pure strain of *Bacillus amyloliquefaciens* NSB4 in MFCs** for producing electricity as well as removing the pollutants from the wastewater.



2. MATERIALS AND METHODS

Sampling of wastewater and its preparation as anolyte for MFC

Wastewater sample was collected in a pre-sterilized bottle from wastewater treatment plant (WWTP), Sharda University, Greater Noida, India. Sample was kept undisturbed for 24-48 h under sterilized conditions in order to ensure the settling down of solid particles. After 48 h of time interval, the liquid supernatant collected, was further sieved through a muslin cloth to remove the unwanted fine granules of sand, wood etc. and was stored at 4°C before usage. The Chemical Oxygen Demand (COD), Total Suspended Solids (TSS) and pH of the black-brown coloured, foul-smelling waste-water was recorded to be 1071.50 mg/L, 2540 mg/L, and 7.8 respectively.

MFC construction, inoculation and operation

A 300 ml, 10 cm × 6 cm plastic container (purchased from local market) was used to design an air-cathode MFC. Four identical chambers were

designed after partitioning the container. The experiments were run in triplicates, in three chambers, while the fourth chamber was kept as control. A piece of carbon cloth (25cm^2) attached to a stainless-steel mesh was placed in the centre of each MFC chamber in order to be used as an anode. Further, a cut of 25cm^2 was made on one of the walls of MFC chamber and a ceramic separator of same dimension was fixed over this cut. The carbon cloth was placed on the outer layer of each separator using a conductive graphite adhesive. Finally, a stainless-steel mesh was attached as current collector. MnO_2 was used as a catalyst on cathode assembly. To ensure the prevention of water crossover, a conductive electric paint (Aerol silicon conformal coating, Grade 9114) was used on the inner side of the separator. Connections for electricity production and measurement were established using the stainless-steel wire end, extended from the mesh of both the electrodes. The wires were further connected to a digital multi-meter via an insulated copper wire, to record the voltage and current output[17-19]. External

resistance was fixed at 10k Ω . Each reactor was surface sterilized using ethanol (70%) and UV rays before placing the anolyte in it. The autoclaved anolyte (prepared as mentioned in section 2.1) was transferred in each chamber of the reactor under aseptic conditions (using a biosafety cabinet). The reactor box was tightly sealed with the top-lid attached with a gasket to avoid any oxygen diffusion. Two separate capped openings (one for inoculation and reference electrode as well as the other for anode connection wire) were maintained. Each anodic chamber (except one, set as control) was inoculated with an overnight grown pure culture of *Bacillus amyloliquefaciens* NSB4 (40 ml each). The MFCs were allowed to run in a batch mode for 15 days at room temperature (25 $^{\circ}$ C). For maintaining an anaerobic environment in the anodic chamber, purging of nitrogen gas was carried out to remove the dissolved oxygen in the anolyte. Digital multi-meter was used to record the voltage results in millivolts. On the drop of voltage (below 300 mV), half of the pre-fed anolyte was replaced with the fresh feed. The experiment was monitored keeping the optimum parameters for all reactors uniform and their average results were recorded.

Electrical measurements

Electrical measurements like voltage, current and power density of the reactor were conducted according to the methods mentioned in previous literature and the voltage was assessed by a digital multimeter (HTC TM) only when the reactor was balanced[20]. After the attainment of balanced voltage by the MFCs, different external resistances were applied through a resistor box ranging from 10 Ω , to 1000k Ω to obtain the polarization results. The current was measured in milli-ampere (mA), next day after the start of the experiment using a fixed external resistance (1000 Ω). Similarly, the voltage was recorded in millivolts (mV). Both these values were calculated using Ohms' law using the following formula.

$$I = V/R$$

Where, V =voltage and R = external resistance applied.

For calculating power, the following formula was used

$$P = IV$$

Where I is the current generated by MFC and V is the voltage generated by MFC

Power density was calculated using the formula

$$Pd = IV/A,$$

Where, A is the surface area of operational electrode which is 25 cm 2 in current study.

Coulombic efficiency (CE) and COD measurement

The efficiency of substrate utilization by the bacteria, *Bacillus amyloliquefaciens* NSB4 was studied by analysing the coulombic efficiency, which is actually the ratio of total coulombs shifted from the substrate towards the anodic surface, to the highest attainable coulombs, if whole organic load is removed to generate the current[21,22]. The COD concentration of the anolyte was recorded according to the standard procedure [23]. Considering the reduction in the COD concentration, the measurement of coulombic efficiency was calculated using the equation given below [24].

$$CE(\%) = \frac{Ms. \int_0^{tb} I. dt}{F. b. Van. \Delta COD} \times 100$$

Where Ms is the molecular weight of O $_2$ (32 g/mol), I is the current density (mA cm $^{-2}$), tb is the operation time (days), F is the Faraday's constant (96,487 C/mol), b= 4 (number of electrons exchanged per mole of Oxygen)

Van is the volume of the anode (L) and Δ COD is the change in COD (g/l) over time tb

Redox reaction study and internal resistance effect

To transfer the electrons to the anode surface, bacteria may either use mobile redox shuttles also called mediators or directly, without involving any mediator via their membrane associated cytochrome compounds[25-27]. Cyclic voltammetry study using electrochemical workstation (Bio-Logic, SP-150, Sharda University, Greater Noida, India) was conducted. The three-electrode system: carbon cloth (working electrode), platinum (reference electrode) and saturated calomel electrode (counter electrode) were used to analyse either of the above mechanism. Oxidation reduction process (redox reaction) was analysed during the electron shifting from the bacteria to the anodic surface and finally towards the cathode. Cyclic voltammograms were recorded between -0.6 to + 0.6 V potential range and 5mV/s scan rate to define the cyclic voltammetry curves. For the examination of the interference caused by the internal resistance created during the MFC run, electrochemical impedance spectroscopy (EIS) was conducted with the frequency range and an amplitude of 100 kHz to 1 Hz and 5.0 mV, respectively[28-30].

SEM analysis of Biofilm

For determining the relation of an anolyte usage, power production and biofilm growth on the electrode surface, scanning electron microscopy

(SEM) was conducted. This study allows us to analyse the attachment of metabolites secreted extracellularly by the exoelectrogens[31]. In this study, several pieces of size 1cm³ were cut aseptically from the anode surface (before and after the power production), keeping the biofilm intact and were prepared for SEM analysis. The anode sample pieces were fixed in glutaraldehyde (2.5% v/v) for 48 h, followed by serial dehydration in ascending alcohol concentration (10%, 30%, 60% and 100%)[32-34], and finally, the samples were desiccated for 48 h. Samples were sent to Sophisticated Analytical Instrumentation Facility (SAIF), Punjab University for SEM imaging analysis.

3. RESULTS AND DISCUSSION

Electricity performance of the strain

Once the settling of the MFC was done, the voltage was monitored regularly up to 15 days across an external resistance of 1k Ω . The operating voltage during the 15 days MFC run was recorded using a digital multi meter and the peak was noticed at 1201 mV on 15th day (Fig. 1) The other electricity associated components like, current, current density and power density were also recorded as shown in Table 1. The results achieved during this study were comparable with the earlier reports[35,36], and witness the high efficiency of *Bacillus amyloliquefaciens* NSB4 for power production from the wastewater.

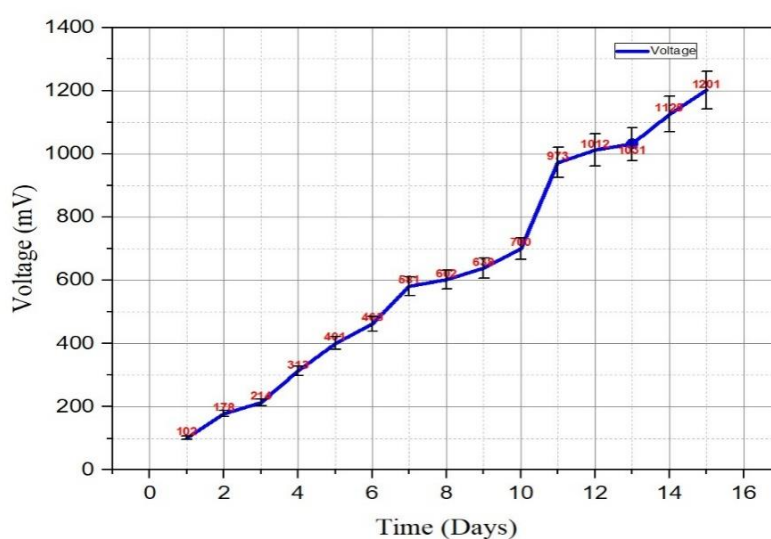


Figure 1. Graph represents the voltage (mV) generation by *Bacillus amyloliquefaciens* NSB4

Table 1. Electrical measurements and COD of the MFC recorded during the experiment

Time (Days)	Voltage (mV)	Current (mA)	Current Density (mA/m ²)	Power (mW)	Power Density (W/m ²)	COD (mg/L)
1	102	0.102	40.8	0.010404	0.04	1071.50
2	178	0.178	71.2	0.031684	0.12	-
3	214	0.214	85.6	0.045796	0.18	-
4	313	0.313	125.2	0.097967	0.39	-
5	401	0.401	160.4	0.160801	0.64	-
6	463	0.463	185.2	0.214369	0.85	-
7	581	0.581	232.4	0.337561	1.35	-
8	602	0.602	240.8	0.362404	1.44	-
9	638	0.638	255.2	0.407044	1.62	-
10	700	0.7	280	0.49	1.96	-
11	973	0.973	389.2	0.946729	3.78	-
12	1012	1.012	404.8	1.024144	4.09	-
13	1031	1.031	412.4	1.062961	4.25	-
14	1125	1.125	450	1.265625	5.06	-
15	1201	1.201	480.4	1.442401	5.77	102.134

Coulombic Efficiency (CE) and COD reduction

The current produced by the strain using wastewater as substrate transferred the coulombs to the anode which was measured by coulombic efficiency. The coulombic efficiency of the strain was found to be 72%, which is higher as compared to previous studies[37-39] and therefore, claimed that our bacteria, *Bacillus amyloliquefaciens* NSB4, is a reliable exoelectrogen to be used in MFC technology. The effluent collected at the end of the experiment was examined to determine the reduction in the organic load while generating volts also. The COD values of the wastewater was found to be decreased from 1071.50 mg/L to 102.134 mg/L, after 15 days of the MFC run process which accounts for 90.46% decline in the COD.

Significant decrement in the COD values of wastewater (Table 1) witnesses as one of the vital parameters for determining the efficiency of the bacteria involved in the mediator-free single-chambered MFC. The results are in agreement with the previous findings (Table 2)[39-59]. Few workers have reported the current density of 366 mA/m²[40] using *Shewanella oneidensis* MR-1 and 369.4mA/m² using *S. oneidensis* and *S. cerevisiae* microbial strains[48]. Similarly, power density ranging from 2.15 mW/m² to 2720 mW/m² has also been reported in literature[40-59]. These findings suggest that the current density of 480.4 mA/m² and the power density of 41.281 mW/m² reported in the current study, are in close agreement with the result reported in literature till date.

Table 2. Comparative study of different bacteria studied for wastewater treatment and power production

Bacteria studied	Type of culture used	MFC used	highest current density	highest Power Density	COD removal Efficiency	Coulombic Efficiency	Ref.
<i>Gluconobacteroxydan</i>	Pure	Dual chambered MFC	Not available	81 mW/m ²	32%	40%	[39]
<i>Shewanellaoneidensis M R-1</i>	Pure	Double chambered	366 mA/m ²	14466 mW/m ³	65%	5.70%	[40]
<i>Pseudomonas aeruginosa PBH03</i>	Pure	Not available	9.01 μ A/cm ²	Not available	Not available	Not available	[41]
<i>Castellaniella sp. A5, Castellaniella sp. B3, and Castellaniella sp. A3</i>	Mixed	single chambered	3.19 A/m ²	320 mW/m ²	91.15 \pm 0.05%	54.81 \pm 4.18%	[43]
<i>G. sulfurreducens, E.coli</i>	Mixed	Not available	NR	918 mW/m ²	Not available	Not available	[44]
<i>P. aeruginosa, E. aerogenes</i>	Mixed	Not available	212 μ A/cm ²	NR	Not available	Not available	[45]
<i>P. aeruginosa, K.variicola</i>	Mixed	Not available	NR	12.88 W/m ³	Not available	Not available	[46]
<i>G. sulfurreducens, C. cellulolyticum</i>	Mixed	Not available	NR	143 mW/m ²	Not available	Not available	[47]
<i>S. oneidensis, S. cerevisiae</i>	Mixed	Not available	369.4 mA/m ²	123.4 mW/m ²	Not available	Not available	[48]
<i>K. pneumonia, L. stakeyi</i>	Mixed	Not available	NR	12.87 W/m ³	Not available	Not available	[49]
<i>S. oneidensis, K.pneumonia</i>	Mixed	Not available	10 mA/m ²	2.15 mW/m ²	Not available	Not available	[50]
<i>S. oneidensis, E.coli</i>	Mixed	Not available	3.0 μ A/cm ²	NR	Not available	Not available	[51]
<i>Rhodospirillumrubrum</i>	Pure	Double chambered	Not available	1.25 W/m ²	Not available	Not available	[52]
<i>R. sphaeroides</i>	Pure	single chambered	Not available	790 mW/m ²	Not available	Not available	[53]
<i>R. palustris</i>	Pure	Not available	Not available	2720 mW/m ²	Not available	Not available	[54]
<i>Ochrobactrumanthropi</i>	Pure	Not available	Not available	89 mW/m	Not available	Not available	[55]
<i>Acidiphiliumcryptum</i>	Pure	Not available	Not available	12.7 mW/m ²	Not available	Not available	[56]
<i>Shewanellaoneidensis M R-2</i>	Pure	Dual chamberedMFC	31 mA/m ²	12.9 mW/m	Not available	81%	[57]
<i>Shewanellabaltica 21</i>	engineered strain	Dual chambered MFC	Not available	1304 mW/m ²	Not available	Not available	[58]
<i>Pseudomonas aeruginosa PBH04</i>	Pure	Not available	125 mA/m ²	26 mW/m ²	Not available	Not available	[59]
<i>Bacillus amyloliquefaciensNSB4</i>	Pure	Single Chambered	0.4804A/m ²	41.281 mW/m ²	90.46%	72%	This study

Polarization study and Cyclic Voltammetry

The curve recorded during the polarization study, displays the effect of external resistances (10 Ω, 100 Ω, 1000 Ω, 10kΩ, 100kΩ and 1000kΩ) on the power generation by the MFC, under particular operating conditions.

Fig. 2 displays the current as well as power. In current study, highest power density recorded was 5.77W/m². These results are also comparable to the previous reports[35] and therefore, highlight the typical role of *Bacillus amyloliquefaciens* NSB4 in power generation. To further confirm the oxidation reduction status of MFC during the substrate utilization and electron transport by the bacteria, cyclic voltammetry (CV) was performed using the Potentiostat (BioLogic SP-150, Department of Life Sciences, Sharda University, Greater Noida, India).

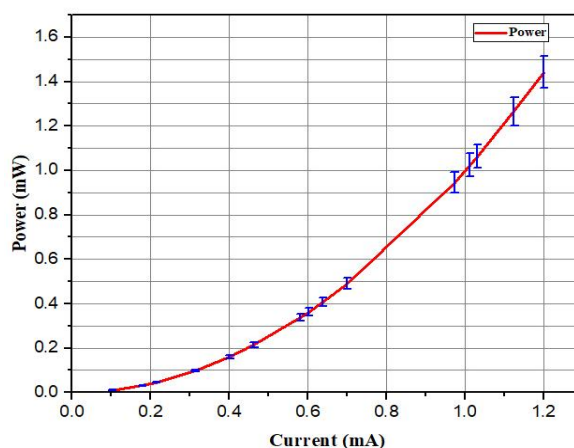


Figure 2. Graph represents the current (mA) and power (mW) produced during the treatment of wastewater by *Bacillus amyloliquefaciens* NSB4

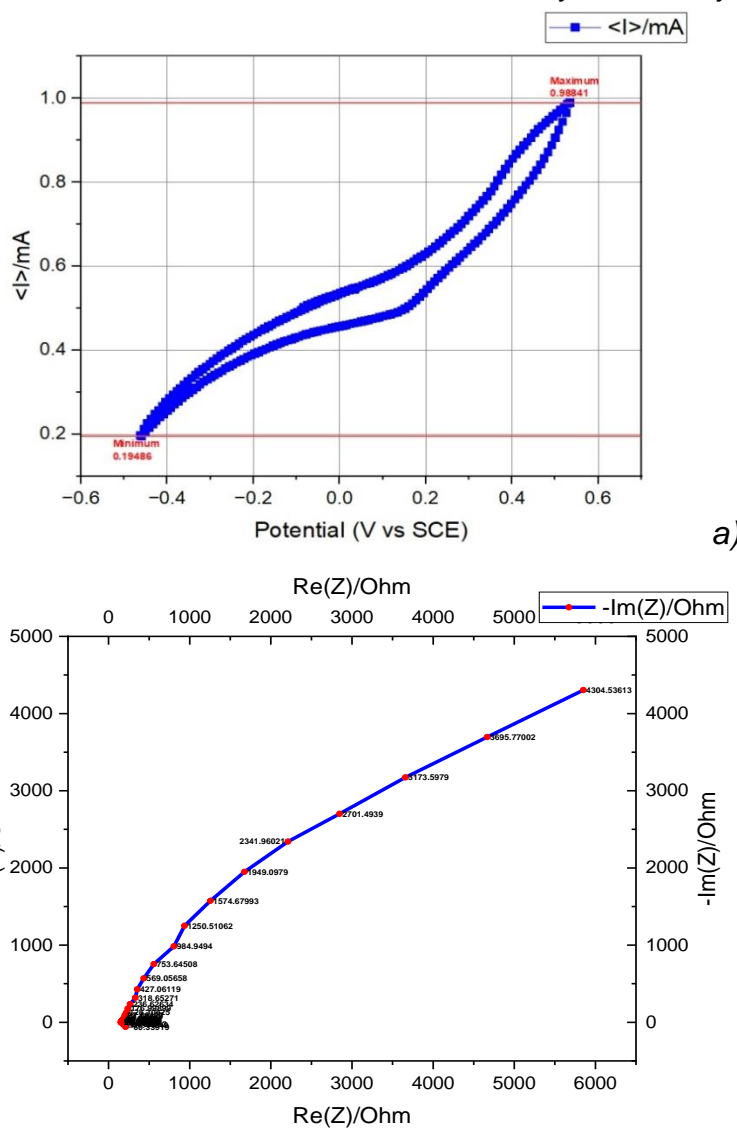
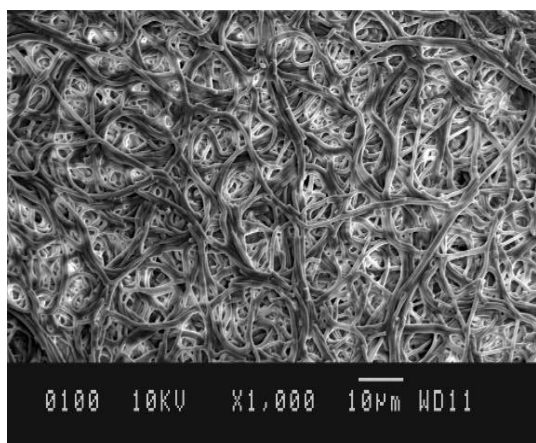


Figure 3. Graph shows (3a) the voltammogram recorded during the oxidation reduction status of the MFC and the graph and (3b) the relation of internal resistance and external resistance of the MFC studied

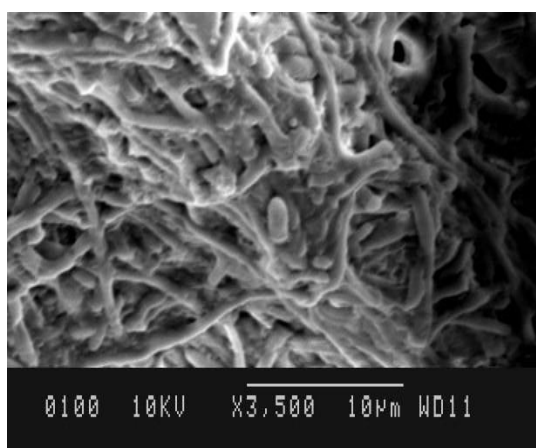
The CV observations revealed the presence of oxidation reduction peaks, associated with the electrode. The anode of the MFC displays oxidation (0.988 mA at 0.533 V) and reduction peak (-0.194 mA at -0.460 V) (Fig. 3a). The position of the redox peak displays the redox capability of the components involved in Extracellular Electron Transfer (EET). Comparatively, the results are in satisfaction with the work already reported [60]. The Electrochemical Impedance Spectroscopy (EIS) was also conducted in this study (Fig. 3b).

SEM observation of biofilm

For analysing the biofilm growth, the anode pieces of both the stages, before and after the power production from the wastewater as well as COD removal, were examined under SEM. No growth was observed before the start of MFC whereas, growth of rod-shaped bacteria was visible on the anode surface post 15 days of operation (Fig. 4a and 4b). This finding clearly displays the exoelectrogen-anode association as well as the transfer of electrons without the aid of any mediator.



a)



b)

Figure 4. Scanning Electron Micrograph shows (4a) no growth on anode surface and (4b) Biofilm attached on the anode surface

4. CONCLUSION

Microbial fuel cell technology exhibits a great applicability in the wastewater treatment and power production. The design as well as the constructing material of the reactor significantly enhances the efficiency of the MFC operation. The pure ceramic material-built separator used in the current study effectively boosted the ion exchange performance of the process. Besides the design of the reactor, the involvement of a pure bacterial strain, *Bacillus amyloliquefaciens* NSB4 as a biocatalyst, also plays a vital role in this technology by acting as an extracellular electron transfer system and generated the electric power. Additionally, the COD reduction efficiency recorded was also quite high, as near about 90.46% reduction in COD of the wastewater was noted before and after the MFC process. Therefore, it can be concluded that the strain *Bacillus amyloliquefaciens* NSB4 could be best utilized as a low-cost and highly-efficient exoelectrogen in a single-chambered mediator-free MFC technology.

Acknowledgements

The corresponding author is thankful to Sharda University for providing the facilities in laboratories for conducting the experimental work.

Funding sources - This work was supported by the Seed Grant fund vide letter no. SU/SF/2023/14 provided by Sharda University, India.

5. REFERENCES

- [1] J.K. Pandey, S.M. Tauseef, S. Manna, R.K. Patel, V. K. Singh, A. Dasgotra (2024) Application of Nanotechnology for Resource Recovery from Wastewater. *Journal of Environmental Management*, 320, 112916, <https://doi.org/10.1016/j.jenvman.2022.112916>
- [2] H. Liu, R. Ramnarayanan, B.E. Logan (2004) Production of electricity during wastewater treatment using a single chamber microbial fuel cell. *Environmental Science & Technology*, 38(7), 2281–2285, <https://doi.org/10.1021/es034923g>
- [3] H. Wang, Z.J. Ren (2013) A comprehensive review of microbial electrochemical systems as a platform technology. *Biotechnology Advances*, 31(8), 1796–1807, <https://doi.org/10.1016/j.biotechadv.2013.09.005>
- [4] M. Kronenberg, E. Trably, N. Bernet, D. Patureau (2017) Biodegradation of polycyclic aromatic hydrocarbons: Using microbial bioelectrochemical systems to overcome an impasse. *Environmental Pollution*, 231, 509–523, <https://doi.org/10.1016/j.envpol.2017.08.064>

- [5] A. T. Hoang, S. Nižetić, K. H. Ng, A. M. Papadopoulos, A. T. Le, S. Kumar, H. Hadiyanto (2022) Microbial fuel cells for bioelectricity production from waste as sustainable prospect of future energy sector. *Chemosphere*, 287, 132285, <https://doi.org/10.1016/j.chemosphere.2021.132285>
- [6] S. D. Kumar, M. Yasasve, G. Karthigadevi, M. Aashabharathi, R. Subbaiya, N. Karmegam, M. Govarthan (2022) Efficiency of microbial fuel cells in the treatment and energy recovery from food wastes: Trends and applications—a review. *Chemosphere*, 287, 132439, <https://doi.org/10.1016/j.chemosphere.2021.132439>
- [7] W. Wang, Q. Zhao, J. Ding, K. Wang, J. Jiang (2021) Development of an MFC-powered BEF system with novel Fe–Mn–Mg/CF composite cathode to degrade refractory pollutants. *Journal of Cleaner Production*, 326, 129348, <https://doi.org/10.1016/j.jclepro.2021.129348>
- [8] J. Li, R. M. Ziara, S. Li, J. Subbiah, B. I. Dvorak (2020) Understanding the sustainability niche of continuous flow tubular microbial fuel cells on beef packing wastewater treatment. *Journal of Cleaner Production*, 257, 120555, <https://doi.org/10.1016/j.jclepro.2020.120555>
- [9] S. V. Mohan, G. Velvizhi, J. A. Modestra, S. Srikanth (2014). Microbial fuel cell: Critical factors regulating bio-catalyzed electrochemical process and recent advancements. *Renewable and Sustainable Energy Reviews*, 40, 779–797, <https://doi.org/10.1016/j.rser.2014.07.145>
- [10] A. ElMekawy, S. Srikanth, S. Bajracharya, H. M. Hegab, P. S. Nigam, A. Singh, S. V. Mohan, D. Pant (2015) Food and agricultural wastes as substrates for bioelectrochemical system (BES): The synchronized recovery of sustainable energy and waste treatment. *Food Research International*, 73, 213–225, <https://doi.org/10.1016/j.foodres.2015.04.026>
- [11] S. Sevda, X. Dominguez-Benetton, K. Vanbroekhoven, H. De Wever, T. Sreerishnan, D. Pant (2013) High strength wastewater treatment accompanied by power generation using air cathode microbial fuel cell. *Applied Energy*, 105, 194–206, <https://doi.org/10.1016/j.apenergy.2013.01.020>
- [12] D. R. Lovley (2006) Microbial fuel cells: Novel microbial physiologies and engineering approaches. *Current Opinion in Biotechnology*, 17(3), 327–332, <https://doi.org/10.1016/j.copbio.2006.04.006>
- [13] Evelyn, Y. Li, A. Marshall, P. A. Gostomski (2014) Gaseous pollutant treatment and electricity generation in microbial fuel cells (MFCs) utilising redox mediators. *Reviews in Environmental Science and Bio/Technology*, 13, 35–51, <https://doi.org/10.1007/s11157-013-9311-0>
- [14] G. D. Saratale, R. G. Saratale, M. K. Shahid, G. Zhen, G. Kumar, H. S. Shin, Y. G. Choi, S. H. Kim (2017) A comprehensive overview on electro-active biofilms, role of exo-electrogens and their microbial niches in microbial fuel cells (MFCs). *Chemosphere*, 178, 534–547, <https://doi.org/10.1016/j.chemosphere.2017.03.074>
- [15] Y. Guo, J. Wang, S. Shinde, X. Wang, Y. Li, Y. Dai, J. Ren, P. Zhang, X. Liu (2020) Simultaneous wastewater treatment and energy harvesting in microbial fuel cells: An update on the biocatalysts. *RSC Advances*, 10(43), 25874–25887, <https://doi.org/10.1039/D0RA05385F>
- [16] A. Vijay, M. Chhabra, T. Vincent (2019) Microbial community modulates electrochemical performance and denitrification rate in a biocathodic autotrophic and heterotrophic denitrifying microbial fuel cell. *Bioresource Technology*, 272, 217–225, <https://doi.org/10.1016/j.biortech.2018.09.043>
- [17] A. Vempaty, A. S. Mathuriya (2023) Strategic development and performance evaluation of functionalized tea waste ash-clay composite as low-cost, high-performance separator in microbial fuel cell. *Environmental Technology*, 44(18), 2713–2724, <https://doi.org/10.1080/09593330.2021.2009072>
- [18] Y. Manjrekar, S. Kakkar, A. Durve-Gupta (2018) Bio-electricity generation using kitchen waste and molasses powered MFC. *IJSRSET*, 5(4), 181–187.
- [19] J. Prasad, R. K. Tripathi (2017) Maximum electricity generation from low-cost sediment microbial fuel cell using copper and zinc electrodes. 1–4.
- [20] A. Hatamian-Zarmi, S. A. Shojaosadati, E. Vasheghani-Farahani, S. Hosseinkhani, A. Emamzadeh (2009) Extensive biodegradation of highly chlorinated biphenyl and Aroclor 1242 by *Pseudomonas aeruginosa* TMU56 isolated from contaminated soils. *International Biodeterioration & Biodegradation*, 63(6), 788–794, <https://doi.org/10.1016/j.ibiod.2009.03.002>
- [21] R. Patel, D. Deb, R. Dey, E. Balas (2020) Microbial fuel cell laboratory setup. In V. E. Balas (Ed.), *Adaptive and Intelligent Control of Microbial Fuel Cells* (pp. 99–108). Springer, https://doi.org/10.1007/978-3-030-46539-7_6
- [22] A. Malyan, G. Mongia, S. Kumar (2022) Catalytic effect of acetate (C₂H₃O₂) on coulombic efficiency and bio-electricity generation from wastewater sample prepared from domestic kitchen waste using dual chamber microbial fuel cell technology. *Journal of Applied and Natural Science*, 14(2), 652–659, <https://doi.org/10.31018/jans.v14i2.3493>
- [23] W. Chen, Z. Liu, Y. Li, X. Xing, Q. Liao, X. Zhu (2021) Improved electricity generation, coulombic efficiency and microbial community structure of microbial fuel cells using sodium citrate as an effective additive. *Journal of Power Sources*, 482, 228947, <https://doi.org/10.1016/j.jpowsour.2020.228947>
- [24] A. E. Greenberg, R. R. Trussell, L. S. Clesceri (1985) *Standard methods for the examination of water and wastewater* (16th ed.). American Public Health Association.
- [25] B. E. Logan, B. Hamelers, R. Rozendal, U. Schröder, J. Keller, S. Freguia, P. Aelterman,

- W.Verstraete, K. Rabaey (2006). Microbial fuel cells: Methodology and technology. *Environmental Science & Technology*, 40(17), 5181–5192, <https://doi.org/10.1021/es0605016>
- [26] A. Genge, R. Khade (2019) Isolation and screening of exoelectrogenic bacteria from wastewater. [Conference presentation], <https://doi.org/10.1016/j.watres.2019.04.001>
- [27] Y. Cao, H. Mu, W. Liu, R. Zhang, J. Guo, M. Xian, H. Liu (2019) Electricigens in the anode of microbial fuel cells: Pure cultures versus mixed communities. *Microbial Cell Factories*, 18(1), 1–14, <https://doi.org/10.1186/s12934-019-1153-2>
- [28] R. M. Allen, H. P. Bennetto (1993) Microbial fuel-cells: Electricity production from carbohydrates. *Applied Biochemistry and Biotechnology*, 39(1), 27–40, <https://doi.org/10.1007/BF02918939>
- [29] Z. Nazeer, E. Y. Fernando (2022) A novel growth and isolation medium for exoelectrogenic bacteria. *Enzyme and Microbial Technology*, 155, 109995, <https://doi.org/10.1016/j.enzmictec.2022.109995>
- [30] B. Thulasinathan, S. Nainamohamed, J. O. E. Samuel, S. Soorangkattan, J. Muthuramalingam, M. Kulanthaisamy, R. Balasubramani, D. D. Nguyen, S. W. Chang, N. Bolan (2019) Comparative study on *Cronobacter sakazakii* and *Pseudomonas otitidis* isolated from septic tank wastewater in microbial fuel cell for bioelectricity generation. *Fuel*, 248, 47–55, <https://doi.org/10.1016/j.fuel.2019.03.057>
- [31] Y. Li, G. Gu, J. Zhao, H. Yu, Y. Qiu, Y. Peng (2003) Treatment of coke-plant wastewater by biofilm systems for removal of organic compounds and nitrogen. *Chemosphere*, 52(6), 997–1005, [https://doi.org/10.1016/S0045-6535\(03\)00318-2](https://doi.org/10.1016/S0045-6535(03)00318-2)
- [32] C. Wang, J. Shen, Q. Chen, D. Ma, G. Zhang, C. Cui, Y. Xin, Y. Zhao, C. Hu (2020) The inhibiting effect of oxygen diffusion on the electricity generation of three-chamber microbial fuel cells. *Journal of Power Sources*, 453, 227889 <https://doi.org/10.1016/j.jpowsour.2020.227889>
- [33] F. L. Torto, M. Relucenti, G. Familiari, N. Vaia, F. Marinozzi, F. Bini, I. Fratoddi, F. Sciubba, R. Cassese, V. Tombolini (2018) The effect of postmastectomy radiation therapy on breast implants. [Conference presentation], <https://doi.org/10.1016/j.radonc.2018.08.008>
- [34] M. Relucenti, S. Miglietta, G. Bove, O. Donfrancesco, E. Battaglione, P. Familiari, C. Barbaranelli, E. Covelli, M. Barbara, G. Familiari (2020) SEM BSE 3D image analysis of human incus bone affected by cholesteatoma ascribes to osteoclasts the bone erosion and VpSEM dEDX analysis reveals new bone formation. *Scanning*, 2020, <https://doi.org/10.1155/2020/5847982>
- [35] M. Relucenti, S. Miglietta, E. Covelli, P. Familiari, E. Battaglione, G. Familiari, M. Barbara (2019) Ciliated cell observation by SEM on the surface of human incudo-malleolar-joint articular cartilage: Are they a new chondrocyte phenotype? *Acta Oto-Laryngologica*, 139(5), 439–443, <https://doi.org/10.1080/00016489.2019.1582341>
- [36] G. M. F. Pierangeli, R. A. Ragio, R. F. Benassi, G. B. Gregoracci, E. L. Subtil (2021) Pollutant removal, electricity generation and microbial community in an electrochemical membrane bioreactor during co-treatment of sewage and landfill leachate. *Journal of Environmental Chemical Engineering*, 9(5), 106205, <https://doi.org/10.1016/j.jece.2021.106205>
- [37] T. Atnafu, S. Leta (2021) Developing and optimization of fragmented electroactive biofilm reactor (FAB) to increase microbial fuel cell bioelectricity generation and treatment performance. [Conference presentation], <https://doi.org/10.1016/j.jece.2021.106205>
- [38] H. Khandelwal, S. Mutyala, M. Kim, Y. E. Song, S. Li, M. Jang, S. E. Oh, J. R. Kim (2022) Colorimetric isolation of a novel electrochemically active *Pseudomonas* strain using tungsten nanorods for bioelectrochemical applications. *Bioelectrochemistry*, 146, 108136, <https://doi.org/10.1016/j.bioelechem.2022.108136>
- [39] S. Tarasov, Y. Plekhanova, V. Kashin, P. Gotovtsev, M. A. Signore, L. Francioso, V. Kolesov, A. Reshetilov (2022) Gluconobacter oxydans-based MFC with PEDOT: PSS/Graphene/Nafion bioanode for wastewater treatment. *Biosensors*, 12(9), 699, <https://doi.org/10.3390/bios12090699>
- [40] S. M. Daud, W. R. W. Daud, M. H. A. Bakar, B. H. Kim, M. R. Somalu, A. Muchtar, J. M. Jahim, S. Muhammed Ali (2020) Low-cost novel clay earthenware as separator in microbial electrochemical technology for power output improvement. *Bioprocess and Biosystems Engineering*, 43, 1369–1379, <https://doi.org/10.1007/s00449-020-02344-0>
- [41] A. Ilshadsabah, T. Suchithra (2022) Identification of novel potent biocatalysts, *Bacillus thuringiensis* STV1324a, *Bacillus aquimaris* STV1324b, and effective augmentation in a bioelectrochemical system for green energy production. *Cleaner Engineering and Technology*, 11, 100580, <https://doi.org/10.1016/j.clet.2022.100580>
- [42] K. Becerril-Varela, J. H. Serment-Guerrero, G. L. Manzanares-Leal, N. Ramírez-Durán, C. Guerrero-Barajas (2021) Generation of electrical energy in a microbial fuel cell coupling acetate oxidation to Fe³⁺ reduction and isolation of the involved bacteria. *World Journal of Microbiology and Biotechnology*, 37(6), 104, <https://doi.org/10.1007/s11274-021-03058-1>
- [43] C. Amanze, X. Zheng, M. Man, Z. Yu, C. Ai, X. Wu, S. Xiao, M. Xia, R. Yu, X. Wu (2022) Recovery of heavy metals from industrial wastewater using bioelectrochemical system inoculated with novel *Castellaniella* species. *Environmental Research*, 205, 112467, <https://doi.org/10.1016/j.envres.2022.112467>

- [44] Y. Qu, Y. Feng, X. Wang, B. E. Logan (2012) Use of a coculture to enable current production by *Geobacter sulfurreducens*. *Applied and Environmental Microbiology*, 78(9), 3484–3487, <https://doi.org/10.1128/AEM.06960-11>
- [45] S. Schmitz, M. A. Rosenbaum (2018) Boosting mediated electron transfer in bioelectrochemical systems with tailored defined microbial cocultures. *Biotechnology and Bioengineering*, 115(9), 2183–2193, <https://doi.org/10.1002/bit.26708>
- [46] M. A. Islam, H. R. Ong, B. Ethiraj, C. K. Cheng, M. M. R. Khan (2018) Optimization of co-culture inoculated microbial fuel cell performance using response surface methodology. *Journal of Environmental Management*, 225, 242–251, <https://doi.org/10.1016/j.jenvman.2018.07.097>
- [47] Z. Ren, T. E. Ward, J. M. Regan (2007) Electricity production from cellulose in a microbial fuel cell using a defined binary culture. *Environmental Science & Technology*, 41(13), 4781–4786, <https://doi.org/10.1021/es070577h>
- [48] T. Lin, X. Bai, Y. Hu, B. Li, Y. Yuan, H. Song, Y. Yang, J. Wang (2017) Synthetic *Saccharomyces cerevisiae*-*Shewanella oneidensis* consortium enables glucose-fed high-performance microbial fuel cell. *AIChE Journal*, 63(6), 1830–1838, <https://doi.org/10.1002/aic.15692>
- [49] M. A. Islam, B. Ethiraj, C. K. Cheng, A. Yousuf, S. Thiruvankadam, R. Prasad, M. M. Rahman Khan (2018) Enhanced current generation using mutualistic interaction of yeast-bacterial coculture in dual chamber microbial fuel cell. *Industrial & Engineering Chemistry Research*, 57(3), 813–821, <https://doi.org/10.1021/acs.iecr.7b03819>
- [50] C. Kim, Y. E. Song, C. R. Lee, B.H. Jeon, J. R. Kim (2016) Glycerol-fed microbial fuel cell with a coculture of *Shewanella oneidensis* MR-1 and *Klebsiella pneumoniae* J2B. *Journal of Industrial Microbiology and Biotechnology*, 43(10), 1397–1403, <https://doi.org/10.1007/s10295-016-1820-0>
- [51] V. B. Wang, K. Sivakumar, L. Yang, Q. Zhang, S. Kjelleberg, S. C. J. Loo, B. Cao (2015) Metabolite-enabled mutualistic interaction between *Shewanella oneidensis* and *Escherichia coli* in a co-culture using an electrode as electron acceptor. *Scientific Reports*, 5(1), 11222, <https://doi.org/10.1038/srep11222>
- [52] M. V. Gomez, G. Mai, T. Greenwood, J. Mullins (2014) The development and maximization of a novel photosynthetic microbial fuel cell using *Rhodospirillum rubrum*. *Journal of Emerging Investigators*, 3, 1–7, <https://doi.org/10.1016/j.jenvman.2014.05.001>
- [53] Y. Cho, T. Donohue, I. Tejedor, M. Anderson, K. McMahon, D. Noguera (2008) Development of a solar-powered microbial fuel cell. *Journal of Applied Microbiology*, 104(3), 640–650, <https://doi.org/10.1111/j.1365-2672.2007.03568.x>
- [54] D. Xing, Y. Zuo, S. Cheng, J. M. Regan, B. E. Logan (2008) Electricity generation by *Rhodospseudomonas palustris* DX-1. *Environmental Science & Technology*, 42(11), 4146–4151, <https://doi.org/10.1021/es800182t>
- [55] Y. Zuo, D. Xing, J. M. Regan, B. E. Logan (2008) Isolation of the exoelectrogenic bacterium *Ochrobactrum anthropi* YZ-1 by using a U-tube microbial fuel cell. *Applied and Environmental Microbiology*, 74(10), 3130–3137, <https://doi.org/10.1128/AEM.02826-07>
- [56] A. P. Borole, H. O'Neill, C. Tsouris, S. Cesar (2008) A microbial fuel cell operating at low pH using the acidophile *Acidiphilium cryptum*. *Biotechnology Letters*, 30, 1367–1372, <https://doi.org/10.1007/s10529-008-9699-2>
- [57] Z.D. Liu, H.R. Li (2007) Effects of bio-and abio-factors on electricity production in a mediatorless microbial fuel cell. *Biochemical Engineering Journal*, 36(3), 209–214, <https://doi.org/10.1016/j.bej.2007.02.019>
- [58] S. Das, R. K. Calay (2022) Experimental study of power generation and COD removal efficiency by air cathode microbial fuel cell using *Shewanella baltica* 20. *Energies*, 15(11), 4152, <https://doi.org/10.3390/en15114152>
- [59] D. E. Holmes, J. S. Nicoll, D. R. Bond, D. R. Lovley (2004) Potential role of a novel psychrotolerant member of the family Geobacteraceae, *Geopsychrobacter electrodiphilus* gen. nov., sp. nov., in electricity production by a marine sediment fuel cell. *Applied and Environmental Microbiology*, 70(10), 6023–6030, <https://doi.org/10.1128/AEM.70.10.6023-6030.2004>
- [60] K. Xiang, Y. Qiao, C. B. Ching, C. M. Li (2009) GldA overexpressing-engineered *E. coli* as superior electrocatalyst for microbial fuel cells. *Electrochemistry Communications*, 11(8), 1593–1595, <https://doi.org/10.1016/j.elecom.2009.06.017>

IZVOD

BACILLUS AMILOLIKUEFACIENS SOJ BAKTERIJA NSB4 ZA PREČIŠĆAVANJE OTPADNIH VODA ZA PRIMENU GORIVIH ČELIJA

Zagađivači u vodnim telima dolaze iz različitih izvora, uključujući, ali ne ograničavajući se na domaće, industrijske, komunalne itd. Zagađenje vode i nedostatak energije su globalni problemi koji zahtevaju značajnu pažnju. Zbog toga je neophodno sintetizovati održivu energiju i transportovati vodu bez otpada do prihvatnih mesta. Zabrinutost zbog nestašice energije i kontaminacije vode podstakla je razvoj tehnologije mikrobnih gorivih ćelija. Mikroorganizmi se koriste od strane elektrohemijske ćelijske prirode MFC-a za anaerobno varenje organskog otpada i proizvodnju energije. Fokusirajući se na jednokomorne MFC-ove bez medijatora koji rade u serijskom režimu, ova studija procenjuje efikasnost novog bakterijskog soja *Bacillus amiloliquefaciens* NSB4, kao egzoelektrogena u smislu prinosa električne energije i eliminacije otpada. Rezultati elektrohemijske karakterizacije soja pokazali su maksimalnu gustinu struje od 0,4804 A/m² i gustinu snage od 41,281 mW/m². Pored toga, Kolumbijska efikasnost (72%) i efikasnost smanjenja COD-a (90,46%) su takođe bile izuzetno visoke. Rast anodnog biofilma tokom MFC procesa pokazao je ključne performanse korišćenog egzoelektrogena. SEM slike biofilma su takođe predstavljene u studiji.

Ključne reči: mikrobne gorivne ćelije, MFC bez posrednika, separator, biofilm, tretman otpadnih voda.

Naučni rad

Rad primljen: 06.03.2024.

Rad korigovan: 29.04.2024

Rad prihvaćen: 22.05.2024.

Muhd Zu Azhan Yahya -

Serguei V. Savilov -

Dr. Sharad Agrawal -

<https://orcid.org/0000-0003-1129-0552>

<https://orcid.org/0000-0002-5827-3912>

<https://orcid.org/0000-0001-6126-1800>

Marija Mitrović¹, Milena Milovanović¹, Nebojša Vasiljević¹,
Milorad Tomić^{1,2*}

¹University of East Sarajevo, Faculty of Technology Zvornik, Zvornik,
Republic of Srpska, Bosnia and Herzegovina; ²Engineering Academy
of Serbia, Belgrade, Serbia

Scientific Paper

ISSN 0351-9465, E-ISSN 2466-2585

<https://doi.org/10.62638/ZasMat1174>



Zastita Materijala 65 (4)
623 – 633 (2024)

The Effect of Anodization and Subsequent Treatments on Corrosion Resistance of Aluminium

ABSTRACT

Aluminium samples were chemically prepared by following operations: degreasing, etching I, etching II, and brightening), prior to anodizing in sulfuric acid. Aluminium surface area was 0.2 dm². The composition of used aluminium samples was determined by the energy dispersive X-ray spectroscopy. Chemically prepared aluminium samples were electrochemically anodized for 45 minutes in a solution of 190 gdm⁻³ H₂SO₄ at room temperature, at a current density of 1.7 Adm⁻². In the anodizing process, the aluminium sample served as the anode, with lead cathodes. After anodizing, the aluminium samples underwent a colouring process in five pairs of solutions (systems), where each system consisted of two solutions of inorganic salts RxA + RxB (x = 1-5, numbers of solutions). Colouring of the anodized aluminium was carried out at room temperature by immersing the samples in each solution for 7 minutes (e.g., R1A + R1B, τ=7 min + 7 min). Each used colouring system provides a different colour: green-yellow, brown, light-grey, blue, and orange-gold. After colouring, the samples were treated in a special solution to improve corrosion resistance and silication, resulting in a change in the obtained colour shade. All obtained colours were stable with very nice appearance, allowing such coloured aluminium to be used for decorative purposes. The corrosion resistance of the coloured anodized aluminium samples was investigated by determining the corrosion potential, corrosion current and polarization resistance using potentiodynamic polarization method, as well as by electrochemical impedance spectroscopy. A common feature of all tested samples is a significant improvement in the corrosion resistance of the anodized aluminium after colouring and subsequent treatment in the corrosion resistance improvement solution, particularly after the additional silane treatment.

Keywords: Aluminium anodization, electrochemical impedance spectroscopy, potentiodynamic polarization, chemical colouring, silication, corrosion resistance.

1. INTRODUCTION

Aluminium is the third most abundant element in the Earth's crust, following oxygen and silicon, and exhibits a range of significant properties. The high mechanical strength of some of its alloys at low specific weight, good electrical and thermal conductivity, corrosion resistance, and various other characteristics make it widely applicable. Primarily used in aviation and military industries, aluminium and its alloys

are now prominent in electronics, chemistry, petroleum refining, machinery, construction, and automotive industries [1-3].

Reaction of aluminium and oxygen in atmospheric conditions, forming an oxide layer is one of the most important characteristic of aluminium. The excellent chemical stability of aluminium can be attributed to the presence of a passive oxide film [4-7]. Experimental measurements of the corrosion rate of high-purity aluminium in solutions with different pH values indicate that the corrosion rate in neutral solutions is very low (a few μAcm⁻²). A significant increase in the corrosion rate occurs in acidic and alkaline solutions, with a higher increase observed in alkaline solutions. The process of

* Corresponding author: Milorad Tomić
E-mail: milorad.tomic@tfzv.us.rs.ba
Paper received: 8.03.2024
Paper accepted: 22.05.2024.

anodic oxidation (anodization) on the surface of aluminium produces an oxide coating with enhanced protective (anticorrosive, anti-abrasive), electro-insulating, and adsorptive properties. This expands the application possibilities of aluminium and its alloys. The proper combination of operating parameters such as temperature, electrolyte type, applied voltage, current density, and duration of anodization are crucial to obtain an oxide film with advanced characteristics. Anodic coatings can be formed on aluminium using a variety of formulated electrolytes with the application of either direct or alternating current. Due to the porosity of the oxide layer, special attention is required for the final treatment of samples to close the pores in the coating and enhance corrosion resistance. Final treatment typically involves rinsing, colouring, and sealing. The oxide film formed on aluminium has good adsorption properties, allowing it to be coloured in various ways, including the use of organic or inorganic substances and electrochemical colouring (direct or alternating current) [8-18]. The colouring process not

only improves corrosion resistance but also provides a decorative effect, significantly expanding the application areas of aluminium.

The aim of this study is to investigate the corrosion resistance of aluminium after each processing stage: chemical preparation, anodization of aluminium in sulfuric acid, chemical colouring of aluminium in different solutions, and subsequent treatment to enhance corrosion resistance. Additionally, the goal was to obtain a final product (aluminium) in various colours and shades that, along with improved corrosion resistance, possesses enhanced decorative properties. This collectively broadens the possibilities of using aluminium as a structural material in various industries.

EXPERIMENTAL PART

Aluminium samples with a surface area of 0.2 dm², whose composition was determined using the Shimadzu EDX-8000 device and is presented in Table 1, were used for experiments.

Table 1. Composition of the aluminium sample expressed in wt. %

Element	Al	Fe	P	Ta	K	Ca	Zn	Sm
Wt.%	98.899	0.267	0.197	0.118	0.109	0.109	0.064	0.059
Element	Ba	Mn	Cr	V	Ga	As	Ni	Tl
Wt.%	0.054	0.036	0.029	0.026	0.014	0.012	0.006	0.003

Aluminium samples were subjected to a chemical preparation process before anodization in sulfuric acid: degreasing, etching I, etching II, and brightening. Degreasing was carried out in a solution: 50% Na₂CO₃, 50% Na₃PO₄·10H₂O, t= 60-70°C, τ= 15 min., 5% water solution, pH= 7.5 – 8.5. Etching I was performed in a solution: 20% NaOH, 2% NaF, τ=2-5 min., t= 70-75°C, and etching II in a solution: 550 cm³dm⁻³ HNO₃, 200 cm³dm⁻³ H₂SO₄, 140 cm³dm⁻³ NaF, τ= 5 min., at room temperature. Brightening was carried out in a solution: 20% HNO₃, 10% HF, τ= 5 min., at room temperature. After chemical preparation, the samples were subjected to anodization process in a solution of 190 gdm⁻³ H₂SO₄, at room temperature, τ= 5 min., and at a current density of 1.7 Adm⁻². After anodization, the aluminium samples underwent a chemical staining process in five different colouring systems, at room temperature. Each system consists of two solutions of inorganic salts, and the colouring time was the same in each of the

solutions (τ=7 min. + 7 min.). The following solutions were used [19]:

1. Solution for achieving yellow colour (R1A + R1B): 50-100 gdm⁻³ K₂Cr₂O₇ + 100-200gdm⁻³ Pb(CH₃COO)₂.
2. Solution for achieving brown colour (R2A + R2B): 10-50 gdm⁻³ K₄[Fe(CN)₆]·3H₂O + 10-100gdm⁻³ CuSO₄.
3. Solution for achieving light grey colour (R3A + R3B):, 10-50 gdm⁻³ Pb(CH₃COO)₂ + 10-50 gdm⁻³ Na₂SO₄.
4. Solution for achieving blue colour (R4A + R4B): 10-15 gdm⁻³ K₄[Fe(CN)₆]·3H₂O + 10-100 gdm⁻³ FeCl₃.
5. Solution for achieving golden yellow colour (R5A + R5B): 10-50 gdm⁻³ Na₂S₂O₃ + 10-50 gdm⁻³ KMnO₄.

After staining, the aluminium samples were treated in a solution of following composition, to improve

corrosion resistance (R_6) [19]: $0.1 \text{ gdm}^{-3} \text{ CoSO}_4$, $5.5 \text{ gdm}^{-3} \text{ CH}_3\text{COONa}$, $3.5 \text{ gdm}^{-3} \text{ H}_3\text{BO}_3$, $\text{pH} = 4.7\text{-}5.7$, at a temperature of $80\text{-}85^\circ\text{C}$ or by immersion for 3 min, in a solution of hot water at $t = 98^\circ\text{C}$ (silane treatment).

Surface of the aluminium samples were observed by Leica EZ4 HD optical microscope. The effect of treatments listed above on the corrosion resistance of aluminium in 3%NaCl was examined by potentiodynamic polarization method and electrochemical impedance spectroscopy. This corrosion measurements were performed using a potentiostat/galvanostat/ZRA Gamry Series GTM 750, in a standard three-electrode cell. The saturated calomel electrode was used as a reference electrode, a Pt electrode was used as a counter electrode and treated aluminium sample was working electrode. Tested sample surface area was 1 cm^2 . The Tafel plots was recorded in the range of $\pm 0.25 \text{ V}$ with respect to the open circuit potential, with a recording speed of 1 mV/s . Electrochemical impedance spectroscopy frequency range was $100\text{kHz} - 10\text{mHz}$, with a 7 mV sinusoidal voltage amplitude, at open circuit potential. The corrosion current density, corrosion potential, cathodic and anodic slope were calculated based on Tafel plots by the DC Corrosion Software for ZRA Gamry Series GTM 750 potentiostat/galvanostat.

The polarization resistance, R_p (Ωcm^2), is calculated according to Stern-Geary equation:

$$R_p = \frac{\beta_a \beta_c}{2.3 j_{\text{corr}} (\beta_c + \beta_a)} \quad (1)$$

Where $\beta_a \beta_a$ and $\beta_c \beta_c$ are anodic and cathodic Tafel slope in V, j_{corr} is corrosion current density in A/cm^2 .

RESULTS AND DISCUSSION

The aluminium samples surfaces were analysed before and after colouring process, and after subsequent silane treatment or immersion in a solution for improving corrosion resistance. Photographs of aluminium surfaces are given in Figures 1-6.

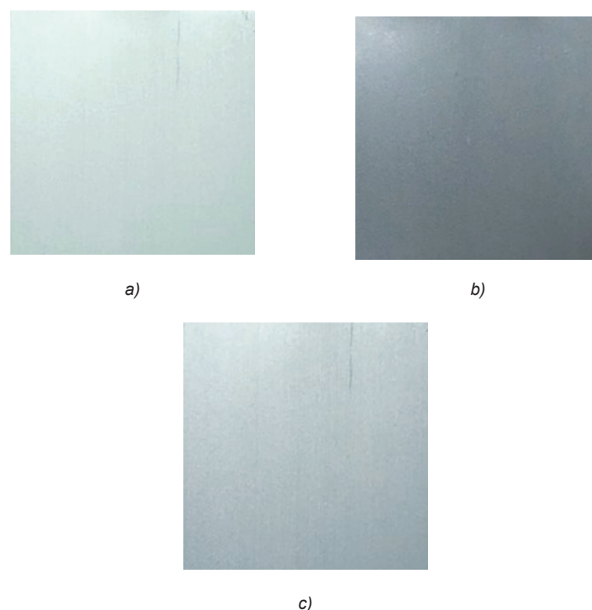


Fig. 1. Photographs of aluminium surface after: a) chemical preparation; b) anodization; c) silane treatment

From Figure 1, it can be observed that the aluminium sample after chemical preparation has a shiny silver colour, which turns into a darker matte colour during anodization in sulfuric acid. After subsequent treatment by silication, it remains a lighter shade similar to that of the chemically prepared sample.

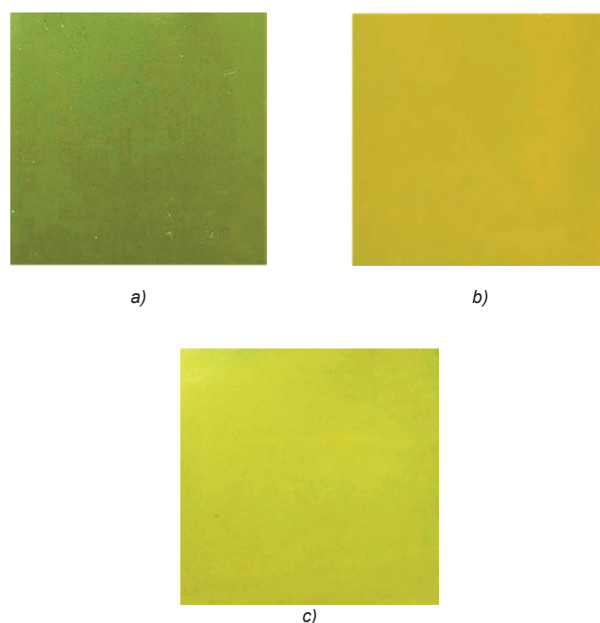


Fig. 2. Photographs of anodized aluminium surface: a) coloured in solutions R1A+R1B; b) after silane treatment; c) after treatment in solution R6

It can be seen from Figure 2 that the colour of the aluminium sample changes significantly after colouring with solutions R1A and R1B, from greenish-yellow to a darker yellow. After the silane treatment, the colour changed to a light yellow-green colour, and after treatment in solution R6, it becomes a light yellow-green shade.

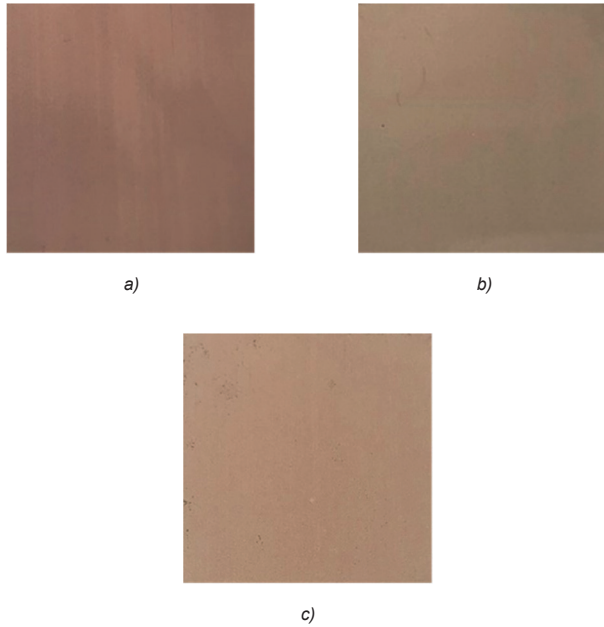


Fig. 3. Photographs of anodized aluminium: a) coloured in solutions R2A+R2B; b) after silane treatment; c) after treatment in solution R6

The surface of anodized aluminium after colouring with solutions R2A+R2B exhibits a brown colour. After subsequent silane treatment and treatment in solution R6, there is a slight change in the shade of brown colour, as seen in Figure 3.

Chemically coloured anodized aluminium in solutions R3A+R3B, and subsequent silane treatment or treatment in solution R6, results in different shades of light grey colour, as shown in Figure 4.

The anodized aluminium samples chemically coloured in solutions R4A+R4B display an intense blue colour, as shown in Figure 5. After subsequent silane treatment or treatment in the solution for improving corrosion resistance, there is a slight change in colour. After treatment in solution R6, the surface of the sample turns into a matte blue.

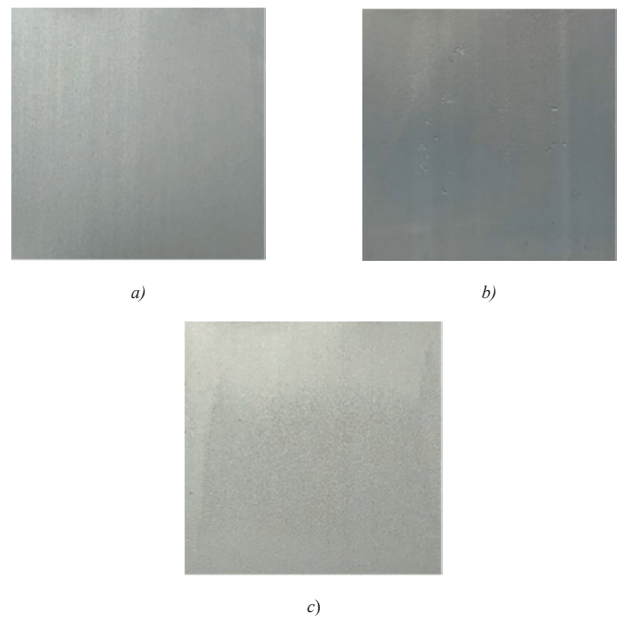


Fig. 4. Photographs of anodized aluminium: a) coloured in solutions R3A+R3B; b) after silane treatment; c) after treatment in solution R6

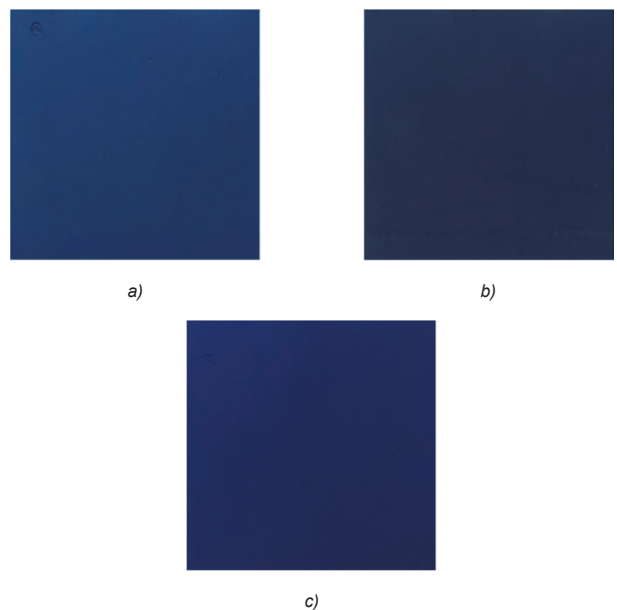


Fig. 5. Photographs of anodized aluminium: a) coloured in solutions R4A+R4B; b) after silane treatment; c) after treatment in solution R6

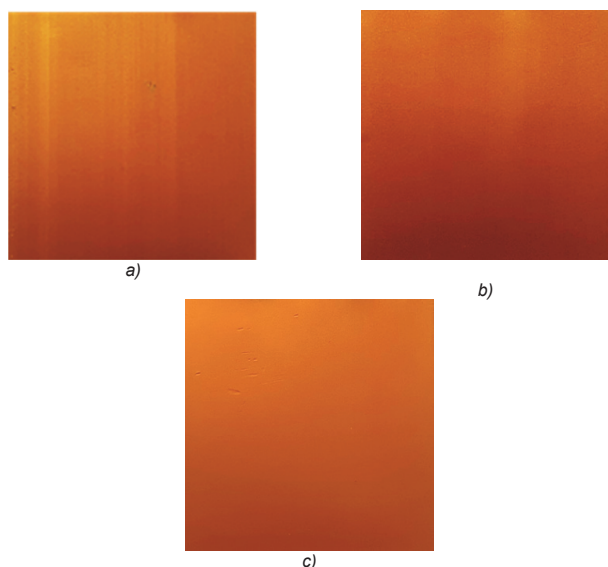


Fig. 6. Photographs of anodized aluminium: a) coloured in solutions R5A+R5B; b) after silane treatment; c) after treatment in solution R6

It can be observed from Figure 6 that aluminium samples chemically coloured in solutions R5A+R5B

exhibit an intense orange-gold colour. After treatment in solution R6, the surface of the sample retains its intense orange-gold colour.

Figures 1-6 demonstrate that through chemical treatment in various inorganic solutions, anodized aluminium can be coloured in different shades, expanding its potential utilization as a structural material for interior and exterior decoration, as well as for creating devices with advanced appearances. Corrosion resistance of aluminium after chemical preparation, anodization, colouring, and subsequent silane treatment by or treatment in a solution for improving corrosion resistance was examined by potentiodynamic polarization method and by electrochemical impedance spectroscopy (EIS). Figures 7–11 depict Tafel polarization diagrams showing the potential (E) dependence on the logarithm of current density ($\log j$). The relevant electrochemical parameters obtained from the polarization curves, including corrosion potential (E_{corr}), corrosion current density (j_{corr}), corrosion rate (π) and polarization resistance (R_p) are shown in Table 2.

Aluminium after:	j_{corr} ($nAcm^{-2}$)	$-E_{\text{corr}}$ (V)	π (μmgod^{-1})	R_p ($M\Omega\text{cm}^2$)
Chemical preparation	3890	0.81	130	0.008
Anodization	21.10	0.58	0.70	4.80
R1A+R1B	111.1	0.68	30.0	0.120
R1A+R1B+silane treatment	0.548	0.59	0.02	56.0
R1A+R1B+R6	1.630	0.66	0.05	21.0
R2A+R2B	49.90	0.59	1.60	8.80
R2A+R2B+silane treatment	0.649	0.57	0.03	33.0
R2A+R2B+R6	35.10	0.64	1.20	3.80
R3A+R3B	1700	0.67	57.0	0.003
R3A+R3B+silane treatment	72.70	0.58	2.30	0.30
R3A+R3B+R6	31.90	0.62	1.10	1.50
R4A+R4B	1600	0.66	54.0	0.04
R4A+R4B+silane treatment	0.481	0.54	0.02	9.00
R4A+R4B+R6	21.10	0.61	0.70	2.00
R5A+R5B	4.900	0.50	0.16	8.70
R5A+R5B+silane treatment	1.890	0.69	0.25	23.0
R5A+R5B+R6	1.610	0.60	0.05	21.0

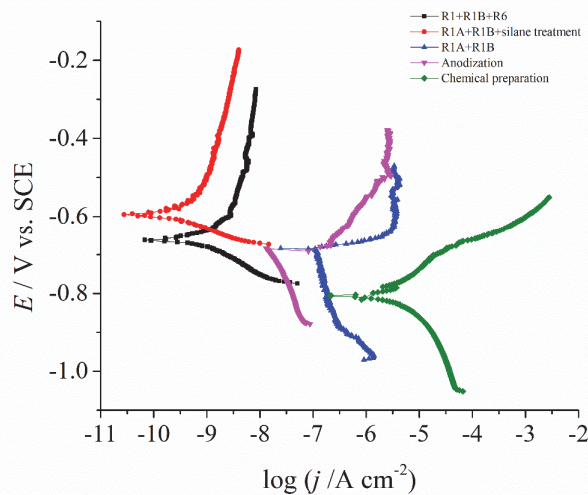


Fig. 7 Tafel plots for aluminium after chemical preparation, anodization, colouring in R1A+R1B, subsequent silane treatment, and treatment in solution R6

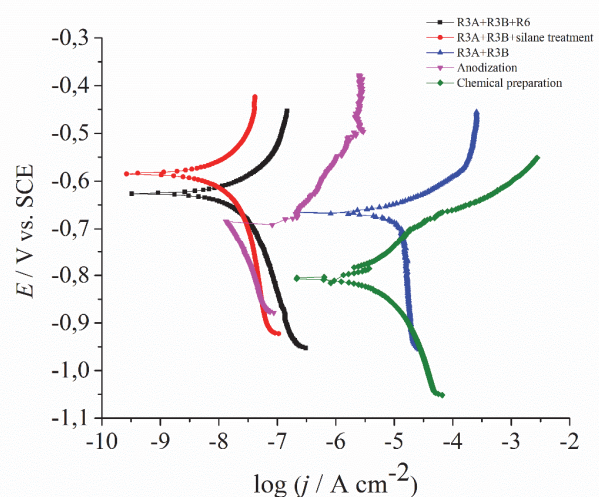


Fig. 9 Tafel plots for aluminium after chemical preparation, anodization, colouring in R3A+R3B, subsequent silane treatment, and treatment in solution R6

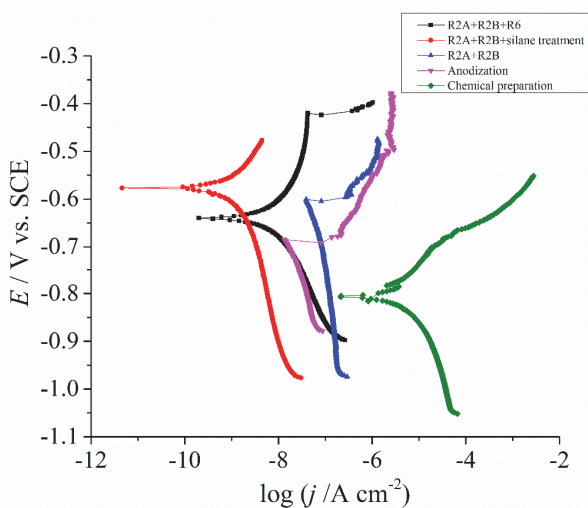


Fig. 8 Tafel plots for aluminium after chemical preparation, anodization, colouring in R2A+R2B, subsequent silane treatment, and treatment in solution R6

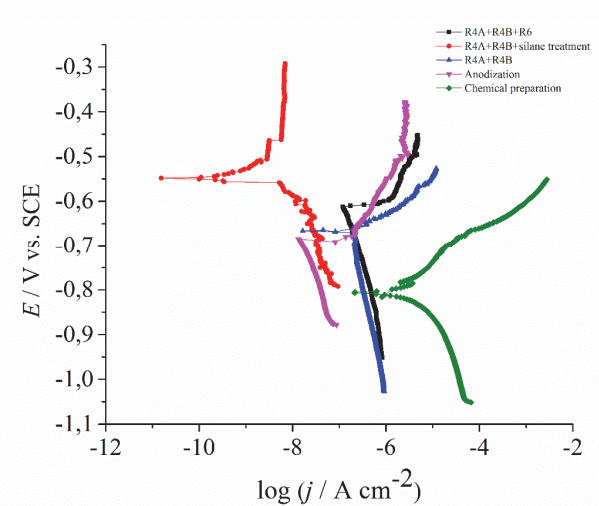


Fig. 10 Tafel plots for aluminium after chemical preparation, anodization, colouring in R4A+R4B, subsequent silane treatment, and treatment in solution R6

From the Figures 7-11 and from the Table 2 it is evident that all examined treatments, i.e. anodization, colouring and silane treatment improves the corrosion resistance of aluminium in saline environment compared to chemical treated aluminium sample. The corrosion current is decreased more than 5 thousand times only by anodization, and by further treatments like colouring and silane treatment the corrosion current value changed from μAcm^{-2} to pAcm^{-2} . The most corrosion resistant aluminium

sample was after colouring and silane treatment, which implies the importance of pore closure for good aluminium corrosion stability. The silane treatment showed better results compared to examine solution for enhancement corrosion resistance (R6). From the results of corrosion rate and polarization resistance it can be seen that aluminium samples coloured in solutions R5A+R5B exhibit the best corrosion resistance.

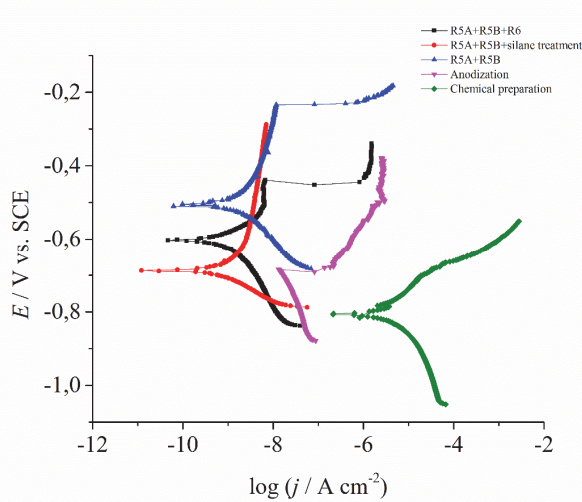
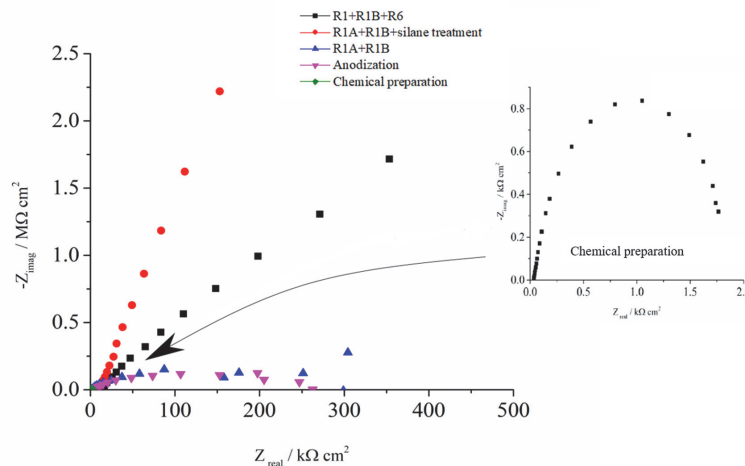
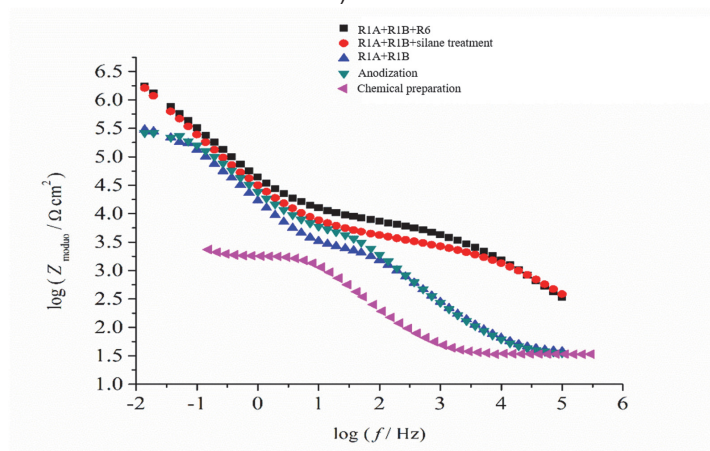


Fig. 11 Tafel plots for aluminium after chemical preparation, anodization, colouring in R5A+R5B, subsequent silane treatment, and treatment in solution R6

In general, the colouring process increases corrosion resistance of anodized aluminium. The best corrosion resistance, i.e., the most positive corrosion potential, is exhibited by aluminium coloured in solutions R5A+R5B ($E_{corr} = -0.50V$), and no subsequent treatment is needed after colouring in these solutions since corrosion parameters are not changing significantly by further treatments. After colouring of anodized aluminium in solutions (R1A+R1B; R2A+R2B; R3A+R3B; and R4A+R4B), the subsequent treatment in solution R6, and especially silication, significantly improves corrosion resistance. Silane treatment proves to be very effective, as it not only enhances the corrosion resistance of coloured samples but also has no significant impact on the colour change before and after treatment.



a)



b)

Fig. 12. a) Nyquist plot and b) Bode plot for aluminium after chemical preparation, anodization, colouring in R1A+R1B, subsequent silane treatment, and treatment in solution R6

Figures 12–17 show graphs depicting the dependence of $-Z_{imag}$ on Z_{real} (Nyquist plots) and the dependence of $\log Z_{moduo}$ on $\log f$ (Bode plots) obtained by electrochemical impedance spectroscopy (EIS) for aluminium samples that were chemically prepared, anodized, coloured in solutions (R1A+R1B; R2A+R2B; R3A+R3B; R4A+R4B; and R5A+R5B), subsequently treated in solution R6, and further treated by silication.

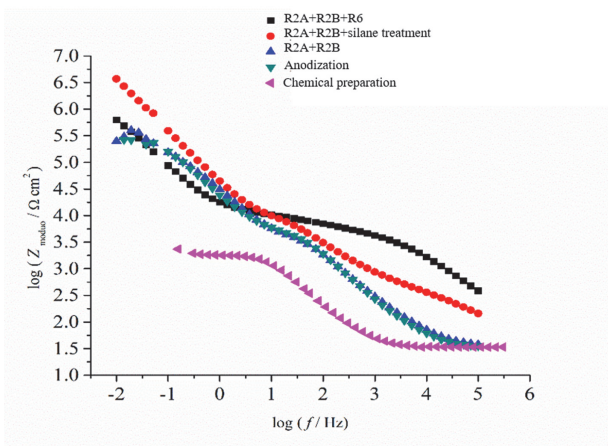
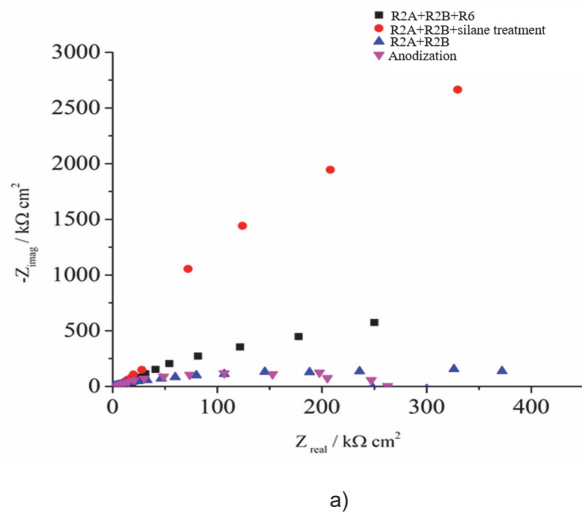


Fig. 13. a) Nyquist plot and b) Bode plot for aluminium after chemical preparation, anodization, colouring in R2A+R2B, subsequent silane treatment, and treatment in solution R6

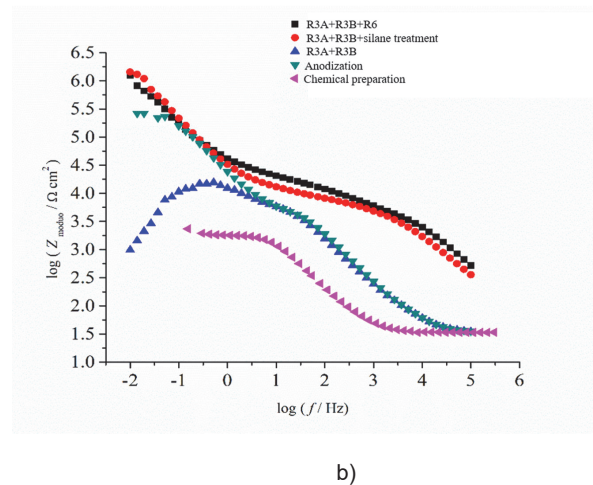
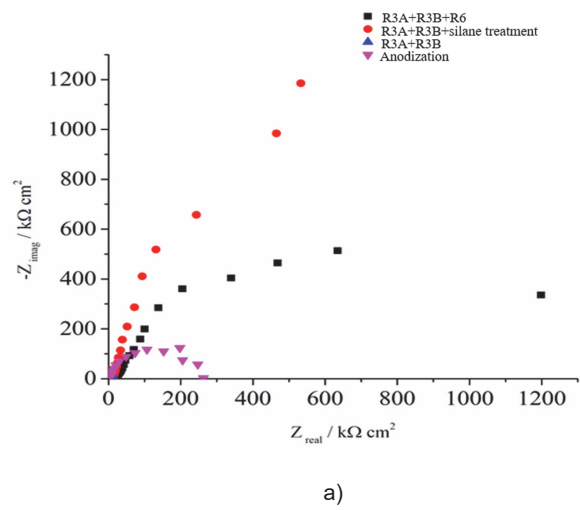


Fig. 14. a) Nyquist plot and b) Bode plot for aluminium after chemical preparation, anodization, colouring in R3A+R3B, subsequent silane treatment, and treatment in solution R6

Based on the Nyquist and Bode plots (Figures 12–15), it can be generally stated that coloured anodized aluminium in solutions (R1A+R1B; R2A+R2B; R3A+R3B; and R4A+R4B), subsequently treated in solution R6, and especially silication, significantly improve corrosion resistance. Moreover, all samples treated by silication exhibit the highest corrosion resistance.

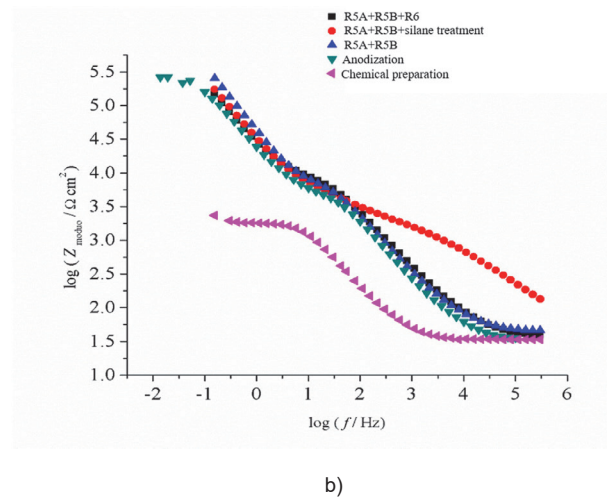
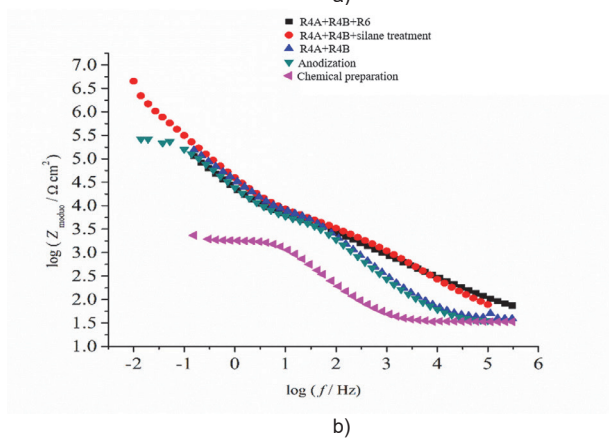
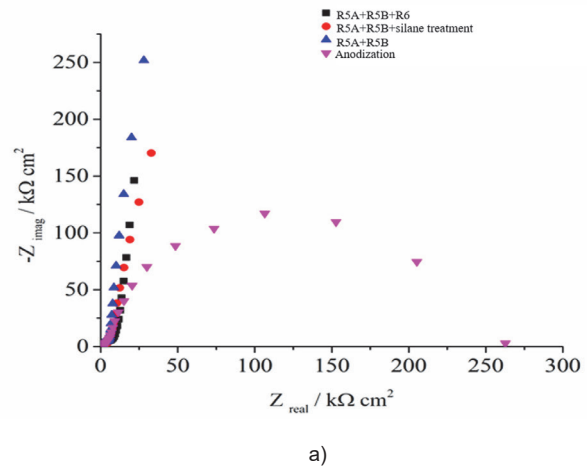
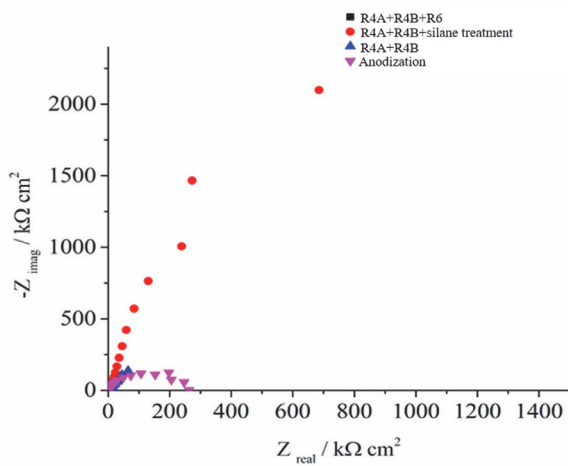


Fig. 15. a) Nyquist plot and b) Bode plot for aluminium after chemical preparation, anodization, colouring in R4A+R4B, subsequent silane treatment, and treatment in solution R6

Fig. 16. a) Nyquist plot and b) Bode plot for aluminium after chemical preparation, anodization, colouring in R5A+R5B, subsequent silane treatment, and treatment in solution R6

From the Nyquist and Bode plots (Figure 16), it is evident that aluminium samples coloured after anodization in solutions R5A and R5B demonstrate the highest corrosion resistance. Aluminium samples coloured in solutions R5A and R5B and subsequently treated in solution R6, as well as those treated by silication, show lower resistance to corrosion. This indicates that aluminium painted in R5A and R5B does not require subsequent treatment.

The results obtained from the Tafel polarization diagrams and corrosion resistance of the examined aluminium samples are in complete agreement with the results from electrochemical impedance spectroscopy (EIS). Anodized aluminium coloured in solutions (R1A+R1B; R2A+R2B; R3A+R3B; and R4A+R4B), after subsequent treatment in solution R6, exhibits improved corrosion resistance, while the

highest corrosion resistance is observed in all samples treated by silication.

CONCLUSION

Anodizing aluminium in sulfuric acid under defined conditions forms an oxide layer with specific characteristics that significantly influence the corrosion resistance of the base metal. By chemically colouring anodized aluminium and subsequent treatments, either with solution R6 or silication, a final product (aluminium) of various colours and shades with improved corrosion resistance is obtained. By chemical colouring of anodized aluminium in the proposed combination of solutions it is possible to obtain the green-yellow, brown colour, light grey, blue, and orange-gold colour. Subsequent treatment

by silication minimally affects shade of colour of the chemically coloured sample, while solution R6, in addition to a slight change in colour shade, mattifies the surfaces. Results gained by potentiodynamic polarization and electrochemical impedance spectroscopy methods showed that colouring of anodized samples in all used pairs of solutions increases corrosion resistance. By applying subsequent treatment in solution R6, and especially silication, corrosion resistance is increased, except for anodized aluminium coloured in solutions R5A+R5B, which had very good corrosion resistance in 3%NaCl after chemical colouring and did not require subsequent treatment. This indicates the reliability of the obtained results and the methods used.

Acknowledgement: This research was financed by the Ministry of Scientific and Technological Development and Higher Education of the Republic of Srpska (Contract No. 19.032/431-1-34/23)

REFERENCE

- [1] R. Vračar, Ž. Živković (1993) Ekstraktivna metalurgija aluminijuma, Naučna knjiga, Beograd .
- [2] M. Antić, M. Smiljanić (2003) Aluminijum i aluminijumske legure, Beograd
- [3] D. Vuksanović, (2018) Uvod u metalurgiju i metale, knjiga, Podgorica
- [4] M.G. Pavlović, M.V. Tomić, Lj.J Pavlović (2005) Electroplating of silver onto aluminum and its alloys", Journal Materials Protection, 46 (2),23-27.
- [5] M. Tomić, Lj. Pavlović, M. Pavlović (2005) Direct electroplating of copper coatings onto aluminium, Journal Materials Protection 46(3), 13-16
- [6] Ki Beom Kim, Byung Chan Kim, Seok Jae Ha ,Myeong Woo Cho (2017) Effect of pre-treatment polishing on fabrication of anodic aluminum oxide using commercial aluminum alloy, J. Mech. Sci. Technol. (31) 4387–4393
- [7] M. T. Wu, I. C. Leu, M. H. Hon (2002) Effect of polishing pretreatment on the fabrication of ordered nanopore arrays on aluminum foils by anodization, JVST B (20) 775-782
- [8] M. Michalska-Domańska et al. (2015) Fabrication of super slippery sheet-layered and porous anodic aluminium oxide surfaces and its anticorrosion property, Appl. Surf. Sci., (355) 487–526
- [9] Craig J. Donahue, Jennifer A. Exline (2014) Anodizing and Coloring Aluminum Alloys, J. Chem. Educ. 2014, 91, 5, 711–715
- [10] P. Vengatesh, M. A. Kulandainathan (2015) Hierarchically ordered self-lubricating superhydrophobic anodized aluminum surfaces with enhanced corrosion resistance, ACS Appl. Mater. Interfaces, (7) 1516–1526
- [11] S. Đorđević, M. Maksimović, M.G. Pavlović, K.I. Popov (2000) Galvanotehnika, Tehnička knjiga, Beograd.
- [12] M. Tomić, Lj. Pavlović, M. Pavlović, M. Stojanović, B. Milošević (2004) The effect of preparation of aluminum surface on surface reflection, Journal Materials Protection, 45(2) 63-67
- [13] M. Tomić, M. Pavlović, Z. Rakočević, Lj. Pavlović (2004) The effect of preparation of aluminum surface on surface roughness, Journal Materials Protection 45(1),5-12
- [14] M. S. de Miera, M. Curioni, P. Skeldon, G.E. Thompson (2010) The behaviour of second phase particles during anodizing of aluminium alloys. Corr. Sci., 52(7), 2489-2497.
- [15] J. Konieczny, K. Labisz, M. Polok-Rubiniec, A. Włodarczyk-Fligier (2016) Influence of aluminium alloy anodizing and casting methods on structure and functional properties, Arch. Metall. Mater, 61(3), 1337-1342.
- [16] U. Donatus, G.E. Thompson, D. Elabar, T. Hashimoto, S. Morsch (2015) Features in aluminium alloy grains and their effects on anodizing and corrosion. Surf. Coat. Tech., 277, 91-98.
- [17] M. Shahzad, M. Chaussimier, R. Chieragatti, C. Mabrú, F. Rezai-Aria (2010) Influence of anodizing process on fatigue life of machined aluminium alloy. Procedia Eng, 2(1), 1015-1024.
- [18] P.B. Madakson, I.A. Malik, S.K. Laminu, I.G. Bashir (2012) Effect of anodization on the corrosion behavior of aluminium alloy in HCl acid and NaOH, Int. J. Mater. Eng., 2(4), 38-42.
- [19] YA. V. Vainep, M. A. Dasoya (1972) Tehnologiya Elektrokhimicheskikh Pokryti, Leningrad.

IZVOD

UTICAJ ANODIZACIJE I NAKNADNIH TRETMANA NA OTPORNOST ALUMINIJUMA NA KOROZIJU

Uzorci aluminijuma površine $0,2 \text{ dm}^2$ pre anodizacije u sumpornoj kiselini podvrgnuti su procesu hemijske pripreme (odmašćivanje, nagrivanje I, nagrivanje II i odmašćivanje). Sastav uzoraka aluminijuma određen je energetsom disperzijom X-zraka na uređaju Shimadzu EDX-8000. Tako pripremljeni uzorci aluminijuma su elektrohemijski anodizovani 45 minuta u rastvoru $190 \text{ gdm}^{-3} \text{ H}_2\text{SO}_4$ na sobnoj temperaturi, pri gustini struje $1,7 \text{ Adm}^{-2}$. U procesu anodizacije kao anoda korišćen je uzorak aluminijuma, a katode su bile od olova. Nakon anodizacije uzorci aluminijuma su podvrgnuti procesu bojenja u pet parova rastvora (sistema), gde se jedan sistem sastoji od dva rastvora neorganskih soli $R_xA + R_xB$ ($x = 1-5$, broj rastvora). Bojenje anodizovanog aluminijuma vršeno je na sobnoj temperaturi potapanjem uzoraka u svaki rastvor po 7 minuta (npr. R1A + R1B, $\tau = 7 \text{ min} + 7 \text{ min}$). Svaki korišćen sistem za bojenje aluminijuma daje različitu boju: zeleno-žutu, braon, svetlo-sivu, plavu i narandžasto-zlatnu boju. Nakon bojenja uzorci su obrađivani u rastvoru za poboljšanje korozione postojanosti i siliranjem, usled čega dolazi do promene dobijene nijanse boje. Sve dobijene boje su stabilne i dekorativne, tako da se ovako obojeni aluminijum može koristiti i u dekorativne svrhe.

Koroziona postojanost obojenih anodiziranih uzoraka aluminijuma ispitivana je određivanjem korozionog potencijala i struje korozije pomoću snimljenih polarizacionih dijagrama, kao i pomoću spektroskopije elektrohemijske impedanse (SIE).

Zajedničko svim ispitivanim uzorcima je značajno poboljšanje korozione postojanosti anodno obrađenog aluminijuma nakon bojenja i naknadne obrade u rastvoru za poboljšanje korozione postojanosti, a posebno nakon naknadne obrade siliranjem

Ključne reči: Anodizacija aluminijuma, spektroskopija elektrohemijske impedanse, polarizacioni dijagrami, hemijsko bojenje, siliranje, koroziona postojanost.

Naučni rad

Rad primljen: 8.03.2024

Rad prihvaćen: 22.05.2024.

The ORCID Ids of all the authors are as follows:

Milorad Tomic: <https://orcid.org/0009-0004-1022-2093>

Marija Mitrovic: <https://orcid.org/0000-0002-3208-016X>

Nebojsa Vasiljevic: <https://orcid.org/0000-0002-3789-9975>

Milena Milovanovic: <https://orcid.org/0009-0008-6545-7024>

Bashir Abdu Muzakkari¹, Amina Salihi Bayero²,
Musa Ibrahim Mohammed³, Pramod Kumar Singh⁴,
Umar Muhammad Jibreel^{2&5}

¹Computer Science Department, Yusuf Maitama Sule University, Kano, Nigeria; ²Chemistry Department, Yusuf Maitama Sule University, Kano, Nigeria; ³Department of Pure and Industrial Chemistry, Bayero University, Kano, Nigeria; ⁴Department of Physics, Sharda School of Basic Sciences and Research, Sharda University, India; ⁵Federal College of Agricultural Produce Technology, Kano, Nigeria.

Review paper

ISSN 0351-9465, E-ISSN 2466-2585

<https://doi.org/10.62638/ZasMat1153>



Zastita Materijala 65 (4)
634 – 644 (2024)

Waste Tyres Pyrolysis Oil (WTPO) as an Alternative Source of Fuel and Chemicals: A Review

ABSTRACT

Waste tyres are dumped and common kind of abandon solid waste. Almost 3 billion tyres are produced each year and each tyre produced will eventually join the waste products and if not properly handled will become pollutant. In many countries disposal of waste tyres is prohibited; as an alternative they should be recovered and recycled instead. In this review pyrolysis was introduced as an alternative way of recycling waste tyres, Pyrolysis allows the dissolution of the waste and it also produces useful by-products. The products obtained during the process are pyrolysis oil, pyrolysis char and condensable gas. Pyrolysis oil is the major product among them, this paper reviewed pyrolysis oil as an alternative sources of fuel to diesel engines and as well to highlight the chemicals obtained in the waste tyres from the pyrolysis oil which mainly depends on the kind of feedstock (i.e. type of tyres e.g truck, cars, bicycle) used in the pyrolysis process. Most of the compounds obtained are Aliphatic and Aromatic hydrocarbons (especially the Polycyclic Aromatic Hydrocarbon PAHs) such as Naphthalene – NAP, Acenaphthylene – ACY, Acenaphthene – ACE, Fluorene – FLU, Phenanthrene – PHE, Anthracene – ANT, Fluoranthene – FLT, Pyrene – PYR, Benzo[a]anthracene – BAA, Chrysene – CRY, Benzo[b]fluoranthene – BBF, Benzo[k]fluoranthene – BKF, Benzo[a]pyrene – BAP, Dibenzo[a,h]anthracene – DBA, Benzo[g,h,i]perylene – BGP, Indeno[1,2,3-cd]pyrene – IND among others. Consequently the pyrolysis oil obtained need further upgrading via a reaction pathways are hydrodesulfurization (HDS), hydrodearomatization (HDA) and hydrocracking (HC) which can be achieved through a 2-stage hydroprocessing strategy regarding WTPO composition in terms of HDS, HAD and HC. Pyrolysis oil from waste tyres can be used as a substitute for diesel and as well as sources of raw materials and fuel to organic chemical industries.

Keywords: waste tyres, pyrolysis, pyrolysis-oil, chemicals, upgrading.

1. INTRODUCTION

The yearly production of discarded tyres has increased dramatically as a result of the transportation and automotive industries fast development. With an anticipated annual growth in market de-

mand of more than 4%, the yearly production of tyres is predicted to be over 3 billion. Additionally, billions of end-of-life tyres will inevitably be created, necessitating trash treatment, disposal, and management. Tyre stockpiling and incorrect disposal harm the environment by creating habitats for insects and rodents, as well as increasing the risk of fire in huge tyre dumps [1] Fig 01.

* Corresponding author: Umar Muhammad Jibreel
E-mail: jibreelumar@gmail.com, jibreelumar@fcapt.edu.ng
Paper received: 20.03.2024.
Paper accepted: 14.06.2024.



Fig 01: Improper dumping of waste tyre

Options for recovering materials from scrap tyres include recycling them into rubber and rubber particles for playground and sports field flooring, as well as using them as application materials in civil engineering. In certain nations, disposing of used tyres in a landfill is part of the treatment and disposal process. But because the rubber and sulfur linkages in waste tyres are strongly cross-linked, the rubber in waste tyres does not break down quickly in landfills

[2]. As a result, society improperly manages or disposes waste tyres by burning them into ashes on a flat piece of ground (Fig. 2), which pollutes the air, produces unwelcome and toxic smoke, and damages habitats by causing illness. For this reason, there has been a push recently to identify more valuable and sustainable resource recovery methods for handling discarded tyres [1].



Fig 02: Improper handling of waste tyres

2. PYROLYSIS AS A WASTE TYRE RECYCLING METHOD

However, because the rubber and sulfur linkages in waste tyres are strongly cross-linked, the rubber in waste tyres does not break down quickly in landfills. For this reason, there has been a push recently to identify more valuable and sustainable resource recovery methods for the process of treating waste tyres which is known as pyrolysis [1].

Pyrolysis is a thermal decomposition process that turns organic molecules into a complicated mixture of solid, liquid, and gaseous components in the absence of oxygen. For many years, this method has been utilized to transform different waste materials—such as biomass, plastics, and rubber—like tyres, into useful goods like carbon black, chemicals, and pyro fuels. Pyrolysis is seen as a promising technology because it produces useful goods and minimize waste volume and environmental effect while managing trash and recovering resources [3-4].

Waste tyres are heated to a certain temperature in the absence of oxygen during the pyrolysis process, which yields useful goods like char, gas, and pyrolysis oil. In a pyrolysis reactor, waste tyres are heated to elevated temperatures (usually between 300°C and 700°C). This process releases gas, char, and oil vapours from the tyres as they break down into smaller molecules [5-6].

3. STAGES IN PYROLYSIS PROCESS

The pyrolysis process is divided into three stages: the initial heating stage, the main pyrolysis stage, and the cooling stage. During the initial heating stage, the temperature of the reactor is raised to the desired temperature. In the main pyrolysis stage, the waste tyres are heated to the desired temperature, and the pyrolysis reactions occur, resulting in the production of pyrolysis oil, gas, and char. Finally, in the cooling stage, the reactor is cooled, and the products are collected [5, 7].

The pyrolysis oil produced from the process can be used as a fuel in boilers, furnaces, and diesel engines after upgrading. The gas produced can be used as a fuel for the pyrolysis process, and the char can be used as a solid fuel or as an additive in rubber products [7].

4. PYROLYSIS APPLICATIONS

Pyrolysis process has been applied in different industries and regions worldwide. In the agriculture

sector, pyrolysis has been used to convert waste agricultural residues into biochar, which can improve crop yields, reduce soil erosion and sequester carbon. In the forestry sector, pyrolysis has been used to convert wood chips and forest residues into bio-oil, which can serve as a feedstock for further processing to obtain transportation fuels [6,8].

In the municipal solid waste sector, pyrolysis has been used to convert household and commercial waste into biochar and non-condensable gases. The biochar can reduce the amount of waste sent to landfills, while the non-condensable gases can generate electricity or used in heating systems [6,8].

In the industrial sector, pyrolysis has been used to convert manufacturing and processing waste into biochar, which can be used as a fuel or carbon sequestration. The process reduces waste disposal costs and greenhouse gas emissions [6,8].

5. TYPES OF PYROLYSIS

There are three main types of pyrolysis: **fast pyrolysis, slow pyrolysis, and intermediate pyrolysis**. Each of these types has different operating temperatures, heating rates, and product yields [9,10].

5.1. Fast Pyrolysis

Fast pyrolysis is a high-temperature process that rapidly heats biomass or waste materials at temperatures between 450°C and 600°C in the absence of oxygen. The heating rates in fast pyrolysis are typically in the range of 10°C/s to 50°C/s. The rapid heating and short residence time of the biomass or waste material in the reactor result in the production of a high yield of liquid bio-oil, which contains a mixture of organic compounds. The liquid bio-oil can be used as a fuel for heat and power generation or as a feedstock for the production of chemicals and materials. The remaining solid residue, known as biochar, can be used as a soil amendment or as a carbon sequestration agent [9,10].

5.2. Slow Pyrolysis

Slow pyrolysis is a low-temperature process that heats biomass or waste materials at temperatures between 300°C and 500°C in the absence of oxygen. The heating rates in slow pyrolysis are typically in the range of 0.1°C/min to 10°C/min. The slow heating and long residence time of the biomass or waste material in the reactor result in the production of a low

yield of liquid bio-oil, which contains a high proportion of water and oxygenated compounds. The remaining solid residue, known as biochar, has a high fixed carbon content and can be used as a soil amendment or as a carbon sequestration agent [9,10].

5.3. Intermediate Pyrolysis

Intermediate pyrolysis is a moderate-temperature process that heats biomass or waste materials at temperatures between 350°C and 450°C in the absence of oxygen. The heating rates in intermediate pyrolysis are typically in the range of 10°C/min to 100°C/min. The intermediate heating and residence time of the biomass or waste material in the reactor result in the production of a moderate yield of liquid bio-oil, which contains a mixture of organic

compounds. The remaining solid residue, known as biochar, can be used as a soil amendment or as a carbon sequestration agent [9,10].

6. PRODUCT TYPES IN PYROLYSIS

The pyrolysis process produces three main end-products, namely **pyro-oil, pyro char, and non-condensable gases**. Pyro-oil is a dark brown liquid with a high water content and a complex mixture of organic compounds. The pyro-oil requires further processing to remove impurities, such as water, acids, and oxygen compounds (Fig 03). The refined pyro-oil can serve as a feedstock for further processing, such as fractional distillation and hydroprocessing, to obtain transportation fuels [11].

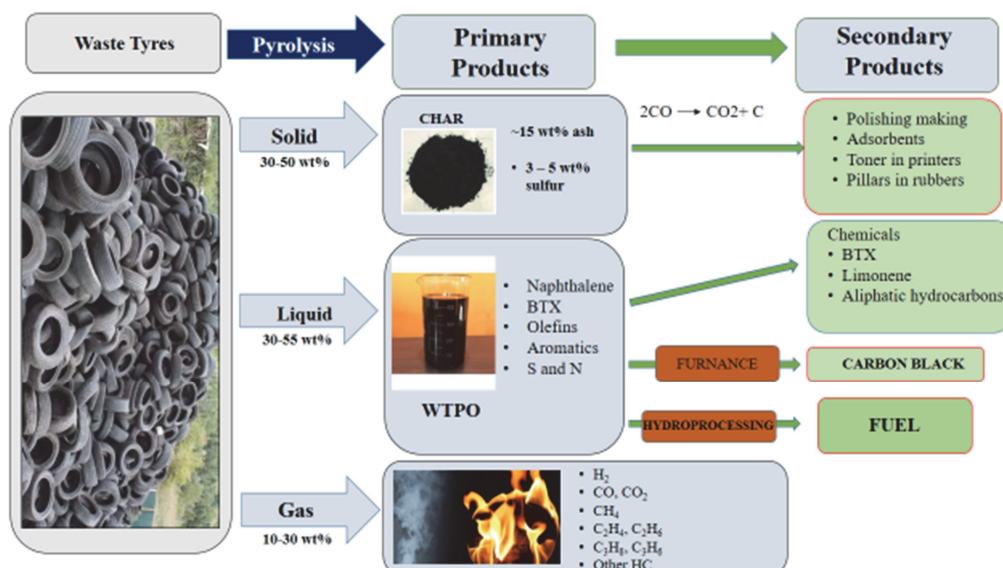


Fig 03: Primary and secondary products from waste tyre pyrolysis.

6.1. Pyrolysis-oil

Pyro-oil is a dark brown liquid that is produced during pyrolysis. It is a complex mixture of organic compounds, such as phenols, ketones, aldehydes, and carboxylic acids. Pyro-oil has a high energy density and can be used as a fuel in various applications, including power generation, heating, and transportation. The main drawback of pyro-oil is its instability, as it degrades rapidly when exposed to air, light and water [12-16]. It contains high water content and requires further processing to remove impurities and obtain transportation fuels. Non-con-

densable gases can generate electricity or used in heating systems [11].

6.2. Pyro char

Pyro-char is a carbon-rich solid material that is produced during pyrolysis. It is a black porous substance that contains high amounts of carbon, and low amounts of volatiles and ash. Pyro-char can be used as a soil amendment, as it increases soil fertility and water retention, and reduces greenhouse gas emissions. It can also be used as a fuel, as it has a high calorific value and burns cleanly [12-16].

It is a solid residue obtained from pyrolysis that can be used as a soil amendment, carbon sequestration, or fuel. The pyro char has high carbon content and can improve soil fertility, water retention, and reduce greenhouse gas emissions [11].

6.3. Non-condensable gases

Condensable gas is a mixture of various gases, such as methane, ethane, propane, and butane. It is produced during pyrolysis when the organic materials are heated and gasified. Condensable gas can be used as fuel in power generation or as a feedstock for chemical synthesis [12-16].

Non-condensable gases are mainly composed of carbon dioxide, carbon monoxide, and methane. The gases can generate electricity or used in heating systems [6, 8].

7. PYROLYSIS OIL AS A FUEL ENERGY

This is the most abundant as well as the most interesting and economically attractive product of the waste tyres pyrolysis. It is a brownish liquid resembling crude oil (Fig 04) and consists basically of:

- (i) The processing liquid as part of the tyre formulation,
- (ii) Organic additives, and
- (iii) Tyre pyrolysis products [17].



Fig 04: Pyrolysis Oil

The calorific value (CV) of pyrolysis oil (PO) can be as high as 44MJkg^{-1} , comparable to valued fuels,

so it requires a separated section to be analyzed in terms of its composition and potential for being used as alternative fuel in diesel engines [17].

7.1. Elemental Composition of Pyrolysis Oil

Despite the different technologies and operational conditions strongly affecting WTPO yield, its composition does not vary as significantly as that of the gaseous fraction (Table 1). Sulfur compounds in waste tyre pyrolysis oil (WTPO) have their origin in the thermal degradation of the organic additives used as vulcanization agent and accelerators in tyre manufacturing [18]. Comparing this data with the elemental analysis of tyres listed in Table 2 which shows the various elemental composition of different kind of tyres: tyres from passenger car tyre (PCT) and truck tyre (TT), bicycle tyre (BT), has higher amounts of C and H are observed in WTPO, together with less oxygen, sulfur and N amount, that has been either removed in the pyrolysis or retained in the solid fraction. The reaction pathways through which sulfur compounds are produced change with pyrolysis conditions (temperature, pressure and residence time) and yield different amounts of sulfurous compounds in WTPO. Some authors have reported values of sulfur in the WTPO of 0.3wt% [18], but the majority of the reported values correspond to ca.1.4wt% [19]. Cleavage of the N-S and C-S bonds of N-N0-caprolactam and benzothiazolic additives in tyres produce caprolactum and benzothiazole in WTPO [20]. Unapumnuk *et al.*, 2008 [21] corroborated the crucial role of temperature on S content in S WTPO, as less S was retained in WTPO removed with increasing temperatures, while heating rate plays no significant role. These authors observed that half of the original sulfur remained in the char.

The amount of O and N present in WTPO is similar to that of S or even higher, with a high H/C ratio representative of aliphatic and aromatic compounds. O and N compounds have their origin in thermal degradation of stearic acid, sulfur compounds, amines and oxygenated oils used in tyre formulation, and should be taken into account when considering WTPO for fuel applications, since pre-treatments are required to remove these elements [18].

Table 1: Composition of WTPO of various authors as reported in literature

Ref	[22] ^a	[23] ^b	[24] ^c	[25] ^a	[26] ^a	[27] ^a	[28] ^a
T ^o C	600	550	500	550	550	650	650
Yield, wt%	53.1	44.6	-	38.0	46.1	48.4	56.0
CV, MJkg ⁻¹	41.2 ^d	41.0	-	40.8 ^d	43.3 ^d	41.6 ^d	42.4 ^d
C, wt%	87.9	85.6	87.2	84.9	85.4	87.6	86.5
H, wt%	10.1	9.6	10.6	9.6	11.4	10.4	11.7
N, wt%	0.5	0.6	0.5	0.1	0.4	< 1	< 1
S, wt%	1.3	1.3	1.2	1.6	0.6	1.4	0.8
O, wt%	0.1	4.0	0.5	3.5	-	-	-
H/C	1.4	1.4	-	1.4	1.6	1.4	1.6

Where: ^a fixed bed reactor.

^b Rotary kiln reactor.

^c Conical spouted bed reactor.

^d Higher.

Table 2: Elemental analysis of different types of tyres

Element (wt%)	PCT ₁	PCT ₂	PCT ₃	BT	TT
C	85.9	82.5	86.4	74.5	83.2
H	8.0	6.4	8.0	6.5	7.7
O	2.3	5.7	3.4	16.4	6.2
N	0.4	0.5	0.5	1.0	1.5
S	1.0	1.1	1.7	1.6	1.4
Ash	2.4	3.8	2.4	-	-

7.2. Molecular Composition of Waste Tyre Pyrolysis Oil

WTPO consists of a very complex mixture of hydrocarbons consisting of : C₆–C₃₇ linear paraffins, particularly C₈–C₁₃; low concentration of alkenes, particularly not condensed butadiene, pentenes, pentadienes and isoprene; high amount of aromatics, naphthenes and terpenes (with a total amount of ca. 65wt%), particularly limonene, BTX, alkylated single-ring aromatics and upto 5-ringbenzopyrenes [17].

As a general trend, the amount of aromatics in WTPO increases with pyrolysis temperature, due to their combination reactions that take place among aliphatic and aromatic free radicals and also to the cyclization of aliphatic chains [29]. Several authors [19, 23, 30] have reported that the aromatic content in WTPO is determined by the original amount of aromatics and olefins in rubber. Olefins and diolefins in particular tend to condense through Diels–Alder, cyclization and dehydrogenation reactions to form aromatics. These reactions are favored at high

temperatures so that the amount of aromatics and polycondensed aromatics in WTPO increases with temperature [23]. Increasing the residence time of volatiles in the pyrolysis reactor also results in the increase of aromatics and polycondensed aromatics yield in WTPO [31].

Sulfur in WTPO is in the form of benzothiazole (BTZ) and dibenzothiophene (DBT) and its alkylated forms; methyl, dimethyl, trimethyl and tetramethyldibenzothiophene (M₁DBT, M₂DBT, M₃DBT, and M₄DBT). Nitrogen in WTPO is in the form of BTZ too, while oxygen appears as hydroxyl compounds such as phenol, 3-methylphenol and 2-ethyl-1-hexanol. As previously mentioned, these hetero atomic molecules represent for a great obstacle for using WTPO in combustion engines or as fuels [17].

8. PYROLYSIS OIL AS ALTERNATIVE SOURCE FOR CHEMICALS

Some of the mentioned molecules composing WTPO have economic interest. WTPO is an impor-

tant source of d-limonene, a high valued chemical used in the formulation of industrial solvents, resins, adhesives, and fragrances, among others [18]. Limonene is acyclic terpene ($C_{10}H_{16}$) that exists in its d- and l- form, as d-limonene and l-limonene. Limonene yields are lower at high temperatures due to secondary reactions taking place, mainly dehydrogenation to form aromatics. Arabiourrutia *et al.*, [32] observed a decrease in d-limonene concentration in WTPO with temperature from 23.4wt% at 425 °C to 5.7wt% at 610 °C in a Conical spouted bed reactor (CSBR). Similarly, Li *et al.*, [23] reported a decrease from 5.4 wt% at 450°C to 0.07 wt% at 650°C in d-limonene yield in WTPO obtained in a rotary kiln reactor. Working in vacuum conditions and decreasing gas residence time can partially avoid sequential reactions of d-limonene [18]. López *et al.*, [24] obtained a 60wt% yield of WTPO with a concentration of d-limonene of 26.8wt% working in a CSBR in vacuum conditions, mainly due to the low residence time of volatiles. In the WTPO obtained in a CSBR, the concentration of d,l-limonene is higher (ca.27wt%) than that in the WTPO obtained using other reactors. Various reaction path ways have been reported in literature for d,l-limonene formation [18], many of them agreeing on poly-isoprene (in the NR) cracking through β -scission and intra molecular cyclization. In parallel, isoprene could dimerize through a Diels–Alder path way. Finally, and if temperature and/or residence time are high enough, d,l-limonene further dehydrogenates to aromatics [33]. Stanciulescu and Ikura [34] used a two-stage distillation to obtain naphtha in the first stage, and d-limonene enriched naphtha in the second one. Then, they used the d-limonene enriched mixture to obtain ethers by alkyl oxidation [32].

WTPO is also a potential source of light aromatics such as benzene, toluene and xylene (BTX, which are valued commodities [18], The BTX com-

position in WTPO is inversely proportional to that of d-limonene, as BTX is formed through d-limonene dehydrogenation. Li *et al.*, [23] have proposed optimal pyrolysis conditions for obtaining high yields of BTX: benzene, 2.09wt%; toluene, 7.05wt%; and xylene 2.01wt%. Furthermore, post pyrolysis selective condensation, distillation, and catalytic pyrolysis can further increase the yields of BTX. Another approach for increasing the BTX proportion in WTPO is using a catalyst in the pyrolysis [17], which is known as catalytic pyrolysis or catalytic cracking. Williams and Brindle [35] used HY and HZSM-5 zeolites in a two-stage pyrolysis process (pyrolysis reactor followed by a catalytic reactor for the gaseous products) and found that generally, increasing the catalyst/feed ratio had a positive effect on BTX yields, with maxima of 5wt% benzene, 24 wt% toluene, 20wt% m- and p-xylenes, and 7wt% o-xylene. The HY zeolite catalyst gave way to higher concentrations of BTX compared to HZSM-5[17]. Olazar *et al.*, [36] observed the following in aromatic yields: 20.2wt%, without catalyst; 32.5wt%, HZSM-5 zeolite catalyst; and 40.5wt%, HY zeolite catalyst; with BTX maximum yields of 4.15 wt% of benzene, 7.39 wt% of toluene, and 6.59 wt% of xylene using HY zeolite.

Even though different waste tyres combination (i.e being tyre of bicycle, car, trucks among others) produced different variety of fuel according to Neoklis and Zorpas, 2019 [37]. Also WTPO can have a lot of polycyclic Aromatic Hydrocarbons (PAHs) as such as Naphthalene – NAP, Acenaphthylene – ACY, Acenaphthene – ACE, Fluorene – FLU, Phenanthrene – PHE, Anthracene – ANT, Fluoranthene – FLT, Pyrene – PYR, Benzo[a]anthracene – BAA, Chrysene – CRY, Benzo[b]fluoranthene – BBF, Benzo[k]fluoranthene – BKF, Benzo[a]pyrene – BAP, Dibenzo[a,h]anthracene – DBA, Benzo[g,h,i]perylene – BGP, Indeno[1,2,3-cd]pyrene – IND were all found in his pyrolysis oil.

9. MAJOR CHARACTERISTICS OF WTPO AND RELATED CHALLENGES

S/N	Property	Characteristics	Issues
1	Sulfur Content	Usually between 0.6 and 1.4 wt%. Sulfur is added to tyres in the vulcanization process. Up to 70% of initial sulfur in tyres remains in recovered carbon black after pyrolysis. The remaining fraction is distributed into pyrolytic gas and TPO. Sulfur compounds in TPO are in the form of thiophene, benzothiazole, benzothiophene, etc.	Sulfur containing compounds are environmental pollutants. During oxidation, SO _x are produced and released as gas products. SO _x also reaches the lubricant oil, causing corrosion problems in combustion systems like internal combustion engines.

2	Nitrogen Content	Usually in the range of 0.4–1.05 wt %, depending on initial tyre composition and attributable to thermal degradation of accelerators such as N,N-di-isopropyl-2-benzothiazole-sulfenamide, 2-(4-morpholinylthio)-benzothiazole, N,N caprolactamdisulphide, and 2-mercaptobenzothiazole incorporated into tyres during formulation. Nitrogen in TPO is commonly found in the form of benzothiazole, also containing sulfur.	High nitrogen levels in the fuel lead to fuel NO _x formation during combustion, which may cause acid rain.
3	Flash Point	Usually lower than 30°C, this low flash point is due to high fraction of volatile compounds in TPO.	High flash point of a liquid fuel is beneficial for storage. A lower flash point is easier for igniting the fuel/air mixture; liquid is considered flammable if its flash point is <60 °C.
4	Aromatic Content	As much as 65 wt% of TPO could be represented by aromatic hydrocarbons, associated with the aromatic nature of rubber (one aromatic ring in the styrene butadiene rubber monomer) and the cyclisation of olefin structures, followed by dehydration and Diels-Alder reactions, favored at high temperature in the pyrolysis process.	Aromatic hydrocarbons are associated with incomplete combustion (due to long IDT) and the tendency to form particulate matter (PM) (act as PM precursors).
5	Final Distillation Point	Final distillation point is usually higher than 550°C., associated with the presence of high molecular weight compounds like polycyclic aromatic hydrocarbons (PAH) and polycyclic aromatic sulfur hydrocarbon (PASH).	Fuel's boiling point affects its vaporization and combustion process. A high final boiling point may decrease the vaporization rate, resulting in incomplete combustion and PM formation.
6	Ignition Delay Time (IDT)	Significant presence of light aromatic (benzene, toluene, and xylene) and <i>iso</i> -paraffinic (limonene) hydrocarbons tends to increase the IDT of TPO, resulting in a low cetane number. These compounds have stable molecular structures, requiring high temperatures and pressures to ignite.	In diesel engines, fuels with high IDTs may increase particulate matter emissions, since combustion begins in the final stage of the expansion cycle when the temperature inside the chamber decreases. Oxidation rate decreases here, leading to increased concentration of unburned hydrocarbons condensing on the surface and increasing the mass of PM

Table as reported by Campuzano *et al* [38]

10. UPGRADING OF WTPO

Among all the processes comprised within are refinery, hydroprocessing is the only one that allows for simultaneously solving the main compositional barriers of WTPO for increasing the value of the feedstock and allow its direct application as a fuel. These barriers can be summarized as: (i) high sulfur content, (ii) high content of aromatics, and (iii) great proportion of molecules within the gas oil boiling point (BP) range. Therefore, the most interesting reaction pathways for WTPO upgrading are hydrodesulfurization (HDS), hydrodearomatization (HDA) and hydrocracking (HC). It is a common industrial strategy to place different cata-

lyst beds in series within a reactor in order to optimize catalyst and reactor performance according to the main hydroprocessing goal [17]. Great achievements can be obtained through a 2-stage hydroprocessing strategy regarding WTPO composition in terms of HDS, HAD and HC. The first hydroprocessing stage, using NiMo catalysts, has allowed for reducing the total amount of sulfur from an initial content of 11,800 ppm in WTPO to ca.2,000 ppm in hydro treated WTPO (HT-WTPO), thanks to the high activity towards hydrogenation reactions of this type of catalysts. Furthermore, 13.2wt% less aromatics and 8wt% less gas oil were obtained working in mild hydrocracking conditions. However, greater achievements in terms of

HAD and HC have been obtained on the second hydroprocessing stage using a PtPd/SiO₂-Al₂O₃ catalyst [17] due to both the higher hydrogenating activity of the metallic phase and cracking ability of the acidic support, which have allowed for further reduction of 18.6wt% of aromatics and almost complete removal of the gas oil lump in upgraded WTPO (Up-WTPO). Additionally, sulfur has reached levels below 100ppm. On the whole, global conversions of 99.2% in HDS, 99.7% in HC and 57% in HAD have been achieved. With very little amount of compounds with in the gas oil lump, and an aromatic content even lower than that of some diesel-type feedstock [39]. Up-WTPO comprises the required features for being co-fed with commercial diesel-type automotive fuels with promising performances in internal combustion engines. It is also to mention that the amount of remaining sulfur in Up-WTPO can be the limiting factor when determining the proportions in the diesel-WTPO blend to be used, in order to avoid excessive aromatic and particulate emissions and comply with the corresponding environmental policies [17].

11. CONCLUSION

Pyrolysis oil from waste tyres can be used as a substitute for diesel and as well as sources of raw materials and fuel to organic chemical industries. Also the oil can have a range of hydrocarbons depending on the composition of the feedstock which was used to undergo the pyrolysis this include aromatic hydrocarbons like benzene, toluene, and Xylene (BTX), as well as aliphatic hydrocarbons such as ethylene, propylene and butenes. Also Oxygenated compounds; compound that contains oxygen such aldehyde, ketones, acids, alcohols and furans. We can also get Polycyclic Aromatic hydro carbons (PAHs) example; Naphthalene, anthracene and phenanthrene. With this WTPO will serves as an alternative fuel instead of fully dependence to natural crude oil.

REFERENCES:

- [1] N. Gao, W. Fengchao, Q. Cui, S. Laura, L. Gartzen, T.W. Paul (2022) Tyre pyrolysis char: Processes, properties, upgrading and applications, *Progress in Energy and Combustion Science*, 93, 101022 <https://doi.org/10.1016/j.pecs.2022.101022>
- [2] L. Bockstal, T. Berchem, Q. Schmetz (2019) Devulcanisation and reclaiming of tyres and rubber by physical and chemical processes: a review, *J Cleaner Prod*; 236, 117574.
- [3] E. E. Okoro, S.E. Sanni, M.E. Emeteri, D.O. Orodu (2019) Process Scheme for the Production of Liquid Fuel From Used Tyres via Fast Pyrolysis, *Procedia Manufacturing.*, 35, 847–853.
- [4] D.Y.C. Leung, C. Wang, K.F. Yung (2017) A review on the pyrolysis of woody biomass to bio-oil: Focus on kinetic models, *Renewable and Sustainable Energy Reviews.*, 67, 16-37. doi:10.1016/j.rser.2016.09.135
- [5] A. Al-Saleh, L.S. Melanie (2014) Waste Tyre Pyrolysis: Influential Parameters and Product Properties, *Curr Sustainable Renewable Energy Rep.*, 1, 129–135
- [6] C. Wu, P.T. Williams, J. Tao (2017) Pyrolysis technologies for municipal solid waste: A review, *Waste Management.*, 69, 497-523. doi:10.1016/j.wasman.2017.07.024
- [7] S. Yaman (2016) Pyrolysis of biomass to produce fuels and chemical feedstocks, *Energy Conversion and Management.*, 113, 31-45.
- [8] M.M. Roy, R.K. Singh (2017) Pyrolysis of municipal solid waste for energy production and waste reduction: A review, *Renewable and Sustainable Energy Reviews.*, 76, 108-122.
- [9] A. Saddawi, P.T. Williams (2018) Characterisation and applications of biochar produced from pyrolysis of waste biomass: A review, *Journal of Environmental Management.*, 217, 56-78.
- [10] F. Ronsse, S. Van Hecke (2017) An overview of slow pyrolysis of biomass. Technological and economic assessment compared to fast pyrolysis and gasification, *Renewable and Sustainable Energy Reviews.*, 74, 742-752. doi:10.1016/j.rser.2017.02.031
- [11] P. Straka, A. Miloš, V. Dan, K. Hugo, S. Pavel, V. Peter (2023) Production of transportation fuels via hydrotreating of scrap tyres pyrolysis oil, *Chemical engineering journal.*, 460, 141764. <https://doi.org/10.1016/j.cej.2023.141764>
- [12] A. E. Ajayi, T.V. Ojumu (2017) Thermal pyrolysis of waste tyres: Production and perspectives of fuel quality of pyrolysis oil - A review, *Journal of Environmental Management.*, 197, 673-686.
- [13] A. Demirbas (2014) Waste management, waste resource facilities and waste conversion techniques, *Energy Conversion and Management.*, 80, 1-9.
- [14] S.E. Hosseini, M.A. Wahid, J.R. Seay, K.A. Schimmel (2018) A review on the pyrolysis of waste tyres: Effect of pyrolysis conditions pathways and methods, *Journal of Analytical and Applied Pyrolysis.*, 130, 142-179.
- [15] G. Luo, S. Liu, X. Huang (2013) Review of pyrolysis of biomass and waste materials: Process simulation and fundamental research, *Energy Conversion and Management.*, 74, 315-321.
- [17] I. Hita, M. Arabiourrutia, M. Olazar, J. Bilbao, J. M. Arandes, P.C. Sánchez (2016) Opportunities and barriers for producing high quality fuels from the pyrolysis of scrap tyres. *Renewable and Sustainable Energy Reviews.*, 56, 745–759
- [18] H. Pakdel, D.M. Pantea, C. Roy (2001) Production of dl-limonene by vacuum pyrolysis of used tyres. *J Anal Appl Pyrolysis.*, 57, 91–107.

- [19] A.M. Cunliffe, P.T Williams (1998) Composition of oils derived from the batch pyrolysis of tyres, *J Anal Appl Pyrolysis.*, 44, 131–152.
- [20] A. Quek, R. Balasubramanian (2013) Liquefaction of waste tyres by pyrolysis for oil and chemicals—A review, *J Anal Appl Pyrolysis.*, 101, 1–16.
- [21] K. Unapumnuk, T.C. Keener, M. Lu, F. Liang (2008) Investigation into the removal of sulfur from tyre derived fuel by pyrolysis, *Fuel.*, 87, 951–956.
- [22] Y. Kar (2011) Catalytic pyrolysis of car tyre waste using expanded perlite. *Waste Management.*, 31, 1772–1782.
- [23] S.Q. Li, Q. Yao, Y. Chi, J. H. Yan, K.F. Cen (2004) Pilot-scale pyrolysis of scrap tyres in a continuous rotary kiln reactor, *Ind Eng Chem Res.*, 43, 5133–5145.
- [24] G. López, M. Olazar, M. Amutio, R. Aguado, J. Bilbao (2009) Influence of tyre formulation on the products of continuous pyrolysis in a conical spouted bed reactor, *Energy Fuels.*, 23, 5423–31.
- [25] A.A. Zabaniotou, G. Stavropoulos (2003) Pyrolysis of used automobile tyres and residual char utilization, *J Anal Appl Pyrolysis.*, 70, 711–722.
- [26] J.D. Martínez, N. Puy, R. Murillo, T. García, M. V. Navarro, A. M. Mastral (2013) Waste tyre pyrolysis – A review, *Renew Sustain Energy Rev.*, 23, 179–213.
- [27] S. Mirmiran, H. Pakdel, C. Roy (1992) Characterization of used tyre vacuum pyrolysis oil: nitrogenous compounds from the naphtha fraction, *J Anal Appl Pyrolysis.*, 22, 205–215.
- [28] E. Aylón, A. Fernández-Colino, M. V. Navarro, R. Murillo, T. García, A. M. Mastral (2008) Waste tyre pyrolysis: comparison between fixed bed reactor and moving bed reactor, *Ind Eng Chem Res.*, 47, 4029–4033.
- [29] M. I. Rodríguez, M. F. Laresgoiti, M. A. Cabrero, A. Torres, M. J. Chomón, B. Caballero (2001) Pyrolysis of scrap tyres, *Fuel Process Technol.*, 72, 9–22
- [30] S. Uçar, S. Karagöz, J. Yanik, M. Saglam, M. Yuksel (2005) Co pyrolysis of scrap tyres with waste lubricant oil, *Fuel Process Technol.*, 87, 53–58
- [31] P.T. Williams, D.T. Taylor (1993) Aromatization of tyre pyrolysis oil to yield polycyclic aromatic hydrocarbons, *Fuel.*, 72, 1469–1474.
- [32] M. Arabiourrutia, G. Lopez, G. Elordi, M. Olazar, R. Aguado, J. Bilbao (2007) Characterization of the liquid obtained in tyre pyrolysis in a conical spouted bed reactor, *Int J Chem React Eng.*, 5, A96.
- [33] X. Zhang, H. Yang, J. Yan (2013) Pyrolysis of waste tyres: A review, *Renewable and Sustainable Energy Reviews.*, 27, 247–258.
- [34] M. Stanculescu, M. Ikura (2007) Limonene ethers from tyre pyrolysis oil: Part2: continuous flow experiments, *J Anal Appl Pyrolysis.*, 78, 76–84.
- [35] P.T. Williams, A.J. Brindle (2003) Aromatic chemicals from the catalytic pyrolysis of scrap tyres, *J Anal Appl Pyrolysis.*, 67, 143–164.
- [36] M. Olazar, R. Aguado, M. Arabiourrutia, G. Lopez, A. Barona, J. Bilbao (2008) Catalyst effect on the composition of tyre pyrolysis products, *Energy Fuels.*, 22, 2909–2916.
- [37] A. A. Neoklis, A. A. Zorpas (2019) Quality protocol and procedure development to define end-of-waste criteria for tyre pyrolysis oil in the framework of circular economy Strategy, *Waste Management.*, 95, 161–170. <https://doi.org/10.1016/j.wasman.2019.05.035>
- [38] F. Campuzano, A. Abdul Gani, Z. Wen, E. Abdul-Hamid, F. A. Andres, D.M. Juan, S.S. Mani (2021) On the distillation of waste tyre pyrolysis oil: A structural characterization of the derived fractions, *Fuel.*, 290, 120041. <https://doi.org/10.1016/j.fuel.2020.120041>
- [39] R. Vihar, T. Seljak, O. S. Rodman, T. Katrašnik (2015) Combustion characteristics of tyre pyrolysis oil in turbo charged compression ignition engine, *Fuel.*, 150, 226–235.

IZVOD

PIROLIZNO ULJE IZ OTPADANIH GUMA (VTPO) KAO ALTERNATIVNI IZVOR GORIVA I HEMIKALIJA: PREGLED

Otpadne gume se odlažu i uobičajena je vrsta napuštanja čvrstog otpada. Skoro 3 milijarde guma se proizvede svake godine i svaka proizvedena guma će se na kraju pridružiti otpadnim proizvodima i ako se njima pravilno ne rukuje postaću zagađivač. U mnogim zemljama odlaganje otpadnih guma je zabranjeno; kao alternativu treba ih oporaviti i reciklirati. U ovom pregledu piroliza je predstavljena kao alternativni način reciklaže otpadnih guma. Piroliza omogućava rastvaranje otpada i takođe proizvodi korisne nusproizvode. Proizvodi dobijeni tokom procesa su pirolizno ulje, pirolizni ugljen i kondenzabilni gas. Pirolizno ulje je glavni proizvod među njima i u ovom radu je dat pregled piroliznog ulja kao alternativnog izvora goriva za dizel motore i istaknute su hemikalije dobijene iz otpadnih guma od piroliznog ulja, koje uglavnom zavise od vrste sirovine, tj. vrste guma (npr. kamion, automobil, bicikl) koji se koriste u procesu pirolize. Većina dobijenih jedinjenja su alifatični i aromatični ugljovodonici (posebno policiklični aromatični ugljovodonici PAH) kao što su naftalen – NAP, acenaftilen – ACI, acenaften – ACE, fluoren – FLU, fenantren – PHE, antracen – ANT, Fluo – PIR, benzo[a]antracen – BAA, krizen – CRI, benzo[b]fluoranten – BBF, benzo[k]fluoranten – BKF, benzo[a]piren – BAP, dibenzo[a,h]antracen – DBA, benzo[g,h,i]perilen – BGP, Indeno[1,2,3-cd]piren – IND između ostalih. Shodno tome, dobijeno pirolizno ulje treba dalju nadogradnju putem reakcionih puteva: hidrodesulfurizacija (HDS), hidrodearomatizacija (HDA) i hidrokreking (HC) koji se mogu postići kroz 2-stepenu strategiju hidroobrade u pogledu sastava VTPO u smislu HDS, HAD i HC. Pirolizno ulje iz otpadnih guma može se koristiti kao zamena za dizel i kao izvor sirovina i goriva za organsku hemijsku industriju.

Ključne reči: otpadne gume, piroliza, pirolizno ulje, hemikalije, nadogradnja.

The ORCID Ids of all the authors are as follows:

1. Bashir Abdu Muzakkari: <https://orcid.org/0000-0001-9432-5313>
2. Pramod Kumar Singh: <https://orcid.org/0000-0002-3155-6621>
3. Umar Muhammad Jibreel: <https://orcid.org/0009-0003-0664-4878>

Pregledni rad

Rad primljen: 20.03.2024.

Rad korigovan: 1.06.2024.

Rad prihvaćen: 14.06.2024.-

Esraa Razaq¹, Shaymaa Abbas Abdulsada^{2*}

^{1,2}Department of Materials Engineering, Faculty of Engineering,
University of Kufa, Iraq

Scientific Paper

ISSN 0351-9465, E-ISSN 2466-2585

<https://doi.org/10.62638/ZasMat1161>



Zastita Materijala 65

(4) 645 - 652 (2024)

Effect of Corrosion Inhibitors on Internal Corrosion in Oil Pipelines: A Brief Review

ABSTRACT

The oil and gas industry primarily relies on pipelines to transport crude and refined petroleum, so transportation of crude oil is mostly handled by pipelines. In view of this, it is impossible to prevent the pipeline surfaces from being continuously exposed to corrosion sources, such as contaminants that contain traces of chromate and sulfur, which can cause corrosion to occur on the pipeline surfaces. It is known that corrosion inhibitors are chemicals that are used in low concentrations for the purpose of reducing or preventing corrosion. The effectiveness of an inhibitor is determined by its ability to react with a metal's surface and produce a protective coating that reduces or prevents corrosion by reacting with the metal's surface. A review of corrosion mechanisms in oil pipelines is presented in this article, along with a description of how corrosion inhibitors can be selected according to the corrosion mechanisms in oil pipelines.

Keywords: Pipelines, Corrosion, Green inhibitors, Carboxylates, Oil.

1. INTRODUCTION

There is a natural tendency for materials, especially metals, to corrode when they react with their environment. Though the mechanisms by which this phenomenon occurs and the consequences that it causes may differ from one another, it is a phenomenon that affects both metallic and non-metallic materials. Corrosion of metallic materials, or rust, is the most common form of corrosion. Iron, in reaction with oxygen and moisture in the air, forms iron oxide (rust). Polymers, for instance, are affected by degradation, which is a type of corrosion. It is important to note that polymers can also degrade if exposed to UV radiation, heat, moisture, and chemicals, in addition to degradation caused by UV radiation, heat, moisture, and chemicals. Even though ceramics are chemically resistant, they may degrade in aggressive environments because of mechanical wear, thermal shock, and chemical attack, despite the fact that they are chemically resistant.

* Corresponding author: Shaymaa Abbas Abdulsada

E-mail: shaymaa.radhi@uokufa.edu.iq

Paper received: 25.03.2024.

Paper accepted: 12.04.2024.

The other type is concrete corrosion, as it is possible for steel reinforcement in reinforced concrete structures to corrode if it is exposed to corrosive chemicals, chloride ions, and carbonation over time. Due to this, the concrete may crack and crumble as a result [1-13]. As mentioned above, the corrosion of metal occurs as a result of chemical reactions between the metal and the environment around it, which causes the metal to slowly disintegrate over time as the environment around it changes [14,18]. As innovative gas fields develop, it is critical that we have the ability to move damp, unprocessed indigenous gases through pipelines and into other inaccessible areas in order to facilitate the advancement of these fields. The importance of understanding corrosion and the methods for preventing it, because of this, cannot be overstated both in terms of safety and economics. Due to the flow of oil inside pipelines, as well as the fact that the pipelines are buried underground, oil pipelines are exposed to internal corrosion as well as external corrosion due to the fact that they are buried underground [18-23].

The use of pipelines for oil and gas delivery is widely recognized as one of the most cost-effective and safest methods. It is still necessary to evaluate corrosion and develop the best mitigation techniques for carbon steel pipelines because they

are prone to corrosion. As one of the primary means of transporting oil and gas, pipelines have many advantages, including their low operating costs, quick and convenient operations, and capacity to transport large amounts of material. There are a number of pipelines around the world that are unfortunately subject to both internal and exterior corrosion, which could have a significant negative impact both economically and environmentally in the long run [21-26]. Oil pipelines transfer liquid petroleum products from one location to another. There are four types of oil pipelines, (1) gathering pipelines, which transport oil over short distances with pipe diameters ranging from

10.2 to 30.2 cm, (2) feeder pipelines, which transport oil product from oil storage tanks or processing plants to gearbox pipelines and are typically larger than gathering lines. (3) transmission pipelines, in addition to the smaller diameter pipelines, these are also used for transporting oil and natural gas over longer distances; between provinces or countries, and (4) distribution lines can be up to 122 cm in diameter and deliver crude oil from production to export or consumption points. Corrosion in crude oil pipelines is one of the most serious issues related

with the presence of water and contaminants such as chlorides, sulphates, CO₂, and H₂S dissolved gases. One method for preserving interior oil pipes from corrosion is to use corrosion inhibitors [27-28].

Corrosion inhibitors are one of the methods used to reduce corrosion in petroleum industry. To ensure optimum inhibition, the inhibitors must be supplied at concentrations greater than a particular minimum. There are numerous techniques for combating corrosion, such as cathodic protection, organic coatings, and the use of high-quality corrosion-resistant alloys, but film-forming inhibitors are still widely regarded as the unrivalled method of defence for mild steel in an acid environment. Film-forming inhibitors are used in industries to build a molecular layer directly on the steel surface and an aliphatic tail as a second layer of hydrocarbon to prevent water from touching the steel surface and causing corrosion. All forms of internal corrosion that are anticipated to occur in pipelines are schematically summarised in Fig. 1 to aid in understanding of the various forms of internal corrosion caused by metal loss or cracking mechanism, which will be covered in more detail later [29-43].

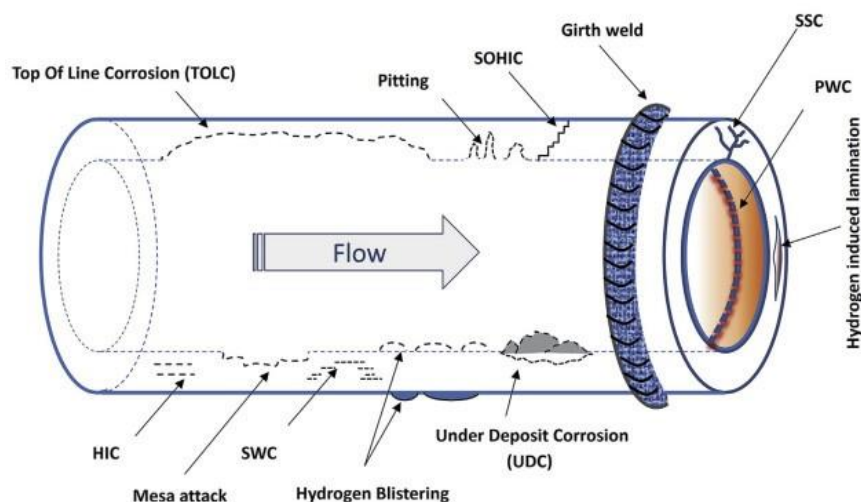


Figure 1. Various types of internal pipeline corrosion in hydrocarbons [43]

2. CAUSES OF OIL FIELD CORROSION

In oil fields, corrosion can often be traced back to the use of drilling fluids that penetrate into the crude oil that is going to be transported later in the process. These fluids include all of the following [44]:

- In certain sectors, organic acids are also present, such as acetic acid, which can cause CO₂ containing devices to corrode faster compared to others. There are hydrocarbon phases; oils with different compositions; and gases like ethane and methane.
- There are dissolved salts such as calcium carbonate, barium sulphate, sodium sulphate, and sodium chloride in the produced water, which can induce scaling. Water injection can cause water breakout and souring, as well as scaling due to chemical mixing and hydrogen sulfide generation.
- There are several acids that can dissolve in water and generate corrosive electrolytes, such as carbon dioxide and hydrogen sulphide, which can produce acidic gases.

3. CORROSION MECHANISM IN OIL PIPELINES

Metal corrosion can be considered as an environmental element that is characterised as the unintentional destruction and degradation of working pipelines in an internal or external environment, as a result of chemical, electrochemical, or biochemical contact with the environment. The process of corrosion, which occurs when chemical or electrochemical reactions occur during the interaction between metallic materials and the environment, is a deteriorating attack on metallic materials. Fig. 2 depicts some types of rusting [45].



Figure 2. Different forms of Corrosion [45]

As far as corrosion in oil and gas refineries and related industries is concerned, there are a number of different forms of corrosion that occur in these facilities. These include microbiologically induced corrosion, erosion, stress corrosion cracking, crevice corrosion, oxygen corrosion, sweet corrosion, and sour corrosion [46]. The material of the pipeline has a significant impact on pipeline corrosion as well.

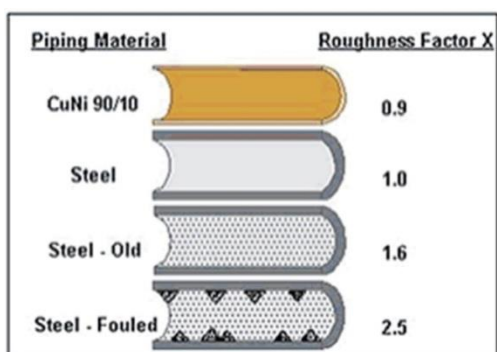


Figure 3. Selection of Piping Materials [47]

The piping material with its varying roughness is shown in Fig. 3. Certain materials, like steel or steel concrete, will increase the rate of corrosion in the pipeline, while other materials, like PVC,

stainless steel, and some special alloys, can extend the lifespan of the pipeline [47].

4. CORROSION INHIBITORS IN OIL PIPELINES

An inhibitor is a chemical that, when introduced in modest doses, reduces the effective corrosion rate. Inhibitors are classified into four categories based on their mechanism and content. The four categories are barrier layer development, neutralising, scavenging, and environmental change. Temperature and water chemistry are two elements that can influence the blockage of petroleum pipelines [44]. Organic compounds are commonly utilised as corrosion inhibitors in oil field applications, where they are applied in modest amounts (less than 0.1%). Because they adsorb on the steel surface and inhibit both the anodic and cathodic reactions, they are frequently classed as mixed inhibitors. Nonetheless, a lot of inhibitor packages that are sold commercially have a tendency to polarise the steel anodically. Known as filmmaking inhibitors, oilfield corrosion inhibitor chemicals also push adsorbed water molecules away from the surface. For instance, jet fuel, a product with a low water content, uses inhibitor compounds, which only function in this way. Nearly all organic molecules used in oil field corrosion inhibitor packages are strongly polar functional compounds, many of which have a nitrogen basis, such as amines, amides, imidazolines, or quaternary ammonium salts. These compounds also include compounds containing P, S, and O, nitrogen heterocyclics, polyoxyalkylated nitrogen-containing compounds, and salts of nitrogenous molecules with carboxylic acids.

Table 1: Fundamental chemical structures of inhibitors used in oilfields [48]

Chemical name	Structure
Primary amine	$R-CH_2-NH_2$
Amide	$R_1-CH_2-C(=O)-NH-R_2$
Imidazoline	 $R-CH_2-N(CH_2-CH_2-NH_2)$
Quaternary ammonium ion	 $(CH_3)_2N^+(CH_2-Ph)CH_2-R$
Polyethoxylated amines	$R-N(CH_2-CH_2-O)_n-OH$

It is frequently disputed whether species in the package actually offers protection because, for

Carboxylates

By forming a hydrophobic coating on the metal surface through the adsorption of a carboxylate group (Lewis base) on Lewis acid, carboxylates can offer corrosion protection. While short-chain fatty acids may encourage corrosion, long-chain fatty acids—like oleic acid, soy fatty acid, TOFA, and polymerized fatty acids—like dimer acids, have long been known to reduce corrosion in a variety of applications. Dicarboxylic acid and its derivatives, known as dicarboxylic esters, have been researched as useful additives for stopping metal corrosion in compositions. Rust development in lubricating oils can be effectively reduced by a synergistic combination of amine derivatives derived from succinic anhydride and tetrapropenyl succinic acid. It should be mentioned, though, that the dicarboxylic acids have a propensity to precipitate when Ca^{2+} or Mg^{2+} ions are present, which would negate their ability to prevent rust [53]. However, an outer negative surface can be generated by carboxylates, and it is possible that the amine carboxylate based inhibitors, Fig. 5, could form a film on the steel surface by associating nitrogen with iron atoms. Consequently, a repulsive force between the carboxylate and the chloride in the media or environment is created. The repelling force is significant at low concentrations of chloride and sulphate, but it becomes less at higher concentrations. Therefore, it is probable that sulphate or chloride seeped into the steel, which is why the film's efficiency decreased [54].

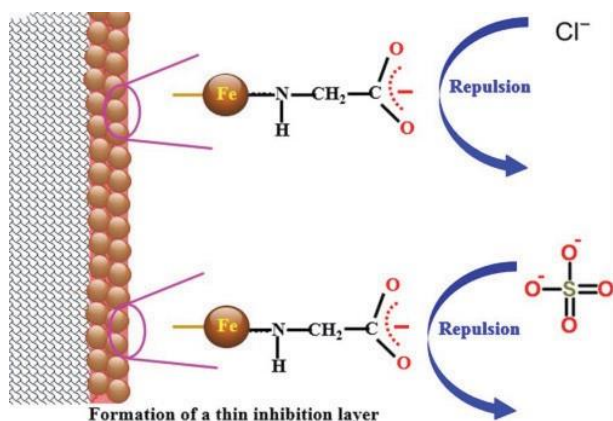


Figure 5. Proposed mechanisms for the inhibition of corrosion of carbon steel by the investigated aminecarboxylate based inhibitors [54].

Amines

Film-forming amines, or fatty amines, are fatty acid derivatives. These components, which have poor alkaline characteristics, have been neutralised by the use of organic acids in the formulation of the corrosion inhibitor or by the action of acid gases in the fluid, converting them to cationic

components with positive charges. Because electrons are re-released on the cathode as a result of corrosion, these cationic components are attached to the cathode and form an oily coating on the metal's surface, preventing acid gases from contacting the cathode while releasing hydrogen. Corrosion inhibitors are classified into functional groups with polar heads, such as fatty acids, amines, imidazoline, oxyalkylated amines, oxygen, sulphur, or phosphorus, and quaternary amine salts. Furthermore, corrosion inhibitors with a long chain of hydrocarbons (typically C14-C18) cling well to the surface [55].

5. CONCLUSION

Overall, it can be concluded that corrosion is an issue of great importance in the oil and gas industry, particularly the pipeline industry, where it can lead to economic losses as well as environmental damage. It is critical to ensure pipeline integrity and safety by understanding the mechanisms of corrosion and applying effective mitigation techniques, such as the use of corrosion inhibitors, in order to prevent corrosion in oil pipelines. A variety of corrosion inhibitors are available, including green inhibitors, organic inhibitors, inorganic inhibitors, carboxylates, and amines, and each of them has its own unique protective mechanism for preventing corrosion in pipelines. The key to successful corrosion prevention is selecting the right inhibitor based on the conditions in the environment and the type of system being treated. It is vital that the oil and gas sector uses corrosion inhibitors and follows regular maintenance methods in order to ensure safe and efficient transportation of oil and gas through pipelines.

6. REFERENCES

- [1] A. Groysman (2009) Corrosion phenomena. In Springer eBooks, 53–108. https://doi.org/10.1007/978-90-481-3477-9_2
- [2] A. A. Shaymaa (2014) Corrosion Inhibitors: Principles and Applications, 1st Edition, LAP LAMBERT Academic Publishing, Germany.
- [3] J. K. B. Balangao (2024) Corrosion of Metals: factors, types and prevention Strategies. J. Chem. Hea. Ri., 14, 79-87. <https://jchr.org/index.php/JCHR/article/view/2120>
- [4] T. W. Quadri, E. D. Akpan, L. O. Olasunkanmi, O. E. Fayemi, E. E. Ebenso (2022) Fundamentals of corrosion chemistry. In Elsevier eBooks, 25–45. <https://doi.org/10.1016/b978-0-323-85405-4.00019-7>
- [5] S. Zehra, M., Mobin, R. Aslam (2022) Corrosion prevention and protection methods. In Elsevier eBooks, 13–26. <https://doi.org/10.1016/b978-0-323-91176-4.00023-4>

- [6] A.I. Al-Mosawi, K. Marossy (2020) Elimination of plasticized poly(vinyl chloride) degradability by using oxydtron: a novel study, *ARPN J. Eng. App. Sci.*, 15, 405-411.
- [7] S. Pyun, (2020). Strategies of metal corrosion protection. *ChemTexts*, 7, 1. <https://doi.org/10.1007/s40828-020-00121-y>
- [8] A.I. Al-Mosawi (2021) A novel evaluation method for dehydrochlorination of plasticized Poly(vinyl chloride) containing heavy metal-free thermal stabilizing syner-gistic agent. *Poly. Adv. Tech.*, 32, 3278–3286. <https://doi.org/10.1002/pat.5339>
- [9] B. A. Omran, M. O. Abdel-Salam (2020) Basic corrosion Fundamentals, aspects and currently applied strategies for corrosion mitigation. In *Adv. mat. rese. tech.*, 1–45. https://doi.org/10.1007/978-3-030-49532-9_1
- [10] A. I. Al-Mosawi (2021) A new generation of cable grade poly(vinyl chloride) containing heavy metal freemodifier. *J. Poly. Res.*, 29, 9. <https://doi.org/10.1007/s10965-021-02798-2>
- [11] P. Pedeferrri (2018) Corrosion in concrete. In *Engineer-ing materials*, 509–548. https://doi.org/10.1007/978-3-319-97625-9_23
- [12] A. I. Al-Mosawi, S. A. Abdulsada (2022) Enhancement of thermal characteristics of flexible poly(vinyl chloride) for automotive applications by using environmentally friendly heavy metal-free modifier. *Journal of Thermoplastic Composite Materials*, 36, 3383–3402. <https://doi.org/10.1177/08927057221129488>
- [13] E.J. Opila, N. S. Jacobson (2013) Oxidation and Corrosion of Ceramics, In: Riedel, R., Chen, I. (eds.) *Ceram. Sci. Tech.*, Wiley-VCH Verlag GmbH & Co. KgaA,. <https://doi.org/10.1002/9783527631971.ch01>
- [14] J. K. Al-Kafaji and A.I. Al-Mosawi (2014) Adding hydrazine to pigments to prevent corrosion of ferrous alloys, *University of Kerbala Journal, Special Issue for 2nd scientific conference, science College, University of Kerbala, Iraq*. <https://doi.org/10.6084/m9.figshare.19180982>
- [15] S. A. Abdulsada, A. I. Al-Mosawi (2022) Corrosion behaviour and surface topography for steel plates used in automotive industry exposed to salty corrosive thermo-accelerated medium. *Épít.*, 74. <https://doi.org/10.14382/epitoanyag-jsbcm.2022.31>
- [16] S. A. Abdulsada, A. I. Al-Mosawi and A.A. Hadi (2017) Studying the effect of eco-addition inhibitors on corrosion resistance of reinforced concrete, *Bio. Eng.*, 1, 81-86. <https://doi.org/10.11648/j.be.20170103.14>
- [17] S. A. Abdulsada, A. I. Al-Mosawi (2023) Analysis of corrosion rate, inhibition efficiency, and economic cost of XD3 reinforced concrete related to inhibitor and plasticiser types, *Eng. Res. Exp.*, 5, 035032. <https://doi.org/10.1088/2631-8695/acee46>
- [18] Z. Albaraqaawee, S. A. Abdulsada, A. I. Al-Mosawi (2024) Analysis of coated samples containing hydroxyapatite/multiwalled carbon nanotubes on 2205 DSS substrate, *Full., Nano. C. Nano.*, 2024. <https://doi.org/10.1080/1536383X.2024.2309943>
- [19] D. S. Freitas (2023) Mechanisms of Corrosion of Pipelines, In: *ABCM - Brazilian Society of Mechanical Sciences and Engineering, de França Freire, J.L., Rennó Gomes, M.R., Guedes Gomes, M. (eds.) Handbook of Pipeline Engineering*. Springer, Cham. https://doi.org/10.1007/978-3-031-05735-9_29-1
- [20] K. Tamalmani, H. Husin (2020) Review on Corrosion Inhibitors for Oil and Gas Corrosion Issues. *Appl. Sci.*, 10, 3389. doi :10.3390/app10103389
- [21] X.X. Chen, Y. Zhao (2017) Research on Corrosion Protection of Buried Steel Pipeline. *Eng.*, 9, 504-509. doi:10.4236/eng.2017.95030
- [22] X. Lei (2024) Visualization and Analysis of Oil and Gas Pipeline Corrosion Research: A Bibliometric Data-Mining Approach, *J. Pip. Syst. Eng. Pract.*, 15. <https://doi.org/10.1061/JPSEA2.PSENG-160>
- [23] Y. Frank Cheng (2015) Pipeline corrosion, *Corr. Eng. Sci. Tech.*, 50, 161-162. <https://doi.org/10.1179/1478422X15Z.000000000357>
- [24] M. Amin (2021) Corrosion Investigation of an Oil and Gas Pipe Section and Prediction of its Future Performance. *University of British Columbia, Vancouver, BC, Canada*. 05.
- [25] D. S. Freitas, A. M. Silva, I. L. M. Gonçalves (2023) Mechanisms of Corrosion of Pipelines, In: *França Freire, J. L., Rennó Gomes, M. R., Guedes Gomes, M. (eds.) Handbook of Pipeline Engineering*. Springer, Cham. https://doi.org/10.1007/978-3-031-05735-9_29-1
- [26] C. M. Silva, M. C. Barreto, W. G. Castinheiras (2023) Pipeline Corrosion Management. In: *França Freire, J.L., Rennó Gomes, M.R., Guedes Gomes, M. (eds.) Handbook of Pipeline Engineering*. Springer, Cham. https://doi.org/10.1007/978-3-031-05735-9_30-1
- [27] H. H. Jasim, R. A. Al-Hussain (2019) Evaluation of Inhibitor Efficiency in Crude Oil Pipeline of Missan OilFields South Iraq. *J. Eng. Sust. Devel.*, 23.
- [28] Pipeline 101 – Four Different Types of Pipelines, *Technical Report, Energy Connections Canada*, 2023.
- [29] A. A. Shaymaa, R. Bak, A. Heczal, I.T. Tamás (2020) Corrosion studies on XD3 reinforced concrete samples prepared by using calcium nitrate as inorganic corrosion inhibitor with different superplasticizers, *KOM – Corr. Mat. Prot. J.*, 64, 11-18, <https://doi.org/10.2478/kom-2020-0002>

- [30] A. A. Shaymaa, I.T. Tamás (2020) Studying chloride ions and corrosion properties of reinforced concrete with a green inhibitor and plasticizers, *Str. Con.*, 21, 1894-1904, <https://doi.org/10.1002/suco.201900580>
- [31] A. A. Shaymaa, I.T. Tamás (2020) Investigations on the resistivity of XD3 reinforced concrete for chloride ions and corrosion with calcium nitrate inhibitor and superplasticizers, *Cem.Wap. Bet.*, 25, 330-343, <https://doi.org/10.32047/cwb.2020.25.4.7>
- [32] A. A. Shaymaa, K. Ferenc, I. T. Tamás (2020) Distribution of corrosion products at the steel-concrete interface of XD3 concrete samples, *Mag. Civ. Eng.*, 100, 10005, <https://doi.org/10.18720/MCE.100.5>
- [33] A. A. Shaymaa, A.I.Al-Mosawi (2016) Using of nucleated waste with a nanoscale particles as a green inhibitor, *Int. J. Mech. & Mech. Eng. IJMME-IJENS*, 16, 27–32.
- [34] A.Shaymaa, F.Éva, I.Tamás (2019) Corrosion testing on steel reinforced XD3 concrete samples prepared with a green inhibitor and two different superplasticizers, *Mat. Corr.*, 70, 1262-1272, <https://doi.org/10.1002/maco.201810695>
- [35] M. Tweek, S. Abdulsada (2023) Improvement corrosion properties of reinforcement concrete by corrosion inhibitors: A brief review. *KOM–Corr. Mat. Prot. J.*, 67, 50-58. doi: 10.2478/kom-2023-0007
- [36] M. Alam, M. Alandis, N. Ahmad, M.Alam (2018) Corrosion Protection of Carbon Steel by Pongamia glabra Oil-Based Polyetheramide Coatings, *Int. J. Elect.I Sci.*, 13, 3124-3135. doi:10.20964/2018.03.52
- [37] W. Chengduan, L. Chuan (2018) Corrosion inhibition of mild steel in HCl medium by S-benzyl-O, O'-bis(2-naphthyl) dithiophosphate with ultra-long lifespan. *Results Phys.* 10, 558–567. doi: 10.1016/j.rinp.2018.07.002
- [38] T. Salman, K.Al-Azawi, I.Mohammed, S.Al-Baghdadi, A.Al-Amiery, T.Gaaz (2018) Experimental and quantum chemical simulations on the corrosion inhibition of mild steel by 3-((5-(3,5-dinitrophenyl)-1,3,4-thiadiazol-2-yl) imino) indolin-2-one. *Results Phys.*, 10, 291–296. doi: 10.1016/j.rinp.2018.02.055
- [39] N. Odewunmi, S. Umoren, Z. Gasem, S. Ganiyu, Q. Muhammad (2015) Electrochemical and quantum chemical studies on carbon steel corrosion protection in 1 M H₂SO₄ using new eco-friendly Schiff basemetal complexes. *J. Taiwan Inst. Chem. Eng.*, 51, 177–185. doi:10.1016/j.jtice.2015.12.021.
- [40] A. Zeino, A. Khaled, Jawich, M.; Obot, I. A. Ismail, H. M. Irshad, A. Zeino, I. H. Toor (2019) Electrochemical Corrosion Performance of Aromatic Functionalized Imidazole Inhibitor Under Hydrodynamic Conditions on API X65 Carbon Steel in 1 M HCl Solution. *Ara. J. Sci. Eng.* 44, 5877–5888. doi: 10.1007/s13369-019- 03745-6
- [41] S. Umoren, U. Eduok (2016) Application of carbohydrate polymers as corrosion inhibitors for metal substrates in different media: A review. *Carbohydr. Polym.* 140, 314–341. doi:10.1016/j.carbpol.2015.12.038
- [42] D. Yadav, B. Maiti, M. Quraishi (2010) Electrochemical and quantum chemical studies of 3,4-dihydropyrimidin-2(1H)-ones as corrosion inhibitors for mild steel in hydrochloric acid solution. *Corros. Sci.*, 52, 3586–3598.
- [43] M. Askari, M. Aliofkhaezrai, S. Afroukhteh (2019) A comprehensive review on internal corrosion and cracking of oil and gas pipelines, *J. Nat. Gas Sci. Eng.*, 71, 102971. doi:10.1016/j.jngse.2019.102971
- [44] Mark E. Orazem (2014) *Underground pipeline corrosion Detection, analysis and prevention*, Woodhead Publishing Series in Metals and Surface Engineering: Number 63.
- [45] J. Joseph P. Akpan, O Udom, F. John (2023) Oil and Gas Pipeline Corrosion Monitoring and Prevention Techniques in The Niger Delta Region, Nigeria: A Re-view. *J. Res. Eng.Com. Sci.*, 1, 43-54. <https://hspublishing.org/JRECS/article/view/114>
- [46] U. Bharatiya, P. Gal, A. Agrawal, M. Shah, A. Sircar (2019) Effect of Corrosion on Crude Oil and Natural Gas Pipeline with Emphasis on Prevention by Ecofriendly Corrosion Inhibitors: A Comprehensive Review. *J. Bio- and Tribo-Corr.* 5(2), 1-12, doi:10.1007/s40735-019-0225-9
- [47] T. Nagalakshmi, A. Sivasakthi (2019) Corrosion Control, Prevention and Mitigation in Oil & Gas Industry, *Int. J. Inno. Tech. Exp. Eng.*, 9, 1568-1572. doi:10.35940/ijitee.B7272.129219
- [48] A. J. McMahon, S. Groves (1995) *Corrosion Inhibitor Guidelines*, BP Sunbury report No. ESR.95.ER.050.
- [49] S. Webster, A. J. McMahon, D. M. E. Paisley, D. Harrop (1996) *Corrosion Inhibitor Test Methods*, BP Sunbury Report No. ESR 95.ER.054.
- [50] F. Hameed, H. Rashida, A. Khadomb (2022) New Developments in Inhibition of the Sweet Environment in a Variety of Corrosive Media: A Review. *Eng. Tech. J.*, 40, 1117- 113. doi:10.30684/etj.2022.132127.1093
- [51] B. E. Brycki, I. H. Kowalczyk, A. Szulc. (2018) Organic corrosion inhibitors. *Corrosion inhibitors, principles and recent applications*, Ch.1, 3-33. doi: 10.5772/in-techopen.72943.
- [52] K. Tamalmani H. Husin (2020) *Review on Corrosion Inhibitors for Oil and Gas Corrosion*, Department of Petroleum Engineering, Universiti Teknologi PETRO-NAS, Bandar Seri Iskandar 32610, Perak, Malaysia.

- [53] Z. Tang (2017) A review of corrosion inhibitors for rust preventative fluids, NTIC (Shanghai) Co., Ltd., Shanghai, China.
- [54] K. A. Al-Sodani, M. Maslehuddin, O.S. Al-Amoudi (2018) Efficiency of generic and proprietary inhibitors in mitigating Corrosion of Carbon Steel in Chloride-Sulfate Environments. Sci Rep 8, 11443. <https://doi.org/10.1038/s41598-018-29413-7>
- [55] M. Askari, M. Aliofkhaeaei, S. Ghaffari, A. Hajizadeh (2018) Film Former Corrosion Inhibitors for Oil and Gas Pipelines - A Technical Review, J. Nat. Gas Sci. & Eng., 2, <https://doi.org/10.1016/j.jngse.2018.07.025>

IZVOD

EFEKAT INHIBITORA KOROZIJE NA UNUTRAŠNJU KOROZIJU U NAFTOVODIMA: KRATAK PREGLED

Industrija nafte i gasa se prvenstveno oslanja na cevovode za transport sirove i rafinisane nafte, tako da se transport sirove nafte uglavnom obavlja cevovodima. S obzirom na ovo, nemoguće je sprečiti da površine cevovoda budu kontinuirano izložene izvorima korozije, kao što su zagađivači koji sadrže tragove hromata i sumpora, koji mogu izazvati pojavu korozije na površinama cevovoda. Poznato je da su inhibitori korozije hemikalije koje se koriste u niskim koncentracijama u svrhu smanjenja ili sprečavanja korozije. Efikasnost inhibitora je određena njegovom sposobnošću da reaguje sa površinom metala i stvori zaštitni premaz koji smanjuje ili sprečava koroziju reagujući sa površinom metala. U ovom članku je dat pregled mehanizama korozije u naftovodima, uz opis načina izbora inhibitora korozije prema mehanizmima korozije u naftovodima.

Ključne reči: cevovodi, korozija, zeleni inhibitori, karboksilati, nafta.

Naučni rad

Rad primljen: 25.03.2024.

Rad prihvaćen: 12.04.2024.

Rad je dostupan na sajtu: www.idk.org.rs/casopis

The ORCID Ids of all the authors are as follows:

1. Shaymaa Abbas: <https://orcid.org/0000-0001-7006-2950>

2. Esraa Razaq: <https://orcid.org/0009-0008-3963-4349>

Bui Xuan Vuong

Faculty of Natural Sciences Education, Sai Gon University, 273 An Duong Vuong St, Ward 3, District 5, Ho Chi Minh City 700000, Vietnam

Scientific paper

ISSN 0351-9465, E-ISSN 2466-2585

<https://doi.org/10.62638/ZasMat1049>



Zastita Materijala 65 (4)
653 - 659 (2024)

Hydrothermal synthesis of bioactive calcium silicate glass

ABSTRACT

This work presents the synthesis of bioactive glass 60SiO₂-40CaO (wt.%) by the hydrothermal method without using acid catalysts in shortened synthesis time. The precursors Si(OC₂H₅)₄ (TEOS), Ca(NO₃)₂·4H₂O were introduced in a hydrothermal system, and heated at 150 °C for 24 hours. The resulting gel was dried at 150 °C for 24 hours, then calcined at 800 °C for 3 hours to achieve bioactive glass. Several physical-chemical methods such as TG-DSC, XRD, SEM, and ICP-OES were used to evaluate the synthetic material. The bioactivity and biocompatibility of synthetic glass were evaluated by in vitro experiments in SBF solution and in cell culture environment. The obtained results show that the synthetic glass is an amorphous material, presenting the bioactivity through the formation of a hydroxyapatite mineral layer after 10 days of soaking in SBF solution, and also showing good biocompatibility with cells L-929.

Keywords: Bioactive glass, bioactivity, artificial bone, hydroxyapatite, cell viability

1. INTRODUCTION

Bioactive glasses (bioglasses) are a type of material that is researched and applied as an artificial bone material used as a component in dental filling cement, culture powder and bone graft in orthopedic surgery to restore and repair damaged and diseased bones [1]. The bioactivity of the material is the ability to form a new layer of hydroxyapatite Ca₁₀(PO₄)₆(OH)₂ (HA) mineral on the surface when the material is implanted in bone defects or damaged bones in the human body. The HA mineral layer has a composition similar to the inorganic composition of human bone, so it is the bridge between the glass graft and natural bone, through which damaged bone parts can be repaired and filled [2,3]. The bioactivity of bioglasses can be tested through “in vitro” experiments according to the method of T. Kokubo & H. Takadama [4]. The glass sample is soaked in SBF solution (Simulated Body Fluid) - a solution with the inorganic ionic components similar to human blood and synthesized in the laboratory. Bioactive glass is synthesized by melting method, or sol-gel method; in which the sol-gel method has been commonly used in recent years.

The sol-gel method is undergone through two main stages: hydrolysis of precursors to create sol, and conversion of sol particles into gel. The resulting gel is processed at a high temperature to obtain a glass material. The sol-gel method overcomes the disadvantages of the melting method such as synthesizing the material system at lower temperatures, the resulting glass systems have a larger specific surface area, leading to higher bioactivity [5 -7]. However, the sol-gel synthesis process requires a long synthesis time because the conversion process from sol to gel usually takes several days. In addition, toxic inorganic acids are often used in the hydrolysis of precursors in the sol-gel synthesis process. In this work, we used a unique method to synthesize two-component bioactive glass SiO₂-CaO. Synthesis experiment was conducted in a hydrothermal system at high temperature, so that the reactions of sol and gel formation could take place quickly. The glass material synthesized in this study was evaluated for their physical-chemical properties, bioactivity and cell biocompatibility.

2. MATERIALS AND METHOD

2.1. Materials

Chemicals for synthesis of bioactive glass 60SiO₂-40CaO (wt.%) consist of calcium nitrate tetrahydrate Ca(NO₃)₂·4H₂O (99%, Sigma-Aldrich); tetraethyl orthosilicate Si(OC₂H₅)₄ (TEOS) (98%, Sigma-Aldrich). Chemicals (over 99%, Merk) for

*Corresponding author: Bui Xuan Vuong

E-mail: bxvuong@sgu.edu.vn

Paper received: 25.03.2024.

Paper accepted: 25.04.2024.

synthesizing SBF solution (Simulated Body Fluid) include $(\text{NH}_4)_2\text{HPO}_4$; $\text{K}_2\text{HPO}_4 \cdot 3\text{H}_2\text{O}$; $\text{MgCl}_2 \cdot 6\text{H}_2\text{O}$; HCl ; NaCl ; KCl ; NaHCO_3 ; CaCl_2 ; $\text{C}_{14}\text{H}_{11}\text{NO}_3$.

2.2. Synthesis process

The 60SiO₂-40CaO (wt.%) glass system was synthesized by a non-catalytic hydrothermal method in this study. Investigation of the temperature factor shows that the hydrothermal reaction did not occur when the reaction mixture was carried out below 140 °C. Gel was formed at 150 °C while above 160 °C the gel was burned due to the decomposition of organic precursors. The H₂O/TEOS molar ratio was chosen to be 10 based on previous researches on bioactive glasses synthesized by the conventional sol-gel method [5-7]. The hydrothermal time was chosen to be 24 hours based on surveys of the reactions according to the above temperatures. According to chemical principles, high temperature leads to the evaporation of water in a closed hydrothermal system, causing high pressure for the reaction system. The pressure of the hydrothermal system, which was not measured in this study, is referred to by the term "self-generated pressure or spontaneous pressure". The value of self-generated pressure will change according to the time of the reaction occurring in the closed system. After investigating factors such as temperature and reaction time, the glass material synthesis process is briefly summarized as follows: mixture of TEOS, Ca(NO₃)₂·4H₂O and distilled water was placed in a hydrothermal system (autoclave) and heated at 150 °C for 24 hours. The resulting gel was dried at 150 °C for 24 hours. From thermal analysis data, the dried gel powder was heated at 800 °C for 3 hours to create a bioglass system.

2.3. In vitro in SBF solution

Glass powder was tested in vitro in SBF solution (Simulated Body Fluid) to check whether it meets the requirements of a biomedical material; that is, to check the bioactivity of the material. This is a quick and simple experiment, intended to carry out a process or reaction in a test tube, in a culture dish outside the living body. In vitro experiment was conducted by soaking glass powder in a solution of simulating human body fluid SBF to investigate the possibility of new bone mineral formation [4]. The SBF solution is a simulated body fluid with a composition of ions similar to blood in the human body, which is synthesized from salt precursors in the laboratory. The glass material powder was soaked in SBF solution for different time periods. The temperature of soaked samples was kept at 37 °C similar to body temperature. The shaking speed for soaked samples was 50 rpm. After soaking periods, the glass material powders

were separated and washed with distilled water to remove excess ions and then rinsed with pure alcohol to completely remove free ions. The powder samples were dried and reserved for analysis of physical-chemical characteristics. The solutions were checked for the content of elements such as Ca, Si, P exchanged between the material and the SBF solution environment.

2.4. In vitro with cells

The glass system was tested in a cell culture environment to evaluate the biocompatibility of the synthetic material. Standard culture medium DMEM (Dulbecco's Modified Eagle Medium – Sigma Aldrich) was used in the experiment [8]. The fibroblast line (L-929 fibroblast) was cultured in a standard environment of 37 °C, with 5% CO₂ and 95% humidity. The existence of cell lines was determined by the MTT colorimetric method. MTT compound with the chemical formula of 3-(4,5-Dimethylthiazol-2-yl)-2,5-diphenyltetrazolium bromide is a yellow tetrazole, which is converted into purple formazan when interacting with mitochondria in living cells. Quantification of formazan through absorbance is determined by measuring at wavelengths from 500 to 570 nm using a UV-Vis spectrophotometer. Formazan quantification allows direct determination of the number of viable cells.

2.5. Methods of analysis and evaluation

TG-DSC (Thermal Gravimetric Analysis-Differential Scanning Calorimetry) is used to determine the calcination temperature that converts dried gel into a glass system. X-ray diffraction (XRD - X Ray Diffraction) is served to determine the phase composition of materials. Scanning electron microscope (SEM - Scanning Electron Microscopy) is a popular tool in materials research, allowing microstructure analysis from the surface of a specimen with high resolution without the need to destroy the sample. The ICP-OES (Inductively Coupled Plasma – Optical Emission Spectroscopy) method is used to analyze the content of Ca, Si, and P elements exchanged between the material sample and the "in vitro" testing environment, thereby evaluating the chemical interactions occurring between the bioglass material sample and the human physiological environment.

3. RESULTS AND DISCUSSION

3.1. Thermal analysis

The result of TG-DSC thermal analysis of the dried gel sample 60SiO₂ – 40CaO (wt.%) is shown in Figure 1. Thermal analysis diagram shows three mass loss ranges on the TG curve. The initial mass loss range of 30 °C to 220 °C with an endothermic peak at 145.2 °C characterizes water removal [9-

10]. The second mass loss in the range from 220 °C to 470 °C with an exothermic peak at 280 °C, is considered to be the dehydration of ethanol because some ethanol may still exist inside the pores of the dried gel [11]. The third mass loss between 470 °C and 660 °C with an endothermic peak at 508.9 °C is attributed to be the decomposition of NO_3^- groups [12-13]. According to previous studies on bioactive glasses synthesized

by the sol-gel method, at a temperature about 900 °C, a phase transition often occurs to form CaSiO_3 mineral [12-14]. Observation show that the $60\text{SiO}_2 - 40\text{CaO}$ (wt.%) glass system is structurally stable in this temperature region without any phase transition occurring. From the TG-DSC thermal analysis, the appropriate temperature for glass heating was chosen to be 800 °C.

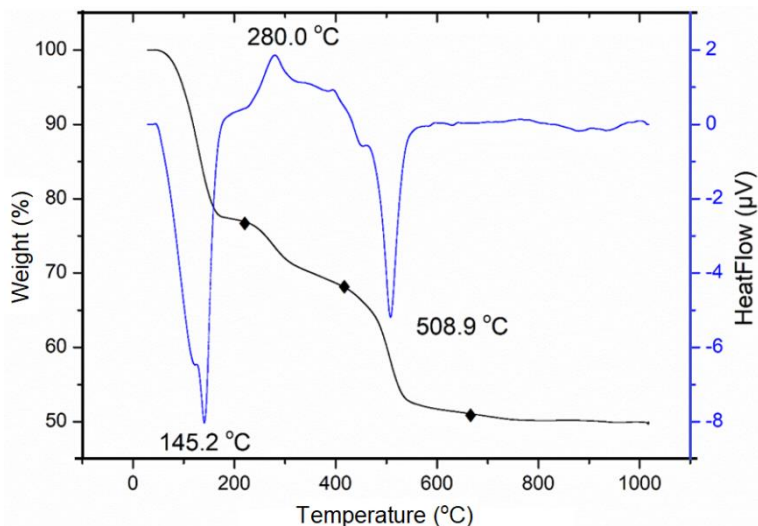


Figure 1. TG-DSC analysis of glass sample $60\text{SiO}_2 - 40\text{CaO}$ (wt.%)

3.2. XRD analysis

Figure 2 shows the XRD pattern of $60\text{SiO}_2 - 40\text{CaO}$ (wt.%) glass material before and after in vitro testing in SBF solution. The XRD pattern of the bioactive glass shows that a broad diffraction halo is observed, the resulting spectral pattern is characteristic of amorphous structural materials. XRD analysis results show that the

$60\text{SiO}_2 - 40\text{CaO}$ (wt.%) bioactive glass synthesized by the non-acid-catalyzed hydrothermal method still maintains amorphous property like the glass prepared by the conventional sol-gel method [15-17]. After 5 days of soaking in SBF solution, the interaction of the material with the SBF environment did not change the feature of the XRD diagram.

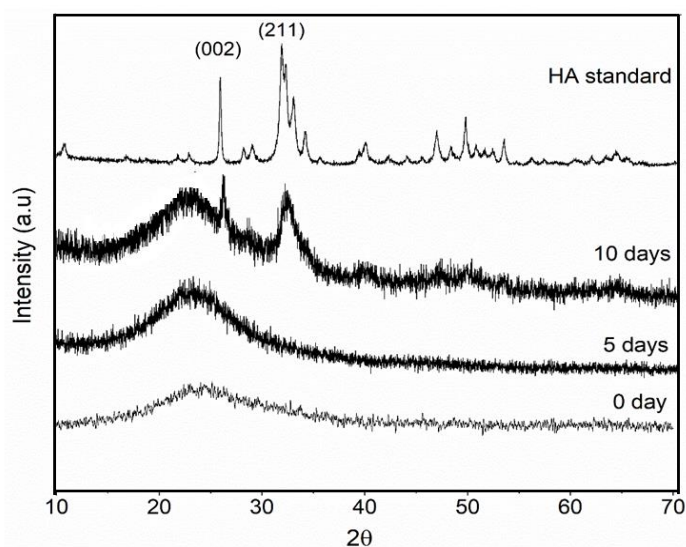


Figure 2. XRD diagrams of glass sample $60\text{SiO}_2 - 40\text{CaO}$ (wt.%) before and after in vitro experiment in SBF solution

This result shows that the 60SiO₂ - 40CaO (wt.%) glass material has not shown bioactivity after 5 days of in vitro experiment. Compared with the previous studies, the glass system synthesized by the modified sol-gel method in this study has lower bioactivity [13, 15-17]. This may be due to the strong structure of the synthetic glass in accordance with the TG-DSC analysis, which gave a fairly high heating temperature to form the glass at 800 °C, and no glass melting at about 900 °C. The durable structure leads to a slow interaction of the material and the SBF environment, which means lower bioactivity. After 10 days of immersion in SBF solution, the hydroxyapatite (HA) mineral phase was identified by the clear appearance of two characteristic peaks at 2θ = 26° (002) and 32° (211) (JCPDS: 09432). The obtained result confirm the bioactivity of the synthetic glass system after 10 days of in vitro experiments in SBF solution.

3.3. SEM observation

Figure 3 presents SEM images of 60SiO₂ - 40CaO (wt.%) glass sample before and after immersion in SBF solution. The original glass material clearly shows irregular aggregation of small particles, creating a rough surface, and a porous structure (Fig. 3a). After 1 day of soaking, the surface changed due to the dissolution of the glass material in the SBF solution (Fig. 3b). The surface appeared small crystals quite uniformly after 5 days of soaking and became clearer after 10 days of soaking (Fig. 3c-3d). After 10 days of immersion in SBF solution, the mineralization process was determined by the formation of new HA crystals covering the surface of the glass samples compared to the original sample. The HA crystals are uniform, and cover the entire surface of the 60SiO₂ - 40CaO (wt.%) bioactive glass material as observed in Fig. 3d.

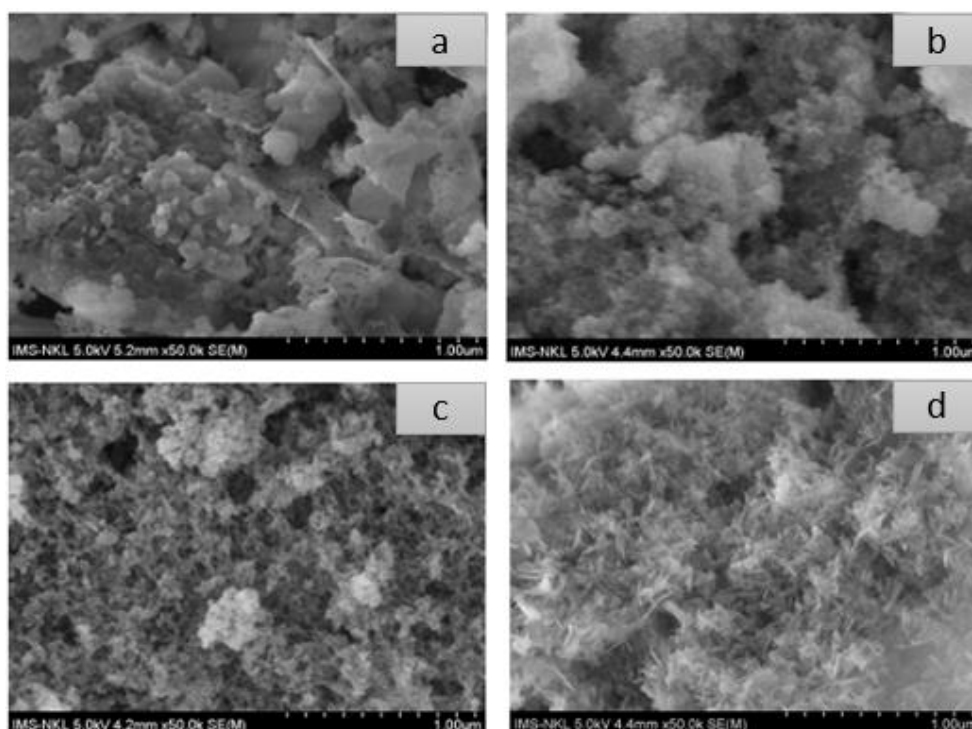


Figure 3. SEM images of glass samples before and after in vitro experiment in SBF solution: a-initial sample; b-sample after 1 day; c-sample after 5 days; and d-sample after 10 days

3.4. Dissolution of glass in SBF solution

The physical-chemical interactions of bioactive glass 60SiO₂ - 40CaO (wt.%) with the experimental environment lead to changes in the concentration of ions in the SBF solution analyzed by the ICP-OES method, as shown in Fig. 4. The elemental concentrations of Si, Ca, and P in the initial SBF solution were 0 ppm, 100.1 ppm, and 31.2 ppm, respectively. The Si concentration

increased rapidly at the beginning of soaking (from 0 to 3 days), then increased moderately from 3 to 5 days, then reached saturation value at the period of 5 to 10 days of soaking. According to previous studies, the increase of Si concentration is explained by the dissolution of the glass network through the release of Si(OH)₄ silicic acid, while the saturation process corresponds to repolymerization of the above acids to create a silica SiO₂ layer [18-21]. The Ca concentration increased at the

beginning of the experiment, due to the rapid exchange of Ca^{2+} released from the glass network and H^+ in the SBF solution [22-24]. Then, the Ca concentration decreased sharply after 3 days and reached saturation after 5 days. The decrease in Ca concentration is explained by its consumption to create the HA mineral layer on the surface of the

bioactive glass [23-24]. No increase in P concentration was observed after the in vitro experiment, which can be explained by the absence of P in the initial glass, as well as the consumption of Ca and P in solution to form the hydroxyapatite mineral layer during the in vitro experiment.

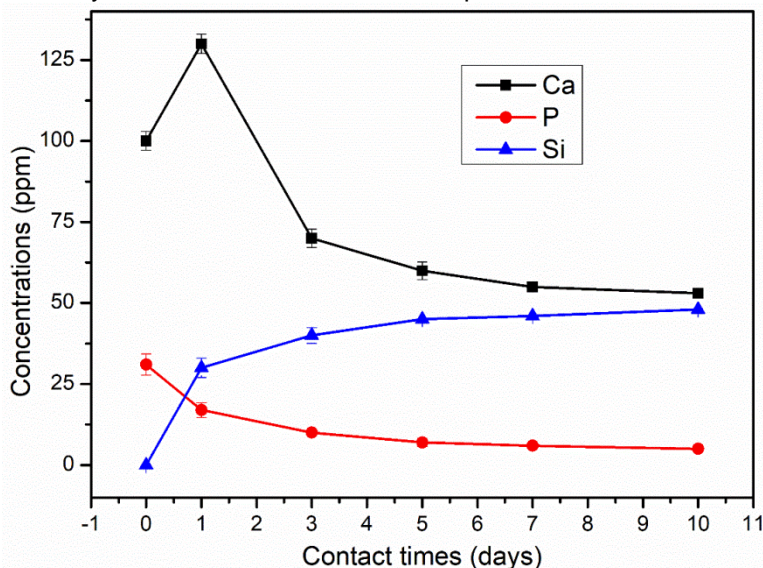


Figure 4. Ionic exchange between glass sample 60SiO₂ - 40CaO (wt.%) and SBF solution

3.5. Biocompatibility with cells

The 60SiO₂ – 40CaO (wt.%) glass system was tested for biocompatibility in cell culture medium.

The viability of fibroblast-like cells (L-929 fibroblast) directly exposed to bioactive glass powder for 24 h is presented in Fig. 5.

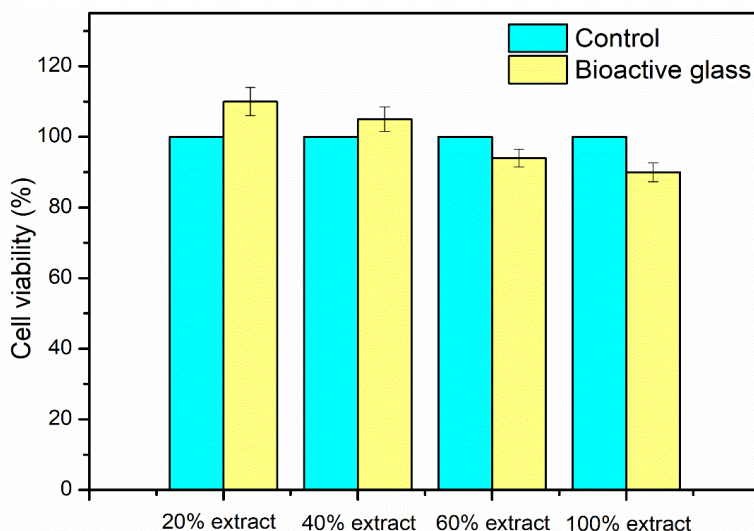


Figure 5. Biocompatibility of glass sample 60SiO₂ - 40CaO (wt.%) in cell culture environment

Cell viability without exposure to bioactive glass was chosen as the control (100%) [8]. According to ISO 10993-5 (Section 5: Cytotoxicity testing, in vitro methods 2009), cell viability is calculated as a percentage compared to the control. In cases where the average cell viability is less than 70%,

the material is cytotoxic. The results obtained showed that cell viability was 110%, 105%, 94%, and 90% for the glass extracts of 20%, 40%, 60% and 100%, respectively. The 20% extract showed the highest cell viability value, while the 60% and 100% extracts showed little difference. The cell

viability values for bioactive glass in this study are equivalent to those of previously studied glass systems synthesized by the sol-gel method [25]. The obtained results show that 60SiO₂-40CaO (wt.%) bioactive glass synthesized by hydrothermal method without catalytic acid exhibits good biocompatibility in cellular environments even in high-concentrated extract.

4. CONCLUSION

Bioactive glass material 60SiO₂-40CaO (wt.%) has been successfully synthesized by the hydrothermal method without using acid catalyst with shortened synthesis time. Synthetic material exhibits an amorphous structure similar the natural structure of glass materials. The bioactivity of the 60SiO₂-40CaO system was confirmed through the formation of a hydroxyapatite (HA) mineral layer after 10 days of in vitro experiment in SBF solution; therefore, it exhibits slower bioactivity than similar glass systems synthesized by the conventional sol-gel method. The diversity of bioactivities when using the new synthesis method in this study brings different application values of bioactive glass materials. Experimental evaluation of biocompatibility in cell culture medium shows that the bioactive glass material in this study has good biocompatibility with the L-929 fibroblast cell line.

5. REFERENCES

- [1] L.L. Hench (1991) Bioceramics: From Concept to Clinic, *Journal of the American Ceramic Society*, 74(7), 1487-1510. <https://doi.org/10.1111/j.1151-2916.1991.tb07132.x>
- [2] L. L. Hench, R. J. Splinter, T. K. Jr. Greenlee (1971) Bonding Mechanisms at the Interface of Ceramic Prosthetic Materials, *Journal of Biomedical Materials Research*, 5(6), 117-141. <https://doi.org/10.1002/jbm.820050611>
- [3] J. Ma, C. Z. Chen, D. G. Wang, X. G. Meng, J. Z. Shi (2010) Influence of the sintering temperature on the structural feature and bioactivity of sol-gel derived SiO₂-CaO-P₂O₅ bioglass, *Ceramics International*, 36(6), 1911-1916. <https://doi.org/10.1016/j.ceramint.2010.03.017>
- [4] T. Kokubo, H. Takadama (2006) How useful is SBF in predicting in vivo bone bioactivity, *Biomaterials*, 27(15), 2907-2915. <https://doi.org/10.1016/j.biomaterials.2006.01.017>
- [5] G. J. Owens, R. K. Singh, F. Foroutan, M. Alqaysi, C. M. Han, C. Mahapatra, H. W. Kim, J. C. Knowles (2016) Sol-gel based materials for biomedical applications, *Progress in Materials Science*, 77, 1-79. <https://doi.org/10.1016/j.pmatsci.2015.12.001>
- [6] Z. Hong, A. Liu, L. Chen, X. Chen, X. Jing (2009) Preparation of bioactive glass ceramic nanoparticles by combination of sol-gel and coprecipitation method, *Journal of Non-Crystalline Solids*, 355 (6), 368-372. <https://doi.org/10.1016/j.jnoncrysol.2008.12.003>
- [7] I. Elgayar, A. E. Aliev, A. R. Boccaccini, R. G. Hill (2005) Structural analysis of bioactive glasses, *Journal of Non-Crystallization Solid*, 361(2), 173-183. <https://doi.org/10.1016/j.jnoncrysol.2004.07.067>
- [8] T.J. Mosmann (1983) Rapid colorimetric assay for cellular growth and survival: Application to proliferation and cytotoxicity assays, *Journal of Immunological Methods*, 65, 55-63. [https://doi.org/10.1016/0022-1759\(83\)90303-4](https://doi.org/10.1016/0022-1759(83)90303-4)
- [9] B.T. Hoa, H.T.T. Hoa, N.A. Tien, N.H.D. Khang, E.V. Guseva, T.A. Tuan, B.X. Vuong (2020) Green synthesis of bioactive glass 70SiO₂-30CaO by hydrothermal method, *Materials Letters*, 274, 128032. <https://doi.org/10.1016/j.matlet.2020.128032>
- [10] A. Saboori, M. Rabiee, F. Moztafzadeh, M. Sheikhi, M. Tahri, M. Karimi (2009) Synthesis, characterization and in vitro bioactivity of sol-gel-derived SiO₂-CaO-P₂O₅-MgO bioglass, *Material Science Engineering C*, 29, 335-340. <https://doi.org/10.1016/j.msec.2008.07.004>
- [11] A.M. El-Kady, A.F. Ali (2012) Fabrication and characterization of ZnO modified bioactive glass nanoparticles, *Ceramic International*, 38, 1195-1204. <https://doi.org/10.1016/j.ceramint.2011.07.069>
- [12] J.R.L. Delben, K. Pereira, S.L. Oliveira, L.D.S. Alencar, A.C. Hernandez, A.A.S.T. Delben (2013) Bioactive glass prepared by sol-gel emulsion, *Journal of Non-Crystalline Solids*, 361, 119-123. <https://doi.org/10.1016/j.jnoncrysol.2012.10.025>
- [13] J. Román, S. Padilla, M. Vallet-Regí (2003) Sol-gel glasses as precursors of bioactive glass ceramics, *Chemistry of Materials*, 15, 798-806. <https://doi.org/10.1021/cm021325c>
- [14] T.A. Tuan, E.V. Guseva, L.H. Phuc, N.Q. Hien, N.V. Long, B.X. Vuong (2020) Acid-free Hydrothermal Process for Synthesis of Bioactive Glasses 70SiO₂-(30-x)CaO-xZnO (x = 1, 3, 5 mol.%), *Proceeding*, 62, 1-12. <https://doi.org/10.3390/proceedings2020062006>
- [15] I. Cacciotti, M. Lombardi, A. B. Antonio, L. Montanaro (2012) Sol-gel derived 45S5 bioglass: synthesis, microstructural evolution and thermal behaviour, *Journal of Material Science: Material Medicine*, 23(8), 1849-1866. <https://doi.org/10.1007/s10856-012-4667-6>
- [16] S. M. Ahmadi, A. Behnamghader, A. Asfnejaad (2017) Sol-gel synthesis, characterization and in vitro evaluation of SiO₂-CaO-P₂O₅ bioactive glass nanoparticles with various CaO/P₂O₅ ratios, *Digest Journal of Nanomaterials and Biostructures*, 12(3), 847-860. <https://doi.org/10.1016/j.ceramint.2015.12.128>
- [17] N. Letaief, H. Oudadesse (2014) New 92S6 mesoporous glass: Influence of surfactant carbon chain length on the structure, pore morphology and bioactivity, *Materials Research Bulletin*, 60, 882-889. <https://doi.org/10.1016/j.materresbull.2014.08.048>
- [18] V. Aina, G. Malavasi, A.F. Pla, L. Munaron, C. Morterra (2009) Zinc-containing bioactive glasses:

- Surface reactivity and behavior towards endothelial cells, *Acta Biomaterialia*, 5, 1211–1222.
<https://doi.org/10.1016/j.actbio.2008.10.020>
- [19] I.Y. Kim, G. Kawachi, K. Kikuta, S.B. Cho, M. Kamitakahara, C.J. Ohtsuki (2008) Preparation of bioactive spherical particles in the CaO–SiO₂ system through sol–gel processing under coexistence of poly (ethylene glycol), *Journal of the European Ceramic* 28, 1595–1602.
<https://doi.org/10.1016/j.jeurceramsoc.2007.11.006>
- [20] P.J. Innocenzi (2003) Infrared spectroscopy of sol–gel derived silica-based films: A spectra-microstructure overview, *Journal of Non-Crystalline Solids*, 316, 309–319.
[https://doi.org/10.1016/S0022-3093\(02\)01637-X](https://doi.org/10.1016/S0022-3093(02)01637-X)
- [21] J. Ding, Y. Chen, W. Chen, L. Hu, G. Boulon (2012) Effect of P₂O₅ addition on the structural and spectroscopic properties of sodium aluminosilicate glass, *Chinese Optics Letters*, 10, 071602.
<https://doi.org/10.3788/col201210.071602>
- [22] X.F. Chen, B. Lei, Y.J. Wang, N.J. Zhao (2009) Morphological control and in vitro bioactivity of nanoscale bioactive glasses, *Journal of Non-Crystalline Solids*, 355, 791–796.
<https://doi.org/10.1016/j.jnoncrysol.2009.02.005>
- [23] Z. Hong, A. Liu, L. Chen, X. Chen, X.J. Jing (2009) Preparation of bioactive glass ceramic nanoparticles by combination of sol–gel and coprecipitation method, *Journal of Non-Crystalline Solids*, 355, 368–372. <https://doi.org/10.1016/j.jnoncrysol.2008.12.003>
- [24] A. Hoppe, N.S. Güldal, A.R. Boccaccini (2011) A review of the biological response to ionic dissolution products from bioactive glasses and glass-ceramics, *Biomaterials*, 32, 2757–2774.
<https://doi.org/10.1016/j.biomaterials.2011.01.004>
- [25] I.A. Silver, J. Deas, M.E. Hska (2001) Interactions of bioactive glasses with osteoblasts in vitro: Effects of 45S5 Bioglass®, and 58S and 77S bioactive glasses on metabolism, intracellular ion concentrations and cell viability, *Biomaterials*, 22, 175–185.
[https://doi.org/10.1016/S0142-9612\(00\)00173-3](https://doi.org/10.1016/S0142-9612(00)00173-3)

IZVOD

HIDROTERMALNA SINTEZA BIOAKTIVNOG KALCIJUM SILIKATNOG STAKLA

U radu je prikazana sinteza bioaktivnog stakla 60SiO₂-40CaO (tež.% hidrotermalnom metodom bez upotrebe kiselih katalizatora za skraćeno vreme sinteze. Prekursori Si(OC₂H₅)₄ (TEOS), Ca(NO₃)₂·4H₂O uvedeni su u hidrotermalni sistem i zagrevani na 150 °C tokom 24 sata. Dobijeni gel je sušen na 150 °C tokom 24 sata, zatim kalcinisan na 800 °C tokom 3 sata da bi se dobilo bioaktivno staklo. Nekoliko fizičko-hemijskih metoda kao što su TG-DSC, XRD, SEM i ICP-OES korišćeno je za procenu sintetičkog materijala. Bioaktivnost i biokompatibilnost sintetičkog stakla su procenjene in vitro eksperimentima u rastvoru SBF i u okruženju ćelijske kulture. Dobijeni rezultati pokazuju da je sintetičko staklo amorfni materijal, koji pokazuje bioaktivnost kroz formiranje mineralnog sloja hidroksiapatita nakon 10 dana namakanja u rastvoru SBF, a takođe pokazuje dobru biokompatibilnost sa ćelijama L-929.

Ključne reči: bioaktivno staklo, bioaktivnost, veštačka kost, hidroksiapatit, vitalnost ćelija

Naučni rad

Rad primljen: 25.03.2024.

Rad prihvacen: 25.04.2024.

Bui XuanVuong -<https://orcid.org/0000-0002-3757-1099>

Etuk Sunday Edet¹, Robert Ubong Williams², Agbasi, Okechukwu Ebuka³, Inyang Namdie Joseph¹

¹Department of Physics, University of Uyo, Uyo, Akwa Ibom State, Nigeria; ²Department of Physics, Akwa Ibom State University, Ikot Akpaden, Mkpāt Enin, Akwa Ibom State, Nigeria; ³Okna Geophysical Services, Eket, Nigeria

Scientific Paper

ISSN 0351-9465, E-ISSN 2466-2585

<https://doi.org/10.62638/ZasMat1051>



Zastita Materijala 65 (4)
660 – 667 (2024)

Influence Of Rice Husk Ash Inclusion On Electrical Characteristics Of Dry Cement Mortar

ABSTRACT

Rice husk is usually generated as waste in large quantities but yet to be optimally utilized. Due to the pollution effects associated with poor approach prevalently adopted for its disposal, volarizing it into economical and sustainable material for building construction is a necessary option to provide solution for future generation. In this research, separate dry mortars were prepared using cement grades 32.5R and 42.5N and the influence of rice husk ash (RHA) inclusion on their electrical characteristics was investigated. The materials used were batched by volume and the RHA was utilized as a partial substitute for cement at 10 % level. All the samples were cured for 21 days and then allowed to dry completely prior to the tests implementation. The results showed decrease in electrical resistance with temperature (ranging from 20°C to 50°C) due to incorporation of the RHA. Though samples with the RHA content possessed ability to act as smart mortars for temperature monitoring/sensing, utilization of cement grade 42.5N ensured a better performance. By utilizing rice husks in such undertakings, their associated disposal problems could be tackled and construction of inexpensive but sustainable building with large temperature sensing capability could be enhanced.

Keywords: Building; Electrical resistance; Temperature sensing; Thermal sensitivity index; Waste

1. INTRODUCTION

Mortar is homogeneous mixture of cementitious material, fine aggregate (sand), and specific amount of water. In building construction, cement mortar is used for plastering over bricks or other forms of masonry. The knowledge acquired from the study of electrical properties of cement-based composites has helped to understand that cement mortar can perform other interesting functions. For instance, Ahmed and Kamal [1] observed that conductive cement mortar has amazing infrastructural applications including building surface heating, pavement de-icing, electromagnetic defence, cathodic protection, and enhancing foundations and buried ground grid systems. Also, Honorio et al [2] found that electrical resistivity and conductivity provide useful information

on the durability of cement-based materials and can be used for monitoring and inspection of concrete structures. Bazari and Chini [3] noticed that it is possible to fully observe the setting time and compressive strength of mortar and concrete by electrical resistance method than in the case of employing common physical tests.

In recent times, researchers have investigated different replacements for conventional materials as well as additives to conventional mortars in order to improve the properties of the cementitious composites. Such filler materials include carbon fiber [4 – 6], graphene [6, 7], carbon black [9 – 12], and carbon nanofiber [13]. The use of carbon nanotube yields reinforced composites that have excellent function properties, such as mechanical properties [14], high-temperature properties [15 – 17], and electrical properties [18 – 21]. Among other factors, the behavior of the composites is influenced by the kind of filler material used. For example, Yoo et al [22] observed that multi-walled carbon nanotubes have

* Corresponding author: Okechukwu, Ebuka Agbasi
E-mail: agbasi.okechukwu@gmail.com
Paper received: 27.03.2024.
Paper accepted: 3.05.2024.

a better enhancement effect on the electrical conductivity of cement paste than graphite nanofibers and graphene. But absolute reliance on these industrial waste materials could hinder sustainable development as some of them are scarce and uneconomical. Therefore, there is need to urgently consider preparation of conductive filler materials from waste that is sustainable.

The aim of this research is to examine the electrical characteristics of dry cement mortars that contain rice husk ash (RHA) as a partial replacement material for cement. In this study, two different grades of cement will be considered and the possible application(s) of the mortars will be predicted. A similar study reported in the literature involved the use of coconut husk ash and one type of cement grade [23]. The choice of rice husk for synthesis of the ash is due to its sustainability as it is continuously abundant and cheaply available in large quantity as an agro-waste. Globally, the annual output of rice husk is at least 80 million tons and over 97 % of the husk is generated in developing countries [24, 25]. Though attempts have been made to use rice husk to prepare ash for enhancement of compressive strength of concrete [26 - 28] and amendment of soil behavior [29, 30], it still remains under-utilized. With persistence of inefficient solid waste management systems in developing countries [31, 32], rice husks are prevalently disposed of by indiscriminate dumping. This situation is detrimental to the environment and needs to be addressed.

2. EXPERIMENTAL PERSPECTIVE

2.1. Materials and their description

Two different grades of Portland limestone cement (CEM II/BL 32.5 R and CEM II/BL 42.5N, both of which are manufactured by Dangote Cement PLC, Obajana Plant), sand (fine aggregate), water (from bore-hole), and rice husks were the major materials utilized in this research. The cement and sand were obtained from a building construction site. The

rice husks were gathered as waste from a local rice mill. These materials were collected in large quantities within Ini Local Government Area, Akwa Ibom State, Nigeria.

2.2. Materials processing and analysis

The husks were soaked in water in order to remove dirt and other forms of impurities from them. They were removed from the water after 2 hours, sun-dried completely, and then incinerated in an open air. The ash obtained was screened using standard US sieve No 200. The fraction of it that passed through the sieve was kept in an air-tight container and labelled RHA. This was necessary to avoid pre-hydration during storage. With the aid of an X-ray diffractometer (Model XRD 3000P, Seifert, Germany), the scanning electron microscopic (SEM) image of the RHA was obtained to reveal its surface structure. Also, the sand was dried in the air before it was subjected to gradation test by sieving technique [33]. Loose density and angle of repose of the RHA, sand, and cement were determined as detailed elsewhere [34]. The RHA and cement were analyzed for chemical composition by adopting the method of Yahaya [35].

2.3. Samples preparation

The mix design used in this research is summarized in Table 1. All batching processes were by volume method. In each case, the cement was replaced with 10 % of the RHA. This proportion of the RHA was chosen based on the fact that it is optimum for significant results [26, 27]. When the materials were thoroughly mixed with water, each mixture was cast into separate Plexiglas molds of cross-section 52 mm x 24 mm and height 14 mm. immediately after casting and compaction, two copper plates (each with a width of 15 mm and a height of 30 mm) were embedded into the mixture. These copper plates served as electrodes and they were at same distances from the ends of the samples. The electrodes spacing and embedment length were 32 mm

Table 1. Design of the materials proportioning

Cement grade	Sample code	Constituent materials	Number of samples prepared and tested	w - c ratio
32.5 R	BCM	Sand and Cement	10	0.5 (Constant)
	RCM	Sand, RHA, and Cement	10	
42.5 N	PCM	Sand and Cement	10	
	CRM	Sand, RHA, and Cement	10	

w - c: Water - cement

and 9 mm respectively. All the samples were demolded after 24 hours and they were cured in a shade by sprinkling equal volumes of water on them twice (morning and evening) daily. The curing was allowed for 21 days after which the samples were allowed to dry completely before they were tested.

2.4. Testing of the samples

Figure 1 shows the schematic diagram of the setup used in this research. The aluminium block measured 80 mm in height and 75 mm in diameter and its use was necessary since the heating element of the hotplate was larger than the sample. In order to ensure that heat flowed upwardly only through the sample, the use of the thermal insulant (of very low thermal conductivity with dimensions 60mm x 60 mm) was necessary. This thermal insulant was provided with a central and circular hole to allow for free passage of heat from the aluminium block. Separate but identical aluminium blocks, thermal insulants, and digital thermometers (Model 305 quipped with type-K probe) were used for different test schedules. Before the commencement of the test, the sample and its electrodes were thickly lagged with cotton wool.

The electrical resistances were measured by means of LCR meter (Model No. 9183, Lutron). The probes of the meter were connected to the electrodes and the control dial on the hotplate was adjusted to a level reasonable enough to ensure a steady heat flow from the heating element. The temperature of the sample was monitored and measured with the aid of the thermometer. During this process, care was taken to ensure that the thermometer probe was in firm contact with the sample's surface as illustrated in the diagram. Temperature readings were taken at 5°C intervals from 20°C. After that, the mean and corresponding standard error values of the resistance were computed for each sample.

The electrical resistivity of the sample was determined using the formula [23]

$$R = \frac{\rho L}{A} \tag{1}$$

where R = mean electrical resistance, A = area of the sample's surface in contact with the electrodes, L = distance between the electrodes.

The value of thermal sensitivity index, β was deduced from the graph of $\ln R$ against the inverse of

absolute value of the temperature, T based on the relation [36, 37]

$$R = R_o \exp \left[\frac{\beta}{T} \right] \tag{2}$$

where R_o = electrical resistance at infinite temperature.

In each case, the temperature coefficient of resistance, α was computed as [38]

$$\alpha = \pm \left[\frac{1}{R_1} \left(\frac{R_2 - R_1}{T_2 - T_1} \right) \right] 100\% \tag{3}$$

where R_1 and R_2 represent the values of electrical resistance obtained at temperatures T_1 and T_2 respectively.

(The negative sign is considered only if R and T relate inversely).

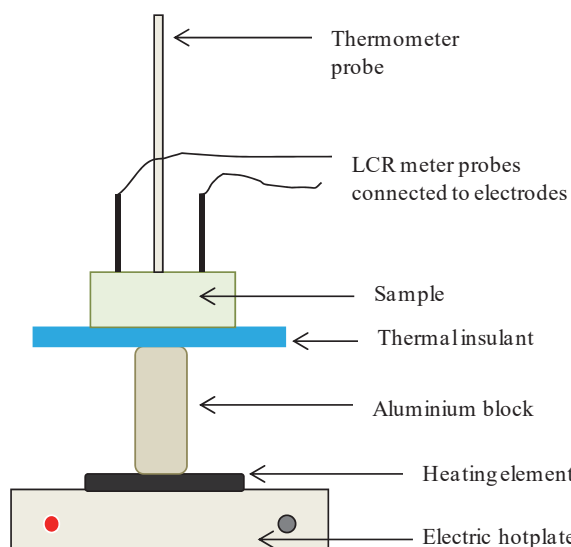


Fig. 1. Schematic features of the experimental setup

3. RESULTS AND DISCUSSION

The index properties of the constituent materials (RHA, sand, and cement) are presented in Table 2. It is clear from the results that sand is the heaviest, followed by cement, and then the RHA. Sand has the least static angle of repose value. Since repose angle of 40° is acceptable for manufacturing purposes [39], it can be adjudged that all the materials in this case are suitable for preparation of the mortars. Considering the fact that angle of repose correlates inversely with particle size of a material [40, 41], it can be inferred that particles of the sand are larger in size than those of the RHA or cement. Figure 2 depicts that the sand contains particles of assorted sizes, thereby making it to be well-graded for use.

Table 2. Particulars of the constituent materials

Parameters	RHA	Sand	Cement	
			32.5 R	42.5 N
Loose density (kgm^{-3})	370.0	1519.0	857.0	853.0
Static angle of repose ($^{\circ}$)	39.1	34.8	39.6	39.9

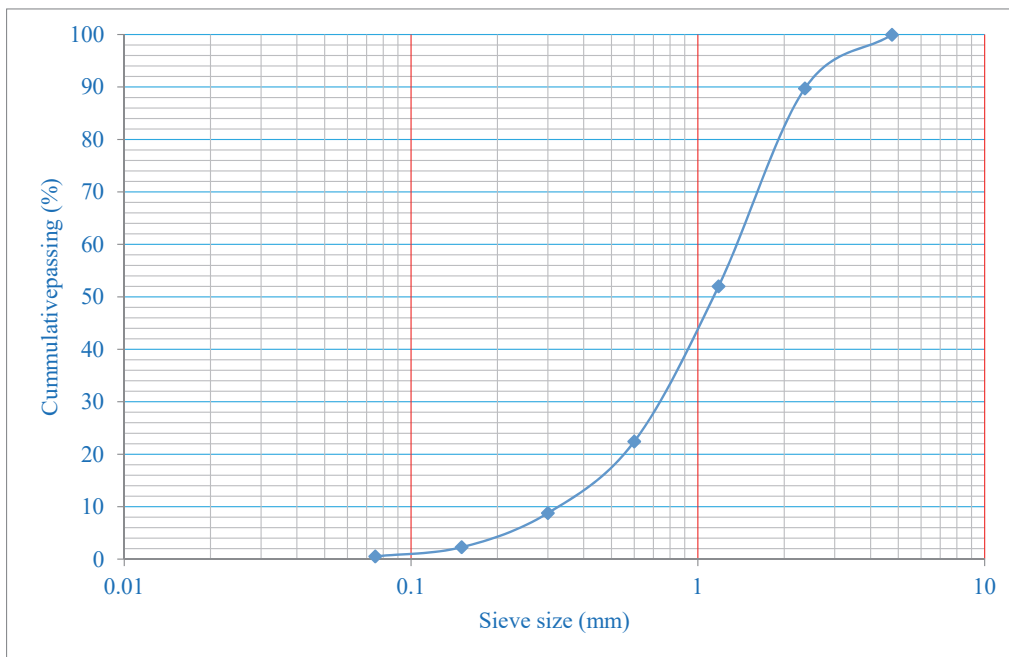


Fig. 2. Grading curve of the sand used

From the results of chemical composition analysis of the RHA and cement (Table 3), it is seen that the most abundant oxide is SiO_2 in the RHA and CaO in both grades of the cement. The loss on ignition (LOI) of cement grade 42.5N is the least while that of cement grade 32.5R is the highest. This is not out of expectation because cement grade 32.5R used in this research contains about 21 % to 30 % of limestone as stated in cement literature. Also, the

value of LOI obtained for the RHA exceeds that of cement grade 42.5N, thereby indicating that it has higher content of carbon-based component than the cement. The proportions of SiO_2 , Al_2O_3 , and Fe_2O_3 in the RHA sum up to a value (71.69 %) which is slightly greater than 70 % required as minimum percentage for pozzolans. Thus, it can be remarked that the RHA utilized in this research is pozzolanic.

Table 3. Chemical composition of the RHA and Cement

Oxides	RHA Formula	Proportion (%) per material		
		Cement		
Name		32.5 R	42.5 N	
Silicon oxide (Silica)	SiO_2	69.88	16.32	20.82
Aluminium oxide (Alumina)	Al_2O_3	1.32	3.60	4.96
Ferric oxide	Fe_2O_3	0.48	2.83	3.20
Magnesium oxide (Magnesia)	MgO	0.59	0.90	2.12
Calcium oxide (Lime)	CaO	0.73	58.25	62.46
Loss on ignition	LOI	8.34	10.31	2.99

Figure 3 shows the monograph of the RHA. It can be clearly seen that the surface of the RHA is irregular in nature and is typical of amorphous ash. Hence, it has the potential for high reactivity.

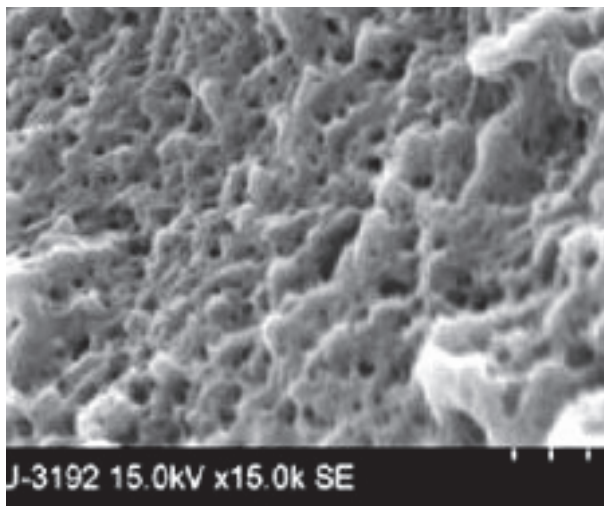


Fig. 3. SEM image of the RHA

It is noticed from the results in Table 4 that at each considered temperature, inclusion of the RHA reduces the electrical resistance of the samples with respect to a particular cement grade. Figure 4 reveals that the electrical resistance in all the cases decreases with increase in temperature of the samples. This means that the samples become more electrically-conductive at higher temperatures. The observed decay pattern of the resistance-temperature relationship typifies a negative temperature coefficient (NTC) thermistor. Robert et al [23] reasoned that such phenomenal tendency is due to activation energy associated with the electron jumping across

interfaces in dry cement-based composites. As such, the observed phenomenon could be utilized for temperature monitoring. On the strength of that consideration, samples with the RHA content would show better performance. Durairaj et al [42] reported that addition of brass fiber as an electrically conductive filler to cement mortar reduced the electrical resistance and also improved self-sensing ability of the mortar at elevated temperatures.

Table 4. Electrical resistance of the samples at various temperatures

Temperature, T ($^{\circ}\text{C}$)	Mean measured electrical resistance, R ($10^6 \Omega$)			
	BCM	RCM	PCM	CRM
20.0	57.06	18.89	56.47	17.98
25.0	25.42	9.94	24.98	9.43
30.0	12.50	5.49	11.64	4.88
35.0	6.65	3.07	5.88	2.79
40.0	2.71	1.86	2.67	1.67
45.0	1.35	1.26	1.28	1.19
50.0	0.96	0.61	0.91	0.51

Based on the electrical resistance values obtained for the samples, CRM has a greater ability than RCM for temperature sensing. The improved self-sensing abilities of the RCM and CRM over the BCM and PCM respectively could be of some great benefits if they are applied for plastering purpose. This is because, in that case, a large sensing volume is possible and in turn, it could save cost as embedded sensors conventionally used for temperature monitoring are very expensive but yet location-specific in their performance [23].

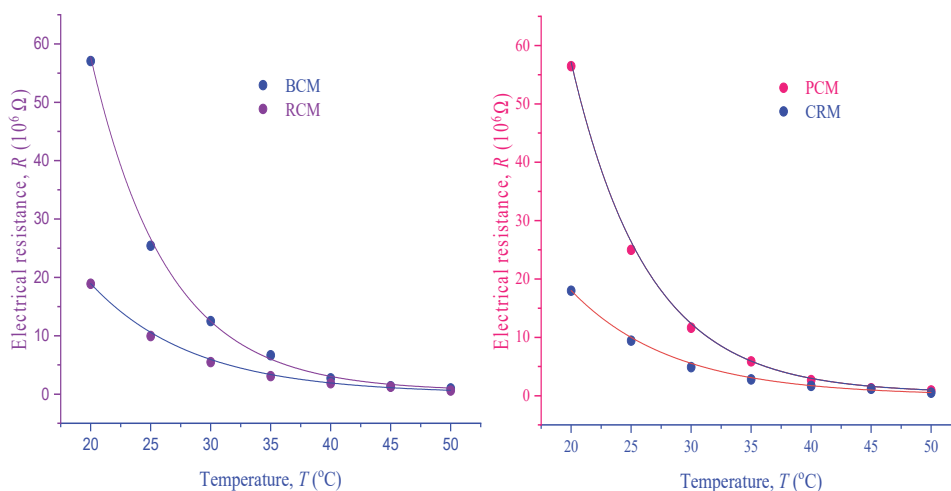


Fig. 4. Electrical resistance – temperature relationships for the samples

The plots in figure 5 agree with linearization of equation 2 above depicting how the thermal sensitivity (β -parameter) relates with inverse values of absolute temperatures of the samples. The summary of the data deduced for the samples from their resistance measurements are shown in Table 5. The electrical resistivity values support the earlier submission that the RHA enhances reduction of electrical resistance of the resulting sample in each case at a given temperature. Accordingly, 66.80 % reduction in electrical resistivity is yielded for preparing RCM over the BCM. Also, 68.06 % decrement is possible in the case of preparing CRM over PCM. This further substantiates the above-stated fact that CRM responds faster than RCM for temperature sensing though both contain the RHA. It also shows that cement grade could influence the electrical behavior of the mortar aside the known fact that it affects the 28-day compressive strength of cementitious materials.

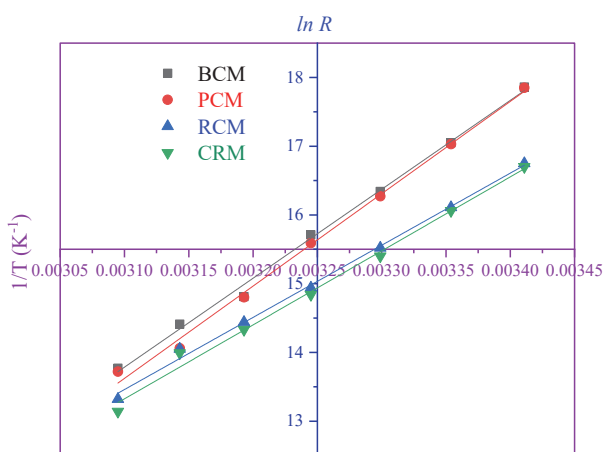


Fig. 5. Plots of $\ln R$ against $1/T$

Table 5. Computed values of electrical parameters of the samples

Sample code	ρ ($10^5 \Omega m$) 20°C	at β (K)	α (% /°C)
BCM	2.41	12937	-3.277
RCM	0.80	10493	-3.226
PCM	2.38	13457	-3.280
CRM	0.76	10763	-3.239

Based on the β -values obtained in this study, it can be averred that RCM and CRM require smaller energy for electrical conduction compared to the BCM and PCM respectively being their counterparts without the RHA content. By implication, the RHA has the potential to lower energy needed by cement

mortar for sensing role. The temperature coefficients of resistance obtained in this study show that the samples could be used as NTC thermistors and temperature sensors

5. CONCLUSION

The investigations carried out in this research revealed that inclusion of 10 % RHA as partial cement substitute caused a significant influence on electrical characteristics of the resulting dry cement mortars. Electrical resistivity and thermal sensitivity index values were lowered as a result of RHA introduction into each plain cement mortar. Electrical resistances of the samples exhibited exponential decay with increase in temperature, thereby indicating that the samples have negative temperature coefficient of resistance. Though samples with the RHA content could be regarded as promising smart mortars, it was observed that utilization of cement grade 42.5N yielded a better self-sensing mortar sample. Thus, if the mortars with RHA content are applied for plastering, building structures can effectively monitor/sense their own temperature without any need for attached sensors.

REFERENCES

- [1] S.M.Ahmed, I.Kamal (2022) Electrical resistivity and compressive strength of cement mortar based on green magnetite nanoparticles and wastes from steel industry. *Case Stud/ Const. Mat.*, 17, e01712, <https://doi.org/10.1016/j.cscm.2022.e01712>
- [2] T.Honorio, H.Carasek, O.Cascudo (2020) Electrical properties of cement-based materials: Multiscale modeling and quantification of the variability. *Const. Build. Mat.*, 245, 11846. <https://doi.org/10.1016/j.conbuildmat.2020.118461>. hal-02486901
- [3] A.A.K.Bazari, M.Chini (2022) Laboratory Evaluation of Electrical Resistance of Concrete. *J. Civ. Eng. Mat. App.* 6, 99 – 111, <https://doi.org/10.22034/jcema.2022.333341.1082>
- [4] C.Vipulanandan, A.Mohammed (2015) Smart cement modified with iron oxide nanoparticles to enhance the piezoresistive behaviour and compressive strength for oil well applications. *Smart Mater. Struct.* 24, 125020.
- [5] M.Chen, P.Gao, F.Geng, L.Zhang, H.Liu (2017) Mechanical and smart properties of carbon fiber and graphite conductive concrete for internal damage monitoring of structure. *Const. Build. Mat.* 142, 320 – 327
- [6] B.Han, L.Zhang, S.Sun, X.Yu, X.Dong, T.Wu, J.Ou (2015) Electrostatic self-assembled carbon nanotube/nano carbon black composite fillers reinforced cement-based materials with multifunctionality. *Compos. Part A Appl. Sci. Manuf.* 79, 103 – 115

- [7] Q.Liu, W.Wu, J.Xiao, Y.Tian, J.Chen, A.Singh (2019) Correlation between damage evolution and resistivity reaction of concrete in-filled with graphene nanoplatelets. *Constr. Build. Mater.*, 208, 482 – 491
- [8] O.E.Ozbulut, Z.Jiang, D.K.Harris (2018) Exploring scalable fabrication of self-sensing cementitious composites with grapheme na-noplatelets, *Smart Mater. Struct.* 7, 115029
- [9] A.Monteiro, P.Cachim, P.M.Costa (2017) Self-sensing piezoresistive cement composite loaded with carbon black particles. *Cem. Concr. Compos.* 81, 59 – 65
- [10] Z.Jiang, O.E.Ozbulut, G.Xing (2019) Self-Sensing Characterization of GNP and carbon black filled cementitious composites. In: *Proceedings of the ASME 2019 Conference on Smart Materials, Adaptive Structures and Intelligent Systems*, Louisville, KY, USA, 9 – 11 September 2019.
- [11] Y.Ding, G.Liu, A.Hussain, F.Pacheco-Torgal, Y.Zhang (2019) Effect of steel fiber and carbon black on the self-sensing ability of concrete cracks under bending. *Constr. Build. Mater.* 2017, 630 – 639.
- [12] G.Yildirim, M.H.Sarwar, A.Al-Dahawi, O.Öztürk, O.Anil, M.Sahmaran (2018) Piezoresistive behavior of CF-and CNT-based reinforced concrete beams subjected to static flexural loading: Shear failure investigation. *Constr. Build. Mater.* 168, 266 – 279
- [13] T.Buasiri, K.Habermehl-Cwirzen, L.Krzeminski, A.Cwirzen (2021) Role of Carbon Nanofiber on the Electrical Resistivity of Mortar under Compressive Load. *Trans. Res. Recl.* 2675, 33 – 37, <https://doi.org/10.1177/0361198120947417>
- [14] F.Gao, W.Tian, Z.Wang, F.Wang (2020) Effect of diameter of multi-walled carbon nanotubes on mechanical properties and microstructure of the cement-based materials. *Const. Build. Mat.* 260, 120452
- [15] F.Gao, W.Tian, X.Cheng (2021) Investigation of moisture migration of MWCNTs concrete after different heatingcooling process by LF-NMR. *Const. Build. Mat.* 288, 123146
- [16] A.Sedaghatdoost, K.Behfarnia (2018) Mechanical Properties of Portland Cement Mortar Containing Multi-Walled Carbon Nanotubes at Elevated Temperatures. *Constr. Build. Mater.* 176, 482–489.
- [17] W.L.Baloch, R.A.Khushnood, W.Khaliq (2018) Influence of Multi-Walled Carbon Nanotubes on the Residual Performance of Concrete Exposed to High Temperatures. *Constr. Build. Mater.* 185, 44–56.
- [18] G.M.Kim, H.N.Yoon, H.K.Lee (2018) Autogenous Shrinkage and Electrical Characteristics of Cement Pastes and Mortars with Carbon. *Constr. Build. Mater.* 177, 428 - 435
- [19] A.Abdulhameed, N.Z.A.Wahab, M.N.Mohtar, M.N.Hamidon, S.Shafie, I.A.Halin (2021) Methods and applications of electrical conductivity enhancement of materials using carbon nanotubes. *J. Electron. Mater.*, 50(6), 3207–3221.
- [20] S.H.Jang, D.P.Hochstein, S.Kawashima, H.Yin (2017) Experiments and micromechanical modeling of electrical conductivity of carbon nanotube/cement composites with moisture. *Cem. Concr. Compos.*, 77, 49–59.
- [21] S.Ding, S.Dong, A.Ashour, B.Han (2019) Development of sensing concrete: principles, properties and its applications. *J. Appl. Phys.*, 126(24), 241101.
- [22] D.Y.Yoo, I.You, S.J.Lee (2018) Electrical and piezoresistive sensing capacities of cement paste with multi-walled carbon nanotubes. *Eng.* 18(2), 371–384.
- [23] U.W.Robert, S.E.Etuk, S.A.Ekong, O.E.Agbasi, N.E.Ekpenyong, S.S.Akpan, E.A.Umana (2022) Electrical characteristics of dry cement-based composites modified with coconut husk ash nanomaterial. *Adv. Mater. Sci.*, 22, 64–77, <https://doi.org/10.2478/adms-2022-0008>.
- [24] T.Honorio, B.Bary, J.Sanahuja, F.Benboudjema (2017) Effective properties of n-coated composite spheres assemblage in an ageing linear viscoelastic framework. *Int. J. Solids Struct.*, 124, 1–13.
- [25] J.C.Nadeau (2002) Water-cement ratio gradients in mortars and corresponding effective elastic properties. *Cem. Concr. Res.*, 32(3), 481–490.
- [26] M.Amin, B.A.Abdelsalam (2019) Efficiency of rice husk ash and fly ash as reactivity materials in sustainable concrete. *Sustain. Environ. Res.*, 29, Article 30, <https://doi.org/10.1186/s42834-019-0035-2>.
- [27] O.Zaid, J.Ahmad, M.S.Siddique, F.Asalam (2021) Effect of Incorporation of Rice Husk Ash instead of Cement on the Performance of Steel Fibers Reinforced Concrete. *Front. Mater.*, 8, 665625, <https://doi.org/10.3389/fmats.2021.665625>.
- [28] B.Bheel, A.W.Abro, I.A.Shar, A.A.Dayo, S.Shaikh, Z.H.Shaikh, (2019) Use of Rice Husk Ash as Cementitious Material in Concrete. *Eng. Technol. Appl. Sci. Res.* 9(3), 4209–4212.
- [29] M.Yin, X.Li, Q.Liu, F.Tang (2022) Rice husk ash addition to acid red soil improves the soil property and cotton seedling growth. *Sci. Rep.*, 12, 1704, <https://doi.org/10.1038/s41598-022-05199-7>.
- [30] P.Saranya, C.M.Sri Gayathiri, K.M.Sellamuthu (2018) Potential Use of Rice Husk Ash for Enhancing Growth of Maize (*Zea mays*). *Int. J. Curr. Microbiol. Appl. Sci.*, 7(3), 899–906, <https://doi.org/10.20546/ijcmas.2018.703.105>.
- [31] U.W.Robert, S.E.Etuk, O.E.Agbasi, S.A.Ekong, E.U.Nathaniel, A.Anonaba, L.A.Nnana (2021) Valorization of Waste carton paper, Melon seed husks and Groundnut shells to thermal insulation panels for structural applications. *Polytechnica.*, 4(2), 97–106, <https://doi.org/10.1007/s41050-021-00034-w>.
- [32] S.A.Ekong, D.A.Oyegoke, A.A.Edema, U.W.Robert (2022) Density and water absorption coefficient of sandcrete blocks produced with waste paper ash as partial replacement of cement. *Adv. Mater. Sci.*, 22(4), 85–97, <https://doi.org/10.2478/adms-2022-0021>.
- [33] ASTM C136/136M (2019) Standard Test Method for Sieve Analysis of Fine and Coarse Aggregates. ASTM International, West Conshohocken, PA.

- [34] U.W.Robert, S.E.Etuk, O.E.Agbasi, U.S.Okorie, Z.T.Abdulrazzaq, A.U.Anonaba, O.T.Ojo (2021) On the hygrothermal properties of sandcrete blocks produced with sawdust as partial replacement of sand. *J. Mech. Behav. Mater.*, 30(1), 144–155, doi.org/10.1515/jmbm-2021-0015.
- [35] M.D.Yahaya (2009) Physico-chemical classification of Nigerian cement. *Aust. J. Technol.*, 12(3), 164–174.
- [36] S.E.Etuk, J.B.Emah, U.W.Robert, O.E.Agbasi, I.A.Akpabio (2021) Comparison of Electrical Resistivity of Soots formed by combustion of Kerosene, Diesel, aviation fuel and their mixtures. *Brilliant Eng.*, 3, 6–10, https://doi.org/10.36937/ben.2021.003.002.
- [37] S.S.Munifah, A.Wiendartun, A.Aminudim (2018) Design of temperature measuring instrument using NTC thermistor of Fe₂TiO₅ based on microcontroller AT mega 328. *J. Phys.: Conf. Ser.*, IOP Publishing, 1–7.
- [38] U.W.Robert, S.E.Etuk, O.E.Agbasi, U.A.Iboh, S.S.Ekpo (2020) Temperature-Dependent Electrical Characteristics of Disc-shaped Compacts fabricated using Calcined Eggshell Nanopowder and Dry Cassava starch. *Powder Metall. Prog.*, 20(1), 12–20, http://dx.doi.org/10.2478/pmp-2020-0002.
- [39] A.O.Adeniran, A.O.Akankpo, S.E.Etuk, U.W.Robert, O.E.Agbasi (2022) Comparative study of electrical resistance of disc-shaped compacts fabricated using calcined clams shell, Periwinkle shell and Oyster shell nanopowder. *Kragujevac J. Sci.*, 44, 25–36, https://doi.org/10.5937/KgJSci2244025A.
- [40] X.Guiling, C.Xiaoping, L.Cai, X.Pan, Z.Changsui (2016) Experimental investigation on the flowability properties of cohesive carbonaceous powders. *J. Partic. Sci. Technol.*, 35(3), 322–329. doi.org/10.1080/02726351.2016.1154910.
- [41] H.Lu, X.Guo, Y.Liu, X.Gong (2015) Effects of particle size on flow mode and flow characteristics of pulverised coal. *Kona Powder Part I.*, 32, 143–53. doi.org/10.14356/kona.2015002.
- [1] [42] R.Durairaj, T.Varatharajan, S.K.Srinivasan, B.G.A.Gurupatham, K.Roy (2022) An Experimental Study on Electrical Properties of Self-Sensing Mortar. *J. Compos. Sci.*, 6, 1–28, https://doi.org/10.3390/jcs6070208.

IZVOD

UTICAJ INKLUZIJE PEPELA OD PIRINČANE LJUSKE NA ELEKTRIČNE KARAKTERISTIKE SUVOG CEMENTNOG MALTERA

Pirinčana ljuska se obično stvara kao otpad u velikim količinama, ali tek treba da se optimalno iskoristi. Zbog efekata zagađenja povezanih sa lošim pristupom koji se uglavnom koristi za njegovo odlaganje, pretvaranje u ekonomičan i održiv materijal za izgradnju zgrada je neophodna opcija za obezbeđivanje rešenja za buduće generacije. U ovom istraživanju odvojeni suvi malteri su pripremljeni korišćenjem cementa 32,5R i 42,5N i ispitan je uticaj pepela pirinčane ljuske (RHA) na njihove električne karakteristike. Korišćeni materijali su dozirani po zapremini i RHA je korišćen kao delimična zamena za cement na nivou od 10%. Svi uzorci su sušeni 21 dan, a zatim ostavljeni da se potpuno osuše pre sprovođenja testa. Rezultati su pokazali smanjenje električnog otpora sa temperaturom (u rasponu od 20°C do 50°C) usled ugradnje RHA. Iako su uzorci sa sadržajem RHA posedovali sposobnost da deluju kao pametni malteri za praćenje/senzivanje temperature, korišćenje cementa 42,5N je obezbedilo bolje performanse. Korišćenjem pirinčanih ljuski u takvim poduhvatima, mogli bi se rešiti njihovi povezani problemi odlaganja i poboljšati izgradnja jeftine, ali održive zgrade sa velikom sposobnošću senzora temperature.

Ključne reči: zgrada; Električna otpornost; Senzor temperature; Indeks toplotne osetljivosti; Gubljenje

Naučni rad

Rad primljen: 27.03.2024.

Rad prihvaćen: 3.05.2024.

The ORCID Ids of all the authors are as follows:

1. Sunday Edet Etuk: <https://orcid.org/0000-0002-2573-8314>
2. Ubong Williams Robert: <https://orcid.org/0000-0001-9979-7176>
3. Okechukwu Ebuka Agbasi: <https://orcid.org/0000-0001-5649-0107>
4. Namdie Joseph Inyang: <https://orcid.org/0000-0002-8798-4692>

Leonid Dvorkin, Vitalii Marchuk, Mykola Kuzlo

National University of Water and Environmental Engineering, Rivne,
Ukraine

Scientific Paper

ISSN 0351-9465, E-ISSN 2466-2585

<https://doi.org/10.62638/ZasMat1170>



Zastita Materijala 65 (4)
668 – 679 (2024)

Influence of Adhesive Additives on the Properties of Bitumen and Asphalt Mixtures

ABSTRACT

This article presents the results of experimental studies of the influence of adhesive additives on the basic properties of modified bitumen and asphalt concrete mixtures based on it. The introduction of adhesive additives improves the basic properties of bitumen, which are necessary for obtaining high-quality asphalt concrete mixtures. Modification of bitumen increases adhesion to glass and crushed stone. Using methods of mathematical planning of experiments, experimental and statistical models of water saturation and compressive strength of asphalt concrete mixtures at temperatures of 20 °C and 50 °C were obtained. The introduction of modifying additives can significantly reduce the water saturation of asphalt concrete mixtures and increase strength at temperatures of 20 °C and 50 °C.

Keywords: bitumen, asphalt mixtures, strength, adhesive additives, penetration, softening point, ductility.

1. INTRODUCTION¹

One of the main tasks of modifying construction bitumen is to improve its adhesion ability to aggregates. The adhesion between mineral components and bitumen is an important criterion that affects the quality of the asphalt mixture, asphalt pavement characteristics and its resistance to damage. Nowadays, there is no generally accepted theory that satisfactorily explains the bonding process.

One of the earliest attempts that was proposed to explain the bonding process is the Mc Bain hypothesis [1], which considers this process as a mechanical “jamming” of the adhesive substance into the pores (or recesses) of the adhesive material. However, the positions put forward by Mc Bain were refuted in subsequent works [2, 3]. Later, considerations of the so-called “specific” adhesion appeared. Adhesion is generally understood as the stickiness that occurs between two dissimilar materials brought

into contact. In the case of stickiness connections, adhesion is the bond between the adhesive and the surface to which the adhesive adheres. When considering adhesion phenomena, it is necessary to take into account cohesion, which is the stickiness within the bonded materials. Currently, the most important theories are the adsorption, electrical, diffusion, and chemical ones.

The adsorption theory of adhesion considers the formation of a bond between the adhesive and the bonded material (substrate) as a result of intermolecular forces. For the first time, the importance of adsorption phenomena for the adhesion process was pointed out [4] in 1926. However, the basics of the adsorption theory of adhesion were developed much later by Debroyne [5] and Mc Laren [6, 7].

According to Mc Laren, the formation of an adhesive layer occurs in two stages. At the first stage, the adhesive molecules move (migrate) to the surface of the substrate and the polar groups of the adhesive molecules approach the polar regions of the substrate, and at the second stage the sorption occurs. At a sufficiently close distance between the adhesive and substrate molecules, molecular forces

* Corresponding author: Leonid Dvorkin
E-mail: dvorkin.leonid@gmail.com
Paper received: 27.03.2024.
Paper accepted: 12.05.2024.

es (dispersion, induction, electrostatic) begin to act, leading to the formation of various bonds (dipole-dipole, dipole-induced dipole, hydrogen bond, etc.).

Being non-polar, bitumen has high water resistance, but mechanical impacts from vehicles accelerate the water penetration into the pores of asphalt concrete, as a result it leads to a decrease the asphalt pavement stability [8]. To reduce the negative effects of moisture, it is necessary to ensure the increased stickiness of the bituminous binder to the mineral components of the asphalt mixture.

Active adhesion is the ability of the binder to completely envelop the aggregate particles during the mixing of the mixture components. This adhesion occurs due to the mutual attraction of positively charged surfactants of bitumen molecules to negatively charged aggregate molecules. This type of interaction allows for the water displacement at the interface and ensures maximum coverage of the mineral material surface with bitumen [9, 10]. In contrast to active adhesion, passive adhesion occurs as a result of external forces, for example, due to increased pressure in the pores of asphalt concrete. Passive adhesion indicates the ability of bitumen to be bonded to the surface of the mineral material throughout the entire service life of asphalt concrete without the risk of destruction of these bonds under the influence of mechanical stress and water [11]. The loss of passive adhesion can cause premature pavement deterioration [12].

The literature describes the main theories that explain the concept of bitumen-aggregate interaction: chemical reaction, surface energy, molecular orientation, and mechanical adhesion [13, 14]. The adhesion between bitumen and aggregate depends on the surface tension of the bitumen, the chemical composition of the bitumen and aggregates, the viscosity of the bitumen, the porosity and purity of the aggregates, the moisture content of the aggregates, and the temperature during the preparation of the asphalt mixture (AM) [15, 16].

Robertson [18] argues that adhesion connecting bitumen and aggregates occurs between the poles of the bitumen and the polar surface of the aggregate. He also asserts that the polarity of the bitumen alone is not sufficient to achieve high adhesion because the bitumen is affected by external mechanical factors. It is assumed that the adhesion between bitumen and aggregate is provided by surface energy because the surface of the aggregate decreases together with the process of the bitumen adsorption [19]. The modifi-

cation of bitumen by surfactant additives is based on the Dupre-Young equation, which relates the work of adhesion W_{aq} to the surface energy of the solid:

$$W_{aq} = v_l - v_l^* (m + \cos \theta), \quad (1)$$

where v_l is the surface energy of a solid; v_l^* is the free surface energy of a solid in an atmosphere of vapor and gases; $m = v_w^* / v_w > 1$ (v_w^* is the surface tension of the liquid oriented under the influence of the force field of the solid surface; v_w is the surface tension of the wetting liquid); θ – is the edge angle of wetting.

It follows from equation (1) that to achieve high adhesive strength, it is important to ensure the necessary wettability of the aggregate with the binder and to reduce the interfacial surface energy, which is achieved by treating the aggregate with surfactants. The decrease in interfacial surface energy during creation of an adsorption-active environment is determined from equation (2).

$$\Delta v_{t,w} = K T, \int_0^c n_s(c) d \ln c \quad (2)$$

where $\Delta v_{t,w}$ is the difference in interfacial surface energy without surfactants and in the presence of surfactants with a concentration of c ; n_s is the adsorption value determined by the number of surfactant molecules adsorbed per 1 cm² of the interface; K is the Boltzmann constant; T is the absolute temperature, °K.

The influence of the adsorption-active medium on the value of rises with an increase in aggregate dispersion and concentration, which is associated with an expansion in the interfacial surface and, accordingly, excess surface energy.

Mechanical adhesion depends on the physical and mechanical properties of the aggregates. An important condition for good adhesion is the wetting of the aggregate, which is necessary for contact between the materials and thus for the establishment of the basic physical and chemical forces that are ultimately responsible for adhesion. Aggregates are generally classified as hydrophobic (acidic aggregates) and hydrophilic (basic aggregates), which react differently to the adhesion process [20]. Authors [21] argue that acidic aggregates, in particular granite, which are most widely used for asphalt mixtures in Ukraine and other European countries, show a high loss of adhesion. In addition, the surface texture of aggregates affects the adhesion capacity, and rough surfaces with a larger contact area are desirable for its increase [14].

Poor adhesion between the bitumen and aggregate leads to binder delamination in the presence of water, which eventually leads to potholes. Moisture damage to the asphalt pavement is considered the main cause of destruction to the asphalt pavement layers. The abrasion resistance of bitumen is also determined by its adhesion to the surface of the aggregate, it must be not only high but also stable over time, which is one of the conditions for the durability of the pavement.

Increasing the adhesion and ensuring the durability of asphalt pavements is possible by modifying bitumen with adhesive additives [22]. The introduction of appropriate additives into the asphalt concrete composition is important to ensure strong stickiness (ad-

hesion) to aggregates [23]. These additives increase the inter-phase adhesion in wet conditions [22].

The purpose of this work is to obtain quantitative characteristics of the influence of the content of bitumen and adhesive additives and their interaction on the basic properties of modified bitumen and asphalt concrete mixtures based on it, which determine the durability of road surfaces.

2. MATERIALS AND METHODS OF RESEARCH

In our research, we used petroleum road bitumen PRB 70/100 that meets the requirements of EN 12591, the characteristics and standard values for which are given in Table 1.

Table 1. Test results of PRB 70/100

Indicator name	Regulatory document	The value for PRB 70/100	Values of indicators
Needle penetration depth (penetration) at 25 °C, 0.1 mm	EN 1426	from 71 to 100 inclusively	77
Softening point, °C	EN 1427	From 45 to 51.	49,5
Tensile strength (ductility) at 25 °C, cm, not less than	DSTU 8825:2019 (Ukr. Standard)	not less than 60	67,6
Adhesion to the glass surface, %	DSTU 9169:2021 (Ukr. Standard)	not less than 18	74 %
Adhesion to the crushed stone surface, %	DSTU 8787:2018 (Ukr. Standard)	not standardized	63 % - 3,5 points

Granite crushed stone with fractions of 5-10 mm, 10-20 mm, and 20-40 mm, bulk density 1420 kg/m³, as well as sand from granite crushing screenings with fractions of 0-5 mm were used, bulk density 1480 kg/m³.

The used as filler non-activated carbonate mineral powder maximum grain size 0.315 mm and bulk density 988 kg/m³ to DSTU B.V.2.7-121-2014 (Ukr.Standard).

The following adhesive additives were used for modification of bitumen:

- Wetfix BE, a cationic surfactant with increased thermal stability, manufactured by Nouryon (Sweden).
- Stardope 130 P, an additive based on vegetable oil phosphates for hot asphalt mixtures, manufactured by Star Asphalt (Italy).

For the obtained modified bitumen binders, standard quality indicators were determined – penetration at 25 °C (Fig. 1), softening point (Fig. 2) and extensibility (ductility) (Fig. 3). For asphalt mixtures were determined water saturation and compressive strength at 20 °C and 50 °C.



Figure 1. Determination of the penetration depth



Figure 2. Determination of softening point using the "Ring and Ball" device



Figure 3. Determination of the bitumen extensibility (ductility)

The method of the adhesion determination is based on the ability of the binder applied to the glass surface to resist peeling under the influence of water. The peeling resistance is determined by the area that remains covered with bitumen binder

Adhesion to glass (C), as ideal adhesive, is determined by the formula:

$$C = \frac{S_p}{S_t} \times 100 \quad (3)$$

where, S_p – area of the plate covered with bitumen, before testing, mm^2

S_t – area of the plate covered with bitumen, after testing, mm^2 .

Determination of adhesion to crushed stone (Fig. 4) is based on the ability of the binder applied to the surface of the crushed stone to resist peeling under the influence of water. The resistance to delamination is determined by the area that remains covered with bitumen binder.

The test results should not differ from each other by more than 0.5 points, otherwise the test should be repeated.

Determination of asphalt concrete samples' water saturation (Fig. 5) and compressive strength at 20 °C and 50 °C were performed according to DSTU B V.2.7-319:2016 (Ukr. Standard). The main idea test of the water saturation is in calculating the mass of water that the sample can absorb at a certain saturation mode. Water saturation (W) is determined by the formula:

$$W = \frac{m_3 - m}{m_2 - m_1} \times 100. \tag{4}$$

where m_3 is the mass of the sample saturated with water and weighted in air, g; m is the mass of the

sample weighted in air, g; m_2 is the mass of the sample kept for 30 minutes in water, weighted in air, g; m_1 is the mass of the sample kept for 30 minutes in water, weighed in water, g.

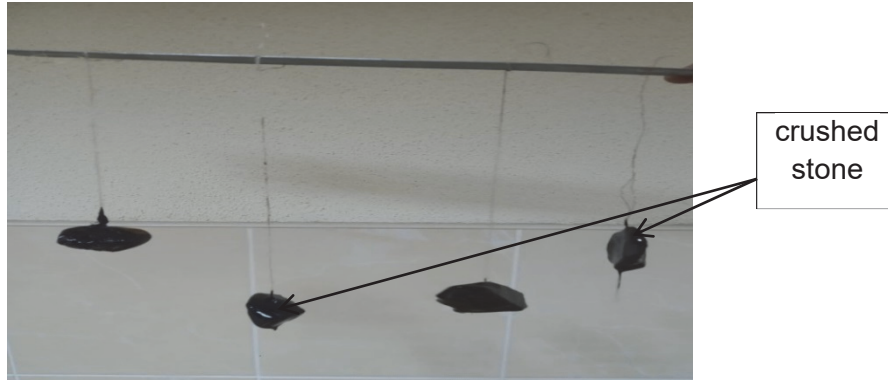


Figure 4. Determination of the adhesion to the crushed stone surface

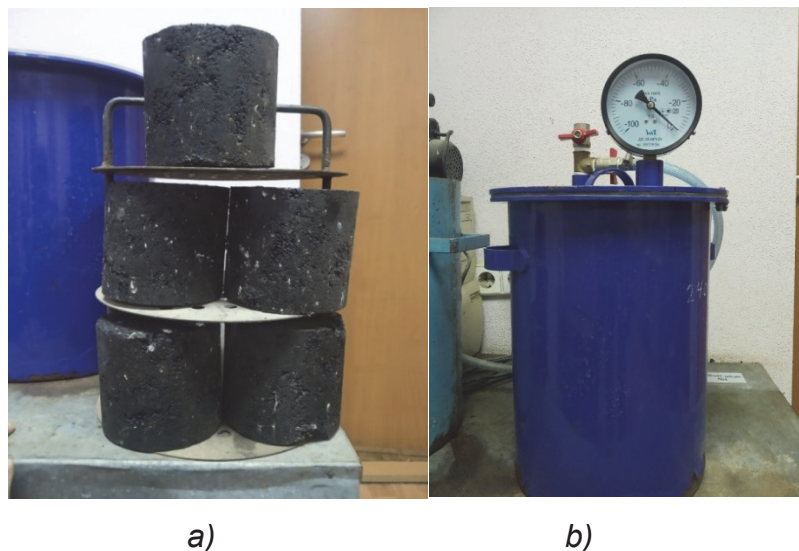


Figure 5. - Samples for determination of water saturation and compressive strength, at 20 °C and 50 °C (a),determination of water saturation (b)

The essence of the asphalt concrete strength test is to determine the compressive strength of laboratory specimens that have been pre-cured in a thermostat at 20 °C and 50 °C, respectively.

The compressive strength (R_c , MPa) is calculated by the formula:

$$R_c = \frac{P}{F} \tag{5}$$

where: P is the destructive load, N ;

F is the cross-sectional area of the sample, m^2 .

The methods of mathematical planning of exper-

iments have been used in research, which promote algorithmization of the experiments according to a certain scheme [24].

The most convenient way is to represent the unknown function as a polynomial:

$$\hat{y} = b_0 + \sum b_i x_i + \sum_{i < j} b_{ij} x_i x_j + \sum b_{ii} x_i^2 + \dots, \tag{6}$$

where b_i, b_{ij}, b_{ii} – regression coefficients; x_i, x_j - factors; k – number of factors.

The experiment has been planned in accordance with a typical matrix, which contains a set of combina-

tions of factors varied relative to a certain origin or zero (basic) level. The permissible area of variation of the factors (factor space) was chosen based on a preliminary study of the object in accordance with the goal.

The results of the experiments were processed using mathematical statistics, obtaining quadratic regression equations for the required number of factors.

To assess the significance of the coefficients and the adequacy of the regression equations, statistical analysis was carried out using Fisher test and Student test.

3. EXPERIMENTAL RESULTS AND THEIR ANALYSIS

Experimental studies were conducted in two stages.

At the first stage, the performance of bitumen modified with adhesive additives Wetfix BE, Stardope 130 P was studied. The bitumen was modified using a laboratory mixer by mingling the bitumen with the additive for 15 minutes at a temperature of $145 \pm 5^\circ\text{C}$, which fully ensured the uniform distribution of the adhesive additive. The obtained research results are shown in Table 2.

On the basis of the experimental data (Table 3), graphical dependences of the bitumen adhesion indicators with glass (Fig. 6 a) and crushed stone (Fig. 6 b) were constructed.

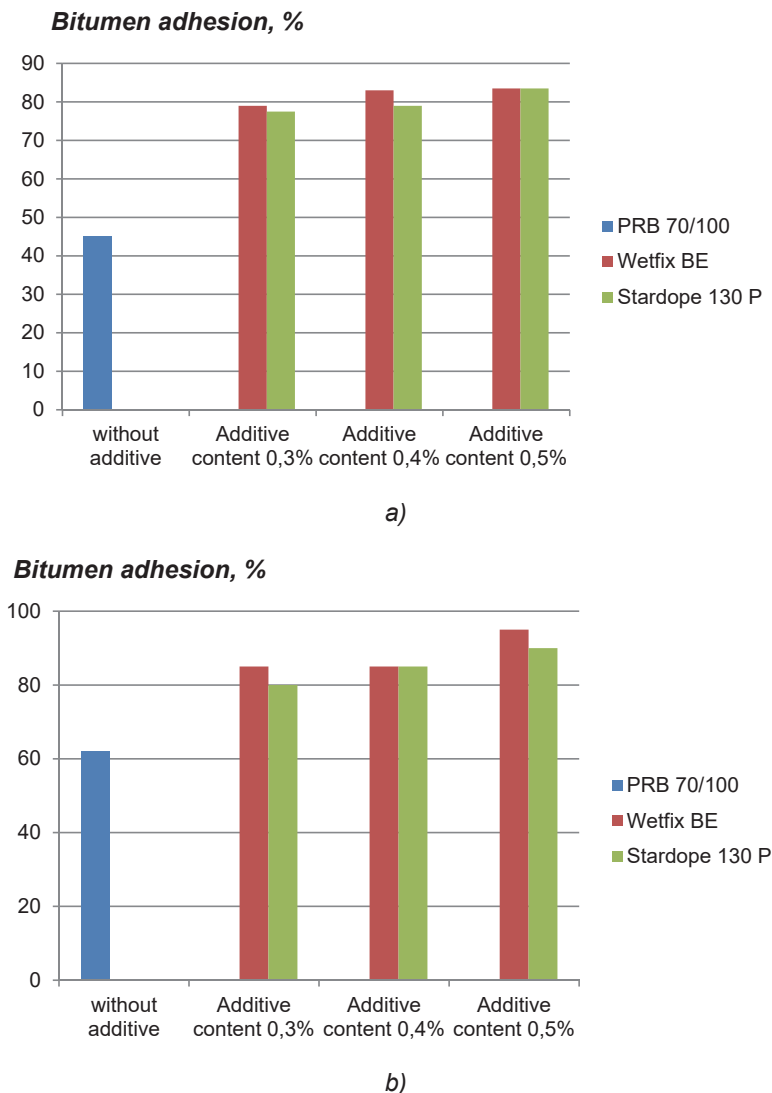


Figure 6. Graphical dependences of bitumen adhesion to glass (a) and crushed stone (b)

Table 2: Bitumen test results

	Indicators														
	Penetration at 25°C, 0.1mm			Temperature of softening, 25°C			Ductility at 25°C, cm			Adhesion to the glass surface, %			Adhesion to the crushed stone surface, points		
PRB 70/100 without additive	77			49,5			67,6			45 %			62		
Additive content, %	0,3	0,4	0,5	0,3	0,4	0,5	0,3	0,4	0,5	0,3	0,4	0,5	0,3	0,4	0,5
Wetfix BE	78	80	80	50	50,2	50,6	68,2	67,8	68,4	79	83	83,5	85	85	95
Stardope 130 P	77	78	79	50,1	50,2	50,5	68	68,2	68,5	77,5	79	83,5	80	85	90

The test results showed that with the addition of adhesive additives to the bitumen, the penetration of the modified bitumen compared to the original PRB 70/100 increases by 0.1 mm at a surfactant Stardope 130 P content of 0.5% in the bitumen, and by 0.2mm at an additive amount of 0.5%. At the same time, the effect of Wetfix BE surfactant is slightly higher.

According to the results obtained, the softening point and elongation of bitumen, which is different from the penetration, practically do not change in the studied range of adhesive additives consumption.

Comparing the results of the original PRB 70/100 with the modified bitumen, the adhesion to glass increases by 32...34% with the addition of 0.3% surfactant, by 34...36% with 0.4%, and by 36...38% with 0.5% in bitumen.

The results of the adhesion of modified bitumen test with crushed stone showed that at 0.3% surfactants in bitumen, the grafting increases by 20%, at 0.4% surfactants in bitumen by 23%, and by 31% at 0.5% surfactants in bitumen.

Therefore, it can be concluded that adhesion additives affect the quality of bitumen, improving them. This primarily applies to adhesion parameters, adhesion to glass and crushed stone. At the same time, the impact of Wetfix BE surfactant is slightly higher compared to Stardope 130 P.

At the second stage, we were exploring the effect of modified bitumen on the main properties of asphalt mixtures. For this purpose, algorithmic experiments were performed in accordance with the three-level two-factor plan B_2 [24]. The conditions for planning experiments are given in Table 3.

Table 3. Conditions for planning experiments

Influencing factors		Levels of variation			Interval
Natural view	Coded view	-1	0	+1	
Bitumen content in the mixture, %, (B)	X_1	4,6	5,0	5,4	0,3
Additive content, % by weight of bitumen, (A)	X_2	0,3	0,4	0,5	0,1

The asphalt mixtures were tested in accordance with DSTU B B.2.7-319:2016 (Ukr. Standard).

At the next stage, during the research, cylinder specimens were manufactured at each point on the basis of modified bitumen in accordance with the composition given in Table 4.

The composition of the asphalt concrete mixture was selected in accordance DSTU B B.2.7-119:2011 (Ukr. Standard). Asphalt mixtures were prepared using a laboratory mixer.

The planning matrix and the experimental results are shown in Table 5.

Table 4. Asphalt mix composition

№	Material	Composition of the mixture (bitumen and additives over 100%), %
1	Crushed stone fr. 20-40 mm	27
2	Crushed stone fr. 10-20 mm	20
3	Crushed stone fr. 5-10 mm	10
4	Screening fr. 0-5 mm	37
5	Mineral powder	6,0
6	PRB 70/100	According to the planning matrix
7	Adhesion additive	According to the planning matrix

Table 5 Planning matrix and experimental data

No.	Coded view		Natural view		Compressive strength at temperature, MPa				Water saturation of samples, %.	
	X_1	X_2	B, %	A, %	20°C		50°C		Wetfix	Stardope
					Wetfix	Stardope	Wetfix	Stardope		
1	1	1	5,4	0,5	4,88	4,80	2,20	2,10	1,1	1,2
2	1	-1	5,4	0,3	4,45	4,20	2,01	1,80	1,5	1,8
3	-1	1	4,6	0,5	4,38	4,25	1,88	1,75	2,2	2,4
4	-1	-1	4,6	0,3	4,14	3,85	1,42	1,35	3,0	3,3
5	1	0	5,4	0,4	4,65	4,50	2,10	2,00	1,5	1,7
6	-1	0	4,6	0,4	4,26	4,00	1,60	1,45	2,6	3,0
7	0	1	5,0	0,5	4,72	4,30	2,08	2,0	1,8	1,9
8	0	-1	5,0	0,3	4,35	4,00	1,87	1,65	2,3	2,4
9	0	0	5,0	0,4	4,51	4,10	1,88	1,75	2,0	2,1
10	0	0	5,0	0,4	4,55	4,20	1,90	1,80	2,0	2,1
11	0	0	5,0	0,4	4,58	4,20	1,88	1,78	1,9	2,1

The study and comparison of surfactants effect on the characteristics of the asphalt mixture was carried out in terms of water saturation, compressive strength at 20 °C and 50 °C.

Based on the data obtained, the experimental-statistical models were built:

When using the Wetfix BE additive

Water saturation

$$W = 2,01 - 0,62 \cdot x_1 - 0,28 \cdot x_2 + 0,1 \cdot x_1 x_2 - 0,01 \cdot x_1^2 - 0,01 \cdot x_2^2 \quad (6)$$

Compressive strength at temperature, 20°C

$$R^{20} = 4,54 + 0,2 \cdot x_1 + 0,17 \cdot x_2 - 0,05 \cdot x_1 x_2 - 0,08 \cdot x_1^2 \quad (7)$$

Compressive strength at temperature, 50°C

$$R^{50} = 1,9 + 0,24 \cdot x_1 + 0,14 \cdot x_2 - 0,07 \cdot x_1 x_2 - 0,07 \cdot x_1^2 + 0,06 \cdot x_2^2 \quad (8)$$

When using the Stardope 130 P additive

Water saturation

$$W = 2,15 - 0,67 \cdot x_1 - 0,33 \cdot x_2 + 0,08 \cdot x_1 x_2 + 0,13 \cdot x_1^2 - 0,07 \cdot x_2^2 \quad (9)$$

Compressive strength at temperature, 20°C

$$R^{20} = 4,16 + 0,23 \cdot x_1 + 0,22 \cdot x_2 + 0,05 \cdot x_1 x_2 + 0,01 \cdot x_1^2 \quad (10)$$

Compressive strength at temperature, 50°C

$$R^{50} = 1,78 + 0,23 \cdot x_1 + 0,18 \cdot x_2 - 0,03 \cdot x_1 x_2 - 0,06 \cdot x_1^2 + 0,04 \cdot x_2^2 \quad (11)$$

Based on the experimental and statistical models (6-11), graphical dependences of water saturation

(Fig. 7) and compressive strength at 20 °C (Fig. 8) and 50 °C (Fig. 9) were drawn.

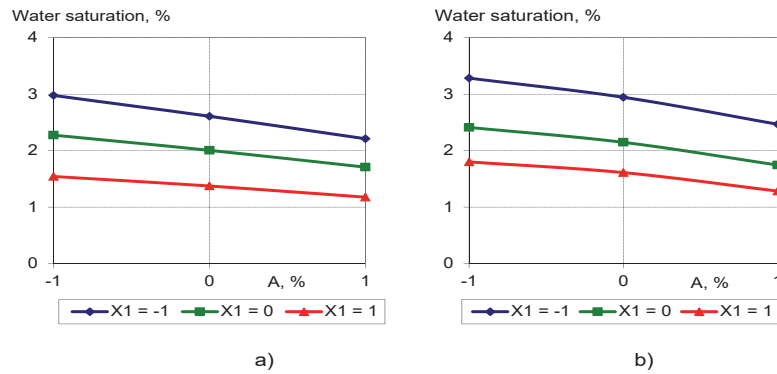


Figure 7. Graphical dependences of water saturation of samples using Wetfix BE (a), Stardope 130 P (b),

Based on the data obtained (Table 5) and graphical dependencies, it can be concluded that modification of bitumen with adhesive additives leads to a decrease in water saturation of the samples and an increase in strength.

Evaluating the Stardope 130 P additive, it can be concluded that with an increase in the content of bitumen and surfactants, water saturation

decreases from 3.3% to 1.3%, with the influence of bitumen being more significant compared to surfactants. It should be noted that, according to the mathematical model (9), there is a certain interaction of the influence factors, in particular, with a smaller amount of bitumen in the mixture, the influence of the additive is more significant.

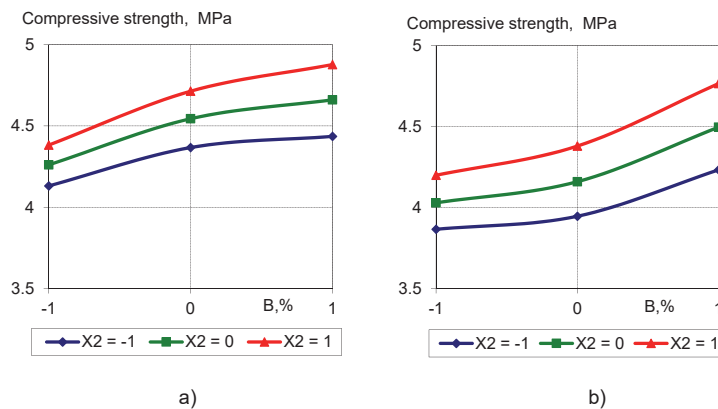


Figure 8. Graphical dependences of the compressive strength at 20°C when using Wetfix BE (a), Stardope 130 P (b)

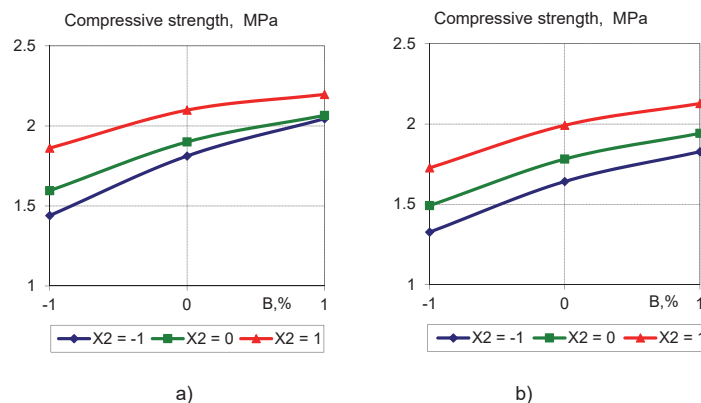


Figure 9: Graphical dependences of the compressive strength at 50°C when using Wetfix BE (a), Stardope 130 P (b)

Varying factors have a similar effect on the compressive strength at temperature 20°C. Under these conditions, the strength increases from 3.8...4.2 MPa to 4.25...4.75 MPa. However, at a temperature of 50°C, the effect is somewhat different the influence of the additive decreasing.

When bitumen amount is up to 5.0%, the increase is more significant compared to the amount of 5.0...5.4%, which can be explained by the excessive amount of modified binder in the asphalt mixture.

Tests of the Wetfix BE additive have shown that an increase in the content of the additive in bitumen also has a positive effect on the properties of asphalt mixtures. The water saturation of the samples decreases from 3.0% to 1.1% at the maximum content of bitumen and additive within the range of variation.

An increase in the compressive strength at temperature 20°C from 4,15...4,4 MPa to 4,45...4,9 MPa can be obtained at the maximum content of bitumen and additives within the range of variation. However, at a bitumen consumption of more than 5.0 % with a minimum content of surfactants, the strength practically does not increase. The influence of the studied factors on the strength at the temperature of 50°C is somewhat different, with the optimal bitumen content in terms of strength being 4.7...5.2%. With a further increase in bitumen, the effect of the additive fades.

To compare the effectiveness of adhesion additives, the properties of asphalt mixtures without surfactant additives were determined. The composition of the mixtures is given in Table 4. The bitumen content was 5%, and the surfactant additives were 0.3%, 0.4%, and 0.5%. The obtained experimental results are shown in Table 6 and graphical dependencies in Figs. 10... 12.

Table 6. Results of experimental data

Type of additive	Additive content, %	Compressive strength at temperature, MPa		Water saturation of samples, %
		20°C	50°C	
Without additive	-	3,2	1,25	3,6
Wetfix BE	0,3	4,35	1,87	2,3
	0,4	4,55	1,9	1,97
	0,5	4,72	2,08	1,8
Stardope 130 P	0,3	4,0	1,65	2,4
	0,4	4,17	1,78	2,1
	0,5	4,3	2,0	1,9

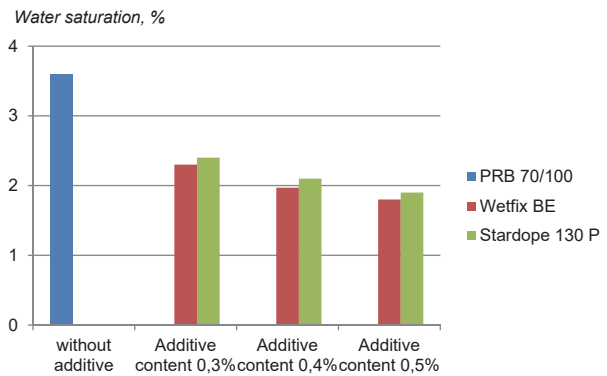


Figure 10: Graphical dependences of water saturation of samples asphalt mixtures

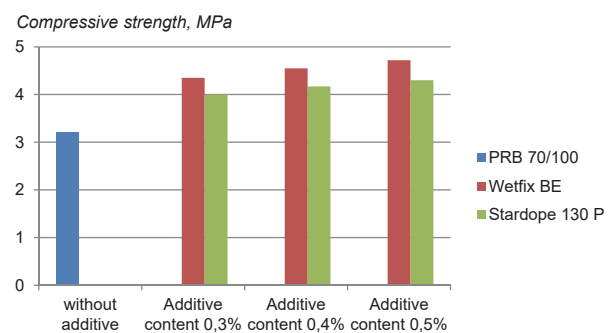


Figure 11. Graphical dependence of compressive strength of asphalt concrete at 20°C

Analyzing the data obtained (Table 6) and the graphical dependences of water saturation and compressive strength at 20°C and 50°C of asphalt mixtures (Figs. 10... 12), it can be concluded that samples without the use of adhesive additives have significantly lower corresponding indicators. The water saturation of asphalt concrete without surfactant additives is more than 3.5%, which does not meet the requirements of the regulatory document ($\leq 3.5\%$) (DSTU B B.2.7-319:2016 (Ukr. Standard)). Thus, it is possible to ensure all regulatory indicators with the use of adhesive additives.

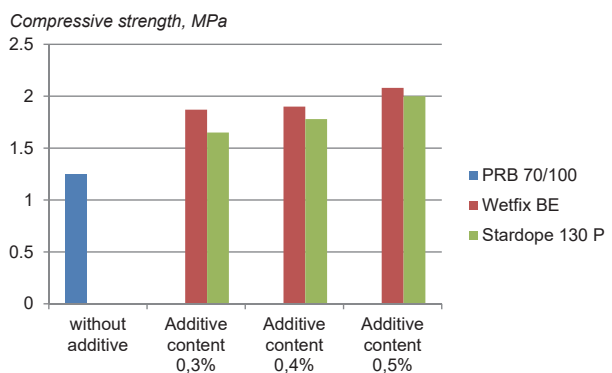


Figure 12. Graphical dependence of compressive strength of asphalt concrete at 50°C

4. CONCLUSIONS

1. The introduction of adhesive additives improves the basic properties of bitumen, which are decisive for obtaining high-quality asphalt concrete mixtures. Modification of bitumen increases adhesion to glass by 75...85%, and to crushed stone by 40...50%.

2. Using methods of mathematical planning of experiments, experimental and statistical models of water saturation and compressive strength of asphalt concrete mixtures at temperatures of 20°C and 50°C were obtained. Analysis of the models made it possible to find the optimal content of adhesive additives depending on the bitumen content in the mixture. The introduction of modifying additives can significantly reduce the water saturation of asphalt concrete mixtures by up to 50%, and increase the strength by 25...40% and 32...65% at temperatures of 20°C and 50°C, respectively.

3. Compositions of asphalt concrete mixtures containing adhesive additives have been proposed that provide the necessary standardized indicators.

4. Further research is planned to be carried out in the direction of the influence of the composition of the asphalt concrete mixture on the effectiveness of the use of modifying additives

5. REFERENCES

- [1] J.McBain, D. Hopkins (1925) On adhesives and adhesive action. *J. Phys. Chem.* 29, 188–204. doi: 10.1021/j150248a008.
- [2] B.V.Deryagin, N.A.Krotova, Adhesion / B.V. Deryagin, N.A. Krotova (1949) Ed. USSR Academy of Sciences, p.12, in Russian.
- [3] N.Krotova (1956) About gluing and adhesion / N.A. Krotova.- Ed. USSR Academy of Sciences, p. 91, in Russian.
- [4] M.Bancroft (1926) *Applied Colloid Chemistry*, McGraw- Hill, New York, – p.81.
- [5] N.De Bruyne (1947) *Aircraft Eng.*, 16(115), 18-23.
- [6] A. Mc Laren, C.J.Seiler (1949) *J.Polymer Sci.*, 4, 63-71. doi: 10.1002/pol.1949.120040105
- [7] A. Mc Laren (1954) Symposium “ Adhesion and Adhesives”, John Wiley and Sons, 1954, p.57.
- [8] L.Ma, A.Varveri, R.Jing, S.Erkensb (2021) Comprehensive review on the transport and reaction of oxygen and moisture towards coupled oxidative ageing and moisture damage of bitumen. *Constr. Build. Mater.*, 283, 122632. doi: 10.1016/j.conbuildmat.2021.122632.
- [9] C.O. Rossi, B.Teltayev, R.Angelico (2017) Adhesion promoters in bituminous road materials: A review. *Appl. Sci.*, 7, 524. doi: 10.3390/app7050524.
- [10] R.Tarefder, A.Zaman (2010) Nanoscale evaluation of moisture damage in polymer modified asphalts. *J. Mater. Civ. Eng.*, 22, 714–725. doi: 10.1061/(ASCE)MT.1943-5533.0000072.
- [11] D.Cihlářová, I.Fencl, S.Cápayová, P.Pospíšil (2018) Use of adhesion promoters in asphalt mixtures. *Slovak J. Civ. Eng.*, 26, 19–24. doi: 10.2478/sjce-2018-0003.
- [12] J.Choudhary, B.Kumar, A.Gupta (2020) Effect of filler on the bitumen-aggregate adhesion in asphalt mix. *Int. J. Pavement Eng.*, 21, 1482–1490. doi: 10.1080/10298436.2018.1549325.
- [13] R.Terrel, J.Shute (1989) Summary Report on Water Sensitivity. Report SHRP-A/IR-89-003. Strategic Highway Research Program, National Research Council, Washington, D.C. <http://onlinepubs.trb.org/Onlinepubs/shrp/shrp-A-IR-89-003/SHRP-AIR-003.pdf>
- [14] R. Moraes, R. Velasquez, H.U. Bahia (2011) Measuring the effect of moisture on asphalt-aggregate bond with the bitumen bond strength test. *Journal of the Transport.* 22(9), 65-71. doi:10.3141/2209-09/
- [15] L. Boulangé, E. Estelle Bonin, M. Saubot (2013) Physicochemical characterizations of the bitumen-aggregate interface to get a better understanding of stripping phenomena. *Road Materials and Pavement Design*, 14 (2), 384-403. doi: 10.1080/14680629.2013.803494.
- [16] P.J. Ramon-Torregrosa, M.A. Rodriguez-Valverde, A. Amirfazli, M.A. Cabrerizo-Vilchez (2008) Factors affecting the measurement of roughness factor of surfaces and implication for wetting studies. *Colloids and Surfaces A: Physicochemical and Engineering Aspects*, 404, 83-93. doi: 10.1016/j.colsurfa.2007.10.032.
- [17] J. Grenfell, N. Ahmad, Y. Liu, A. Apeagyei, D. Large, G. Airey (2014) Assessing asphalt mixture moisture susceptibility through intrinsic adhesion, bitumen stripping and mechanical damage. *Road Materials and Pavement Design*, 15, 131-152. doi: 10.1080/14680629.2013.863162.
- [18] R.Robertson (2000) Chemical properties of asphalts and their effects on pavement performance. *Transportation Research Circular* 499, 49-54. <http://onlinepubs.trb.org/onlinepubs/shrp/SHRP-91-510.pdf>.
- [19] J.M. Rice (1958) Relationship of aggregate characteristics to the effect of water on bituminous paving mixtures. Symposium on Effect of Water on Bituminous Paving Mixtures, ASTM STP, 240, 17-34. <https://onlinepubs.trb.org/Onlinepubs/sr/sr98.pdf>.
- [20] A.Tarrer, V.Wagh (1991) The Effect of the physical and chemical characteristics of the aggregate on bonding. SHRP-A/UIR-91-507, p.31. <http://onlinepubs.trb.org/onlinepubs/shrp/SHRP-91-507.pdf>.
- [21] M.Paliukaitė, V. Vorobjovas, M. Bulevičius, V. Andrejevas (2016) Evaluation of Different Test Methods for Bitumen Adhesion Properties, *Transportation Research Procedia*, 14, 724-731, ISSN 2352-1465, doi: 10.1016/j.trpro.2016.05.339.
- [22] K.Pstrowska, V.Gunka, I. Sidun, Y.Demchuk, N.Vytrykush, M.Kułażyński, M.Bratychak (2022) Adhesion

in Bitumen/Aggregate System: Adhesion Mechanism and Test Methods. *Coatings*, 12, 1934. doi: 10.3390/coatings12121934.

- [23] Y. Kim, I. Pinto, S.W. Park (2012) Experimental evaluation of anti-stripping additives in bituminous mixtures through multiple scale laboratory test results.

Construction and Building Materials, 29, 386-393. doi: 10.1016/j.conbuildmat.2011.10.012.

- [24] L.Dvorkin, O.Dvorkin, Y.Ribakov (2011) *Mathematical experiments planning in concrete technology*. Nova Science Publishers.

IZVOD

UTICAJ ADITIVA LEPILA NA SVOJSTVA BITUMENA I ASFALTNIH SMEŠA

U ovom radu su prikazani rezultati eksperimentalnih istraživanja uticaja adhezivnih aditiva na osnovna svojstva modifikovanih bitumenskih i asfaltbetonskih mešavina. Uvođenjem adhezivnih aditiva poboljšavaju se osnovna svojstva bitumena, neophodna za dobijanje visokokvalitetnih asfaltbetonskih mešavina. Modifikacija bitumena povećava adheziju na staklo i drobljeni kamen. Korišćenjem metoda matematičkog planiranja eksperimenata dobijeni su eksperimentalni i statistički modeli zasićenosti vodom i čvrstoće na pritisak asfaltbetonskih mešavina na temperaturama od 20°C i 50°C. Uvođenje modifikujućih aditiva može značajno smanjiti zasićenje vodom asfaltbetonskih mešavina i povećati čvrstoću na temperaturama od 20 °C i 50 °C.

Ključne reči: bitumen, asfaltne mešavine, čvrstoća, adhezivni aditivi, penetracija, tačka omekšavanja, duktilnost.

The ORCID Ids of all the authors are as follows:

Leonid Dvorkin: <https://orcid.org/0000-0001-8759-6318>

Vitalii Marchuk: <https://orcid.org/0000-0003-0999-0402>

Mykola Kuzlo: <https://orcid.org/0000-0001-9242-2478>

Naučni rad

Rad primljen: 27.03.2024.

Rad korigovan 4.05.2024.

Rad prihvaćen: 12.05.2024.

Lyudmila Nyrkova, Vitaliy Knysh, Sergiy Solovey, Svetlana Osadchuk

E.O Paton Electric Welding Institute of National Academy of Sciences of Ukraine, Kyiv, Ukraine

Scientific Paper

ISSN 0351-9465, E-ISSN 2466-2585

<https://doi.org/10.62638/ZasMat1052>



Zastita Materijala 65 (4)
680 – 689 (2024)

Influence of Different Methods of Surface Treatment on Corrosion Resistance of Low-Alloy Steel

ABSTRACT

The influence of mechanical methods of surface treatment (polish and polish with the next strengthening by high-frequency mechanical pinning, HFMP) on the corrosion resistance of low-alloy steel 15HSND were presented. The deficiencies of surface strengthening by HFMP with one impact peen were analyzed, and an instrument in which shock elements are situated in a few rows was suggested. Speed of HFMP for the surfaces 35 sm²/min was recommended. The differences in structure and microhardness of near-surface layers of 15HSND steel with polished surface and the polished surface with next strengthening by HFMP were established after investigations in the salt fog chamber and moisture chamber during 1200 hours. Application of HFMP technology increases of corrosion resistance of steel: corrosion rate after neutral salt fog decreased from 2,543 mm/year on the polished surface to 2,096 mm/year after HFMP treatment, and after increased humidity and temperature, from 0,104 mm/year to 0,080 mm/year.

Keywords: accelerated climatic tests, corrosion resistance, high-frequency mechanical peening, low-alloy steel, metallography

1. INTRODUCTION

To increase the corrosion resistance and corrosion fatigue of machine parts and structural elements, various methods of surface machining are widely used, which are aimed at reducing roughness, changing the structure of the surface layer of metal, introducing residual compressive stresses, etc. [1-5]. In recent years, there has been an increasing number of publications dedicated to researching the effectiveness of high-frequency mechanical peening (HFMP) with impact elements using ultrasound energy [6-12], which shows the expediency of strengthening the surface by HFMP technology in order to increase the corrosion resistance of various metals (stainless steels, aluminum,

and zirconium-niobium alloys). The purpose of the work was to compare the effects of different surface treatment methods, namely grinding and grinding followed by strengthening by HFMP technology, on the corrosion resistance of weather-resistant steels. The research was carried out on specimens with dimensions of 70'50×10 mm, made of low-alloy steel 15HSND, which is widely used for the execution of elements of welded metal structures, in particular, bridge structures, has increased strength, is well welded, is stable in atmospheric conditions, and is capable of working in the temperature range from -70 °C to 45 °C.

2. EXPERIMENTAL

The investigations were carried out on low alloy 15HSND steel ($\sigma_{YS} = 400$ MPa, $\sigma_{TS} = 565$ MPa) such a chemical composition (weigh part, %): 0,142C, 0,466 Si, 0,31 Ni, 0,020 S, 0,013 P, 0,66 Cr and 0,37 Cu.

* Corresponding author: Kaushalendra Kumar Dubey
E-mail: lnyrkova@gmail.com
Paper received: 28.03.2024.
Paper accepted: 29.05.2024.

Specimens with a polished surface and a surface treated (on all sides) using HFMP technology were used. Corrosion tests were performed on the surface treated by the following methods: polished (P) and polished + HFMP (G + HFMP) according to the procedure, described in [13]. Corrosion tests were carried out under the following conditions: exposure to neutral salt fog and elevated temperature of 35 °C with a humidity of about 98% in a salt fog chamber (hereinafter the SF-1 chamber) and exposure to an elevated humidity of 98% and a temperature of 40 °C in a humidity chamber G4 (further chamber G4). The corrosion rate of the specimens was determined by masometry method. Corrosion rate was estimated by the formula:

$$v_{\text{cor}} = \frac{8760 \times \Delta m}{dST} \quad (1)$$

where $\Delta m = m_1 - m_2$ the corrosion losses of the specimen, g;

m_1 is the specimen weight before testing, g;

m_2 is the specimen weight after corrosion tests;

S is the specimen surface area, m²;

T is the study duration, hours;

8760 is the number of hours in a year;

d – steel density, equal to 6.7 g/cm³.

Before and after the corrosion studies, the condition of the near-surface layers was monitored by the metallographic method. Metallographic sections were prepared according to standard methods. Grinding and polishing of the grindstones was carried out in ring mandrels with protacryl fixation of the specimen, the near-surface layers were examined for a length of ~ (15-20) mm, the total dimensions of these layers were about (30-40) mm.

Metallographic studies were carried out on a NEOPHOT 32 and NEOPHOT 21 microscope, and a digital image of the structure was obtained using a digital camera Olympus C 5050 and SIGETA UC-MOS. Micro hardness was measured on a Leco micro hardness tester M-400 at a load of 25 g (0.25 N), 50 g (0.49 N), 100 g (0.98 N). The grain size was determined according to ISO 4499-2.

3. RESULTS AND DISCUSSION

3.1 Selection of optimal strengthening parameters by high frequency peening technology

To increase the fatigue resistance of welded joints using HFMP technology, a narrow transition zone of the weld metal to the base metal is processed. Processing is carried out with both automatic and manual tools with one impact element or several impact elements located in a row, thanks to which a characteristic groove is formed. A riveted (plastically deformed) layer of metal with a depth of up to 1 mm is located under the groove (**Fig. 1**). It is known [14] that there is a satisfactory correlation between the depth of the groove and the durability of welded joints, and ensuring the required depth of the groove can serve as a criterion for quality processing. A methodical approach to establishing optimal parameters for strengthening local zones of machine parts or welded joints in order to increase their resistance to fatigue is described in [15].

A number of features must be taken into account when strengthening surfaces. With an increase in the duration of forging, corrosion resistance initially increases, after which, with a further increase in forging time, corrosion resistance may decrease [8]. The work [16] gives the results of processing a flat surface with a tool with one impact element, which was displaced by 1 mm after each pass. It was shown that increasing the number of tools passes from one to three reduced the efficiency of the HFMP and led to the appearance of defects. However, the authors of the work [16] did not take into account that this approach to surface treatment leads to the artificial formation of internal defects (mainly in the form of subsurface cracks) due to the fact that high flows of riveted metal near the groove were wrapped and re-riveted when the tool was moved by 1 mm. Thus, discontinuities were artificially formed between layers of riveted metal.

Taking into account the above, a hand tool with a removable nozzle was developed for strengthening flat surfaces, in which the impact elements were arranged in several rows. Surface treatment is recommended to be strengthened with circular reciprocating movements at a speed of 35 cm²/min. At the same time, the depth of the strengthened metal layer reached 130-150 microns.

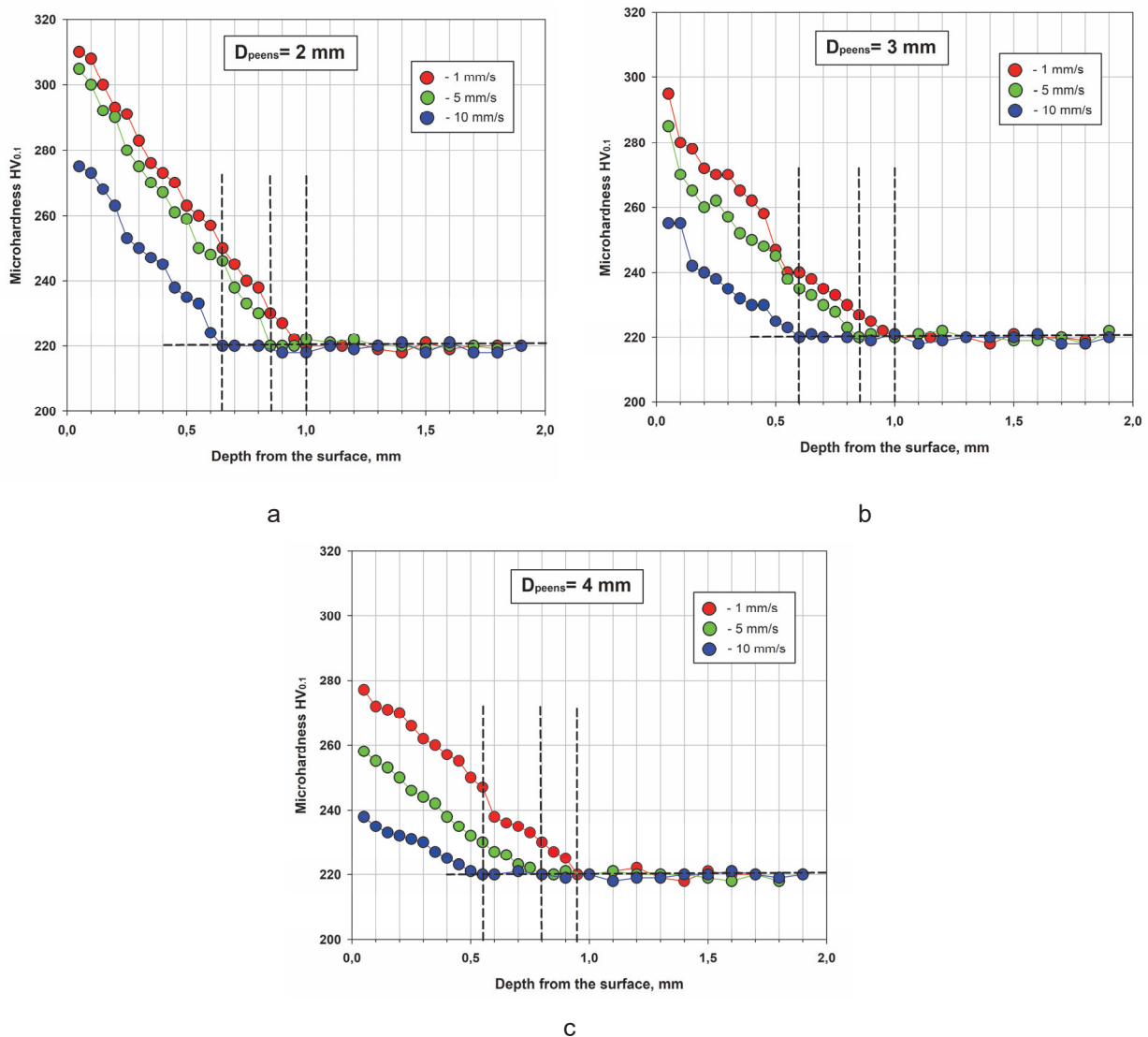


Fig. 1. Dependence of microhardness of near surface metal layer, strengthened by HFMP by using of one-row head with the diameter of cylindrical firing-pins of 2 mm (a), 3 mm (b) and 4 mm (c) from the distance from the bottom of groove to the depth of metal. Speed of implementation of HFMP (Reproduced with permission [15])

3.2 Corrosion and metallographic studies

After choosing the optimal parameters of the HFMP technology, comparative studies of the effect of surface treatment methods on the corrosion resistance of 15HSND steel were carried out. In Fig. 2

show photographs of the microstructure of the near-surface layers of 15HSND steel with a polished surface (Fig. 2, a) (hereinafter P) and a surface processed by HFMP (hereinafter P+ HFMP) technology (Fig. 2, b).

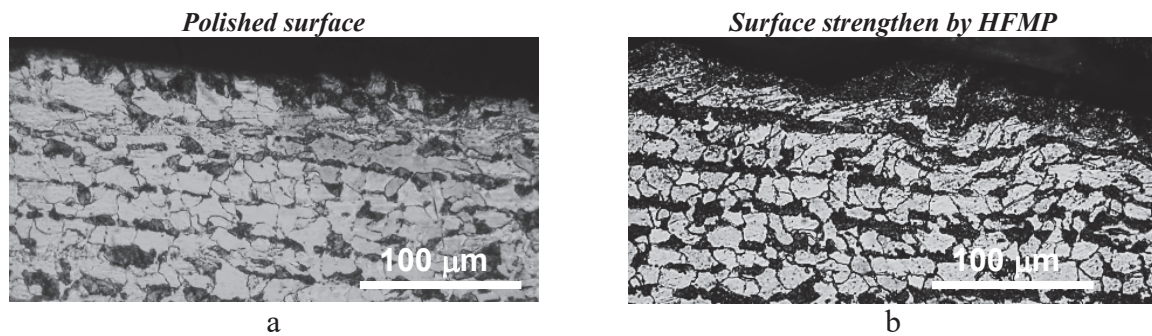


Fig. 2. Microstructure of near surface layers of 15HSND steel with polished surface (P) (a) and surface strengthened by HFMP (b) in the initial state

It should be noted that the surface P is not completely flat (**Fig. 2, a**) in some areas of the near-surface layers, a different degree of plastic deformation is observed, which leads to a change in the shape of the grains of ferrite and pearlite, with a shape factor from 1.8 to 4, the depth of penetration of plastic deformation is from 0.03 mm to 0.08 mm. After HFMP (**Fig. 2, b**), the surface of the specimen acquired uneven waviness, in the zone with more intensive deformation - from 0.06 mm to 0.08 mm. A change in the shape of the grains, their extraction with a shape factor from 3 to 5, grinding and the more frequent appearance of second-phase dispersed discharges were noted. In the zone with a lower degree of deformation, with a depth of 0.09 mm

to 0.13 mm, practically no change in the shape of the grains was observed, only the distortion of the ferrite-pearlite striation of the structure was noted.

The results of measuring the micro-hardness of ferrite grains in the near-surface layers of the studied steel, subjected to various types of surface treatment, are presented in Table 1, from which it can be seen that processing using the HFMP technology somewhat (about 1.07–1

Photographs of specimens at the initial state (before corrosion tests) with polished surface (**Fig. 3, a**) and surface strengthened by HFMP (**Fig. 4, a**) and after exposure in SF-1 (**Fig. 3, b, c, Fig. 4, b, c**) and G4 (**Fig. 3, d, e, Fig. 4, d, e**) are shown below.

TABLE 1. Micro-hardness of ferrite grains in the near surface layers of 15HSND steel after the different methods of surface treatment before investigations

The method of surface treatment	Micro-hardness of ferrite grains, HV _{0,25 H}		Coefficient of hardening of ferrite grains ^[a]
	near the surface (at a distance 0,02-0,04 mm)	in the volume of metal (with the injection step 0,08 – 0,12 mm)	
P	<u>153–161–172–77–168*</u> 166	<u>147–153–161–161–153</u> 155	1,07
P+HFMP	<u>199–178–169–181–172</u> 180	<u>160–153–154–154–147</u> 154	1,17

^[a] Coefficient of hardening of ferrite grains, micro-hardness of ferrite grains: in the numerator – measured, in the denominator - average.

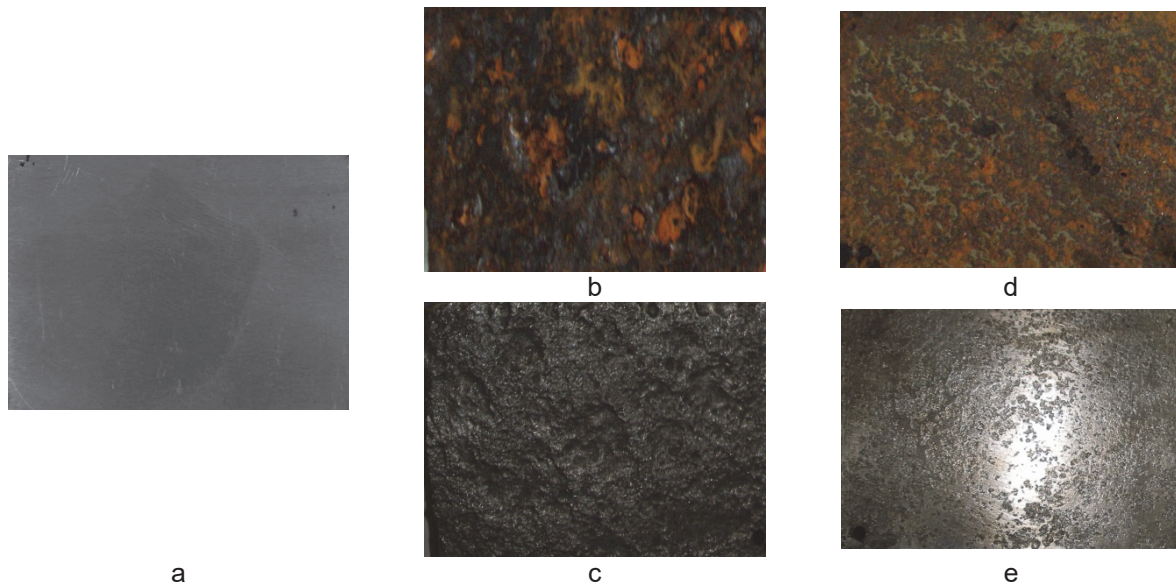


Fig. 3. Appearance of surface of 15HSND steel specimens with polished surface (P) before (a) and after investigations (b, c, d) in the salt fog chamber SF-1 (b, c) and moisture chamber G4 (d, e) during 1200 hours

Analyzing the experimental results, it can be noted that after the tests under the influence of neutral salt fog and elevated temperature, all the examined specimens (with surfaces P and P+HFMP) were covered with a thick layer of corrosion products of uneven thickness of brown-black color (**Fig. 3, b, Fig. 4, b**), which were firmly attached to the surface and were very difficult to remove. Areas of the surface without corrosion products with a metallic luster were not observed. After removing the cor-

rosion products, it was noted that the surface is uneven, and corrosion spots are visible over the entire area, with ulcers and pitting inside (**Fig. 3, c, Fig. 4, c**). There are also no areas not affected by local corrosion. Areas with the remains of the reinforcing layer are not visually visible on specimens strengthened by HFMP technology. The corrosion rate after 1200 hours was 2.543 mm/year on the surface of P and 2.096 mm/year on the surface of P+HFMP (**Fig. 5**).

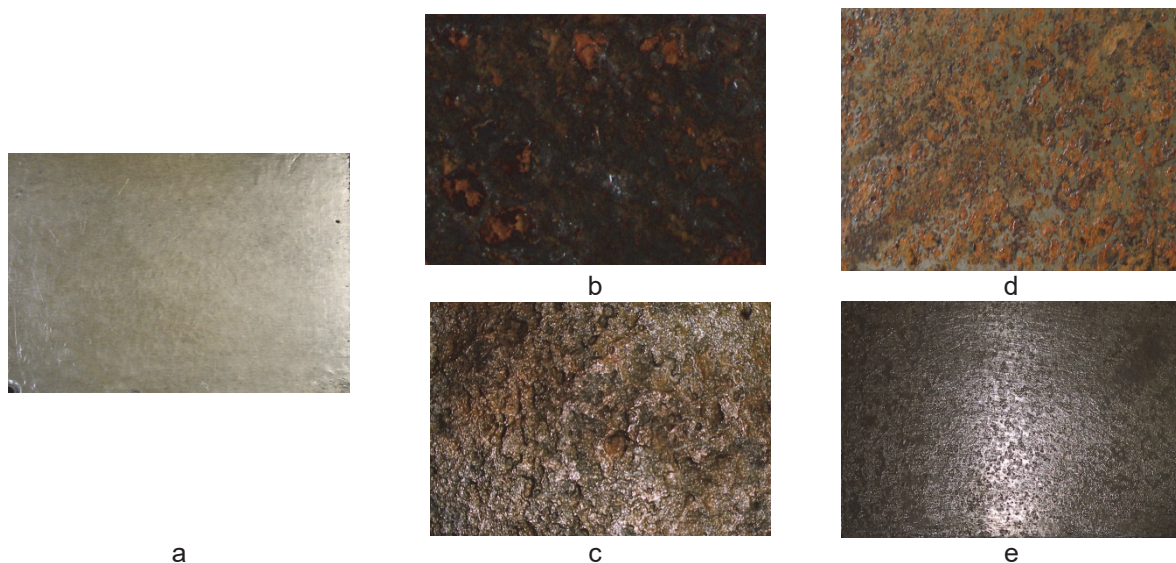


Fig. 4. Appearance of surface of 15HSND steel specimens with surface strengthened by HFMP before (a) and after investigations (b, c, d, e) in the salt fog chamber SF-1 (b, c) and moisture chamber G4 (d, e) during 1200 hours

After tests in G4, specimens with the surface P and P+HFMP (**Fig. 3, d, Fig. 4, d**), are covered with an uneven layer of brown corrosion products with black spots. Areas of the surface with almost no corrosion products with a metallic luster are noted, which occupy about 5-7%. After removal of corrosion products, corrosion spots are visible on the surface, smaller in size than after exposure in SF-1, inside some of them pitting has formed, there are areas practically unaffected by local corrosion (**Fig. 3, e, Fig. 4, e**). The corrosion rate was 0.104 mm/year on the P surface and 0.080 mm/year on the P+HFMP surface (**Fig. 5**).

Thus, surface treatment of HFMP contributed to some extent to increase the corrosion resistance of the studied steel.

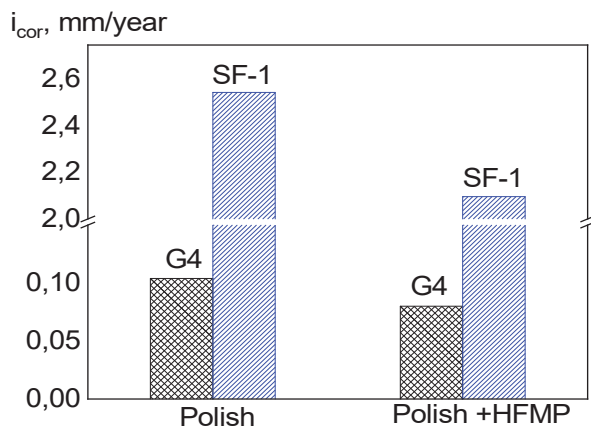


Fig. 5. Comparative diagram of corrosion rate of 15HSND steel with polished surface (P) and surface strengthened by HFMP after accelerated corrosion tests in the salt fog chamber SF-1 and moisture chamber G4 after 1200 hours

After the corrosion studies, metallographic studies were carried out, during which the type of corrosion, the size and distribution of corrosion damages were determined. The type of corrosion was determined by comparing it with the types of corrosion defects given in GOST 9.908 (appendix 2), distribution – according to GOST 9.908 (appendix 3) [17]. Corrosion resistance indicators were determined quantitatively and qualitatively. During the influence of the surface treatment method on the corrosion resistance of the specimens before and after the action of climatic factors, the following types of corrosion damage were detected:

– continuous uniform corrosion, which is characterized only by surface unevenness;

– local uneven corrosion, in which only part of the surface is susceptible to corrosion damage;

– spot corrosion – a small (shallow) corrosion lesion, usually of an irregular shape with different sizes of the corrosion damage area;

– corrosion by ulcers; surface damage, the depth and width of which are almost the same;

– subsurface corrosion – corrosion damage that occupies a small area on the surface of the specimen and is concentrated mainly under the surface of the metal;

– intergranular corrosion (IGC) – a corrosion lesion characterized by the presence of a corroded zone along the boundaries of metal grains, which may touch the boundaries of all grains or selectively the grains of individual structural components;

– selective corrosion – corrosion damage to which individual grains of any structural component are exposed, including that which is accompanied by the formation of corrosion products that can have different depths of occurrence.

The total length of the studied near-surface layers is 15 mm × 2.

3.3 Results of metallographic studies of specimens after exposure to neutral salt fog and temperature

Some types of surface damage after exposure in SF-1 and G4 are shown in **Fig. 6, b, c**. After exposure in SF-1, continuous uneven corrosion was observed in the surface layers of the specimen with surface P (**Fig. 6, a**), against the background of which deep corrosion lesions were observed in the form of corrosion spots, for example, 2.8 × 0.5 mm, 2.1 × 0.7 mm in size and, less often, corrosion ulcers, for example, in size 1.7 × 1.58 mm. IGC, which started from the boundaries of the ferrite and pearlite grains, and selective corrosion along the pearlite grains were also detected. In addition, in the near-surface layers at a depth of 0.02-0.03 mm, separately located areas with subsurface corrosion from 0.38 mm to 0.413 mm in length were found.

The surface of the specimen P+HFMP was exposed to continuous uneven corrosion (**Fig. 6, b**): mainly, spot corrosion of various sizes, for example, from 0.13×0.03 mm to 1.56×0.26 mm, was detected; in the near-surface layers - by subsurface corrosion of various areas, for example, 0.38×0.012 mm, 0.1×0.007 mm, mainly at a depth of 0.05-0.07 mm, with direct access to the surface of the v; IGC along the boundaries of ferrite grains at a depth of nearly 0.1 mm; selective corrosion of pearlite grains.

Corrosion lesions are less deep compared to the surface P: for example, 0.7×0.01 mm, 0.15×0.007 mm, and corrosion by ulcers, for example, 0.15×0.13 mm.

The results of metallographic studies of specimens of the base metal of 15HSND steel after exposure to high humidity and temperature. A feature

of the surface of the specimens after exposure in G4 is the presence of a large number of areas with subsurface corrosion of different lengths (0.1–1.32 mm) and depths (0.01–0.07 mm), mainly with direct access to the surface.

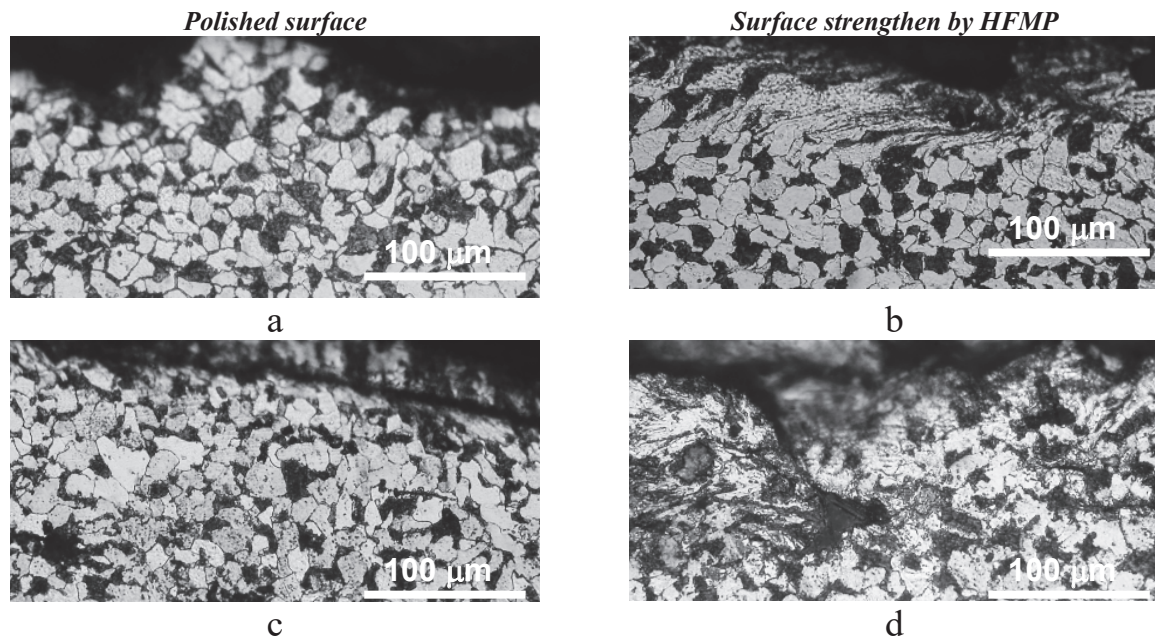


Fig. 6. Microstructure of near surface layers of 15HSND steel with polished surface (P) (a, c) and surface strengthened by HFMP (b, d) after investigations in the salt fog chamber SF-1 (a, b) and moisture chamber G4 (c, d) during 1200 hours.

In the near-surface layers of the specimen with surface P, continuous uneven corrosion was recorded after the tests (**Fig. 6, c**, and **Table 2**). In addition, relatively shallow (0.03–0.08 mm) corrosion damage is observed, mainly in the form of spots, for example, 0.3×0.05 mm and 0.11×0.017 mm in size; shallow IGC from the boundary of elongated pearlite grains; and more intense selective corrosion along the grains of the pearlite component.

A plastically deformed layer of ferrite and pearlite grains with a depth of 0.01 to 0.13 mm and a grain shape factor (K_{gsh}) equal to 3–50 is observed in the

near-surface layers of the specimen with a surface of P+HFMP. The near-surface layers of the specimen were subjected to continuous uneven corrosion (**Fig. 6, d**), relatively shallow (0.026–0.1 mm) spot corrosion was recorded (**Table 2**). In addition, there are areas with subsurface corrosion of different areas, lengths (0.06–0.9 mm), and depths of occurrence (0.01–0.07 mm), both with direct exit and without exit to the metal surface. IGC is not intense and spreads along the boundaries of both ferrite and pearlite grains; selective corrosion of pearlite grains is observed.

Table 2. Corrosion damage parameters in the near surface layers of 15HSND steel

Surface treatment method	Tests conditions	Deformed layer depth, mm	Spot corrosion			Subsurface corrosion			Intergranular corrosion			Selective corrosion
			Damage degree, %	Penetration depth, mm	Total projection of the affected area, mm ²	Damage degree, %	Penetration depth, mm	Total projection of the affected area, mm ²	Damage degree, %	Penetration depth, mm	Total projection of the affected area, mm ²	
P	SF-1	-	42,9	0,05-1,0	17,16	6,03	0,01-0,07	2,41	0,88	0,003-0,06	0,35	along pearlite grains
P+HFMP	SF-1	0,02-0,066	80	0,013-0,163	25,6	0,93	0,017-0,065	0,3	0,5	0,022-0,044	0,16	along pearlite grains at a depth of 0.3 mm
P	G4	0,007-0,017	8	0,03-0,08	2,41	14,2	0,01-0,07	4,27	0,18	0,03	0,054	
P+HFMP	G4	0,01-0,132	27,7	0,026-0,065	8,32	10	0,017-0,035	3,01	along the boundaries of individual ferrite grains			

According to the results of measuring the micro-hardness of ferrite grains in the near-surface layers of 15HSND steel subjected to various methods of surface treatment, no difference in micro-hardness was found after tests in SF-1 and G4. In order to assess the effect of the applied methods of metal processing on its corrosion resistance under various conditions, the degree of damage to the specimens by corrosion, in addition to the depth of corrosion penetration, was determined not only by the area but also by the total projection of the damaged plane in the cross-section of the specimen, related to its total length, the results of which are given in **Table 2**.

After research in conditions of neutral salt fog (**Table 2**), the depth of penetration of the detected types of corrosion damage in the near-surface layers of 15HSND steel is different: the greatest depth of spot corrosion (1 mm) is recorded on the surface P, the smallest (0.163 mm) is on the surface P+HFMP; the depth of subsurface corrosion for all methods of surface treatment is almost the same - (0.065-0.07 mm), but on the surface P+HFMP the number of areas with this type of corrosion is less than on the surface P. The smallest depth of IGC (0.044 mm) is established in the near-surface layers on the surface P+HFMP, the largest (0.06 mm) – after on the surface P. After research in conditions of high humidity and temperature, the manifestation of corrosion damage in the near-surface layers of the metal is,

in general, similar to the above. Thus, research has established that more intense corrosion in the near-surface layers of metal occurs in conditions of neutral salt fog, in which the depth of penetration of all detected types of corrosion is greater compared to conditions of high humidity. The highest corrosion resistance is provided by the surface layers of 15HSND steel subjected to high-frequency mechanical forging, despite some disagreement regarding the degree of damage by spot corrosion.

4. CONCLUSIONS

An analysis was carried out regarding the selection of the most technologically effective parameters for strengthening low-alloy steels using the HFMP technology. To strengthen the surfaces, it is recommended to use a removable nozzle in which the impact elements are located in several rows. The speed of HFMP should be 35 cm²/min.

According to the results of metallographic studies, it was established that processing using HFMP technology strengthens the ferrite component of the near-surface layers of low-alloy steel 15HSND by about 1.07–1.17 times compared to the polished surface.

The influence of various methods of surface treatment of low-alloy steel 15HSND (grinding and processing using HFMP technology) on its corrosion resistance under the influence of climatic factors was studied. It was established that the surface after

HFMP treatment helps to some extent increase the corrosion resistance of the studied steel: the corrosion rate after exposure to neutral salt fog after 1200 hours decreases from 2.543 mm/year on a polished surface to 2.096 mm/year after HFMP treatment, and after exposure to high humidity and temperature – from 0.104 mm/year to 0.080 mm/year, respectively.

The corrosion rate of steel with a polished surface is lower, but the HFMP technology is planned to be used in the future to increase the durability against corrosion-fatigue failure.

ACKNOWLEDGEMENTS

This work was carried out under the support of the National Academy of Sciences of Ukraine (State registration number 0112U000615).

CONFLICT OF INTEREST

The authors declare no financial or commercial conflict of interest.

REFERENCES

- [1] M.Mhaede (2012) Influence of surface treatments on surface layer properties, fatigue and corrosion fatigue performance of AA7075 T73, *Materials & Design*, 41, 61-66. DOI: 10.1016/j.matdes.2012.04.056
- [2] Z.M.Bogdanowicz, B.M.Nasiłowska, M.Wojucki (2015) Shot peening effect on 904 L welds corrosion resistance, *Journal of Constructional Steel Research*, 115, 276-282. DOI: 10.1016/j.jcsr.2015.08.041
- [3] A.Ahmed, M. Mhaede, M. Wollmann, L.Wagner (2014) Effect of surface and bulk plastic deformations on the corrosion resistance and corrosion fatigue performance of AISI 316L, *Surface and Coatings Technology*, 259, 448-455. DOI: 10.1016/j.surfcoat.2014.10.052
- [4] W.Gao, D. Wang, F. Cheng, C. Deng, Y.Liu, W. Xu (2015) Enhancement of the fatigue strength of underwater wet welds by grinding and ultrasonic impact treatment, *Journal of Materials Processing Technology*, 223, 305-312. DOI: 10.1016/j.jmatprotec.2015.04.013
- [5] T.Balusamy, T.Narayanan, K. Ravichandran, S. Park, M. Lee (2013) Influence of surface mechanical attrition treatment (SMAT) on the corrosion behaviour of AISI 304 stainless steel, *Corr. Sci.*, 74, 332-344. DOI: 10.1016/j.corsci.2013.04.056
- [6] B.Mordyuk, G. Prokopenko, M. Vasylyev, M. Lefimov (2007) Effect of structure evolution induced by ultrasonic peening on the corrosion behavior of AISI-321 stainless steel, *Materials Science and Engineering: A*, 458 (1-2), 253-261. DOI: 10.1016/j.msea.2006.12.049
- [7] V.Knysh, S. Solovei, A. Kadyshchev, L. Nyrkova, S. Osadchuk (2017). Influence of high-frequency peening on the corrosion fatigue of welded joints. *Materials Science*, 53, 7-13. DOI: 10.1007/s11003-017-0036-4
- [8] V. Knysh, S. Solovei, L. Nyrkova, S. Osadchuk (2020). Influence of marine media on the fatigue strength of butt welded joints of 15KhSND steel hardened by high-frequency mechanical impacts. *Materials Science*, 55, 812-821. DOI: 10.1007/s11003-020-00374-5
- [9] A.Abdullah, M. Malaki, A. Eskandari (2012) Strength enhancement of the welded structures by ultrasonic peening, *Materials & Design*, 38, 7-18. DOI: 10.1016/j.matdes.2012.01.040
- [10] T.Kravtsov, V.Sevryukov, (2001) *Ultrasonic treatment of ship parts and welded structures*. Monograph, Nikolaev, UGMTU. 216 p.
- [11] L.Lobanov, V.Kirian, V.Knysh, G.Prokopenko (2006) Improvement of fatigue resistance of welded joints in metal structures by high-frequency mechanical peening, *The Paton Welding Journal*, 9, 2-8. <https://paton-publishinghouse.com/eng/journals/tpwj/2006/09/00>
- [12] V.Degtyaryov, B.Shulginov, V.Knysh (2009) Deformation criterion of the efficiency of strengthening of welded joints by high-frequency mechanical peening, *The Paton Welding Journal*, 10, 39-41. <https://paton-publishinghouse.com/eng/journals/tpwj/2009/10/09>
- [13] V.Knysh, S. Solovei, I. Bogajch(2011) Optimisation of the process of strengthening of welded joints of 09G2S steel by high-frequency mechanical peening, *The Paton Welding Journal*, 5, 20-24. <https://paton-publishinghouse.com/eng/journals/tpwj/2011/05/04>
- [14] V.Knysh, S. Osadchuk, S. Solovei, L. Nyrkova, A. Rybakov (2019) Procedure of accelerated corrosion testing for modeling the long-term effect of moderate climate atmosphere on welded joints, *The Paton Welding Journal*, 11, 44-49. DOI: 10.15407/tpwj2019.11.08
- [15] Y.Feng, S. Hu, D. Wang, L. Cui (2016) Formation of short crack and its effect on fatigue properties of ultrasonic peening treatment S355 steel, *Materials & Design*, 89, 507-515. DOI: 10.1016/j.matdes.2015.10.009
- [16] GOST 9.908-85. Unified system of corrosion and ageing protection. Metals and alloys. Methods for determination of corrosion and corrosion resistance indices.

IZVOD

UTICAJ RAZLIČITIH METODA POVRŠINSKE OBRADE NA OTPORNOST NISKOLEGIRANOG ČELIKA NA KOROZIJU

Prikazan je uticaj mehaničkih metoda površinske obrade (poliranje i poliranje sa sledećim ojačanjem visokofrekventnim mehaničkim piningom, HFMP) na otpornost na koroziju niskolegiranog čelika 15HSND. Analizirani su nedostaci površinskog ojačanja HFMP-om sa jednim udarnim peenom i predložen je instrument u kome su udarni elementi smešteni u nekoliko redova. Preporučena je brzina HFMP-a za površine 35 sm²/min. Razlike u strukturi i mikrotvrdoći pripovršinskih slojeva 15HSND čelika sa poliranom površinom i polirane površine sa sledećim ojačanjem pomoću HFMP utvrđene su nakon ispitivanja u slanoj komori i komori za vlagu tokom 1200 sati. Primena HFMP tehnologije povećava otpornost čelika na koroziju: stopa korozije nakon neutralne slane magle smanjena je sa 2.543 mm/godišnje na poliranoj površini na 2.096 mm/godišnje nakon HFMP tretmana, a nakon povećane vlažnosti i temperature sa 0.104 mm/godišnje na 0.080 mm/god.

Ključne reči: ubrzana klimatska ispitivanja, otpornost na koroziju, visokofrekventno mehaničko kaljenje, niskolegirani čelik, metalografija

Naučni rad

Rad primljen: 28.03.2024.

Rad korigovan: 15.05.2024.

Rad prihvaćen: 29.05.2024.

The ORCID Ids of all the authors are as follows:

1. Lyudmila Nyrkova: <https://orcid.org/0000-0003-3917-9063>

2. Vitaliy Knysh: <https://orcid.org/0000-0003-1289-4462>

3. Sergiy Solovey: <https://orcid.org/0000-0002-1126-5536>

4. Svetlana Osadchuk: <https://orcid.org/0000-0001-9559-0151>

Monika Srivastava^{1*}, Ikhwan Syafiq Mohd Noor²,
Muhd Zu Azhan Yahya³, R. C. Singh¹

¹Centre for Solar Cell and Renewable Energy, Department of Physics, Sharda University, Greater Noida, India, ²Physics Division, Centre of Foundation Studies for Agricultural Sciences, Universiti Putra Malaysia, UPM Serdang, 43400, Selangor Darul Ehsan, Malaysia, ³Muhd Zu Azhan Yahya Faculty of Defence Science and Technology, Universiti Petrahanan Nasional Malaysia (UPNM), Kuala Lumpur, Malaysi

Scientific paper

ISSN 0351-9465, E-ISSN 2466-2585

<https://doi.org/10.62638/ZasMat1257>



Zastita Materijala 65 (4)
690 - 702 (2024)

Synthesis and scalable process for fabrication of Perovskite Solar Cells using organic and inorganic hole transport materials

ABSTRACT

The Organic Inorganic Lead Iodideperovskite material has emerged as a pioneer in being an active material for third generation solar cells. Apart from the synthesis, the scalable mechanism which is being used for the deposition process, greatly influences the performance of the cell owing to its impact on the morphology, uniform thickness and interface between two functional layers. This study briefly discusses the various deposition processes involved in assembling the layers of perovskite solar cells (PSC). Hole transport materials (HTM) are the crucial part of the PSC providing efficient transport of the charge carriers. However the effect of organic and inorganic HTMs is highly pronounced in the PSCs. This study also discusses the effect of organic and inorganic HTM on the stability and efficiency of the sandwich structured PSC.

Keywords: Perovskite, Solar energy, PCE, Hole transport material

1. INTRODUCTION

As we know that across the world the energy consumption is continuously increasing and is estimated to elevate by approximately 48% by the end of 2040, as stated by Energy Information Administration (EIA, 2015). This surge in the energy consumption is primarily due to growth in population and living standard of the people which translates into greater use of energy products. Clean and renewable energy sources are needed to dominate this domain for sustainable developments (McGeoch *et al.*, 2010). Solar cells are the effective way to harness the sun's energy to convert it into electricity and thus provide the opportunity to overcome humanity's continued increase in demand and consumption of available energy (Service, 2005). Compared to other means, for example photochemical reaction and solar thermal, solar cells offer an efficient and safer way to meet the energy demands across the globe. However, it has the capacity to efficiently transport and store energy. Thus, the main aim of this technology is to use solar energy in the most efficient way.

In 1954, the first known silicon solar cell was fabricated at Bell laboratories. The solar cell achieved an efficiency of 6%. Three generations of solar cells are under development in 60 years, based on the device engineering and the fundamental understanding of these photovoltaics. Silicon based solar cells that achieve efficiency as high as 26%, also classified as of the first generation, are the most successful commercially. The second generation of photovoltaics includes thin film solar cell technologies such as Copper Indium Gallium Selenide (CIGS), Cadmium Telluride (CdTe), and Gallium Arsenide (GaAs) also shows promising efficiencies. Gallium arsenide solar cells show a record efficiency of 29.3% under solar illumination condition (Polman *et al.*, 2016). But due to scarcity and toxicity of second generation, the third generation, have emerged, which includes the organic solar cells (OSC), Dye Sensitized Solar Cells (DSSC) and Perovskite Solar Cells (PSC) (Sengul and Theis, 2011; Gratzel, 2009). The third generation of solar cell technology is commonly known as an emerging generation of technologies. It encompasses a diverse array of solar cells that exhibit enhanced photovoltaic characteristics. These solar cells are characterized by their affordability, solution-based processing, and straightforward manufacturing processes that do not compromise their efficiency (Roy *et al.*, 2022).

The metal halide based perovskites have proved themselves as a promising photovoltaic

*Corresponding author: Monika Srivastava

E-mail: monika.srivastava@sharda.ac.in

Paper received: 07.03.2024.

Paper corrected: 23.05.2024.

Paper accepted: 06.06.2024.

material in the photovoltaic applications. The term 'Perovskite' follows the same crystal structure as CaTiO_3 and they are expressed as ABX_3 , where 'A' is the methyl ammonium (organic) cation, 'B' is the Pb cation and X is the halide ion. These cations and anions can be easily changed to tune the bandgap of the perovskite material. The metal halide perovskites have a number of applications for photovoltaic devices, Light emitting diodes, sensors etc. the year 2009 marks the first demonstration of a PSC with an efficiency of 3.8% (Kojima et al., 2009). This work garnered the interest of the scientific community towards the high absorption coefficient of PSCs. However the initial reported works were based on the liquid electrolyte PSC, therefore it leads to the leakage of the electrolyte causing low efficiency and instability. However, the year 2012, was a breakthrough in the area of PSCs which uses the HTM instead of the liquid electrolyte for the fabrication purpose. This increases the (PCE) efficiency of the PSC upto 10% (Kim et al., 2012; Lee et al; 2012). However, with certain modifications, the PCE of the perovskite solar cells have obtained an efficiency of ~ 25.4% within a duration of 10 years. It is discussed in this paper about the recent progress in the fabrication of PSCs and focus on the challenges which are faced for its commercialization. Perovskite solar cells (PSCs) boast several benefits, including their lightweight nature, adjustable bandgap of the sensitizer material, ease of production, and scalability. However, despite their potential, they are still in the early stages of industrialization compared to other solar technologies. A significant challenge is that efficient PSCs often use gold (Au) as an electrode, which adds to the cost of the devices. Finding a low-cost alternative for the electrode could mitigate

this issue. Additionally, most top-performing PSCs are based on lead (Pb), which introduces concerns about toxicity. Efforts are underway to find non-toxic alternatives to Pb, yet no Pb-free PSC has surpassed the performance of Pb-based counterparts so far. The scientific community continues to explore alternatives to eliminate the toxicity issue. Substances like Sn, Rb, Ge, Bi, and antimony (Sb) have been identified as potential candidates for creating toxin free metal halide perovskite materials. Among these, Sn has shown the most promising performance in PSCs. However the Sn based PSC were not able to attain the efficiency and stability of Pb based PSCs. This may be due to oxidation of Sn and also poor band matching between the perovskite, ETL and HTL. Nishimura et al., addressed this problem by partially substituting formamidium ion with ethyl ammonium ion which enhances the photo conversion efficiency of the PSC to 13%. Min et al., took a completely different approach where an interface layer was introduced between the ETL and the Perovskite layer which eliminated the need of surface passivation. With this modification, the PSC attained an efficiency of 25.5% with retention of 90% efficiency even after 500 h.

1.2 Structure of the Perovskites:

The organic-inorganic lead iodide perovskite material has a general formula of ABX_3 . In this, the cations "A" and "B" are occupied at the cubic and octahedral sites, respectively, where X can be any of the following: oxygen, carbon, nitrogen, or halogen. The cation 'A' is placed at cubic octahedral site and the cation B is occupied at the octahedral site, where (X = oxygen or halogen).

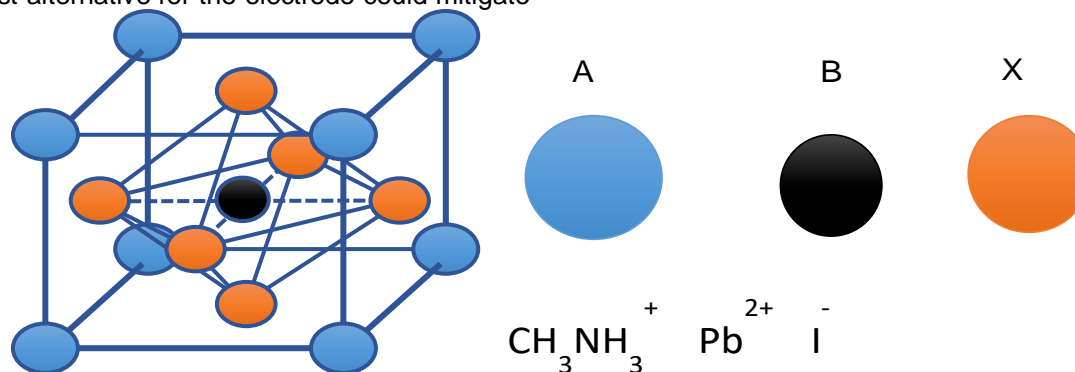


Figure 1: Structure of MAPbI_3

Thus the charge neutrality is achieved by the monovalent A and divalent B cations through the perovskite holding halogen anions. Methyl Ammonium lead iodide (MAPbI_3) has extraordinary optical and electronic characteristics (Baikie et al., 2013) where the band gap is 1.58 eV and an absorption which starts from 800 nm and is having

high absorption coefficient. The MAPbI_3 has low binding energy of 50 meV which results in easy generation of the excitons even at room temperature (Ponseca et al., 2015). Therefore, the excitons which are generated exhibit a display of small masses bringing about high transporter mobilities of $27 \pm 7 \text{ cm}^2 \text{ V}^{-1}\text{s}^{-1}$ for electrons and

$105 \pm 3 \text{ cm}^2 \text{ V}^{-1} \text{ s}^{-1}$ for holes. In addition excitons produced have a long diffusion length around 100 nm to 1000 nm. (Dong et al., 2015, Assadi et al., 2018).

2. SCALABLE TECHNIQUES FOR THE PSC

2.1. Vacuum Deposition:

In the year 1999, Mitzi et al., were the first one to use vacuum deposition in which organic inorganic compounds were deposited on a substrate. This technique controls the film composition and thickness giving high reproducibility. Snaith et al., used this technique to deposit MAPbI_3 to obtain excellent uniformity of the film, thus obtained an efficiency of 15% (Liu et al., 2013). The previous works suggests that the

perovskite film deposited with the help of vapour deposition method give considerably improved efficiency. Since this technique is free from any toxic solvent therefore it still holds its importance in the field even though the process is expensive (Fig. 2 A). Recent advancements in vacuum deposition techniques have significantly benefited the development of perovskite materials, including those with mixed halides (Longo et al., 2018), low bandgap properties (Iguar-Muñoz et al., 2020), and formamidinium-based PSCs (Chiang et al., 2020; Feng et al., 2021). Notably, a peak efficiency of 21.32% was achieved in small-size cells (Feng et al., 2021), and 18.13% efficiency was reported for mini-modules with 21 cm^2 as an effective device area (Li J. et al., 2020).

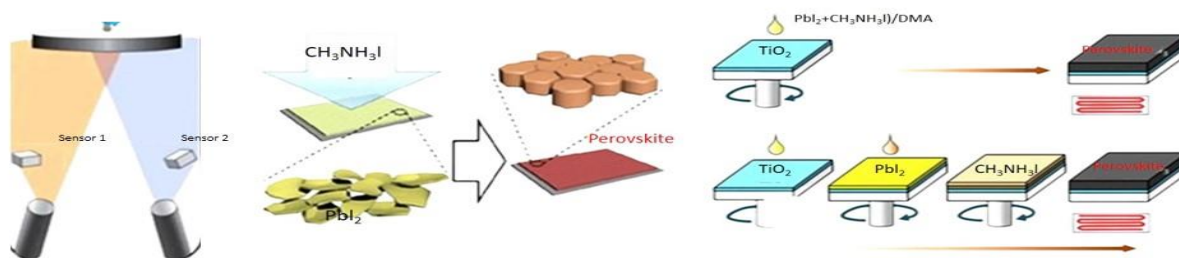


Figure 2. (A) Vacuum Deposition of Perovskite material (B) Vapour Deposition of perovskite material. (C) Deposition methods (One step and two step) of perovskite material.

2.2. One step deposition

The one step deposition method is a solution processed method which is favourably used for the deposition of perovskite layer on the substrate. In this method the precursor is prepared by mixing Methyl ammonium iodide (MAI) and lead iodide (PbI_2) in N,N-Dimethyl formamide (DMF) with continuous stirring at 60°C for 6 hours. The prepared solution is spin coated on the substrate to obtain a uniform thickness (Fig. 2C). The Perovskite layer coated is then kept on the hot plate for 30 minutes at 70°C to evaporate the solvent. This method is simple to be conducted in laboratory. However, in order to obtain compact and pinhole free perovskite layer, this process is followed by applying the antisolvent on the functional layer. The antisolvents generally used are toluene (Jeon et al., 2014), chlorobenzene (Bi et al., 2016) and diethyl ether (Gao et al., 2018), fullerene (Wu et al., 2016). Some researchers have reported that polymer dissolved in antisolvents reduce the trap sites and non radiative recombination loss (Quin et al., 2018).

2.3. Two Step deposition Method

This method is also a very commonly used for deposition of perovskite materials to ease the reproducibility process. In this method, at first the

substrate is coated with PbI_2 solution through spin coating and then MAI solution is coated on it. In another process of two step deposition, the MAI is applied by dip coating on the PbI_2 coated substrate for 20 Sec. The two step deposition method has a better film morphology and give more efficient PSCs as compared to one step deposition method (Srivastava et al., 2021) (Fig. 2 C). However this process has a limitation of conversion of PbI_2 to Perovskite, thus leading to poor efficiency and stability of the PSC (Chiang et al., 2017; Xu et al., 2019). These unconverted PbI_2 often lead to the degradation of the PSC and also impedes the carrier transportation. (Jiang et al., 2016).

2.4. Vapour Assisted Deposition Method

As compared to other processes the vapour deposited perovskite film demonstrate a superior uniformity and thus resulting in better performance of the solar cell (fig 2 B). One clear benefit of using vapor deposition compared to solution processing is the capability to create multi-layered thin films across extensive surfaces. Vapor deposition is an established method employed in various sectors, including the glazing, liquid-crystal display, and thin-film solar cell industries. This technique enables the precise optimization of electronic contacts at interfaces by applying multilayers that have specific doping levels, as seen in the

crystalline silicon 'heterojunction with thin intrinsic layer' solar cells and in thin-film solar cells. Furthermore, this method is also applied in the development of organic light-emitting diodes. One of the studies uses vapour deposition of PbI_2 followed by blade coating of perovskite solution. This method avoids the use of toxic solvents and also is efficiently applicable for large area PSCs (Zhang et al., 2024). In addition, the interface recombination and regulated of perovskite crystallization is achieved by introduction of urea additives.

Not only the deposition of the perovskite layer affects the efficiency of the PSC but also the process applied for the deposition of other functional layers such as HTM and Electron transport layer affects the performance of the cell. In one of the recent study the performance of the solar cell is enhanced and also the cost of fabrication is reduced by depositing thin TiO_2 films (ETL) by sputtering method without thermal at ambient temperature. When compared to thermally sintered TiO_2 films, the sputtered films showed advantages in carrier concentration, electron mobility, and hole-blocking capabilities along with well-matched band alignment and defect reduction with appropriate UV treatment (Yoo et al., 2024). There are certain other wide band gap materials

which are used as ETL other than TiO_2 such as ZnO and SnO_2 . In one of the studies, the ETL SnO_2 is modified by adding non-ionic polymeric polyacrylamide (PAM) which prevents the formation of clusters in the SnO_2 layer that improves the efficiency by reaching a PCE of 21.61% (Chen et al., 2024).

3. SANDWICHED STRUCTURED PEROVSKITE SOLAR CELLS

There has been a number of works in the area of sandwich structured PSCs. At first Park et al., worked on the sandwich based perovskite solar cells on the same structure as the DSSC only the Dye was replaced by perovskite sensitizer. Using this sensitization concept the PCE obtained was 9.7% , photocurrent density (J_{sc}) of 17.6 mA/cm^2 , and open-circuit voltage (V_{oc}) of 888 mV (Naam Gyu Park, 2015). In this type of structure the hole transport material was infiltrated inside the mesoporous oxide layer. In another work by (Rahul et al., 2017) the sandwich structured perovskite solar cells were fabricated at room temperature without the HTM, in the presence of solid polymer electrolyte. The flow chart and mechanism of the sandwich structured perovskite solar cell used in the present work is demonstrated as under in figure 3.

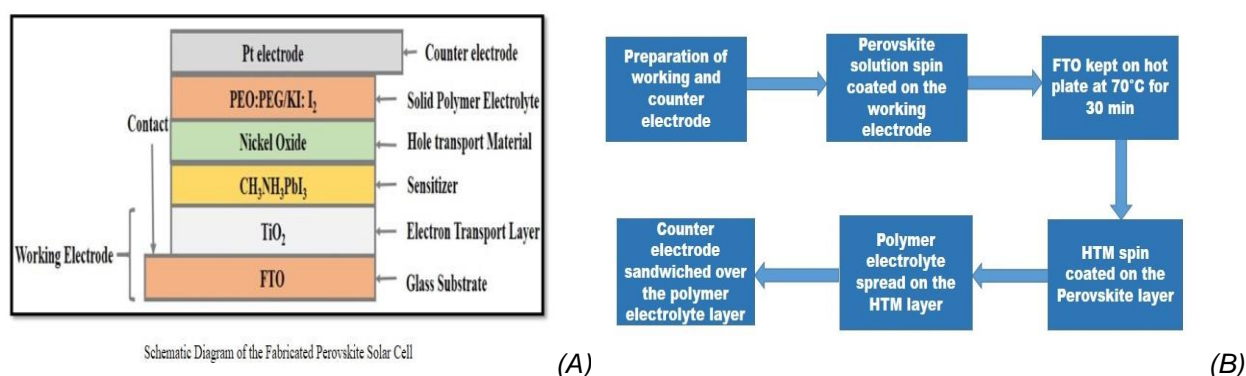


Figure 3. (A) Flowchart and (B) schematic diagram of Sandwich structured Perovskite solar cell

As shown in the figure 3, the fabrication of the perovskite solar cell, requires a working electrode and a counter electrode, blocking layer, electron transport layer, hole transport layer, PEO:PEG based solid polymer electrolyte and the perovskite material. As we know the working of a solar cell is based on three basic phenomenon i.e. charge generation, charge separation and charge collection. In the case of perovskite solar cell charge generation is absorption coefficient (Assadi et al., 2018), it absorbs the radiations, its bound electrons in highest occupied molecular orbital (HOMO) absorb this energy and move to the lowest unoccupied molecular orbital (LUMO) of the

perovskite cell. The electron transport layer, in the present research work specifically TiO_2 . The photo-excited electrons produced in this process are injected in the conduction band of electron transport layer TiO_2 which is referred to as charge separation process. The same procedure follows for the holes which are created in the HOMO of the perovskite layer, similarly through the HTM the holes are separated and transported further. The photo-injected electrons are transported through the porous TiO_2 and holes are transported through the HTM (organic or inorganic) and they get eventually collected on FTO and transported through the outer circuit to give photo current. The

role of solid polymer electrolyte is also very crucial in the sandwich structured solar cells as they aid in efficient charge transfer to the respective electrode. They also acts as a means to regenerate the sensitizer material (Srivastava et al.,2022). They also contribute in having a better contact between the hole transport material and the platinum electrode especially in the sandwich structured solar cell.

3.1. Synthesis of Processes involved in the PSC

3.1.1. Material Synthesis

For the preparation of hybrid organic inorganic lead based perovskite material MAPbI_3 , we first prepare methyl ammonium iodide (MAI) by mixing 20 ml HI and 20 ml Methylamine in a round bottom flask under ice bath treatment (Srivastava et al., 2021) for two hours. The solution prepared is kept in vacuum oven at 60°C for 24 hours. The yellow color precipitate is washed thoroughly with diethyl ether until a white colour precipitate is formed. Once MAI is prepared, it is mixed with an equal molar ratio of 1:1 with PbI_2 in N, N-Dimethyl Formamide (DMF) and stirred continuously for 6 hours at 60°C to obtain a yellow colour perovskite (MAPbI_3) solution.

3.1.2. Preparation of working and the counter electrode

The Working (WE) and counter electrode (CE) are two crucial parts of the PSC for its laboratory scale preparation. For this, we take the FTOs of size of $1.5 \times 1.5 \text{ cm}^2$, for cleaning of FTOs, they are sonicated in water and then in Acetone for three hours respectively. For WE, the FTO is coated with blocking layer (BL) Ti(IV) bis(ethyl acetoacetato)-diisopropoxide solution (2 wt% in 1-butanol) is applied and by the spin coating method it is evenly spread over the surface of glass substrate (leaving contact area with help of a scotch tape) and annealed at 500°C for 30 min in a muffle furnace (Xu et al., 2016, El Henawey et al., 2016). After this blocking layer coated with FTO, is covered with two layers of scotch tape at both ends, then porous TiO_2 is applied to it by the Doctor Blading method. After applying TiO_2 , the FTO is sintered at 500°C for 30 min. A porous TiO_2 film of $10 \mu\text{m}$ with pore diameter of 10-15 nm is obtained because of the sintering process. For the counter electrode the solar cell is prepared by spin coating then sintering at 500°C of a thin layer of H_2PtCl_6 on another piece of FTO-coated glass substrate (Yang et al. 2015). The polymer electrolyte which is specifically used in the present research work is the solid polymer electrolyte, which is prepared by dissolving

polyethylene oxide (PEO) and polyethylene glycol (PEG) and the redox couple i.e., 10% KI and I_2 (10% of KI) in 5 ml of acetonitrile. The solution is stirred continuously for 3-4 days until a homogeneous solution is prepared.

3.2. Fabrication Process:

3.2.1. Fabrication of the PSC

The fabrication of the PSC includes the following essential components: first is the Fluorine doped Tin oxide (FTO) coated glass substrate. Second, porous, nanocrystalline semiconducting TiO_2 for working electrode, third is the coating of MAPbI_3 perovskite sensitizer, fourth is the hole transport material (HTM), fifth is a secondary component i.e. polymer electrolyte and sixth is (H_2PtCl_6) platinum coated counter electrode. The method to prepare the working and the counter electrode has already been discussed in the previous section. The MAPbI_3 perovskite material and the inorganic HTMs have been synthesised in the laboratory. The perovskite solution is deposited through spin coating on the mesoporous layer of TiO_2 on the glass substrate and is then placed on hot plate for 30 min at 70°C . The HTM is then drop casted on the perovskite layer. The final step of fabrication consists of sandwiching the counter electrode on the working electrode (fig. 3 B).

4. RESULT AND DISCUSSION

4.1. MAPbI_3 based Perovskite Solar Cell

When the $\text{CH}_3\text{NH}_3\text{PbI}_3$ sample is examined in daylight, a yellow colour solution is visible. Under UV light at a shorter wavelength (254 nm), the same solution emits a green colour (Fig. 4) radiation, which corresponds to 550 nanometers, in value. It indicates that photons absorb light at shorter wavelengths and radiate at longer wavelengths. This implies the presence of fluorescence in the perovskite material. The absorbance curve shows that there is a slight peak at 530 nm, which is followed by a sharp rise in the curve. The band gap energy E_g , according to the figure, 4 (b) is 2.78 eV. The surface morphology of the perovskite surface is described by SEM analysis of a thin film of the material on a glass sheet. Figure. The SEM image of the $\text{CH}_3\text{NH}_3\text{PbI}_3$ thin film is shown in Figure 4(d) below, which also features flowery islands with a rod-like structure. These features demonstrate the crystalline behavior of methyl ammonium lead iodide-based perovskites, as suggested by their structural description. It establishes the porous nature of the perovskite film when magnified to a higher degree.

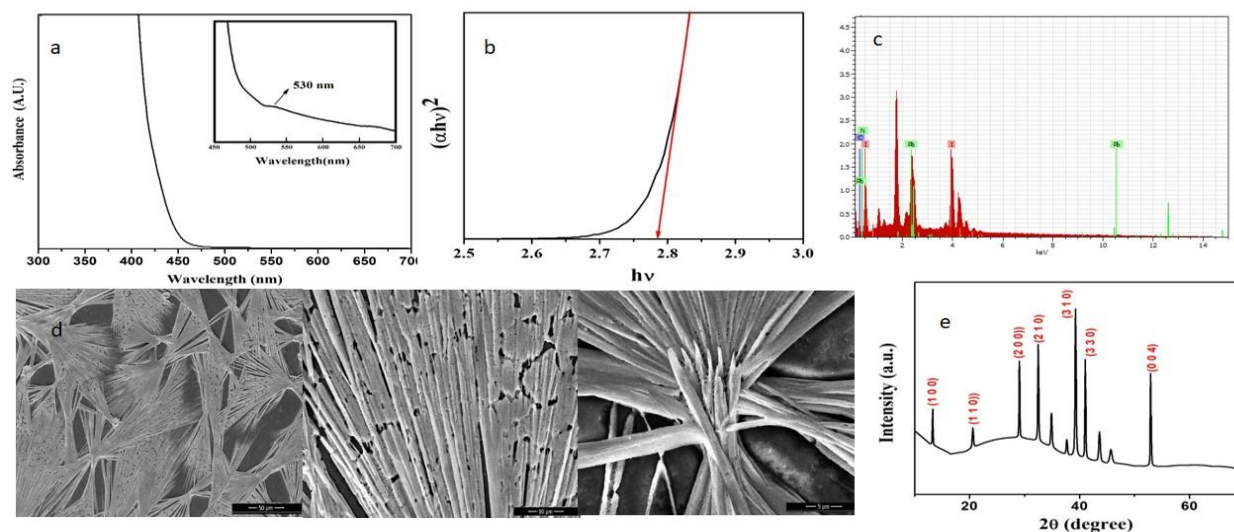


Figure 4. (a) UV absorbance curve of MAPbI_3 (b) Tauc's plot of MAPbI_3 (c) EDX Analysis of MAPbI_3 (d) SEM images of MAPbI_3 (e) XRD of MAPbI_3

This makes it more likely for HTM to permeate the perovskite material and improve the interface. The MAPbI_3 rod-shaped structures, as demonstrated, are advantageous for effective charge transfer applications and superior light harvesting because these rods can actually absorb both the surrounding wave and the portion of a wave that is incident directly on them. According to earlier research, the perovskite solution coated on FTO using the spin coating method has a rod-shaped structure, which means that the FTO substrate is not completely covered. This is explained by the fact that methyl ammonium iodide and lead iodide have different solubilities (Ahn et al., 2015; Park Naam Gyu (2016)). Due to the variance in crystal growth rate caused by the evaporation of the solvent DMF and the high solubility of MAI and low solubility of lead iodide, this can occasionally result in poor morphology. The perovskite EDX image, as shown in . Figure 4(c), amply demonstrates the presence of each component i. E. , lead (Pb), nitrogen (N), carbon (c), and iodine (I). However, the fact that DMF was used as the solvent for the perovskite material also indicates the presence of oxygen. The elemental composition of perovskite contains oxygen due to the fact that DMF has a boiling point of 153 °C and can be heated to 70 °C when spin-coated. The methyl ammonium lead iodide structural characteristics are determined by the XRD measurements (Fig. 4 e). Using Scherer's formula and the XRD pattern, the crystallite size was determined to be 45.82 nm. Significant peaks are visible in the perovskite material's XRD pattern at

13.26°, 20.56°, 29.03°, 32.45°, 39.25°, 41.05°, and 52.91°. These peaks are in close agreement with peaks previously reported (Rajamanickam et al. 2016.). These 2θ values represent (1 0 0), (1 1 0), (2 0 0), (2 1 0), (3 1 0), (3 3 0), and (0 0 4), in that order. This suggests that MAPbI_3 has a cubical structure. Nevertheless, it also implies that the perovskite material undergoes a phase transition from a tetragonal to a cubic crystal structure at 330.4 K, or roughly 67°C (Baikie et al. 2013, as the perovskite solution is heated to 70°C after being spin coated on the FTO, potentially resulting in a phase transition in the perovskites. In the XRD pattern, a hump that ranges from 2θ= 20° to 2θ= 35° is clearly visible.

4.2. PSC using organic Hole transport Material

Numerous studies have been conducted on the production of PSC with organic hole transport materials. Hole transporting materials (HTMs) are primarily used in devices to make it easier for holes to gather and move after being injected from the light harvester. This helps to ensure that electrons and holes are effectively separated. For perovskite solar cells (PSCs) to function properly, this procedure is essential. HTMs need to possess specific qualities in order to achieve high-performing PSCs. These qualities include: (1) proper HOMO levels that align with the valence band energy (VBE) of perovskite materials, which is essential for hole injection and transport across different interfaces; (2) notable hole mobility and resistance to photochemical degradation; and (3) the capacity to dissolve well in organic solvents.

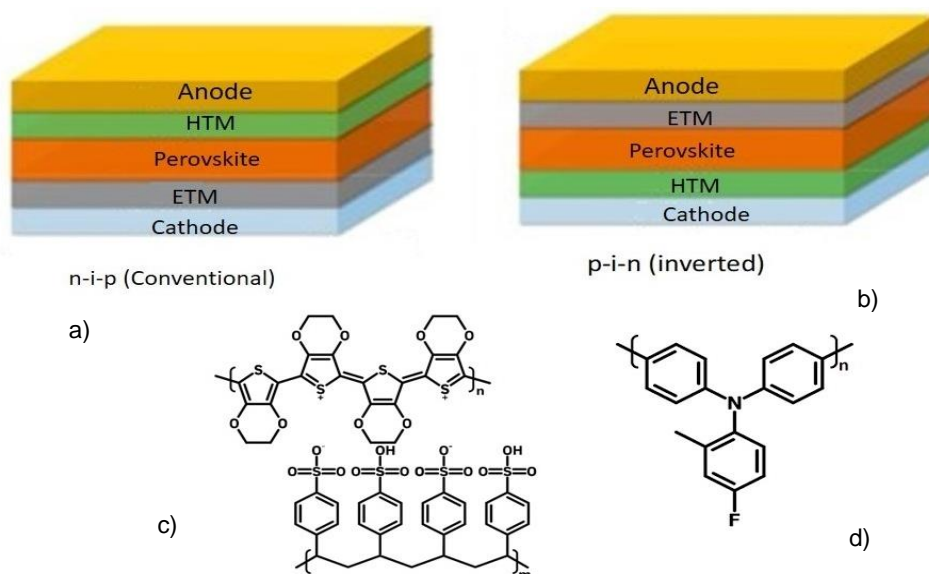


Figure 5. Solid-state perovskite solar cells typically have two device structures as shown in: (a) an inverted planar heterojunction structure and (b) a conventional planar heterojunction structure (c) Widely used organic HTMs have molecular structures as shown in figure 5. (Fu et al., 2022)

As of now 2,2',7,7'-Tetrakis[N,N-di(4-methoxyphenyl) amino]-9,9'-spirobifluorene (spiro-OMeTAD) is recognized as one of the most effective HTMs in perovskite solar cells (PSCs) due to its fulfilment of many previously mentioned criteria. Historically, Spiro-OMeTAD has been employed as a functional transport material in both light emitting diodes and dye-sensitized solar cells, with extensive efforts made towards optimizing its composition and characteristics. Despite its advantages, the high cost of Spiro-OMeTAD, attributed to its complex synthesis process, the need for costly sublimation steps, and the use of toxic and corrosive chemicals, significantly hampers its potential for widespread application in the future (Fu et al., 2022). Currently, 2,2',7,7'-Tetrakis[N,N-di(4-methoxyphenyl) amino]-9,9'-spirobifluorene (spiro-OMeTAD) stands out as a highly efficient HTM in perovskite solar cells (PSCs), meeting many of the essential requirements previously described. In the past, spiro-OMeTAD has served as an effective transport material in technologies such as light emitting diodes and dye-sensitized solar cells, with significant optimization of its formula and properties undertaken. However, its widespread adoption is hindered by the prohibitive cost, roughly 500 euros per gram, which is a consequence of its complicated production process, expensive sublimation procedures, and the employment of hazardous and corrosive substances.

4.3. Perovskite Solar Cells performance with PEDOT:PSS as HTM

To fabricate the perovskite layer, two separate solutions were prepared. Initially, a solution of PbI_2 in DMF with a density of 462 mg/mL was made,

alongside a solution of $\text{CH}_3\text{NH}_3\text{I}$ in isopropanol at a density of 10 mg/mL. The PbI_2 solution was then applied to the working electrode by spin-coating at a speed of 1000 rpm for a duration of 60 seconds. Following this, the FTO glass coated with the yellow PbI_2 film was dipped into the $\text{CH}_3\text{NH}_3\text{I}$ solution for 20 seconds, which changed its color to dark brown. Afterwards, this FTO glass, now coated with the perovskite film, was heated at 70°C for 30 minutes on a hot plate.

Then, 20 mL of PEDOT:PSS, which acts as an efficient hole transport material, was deposited on the perovskite film using the drop-casting method. The counter electrode was produced by applying an H_2PtCl_6 solution to a separate piece of FTO glass via spin-coating, followed by annealing it at 500°C for 30 minutes. This platinum counter electrode was then positioned atop the working electrode, culminating in the creation of a sandwich structure. The assembly of this perovskite solar cell was carried out in ambient conditions, where the temperature stood at 35°C and the relative humidity at 69%.

4.4. Fabrication of PSC using Inorganic HTMs

Inorganic compounds with effective band gap compatibility, suitable conductivity have proved to be a replacement for the organic HTMs in the PSCs. One of the effective HTM is copper thiocyanate CuSCN . Qin and colleagues pioneered the use of copper thiocyanate (CuSCN) as a hole transport material (HTM) in the construction of PSCs. They observed that solar cells incorporating CuSCN as an HTM demonstrated a PCE of 12.4% under 1 sun condition, compared to 6.7%.

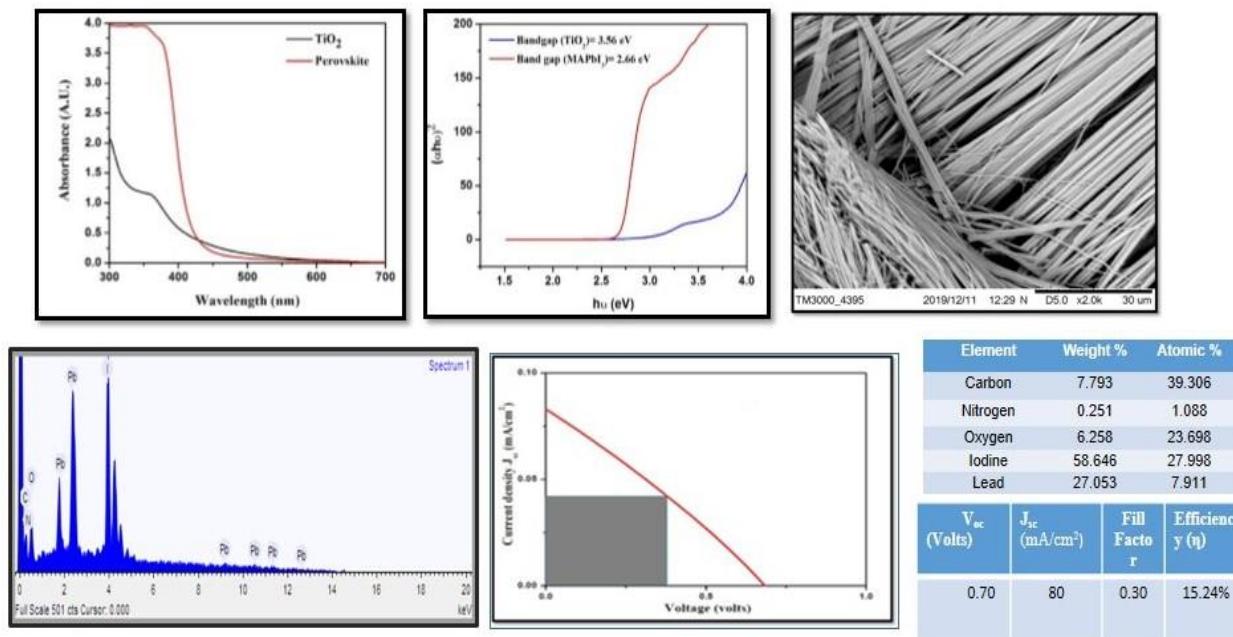


Figure 6. (A) and (B) represents the absorbance and bandgap of two step deposition of MAPbI_3 . (C) represents the EDAX of MAPbI_3 (D) PCE curve of PSC using PEDOT:PSS as HTM

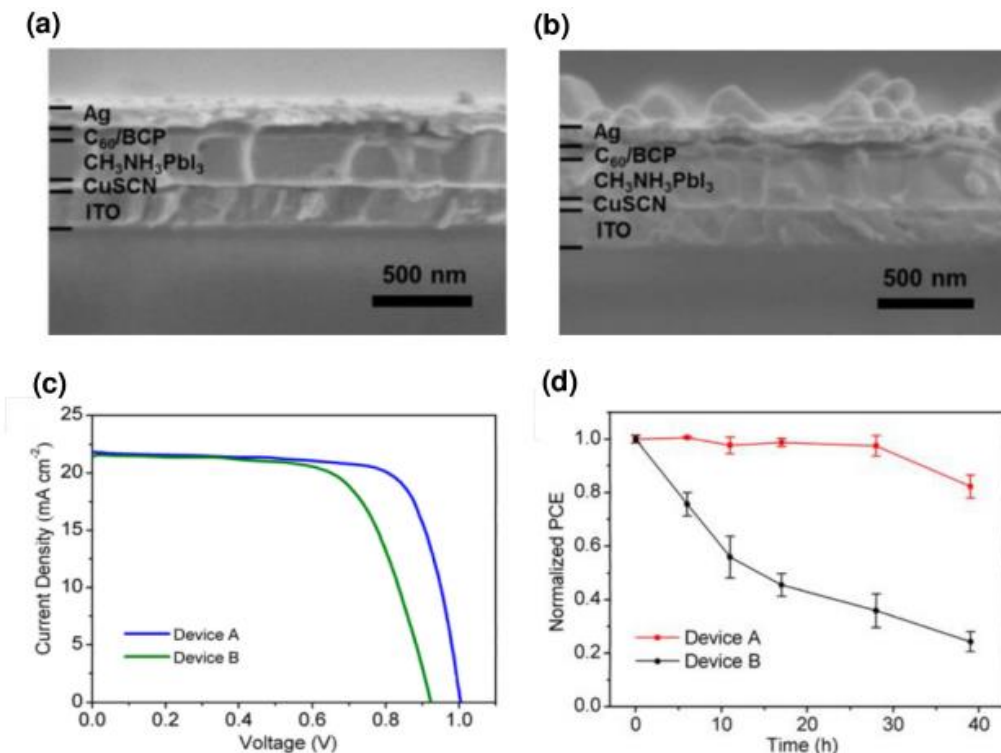


Figure 7. Cross-sectional pictures of SEM showing the PSC, with the one-step fast deposition-crystallization method (Device A) (a) and (b) two-step sequential deposition process (Device B). (c) JV characteristics of Devices A and B under AM 1.5G $100 \text{ mW}/\text{cm}^2$ simulated sunlight at a scan rate of 0.5 V s^{-1} (d) The corresponding IPCE spectra of Devices A and B. (Ye et al., 2015)

For cells without CuSCN. The incident photon-to-current efficiency (IPCE) spectra indicated that the inclusion of CuSCN HTM enhances internal

quantum efficiency, along with more effective charge injection and collection in PSCs. These findings underscore the potential of CuSCN as an

effective and affordable HTM option for PSCs. Following this, Ye and colleagues showed that inverted planar PSCs utilizing CuSCN HTM achieve a PCE of 16.6%, rivaling traditional cells that use organic hole conductors. These devices, constructed with high-quality $\text{CH}_3\text{NH}_3\text{PbI}_3$ films atop a CuSCN layer through a rapid one-step deposition-crystallization method (referred to as Device A), have smoother surfaces and less interfacial contact resistance between the perovskite layer and the selective contacts. This was in sharp contrast to films produced using a two-step sequential deposition process (referred to as Device B) (Figure 7).

Nickel oxide is another common inorganic HTM. Strong environmental stability, a broad band gap, of 5.4 eV, and a valence band (VB) that closely resembles that of perovskite are some of its distinguishing features. Because of these characteristics, NiOx can be used in place of the organic PEDOT:PSS HTMs in PSCs. The

application of a NiO interlayer as a HTM in a planar heterojunction solar cell was demonstrated by Jeng and colleagues. PCBM ([6,6]-phenyl C61-butyric acid methyl ester) was used as the electron transport layer. The PCE of this configuration was 71.8 %, which is significantly higher than 30.9 % PCE of devices that use the organic HTM PEDOT:PSS. Because of the better energy band levelling between the NiO and the perovskite light absorber, the performance is improved. Wang et al. demonstrated in a different study the efficiency of organo-metallic inverted hybrid PSCs, attaining a PCE of 9.51%. As a p-type electrode material within the PSC, this study used mesoscopic NiOx in nanocrystalline form, which improved charge transport at the NiOx/perovskite interface. With an open-circuit voltage (V_{oc}) of [6,6]-phenyl C61-butyric acid methyl ester, mesoscopic NiOx, perovskite, and PCBM (p-i-n active layer structure), the device's photovoltaic parameters were noteworthy.

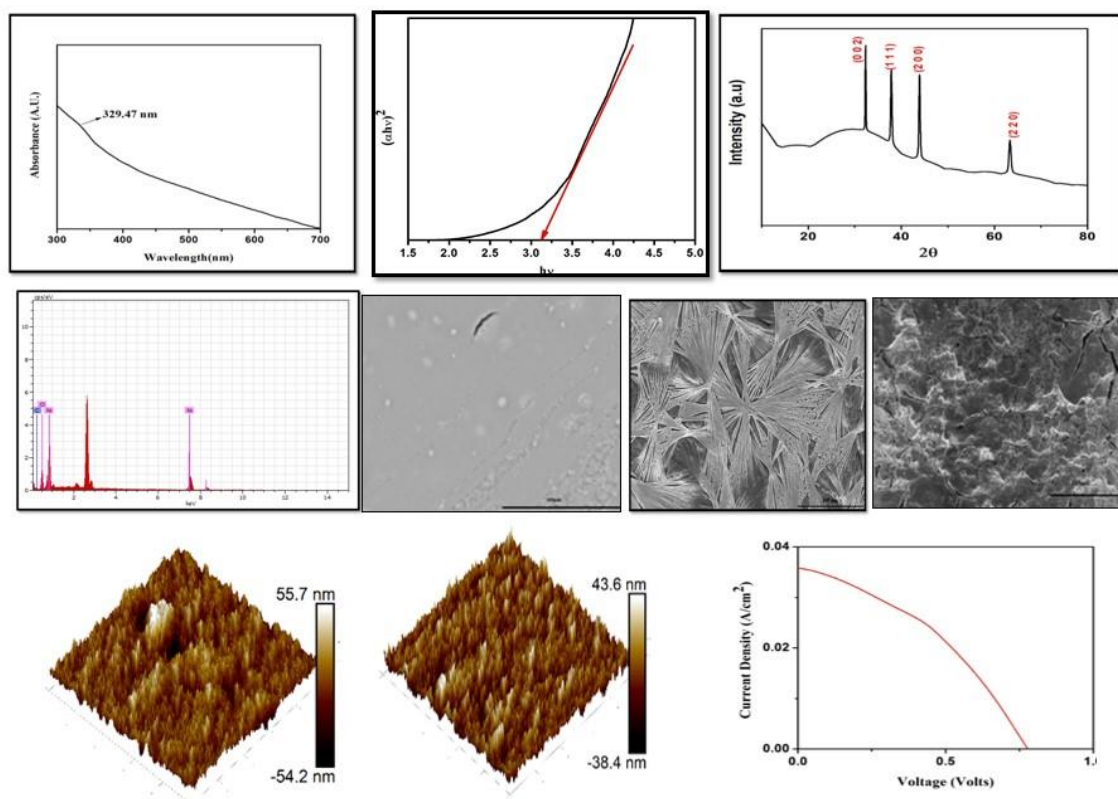


Figure 8. Representation of the various characteristics features of NiO and PCE graph

CuI stands out as a highly effective, cost-efficient, stable, wide bandgap semiconductor with notable conductivity, making it an excellent choice for use as a HTM in PSCs. Christians and colleagues engineered PSCs utilizing CuI as the HTM through a drop-casting technique, achieving a PCE of 6% alongside remarkable photocurrent stability. Through impedance spectroscopy, it was

discovered that CuI-based cells exhibit electrical conductivity that is two orders of magnitude higher than that of cells using spiro-OMeTAD as the HTM, which significantly enhances the fill factor (FF) values.

Further, stability assessments comparing CuI and spiro-OMeTAD-based solar cells revealed that CuI solar cells maintained a consistent current,

whereas the spiro-OMeTAD cells experienced a reduction in short-circuit current density (J_{sc}) by about 10%, as illustrated in This evaluation was conducted under continuous 100 mW/cm² AM 1.5G illumination for 2 hours without encapsulation in ambient conditions. One of the studies uses a sandwich configuration to study the synthesis of polymer electrolyte and hole transport material (HTM) and their application in a PSC in a standard room environment. Solution-processed spin-coating was used to assemble a planar structure made of WE/TiO₂/CH₃NH₃PbI₃/HTM/electrolyte/CE. With an open-circuit voltage (V_{oc}) of 0.63 V, a short-circuit current density (J_{sc}) of 33 mA/cm², and a fill factor of 0.65, the PSC's electrical

performance was assessed using a solar simulator. The results showed an efficiency of 13.64 percent (Figure 9). This research highlights the innovative aspect of fabricating a sandwich-structured PSC in ambient conditions with a notably high efficiency (Srivastava et al., 2023). Various research work is going on, in the field of bifacial perovskite solar cells where Cu doped NiO is used as a hole transport material. In such type of solar cells, the single walled CNTs (carbon nano tubes) are used as both front and back electrodes which offers high transparency, conductivity and stability. Such type of cells are capable of generating high power density of 36% (Zhang et al., 2024)

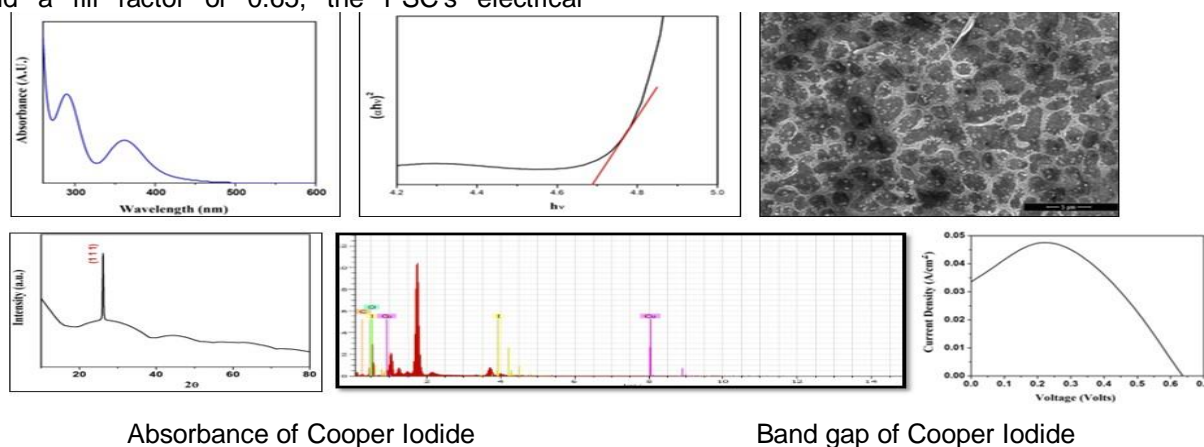


Figure 9. Representation of the various characteristics features of CuI and PCE.graph

5. CONCLUSION

This paper addresses various scalable techniques for the fabrication of various functional layers of a PSC. It also clarifies the techniques used in the deposition process plays a very crucial role in enhancing the efficiency and stability of the PSC. It signifies the fact that HTM characteristics are intimately linked to a number of variables, such as molecular stacking, energy levels, hole mobility, and film-forming capabilities. To maximize the performance of HTMs, it is imperative to thoroughly take into account the effects of a number of factors. Two of the most important PSC concerns to take into account are lowering the price of solar cells and enhancing their stability for possible uses. Inorganic HTMs that are affordable, easily synthesized, extremely stable, long-lasting, and transparent (both in the visible and near-IR range) are used in this article to address these problems. In addition, fabrication costs are less than those of organic HTMs. The highest PCE of 19 % and 16.6 % was recently recorded by copper-based inorganic HTMs such as CuO and CuSCN in PSCs. Thus, by altering the morphology of the perovskite film, mixing organic and inorganic

materials, altering the deposition processes, and changing the metal oxides, PSCs' power conversion efficiency and stability were increased. Furthermore, it was discovered that inorganic HTMs were more economically feasible than organic HTMs.

Acknowledgement

We are extremely thankful to Seed Fund (SU/SF/2023/02) provided by Sharda University to support this research.

6. REFERENCES

- [1] U.EIA (2015) Analysis of the impacts of the Clean Power Plan, US Energy Information Administration, Washington DC, pp.1-96.
- [2] M.A.McGeoch, S.H. Butchart, D. Spear, E. Marais, E. Kleyhans, A. Symes, J.Chanson, M. Hoffmann (2010) Global indicators of biological invasion: species numbers, biodiversity impact and policy responses, Diversity and Distributions, 16(1), 95-108. <http://doi/10.1111/j.1472-4642.2009.00633.x>
- [3] R.F.Service (2005) Solar energy. Is it time to shoot for the sun?, Science (New York, NY), 309(5734), 548-551. <http://doi/10.1126/science.309.5734.548>.

- [4] H. Şengül, T. L. Theis, (2011)., An environmental impact assessment of quantum dot photovoltaics (QDPV) from raw material acquisition through use. *Journal of Cleaner Production*, 19(1), 21-31. <http://doi/10.1016/j.jclepro.2010.08.010>.
- [5] M. Grätzel, (2009)., Recent advances in sensitized mesoscopic solar cells. *Accounts of chemical research*, 42(11), 1788-1798. <https://doi.org/10.1021/ar900141y>.
- [6] P.Roy, A.Ghosh, F.Barclay, A.Khare, E.Cuce (2022) Perovskite solar cells: a review of the recent advances. *Coatings*, 12(8), 1089. <https://doi.org/10.3390/coatings12081089>.
- [7] K.Nishimura, M. Amarudin, D.Hirofani, K Hamada, Q. Shen, S. Iikubo,S.Hayase (2020) Lead-free tin-halide perovskite solar cells with 13% efficiency. *Nano Energy*, 74, 104858. <https://doi.org/10.1016/j.nanoen.2020.104858>.
- [8] A. Kojima, K. Teshima, Y. Shirai, T. Miyasaka (2009) Organometal halide perovskites as visible-light sensitizers for photovoltaic cells. *Journal of the American chemical society*, 131(17), 6050-6051. <https://doi.org/10.1021/ja809598r>.
- [9] H.S. Kim, C. R. Lee, J.H. Im, K.B. Lee, T. Moehl, A. Marchioro, N. G. Park (2012) Lead iodide perovskite sensitized all-solid-state submicron thin film mesoscopic solar cell with efficiency exceeding 9%. *Scientific reports*, 2(1), 591. <http://doi/10.1038/srep00591>.
- [10] J. W. Lee, H.S. Kim, N. G. Park (2016) Lewis acid–base adduct approach for high efficiency perovskite solar cells. *Accounts of chemical research*, 49(2), 311-319. <https://doi.org/10.1021/acs.accounts.5b00440>.
- [11] T. Baikie, Y. Fang, J. M. Kadro, M. Schreyer, F. Wei, S. G. Mhaisalkar, T. White (2013) Synthesis and crystal chemistry of the hybrid perovskite (CH₃NH₃)PbI₃ for solid-state sensitised solar cell applications. *Journal of Materials Chemistry A*, 1(18), 5628-5641. doi: <https://doi.org/10.1039/C3TA10518K>.
- [12] Q. Dong, Y. Fang, Y. Shao, P. Mulligan, J. Qiu, L. Cao, J. Huang, (2015) Electron-hole diffusion lengths > 175 µm in solution-grown CH₃NH₃PbI₃ single crystals. *Science*, 347(6225), 967-970. <https://doi.org/10.1126/science.aaa5760>.
- [13] Jr. Ponceca, T.J. Savenije, M. Abdellah, K. Zheng, A. Yartsev, T. Pascher, V. Sundström (2014) Organometal halide perovskite solar cell materials rationalized: ultrafast charge generation, high and microsecond-long balanced mobilities, and slow recombination. *Journal of the American Chemical Society*, 136(14), 5189-5192. <https://doi.org/10.1021/ja412583t>.
- [14] M.K. Assadi, S. Bakhoda, R. Saidur, H. Hanaei (2018) Recent progress in perovskite solar cells. *Renewable and Sustainable Energy Reviews*, 81, 2812-2822. <https://doi.org/10.1016/j.rser.2017.06.088>
- [15] D. B. Mitzi, M.T. Prikas, K. Chondroudis (1999) Thin film deposition of organic–inorganic hybrid materials using a single source thermal ablation technique. *Chemistry of materials*, 11(3), 542-544. <https://doi.org/10.1021/cm9811139>.
- [16] M.M Lee, J. Teuscher, T. Miyasaka, T.N. Murakami, H.J. Snaith (2012) Efficient hybrid solar cells based on meso-structured organometal halide perovskites. *science*, 338(6107), 643-647. <https://doi.org/10.1021/cm9811139>
- [17] G. Longo, C. Momblona, M.G. La-Placa, L. Gil-Escrig, M. Sessolo, H. J. Bolink, (2017) Fully vacuum-processed wide band gap mixed-halide perovskite solar cells. *ACS energy letters*, 3(1), 214-219. <https://doi.org/10.1021/acseenergylett.7b01217>
- [18] A. M. Igual-Muñoz, J. Ávila, P.P. Boix, H. J. Bolink (2020) FAPb_{0.5}Sn_{0.5}I₃: A narrow bandgap perovskite synthesized through evaporation methods for solar cell applications. *Solar RRL*, 4(2), 1900283. <https://doi.org/10.1002/solr.202070024>
- [19] Y.H. Chiang, M. Anaya, S. D. Stranks (2020) Multisource vacuum deposition of methylammonium-free perovskite solar cells. *ACS Energy Letters*, 5(8), 2498-2504. <https://doi.org/10.1021/acseenergylett.0c00839>
- [20] J. Feng, Y. Jiao, H. Wang, X. Zhu, Y. Sun, M. Du, Y. Cao, D. Yang, S.F. Liu (2021) High-throughput large-area vacuum deposition for high-performance formamidinium-based perovskite solar cells, *Energy & Environmental Science*, 14(5), 3035-3043. doi: 10.1039/D1EE00656Ka.
- [21] J. Li, H. Wang, X.Y. Chin, H.A. Dewi, K. Vergeer, T.W. Goh, J.W.M. Lim, J.H. Lew, K.P. Loh, C. Soci, T.C. Sum (2020) Highly efficient thermally co-evaporated perovskite solar cells and mini-modules, *Joule*, 4(5), 1035-1053. doi: 10.1016/j.joule.2020.03.007.
- [22] P. Zhang, M. Li, W.C. Chen (2022) A perspective on perovskite solar cells: emergence, progress, and commercialization, *Frontiers in Chemistry*, 10, 802890. doi: 10.3389/fchem.2022.802890.
- [23] N.J. Jeon, J.H. Noh, Y.C. Kim, W.S. Yang, S. Ryu, S.I. Seok (2014) Solvent Engineering for High-Performance Inorganic–Organic Hybrid Perovskite Solar Cells, *Nature Materials*, 13(9), 897-903. doi: 10.1038/nmat4014.
- [24] D. Bi, C. Yi, J. Luo, J.D. Décoppet, F. Zhang, S.M. Zakeeruddin, X. Li, A. Hagfeldt, M. Grätzel (2016) Polymer-templated nucleation and crystal growth of perovskite films for solar cells with efficiency greater than 21%, *Nature Energy*, 1(10), 1-5. doi: 10.1038/nenergy.2016.189.
- [25] Y. Gao, L. Yang, F. Wang, Y. Sui, Y. Sun, M. Wei, J. Cao, H. Liu (2018) Anti-solvent surface engineering via diethyl ether to enhance the photovoltaic conversion efficiency of perovskite solar cells to 18.76%, *Superlattices and Microstructures*, 113, 761-768. <https://doi.org/10.1016/j.spmi.2017.12.014>

- [26] Y. Wu, X. Yang, W. Chen, Y. Yue, M. Cai, F. Xie, E. Bi, A. Islam, L. Han (2016) Perovskite solar cells with 18.21% efficiency and area over 1 cm² fabricated by heterojunction engineering, *Nature Energy*, 1(11), 1-7.
<https://doi.org/10.1038/nenergy.2016.215>
- [27] P.L. Qin, G. Yang, Z.W. Ren, S.H. Cheung, S.K. So, L. Chen, J. Hao, J. Hou, G. Li (2018) Stable and efficient organo-metal halide hybrid perovskite solar cells via π -conjugated Lewis base polymer induced trap passivation and charge extraction, *Advanced Materials*, 30(12), 1706126.
<https://doi.org/10.1002/adma.201706126>.
- [28] M. Srivastava, P.K. Singh, R.C. Singh (2022) Comparative study of PSCs formed by one step and sequential deposition of CH₃NH₃PbI₃ using PEDOT: PSS as HTM, *Materials Today: Proceedings*, 49, 3340-3344.
<https://doi.org/10.1016/j.matpr.2021.03.318>
- [29] C.H. Chiang, M.K. Nazeeruddin, M. Grätzel, C.G. Wu (2017) The synergistic effect of H₂O and DMF towards stable and 20% efficiency inverted perovskite solar cells, *Energy & Environmental Science*, 10(3), 808-817.
<https://doi.org/10.1039/C6EE03539H>.
- [30] X. Xu, M. Li, Y.M. Xie, Y. Ma, C. Ma, Y. Cheng, et al. (2019) Porous and Intercrossed PbI₂-CsI Nanorod Scaffold for Inverted Planar FA-Cs Mixed Cation Perovskite Solar Cells, *ACS Applied Materials & Interfaces*, 11(6), 6126-6135.
<https://doi.org/10.1021/acsami.8b21835>
- [31] Q. Jiang, L. Zhang, H. Wang, X. Yang, J. Meng, H. Liu, Z. Yin, J. Wu, X. Zhang, J. You (2016) Enhanced electron extraction using SnO₂ for high-efficiency planar-structure HC(NH₂)₂PbI₃-based perovskite solar cells, *Nature Energy*, 2(1), 1-7.
<https://doi.org/10.1038/nenergy.2016.187>
- [32] J. Zhang, X. Ji, X. Wang, L. Zhang, L. Bi, Z. Su, X. Gao, W. Zhang, L. Shi, G. Guan, A. Abudula (2024) Efficient and Stable Inverted Perovskite Solar Modules Enabled by Solid-Liquid Two-Step Film Formation, *Nano-Micro Letters*, 16, 190-190.
<https://doi.org/10.1007/s40820-023-00943-6>
- [33] Y. Yoo, G. Seo, H.J. Park, J. Kim, J. Jang, W. Cho, J.H. Kim, J. Shin, J.S. Choi, D. Lee, S.W. Baek (2024) Low-temperature rapid UV sintering of sputtered TiO₂ for flexible perovskite solar modules, *Journal of Materials Chemistry A*, 12(3), 1562-1572.
<https://doi.org/10.1039/D3TA01474A>
- [34] J. Zhang, X.G. Hu, K. Ji, S. Zhao, D. Liu, B. Li, P.X. Hou, C. Liu, L. Liu, S.D. Stranks, H.M. Cheng (2024) High-performance bifacial perovskite solar cells enabled by single-walled carbon nanotubes, *Nature Communications*, 15(1), 2245.
<https://doi.org/10.1038/s41467-024-20085-1>
- [35] N.G. Park (2015) Perovskite solar cells: an emerging photovoltaic technology, *Materials Today*, 18(2), 65-72.
<https://doi.org/10.1016/j.mattod.2014.07.007>.
- [36] P.K. Singh, R. Singh, V. Singh, S.K. Tomar, B. Bhattacharya, Z.H. Khan (2017) Effect of crystal and powder of CH₃NH₃ on the CH₃NH₃PbI₃ based perovskite sensitized solar cell, *Materials Research Bulletin*, 89, 292-296.
<https://doi.org/10.1016/j.materresbull.2016.12.018>
- [37] M. Srivastava, K. Surana, P.K. Singh, R. Ch (2021) Nickel oxide embedded with polymer electrolyte as efficient hole transport material for perovskite solar cell, *Engineered Science*, 17, 216-223.
<https://doi.org/10.30919/es8d474>
- [38] Y. Xu, L. Zhu, J. Shi, X. Xu, J. Xiao, J. Dong, H. Wu, Y. Luo, D. Li, Q. Meng (2016) The Effect of Humidity upon the Crystallization Process of Two-Step Spin-Coated Organic-Inorganic Perovskites, *ChemPhysChem*, 17(1), 112-118.
<https://doi.org/10.1002/cphc.201500928>
- [39] M.I. El-Henawy, R.S. Gebhardt, M.M. El-Tonsy, S. Chaudhary (2016) Organic solvent vapor treatment of lead iodide layers in the two-step sequential deposition of CH₃NH₃PbI₃-based perovskite solar cells, *Journal of Materials Chemistry A*, 4(5), 1947-1952.
<https://doi.org/10.1039/C5TA08032A>
- [40] N. Ahn, D.Y. Son, I.H. Jang, S.M. Kang, M. Choi, N.G. Park (2015) Highly reproducible perovskite solar cells with average efficiency of 18.3% and best efficiency of 19.7% fabricated via Lewis base adduct of lead (II) iodide, *Journal of the American Chemical Society*, 137(27), 8696-8699.
<https://doi.org/10.1021/jacs.5b04930>
- [41] N.G. Park, M. Grätzel, T. Miyasaka, K. Zhu, K. Emery (2016) Towards stable and commercially available perovskite solar cells, *Nature Energy*, 1(11), 1-8.
<https://doi.org/10.1038/nenergy.2016.139>.
- [42] N. Rajamanickam, S. Kumari, V.K. Vendra, B.W. Lavery, J. Spurgeon, T. Druffel, M.K. Sunkara (2016) Stable and durable CH₃NH₃PbI₃ perovskite solar cells at ambient conditions, *Nanotechnology*, 27(23), 235404. <https://doi.org/10.1088/0957-4484/27/23/235404>
- [43] T. Baikie, Y. Fang, J.M. Kadro, M. Schreyer, F. Wei, S.G. Mhaisalkar, M. Graetzel, T.J. White (2013) Synthesis and crystal chemistry of the hybrid perovskite (CH₃NH₃)PbI₃ for solid-state sensitised solar cell applications, *Journal of Materials Chemistry A*, 1(18), 5628-5641.
<https://doi.org/10.1039/C3TA10518K>.
- [44] S. Ye, W. Sun, Y. Li, W. Yan, H. Peng, Z. Bian, Z. Liu, C. Huang (2015) CuSCN-based inverted planar perovskite solar cell with an average PCE of 15.6%, *Nano Letters*, 15(6), 3723-3728.
<https://doi.org/10.1021/acs.nanolett.5b00683>.
- [45] J.Y. Jeng, K.C. Chen, T.Y. Chiang, P.Y. Lin, T.D. Tsai, Y.C. Chang, T.F. Guo, P. Chen, T.C. Wen, Y.J. Hsu (2014) Nickel oxide electrode interlayer in CH₃NH₃PbI₃ perovskite/PCBM planar-heterojunction hybrid solar cells, *Advanced Materials*, 26(24), 4107-4113.
<https://doi.org/10.1002/adma.201400772>

- [46] K.C. Wang, J.Y. Jeng, P.S. Shen, Y.C. Chang, E.W.G. Diau, C.H. Tsai, T.Y. Chao, H.C. Hsu, P.Y. Lin, P. Chen, T.F. Guo (2014) P-type mesoscopic nickel oxide/organometallic perovskite hetero-junction solar cells, *Scientific Reports*, 4(1), 4756. <https://doi.org/10.1038/srep04756>
- [47] Y.Yoo, G.Seo, J.H.Park, J.Kim, J.Jang, H.Cho, J.Kim, J.Shin, J.Choi,D.Lee, W.Baek (2024) Low-temperature rapid UV sintering of sputtered TiO₂ for flexible perovskite solar modules. *Journal of Materials Chemistry A*, 12(3), 1562-1572. <https://doi.org/10.1039/D3TA05666J>

IZVOD

SINTEZA I SKALABILNI PROCES ZA PROIZVODNJU PEROVSKITNIH SOLARNIH ČELIJA KORIŠĆENJEM ORGANSKIH I NEORGANSKIH MATERIJALA ZA TRANSPORT RUPA

Organsko neorganski olovni jodid perovskit materijal se pojavio kao pionir u tome da bude aktivan materijal za treću generaciju solarnih ćelija. Osim sinteze, skalabilni mehanizam koji se koristi za proces depozicije, u velikoj meri utiče na performanse ćelije zahvaljujući svom uticaju na morfologiju, ujednačenu debljinu i interfejs između dva funkcionalna sloja. Ova studija ukratko govori o različitim procesima taloženja uključenim u sastavljanje slojeva solarnih ćelija perovskita (PSC). Materijali za transport rupa (HTM) su ključni deo PSC koji obezbeđuju efikasan transport nosača punjenja. Međutim, efekat organskih i neorganskih HTM je veoma izražen u PSC. Ova studija, takođe, razmatra uticaj organskog i neorganskog HTM na stabilnost i efikasnost sendvič strukturisanog PSC.

Ključne reči: perovskit, solarna energija, PCE, materijal za transport rupa

Naučni rad

Rad primljen: 07.03.2024.

Rad korigovan: 23.05.2024.

Rad prihvaćen: 06.06.2024.

Ikhwan Syafiq Mohd Noor
Muhd Zu Azhan Yahya

<https://orcid.org/0000-0003-0983-782X>

<https://orcid.org/0000-0003-1129-0552>

Sushant Kumar^{1*}, Manoj K. Singh^{2*}, Muhd Zu Azhan Yahya³,
Ikhwan Syafiq Mohd Noor⁴, Pramod K. Singh^{1*}

¹Center for Solar Cells and Renewable Energy, School of Basic Sciences and Research, Sharda University, Greater Noida, Uttar Pradesh 201306, India, ²Energy Conversion & Storage Lab, Department of Applied Science & Humanities, Rajkiya Engineering College Banda, AKTU, Uttar Pradesh, India, ³Faculty of Defence Science and Technology, Universiti Pertahanan Nasional Malaysia (UPNM), Kuala Lumpur, Malaysia, ⁴Ionic Materials and Energy Devices Laboratory, Physics Department, Faculty of Science, Universiti Putra Malaysia, UPM Serdang, Selangor Darul Ehsan, Malaysia

Scientific Paper

ISSN 0351-9465, E-ISSN 2466-2585

<https://doi.org/10.62638/ZasMat1050>



Zastita Materijala 65 (4)
703 – 711 (2024)

Structural, Electrochemical, and Dielectric Studies of Phytigel and 1-ethyl-3-methylimidazolium Tricyanomethanide-based Bio-polymer Electrolytes

ABSTRACT

The present work is focused on the synthesis and detailed study of biopolymer phytigel and ionic liquid 1-ethyl-3-methylimidazolium tricyanomethanide (EMIm[TCM]) blended polymer electrolyte films for energy applications. Here, biopolymer phytigel-based polymeric films are synthesized with different concentrations of ionic liquid (EMIm[TCM]) using the solution cast technique. The synthesized films are characterized for their structural, electrochemical, and dielectric properties using different characterization tools i.e., XRD, FTIR, Electrochemical Impedance Spectroscopy, Linear Sweep Voltammetry, and Wagner polarization technique. The film with 30wt% EMIm[TCM] shows a maximum conductivity of $3.64 \times 10^{-4} \text{ S cm}^{-1}$ and an electrochemical stability window of 3.1 V. The dielectric properties such as dielectric constant (κ), dielectric loss tangent ($\tan\delta$), relaxation time, and frequency are also studied for the prepared pure phytigel and phytigel/EMIm[TCM] polymeric films.

Keywords: Biodegradable polymers, Phytigel, Ionic liquid, 1-ethyl-3-methylimidazolium tricyanomethanide, Polymer electrolyte

1. INTRODUCTION:

Electrochemical devices such as batteries, supercapacitors, dye-sensitized solar cells (DSSCs), etc. mostly consist of electrodes, electrolytes, and separators [1]. Electrolyte is one of the key components which is responsible for the performance of any electrochemical device [2]. Traditionally, liquid electrolytes such as H_2SO_4 , KOH, ZnCl_2 , ZnSO_4 , NaCl, etc are being used in electrochemical devices that have certain limitations such as – leakage, evaporation, bulky design, etc. which affect the performance of the devices [3, 4]. To overcome such limitations, polymer electrolytes can be taken into consideration. Polymer electrolytes are mostly containing a host polymer, ionic

species (salts, ionic liquids, fillers, etc.), and a plasticizer [5–7]. Based on their origin, polymers can be divided into two types i.e., synthetic polymers and natural polymers. Most of the research is done on polymer electrolytes based on synthetic polymers like – PVDF-HFP, PEO, PMMA, PEMA, etc. which are made up of petroleum resources and take a lot of time to degrade [8]. Taking this limitation of synthetic polymers into consideration, natural bio-degradable polymers such as corn starch, agarose, phytigel, etc. become a new interest for researchers [9]. Biopolymers are environment friendly and abundant in nature that is why a lot of research is going on to develop solid or gel polymer electrolytes using natural polymers as a host material. The biopolymer-based electrolytes which are doped with only salts show less ionic conductivity, mostly in the order of $\sim 10^{-5} \text{ S cm}^{-1}$ [10]. To increase the ionic conductivity of the biopolymer-based electrolytes certain approaches can be followed such as making blends or composites, doping of fillers or

* Corresponding authors: pramodkumar.singh@sharda.ac.in (PKS); mksingh@recbanda.ac.in (MKS); thekumar-sushant@gmail.com (SK)

Paper received: 30.03.2024.

Paper accepted: 5.06.2024.

nanofillers, co-polymerization, or using ionic liquids as ionic species in polymers, etc [10–14]. Ionic liquids are the salt that have a low vapor pressure and they are non-flammable in nature. Mostly ionic liquids are present in molten state at temperatures less than 100°C [15]. Along with high ionic conductivity they possess high chemical and electrochemical stability [16]. Ionic liquids behave as ionic species as well as a plasticizer [17]. Various biopolymers have been used as a host-polymer for the preparation of a bio-polymer-based polymer electrolyte such as arrowroot [18], corn starch [19], chitosan [20], agar-agar [21], carrageenan [22], gellan gum [23], pectin [24], methyl cellulose [25], etc. In the present study, a biopolymer phytigel is chosen as a host polymer because of its low cost, environment-friendly and non-hazardous nature, thermal resistance, easy chemical modifications, and ability to form films [26]. Ionic liquid- 1-ethyl-3-methylimidazoliumtricyanomethanide (EMIm[TCM]) has been used as an ionic species as well as a plasticizer to increase the ionic conductivity of the polymeric film. The polymer electrolyte films are synthesized by blending phytigel with different weight percentages of EMIm[TCM] and then characterized for structural, optical, and electrochemical properties using different characterization tools such as X-ray diffractometer (XRD), Fourier transform infrared spectroscopy (FTIR), Electrochemical impedance spectroscopy (EIS), Linear sweep voltammetry (LSV), Wagner polarization technique (t_{ion}). Dielectric studies such as dielectric constant, dielectric loss tangent ($\tan\delta$), relaxation time and frequency, etc. are also done.

2. EXPERIMENTAL:

2.1. Preparation of polymer electrolytes.

Phytigel and Dimethyl sulfoxide (DMSO, purity $\geq 99.9\%$) are procured from Sigma-Aldrich and EMIm[TCM] is procured from Tokyo Chemical Industry Co. Ltd. First, host biopolymer phytigel (200 mg) is dissolved into DMSO with constant stirring using magnetic stirrer for 12 hours at 60°C, then different weight percent of ionic liquid EMIm[TCM] is added to the solutions and again stirred for 12 hours at room temperature. After complete dissolution, all the solutions are poured into glass petri dishes and kept in a vacuum oven at 60°C until the complete evaporation of common solvent (DMSO). After the complete evaporation of the solvent, the polymeric films are peeled out from the petri dishes and stored in a vacuum for further characterization. After 40wt% con-

centration, the ionic liquid starts to come out from the polymeric films that's why the films are only synthesized with 0wt% to 40wt% blending of ionic liquid.

2.2. Instrumentation.

X-ray diffraction (XRD) patterns of the phytigel-based polymeric films were performed using XPERT-Pro X-ray diffractometer with Cu-K α radiation ($\lambda = 1.54 \text{ \AA}$) in the range from 10° to 80°. FTIR spectroscopy was performed by PerkinElmer Spectrum version 10.4.00. The electrochemical impedance spectroscopy (EIS), Linear sweep voltammetry (LSV), Wagner polarization technique, and dielectric studies of the polymeric films were carried out by using an electrochemical workstation (CHI-604D, USA).

3. RESULT AND DISCUSSION.

3.1. Structural Studies

X-ray diffraction-

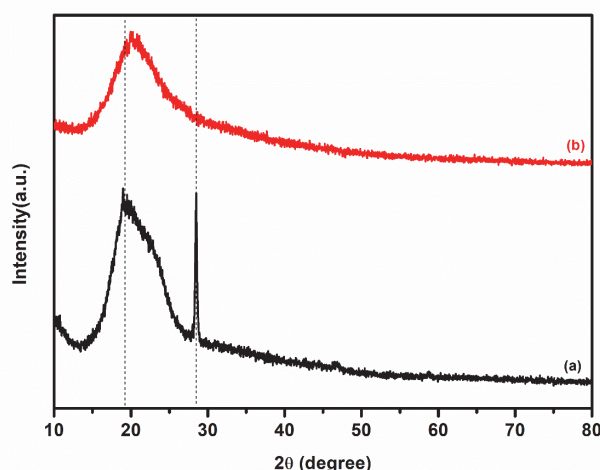


Figure 1. XRD plots of: (a) pure phytigel and (b) phytigel/30wt%EMImTCM film

To study the structural properties of the polymeric films, X-ray diffraction is performed using XPERT-Pro X-ray diffractometer with Cu-K α radiation ($\lambda = 1.54 \text{ \AA}$) in the range from 10° to 80° as shown in figure 1. The XRD patterns for pure phytigel show two predominant peaks, a broad peak at 19.14° and a sharp peak at 28.5° which indicates the semicrystalline nature of the host polymer phytigel [26]. From the XRD patterns of phytigel/EMIm[TCM] it can be seen that the sharp peak present in phytigel at 28.5° disappears and the peak at 19.14° becomes more broad which shows the decrease in the crystalline nature of phytigel on adding of EMIm[TCM] ionic liquid in it.

Fourier Transform Infrared Spectroscopy (FTIR):

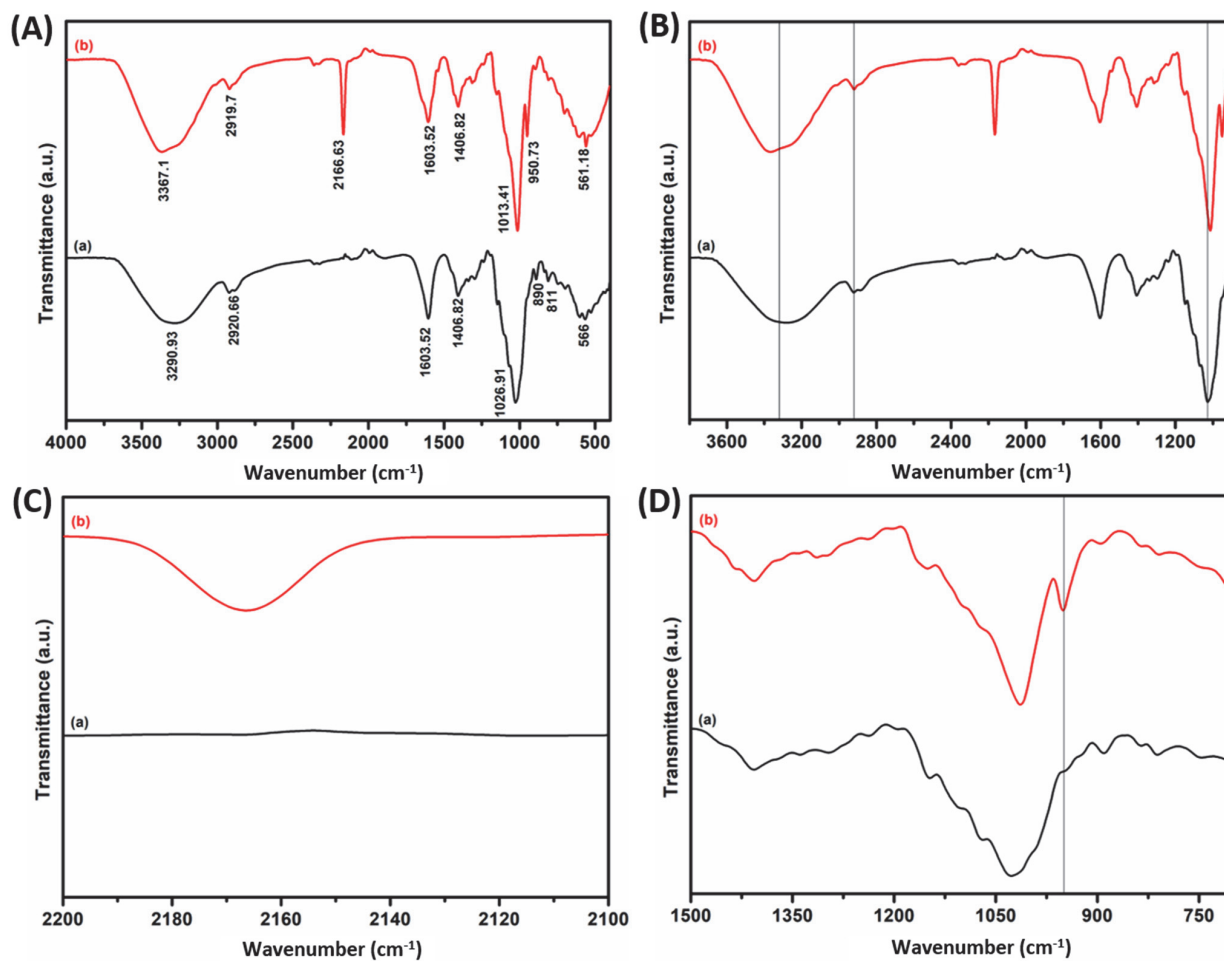


Figure 2. (A) FTIR spectra and its expanded representation in (B) 900 cm^{-1} to 3800 cm^{-1} , (C) 2100 cm^{-1} to 2200 cm^{-1} , and 800 cm^{-1} to 1500 cm^{-1} for (a) pure phytigel and (b) phytigel/30wt%EMIm[TCM]

FTIR spectroscopy has been used to determine the complexation and interaction between biopolymer and ionic liquid doped biopolymer. For this a FTIR spectroscopy of pure phytigel and maximum conducting EMIm[TCM] blended phytigel polymer films has been carried out using PerkinElmer Spectrum version 10.4.00 as shown in figure 2(a). Table 1 shows some important peaks related to host polymer phytigel and ionic liquid EMIm[TCM]. Pure phytigel shows two characteristic peaks related to O-H stretching of alcohol at 3290, 2920 cm^{-1} , also it shows two peaks representing the C=O stretching and C=C bending of alkene in phytigel at 1603 and 1026 cm^{-1} respectively and at 1406 it shows a sharp medium peak showing the C-H bending of alkanes. It can be seen from the graph that the

peaks at 3290, 2920 and 1026 cm^{-1} are shifted to 3367, 2919 and 1013 cm^{-1} in phytigel/EMIm[TCM] (figure 2B) along with this it shows two new peaks at 2166 and 950 cm^{-1} showing the C≡N of anion [C(CN)₃]⁻ and C=C bending of cation EMIm⁺ of ionic liquid respectively [28, 29] and the archetypal channel material is poly(3,4-ethylenedioxythiophene) (figure 2 C&D). These observations clearly state that almost all the FTIR peaks of host polymer phytigel are present in phytigel/EMIm[TCM] films without disappearing of any major peaks also showing presence of two significant peak related to the ionic liquid EMIm[TCM], which clearly shows the complex nature of the samples and the considerable changes occurs due to interaction of ionic liquid ions [30].

Table 1. Functional groups corresponding to the different FTIR bands present in FTIR spectra of pure phytigel and phytigel/30wt%EMIM[TCM].

	IR bands (cm ⁻¹)	Functional group (Mode of Vibration/Chemical bond)
Phytigel	3290	O-H stretching, alcohol
	2920	O-H stretching, alcohol
	1603	N-H bending, amine
	1406	C-H bending, alkane
	1026	C-N stretching, amine
EMIm⁺	1013	C=C bending, alkene
	561	Ring in-plane sym. bending
[C(CN₃)]⁻	2166	C≡N

3.2. Dielectric and Electrochemical Studies

Electrochemical Impedance Spectroscopy-

To study the electrochemical properties of prepared polymer electrolytes, electrochemical impedance spectroscopy (EIS) measurement has been done for the prepared polymeric films consisting different concentration of ionic liquid (0-40 wt%). The impedance spectroscopy of the cell: SS | Phytigel/EMImTCM | SS (SS is stainless steel electrodes) has been done in the frequency range of 100 Hz to 1 MHz. Using the EIS data, Nyquist plots are drawn for all the polymeric films with 0wt% to 40wt% ionic liquid. The Nyquist plot for phytigel/30wt%EMIm[TCM] is shown in figure 3A. Ionic conductivity for all the films has been calculated from Nyquist plot using the following equation (Eq. 1)-

$$\sigma = \frac{1}{R_b} \times \frac{t}{A} \quad (1)$$

Where, σ is ionic conductivity, R_b is bulk resistance, t is thickness of the polymeric film and A is the area of contact. The calculated ionic conductivity of pure phytigel film, ionic liquid and phytigel/EMIm[TCM] film is shown in figure 3B and listed in table 2. The ionic conductivity increases with the increase in the concentration of ionic liquid in polymeric films and it attains a maximum at 30wt% of IL and after that it starts to decrease (figure 3B). It is well known that the expression for conductivity is $\sigma = nq\mu$ where, σ is conductivity, n is number of charge carriers, q is electronic charge and μ is mobility, in present case the ionic conductivity increases because the n and μ are increasing as ionic liquid is working as an ionic species as well as plasticizer (which provides easy passes to ions). The decrease in conductivity beyond blending of 30wt% ionic liquid is may be due to the steric hindrance in between ions which causes obstacle in ionic movement on the way to the respective electrodes [31].

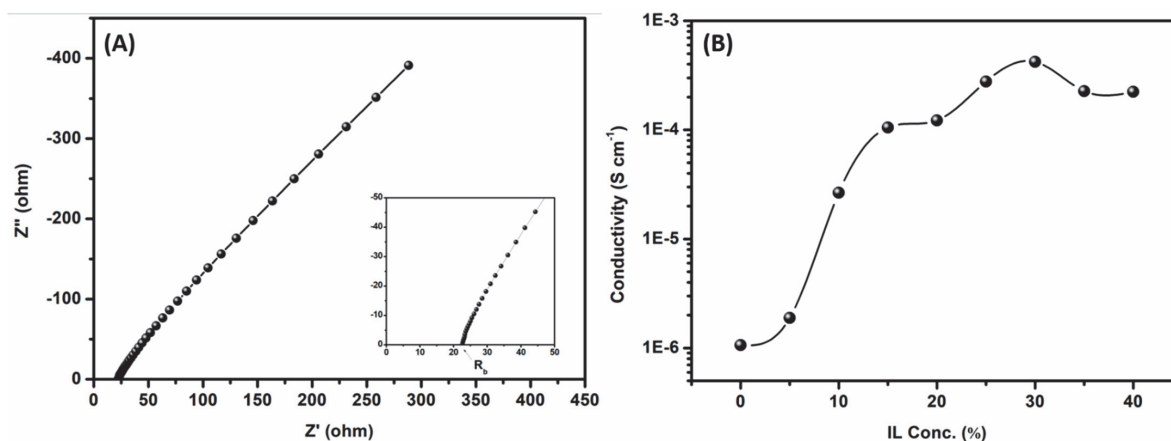


Figure 3. (A) Nyquist plot of phytigel/30wt% EMIm[TCM], (B) Ionic conductivity vs EMIm[TCM] concentration

Table 2. The ionic conductivity, Relaxation frequency, and Relaxation time corresponding to polymeric films consist of different weight percent of ionic liquid in phytigel.

Polymeric film	Ionic conductivity (S cm ⁻¹)	Relaxation frequency (f _{max} , Hz)	Relaxation time ($\tau = \frac{1}{2\pi f_{max}}$, sec)
Pure Phytigel	1.06×10^{-6}	227	7.01×10^{-4}
Phytigel/EMImTCM (5wt%)	1.88×10^{-6}	16883	9.43×10^{-6}
Phytigel/EMImTCM (10wt%)	2.65×10^{-5}	147186	1.08×10^{-6}
Phytigel/EMImTCM (15wt%)	1.05×10^{-4}	560389	2.84×10^{-7}
Phytigel/EMImTCM (20wt%)	1.22×10^{-4}	191147	8.33×10^{-7}
Phytigel/EMImTCM (25wt%)	2.77×10^{-4}	354441	4.49×10^{-7}
Phytigel/EMImTCM (30wt%)	3.64×10^{-4}	311648	5.10×10^{-7}
Phytigel/EMImTCM (35wt%)	2.26×10^{-4}	357695	4.45×10^{-7}
Phytigel/EMImTCM (40wt%)	2.23×10^{-4}	429211	3.70×10^{-7}

Dielectric studies: Dielectric studies are necessary to explore the dissipation of electric energy in various optical and electronic devices. The dielectric constant values are calculated at three different frequencies i.e., 825200, 99610, and 8301 Hz using the formula $\kappa = \frac{C}{C_0}$, where, κ is dielectric constant, C is capacitance and C_0 is the capacitance at vacuum. The variation of dielectric constant for all polymeric film with respect to different wt% of ionic liquid shown in figure 4. It can be clearly seen from figure 4 that dielectric constant is also following almost the same trend as ionic conductivity with respect to concentration of ionic liquid. The increase in dielectric constant trend with respect to increase in ionic liquid concentration is indicating that the major charge carriers in the polymer electrolyte films are ions.

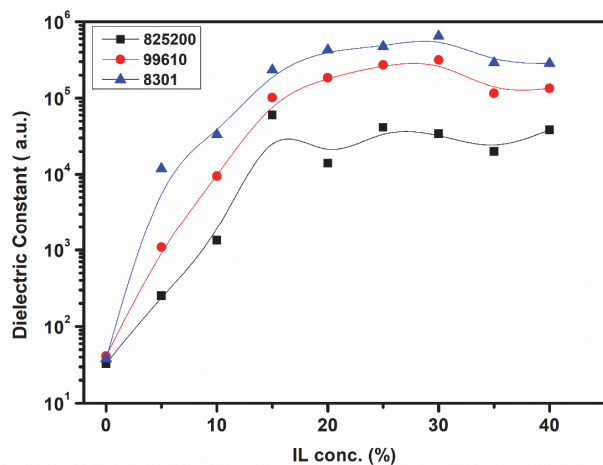


Figure 4. Variation of dielectric constant with respect to EMIm[TCM] concentration at 825200, 99610, 8301 Hz.

The complex permittivity (ϵ^*) provide a detail information about the polarized mechanism which is expressed by the following equation (Eq. 2)-

$$\epsilon^* = \epsilon' - j\epsilon'' \quad (2)$$

Where ϵ' and ϵ'' are representing the real and imaginary parts of complex permittivity, which is expressed by Eq. (3 & 4)

$$\epsilon' = \frac{-Z''}{\omega C_0(Z'^2 + Z''^2)} \quad (3) \quad \text{and} \quad \epsilon'' = \frac{-Z'}{\omega C_0(Z'^2 + Z''^2)} \quad (4)$$

Where, z' and z'' are the real and imaginary part of impedance, $\omega = 2\pi f$ is the angular frequency, $C_0 = (\epsilon_0 A/t)$, A is cross-section area, t is the thickness of polymer electrolytes. Figure 5 represents the variation of ϵ' and ϵ'' with frequency for polymeric films with ionic liquid concentration of 0wt% to 40wt%. Figure 5 A&B reveals that ϵ' and ϵ'' has high values at lower frequencies, which may be due to the alignment of dipoles with applied field and accumulation of charges near blocking electrode-electrolyte interface (space charge effect). The ϵ' and ϵ'' starts to decrease with increasing in frequency, since the dipoles are not able to align with the rapid changing of applied AC field also, with the increasing frequency the diffusion of ions does not take place at available sites [32]. The value for ϵ' and ϵ'' is also vary with different concentration of EMIm[TCM], the highest value for ϵ' and ϵ'' is comes out for the polymer electrolyte film with 30wt% of EMIm[TCM]. It may be because of the increase in charge carriers and mobility of ions with increase in concentration of ionic liquid.

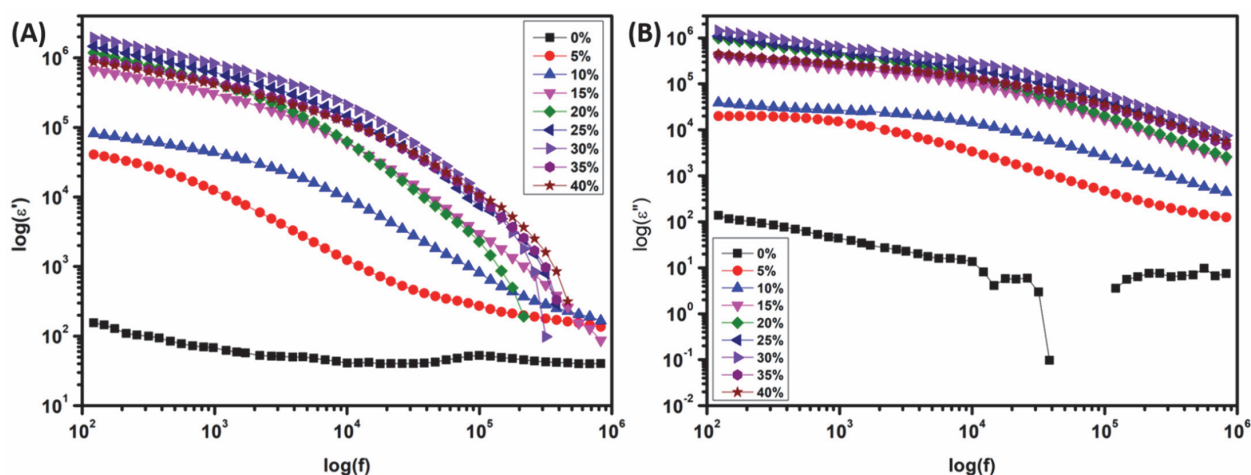


Figure 5. Variation of ϵ' and ϵ'' with respect to frequency for all polymeric films.

Dielectric loss or loss tangent is also calculated for the polymeric films which is represented by $\tan(\delta)$ and expressed mathematically as (Eq. 5)-

$$\tan(\delta) = \frac{\epsilon''}{\epsilon'} \quad (5)$$

Where, ϵ' and ϵ'' are real and imaginary part of dielectric constant. The variation of $\tan(\delta)$ with frequency for all prepared polymeric films is shown in figure 6. The loss tangent ($\tan(\delta)$) decreases with the increasing frequency and attains a maximum point at certain frequency known as relaxation frequency, in the presence of restful dipoles and again starts to decrease. Relaxation time (τ), which is reciprocal of relaxation frequency is also calculated for the phytigel and phytigel/EMIm[TCM] polymer films, which are listed in table 2. The phytigel based films consisting of ionic liquid more than 10% are showing relaxation time in the order of 10^{-7} seconds which shows the fast ionic movement in them.

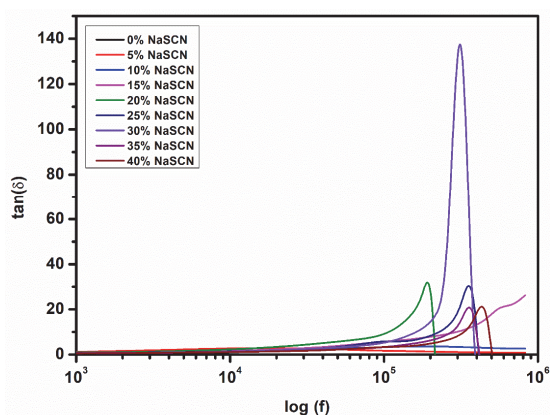


Figure 6. Variation of dielectric loss ($\tan \delta$) with respect to frequency for pure phytigel and EMIm[TCM] blended phytigel films.

Linear Sweep Voltammetry:

The Electrochemical stability window (ESW) i.e., working potential is a very important parameter of any electrolyte for their application practical devices. To determine the working potential window of the maximum conducting (phytagel/30wt%EMIm[TCM]) film the linear sweep voltammetry is performed shown in figure 7. The working potential range of the phytigel/30wt%EMIm[TCM] is comes out from -1.69 V to 1.42 V i.e., ~ 3.1 V which is sufficient for their application in electrochemical energy devices such as supercapacitors, batteries, dye sensitized solar cells etc.

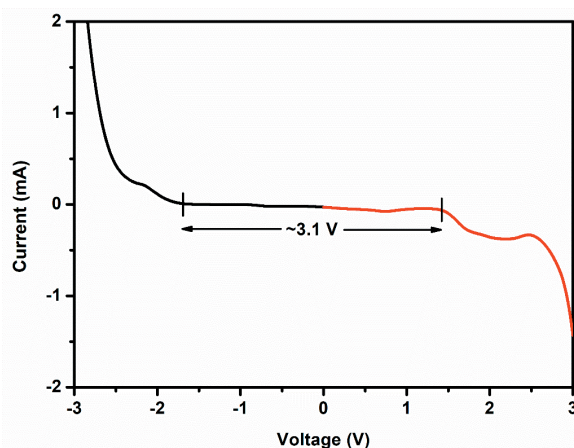


Figure 7. Linear Sweep Voltammetry (LSV) plot for phytigel/30wt% EMIm[TCM]

Ionic transport number:

Wagner polarization technique is used to calculate the total ionic transport number (t_{ion}) of the polymer electrolyte film phytigel/30wt%EMIm[TCM].

Cell SS|phytagel/30wt%EMIm[TCM]|SS is polarized with a 7.5V potential. The current vs time plot for phytigel/30wt%EMIm[TCM] is shown in figure 8. The total ionic transport number (t_{ion}) has been calculated using the following expression (Eq. 6)-

$$t_{ion} = 1 - \frac{i_e}{i_t} \quad (6)$$

Where, i_e is the remaining current and i_t is the total current. The value of t_{ion} is comes out to be ~ 0.99 which shows that the ionic charge carriers are predominant in the prepared polymer electrolyte film.

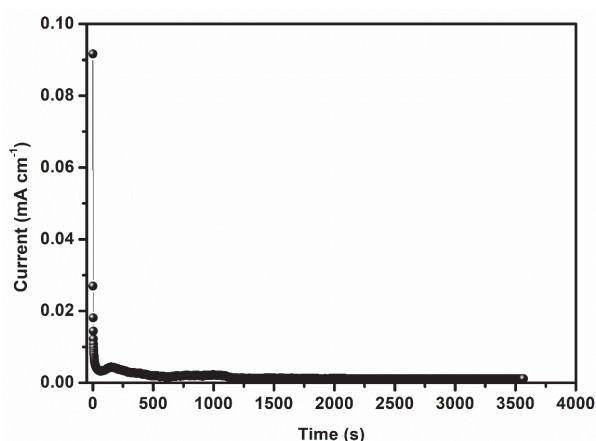


Figure 8. Potentiostatic current vs time plot (t_{ion}) for phytigel/30wt%EMIm[TCM].

Conclusion. Ionic liquid 1-ethyl-3-methylimidazolium tricyanomethanide and biopolymer phytigel blended polymer electrolyte films are successfully synthesized using solution cast technique. The XRD studies shows the semi-crystalline nature of host polymer phytigel and also evident the increase in amorphous phase with blending of ionic liquid. FTIR reveals the presence of different functional groups and interaction of ionic liquid ions with polymer chain of phytigel. The polymer electrolyte film with 30wt% of ionic liquid concentration shows the maximum conductivity value of 3.64×10^{-4} . The dielectric plots follow the same trend as ionic conductivity. The relaxation time calculated from dielectric loss tangent graph is comes out in the order of 10^{-7} for the films >10 wt% of EMIm[TCM] indicating the fast ionic movement. The t_{ion} value of maximum conducting film, calculated using DC polarization is comes out to be ~ 0.99 which shows the predominant ionic charge carriers in prepared polymer electrolyte films. The maximum conducting film is electrochemical stable upto $\sim 3.1V$.

Conflict of Interest:

The authors declare no conflict of interest.

REFERENCE:

- [1] A.Rajapriya, S.Keerthana, N.Ponpandian (2023) Fundamental understanding of charge storage mechanism. In: *Smart Supercapacitors*. Elsevier, p. 65–82. doi: <https://doi.org/10.1016/B978-0-323-90530-5.00034-4>
- [2] L.Xia, L.Yu, D.Hu, et al. (2017) Electrolytes for electrochemical energy storage. *Materials Chemistry Frontiers*, 1, 584–618. doi: 10.1039/C6QM00169F
- [3] A.Singh, P.S.Dhapola, S.Kumar, et al. (2022) Highly conducting ionic liquid doped polymer electrolyte for energy storage applications. *Journal of Science: Advanced Materials and Devices*, 7, 100511. doi: <https://doi.org/10.1016/j.jsamd.2022.100511>.
- [4] G-R.Zhu, Q.Zhang, Q-S.Liu, et al. (2023) Non-flammable solvent-free liquid polymer electrolyte for lithium metal batteries. *Nat Commun*, 14, 4617. doi: <https://doi.org/10.1038/s41467-023-40394-8>.
- [5] S.B.Aziz, O.G.Abdullah, R.T.Abdulwahid, et al. (2023) EDLC performance of plasticized NBG electrolyte inserted with Ba (NO₃)₂ salt: Impedance, electrical and electrochemical properties. *Electrochimica Acta*, 467, 143134. doi: <https://doi.org/10.1016/j.electacta.2023.143134>
- [6] H.Niu, M.Ding, N.Zhang, et al. (2023) Preparation of imidazolium based polymerized ionic liquids gel polymer electrolytes for high-performance lithium batteries. *Materials Chemistry and Physics*, 293, 126971. doi: <https://doi.org/10.1016/j.matchemphys.2022.126971>
- [7] P.Rawat, A.L.Saroj (2023) Effect of ionic liquid on plasticized CS-PVP-Nal based bio-polymer blend electrolytes: Structural, thermal, dielectric and ion transport properties study. *Materials Science and Engineering: B*, 288, 116215. doi: <https://doi.org/10.1016/j.mseb.2022.116215>
- [8] S.Kumari, A.Rao, M.Kaur, et al. (2023) Petroleum-Based Plastics Versus Bio-Based Plastics: A Review. *Nature Environment & Pollution Technology*, 22. doi: <https://doi.org/10.46488/NEPT.2023.v22i03.003>
- [9] S.Konwar, P.K.Singh, P.Dhapola, et al. (2023) Developing Biopolymer-Based Electrolytes for Supercapacitor and Dye-Sensitized Solar Cell Applications. *ACS Applied Electronic Materials*, 5, 5503–5512. doi: <https://doi.org/10.1021/acsaelm.3c00736>
- [10] R.T.Abdulwahid, S.B.Aziz, M.F.Z.Kadir (2023) Replacing synthetic polymer electrolytes in energy storage with flexible biodegradable alternatives: sustainable green biopolymer blend electrolyte for supercapacitor device. *Materials Today Sustainability*, 23, 100472. doi: <https://doi.org/10.1016/j.mtsust.2023.100472>

- [11] M. Kani Ajay Babu, S.S.Jayabalakrishnan, S.Selvasekarapandian, et al. (2023) Development and characterization of biopolymer electrolyte based on gellan gum for the fabrication of solid-state sodium-ion battery. *Ionics*, 29, 5249–5265. doi: <https://doi.org/10.1007/s11581-023-05210-9>
- [12] J.L.Shamshina, P.Berton (2023) Renewable biopolymers combined with ionic liquids for the next generation of supercapacitor materials. *International Journal of Molecular Sciences*, 24, 7866. doi: <https://doi.org/10.3390/ijms24097866>
- [13] M.S.A.Rani, N.S.Isa, N.M.Nurazzi, et al. (2023) Effect of SiO₂ ceramic filler on carboxymethyl cellulose from palm oil empty fruit bunch-based nanocomposite biopolymer electrolyte. In: *Synthetic and Natural Nanofillers in Polymer Composites*. Elsevier, pp. 127–139. doi: <https://doi.org/10.1016/B978-0-443-19053-7.00022-6>
- [14] F.C.Tavares, C.M.Cholant, E.C.Kohlrausch, et al. (2023) Ionic liquid boosted conductivity of biopolymer gel electrolyte. *Journal of the Electrochemical Society*, 170, 084501. doi: [10.1149/1945-7111/ace937](https://doi.org/10.1149/1945-7111/ace937)
- [15] M.J.Park, I.Choi, J.Hong, et al. (2013) Polymer electrolytes integrated with ionic liquids for future electrochemical devices. *J of Applied Polymer Sci*, 129, 2363–2376. doi: <https://doi.org/10.1002/app.39064>
- [16] G.A.Tiruye, D.Muñoz-Torrero, J.Palma, et al. (2016) Performance of solid state supercapacitors based on polymer electrolytes containing different ionic liquids. *Journal of Power Sources*, 326, 560–568. doi: <https://doi.org/10.1016/j.jpowsour.2016.03.044>
- [17] A.S.F.M.Asnawi, M.H.Hamsan, S.B.Aziz, et al. (2021) Impregnation of [Emim]Br ionic liquid as plasticizer in biopolymer electrolytes for EDLC application. *Electrochimica Acta*, 375, 137923. doi: <https://doi.org/10.1016/j.electacta.2021.137923>
- [18] S.Romano, S.De Santis, A.Martinelli, et al. (2023) Starch films plasticized by imidazolium-based ionic liquids: Effect of mono-and dicationic structures and different anions. *ACS Applied Polymer Materials*, 5, 8859–8868. doi: <https://doi.org/10.1021/acscpm.3c01235>
- [19] S.Konwar, A.Singh, P.K.Singh, et al. (2023) Highly conducting corn starch doped ionic liquid solid polymer electrolyte for energy storage devices. *High Performance Polymers*, 35, 63–70. doi: <https://doi.org/10.1021/acscpm.3c01235>
- [20] C.Naveen, M.Muthuvinayagam. (2023) Studies on electrical properties of Chitosan-PVA based biopolymer electrolytes for electrochemical devices. *Journal of Polymer Research*, 30, 353. doi: <https://doi.org/10.1007/s10965-023-03741-3>
- [21] S.Sowmiyaa, C.Shanthia, S.Selvasekarapandian (2023) Development of sodium-ion conducting biopolymer electrolyte membrane based on Agar-Agar with sodium perchlorate (NaClO₄) using ethylene carbonate (EC) as a plasticizer for primary Na-ion battery. *DIGEST JOURNAL OF NANOMATERIALS AND BIOSTRUCTURES*, 18, 1537–1555. doi: <https://doi.org/10.15251/DJNB.2023.184.1537>
- [22] P.S.Rudati, Y.Dzakiyyah, R.Fane, et al. (2023) Biopolymer Kappa Carrageenan with Ammonium Chloride as Electrolyte for Potential Application in Organic Battery. *Key Engineering Materials*, 950, 11–16. doi: <https://doi.org/10.4028/p-FW7xiu>
- [23] M.Kani Ajay Babu, S.S.Jayabalakrishnan, S.Selvasekarapandian, et al. (2023) Development and characterization of biopolymer electrolyte based on gellan gum for the fabrication of solid-state sodium-ion battery. *Ionics*, 29, 5249–5265. doi: <https://doi.org/10.1007/s11581-023-05210-9>
- [24] S.Eswaragomathy, S.Selvanayagam, S.Selvasekarapandian, et al. (2023) Preparation of pectin biopolymer electrolyte for zinc-ion battery application. *Ionics*, 29, 2329–2340. doi: <https://doi.org/10.1007/s11581-023-05005-y>
- [25] D.Singh, S.Kumar, A.Singh, et al. (2022) Ionic liquid–biopolymer electrolyte for electrochemical devices. *Ionics*, 28, 759–766. doi: <https://doi.org/10.1007/s11581-021-04372-8>
- [26] K.Karuppasamy, D.Vikraman, K.Jang, et al. (2021) Bio-inspired proton conducting phytigel derived zwitterionic complex membranes for fuel cells. *Intl J of Energy Research*, 45, 17120–17132. doi: <https://doi.org/10.1002/er.5386>
- [27] X.Wu, A.Surendran, J.Ko, et al. (2019) Ionic-Liquid Doping Enables High Transconductance, Fast Response Time, and High Ion Sensitivity in Organic Electrochemical Transistors. *Advanced Materials*, 31, 1805544. doi: <https://doi.org/10.1002/adma.201805544>
- [28] S.Kumar, P.K.Singh, D.Agarwal, et al. (2022) Structure, Dielectric, and Electrochemical Studies on Poly(Vinylidene Fluoride-Co-Hexafluoropropylene)/IonicLiquid 1-Ethyl-3-Methylimidazolium Tricyanomethanide-Based Polymer Electrolytes. *Physica Status Solidi (a)*, 219, 2100711. doi: [10.1002/pssa.202100711](https://doi.org/10.1002/pssa.202100711)
- [29] R.Singh, B.Bhattacharya, H-W.Rhee, et al. (2015) Solid gellan gum polymer electrolyte for energy application. *International Journal of Hydrogen Energy*, 40, 9365–9372. doi: <https://doi.org/10.1016/j.ijhydene.2015.05.084>
- [30] G.Nath, P.S.Dhapola, N.Sahoo, et al. (2022) Polyvinylpyrrolidone with ammonium iodide and plasticizer ethylene carbonate solid polymer electrolyte for supercapacitor application. *Journal of Thermoplastic Composite Materials*, 35, 879–890. doi: <https://doi.org/10.1177/0892705720925115>
- [31] D.Kumar, K.Gohel, D.K.Kanchan, et al. (2020) Dielectrics and battery studies on flexible nanocomposite gel polymer electrolyte membranes for sodium batteries. *Journal of Materials Science: Materials in Electronics*, 31, 13249–13260. doi: <https://doi.org/10.1007/s10854-020-03877-8>

IZVOD**STRUKTURALNA, ELEKTROHEMIJSKA I DIELEKTRIČNA
ISTRAŽIVANJA FITAGELA I 1-ETIL-3-METILIMIDAZOLIJUMA
BIO-POLIMER ELEKTROLITA NA BAZI TRICIJANOMETANIDA**

Ovaj rad je fokusiran na sintezu i detaljno proučavanje biopolimernih fitagela i jonske tečnosti 1-etil-3-metilimidazolijum tricijanometanida (EMIm[TCM]) mešanih polimernih elektrolitnih filmova za energetske primene. Ovde se polimerni filmovi, na bazi biopolimera fitagela, sintetišu sa različitim koncentracijama jonske tečnosti (EMIm[TCM]) korišćenjem tehnike livenja rastvora. Sintetizovani filmovi su okarakterisani zbog svojih strukturnih, elektrohemijskih i dielektričnih svojstava korišćenjem različitih alata za karakterizaciju, kao što su XRD, FTIR, spektroskopija elektrohemijske impedanse, linearna voltometrija i Vagnorova tehnika polarizacije. Film sa 30wt% EMIm[TCM] pokazuje maksimalnu provodljivost od $3,64 \times 10^{-4} \text{ S cm}^{-1}$ i prozor elektrohemijske stabilnosti od 3,1 V. Dielektrična svojstva kao što su dielektrična konstanta (k), tangenta dielektričnog gubitka ($\tan\delta$), vreme relaksacije i učestalost su takođe proučavani za pripremljene čiste fitagel i fitagel/EMIm[TCM] polimerne filmove. Ključne reči: biorazgradivi polimeri, fitagel, jonska tečnost, 1-etil-3-metilimidazolijum tricijanometanid, polimerni elektrolit

Naučni rad

Rad primljen: 30.03.2024.

Rad korigovan: 27.05.2024.

Rad prihvaćen: 5.06.2024.

The ORCID Ids of all the authors are as follows:

1. Sushant Kumar: <https://orcid.org/0000-0002-9326-1132>
2. Manoj K. Singh: <https://orcid.org/0000-0001-7006-290X>
3. M.Z.A. Yahya: <https://orcid.org/0000-0003-1129-0552>
4. I.M. Noor: <https://orcid.org/0000-0003-0983-782X>
5. Pramod K. Singh: <https://orcid.org/0000-0002-3155-6621>

Liubov Melnyk¹, Lev Chernyak^{1*}, Valentin Sviderskyi¹,
Ludmila Vovchenko², Viktoria Yevpak¹

Department of Chemical Technology of Composite Materials, National
Technical University of Ukraine "Igor Sikorsky Kyiv Polytechnic Institute",
Kyiv, Ukraine

Scientific Paper

ISSN 0351-9465, E-ISSN 2466-2585

<https://doi.org/10.62638/ZasMat1171>



Zastita Materijala 65 (4)
712 – 723 (2024)

Comparative Study of Various Volcanic Materials as Fillers in Polymer Composites

ABSTRACT

The object of the study was composite materials using rocks of volcanic origin as a filler (60-90 wt.%) and aqueous dispersions of polymers Latex 2012 and Policril 590 as a matrix. The peculiarities of the chemical and mineralogical composition and surface properties of perlite and zeolite as factors of interaction with the binder in the formation of the composite structure are shown. Differences in lyophilicity coefficients and effective specific surface of zeolite and perlite were determined, which are 0.318 versus 0.189 and 11.68 versus 2.20 m²/g, respectively. The influence of a high concentration of fillers on the formation of the pore structure and indicators of physical and mechanical properties of composites is evaluated. The possibility of adjusting the properties of the composites in the following range was established: water absorption in the range of 2.63-14.16 wt.%, open porosity 3.58-21.35 %, residual strain 0.1-0.3, Young's modulus 19.7-677.5 MPa.

Keywords: composite, filler, perlite, zeolite, concentration, copolymer, porosity, properties.

INTRODUCTION

The development of scientific and technical principles of polymer composite materials technology is the subject of numerous studies [1-3]. A significant role of composite fillers has been recognised, the use of which can significantly reduce the amount of required binder polymers and improve the properties of materials [4-6].

According to the modern material science concept of the composition structure properties relationship, the characteristics of composites depend on the types of filler and matrix, manufacturing technology and parameters. At the same time, the degree of bonding of the components, their concentration and uniformity of volume distribution determine the structure parameters, general physical, mechanical and special properties of composites.

Natural materials such as chalk, kaolin, and graphite are mainly used as dispersed fillers [7-9].

* Corresponding author: Lev Chernyak
E-mail: lpchernyak@ukr.net
Paper received: 30.03.2024.
Paper accepted: 7.06.2024.

One of the areas of expansion of the raw material base of fillers is the study and use of by-products of non-metallic materials extraction [10].

In this regard, developments in the use of rocks of volcanic origin, common in the world and Ukraine, among which perlite and zeolite play a significant role, are of particular interest [11, 12].

Perlite is a rock of volcanic origin. At the edge of a lava flow, at the points of contact between magma melts and the ground, volcanic glass, obsidian, is formed after the lava has cooled rapidly. Subsequently, groundwater seeps through the obsidian, undergoing the process of its hydration and the formation of perlite [13].

Perlite is characterised by a fine concentric-shell structure. Perlite differs from other volcanic rocks in that it contains constitutional water (more than 1%). The porosity can range from 8 to 40 % [14].

The use of perlite in composite materials has a number of advantages, such as low density, good thermal insulation properties, resistance to fire, moisture and chemical resistance.

Bituminised perlite is a rather interesting material

used in the manufacture of roofinsulation. Perlite is first treated with bitumen in the factory. When a solvent is added to it, it becomes adhesive. This helps to form quite strong insulation layers of various shapes [15].

According to the genetic criterion, all existing varieties of perlite are divided into two large groups: primary hydrated rock and secondary hydrated rock or primary perlite and secondary perlite.

In most cases, primary perlites have a porous or pumice-like texture, with the amount of structural water ranging from 1.5 to 4.5%. Such perlites include those from deposits in Armenia, Georgia, America, Greece, and Turkey.

Secondary pearls can be represented by massive and loose varieties with a water content of 4.5 to 9.5%. These include perlites from deposits in Ukraine, Mongolia, and China.

Zeolite also belongs to rocks of volcanic origin [16-18]. It is known that zeolites are characterised by the development of molecular-sized pores - uniformly sized channels and cavities that create a large specific surface area. In addition to structural features, it is important to note the distribution and significant reserves of natural zeolite deposits, including in Ukraine [19].

Natural zeolites are aqueous aluminosilicates with a skeletal structure that have uniform pores of molecular size.

In Ukraine, the zeolite deposit is located in Sokyrynsia village (Zakarpattia region). The zeolite of the Sokyrynsia deposit contains a large amount of clinoptilolite. Sufficient mechanical strength of clinoptilolite, resistance to high temperatures [20], aggressive environments and ionising radiation, selectivity to cations of alkaline, alkaline earth, rare earth, scattered and some heavy metals, absorption capacity and sieve effect - all this leads to the wide use of the mineral.

Developments in the use of new types of raw materials, including zeolite and perlite, require consideration of their physical and chemical composition, impact on the structure formation and characteristics of the systems under study and product properties.

One of the ways to improve the properties of polymers is to fill them with structurally active additives, the addition of which ensures the formation of a given phase and supramolecular structure of the matrix. Currently, layered and skeletal natural minerals, including natural zeolite and perlite, are often used as modifiers

of various polymer matrices (polytetrafluoroethylene, polyethylenes, polyester resins, rubbers, etc.).

It is known that the introduction of zeolites into a polymer improves the functional properties of polymer composite materials (PCM). Work [21] shows an improvement in the strength of an epoxy material by 43% when zeolite of natural origin is introduced as a modifier. Various technological methods are used to enhance the adhesive interaction at the polymer-filler interface, which leads to a significant change in the structural organisation of a heterogeneous system. For example, mechanochemical activation of the filler can increase the specific surface area of particles by 1.5-2 times. Effect of mechanical impact activated zeolite was found when it was introduced into polytetrafluoroethylene (PTFE): in the work [22], an increase in deformation-strength properties and wear resistance of PCM based on PTFE and activated zeolite was recorded compared to PCM with unactivated zeolite. Structural studies of the PCMs, carried out using scanning electron and atomic force microscopy, infrared spectroscopy and X-ray diffractometry, confirm the transformation of the supramolecular structure of PTFE from lamellar to spherical under the influence of activated zeolite particles. Thus, the dependence of the functional parameters of PCMs on the level of adhesive interaction between the polymer matrix and the filler is obvious, which, in turn, is directly related to such a characteristic of the filler as microporosity.

Perlite has a similar effect. The authors of [23] found a significant effect of perlite nanofiller on the mechanical and thermal properties of composites with a polyethylene matrix, and an increase in the elastic modulus with an increase in the filler concentration was also noted.

A number of research groups have determined the effect of perlite particle size on the mechanical and electrical properties of a polypropylene-based composite and found that a smaller perlite size can lead to an increase in the mechanical properties of polymer composites by reducing shrinkage [24].

It is important that the use of raw materials of different genesis as a filler makes it possible to comprehensively address the issues of composite quality and resource conservation. At the same time, developments in the use of new types of fillers require consideration of the peculiarities of their physical and chemical composition as a factor influencing the characteristics of the systems under study and the properties of the composite material. This was the aim of

this work in relation to composites based on perlite and zeolite with a polymeric binder.

EXPERIMENTAL

Materials and Research Methods

The object of study was composite materials based on copolymer-filler systems. Perlite of the Berehove deposit and zeolite of the Sokyrmysia deposit (Transcarpathian region, Ukraine) were chosen as fillers.

Aqueous dispersions of Latex 2012 copolymer and Policril 590 polymer were used as a matrix for the composite (Table 1). At the same time, the choice of binders is based on their presence in a water-dispersed state, which is important for practical implementation in technology, the specified differences in chemical composition and indicators of physical properties.

Table 1 Characteristics of binders

Features.	Indicators.	
	Latex 2012	Policril 590
Chemical composition	Styrene-butadiene	acrylic
Styrene content, %.	30	-
Physical condition	White aqueous dispersion	White aqueous dispersion
Dry matter content, %.	51.0	53.5-55.0
Particle size, nm	140	200
Viscosity, MPa-s	200	<1000
pH	5.5	5.5-7.5
Temperature (MTU), °C	< 5	0

The IR spectra in the range of 4000-400 cm^{-1} were recorded using a Specord IR-75 spectrophotometer (manufactured by Carl Zeiss, Germany).

The specific surface area was determined by the BET method, which is based on the adsorption of nitrogen vapour at temperature of minus 195 °C by a molecular layer on the surface of the test powder.

The particle size distribution was determined by the sieve method.

The abrasive resistance of the samples was determined in accordance with DSTUB.V.2.7-212:2009 on a Beme-type abrasive wheel, and the mechanical properties - 'Loading-unloading' diagrams were studied at room temperature using an automated arrangement consisting of IMASH-20-78, analog-digital converter (ADC), personal computer (PC), and connecting cables. The measurements were performed in a vacuum of 10^{-5} Torr [25].

The technology of manufacturing a composite based on the copolymer-filler system consisted of the following operations:

- Mechanical activation of the filler and binder in a ball mill (20 minutes);

- Forming of blanks (by mould volume) and their maturation (48 hours at room temperature);
- Heat treatment of the workpieces (gradual increase in temperature and holding for 1 hour at 80° C);
- Cold pressing of cylindrical samples with a diameter of 10 mm.

RESULTS AND DISCUSSION

The nature of the filler plays an important role in the creation of polymer composite materials, so it is essential to study their properties first.

The chemical composition of the studied fillers, the results of their X-ray phase analysis, lyophilicity, and the energy state of the surface of the considered fillers are described in our previous work [26].

The experimental fillers have a specific surface area, which is directly related to their mineral phase composition. For example, the specific surface area for zeolite is larger than that of perlite determined by the BET method (11.68 against 2.20 m^2/g) (Table 2).

Table 2 Lyophilicity and energy state of fillers surface

Material	Surface area (BET), m ² /g	Coefficient of lyophilicity	Coefficient of wetting during inflow	
			water	benzene
Perlite	2.20	0.189	0.17	0.87
Zeolite	11.68	0.318	0.16	0.52

Perlite has a slightly higher wettability with both water and benzene (0.17 with water, 0.87 with benzene) compared to zeolite (0.16 with water, 0.52 with benzene).

The coefficient of lyophilicity has an inverse relationship and is higher for zeolite (0.318) compared to (0.189) for perlite.

The key parameter that determines the choice of a filler is its dispersion and the percentage of different fractions, i.e., the particle size distribution (Fig. 1).

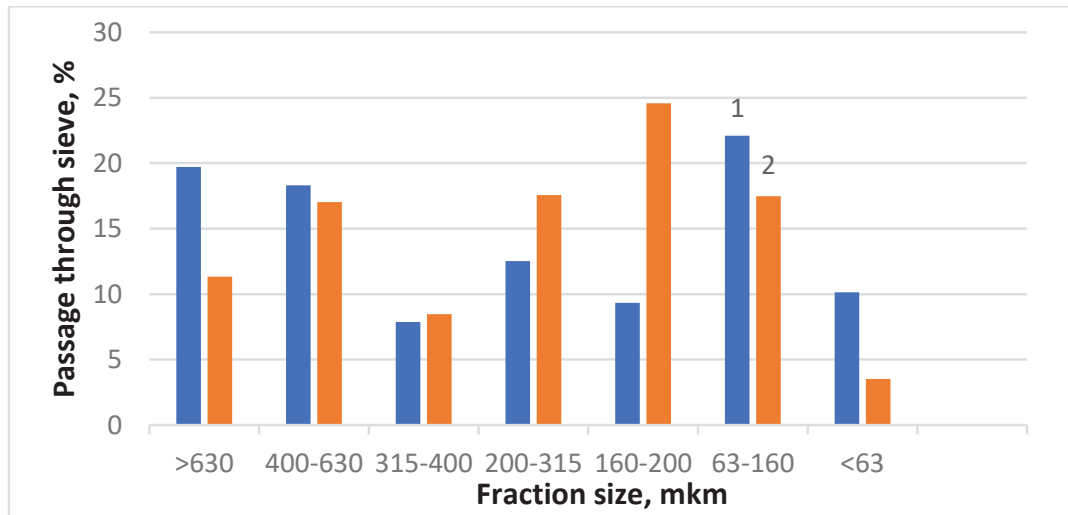


Fig. 1. Particle distribution by fractions of perlite (1) and zeolite (2) samples

It was found that among the studied fillers, the highest content was found in the particle size fraction of 63-160 μm for zeolite, which is 22.1%. Perlite has a maximum content of 27.58% in the larger fraction of 200-315 μm .

In order to study the chemical composition of the fillers and their interaction with the binder in more detail, infrared spectroscopy was performed (Fig. 2).

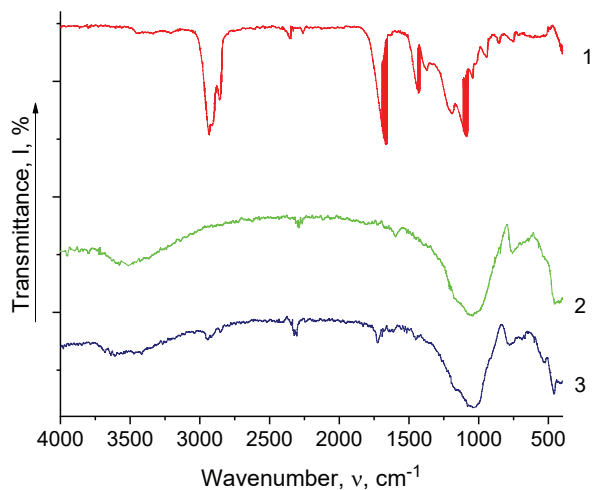


Fig. 2. a. Infrared spectroscopy of samples: 1 - Policril 590, 2 - Perlite, 3 - Perlite + Policril 590

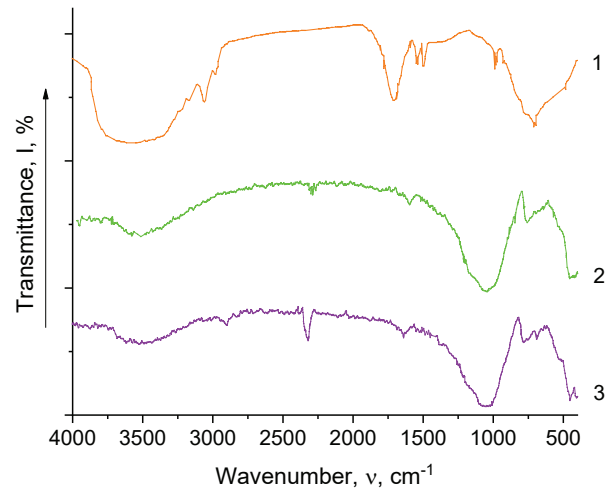


Fig. 2. b. Infrared spectroscopy of the samples: 1 - Latex 2012, 2 - Perlite; 3 - Perlite + Latex 2012

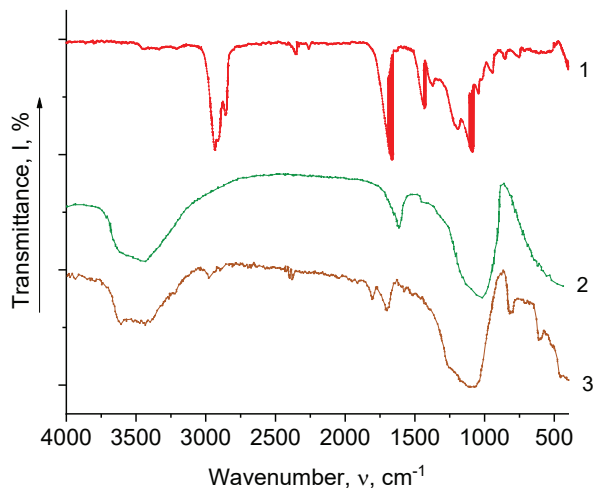


Fig. 2. c. Infrared spectroscopy of the samples: 1 - Policril 590, 2 - Zeolite, 3 - Zeolite + Policril 590

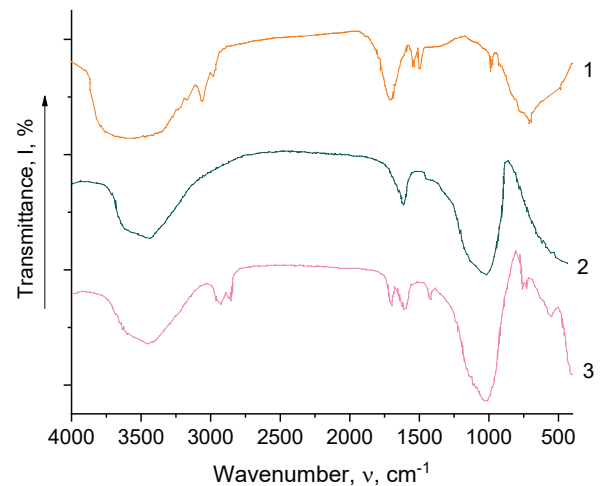


Fig. 2. d. Infrared spectroscopy of the samples: 1 - Latex 2012, 2 - Zeolite, 3 - Zeolite + Latex 2012

These features of the surface properties of perlite particles correlate with the results of infrared spectroscopic analysis, which showed the presence and characteristics of simple compounds, functional groups, and chemical bonds (Fig. 2. a, curve 2). Among the latter, first of all, it is necessary to note the vibrations of the structure-forming bridging and non-bridging Si-O-Si bonds (valence interval 640-690 cm^{-1} , Si-O-Al (710-780 cm^{-1}). There are also characteristic absorption bands responsible for the deformation vibrations of the Si-O^- (440-436 cm^{-1}) and Si-O-Al (507-593 cm^{-1}) bonds.

Analysis of the position of the absorption band maxima characteristic of the valence vibrations of Si-

O-Si bonds on the IR spectra showed the presence of a relatively narrow interval (1000-1080 cm^{-1}) for perlite.

It should be noted that there are absorption bands responsible for differential vibrations of adsorbed water at 1620-1640 cm^{-1} . As for zeolite (Fig. 2. c, curve 2), the intense band appearing in the range of 3400-3500 cm^{-1} is the result of the vibration of OH groups of water. The band appearing in the range of 1600-1650 cm^{-1} is the result of molecularly bound water in the structure. The vibration ranges at a distance of 950-1250 cm^{-1} are the result of structural units of the alumina-silicate lattice of Si(Al)-O zeolite. Based on this structural analysis, it is con-

firmed that this is a nanoporous aluminosilicate material with a defined structure and the presence of free and chemically bound water.

When studying the interaction between the filler and binder using infrared spectroscopy (Fig. 2. a, curve 1), it was found that the acrylic dispersion of Policril 590 is characterised by an absorption band at 1670 cm^{-1} , which corresponds to the monomeric links of acrylate [27] and is the result of asymmetric and symmetric valence vibrations of C=O in the carboxyl group. Vibrational vibrations of the C=C bond correspond to the absorption band at 1435 cm^{-1} , the presence of a CH bond is indicated by the absorption bands at 1100 cm^{-1} [28]. As for the Policril 590 – Perlite system (Fig. 2 a, curve 3), the curve is more consistent with the absorption curve characteristic of perlite, but there are certain nuances: in particular, a slight absorption band at 2280 cm^{-1} , corresponding to the C=C bond, and at 1740 cm^{-1} , characteristic of the C=O bond of the polymer, appeared, but the intensity of these bands is insignificant compared to the original Policril 590 with some shift, which may confirm the presence of interaction in the system. The same patterns are observed when using zeolite (Fig. 2. c, curve 3).

As for the styrene-butadiene dispersion Latex 2012 (Fig. 2. d, curve 1), the saturation band at 2980 cm^{-1} is responsible for the CH compound in the aromatic ring, and the saturation band at 1525 cm^{-1} is directly responsible for the presence of the ring itself. The absorption band at 2852 cm^{-1} confirms the presence of the CH_2 group, and at 1500 cm^{-1} – the presence of the butadiene double bond. [29].

For the composite material based on the Latex 2012 – Zeolite system (Fig. 2. d, curve 3), we assume that physical sorption occurs, as evidenced by the presence of a band of 2920 cm^{-1} corresponding to the -CH bond of the styrene aromatic ring, and a decrease in the intensity of the shift of the band 1525 cm^{-1} C=C characteristic of the butadiene component.

Similar patterns are observed when using perlite (Fig. 2. b, curve 3).

Samples of the composite material were obtained on the basis of binary systems of the studied fillers (perlite and zeolite) with a binder (Table 3). The concentration of fillers with a particle size of ≤ 1 mm varied from 65 to 90 wt.%, and the concentration of binders - from 35 to 10 wt.%, respectively.

Table 3 Composition and properties of the composite material

Composition of the composite	Filler concentration, C, wt. %	Indicators				
		Water absorption after 24 hours, %	Open porosity, %	Total porosity, %	Average density, g/cm^3	Abrasion resistance, g/cm^2
Policril 590 + Perlite	65	2.63	3.58	7.67	1.36	0.026
	75	6.45	9.02	17.70	1.40	0.026
	85	7.08	11.13	30.99	1.57	0.026
	90	8.41	13.55	35.72	1.61	0.034
Latex 2012 + Perlite	65	3.42	4.67	5.42	1.37	0.015
	75	4.16	5.96	13.87	1.43	0.016
	85	7.89	12.67	24.43	1.61	0.040
	90	8.59	14.38	31.73	1.67	0.060
Policril 590 + Zeolite	65	3.35	4.84	11.50	1.44	0.011
	75	3.73	5.64	20.61	1.51	0.013
	85	8.21	13.27	30.01	1.61	0.017
	90	9.28	15.46	34.03	1.66	0.022
Latex 2012 + Zeolite	65	3.91	5.29	7.23	1.35	0.012
	75	6.36	9.32	19.76	1.46	0.013
	85	13.90	20.41	24.70	1.47	0.026
	90	14.16	21.35	28.79	1.51	0.045

According to the test results, the physical and mechanical properties of composites significantly depend on the type and concentration of the filler. When using both fillers, an increase in water absorption and a decrease in the average density are observed with an increase in their concentration. At the same time, the degree of change in these indicators in the specified range of filler concentrations is significantly different. Thus, when comparing composites based on acrylic dispersion (Policril 590) using different fillers, it should be noted that water absorption when using zeolite with an increase in its concentration varies within 3.35-9.28 wt.%, which is slightly higher compared to composites using perlite (2.63-8.41 %). When replacing the binder with Latex 2012, this trend is observed, but the values increase slightly. Thus, for composites with perlite, they range from 3.42-8.59 wt.% against 3.91-14.16 wt.% when using zeolite.

The analysis of the structure of the prototypes showed (Table 3) that there is a linear dependence of the increase in porosity on the concentration of the filler.

Thus, when comparing composites based on Policril 590 dispersion using perlite, it should be noted that the open porosity with an increase in its concentration varies within 3.58-13.55 %, which is slightly lower compared to composites with zeolite (4.84-15.46 %). When replacing the binder with Latex 2012, this trend persists, but the values increase slightly: 4.67-14.38 % for perlite versus 5.29-21.35 % for zeolite.

For composites using perlite, when binders are replaced with Policril 590 by Latex 2012, the initial values of the total porosity increase from 7.64-35.72 % against 5.42-31.73 %. When using zeolite and replacing the binders from Policril 590 with Latex 2012, the values of the total porosity decrease from 11.50-34.03 % to 7.23-28.76 %, respectively.

Obviously, these features indicate differences in the pore structure of the studied composites, since the analysis of the sample structure showed (Fig. 3) that the use of a binder with a higher viscosity (Policril 590) at the same filler concentration leads to an increase in the porosity of the composite samples.

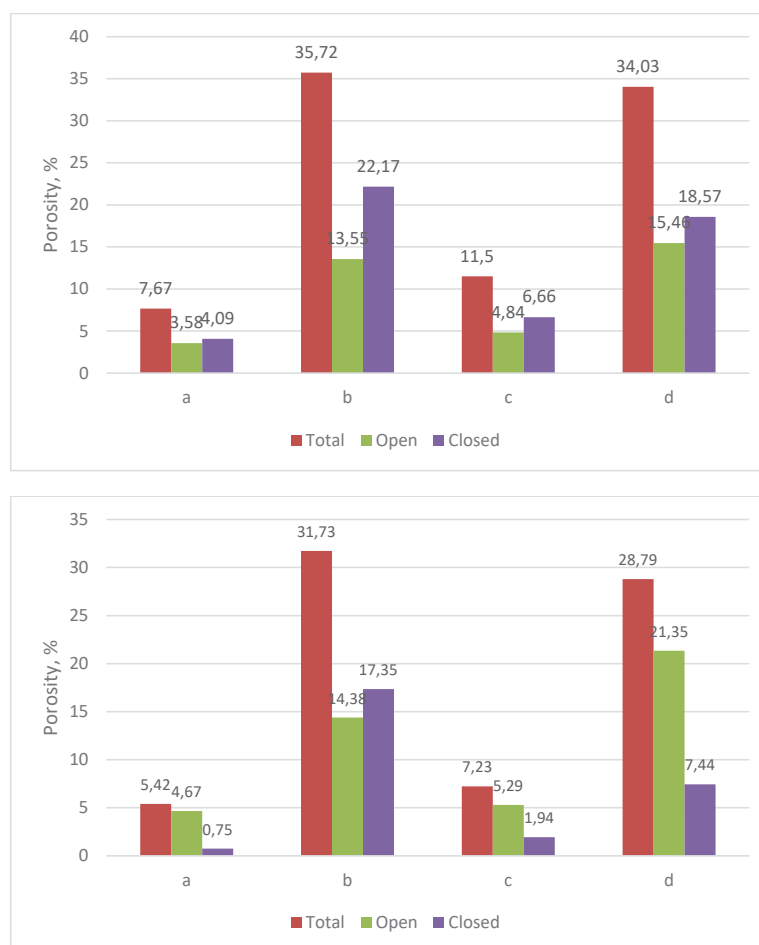


Fig. 3. Porosity of composites based on Policril 590 (1) and Latex 2012 (2) at the concentration of perlite 65.0 (a), 90.0 wt.% (b) and zeolite 65.0 (c), 90.0 wt.% (d)

Among the performance characteristics of the studied composites, the abrasion indicators indicate increased abrasion resistance of the material.

We also studied the mechanical properties of composites using polymeric binders and two types

of fillers - perlite and zeolite - under uniaxial compression of these samples. Figs. 4-5 show the load-strain diagrams for composites with perlite filler using two types of binders, Policril 590 and Latex 2012.

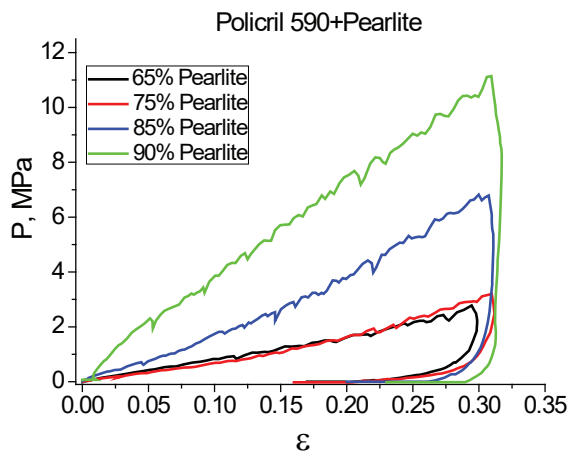


Fig. 4. Dependence of deformation on load for CM system Policril 590 + Perlite

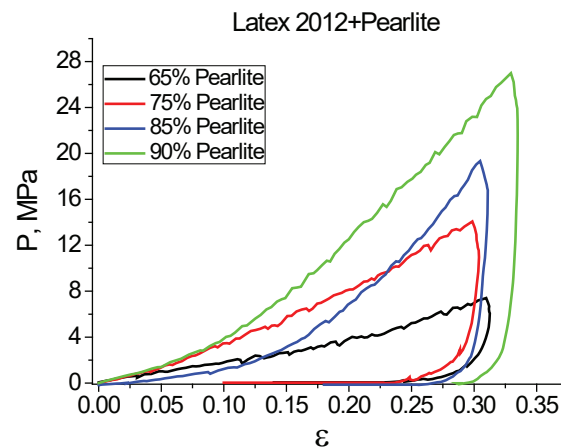


Fig. 5. Dependence of deformation on load for CM system Latex 2012 + Perlite

The elastic ϵ_{el} and residual (plastic) ϵ_{pl} strains and Young's modulus $E=P/\epsilon_{el}$ were determined from the load-strain diagrams, the data are presented in Table 3. For a comparative analysis of the mechanical properties of different types of CM samples, the values of the ultimate load were chosen so that the total deformation of the samples was approximately the same, $\epsilon_{total} = \epsilon_{el} + \epsilon_{pl} \approx 0.30$.

As can be seen from the data presented, with an increase in the content of perlite in composites of both types (with Policril 590 and Latex 2012 binders), the value of the ultimate load increases, which indicates an improvement in the strength characteristics. It is worth noting that these composites have

rather high residual strains (ϵ_{pl}), the value of which increases with increasing perlite content in the composites, since the ultimate load for high composites filling increases.

Similarly, as can be seen from Table 4, the increase in the perlite content in the composites materials also increases the Young's modulus, despite the rather significant residual deformations in these composites materials. Moreover, the Young's modulus is much higher for the composites materials with Latex 2012 binder, increasing from 41.9 MPa for the perlite content of 65 wt% to 677.5 MPa for the composites materials with 90 wt% perlite.

Table 4 Strength and elastic characteristics of samples using Perlite

Perlite content, wt. %	Maximum load, P MPa	ϵ_{total}	ϵ_{pl}	ϵ_{el}	Young's modulus, E, MPa
CM system Policril 590 + Perlite					
65	2.77	0.29	0.17	0.12	23.1
75	3.18	0.31	0.16	0.15	20
85	6.85	0.31	0.20	0.11	62.3
90	11.20	0.31	0.23	0.08	140.0
CM system Latex 2012 + Perlite					
65	7.12	0.31	0.14	0.17	41.9
75	14.1	0.30	0.10	0.20	70.5
85	19.30	0.30	0.18	0.12	160.0
90	27.1	0.33	0.29	0.04	677.5

Similar results of the study of mechanical characteristics for the CM with zeolite filler are presented in Figs. 6-7 and Table 5. For these composites, there is also an increase in Young's modulus with increasing filler content, but this dependence is not monotonic: for Policril 590 + 90 wt.% Zeolite composites, a

decrease in both the ultimate load for deformations $\epsilon_{total} \approx 0.30$ and the effective Young's modulus was observed, which may indicate a deterioration in the strength characteristics of composites with such a high filling.

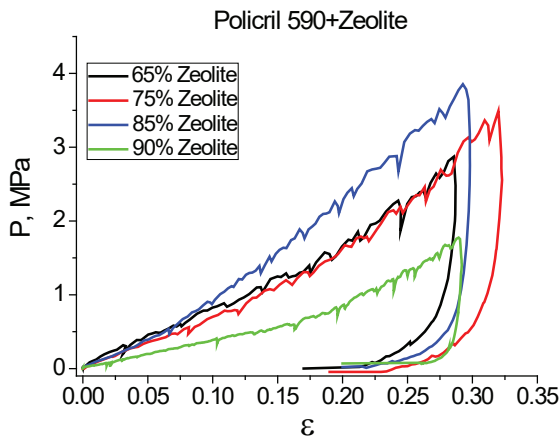


Fig. 6. Dependence of deformation on the load for CM system Policril 590 + Zeolite

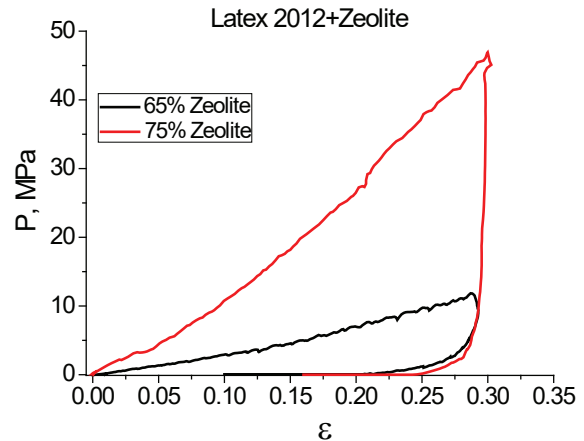


Fig. 7. Dependence of deformation on load for CM system Latex 2012 + Zeolite

Table 5 Strength and elastic characteristics of samples using Zeolite

Zeolite content, wt.%.	Maximum load, P MPa	ϵ_{total}	ϵ_{pl}	ϵ_{el}	Young's modulus, E, MPa
CM system Policril 590 + Zeolite					
65	2.88	0.29	0.17	0.11	26.2
75	3.48	0.32	0.19	0.13	26.7
85	3.90	0.29	0.20	0.09	43.3
90	1.77	0.29	0.20	0.09	19.7
CM system Latex 2012 + Zeolite					
65	11.8	0.29	0.11	0.18	65.6
75	46.9	0.30	0.16	0.14	335.0

Fig. 8 shows comparative graphs for the ratio between plastic and elastic deformations $\epsilon_{pl} / \epsilon_{el}$ at the maximum ultimate load and the effective Young's

modulus E for all the studied CM samples depending on the filler concentration and type of polymer binder.

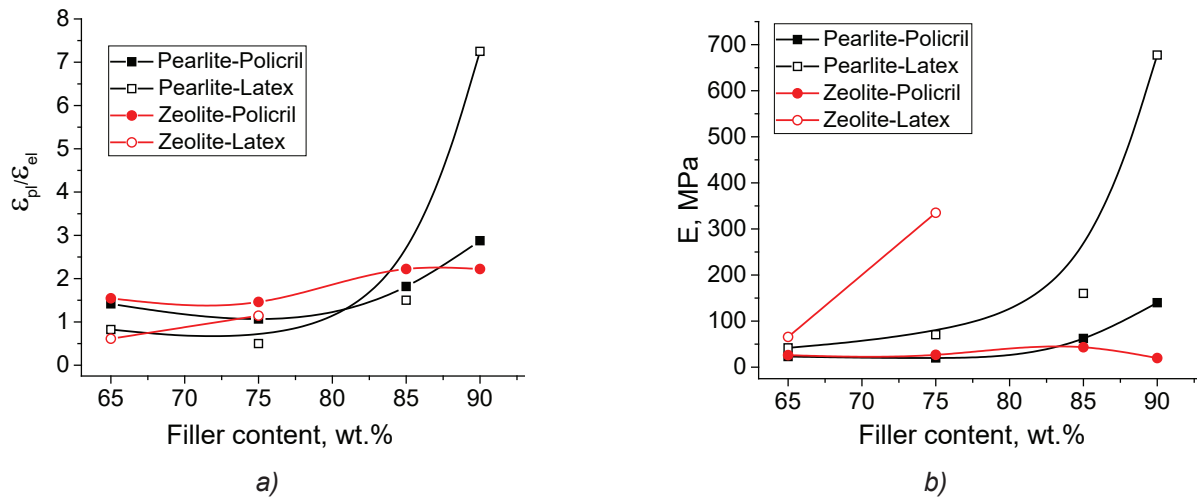


Fig. 8. The ratio between plastic and elastic deformations and effective Young's module versus filler content for CM systems Binder + Filler

As can be seen from Figures 8 a, b, with increasing filler content, the value of $\epsilon_{pl}/\epsilon_{el}$ gradually increases, which correlates with an increase in the ultimate load P_{max} , and this increase is most dramatic for the Latex 2012 + Perlite system. The concentration dependence of the effective Young's modulus E for these systems is fully correlated with the data for $\epsilon_{pl}/\epsilon_{el}$, since $E \sim 1/\epsilon_{el}$; the maximum effective Young's modulus was observed for CM Latex 2012 + 90 wt.% Perlite.

Comparing all the studied systems with each other, it can be concluded that the main role in determining the mechanical characteristics of composites is played by the type of binder and filler concentration. For example, CM with Latex 2012 binder have a significantly higher Young's modulus compared to composites based on Policril 590, which increases with the increase in filler content (perlite or zeolite) and indicates an improvement in strength characteristics.

CONCLUSIONS

1. The developed composite materials, intended primarily for use in the field of construction, differ from the well-known high concentration of fillers, which are by-products of the extraction of volcanic rocks, which contributes to a comprehensive solution to the issues of expanding the raw material base for the production of polymer composites and resource saving.

2. The peculiarities of using perlite and zeolite as fillers in the concentration of 65-90 wt. % for the manufacture of composite materials using Latex 2012 copolymer and Policril 590 polymer as a matrix are studied.
3. The differences in the chemical and mineralogical composition and surface properties of perlite and zeolite as factors influencing the formation of the structure and indicators of physical and mechanical properties of the developed composites are determined.
4. The influence of high concentration of fillers and binder types on the pore structure and properties of the composite material is considered. The possibility of providing increased abrasive resistance of composites at controlled water absorption in the range of 2.63-14.16 wt.%, open porosity of 3.58-21.35 %, residual deformation of 0.1-0.3, and Young's modulus of 19.7-677.5 MPa was noted.

REFERENCES

- [1] S.Grove (2018) *Composite Materials and Structures for Engineering Students*. Kindle Direct Publishing.
- [2] L.Melnyk (2017) Research of electrical properties of epoxy composite with carbon fillers. *Technology Audit and Production Reserves*, 3(1(35)), 28-34. <https://doi.org/10.15587/2312-8372.2017.104807>.
- [3] S.S.Ray, M.Okamoto (2003) Polymer/layered silicate nanocomposites: a review from preparation to processing. *Progress in Polymer Science*, 28(11), 1539-1641. <https://doi.org/10.1016/j.progpolymsci.2003.08.002>.

- [4] B.Tarhan, M.Tarhan (2021) Utilization of perlite as an alternative raw material in the production of ceramic sanitaryware. *Journal of Thermal Analysis and Calorimetry*, 147(5), 3509-3518. <https://doi.org/10.1007/s10973-021-10784-5>.
- [5] R.Rothon (2017) *Fillers for polymer applications*. Springer.
- [6] T.V.Kumar, M.Chandrasekaran, P.Mohanraj, R.Balasuubramanian, R.Muraliraja, V.Shaisundaram (2018) Fillers preparation for polymer composite and its properties – a review. *International Journal of Engineering & Technology*, 7(3.3), 212. <https://doi.org/10.14419/ijet.v7i2.33.13889>.
- [7] R.N.Rothon (2002) *Particulate fillers for polymers*. Smithers Rapra Publishing.
- [8] J.W.Kaczmar, J.Pach, R.Kozłowski (2007) Use of natural fibres as fillers for polymer composites. *International Polymer Science and Technology*, 34(6), 45-50. <https://doi.org/10.1177/0307174x0703400610>.
- [9] L.I.Melnyk (2009) *Patterns of formation and application of heat-resistant conductive siloxane-graphite materials*. Dissertation abstract.
- [10] İ.Uzun, S.Terzi (2012) Evaluation of andesite waste as mineral filler in asphaltic concrete mixture. *Construction and Building Materials*, 31, 284-288. <https://doi.org/10.1016/j.conbuildmat.2011.12.093>.
- [11] L.Melnyk, L.Chernyak, V.Svidersky, O.Belousov, A.Nehreyko (2020) Structure and properties of polymer composite based on natural zeolite. *French-Ukrainian Journal of Chemistry*, 8(1), 12-18. <https://doi.org/10.17721/fujcv8i1p12-18>.
- [12] A.Mohamed, S.Basfar, S.Elkatatny, B.Bageri (2020) Impact of Perlite on the properties and stability of Water-Based mud in Elevated-Temperature Applications. *ACS Omega*, 5(50), 32573-32582. <https://doi.org/10.1021/acsomega.0c04853>.
- [13] A.Sukhovi, L.Chursina, G.Tikhosova, N.Nezhluhenko (2020) New fillers for polymer composite materials. *Bulletin of the Kherson National Technical University*, 2(73), 61-68. <https://doi.org/10.35546/kntu2078-4481.2020.2.7>.
- [14] Z.Khosraftar, H.Masoumi, A.Ghaemi (2023) On the performance of perlite as a mineral adsorbent for heavy metals ions and dye removal from industrial wastewater: A review of the state of the art. *Case Studies in Chemical and Environmental Engineering*, 8, 100385. <https://doi.org/10.1016/j.cscee.2023.100385>.
- [15] H.Binici, K.Firdevs (2015) Production of perlite based thermal insulating material. *International Journal of Academic Research and Reflection*, 3(7), 47-54.
- [16] S.Narayanan, W.Batchelor, P.Webley (2013) A review on the use of zeolites to create valuable paper products and paper-like adsorbent materials. *Appita Journal*, 66(3), 235-245.
- [19] F.A.Mumpton (1981) *Mineralogy and geology of natural zeolites*.
- [20] F.A.Mumpton (1977) *Mineralogy and Geology of Natural Zeolites*. Brockport.
- [21] L.Bačáková, M.Vandrovcová, I.Kopová I.Jirka (2018) Applications of zeolites in biotechnology and medicine – a review. *Biomaterials Science*, 6(5), 974-989. <https://doi.org/10.1039/c8bm00028j>.
- [22] L.Maxim, R.Niebo, E.McConnell (2014) Perlite toxicology and epidemiology – a review. *Inhalation Toxicology*, 26(5), 259-270. <https://doi.org/10.3109/08958378.2014.881940>.
- [23] M.Barczewski, A.Hejna, P.Kosmela, O.Mysiukiewicz, A.Piasecki, K.SaŁasińska (2022) High-density Polyethylene - Expanded Perlite Composites: Structural Oriented Analysis of Mechanical and Thermomechanical Properties. *Materiale Plaste*, 59(3), 52-63. <https://doi.org/10.37358/mp.22.3.5605>.
- [24] M.Spoerk, J.Sapkota, G.Weingrill, T.Fischinger, F.Arbeiter, C.Holzer (2017) Shrinkage and warpage optimization of expanded-perlite-filled polypropylene composites in extrusion-based additive manufacturing. *Macromolecular materials and engineering*, 302(10), 1700143.
- [25] A.L.Page, A.A.Elseewi, I.R.Straughan (1979) Physical and chemical properties of fly ash from coal-fired power plants with reference to environmental impacts. In *Residue Reviews: Residues of Pesticides and Other Contaminants in the Total Environment* (pp. 83-120). Springer New York.
- [26] L.Melnyk, L.Chernyak (2022) Analysis of volcanic rocks as fillers for polymer composites. *Modern Engineering and Innovative Technologies*, 22(01), 42-46. <https://doi.org/10.30890/2567-5273.2022-22-01-008>.
- [27] E.Fischer, D.Cuccato, G.Storti, M.Morbidei (2018) Effect of the charge interactions on the composition behavior of acrylamide/acrylic acid copolymerization in aqueous medium. *European Polymer Journal*, 98, 302-312. <https://doi.org/10.1016/j.eurpolymj.2017.11.022>.
- [28] Y.A.Yakovleva, N.A.Barykin, O.S.Eltsov (2016) Identification of the monomeric composition of poly(styrene)acrylates. *Chimica Techno Acta*, 3(3), 193-212. <https://doi.org/10.15826/chimtech.2016.3.3.014>.
- [29] T.Guo, J.Song, Y.Jin, Z.Sun, L.Li (2019) Thermally stable and green cellulose-based composites strengthened by styrene-co-acrylate latex for lithium-ion battery separators. *Carbohydrate Polymers*, 206, 801-810. <https://doi.org/10.1016/j.carbpol.2018.11.025>.

IZVOD

KOMPARATIVNO PROUČAVANJE RAZLIČITIH VULKANSKIH MATERIJALA KAO PUNILA U POLIMERNIM KOMPOZITIMA

Predmet studije bili su kompozitni materijali koji koriste stene vulkanskog porekla kao punilo (60-90 tež. %) i disperziju Latex 2012 i Policril 590 kao a matrica. Osobnosti hemijskih i mineraloških sastava i površinska svojstva perlita i zeolita kao interakcija sa faktorima u formaciji prikazane su u kompozitnim strukturama . Utvrđene su razlike u koeficijentima liofilnosti i efektivne specifične površine zeolita i perlita, koje su 0,318 prema 0,189 i 11,68 prema 2,20 m²/g, respektivno. Uticaj visoke koncentracije punila na formiranje strukture pora i indikatora i sastava i mehaničkih i fizičkih svojstava je procenjeno. Mogućnost prilagođavanja svojstva kompozita u sledećem opsegu je uspostavljena: voda apsorpcija u 4,16 mas. %, otvorena poroznost 3,58-21,35 %, rezidualna deformacija 0,1-0,3 , Youngov modul 19,7-677,5 MPa.

Ključne reči: kompozit, punilo, perlit, zeolit, koncentracija, kopolimer, poroznost, svojstva.

Naučni rad

Rad primljen: 30.03.2024.

Rad prihvaćen: 7.06.2024.

The ORCID Ids of all the authors are as follows:

Liubov Melnyk: <http://orcid.org/0000-0001-5139-3105>

Lev Chernyak: <https://orcid.org/0000-0001-8479-0545>

Valentin Svidersky: <https://orcid.org/0000-0002-4457-6875>

Ludmila Vovchenko: <https://orcid.org/0000-0002-0783-4310>

Viktorija Yevpak: <https://orcid.org/0009-0006-0747-2942>

Sirisha Korrai^{1*}, B. Vinay Sagar², Madhavi Earle^{3*},
Sangeetha Sankhyayani Achanta⁴, Hemanshu Mediboyana⁵

¹Department of Basic Sciences & Humanities, Vignan's Institute of Information Technology (A), Duvvada, Visakhapatnam-530049, India;

²Department of Environmental Sciences, Andhra University, Visakhapatnam, India; ³NSRIT College, Visakhapatnam, Andhra Pradesh, India; ⁴Department of Environmental sciences, Archarya Nagarjuna University, Andhra Pradesh, India; ⁵Centre for the Environment, Indian Institute of Technology, Guwahati, Assam

Scientific paper

ISSN 0351-9465, E-ISSN 2466-2585

<https://doi.org/10.62638/ZasMat1172>



Zastita Materijala 65 (4)
724 – 733 (2024)

Evaluating the water quality of a Kondakarla Ava Lake for Agricultural Endeavours in Visakhapatnam, India

ABSTRACT

Global population growth is placing a pressure on freshwater resources. Freshwater resources are becoming scarcer in terms of both quantity and quality due to the rising demand. Assessing water quality of surface water bodies for irrigation is essential as water with poor quality can pose health risks. The study involved observing the physicochemical parameters of Kondakarla Ava Lake from six different sampling locations. The study revealed that it could not use directly for drinking purposes as per NSFQI. According to parameters like RSC, SAR, PI, % Na, and IWQI, water quality is appropriate for irrigation. It is further strengthened by the USSL diagram showing that the Kondakarla Ava Lake samples fall under the categories C3S1 and C4S1, which indicates that water has low sodium peril and high to very high salinity. The Wilcox diagram showed the grouping of the samples under three categories: excellent, good to permissible, and doubtful.

Keywords: Eutrophication; Potability; Water Quality Index; Overall Index of Pollution; Principal Component Analysis; Irrigation.

1. INTRODUCTION

Water considered the most precious resource on the planet, plays an indispensable role in human survival. Although about 70% of the earth's surface is surrounded by water, only 3% of it is considered to be freshwater which is suitable for human use. And it is estimated that approximately 0.4 percent of the earth's usable and drinkable water is shared among the 7.8 billion inhabitants.

Deep down from the history of human civilisation, surface water bodies like rivers and lakes are prone to heavy pollution as they are easily accessible for waste disposal. Natural and anthropogenic processes significantly influence the surface water quality [1]. Industrialisation, urbanisation, and modern agricultural practices drastically impact on water quality [2, 3, 4, 5, 6, 7]. In the recent decade, there has been a considerable enhancement in the population and their utilisation of resources, generating sewage and its run-off, proportionally increasing the nutrient inputs for Eutrophication [8].

Water quality and loss of dire habitats and other pollutants in the water bodies generate immense stress on the aquatic ecosystems resulting in the deterioration of the biodiversity, which might ultimately decrease the life quality for the local inhabitants [9]. With the ever-increasing human interferences and the ill effects of pollution, it is obligatory to determine water quality before it is deemed fit for human use.

To assess the quality of these water bodies, some frequently used Water Quality Index (WQI) in open domains are as follows [10]. Surface water is considered as an essential resource for irrigation, making it easier to cultivate crops nearby. A sizable area of land may benefit from using lake water for irrigation, which would raise agricultural productivity and sustain local lives. Furthermore, the necessity of sustainable water management techniques is highlighted by the relationship between environmental protection and agricultural activities. The long-term sustainability of agriculture and the health of ecosystems and societies depend on a harmonious balance between environmental preservation and productivity.

A technique such as SAR (Sodium Absorption Rate) is the additional index used to evaluate the suitability of water used in irrigation [11]. Statistical approaches were employed to endow with

*Corresponding author: Madhavi Earle and Sirisha Korrai

E-mail: siritejvardhan07@gmail.com

Paper received: 17.04.2024.

Paper accepted: 22.05.2024.

representative and reliable chemical analysis of the water quality. The non-linear nature of the environmental information formulates spacio-temporal differences in water quality, which are usually difficult to interpret [12]. In this study, we made use of multivariate statistical tools like Correlation and Principal Component Analysis (PCA) as these are extensively used as unbiased techniques for the study of water quality facts for deriving important conclusions [13 &14].

2. METHODOLOGY

2.1 Study area

Kondakarla Ava wetland is one of the leading natural freshwater lakes of Andhra Pradesh and is 50 km southwest of Visakhapatnam, India. It lies between 17° 35' 30" N, 17°36'02"N latitudes, and 82° 59' 27" E and 83° 01' 02" E longitudes (Fig 1).

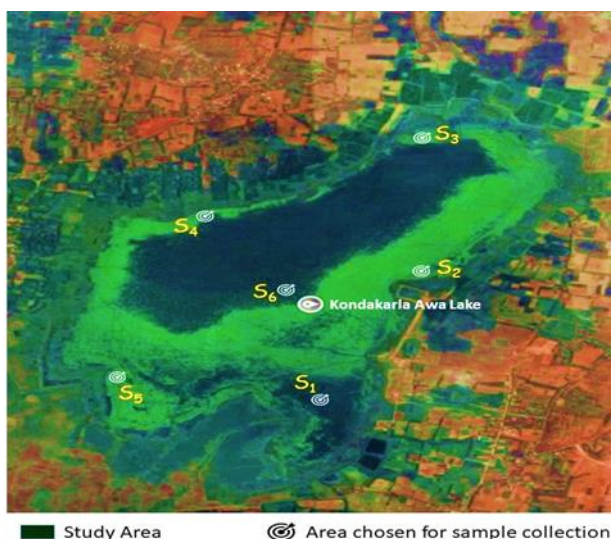


Figure 1. Study area

The Kondakarla Ava wetland is a share of the Sarada riverine structure and is categorised as a perpetual, warm, eutrophic shallow freshwater lentic body. The total water spread of the Kondakarla Ava wetland is about 753.93 hectares, with a self-catchment area of about 2538.19 hectares. The twelve-monthly rainfall in the present study area is about 955 mm, with mean temperatures varying from 23.5⁰ C to 31.2⁰ C.

2.2. Sample collection and Physico-chemical analysis

The water samples were collected in a pre-cleaned polyethylene bottle for six months (i.e., Pre-monsoon (March to May, 2023) and Post-monsoon (October to December, 2023) from six different sampling locations. To obtain the lake's overall water quality, consider the mean values independently in pre-and post-monsoon seasons.

A continuous lake water quality monitoring was done in both seasons, which involved a comprehensive physicochemical analysis. The analysis of essential cations (Ca⁺², Mg⁺², K⁺, Na⁺) and anions (Cl⁻, SO₄⁻², NO₃⁻³, PO₄⁻³) and other general parameters like pH, Temperature, BOD, DO, TS, TSS, TDS, and TH were conducted using standard analytical procedures as stipulated by APHA (2005) [15]. Each parameter was examined thrice for consistency in the obtained values. The irrigational Water Quality Index, Sodium Absorption Rates (SAR), and Percent Sodium (% Na) were investigated in all collected samples to check the suitability for irrigation.

In contrast, assessing its suitability for drinking, NSFQI was used along with a comparison of observed values with that of the Bureau of Indian Standards (BIS 1998). The Overall Index of Pollution (OIP) was utilised to analyse the overall quality of lake water. *Evaluation of potable water quality comparison with standards stipulated by BIS, 1998.* The observed physicochemical values were compared with the criteria specified by the BIS[16], 1998, to acknowledge their usage for drinking purposes.

2.3 National Sanitation Foundation Water Quality Index (NSFWQI)

Water quality valuation can be used as a tool to provide valuable facts for strategic planners and decision-makers [8]. WQI is a sole entity that converts detailed water quality data into a simple form that generally helps express the overall water quality in a particular region at a specific period.

By calculating the NSFQI, the suitability of the water sample for human consumption can be determined. Horton [17], has suggested the first WQI followed by other indices, which included the National Sanitation Foundation (NSF) by the US, which is putative as a more user-oriented WQI based on the opinions of experts or panellists [18]. The NSFQI, employed to estimate the water quality of Kondakarla Lake, is precisely expressed as:

$$NSFWQI = \sum_{n=1}^n (SI_i)$$

Where SI_i=Sub index for ith water quality parameter and was calculated by using the Equation 1 below:

$$SI = W_i q_i \quad (Eq 1)$$

Where

W_i= Relative Weight (in terms of importance) associated with water quality parameters which is given Equation 2:

$$W_i = \frac{w_i}{\sum_{n=1}^n w_i} \quad (Eq 2)$$

and q_i = quality rating and it is measured by using Equation 3:

$$q_i = (C_i / S_i) * 100 \quad (\text{Eq 3})$$

For the study, standard software is employed to calculate NSFQI [19]. The scores range from 0 to 100. The WQI scores were categorised into five types as Excellent; Good; Medium; Bad; and Very Bad, usually meant to summarise the water quality of that particular area.

2.4. Overall Index of Pollution (OIP)

For the valuation of overall surface water quality in Indian conditions, Sargaonkar and Deshpande in the year 2003 [20], developed a unique index named Overall Index of Pollution (OIP), based on a general classification scheme. Water quality is classified into five classes as follows in Fig. 2. The index was calculated using the following scientific expression:

$$OIP = \sum_{i=1}^n P_i / n$$

Where

P_i = Pollution Index of i th parameter; n = number of parameters.

$P_i = V_i / S_i$ (observed value of the parameter) / S_i (standard value of the parameter).

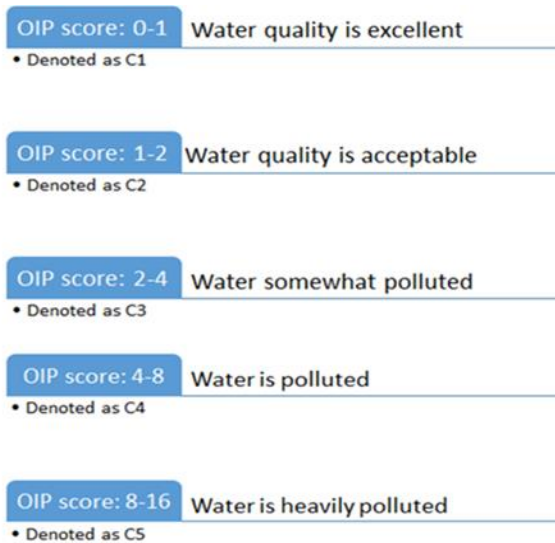


Figure 2. OIP score

2.5. Evaluation of irrigation water quality

The appropriateness of surface water for irrigation was evaluated by using different types of indices like Residual Sodium Carbonate (RSC), Sodium Percentage (Na%), and Sodium Adsorption Ratio (SAR), Permeability Index, Chloride and Electrical Conductivity (EC). The irrigation water classifications, based on the above physicochemical and statistical parameters, are represented in Table 1.

2.6. Permeability and Infiltration Hazard

The ubiquitous water quality factor governing the regular rate of water penetration is the relative and absolute concentrations of cations that include Na^+ , Mg^{2+} , and Ca^{2+} in the water, also acknowledged as the Sodium Adsorption Ratio (SAR). The SAR value of irrigation measures the relative quantities of Na^+ to Ca^{2+} and Mg^{2+} and is calculated using the formula given by Richards in the year 1954. The procedure is represented below:

$$SAR = \frac{\text{Na}^+}{\sqrt{\frac{\text{Ca}^{2+} + \text{Mg}^{2+}}{2}}}$$

where ion concentrations are in milliequivalents per litre (meq/l) units.

Water quality is considered excellent for irrigation if the values range below 10.

2.7. Percent Sodium (% Na)

The sodium content in the irrigation waters is further expressed in terms of % Na (amounts expressed in meq/l) and this is computed using the below method:

$$\% \text{Na} = \{(\text{Na}^+ + \text{K}^+) / (\text{Ca}^{2+} + \text{Mg}^{2+} + \text{Na}^+ + \text{K}^+)\} * 100$$

2.8. Residual Sodium Carbonate (RSC)

Richards, 1954 [21] determined the harmful effects of carbonate (CO_3^{2-}) and bicarbonate (HCO_3^-) on irrigation water; stated as Residual Sodium Carbonate (RSC), which is computed using the below method where ion concentrations are represented in meq/l:

$$RSC = (\text{CO}_3^{2-} + \text{HCO}_3^-) - (\text{Ca}^{2+} + \text{Mg}^{2+})$$

2.9. Permeability Index (PI)

The soil permeability usually influences the proper usage of water for irrigation, which generally depends on the concentrations of cations like Na^+ , Ca^{2+} , and Mg^{2+} along with anions like HCO_3^- present in the soil. The formula used to compute the Permeability Index was put forward by [22] Doneen (1964) is as follows:

$$PI = \{(\text{Na}^+ + \sqrt{\text{HCO}_3^-}) / (\text{Ca}^{2+} + \text{Mg}^{2+} + \text{Na}^+)\} * 100$$

2.10. Irrigational Water Quality Index (IWQI)

Further, a complex irrigational water quality examination was carried out using the Irrigation Water Quality Index (IWQI), which uses various irrigation water quality indicators, which were further generalised and then presented in a single value (ranges from 0 to 100)- as in Table.2.

To process this index, we depend on the standards stated by the FAO paper No. 29 [23,24] along with a few specifications on the local studies. Q_i value was intended using the below equation:

$$Q_i = q_{imax} - \left\{ \frac{[(x_{ij} - x_{inf}) * q_{iamp}]}{x_{amp}} \right\}$$

Where q_{imax} is regarded as the maximal value of q_i for the class; x_{ij} is the measured value of chemical parameters; x_{inf} is termed as the minimal limit of the class to each parameter belongs; q_{iamp} is class amplitude; and x_{amp} is upper limit of the last class of each parameter. Finally, Irrigation Water Quality Index (IWQI) has been estimated using the below equation:

$$IWQI = \sum_{i=1}^n Q_i * w_i$$

IWQI is termed as a nondimensional index of irrigation water quality which usually ranges from 0 to 100, where Q_i is the quality measurement of the parameter, (i^{th}) a number from (0 to 100) is a function of its concentration. W_i is the normalised weight of the i^{th} parameter.

3. RESULTS AND DISCUSSION

3.1. Parameters for drinking water quality assessment

The examination of the surface water quality of the lake is essential for the maintenance and

existence of aquatic flora and fauna. The minimum, maximum, mean, and standard deviation values of each parameter in pre and post-monsoon for each station are depicted in Table 2.

Ca^{2+} and Mg^{2+} ions are probably due to the leaching of the minerals like dolomites, limestone, anhydrite and gypsum [25].

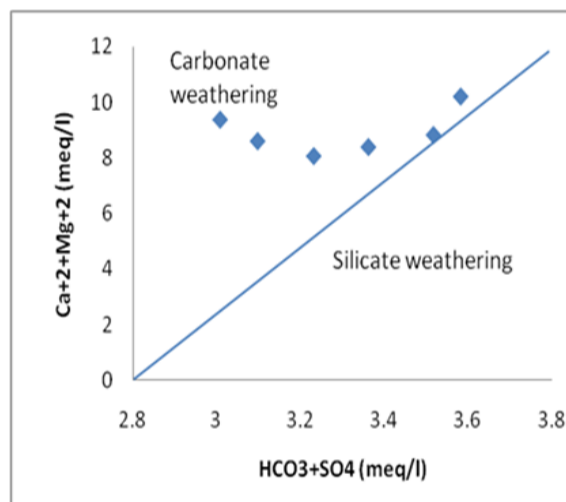


Figure 3. Scatter plot for $Ca^{2+} + Mg^{2+}$ Vs $HCO_3^- + SO_4^{2-}$

Table 1. The organisation of water for irrigation purposes based on physicochemical and statistical parameters

Parameter	Range in meq/l	Quality concerning the suitability for irrigation
Sodium Adsorption Ratio (SAR) (Richards, 1954)	0-10	Excellent
	10-18	Good
	18-26	Fair
	Above 26	Poor
Residual Sodium Carbonate (RSC) (Richards, 1954)	<1.25	Good
	1.25-2.5	Medium
	>2.5	Bad
Percent Sodium (% Na) (Wilcox, 1955)	<20	Excellent
	20-40	Good
	40-60	Permissible
	60-80	Doubtful
	>80	Unsuitable
Permeability Index (PI) (Doneen, 1964)	>75	Class I – Good
	25-75	Class II – Suitable
	<25	Class III – Unsuitable
Chloride (Cl ⁻ in meq/L) (Doneen, 1958)	>5	Class I – Good
	5-10	Class II – Hazardous
	<10	Class III – Very Hazardous
Electrical Conductivity (EC, μ S/cm)(Wilcox, 1955)	<250	Excellent
	250-750	Good
	750-2250	Permissible
	2250-5000	Doubtful
	>5000	Unsuitable
Irrigation Water Quality Index (IWQI)	80-100	Class I - Excellent
	60-80	Class II - Good
	45-60	Class III - Permissible

In particular, calcium can also be attained from the cation exchange process [26]. A scattered diagram (Fig.3) of $\text{Ca}^{2+} + \text{Mg}^{2+}$ Vs. $\text{HCO}_3^- + \text{SO}_4^{2-}$ [27] reflects that majority (i.e., five out of six samples) of the collected samples of the study area drop above the equi-line, which indicates that carbonate weathering plays a significant role in supplying these ions to the Kondakarla lake.

3.2. National Sanitation Foundation Water Quality Index (NSFWQI)

This study's computed NSFWQI values ranged from 43 to 57 meq/l. From these calculated values, it was evident that the quality of this lake water during the study period was graded as a medium quality category in the sampling stations S1 and S2, while the rest (S3 to S6) were categorised as bad. Hence this lake water is not suggestible for direct consumption by humans (Table 3). The computed NSFWQI values were categorised into five types (Fig. 3).

3.3. Overall Index of Pollution (OIP)

To determine the overall status of the water quality, OIP is computed. The computed values showed that the lake is excellent. The observed OIP values were 0.53 and 1.41 (Table 4). As per the classification given by [28], the present lake water quality during the study period was labelled as C1 category for five samples (S1, S2, S3, S4, and S6); while S5 falls under the C2 category (Fig.2).

3.4. Parameters for irrigational water quality assessment

3.4.1. Sodium Absorption Ratio (SAR)

According to the classification (Table 3), the quality of the study area was Excellent during the study period. The computed values of SAR were observed to be 4.17 meq/l and 3.606 meq/l during the study period.

3.4.2. Percent Sodium (% Na)

The most widely recommended % sodium for water for irrigation purposes should not exceed 50-60 to prevent its detrimental difficulties on the soil. The computed values of PI were 55.04 meq/l and 59.9 meq/l during the study period.

3.4.3. Residual Sodium Carbonate (RSC)

The excess quantity of CO_3^{2-} and HCO_3^- is known as Residual Sodium Carbonate (RSC). The observed values of RSC in the selected area range from -5.19 to -7.24, i.e., all the values fall under the excellent and safe category for irrigation (Table 2 & 3).

3.4.4. Permeability Index (PI)

Na^+ , Ca^{+2} , Mg^{+2} and HCO_3^- concentrations influence soil permeability [29]. Hence, the PI values were calculated using cations and anions to assess the water quality. The PI values in the present study ranged from 55.04 to 59.9, i.e., all the samples collected were suitable for irrigation (Tables 2 & 3).

3.4.5. Irrigational Water Quality Index (IWQI)

As per the classification (Table 2), all the samples in the present study area range from 70.23 to 84.79, i.e., they range from good to excellent for irrigation. The water quality is evaluated using different indices, and the data is presented in Table 3.

3.5. Correlation analysis

Correlation is a bivariate technique that signifies the association between two random variables, which provides a quick view of the water quality monitoring processes. Spearman's rank coefficients of correlation among twelve Physico-chemical parameters (i.e., EC, pH, Ca^{+2} , Mg^{+2} , Na^+ , K^+ , HCO_3^- , Cl^- , SO_4^{2-} , PO_4^{3-} , NO_3^- , K^+ and IWQI) was computed for analysis of correlation (Table 4), to identify the association between different random properties.

The highest correlation coefficients (nearer to -1.0 or +1.0) reflect the existing association between two variables. Suppose it is nearer to zero, demonstrating no connection among them [31]. In the present study, pH showed the most negligible correlation, while EC showed the highest correlation with maximum parameters. The rest of the parameters also exhibited a more or less strong positive correlation.

Table 2. Analytical results of the lake Kondakarla Ava

Parameters	Site 1		Site 2		Site 3	
	Pre-monsoon	Post – Monsoon	Pre-monsoon	Post - Monsoon	Pre-monsoon	Post - Monsoon
Temperature (oC)	26.3	30.5	26.5	27.5	25.2	27.5
pH	8.03	8.6	7.7	8.82	8.1	8.5
Turbidity (NTU)	7.8	8.4	6.9	7.6	7.4	8.2
EC ($\mu\text{S}/\text{cm}$)	476.6	520.4	433.2	498.1	467.2	514.1
Total Hardness (mg/l)	359.69	478.04	429.235	488.4245	351.6	412
Total Alkalinity (mg/l)	145.1	298.4	186.3	261.1	144.8	278.44

TDS (mg/l)	1020	1300	754	838	1121	1452
DO (mg/l)	8.1	11.6	8.2	12.4	8.4	10.4
BOD (mg/l)	2.8	10.3	1.9	7.2	3.9	10.2
Ca ²⁺ (mg/l)	67.53	95.3	112.2	67.65	72.97	96.42
CaH (mg/l)	168.622	237.96	280.16	287.8	168.742	239.08
Mg ²⁺ (mg/l)	46.4	58.3	37.1	49.3	46.52	59.42
MgH (mg/l)	149.07	240.07	191.07	203.01	191.19	241.19
Cl ⁻ (mg/l)	89.3	164.1	43.4	101.3	89.42	165.22
HCO ₃ ⁻ (mg/l)	152.3	201.2	152.3	196.6	116.41	202.32
SO ₄ ⁻ (mg/l)	19.3	25.35	15.21	20.51	20.12	26.47
NO ₃ ⁻ (mg/l)	1.12	3.34	2.14	1.14	0.65	4.46
PO ₄ ⁻ (mg/l)	0.25	1.27	0.1	0.4	0.37	2.39
Na ⁺ (mg/l)	81.5	101.86	94.7	96.2	95.7	102.98
K ⁺ (mg/l)	18.3	34.6	10.2	21.3	19.14	35.72

Parameters	Site 4		Site 5		Site 6	
	Pre-monsoon	Post-Monsoon	Pre-monsoon	Post-Monsoon	Pre-monsoon	Post-Monsoon
Temperature (°C)	25.1	28.5	26.8	30.2	24.3	27.6
pH	7.8	8.2	7.89	8.4	7.5	8.21
Turbidity (NTU)	7.1	7.4	7.3	8.2	7.2	7.8
EC (µS/cm)	424.1	472.3	446.4	522.3	443.1	491.7
Total Hardness (mg/l)	431.2	474.7	354.4	441.1	414.7	472.4
Total Alkalinity (mg/l)	174.32	254.1	175.4	274.2	167.3	265.4
TDS (mg/l)	784	1021	1189	1302	1122	1347
DO (mg/l)	8.3	11.8	8.4	10.6	8.7	11.7
BOD (mg/l)	3.2	7.3	4.8	11.2	1.4	6.3
Ca ²⁺ (mg/l)	113.6	116.7	69.85	99.62	114.3	100.74
CaH (mg/l)	281.56	285.4	170.942	242.28	174.062	245.4
Mg ²⁺ (mg/l)	36.2	51.7	48.72	62.62	51.84	65.74
MgH (mg/l)	150.47	247.51	193.39	205.41	196.51	244.39
Cl ⁻ (mg/l)	44.8	103.7	91.62	168.42	94.74	171.54
HCO ₃ ⁻ (mg/l)	117.81	199	154.5	208.64	157.62	205.52
SO ₄ ⁻ (mg/l)	16.61	22.91	22.32	29.67	25.44	32.79
NO ₃ ⁻ (mg/l)	2.05	10.78	4.34	7.66	7.46	3.54
PO ₄ ⁻ (mg/l)	1.5	2.8	1.21	5.59	1.22	1.54
Na ⁺ (mg/l)	82.9	98.6	97.9	106.18	101.02	109.3
K ⁺ (mg/l)	11.6	23.7	21.34	42.04	24.46	38.92

Table 3. Quality of water based on different indicators

	S1	Water quality-status	S	Water quality-status	S3	Water quality-status	S4	Water quality-status	S5	Water quality-status	S6	Water quality-status
NSFWQI	50	Medium	57	Medium	48	Bad	46	Bad	43	Bad	49	Bad
OIP	0.76	Excellent	0.53	Excellent	0.91	Excellent	0.99	Excellent	1.41	Acceptable	0.92	Excellent
IWQI	77.65	Good	70.23	Good	79.3	Good	74.42	Good	81.47	Excellent	84.79	Excellent
PI	59.16	Suitable	59.11	Suitable	59.51	Suitable	55.04	Suitable	59.9	Suitable	56.15	Suitable
RSC	-5.48	Safe	-5.19	Safe	-5.98	Safe	-6.78	Safe	-5.84	Safe	-7.24	Safe
SAR	3.895	Excellent	4.137	Excellent	4.167	Excellent	3.645	Excellent	4.226	Excellent	4.046	Excellent
Na%	46.81	Permissible	49.54	Permissible	48.16	Permissible	44.54	Permissible	47.95	Permissible	45.33	Permissible

Table 4. Correlation matrix for analysed parameters

	EC	pH	Ca ²⁺	Mg ²⁺	TDS	Na ⁺	K ⁺	HCO ₃ ⁻	Cl ⁻	SO ₄ ²⁻	PO ₄ ⁻	NO ₃ ⁻	IWQ _I
EC	1												
pH	0.331	1											
Ca ²⁺	0.824	0.006	1										
Mg ²⁺	0.742	-0.174	0.64	1									
TDS	0.871	0.124	0.871	0.973	1								
Na ⁺	0.916	-0.11	0.811	0.914	0.981	1							
K ⁺	0.784	0.472	0.742	0.412	0.873	0.617	1						
HCO ₃ ⁻	0.947	0.227	0.631	0.88	0.911	0.874	0.747	1					
Cl ⁻	0.914	0.413	0.711	0.628	0.899	0.887	0.712	0.874	1				
SO ₄ ²⁻	0.875	-0.241	0.841	-0.852	0.926	0.712	0.624	0.799	0.742	1			
PO ₄ ⁻	0.041	-0.02	0.648	0.245	0.939	0.354	0.124	0.878	0.841	0.719	1		
NO ₃ ⁻	0.215	-0.041	0.731	0.124	0.901	0.133	0.233	0.851	0.872	0.784	0.471	1	
IWQ _I	-0.972	0.217	-0.871	0.947	-0.972	-0.974	-0.817	-0.896	-0.981	-0.857	-0.523	0.291	1

3.6. Principal Component Analysis (PCA)

Further analysis of factor loadings showed that EC, TH, TDS, BOD, TA, Ca²⁺, Mg²⁺, Na⁺, K⁺, HCO₃⁻, Cl⁻, SO₄²⁻, PO₄³⁻, and NO₃⁻ were found to be the major factors affecting the water quality in the selected area (Table 5). For factor 1, EC, TH, TDS, Mg²⁺, Na⁺, K⁺, HCO₃⁻, Cl⁻ and PO₄⁻ showed high positive loading value (> 0.9). These are the most significant variables for the first factor and were mentioned to be the most responsible variables for pollution loads in the Kondakarla Ava Lake during the study period. Factor 2 is heavily loaded with TA, BOD, Ca²⁺ and Na⁺, reflecting the influence of organic matter that may have intruded from domestic and agricultural run-off. High positive loading of Ca²⁺ and Na⁺ confirms the discharge of agricultural run-off [30]. The third factor is highly loaded with SO₄⁻ and NO₃⁻, which is attributed to agricultural run-off associated with excessive usage of organic and chemical fertilisers.

Thus, the water is heavily polluted with organic and inorganic pollutants which are attributed to agricultural run-off or the dumping of domestic wastewater into the lake. The lake is eutrophic (heavily flooded with algal blooms) and is one of the evident factors for its deterioration.

3.7. United States Salinity Laboratory (USSL) Diagram

A total reflection of the effect of SAR & EC on the quality of soil is determined by the USSL diagram. The USSL graph for the present study samples shows that samples 1, 2, 4, 5, and 6, which account for about 83.33 %, fall under C3S1 (low sodium and high salinity category), and sample 3, which represents 16.6 % of the samples, fall under C4S1 (low sodium and very high salinity category). Thus, this diagram (Fig 3) shows that this water can be used for irrigation purposes, with frequent leaching, good drainage, and intensive management support.

Table 5. Factorial loads of Kondakarla Lake

Variables	F1	F2	F3
pH	-0.3611	0.255	0.21
EC (µS/cm)	0.942	0.032	0.014
Total Hardness (mg/L)	0.911	0.047	-0.022
Total Alkalinity (mg/L)	0.122	0.957	-0.735
TDS (mg/L)	0.9238	-0.536	0.321
DO (mg/L)	-0.9404	-0.447	0.112
BOD (mg/L)	0.7957	0.957	-0.7431
Ca ²⁺ (mg/L)	0.472	0.914	0.176
Mg ²⁺ (mg/L)	0.969	-0.386	-0.623
Cl ⁻ (mg/L)	0.9293	0.447	0.1373
HCO ₃ ⁻ (mg/L)	0.9973	0.764	-0.361
SO ₄ ⁻ (mg/L)	0.223	0.112	0.947
NO ₃ ⁻ (mg/L)	0.321	0.258	0.918
PO ₄ ⁻ (mg/L)	0.971	0.291	-0.112
Na ⁺ (mg/L)	0.952	0.912	-0.551
K ⁺ (mg/L)	0.982	0.345	0.1373

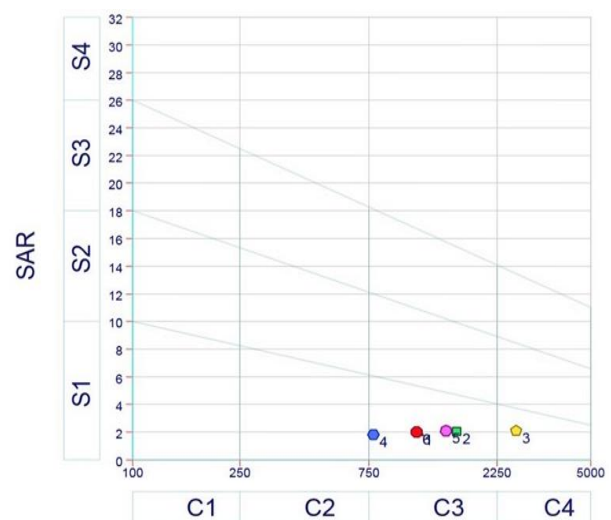


Figure 4. USSL Salinity diagrams indicating the classification of irrigation waters

3.8. Wilcox Diagram

Wilcox diagram represents the effect of % Na and EC on the soil and crops. As per the Wilcox classification (Fig 5), sample 4 falls under Excellent (16.66 %); samples 1,2, 5, and 6 (about 66.66%) fall under the good to permissible section, and sample 3 (16.66 %) fall under doubtful.

Thus, the study stated that as per the USSL diagram, the samples fall under highly saline to very highly saline, making them unsuitable for irrigation under normal conditions. In contrast, as per Wilcox classification, most samples drop below the good to permissible category.

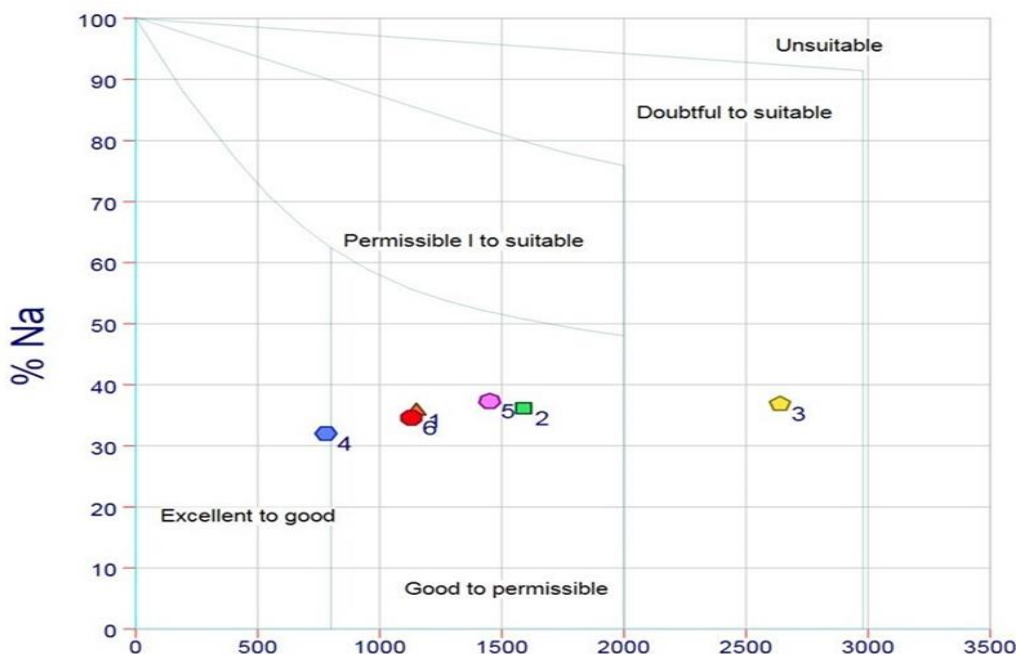


Figura 5. Wilcox diagram depicting the classification of irrigation water based on % Na and EC

4. CONCLUSION

The study aims in determining the suitability of the lake water of Kondakarla Ava of Visakhapatnam for human consumption along with irrigation. The study found that the water is unsuitable for drinking depending on the NSWQI values, as they range from medium to lousy category. Based on values of RSC, SAR, PI, % Na, and IWQI, all the samples were detected to be appropriate for irrigation. This evaluation was further supported by obtained OIP values, in which all samples fall under the excellent category. The statistical analysis, including Principal Component Analysis and correlation analysis, stressed the influence of agricultural run-off and wastewater discharge as the primary source of pollution loads. The values plotted on the USSL diagram showed that the samples of the Kondakarla Ava Lake fall under the categories C3S1 and C4S1, which indicates that they are low sodium hazards and high to very high salinity. The Wilcox diagram, on the other hand, shows that the samples fall under three categories excellent, good to permissible, and doubtful.

Acknowledgements

The authors thank Andhra University for providing laboratory space for analysis.

5. REFERENCES

- [1] [1] T.G.Kazi, M.B.Arain, M.K.Jamali, N.Jalbani, H.I.Afridi, R.A.Sarfraz, J.A.Baig, A.Q.Shah (2009) Assessment of water quality of polluted lake using multivariate statistical techniques: a case study. *Ecotoxicol Environ Saf.* Feb; 72(2), 301-9.doi: 10.1016/j.ecoenv.2008.02.024. Epub 2008
- [2] [2] H.P.Jarvie, B.A.Whitton, C.Neal (1998) Nitrogen and phosphorus in east coast British Rivers: speciation, sources and biological significance. *Sci Total Environ*, 210(211), 79–109. [https://doi.org/10.1016/S0048-9697\(98\)00109-0](https://doi.org/10.1016/S0048-9697(98)00109-0).
- [3] [3] A.R.Karbassi, S.MMonavari, G.R.NabiBidhendi, J. Nouri, K. Nematpour (2008) Metal pollution assessment of sediment and water in the Shur River. *Environ Monit Assess*, **147**, 107–116. <https://doi.org/10.1007/s10661-007-0102-8>
- [4] [4] A.H.Mahvi, J.Nouri, R.Nabizadeh, A.A.Babaei (2005) Agricultural activities impact on groundwater nitrate pollution. *Int J Environ Sci Tech*, 2(1), 41–47. [Online]. Available: <https://doi.org/10.1007/BF03325856>

- [5] J.Nouri, A.H.Mahvi, G.R. Jahed, A.A.Babaei (2008) Regional distribution pattern of groundwater heavy metals resulting from agricultural activities. *Environ. Geo.*, 55(6), 1337-1343. [Online]. Available: <https://doi.org/10.1007/s00254-007-1081-3>
- [6] V.Simeonov, P.Simeonova, R.Tsitouridou (2004) Chemometric quality assessment of surface waters: two case studies. *Eco ChemEng*, 11(6), 449–469.
- [7] V.S.Simeonov, J.Samara, C.Zachariadis, G.Voutsas, D.Anthemidis, A.Sofoniou, M.Kouimtzis (2003) Assessment of the Surface Water Quality in Northern Greece. *Water research*, 37, 4119-24.[Online]. Available: [https://doi.org/10.1016/S0043-1354\(03\)00398-1](https://doi.org/10.1016/S0043-1354(03)00398-1)
- [8] P.R.Chaudhari, D.V.Ahire, V.D.Ahire, M. Chakravarty, S. Maity (2013) Soil Bulk Density as related to Soil Texture, Organic Matter Content and available total Nutrients of Coimbatore Soil. *Int. J. Scientific and Res. Publications*, 3(2), 67-75.
- [9] J.A.Herrera-Silveira, S.M.Morales-Ojeda (2008) Evaluation of the health status of a coastal ecosystem in southeast Mexico: Assessment of water quality, phytoplankton and submerged aquatic vegetation. *Marine Pollution Bulletin*, 59(1-3), 72-86. [Online]. Available: <https://doi.org/10.1016/j.marpolbul.2008.11.017>.
- [10] T.Poonam, B.Tanushree, C. Sukalyan (2015) Water quality indices-important tools for water quality assessment: a review.*Int. J. Adv. Chem.*, 1(1), 15-28.
- [11] K.S. Srivastava, L.A. Ramanathan (2008) Geochemical Assessment of Groundwater Quality in Vicinity of Bhalswa Landfill.Delhi; India by Using Graphical and Multivariable Statistical Methods. *Environmental Geology*, 53, 1509-1528.
- [12] W.Dixon, B.Chiswell (1996) Review of Aquatic Monitoring Program Design. *Water Research*, 30, 1935-1948.
- [13] C.R.Surakasi, S.H.Doke (2019) Assessment of groundwater quality in the vicinity of landfill site: A case study of Dhapa landfill site, Kolkata. *Applied Water Science*, 9(2), 42-49. Available: <https://doi.org/10.1007/s13201-019-1088-1>.
- [14] K.Singh, A.Malik, D.Mohan, S.Sinha (2004) Multivariate Statistical Techniques of the Evaluation of Spatial and Temporal Variations in Water Quality of Gomti River (India) – A Case Study. *Water research*, 38, 3980-92.[Online]. Available: <https://doi.org/10.1016/j.watres.2004.06.011>.
- [15] APHA (2005) Standard Methods for Examination of Water and Wastewater. American Public Health Association, Washington, D.C.
- [16] Bureau of Indian Standards (BIS) (1998) Drinking water specifications (revised 2003) IS:10500.
- [17] R.K.Horton (1965) An index number system for rating water quality. *J Water Pollut. Control Fed.*, 37(3), 300-306.
- [18] R.M. Brown, N.J. McClelland, R.A. Deininger, R.G. Tozer (1970) Avater quality index--Do we dare? *Water and Sewage Works*, vol. 117, p. 339.
- [19] B.Oram (2012) Water Quality Index Calculator. Field Manual for Water Quality Monitoring, Pennsylvania, USA.
- [20] A. Sargaonkar, V. Deshpande (2003) Development of an Overall Index of Pollution for Surface Water Based on a General Classification Scheme in Indian Context. *Environmental monitoring and assessment*, 89, 43-67.[Online]. Available: <https://doi.org/10.1023/A:1025886025137>
- [21] L.M. Richards (1954) Diagnosis and Improvement of Saline and Alkaline Soils. *Agriculture Handbook*, No. 60, US Salinity Laboratory, USDA.
- [22] L.D.Doneen (1964) Water quality for agriculture. Department of Irrigation, University of California, Davis.
- [23] R.S.Ayers, D.W.Westcot (1999) The water quality in agriculture. 2nd ed., UFPB, FAO Irrigation and drainage, Campina Grande.
- [24] R.S.Ayers and D.W.Westcot (1985) Water Quality for Agriculture. FAO Irrigation.
- [25] N. Bhat, A. Bhat, S. Nath, B. Singh, D. Guha (2016) Assessment of Drinking and Irrigation Water Quality of Surface Water Resources of South-West Kashmir, India. *Journal of Civil & Environmental Engineering*, 6, 78-85.
- [26] R.M.Garrels (1976) Survey of Low Temperature Water Mineral Relations in Interpretation of Environmental Isotope and Hydrogeochemical Data in Groundwater Hydrology, Vienna, International Atomic Energy Agency, p. 65–84.
- [27] P.Datta, S.Tyagi (1996) Major ion chemistry of groundwater in Delhi area: Chemical weathering processes and groundwater flow regime. *Journal of the Geological Society of India*, 47, 179-188.
- [28] C.N. Sawyer, P.L. McCarty (1978) Chemistry for Environmental Engineering. 3rd ed., McGraw-Hill Book Co., New York.
- [29] S.K. Singh, P.K. Srivastav, D. Singh, D. Han, S.K. Gautam, A.C. Pande (2015) Modeling ground water quality over a humid subtropical region using numerical indices, earth observation datasets and X ray diffraction techniques, A case study of Allahabad district India. *Environmental Geochemical Health*, 37(1), 157–180.
- [30] H. Juahir, S.M. Zain, M.K. Yusoff, T.I.T. Hanidza, A.S.M. Armi, M.E. Toriman, M. Mokhtar (2011) Spatial water quality assessment of Langat River basin (Malaysia) using environmetric techniques. *Environ. Monit.Assess.*, 173, 625-641.
- [31] K.S. Srivastava, L.A. Ramanathan (2008) Geochemical Assessment of Groundwater Quality in Vicinity of Bhalswa Landfill.Delhi; India by Using Graphical and Multivariable Statistical Methods. *Environmental Geology*, 53, 1509-1528.

IZVOD

KUMULATIVNI PRISTUP ZA PROCENU KVALITETA POVRŠINSKE VODE JEZERA KONDAKARLA AVA, VISAKHAPATANAM, INDIJA

Globalni rast stanovništva vrši pritisak na slatkovodneresurse. Slatkovodni resursi postaju sve oskudniji u pogledu količine i kvaliteta zbog rastuće potražnje. Procena kvaliteta vode površinskih vodnih tela za navodnjavanje je od suštinskog značaja jer voda lošeg kvaliteta može predstavljati rizik po zdravlje. Studija je uključivala posmatranje fizičko-hemijskih parametara jezera Kondakarla Ava sa šest različitih lokacija za uzorkovanje. Studija je otkrila da se ne može koristiti direktno za piće prema NSFVKI. Prema parametrima kao što su RSC, SAR, PI, % Na i IVKI, kvalitet vode je odgovarajući za navodnjavanje. Dodatno je ojačan USSL dijagramom koji pokazuje da uzorci jezera Kondakarla Ava spadaju u kategorije C3S1 i C4S1, što ukazuje da vodama nisku opasnost od natrijuma i visok do veoma visok salinitet. Vilcok dijagram je pokazao grupisanje uzoraka u tri kategorije: odlično, dobro do dozvoljeno i sumnjivo.

Ključnereči: eutrofikacija, Potabiliti, Indeks kvaliteta vode, Ukupan indeks zagađenja, Glavni analiza komponenti, Navodnjavanje

Naučni rad

Rad primljen: 17.04.2024.

Rad prihvaćen: 22.05.2024.

The ORCID Ids of all the authors are as follows:

1. Dr Madhavi Earle: <https://orcid.org/000-0001-9945-0201>
2. Dr SirishaKorrai: <https://orcid.org/0000-0002-7215-8128>
3. Dr B. VinaySagar: <https://orcid.org/0009-0004-4522-9084>
4. Sangeetha S Achanta: <https://orcid.org/0009-0002-6342-1251>
5. HemanshuMediboyana: <https://orcid.org/0000-0002-0324-6909>

Rawnaq Jima'a¹, Naser Shaalan², Muna Bufaroosha^{3*}, Gamal A. El-Hiti⁴, Benson M. Kariuki⁵, Dina S. Ahmed⁶, Emad Yousif^{7**}

¹Department of Chemistry, College of Science, University of Diyala, Diyala, Iraq; ²Department of Chemistry, College of Science for Women, University of Baghdad, Baghdad, Iraq; ³Department of Chemistry, College of Science, United Arab Emirates University, Al-Ain, United Arab Emirates; ⁴Department of Optometry, College of Applied Medical Sciences, King Saud University, Riyadh, Saudi Arabia; ⁵School of Chemistry, Cardiff University, Main Building, Park Place, Cardiff, UK; ⁶Department of Chemical Industries, Institute of Technology-Baghdad, Middle Technical University, Baghdad, Iraq; ⁷ Department of Chemistry, College of Science, Al-Nahrain University, Baghdad, Iraq

Scientific Paper

ISSN 0351-9465, E-ISSN 2466-2585

<https://doi.org/10.62638/ZasMat1045>



Zastita Materijala 65 (4)
734 – 747 (2024)

Synthesis and Properties of New Metal Complexes Containing Heterocyclic Moieties and Investigation of the Role of the Metal in Carbon Dioxide Gas Capture

ABSTRACT

The continuous release of carbon dioxide (CO₂) into the atmosphere will inevitably lead to greater environmental damage. The capture and storage of CO₂ is one strategy to mitigate the harm associated with its high concentrations in the atmosphere. The design and synthesis of new materials to act as storage media for CO₂ is currently an important challenge for researchers. In this regard, the investigation into the synthesis of new organometallic materials and their potential as CO₂ storage media is reported. Therefore, the current work aimed to produce new materials using a simple procedure and investigate their properties, including factors affecting their CO₂ adsorption. Four metal complexes containing heterocyclic units were synthesized using a simple method, and their structures were confirmed using several techniques. The surface morphology of the materials was inspected by microscopy. The metal complexes exhibited tunable particle sizes with diameters that ranged from 16.77 to 97.62 nm and a Brunauer–Emmett–Teller surface area of 1.20–4.01 m²/g. The materials can capture CO₂ at 323 K and 40 bars, with the manganese-containing complex showing the highest CO₂ storage capacity (13.1 cm³/gm).

Keywords: synthesis, metal complexes, carbon dioxide capture, surface area, surface morphology

1. INTRODUCTION

The level of carbon dioxide (CO₂) in the atmosphere is on an upward curve correlated with the growing demand for energy and resources (e.g., power stations and the pharmaceutical industry) and the associated high demand for fossil fuels [1]. Currently, the concentration of CO₂ in the atmosphere is over 50% higher than the level at the end of the 19th century [2]. The increase in CO₂ levels is linked to rises in the surface temperature of the Earth, sea level, and the acidity of ocean water, for example, leading to serious environmental and socioeconomic

problems [3–6]. It is challenging to reduce CO₂ emissions into the atmosphere rapidly due to the continuous high demand for fossil fuels, and so a multifaceted strategy is needed to control the levels. One approach is to find reliable alternative sources of energy to replace the use of fossil fuels, and, indeed, much attention has been paid to renewable sources such as wind, solar, nuclear, and biomass as a strategy to reduce CO₂ emissions into the atmosphere [7, 8]. However, renewable sources currently fall far short of the capacity required to meet the global demand for energy and generally cannot compete with fossil fuels in terms of cost [9].

Another way to address the unsustainable levels of the gas in the atmosphere is CO₂ capture. For this to be successful, the design and use of new adsorbent materials to capture CO₂ requires exploration [10–13]. Several processes have been used

* Corresponding author: Muna Bufaroosha, Emad Yousif
E-mail: *muna.bufaroosha@uaeu.ac.ae, **emad_yousif@hotmail.com

Paper received: 31.03.2024.

Paper accepted: 5.06.2024.

to capture CO₂ from the atmosphere [14–20]. For example, amines (e.g., ethanolamine and ammonia) have been employed to remove CO₂ from natural gas [21]. However, there are associated risks with the use of amines since they are volatile and hazardous. The process of CO₂ capture often involves the separation of the gas and its adsorption at high pressure [22]. Thus, many new porous materials have been tested as storage media [23, 24]. Porous materials designed for CO₂ capture should meet certain requirements; they should be stable, polar, have large enough surface area and pore size, be easy to synthesize, be cheap to produce, have a long shelf life, be recyclable, and not pose a danger to the environment [25–28]. Examples of materials that have been tested as CO₂ adsorbents include metal-organic frameworks, carbon-based materials, zeolites, cross-linked polymers, and inorganic materials [29–32]. Metal oxides have been used with metal carbonates as materials in a chemical looping process, but their adsorption capacity is limited [33,34]. Additionally, carbon materials (e.g., activated carbons) are not suitable for flue gases due to their hydrophilic properties and poor selectivity [35–39]. Porous materials, including organic polymers, are used as CO₂ adsorbents due to their low heat of adsorption and high surface area [40–42]. However, the synthetic procedures for these materials are not environmentally friendly [43].

Organometallic compounds (e.g., metal–organic frameworks) have been used in many applications, such as storage and separation media, catalysts, and sensors [44]. However, there are problems associated with the use of organometallics that need to be addressed to enable their commercialization. The most common issues are their toxicity, regeneration, and reuse. Some success has been reported with organometallic regeneration and reuse [44]. However, further research is still needed to improve materials efficiency, cost of production, cleanliness, and simplicity of the process. Recently, success has been achieved in capturing CO₂ using polymeric materials [45–47], heterocycles [48,49], and organometallics [50–53]. Heterocycles such as thiophenes have useful applications in medicine, optoelectronic conductive devices, catalysis, and the production of dyes, plasticizers, and resins [54,55]. The current work explores the synthesis of new complexes containing different metals and heterocyclic units, such as thiophene. While recognizing that they do not show the levels required for application, an additional aim is to use the compounds as a model to

explore how the metal identity influences the CO₂ absorption in such materials.

EXPERIMENTAL

General

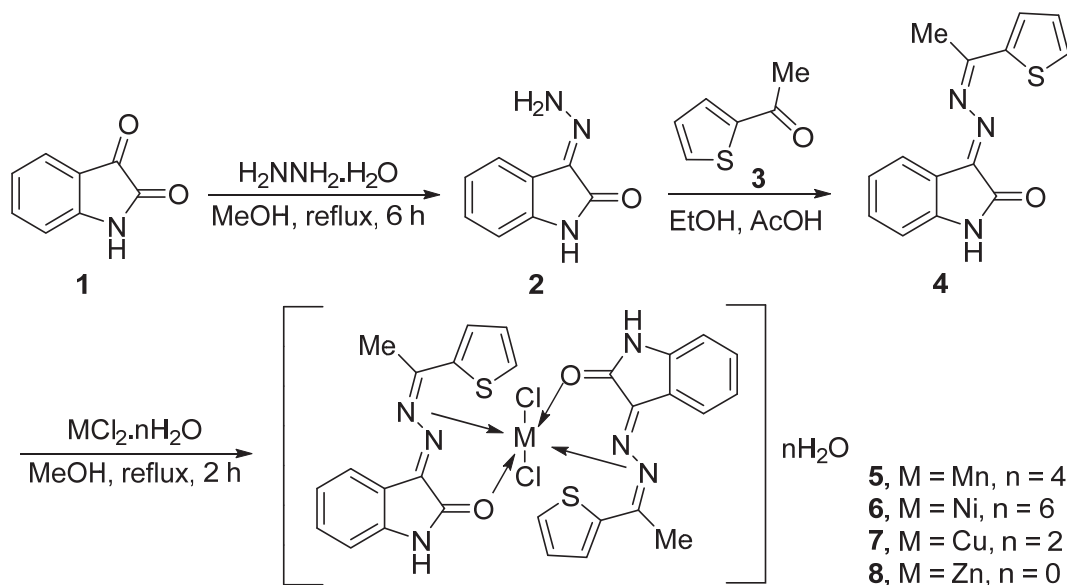
Chemicals, solvents, and reagents (analytical grades) were obtained from Merck (Gillingham, UK) and used as received. Melting points were measured on a Gallenkamp melting point apparatus. The FTIR spectra (KBr disks) were recorded on a Shimadzu IR Prestige-21 single-beam Fourier Transform Infrared spectrophotometer (400–4000 cm⁻¹). A Shimadzu-1800 double-beam UV-Vis spectroscopy was used to record the electronic absorption spectra (200–1100 nm; 10⁻³ M in DMF). A Bruker BM6 magnetic monitor was used to measure the magnetic susceptibility of complexes. Molar conductance (10⁻³ M in DMF) was calculated using a WTW ProfiLine Oxi3205 conventional portable meter. The NMR spectra were recorded on Bruker DRX300NMR spectrometry in DMSO-*d*₆. The electron impact (70 eV) mass spectrum of the ligand was conducted on a Shimadzu GCMS-QP2010-plus mass spectrometer that was equipped with a DB-5MS column (30 m × 0.25 mm I.D. × 0.1 μm). The injector temperature was kept at 260 °C, and the oven temperature started at 50 °C for 2 minutes, increased to 210 °C (3 °C/min), and then to 270 °C (10 °C/min). The carrier gas used was helium, with a pressure of 69 kPa. The complexes were dried for 4 hours at 60 °C using a vacuum oven to dry samples. The specific surface area of complexes was measured using the Brunauer-Emmett-Teller (BET) method. Pore sizes and volumes were measured via the Barrett-Joyner-Halenda (BJH) method. The CO₂ uptake measurements (three times) were performed on an H-sorb 2600 high-pressure volumetric adsorption instrument. The complex (1 g) was first degassed for 1 h at 50 °C in a vacuum oven to remove any traces of either water or solvent that are trapped within the pores of the complexes. Based on our previous work, the pressure and the temperature were set at 40 bar and 323 K, respectively [48–50]. The gas uptake experiment was then replicated three times under identical conditions to determine the optimum pressure. A ZEISS Sigma VP (10 kV) was used to record the field emission scanning electron microscopy (FESEM) images. The energy dispersive x-ray (EDX) and mapping tests for the complexes were performed on Oxford Instruments equipment.

A Veeco instrument was used to record the atomic force microscopy (AFM) images.

Synthesis of 3-hydrazone-1,3-dihydroindole-2-one (2)

A solution of 1*H*-indole-2,3-dione (1; 1.00 g, 6.8 mmol) in MeOH (10 mL) was added dropwise

to a stirred solution of hydrazine monohydrate (0.34 g, 6.8 mmol) in MeOH (10 mL). The mixture was refluxed for 6 hours, and the yellow solid formed was filtered, washed with MeOH, and dried at 50 °C to give pure 2 (Scheme 1) in 80% yield, M.P. 187–188 °C. FTIR (cm⁻¹): 3369, 3197, 1689, 1560, 1461.



Scheme 1. Synthesis of metal complexes 5–8.

Synthesis of 3-[(1-Thiophen-2-yl)ethylidene]hydrazone-1,3-dihydroindole-2-one (4)

A solution of 2 (1.00 g, 6.2 mmol) in EtOH (10 mL) was added dropwise to a stirred solution of 1-(thiophen-2-yl)ethan-1-one (3; 0.78 g, 6.2 mmol) in EtOH (10 mL) containing glacial AcOH (0.5 mL). The mixture was refluxed for 4 hours, and the orange solid formed was collected by filtration, washed with EtOH, recrystallized using a mixture of MeOH and EtOH (1:1 by volume), and dried at 50 °C to give pure 4 (Scheme 1) in 75% yield, M.P. 234–236 °C. FTIR (cm⁻¹): 3372, 3201, 1688, 1612, 1465. UV (nm): 249, 313. ¹H NMR (400 MHz; DMSO-d₆): 2.51 (s, 3H, Me), 6.86 (t, 8 Hz, 1H, Ar), 6.97 (t, 8 Hz, 1H, Ar), 7.16 (d, 8 Hz, 1H, Ar), 7.22

(d, 8 Hz, 1H, Ar), 8.56 (d, 5 Hz, 1H, thiophene), 8.75–8.78 (m, 2H, thiophene), 10.70 (s, 1H, NH). ¹³C NMR (100 MHz; DMSO-d₆): 39.3, 110.1, 117.9, 121.8, 122.7, 123.2, 126.7, 127.5, 129.0, 129.2, 139.1, 141.0, 163.3, 166.4. EI-MS (m/z, %): 270 (M⁺, 100), 197 (15), 160 (55).

Synthesis of metal complexes 5–8

A mixture of metal chloride (1.8 mmol) and 4 (0.97 g, 3.6 mmol) in MeOH (10 mL) was refluxed for 2 h. The colored complexes obtained were collected by filtration, washed with MeOH, and dried to give 5–8 (Scheme 1) in good yields (Table 1). The solids obtained are highly insoluble in most solvents, and therefore, no crystallization process was performed.

Table 1. Color, melting point, yield, and elemental analysis of metal complexes 5–8

Complex	Metal	Color	M.P (°C)	Yield (%)	Analysis (%); Found (Calculated)		
					C	H	M
5	Mn	Reddish brown	213–215	66	45.56 (45.66)	4.09 (4.11)	7.29 (7.46)
6	Ni	Yellow	200–203	65	43.20 (43.32)	4.37 (4.41)	7.37 (7.56)
7	Cu	Dark brown	177–179	60	47.31 (47.43)	3.65 (3.70)	8.87 (8.96)
8	Zn	Light yellow	218–221	75	49.74 (49.83)	3.34 (3.29)	9.52 (9.69)

Results and Discussion

Synthesis of metal complexes

Compound **4** was obtained in 75% yield, as shown in Scheme 1. The mass spectrum of **4** showed a pseudo molecular ion peak (MH^+) at $m/z = 270$. Its 1H NMR spectrum showed the presence of the methyl and NH protons as singlet signals at 2.51 and 10.70 ppm, respectively. The ^{13}C NMR spectrum of **4** showed the carbonyl carbon at 166.4 ppm. The reaction of **4** with metal chlorides leads to the formation of metal complexes **5–8** (Scheme 1) in rea-

sonable yields (Table 1). The structures of **5–8** were confirmed by the FTIR (Table 2), electronic (Table 3), and NMR (Table 4) spectral data.

The coordination took place between the metal and oxygen rather than the sulfur. The lone pairs of electrons of the sulfur atom are involved in thiophene aromaticity and are not available for coordination. In addition, the high melting points of the synthesized complexes indicate their high stability in the air. The complexes decomposed at temperatures higher than 200 °C.

Table 2. Selected FTIR absorption bands (cm^{-1}) of **5–8**

Complex	Metal	OH	NH	C=O	C=N	M–N	M–O	M–Cl
5	Mn	3360	3161	1762	1658	524	501	289
6	Ni	3360	3163	1730	1658	524	501	289
7	Cu	3450	3196	1732	1618	480	457	277
8	Zn	—	3161	1691	1652	524	501	289

FTIR spectroscopy of **5–8**.

The FTIR spectra of **5–8** showed the presence of absorption bands corresponding to the C=N bonds in thiophene that appeared in the regions of 1618–1658 cm^{-1} (Table 2). They also showed absorption bands that are corresponding to the carbonyl group at 1691–1730 cm^{-1} . There was a shift in the carbonyl group position compared with compound **4**, indicating that coordination has taken place. Indeed, new absorption bands corresponding to the M–N, M–O, and M–Cl bonds appeared in the regions of 480–534, 457–501, and 277–289 cm^{-1} , respectively [56, 57].

Molar conductivity, magnetic moment, and UV spectroscopy of **5–8**

The electronic spectra (200–1100 nm) of **5–8** were measured in DMF at 20 °C. The UV spectrum of the Mn complex showed bands at 267 and 317 nm corresponding to the $\pi-\pi^*$ and $n-\pi^*$ transitions, respectively (Table 3). The spectrum does not show d–d transitions except a band at 395 nm, which was attributed to charge transfer (CT) since the multiplicities in the ground and excited states are different. This result is consistent with the magnetic moment

($\mu_{eff} = 6.26$ BM), indicating an octahedral geometry [58,59].

The UV spectrum of the Ni complex showed bands at 260 and 312 nm that were assigned to the $\pi-\pi^*$ and $n-\pi^*$ transitions, respectively. In addition, three bands in the visible region at 400, 500, and 810 nm were attributed to the spin-allowed transitions $^3A_2g(F) \rightarrow ^3T_1g(P)$, $^3A_2g(F) \rightarrow ^3T_1g(F)$, and $^3A_2g(F) \rightarrow ^3T_2g(F)$, respectively.

The magnetic moment (2.68 BM) of the Ni complex was in the normal range for octahedral arrangement [58, 59]. For the Cu complex, three absorption bands appearing at 211, 268, and 380 nm were attributed to $\pi-\pi^*$, $n-\pi^*$ transitions, and the CT, respectively. The broad band centered at 635 nm was attributed to $^2Eg \rightarrow ^2T_2g$ transitions. The d–d bands were strongly indicative of the distorted octahedral geometry, which was confirmed by magnetic susceptibility (1.89 BM) [60].

The electronic spectrum of the Zn complex showed a charge transfer band at 407 nm as well as two bands at 275 and 329 nm due to $\pi-\pi^*$ and $n-\pi^*$ transitions, respectively [58]. The molar conductivity recorded indicates that complexes **5–8** are non-electrolytes.

Table 3. Molar conductivity, magnetic moment, and electronic spectral data of metal complexes 5–8

Complex	Metal	Conductivity ($\text{Ohm}^{-1} \text{cm}^2 \text{mol}^{-1}$)	μ_{eff} (BM)	Band (nm)	Assignment
5	Mn	10	6.26	267	$\pi-\pi^*$
				317	$n-\pi^*$
				395	CT
6	Ni	20	3.68	260	$\pi-\pi^*$
				312	$n-\pi^*$
				400	${}^3A_2g(F) \rightarrow {}^3T_1g(P)$
				500	${}^3A_2g(F) \rightarrow {}^3T_1g(F)$
7	Cu	32	1.89	211	$\pi-\pi^*$
				268	$n-\pi^*$
				280	CT
				635	${}^2Eg \rightarrow {}^2T_2g$
8	Zn	3	Diamagnetic	275	$\pi-\pi^*$
				329	$n-\pi^*$
				407	CT

NMR Spectroscopy of 5–8

The structures of **5–8** were confirmed by the NMR spectral data (Table 4). It was not possible to record the NMR spectrum of the Mn complex using the standard technique at room temperature due to its poor solubility in a variety of deuterated solvents [58,61]. The ${}^1\text{H}$ NMR spectra of the metal complexes showed the methyl protons as singlets in the 2.18–2.38 ppm re-

gion. In addition, the NH protons appeared as singlets at the 10.01–10.70 ppm region. The carbonyl carbons appeared downfield (166.2–168.6 ppm) in the ${}^{13}\text{C}$ NMR spectra, while the methyl carbons appeared at high field (27.2–27.8 ppm). It should be noted that the mass spectra of the synthesized complexes **5–8** were very poor and provided no useful information, presumably due to their low volatility.

Table 4. NMR spectral data of metal complexes 6–8

Complex	Metal	${}^1\text{H}$ NMR	${}^{13}\text{C}$ NMR
6	Ni	2.38 (s, 3H, Me), 6.79 (t, 8 Hz, 1H, Ar), 6.83 (t, 8 Hz, 1H, Ar), 6.99 (d, 8 Hz, 1H, Ar), 7.19 (d, 8 Hz, 1H, Ar), 8.60, (d, 4 Hz, 1H, thiophene), 8.82–8.87 (m, 2H, thiophene), 10.70 (s, 1H, NH)	27.3, 110.4, 117.8, 122.7, 126.7, 127.4, 129.2, 134.4, 135.4, 139.0, 144.5, 145.4, 163.2, 168.6
7	Cu	2.38 (s, 3H, Me), 6.72 (t, 8 Hz, 1H, Ar), 6.87 (t, 8 Hz, 1H, Ar), 7.14 (d, 8 Hz, 1H, Ar), 7.31 (d, 8 Hz, 1H, Ar), 8.65, (d, 4 Hz, 1H, thiophene), 8.72–8.77 (m, 2H, thiophene), 10.70 (s, 1H, NH)	27.8, 110.0, 112.6, 118.2, 121.6, 123.2, 125.1, 129.7, 133.1, 138.8, 144.5, 151.1, 159.8, 166.2
8	Zn	2.18 (s, 3H, Me), 6.82 (t, 8 Hz, 1H, Ar), 6.82 (t, 8 Hz, 1H, Ar), 6.91 (d, 8 Hz, 1H, Ar), 7.13 (d, 8 Hz, 1H, Ar), 7.91, (d, 4 Hz, 1H, thiophene), 8.69–8.79 (m, 2H, thiophene), 10.01 (s, 1H, NH)	27.2, 110.5, 117.9, 121.5, 122.7, 126.3, 127.5, 129.3, 134.3, 135.3, 139.1, 140.9, 163.3, 166.4

EDX Mapping of 5–8

The elemental contents of **5–8** were confirmed using the energy-dispersive X-ray analysis (EDX). The EDX images provide a rough estimate of metal contents. However, it is not as precise as the results obtained from the elemental analysis. Figure 1 shows the EDX mapping graphs for the synthesized metal

complexes, and they reveal all the elements within the structures of metal complexes. Figure 1 showed a lower percentage for Zn compared with those shown for appeared for the other metals. It should be noted that the structures and quantity of water for the metal complexes (Scheme 1) were suggested based on the elemental analysis (Table 1).

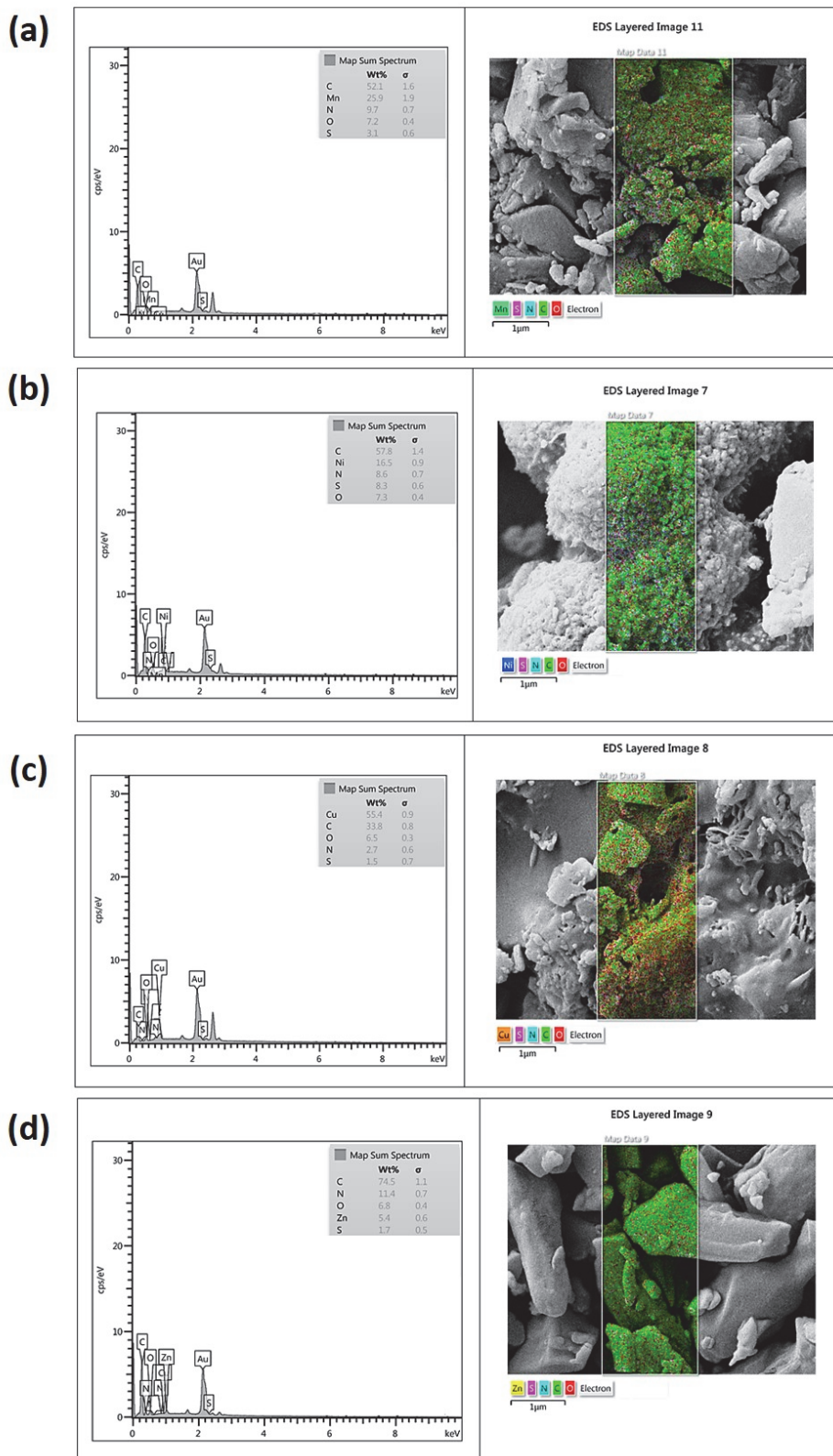


Figure 1. EDX mapping images of complexes containing (a) Mn, (b) Ni, (c) Cu, and (d) Zn.

Surface morphology of 5–8

The morphology, particle sizes, and porosity of metal complexes 5–8 were examined using various

microscopy techniques. FESEM provided clear and undistorted images of the surface of complexes 5–8 (Figure 2). FESEM images indicate the uniformity, amorphous nature, and roughness of surfaces. The

roughness of the surface can influence the adsorption of CO₂. The increase in the roughness of materials leads to a greater surface area for gas adsorption [62]. In addition, the FESEM images showed the existence

of a range of particle sizes. Complexes 5–8 have irregular pore sizes with particle diameters in the range of 37–189, 35–69, 31–263, and 26–241 nm for the complexes containing Mn, Ni, Cu, and Zn, respectively [63].

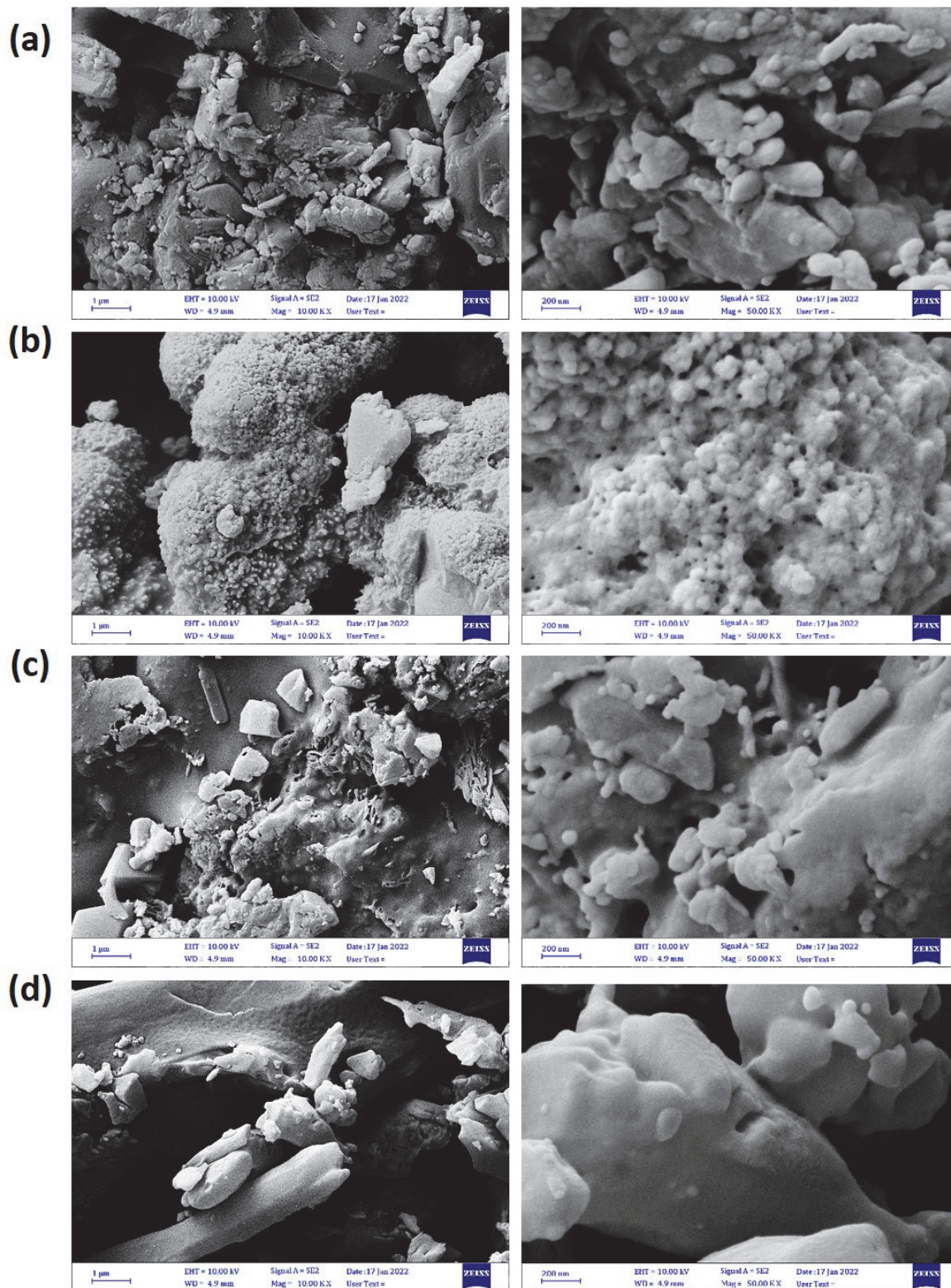


Figure 2. FESEM image of complexes containing (a) Mn, (b) Ni, (c) Cu, and (d) Zn.

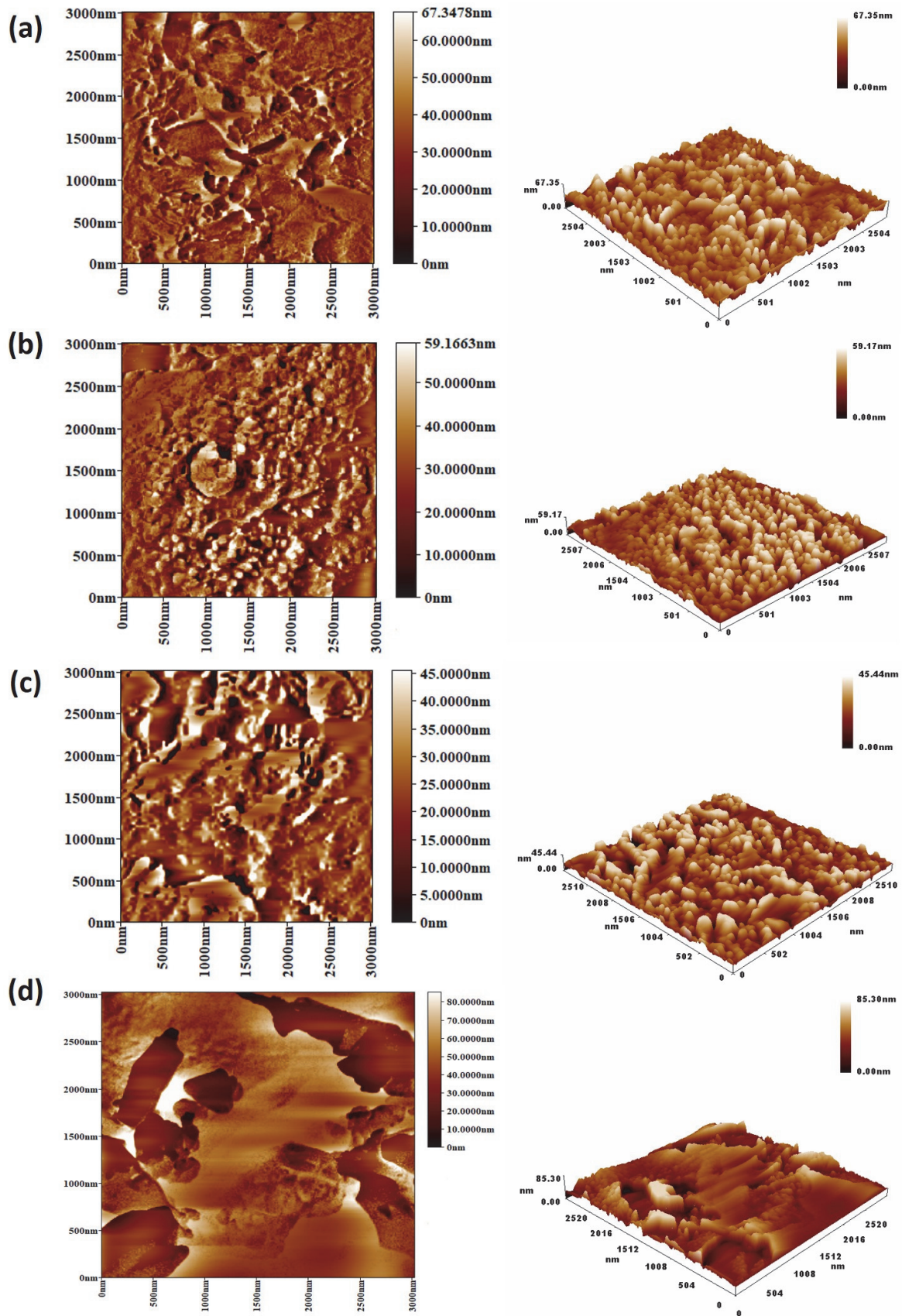


Figure 3. AFM images of complexes containing (a) Mn, (b) Ni, (c) Cu, and (d) Zn.

The AFM (two and three-dimensional) images provided information about the surface porosity and roughness (Figure 3). The AFM images indicated that the surface of the metal complexes is rough and highly porous. The roughness factor for the surface of metal complexes containing Mn, Ni, Cu, and Zn was 356, 175, 124, and 238, respectively. The particle sizes were 31.3–207.8, 33.5–117.5, 83.7–386.6, and 67.0–460.9 nm for complexes containing Mn, Ni, Cu, and Zn, respectively. It was clear that the particle sizes measured by the AFM in the Cu and Zn-based samples were more or less correlated with those obtained from the FESEM. However, the AFM provides much larger particle sizes in the Cu and Zn complex-

es compared to those provided by the FESEM. It is not clear why this variation took place, but it could be that the particle sizes were just visually estimated from the FESEM.

The BET surface area of 5–8

The BET surface area determines the adsorption capacity of adsorbents, and additionally, the porosity provides information about their chemical and physical interactions with the adsorbed gas. Therefore, the nitrogen isotherms, along with the pore size distribution of complexes containing Mn, Ni, Cu, and Zn, were determined (Figure 4).

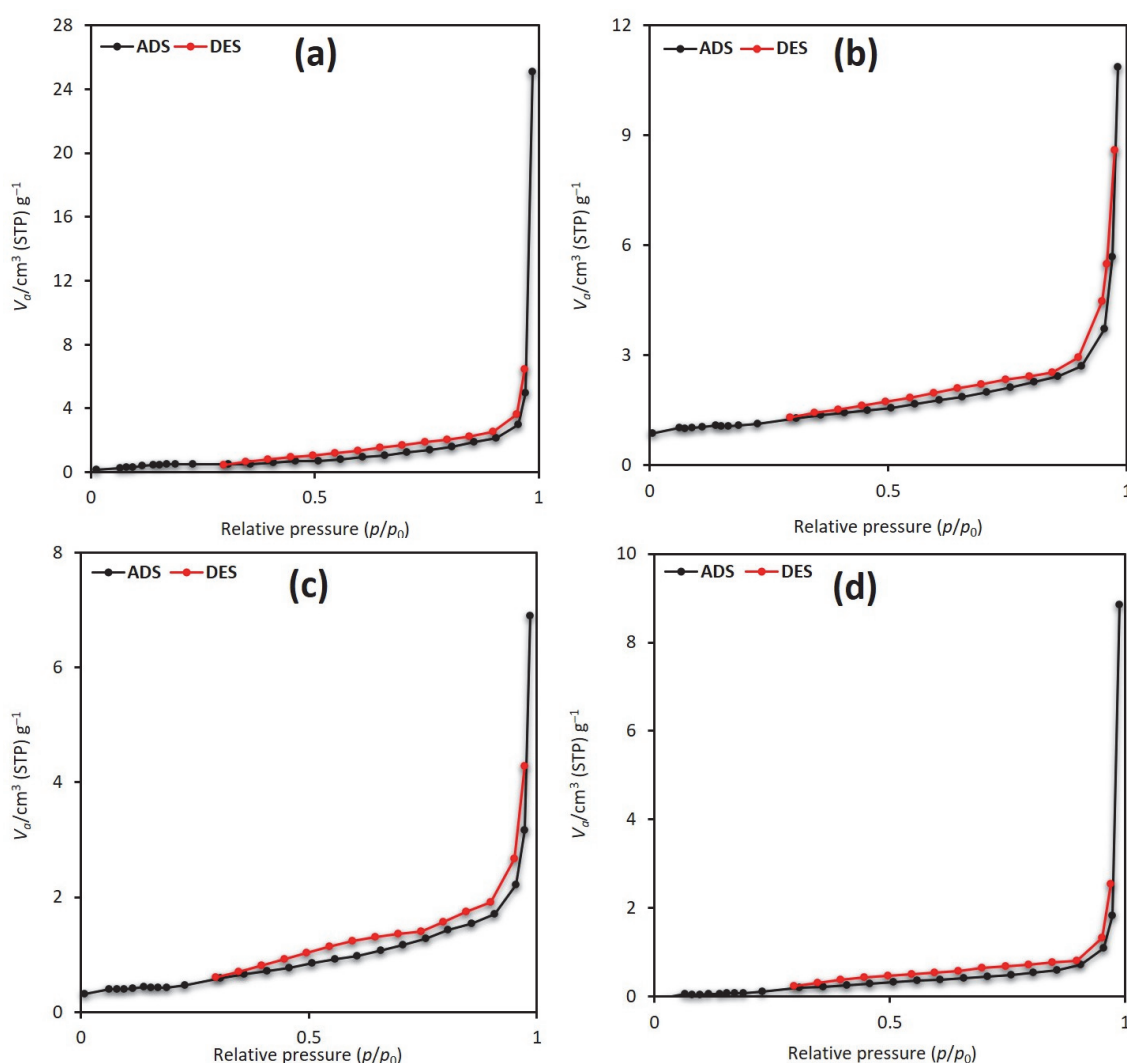


Figure 4. The N₂ adsorption isotherms of complexes containing (a) Mn, (b) Ni, (c) Cu, and (d) Zn.

The interactions between the metal complexes and CO₂ were relatively weak [64]. The isotherms indicated that the structures of complexes are type IV mesoporous. No identifiable monolayer formation was found. The nitrogen adsorption isotherms ($P/P^0 = 0.9$)

were used to calculate the BET surface area and pore volume. The desorption data was used to estimate the average pore diameter (Table 5). The BET surface area of metal complexes was low (1.20–4.01 m²/g), and the pore volume and diameter were in the ranges

0.011–0.039 cm³/g and 16.77–97.62 nm, respectively. The Mn complex has the highest BET surface area (4.01 m²/g), pore volume (0.039 cm³/g), and diameter (97.62 nm). It seems likely that interparticle sorption takes place at the high relative pressure used, leading to a steep increase in the uptake graphs.

Table 5. Surface area and pore size distribution of metal complexes obtained by the N₂ adsorption

Complex	Metal	S _{BET} (m ² /g)	Pore volume (cm ³ /g)	Average pore diameter (nm)
5	Mn	4.01	0.039	97.62
6	Ni	1.20	0.011	16.77
7	Cu	1.59	0.014	26.30
8	Zn	1.62	0.017	45.77

The CO₂ uptake of 5–8

The pores' size and the type and strength of interactions between adsorbent and CO₂ (e.g., Van der Waal forces or hydrogen bonding) control CO₂ adsorption. High energy is required to adsorb CO₂ if the aperture size is small compared to the molecular size,

as repulsive forces could dominate [65]. In addition, the effect of pores' volume of absorbent materials is important for gas uptake capacity [66], with materials with large pores volumes having the space to store more CO₂ [67]. The chosen conditions for the CO₂ uptake process were based on our previous related work [45–53]. The CO₂ uptake recorded at 323 K and 40 bars for the complexes containing Mn, Ni, Cu, and Zn were 13.1, 10.1, 4.3, and 10.8 cm³/g, respectively (Figure 5). In terms of wt %, the CO₂ uptake was 2.6, 2.0, 0.9, and 2.1% for the Mn, Ni, Cu, and Zn complexes, respectively. The Mn complex led to the highest CO₂ uptake compared to the others. The Mn complex has the highest BET surface area and pore volume and diameter. In addition, the Mn atom has the lowest atomic radii compared with the other metals. Generally, the CO₂ uptake by complexes is reasonable since the complexes have a small surface area. This provides a sound starting point for the optimization of the chemical and physical properties to improve the interactions and capacity of the materials. We have not attempted to study the stability of the complexes. However, we believe they are highly stable since physisorption mainly takes place in the adsorption of CO₂. Therefore, the complexes should remain intact during and after the adsorption process.

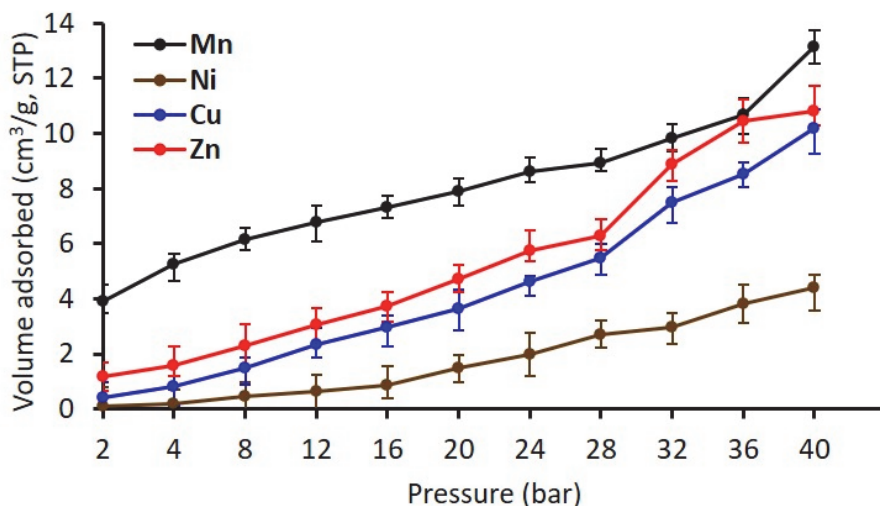


Figure 5. The CO₂ adsorption isotherms for the metal complexes.

It is believed that the CO₂ adsorption mechanism is dependent on both the aromatic moieties, polarity of heteroatoms, and the Lewis acid center in the complexes used. We believe that physisorption is involved in CO₂ adsorption by the newly synthesized metal complexes. Physisorption plays an important role in the adsorption of gas due to the interaction between the polarized bonds within both the com-

plexes and CO₂ [68]. Table 6 shows the CO₂ uptake (wt %) over various storage media that have been reported recently in comparison to those achieved using the currently synthesized metal complexes. Clearly, multiple factors are controlling the adsorbent's efficacy toward CO₂ uptake. The most common factors are the surface area, pores volume and diameter, and surface morphology.

Table 6. Surface area and CO₂ uptake of recently synthesized adsorbents

Adsorbent	S _{BET} (m ² /g)	CO ₂ (wt)	T (K), P (bar)	Ref
Thiophene-metal complexes	1.2–4.0	0.9–2.6	323, 40	Current
Polyphosphates–1,4-diaminobenzene	82.7–213.5	2.0–6.0	323, 40	45
Polysilicates	8.2–18.0	2.2–6.0	323, 40	46
Polyphosphates–benzidine	24.8–30.0	1.8–14.0	323, 50	47
Trimethoprim Schiff bases	4.2–20.3	6.0–10.3	313, 40	48
Melamine Schiff bases	5.2–11.6	6.1–10.0	323, 40	49
Metal-fusidate complexes	31.2–46.9	6.3–7.2	323, 50	50
Valsartan-metal complexes	16.0–22.8	4.8–6.8	323, 40	51
Carvedilol metal complexes	6.1–9.1	2.1–3.5	323, 40	52
Telmisartan metal complexes	32.4–130.4	3.3–7.1	323, 50	53

Conclusions

Four complexes containing heterocyclic units and metals were synthesized, and their structures were confirmed spectroscopically. Their physical properties and surface morphology were assessed. The materials have a diameter ranging from 16.77 to 97.62 nm and a specific surface area in the range of 1.20–4.01 m²/g. The highest CO₂ storage capacity was achieved with the complex containing manganese, followed by the others in the order of zinc, copper, and nickel. The manganese complex has the largest surface area, pores' volume, and average diameter compared with the others. In addition, the manganese-containing complex has the highest surface roughness factor. The results obtained open gates for designing a better storage media for CO₂. However, the toxicity that might be associated with these materials, their regeneration, and reuse need to be assessed.

Acknowledgments

We thank Al-Nahrain University for its technical support.

Funding

G. A. El-Hiti acknowledges the support received from the Researchers Supporting Project (number RSP20244R404), King Saud University, Riyadh, Saudi Arabia.

Conflicts of Interest

The authors declare no conflict of interest requiring disclosure in this article.

REFERENCES

1. A.L. Yaumi, M.Z. Abu Bakar, B.H.Hameed (2017) Recent advances in functionalized composite solid materials for carbon dioxide capture. *Energy*, 124, 461–480, <https://doi.org/10.1016/j.energy.2017.02.053>
2. A. Mardani, D. Streimikiene, F. Cavallaro, N. Loganathan, M. Khoshnoudi (2019) Carbon dioxide (CO₂) emissions and economic growth: a systematic review of two decades of research from 1995 to 2017. *Sci. Total Environ.*, 649, 31–49, <https://doi.org/10.1016/j.scitotenv.2018.08.229>.
3. H.Sun, Q.Xin, Z.Ma, S.Lan (2019) Effects of plant diversity on carbon dioxide emissions and carbon removal in laboratory-scale constructed wetland. *Environ. Sci. Pollut. Res.*, 26, 5076–5082, <https://doi.org/10.1007/s11356-018-3988-5>.
4. K. B. Boamah, J. Du, I. A. Bediako, A. J. Boamah, A. A. Abdul-Rasheed, S. M. Owusu (2017) Carbon dioxide emission and economic growth of China—the role of international trade. *Environ. Sci. Pollut. Res.*, 24, 13049–13067, <https://doi.org/10.1007/s11356-017-8955-z>.
5. E. S. Sanz-Pérez, C. R. Murdock, S. A. Didas, C. W. Jones (2016) Direct capture of CO₂ from ambient air. *Chem. Rev.*, 116, 11840–11876, <https://doi.org/10.1021/acs.chemrev.6b00173>.
6. Z. Liu, Z. Deng, S. J Davis, C. Giron, P. Ciais (2022) Monitoring global carbon emissions in 2021. *Nat. Rev. Earth Environ.*, 3, 217–219, <https://doi.org/10.1038/s43017-022-00285-w>.
7. A.Qazi, F.Hussain, N.A.Rahim, G.Hardaker, D. Alghazzawi, K. Shaban, K. Haruna (2019) Towards sustainable energy: a systematic review of renewable energy sources, technologies, and public opinions. *IEEE Access*, 7, 63837, <https://doi.org/10.1109/ACCESS.2019.2906402>.
8. N. A. Ludin, N. I. Mustafa, M.M. Hanafiah, M. A. Ibrahim, M. A. Teridi, S. Sepeai, A. Zaharim, K. Sopian (2018) Prospects of life cycle assessment of renewable energy from solar photovoltaic technologies: a review. *Renew. Sust. Energ. Rev.*, 96, 11–28, <https://doi.org/10.1016/j.rser.2018.07.048>.
9. Y. Ouyang, H. Yang, P. Zhang, Y. Wang, S. Kaur, X. Zhu, Z. Wang, Y. Sun, W. Hong, Y. F. Ngeow, H. Wang (2017) Synthesis of 2,4-diaminopyrimidine core-based

- derivatives and biological evaluation of their anti-tubercular activities. *Molecules*, 22, 1592, <https://doi.org/10.3390/molecules22101592>.
10. A. I. Osman, M. Hefny, M. I. Maksoud, A. M. Elgarahy, D. W. Rooney (2021) Recent advances in carbon capture storage and utilisation technologies: a review. *Environ. Chem. Lett.*, 19, 797–849, <https://doi.org/10.1007/s10311-020-01133-3>.
 11. T. Wilberforce, A. Olabi, E. T. Sayed, K. Elsaid, M. A. Abdelkareem (2021) Progress in carbon capture technologies. *Sci. Total. Environ.*, 761, 143203, <https://doi.org/10.1016/j.scitotenv.2020.143203>.
 12. O. Jankovský, M. Lojka, A. M. Lauermannová, F. Antončík, M. Pavlík, D. Sedmidubský (2020) Carbon dioxide uptake by MOC-based materials. *Appl. Sci.*, 10, 2254., <https://doi.org/10.3390/app10072254>.
 13. K. Goh, H. E. Karahan, E. Yang, T. H. Bae (2019) Graphene-based membranes for CO₂/CH₄ separation: key challenges and perspectives. *Appl. Sci.*, 2784. <https://doi.org/10.3390/app9142784>.
 14. I. S. Omodolor, H. O. Otor, J. A. Andonegui, B. J. Allen, A. C. Alba-Rubio (2020) Dual-function materials for CO₂ capture and conversion: a review. *Ind. Eng. Chem. Res.*, 59, 17612–17631, <https://doi.org/10.1021/acs.iecr.0c02218>.
 15. H. Muslemani, X. Liang, K. Kaesehage, J. Wilson (2020) Business models for carbon capture, utilization and storage technologies in the steel sector: a qualitative multi-method study. *Processes*, 8, 576, <https://doi.org/10.3390/pr8050576>.
 16. S. F. Cannone, A. Lanzini, M. A. Santarelli (2021) Review: on CO₂ capture technologies with focus on CO₂-enhanced methane recovery from hydrates. *Energies*, 14, 387, <https://doi.org/10.3390/en14020387>.
 17. S. Shukrullah, M. Y. Naz, N. M. Mohamed, K. A. Ibrahim, N. M. Abdel-Salam, A. Ghaffar, (2019) CVD synthesis, functionalization and CO₂ adsorption attributes of multiwalled carbon nanotubes, *Processes*, 7, 634, <https://doi.org/10.3390/pr7090634>.
 18. J. Li, Y. Hou, P. Wang, B. Yang (2019) A review of carbon capture and storage project investment and operational decision-making based on bibliometrics. *Energies*, 12, 23, <https://doi.org/10.3390/en12010023>.
 19. A. Raza, R. Gholami, R. Rezaee, V. Rasouli, M. Rabbie (2019) Significant aspects of carbon capture and storage—a review. *Petroleum*, 5, 335–340, <https://doi.org/10.1016/j.petlm.2018.12.007>.
 20. E. Schuler, M. Morana, N. R. Shiju, G. J. Gruter (2022) A new way to make oxalic acid from CO₂ and alkali formats: using the active carbonite intermediate. *Sustain. Chem. Clim. Action*, 1, 100001, <https://doi.org/10.1016/j.scca.2022.100001>.
 21. S. Builes, P. López-Aranguren, J. Fraile, L. F. Vega, C. Domingo (2015) Analysis of CO₂ adsorption in amine-functionalized porous silicas by molecular simulations. *Energy Fuels*, 29, 3855–3862, <https://doi.org/10.1021/acs.energyfuels.5b00781>.
 22. D. M. D'Alessandro, B. Smit, J. R. Long (2010) Carbon dioxide capture: prospects for new materials. *Angew. Chem. Int. Ed.*, 49, 6058–6082, <https://doi.org/10.1002/anie.201000431>.
 23. A. Mukherjee, J. A. Okolie, A. Abdelrasoul, C. Niu, A. K. Dalai (2019) Review of post-combustion carbon dioxide capture technologies using activated carbon. *J. Environ. Sci.*, 83, 46–63, <https://doi.org/10.1016/j.jes.2019.03.014>.
 24. A. A. Okesola, A. A. Oyedeji, A. F. Abdulhamid, J. Olowo, B. E. Ayodele, T. W. Alabi (2018) Direct air capture: A review of carbon dioxide capture from the air. *IOP Conf. Ser: Mater. Sci. Eng.*, 413, 012077, <https://doi.org/10.1088/1757-899x/413/1/012077>.
 25. Z. Asadi-Sangachini, M. M. Galangash, H. Younesi, M. Nowrouzi (2019) The feasibility of cost-effective manufacturing activated carbon derived from walnut shells for large-scale CO₂ capture. *Environ. Sci. Pollut. Res.*, 26, 26542–26552, <https://doi.org/10.1007/s11356-019-05842-3>.
 26. J. A. Gibson, E. Mangano, E. Shiko, A. G. Greenaway, A. V. Gromov, M. M. Lozinska, D. Friedrich, E. B. Campbell, P. A. Wright, S. Brandani (2016) Adsorption materials and processes for carbon capture from gas-fired power plants: AMPGas. *Ind. Eng. Chem. Res.*, 55, 3840–3851, <https://doi.org/10.1021/acs.iecr.5b05015>.
 27. S. Y. Lee, S. J. Park (2015) A review on solid adsorbents for carbon dioxide capture. *J. Ind. Eng. Chem.*, 23, 1–11, <https://doi.org/10.1016/j.jiec.2014.09.001>.
 28. K. Sumida, D. L. Rogow, J. A. Mason, T. M. McDonald, E. D. Bloch, Z. R. Herm, T. H. Bae, J. R. Long (2012) A review on solid adsorbents for carbon dioxide capture. *Chem. Rev.*, 112, 724–781, <https://doi.org/10.1021/cr2003272>.
 29. C. Lu, T. Ben, S. Qiu (2016) Synthesis and gas storage application of hierarchically porous materials. *Macromol. Chem. Phys.*, 217, 1995–2003, <https://doi.org/10.1002/macp.201600221>.
 30. Japip, H. Wang, Y. Xiao, T. S. Chung (2014) Highly permeable zeolitic imidazolate framework (ZIF)-71 nano-particles enhanced polyimide membranes for gas separation. *J. Membr. Sci.*, 467, 162–174. <https://doi.org/10.1016/j.memsci.2014.05.025>.
 31. Q. Huang, M. Eić (2013) Commercial adsorbents as benchmark materials for separation of carbon dioxide and nitrogen by vacuum swing adsorption process. *Sep. Purif. Technol.*, 103, 203–215, <https://doi.org/10.1016/j.seppur.2012.10.040>.
 32. A. Ö. Yazaydin, A. I. Benin, S. A. Faheem, P. Jakubczak, J. J. Low, R. R. Willis, R. Q. Snurr (2019) Enhanced CO₂ adsorption in metal-organic frameworks via occupation of open-metal sites by coordinated water molecules. *Chem. Mater.*, 21, 1425–1430, <https://doi.org/10.1021/cm900049x>.
 33. S. C. Lee, H. J. Chae, S. J. Lee, B. Y. Choi, C. K. Yi, J. B. Lee, C. K. Ryu, J. C. Kim (2008) Development of regenerable MgO-based sorbent promoted with K₂CO₃ for CO₂ capture at low temperatures. *Environ. Sci. Technol.*, 42, 2736–2741, <https://doi.org/10.1021/es702693c>.
 34. S. Wang, S. Yan, X. Ma, J. Gong (2011) Recent advances in capture of carbon dioxide using alkali-metal-based oxides. *Energy Environ. Sci.*, 4, 3805–3819, <https://doi.org/10.1039/c1ee01116b>.

35. L. Hauchhum, P. Mahanta (2014) Carbon dioxide adsorption on zeolites and activated carbon by pressure swing adsorption in a fixed bed. *Int. J. Energy Environ. Eng.*, 5, 349–356, <https://doi.org/10.1007/s40095-014-0131-3>.
36. P. Staciwa, U. Narkiewicz, D. Sibera, D. Moszyński, R. J. Wróbel, R. D. Cormia (2019) Carbon spheres as CO₂ sorbents. *Appl. Sci.*, 9, 3349, <https://doi.org/10.3390/app9163349>.
37. A. S. Aquino, M. O. Vieira, A. S. Ferreira, E. J. Cabrita, S. Einloft, M. O. De Souza (2019) Hybrid ionic liquid–silica xerogels applied in CO₂ capture. *Appl. Sci.*, 9, 2614, <https://doi.org/10.3390/app9132614>.
38. Y. -C. Chiang, C. -Y. Yeh, C. -H. Weng (2019) Carbon dioxide adsorption on porous and functionalized activated carbon fibers. *Appl. Sci.*, 9, 1977, <https://doi.org/10.3390/app9101977>.
39. J. Choma, M. Kloske, A. Dziura, K. Stachurska, M. Jaroniec (2016) Preparation and studies of adsorption properties of microporous carbon spheres. *Eng. Prot. Environ.*, 19, 169–182, <https://doi.org/10.17512/ios.2016.2.1>.
40. R. Dawson, A. I. Cooper, D. J. Adams (2012) Nanoporous organic polymer networks. *Prog. Polym. Sci.*, 37, 530–563, <https://doi.org/10.1016/j.progpolymsci.2011.09.002>.
41. S. Choi, J. H. Drese, C. W. Jones (2009) Adsorbent materials for carbon dioxide capture from large anthropogenic point sources. *ChemSusChem*, 2, 796–854, <https://doi.org/10.1002/cssc.200900036>.
42. W. Wang, M. Zhou, D. Yuan (2017) Carbon dioxide capture in amorphous porous organic polymers. *J. Mater. Chem. A*, 5, 1334–1347, <https://doi.org/10.1039/c6ta09234a>.
43. S. E. M. Elhenawy, M. Khraisheh, F. AlMomani, G. Walker (2020) Metal-organic frameworks as a platform for CO₂ capture and chemical processes: adsorption, membrane separation, catalytic-conversion, and electrochemical reduction of CO₂. *Catalysts*, 10, 1293, <https://doi.org/10.3390/catal10111293>.
44. P. Kumar, B. Anand, Y. F. Tsang, K. -H. Kim, S. Khullar, B. Wang (2019) Regeneration, degradation, and toxicity effect of MOFs: opportunities and challenges. *Environ. Res.*, 176, 108488, <https://doi.org/10.1016/j.envres.2019.05.019>.
45. H. A. Satar, A. A. Ahmed, E. Yousif, D. S. Ahmed, M. F. Alotibi, G. A. El-Hiti (2019) Synthesis of novel heteroatom-doped porous-organic polymers as environmentally efficient media for carbon dioxide storage. *Appl. Sci.*, 9, 4314, <https://doi.org/10.3390/app9204314>.
46. S.H., Mohamed, A. S. Hameed, E. Yousif, M. H. Alotabi, D. S. Ahmed, G. A. El-Hiti (2020) New porous silicon-containing organic polymers: synthesis and carbon dioxide uptake. *Processes*, 8, 1488, <https://doi.org/10.3390/pr8111488>.
47. D. S. Ahmed, G. A. El-Hiti, E. Yousif, A. S. Hameed, M. Abdalla (2017) New eco-friendly phosphorus organic polymers as gas storage media. *Polymers*, 9, 336, <https://doi.org/10.3390/polym9080336>.
48. A. A. Yaseen, E. T. B. Al-Tikrity, G. A. El-Hiti, D.S.Ahmed, M.A.Baashen, M.H. Al-Mashhadani, E. Yousif (2021) A process for carbon dioxide capture using Schiff bases containing a trimethoprim unit. *Processes*, 9, 707, <https://doi.org/10.3390/pr9040707>.
49. R. M. Omer, E. T. B. Al-Tikrity, G. A. El-Hiti, M. F. Alotibi, D. S. Ahmed, and E. Yousif (2020) Porous aromatic melamine Schiff bases as highly efficient media for carbon dioxide storage. *Processes*, 8, 17, <https://doi.org/10.3390/pr8010017>.
50. Z. N. Mahmood, M. Alias, G. A. -R. El-Hiti, D. S. Ahmed, E. Yousif (2021) Synthesis and use of new porous metal complexes containing a fusidate moiety as gas storage media. *Korean J. Chem. Eng.*, 38, 179–186, <https://doi.org/10.1007/s11814-020-0692-1>.
51. A. Mohammed, E. Yousif, and G. A. El-Hiti (2020) Synthesis and use of valsartan metal complexes as media for carbon dioxide storage. *Materials*, 13, 1183, <https://doi.org/10.3390/ma13051183>.
52. O. G. Mousa, E. Yousif, A. A. Ahmed, G. A. El-Hiti, M. H. Alotabi, D. A. Ahmed (2020) Synthesis and use of carvedilol metal complexes as carbon dioxide storage media. *Appl. Petrochem. Res.*, 10, 157–164, <https://doi.org/10.1007/s13203-020-00255-7>.
53. A. G. Hadi, K. Jawad, E. Yousif, G. A. El-Hiti, Alotabi, D. S. Ahmed (2019) Synthesis of telmisartan organotin(IV) complexes and their use as carbon dioxide capture media. *Molecules*, 24, 1631, <https://doi.org/10.3390/molecules24081631>.
54. M. Nakao, M. Toguchi, K. Horikoshi, S. Kitaike, S. Sano (2022) Synthesis of novel 2,3-disubstituted thiophenes via tandem thia-Michael/aldol reactions of allenyl esters. *Heterocycles*, 104, 379–388, <https://doi.org/10.3987/COM-21-14575>.
55. B. A. Baldo, N. H. Phan (2017) Drug Allergy: Clinical Aspects, Diagnosis, Mechanism, Structure–Activity Relationship; 2nd Ed., Springer Cham, London, UK, 134–162, <https://doi.org/10.1007/978-3-030-51740-3>.
56. A. J. Abdulghani, R. Kh. Hussain (2015) Synthesis and characterization of Schiff base metal complexes derived from cefotaxime with 1*H*-indole-2,3-dione (isatin) and 4-*N,N*-dimethylaminobenzaldehyde. *Open J. Inorg. Chem.*, 5, 83–101, <https://doi.org/10.4236/ojic.2015.54010>.
57. N. Hasani, M. N. A. Al-Jibouri (2017) Synthesis, characterization, and DFT study of some transition metal complexes with Schiff base derived from 2-acetylthiophene and L-methionine. *Res. Chem. Intermed.*, 43, 4585–4610, <https://doi.org/10.1007/s11164-017-2898-3>.
58. M. A. Ayoub, E. H. Abd-Elnasser, M. A. Ahmed, M. G. Rizk (2018) Some new metal(II) complexes based on bis-Schiff base ligand derived from 2-acetylthiophene and 2,6-diaminopyridine: synthesis, structural investigation, thermal, fluorescence and catalytic activity studies. *J. Mol. Struct.*, 1163, 379–387, <https://doi.org/10.1016/j.molstruc.2018.03.006>.
59. F. A. El-Saied, M. M. E. Shakhdofa, A. S. El-Tabi, M. M. Abdel-Zaher, N. Morsy (2017) Coordination versatility of N₂O₄ polydentate hydrazonic ligand in Zn(II), Cu(II), Ni(II), Co(II), Mn(II), and Pd(II) complexes and antimicrobial evaluation. *Beni-Suef Univ. J. Basic Appl. Sci.*, 6, 310–320, <https://doi.org/10.1016/j.bjbas.2017.09.005>.

60. C. A. Housecroft, A. G. Sharpe (2012) *Inorganic Chemistry*; 4th Ed., Pearson Education Limited, England, UK, 1213 pp. ISBN 0273742752, 9780273742753.
61. H. O. Echekwube, P.O. Ukooha, O. T. Ujam, C. O. Nwuche, J. N. Asegbeloyin, A. Ibezim (2019) Synthesis and in silico investigation of Schiff base derivatives of 1H-indole-2,3-diones and their Co(II) and Ni(II) complexes as antimicrobial agents. *Braz. J. Biol. Sci.*, 6, 63–85, <https://doi.org/10.21472/bjbs.061207>.
62. X. Yu, K. Regenauer-Lieb, F. Tian (2019) Investigation of effects of surface roughness on coal seam gas transport using a fractal-based lattice Boltzmann method. *ASEG Extended Abstracts*, 1, 1–2, <https://doi.org/10.1080/22020586.2019.12073014>.
63. B. R. Vergis, N. Kottam, R. H. Krishna, B. N. Nagabhushana (2019) Removal of Evans Blue dye from aqueous solution using magnetic spinel ZnFe₂O₄ nanomaterial: adsorption isotherms and kinetics. *Nano-Struct. Nano-Objects*, 18, 100290, <https://doi.org/10.1016/j.nanoso.2019.100290>.
64. K. A. Cychosz, M. Thommes (2018) Progress in the physisorption characterization of nanoporous gas storage materials. *Engineering*, 4, 559–566, <https://doi.org/10.1016/j.eng.2018.06.001>.
65. H. Furukawa, O. M. Yaghi (2009) Storage of hydrogen, methane, and carbon dioxide in highly porous covalent organic frameworks for clean energy applications. *J. Am. Chem. Soc.*, 131, 8875–8883, <https://doi.org/10.1021/ja9015765>.
66. Y. Peng, V. Krungleviciute, I. Eryazici, J. T. Hupp, O. K. Farha, T. Yildirim (2013) Methane storage in metal-organic frameworks: current records, surprise findings, and challenges. *J. Am. Chem. Soc.*, 135, 11887–11894, <https://doi.org/10.1021/ja4045289>.
67. M. Razavian, S. Fatemi, M. A. Masoudi-Nejad (2014) Comparative study of CO₂ and CH₄ adsorption on silicalite-1 fabricated by sonication and conventional method. *Adsorpt. Sci. Technol.*, 32, 73–87, <https://doi.org/10.1260/0263-6174.32.1.73>.
68. A.A.Abd, S.Z.Naji, A.S.Hashim, M.R.Othman (2020) Carbon dioxide removal through physical adsorption using carbonaceous and non-carbonaceous adsorbents: a review. *J. Environ. Chem. Eng.*, 8, 104142, <https://doi.org/10.1016/j.jece.2020.104142>.

IZVOD

SINTEZA I SVOJSTVA NOVIH METALNIH KOMPLEKSA KOJI SADRŽE HETEROCIKLIČNE GRUPE I ISTRAŽIVANJE ULOGE METALA U HVATANJU GASA UGLJEN-DIOKSIDA

Kontinuirano oslobađanje ugljen-dioksida (CO₂) u atmosferu će neizbežno dovesti do veće štete po životnu sredinu. Sakupljanje i skladištenje CO₂ je jedna od strategija za ublažavanje štete povezane sa visokim koncentracijama CO₂ u atmosferi. Dizajn i sinteza novih materijala koji će delovati kao medij za skladištenje CO₂ je trenutno važan izazov za istraživače. S tim u vezi, objavljeno je istraživanje sinteze novih organometalnih materijala i njihovog potencijala kao medija za skladištenje CO₂. Stoga je trenutni rad imao za cilj da proizvede nove materijale koristeći jednostavnu proceduru i istraži njihova svojstva, uključujući faktore koji utiču na njihovu adsorpciju CO₂. Četiri metalna kompleksa koji sadrže heterociklične jedinice sintetizovana su jednostavnom metodom, a njihove strukture su potvrđene korišćenjem nekoliko tehnika. Morfologija površine materijala je pregledana mikroskopski. Metalni kompleksi su pokazali podesive veličine čestica sa prečnicima koji su se kretali od 16,77 do 97,62 nm i Brunauer-Emmett-Teller-ovom površinom od 1,20-4,01 m²/g. Materijali mogu uhvatiti CO₂ na 323 K i 40 bara, pri čemu kompleks koji sadrži mangan pokazuje najveći kapacitet skladištenja CO₂ (13,1 cm³/gm).

Ključne reči: sinteza, metalni kompleksi, hvatanje ugljen-dioksida, površina, morfologija površine

The ORCID Ids of all the authors are as follows:

1. Rawnaq Jima'a: <https://orcid.org/0000-0002-3706-2227>
2. Naser Shaalan: <https://orcid.org/0000-0002-2875-5056>
3. Muna Bufaroosha: <https://orcid.org/0000-0003-4799-3356>
4. Gamal A. El-Hiti: <https://orcid.org/0000-0001-6675-3126>
5. Benson M. Kariuki: <https://orcid.org/0000-0002-8658-3897>
6. Dina S. Ahmed: <https://orcid.org/0000-0003-2205-4061>
7. Emad Yousif: <https://orcid.org/0000-0003-1458-4724>

Naučni rad

Rad primljen: 31.03.2024.

Rad korigovan: 20.05.2024.

Rad prihvaćen: 5.06.2024.

Amina Salihi Bayero¹, Nura Alhaji Yaro², Musa Ibrahim Mohammed³, Pramod Kumar Singh⁴, Bashir Abdu Muzakkari⁵, Umar Muhammad Jibreel^{1,6}

¹Chemistry Department, Yusuf Maitama Sule University, Kano-Nigeria;

²Maryam Abacha American University of Nigeria, Kano-Nigeria;

³Department of Pure and Industrial Chemistry, Bayero University, Kano-Nigeria; ⁴Department of Physics, Sharda School of Basic Sciences and Research, Sharda University, India; ⁵Department of Computer Science, Yusuf Maitama Sule University, Kano -Nigeria; ⁶Federal College of Agricultural Produce Technology, Kano-Nigeria

Scientific Paper

ISSN 0351-9465, E-ISSN 2466-2585

<https://doi.org/10.62638/ZasMat1046>



Zastita Materijala 65 (4)
748 – 755 (2024)

Pyrolysis Char from Waste Tyres its Characteristics, Upgrading and Application

ABSTRACT

The pyrolysis of waste tyres can recycle energy and produce reusable products (oil, char and gas). Although there are many reviews in the literature in regard to the pyrolysis characteristics of waste tyres, but this paper critically looked as pyrolysis char as one of the useful product. Its physical characteristics include pore diameter, pore volume, specific surface area, and composition. The common detection techniques of the physical characteristics include elemental analysis, proximate analysis, SEM, EDS, TGA, XRF, BET, and Raman spectroscopy. The chemical characteristics of tyre char mainly include calorific value, the surface functional groups (i.e phenols, alcohols, carboxylic acid and C-O/C-O-C chemical structures) which can be determined by FT-IR, XRD. The higher sulfur retention on the surface of tyre char is obtained at low temperature compared with that obtained at high temperature. Tyre char could also be directly used as a catalyst material to decrease the operational cost, and improve the quality of pyrolysis oil and gas. The modified tyre char with high specific surface area and lower ash content could be used as an activated carbon adsorbent material, catalyst and catalyst support, capacitor electrode to create higher commercial value, as an adsorbent, in batteries and so on. It is suggested that the recycling applications of tyre char should be developed, which can create a high level of potential economic prospects for the waste tyre pyrolysis industry.

Keywords: Pyrolysis, Waste tyres, Char, Modification, Carbon black.

1. INTRODUCTION

Over time, pyrolysis technology has advanced and become sufficiently refined to be considered a quick and effective means of addressing the environmental issues arising from waste tyres. Pyrolysis oil, char, and gas are the three primary products that are derived from pyrolyzing tyres under mild conditions. Nevertheless, the direct use of these products as energy sources is constrained by their high sulfur concentration and composition [1]. The pyrolysis process yields nearly no waste byproducts, and the steel, rubber, carbon black, additives

and other components present in the discarded tyre may be recovered [2].

Fig. 1 illustrates the products and by-products from waste tyre pyrolysis. Improving the quality of pyrolysis products is the primary obstacle to the full-scale development of the waste tyre pyrolysis process, even with appropriate processing and modification. Numerous large-scale tyre pyrolysis projects have reportedly failed to achieve complete commercial success because of the low value of the goods that are produced [3].

In the realm of waste tyre treatment, pyrolysis is a promising technique for recycling and recovering energy and fuels. It has the potential to satisfy the three pillars of solid waste treatment: pollution mitigation, resource recovery, and reduction. In contrast to alternative therapeutic approaches (i.e. com-

* Corresponding author: Umar Muhammad Jibreel
E-mail: jibreelumar@gmail.com and jibreelumar@fcapt.edu.ng
Paper received: 31.03.2024.
Paper accepted: 15.06.2024.

bustion, retread, and landfill) [4-6]. Since pyrolysis reduces secondary pollutants in the environment and has the potential to increase product economic value, it has been extensively studied as a recovery

technique. In order to produce gases and condensable oil, the procedure breaks down the organic components of discarded tyres, and solid char [7,8].

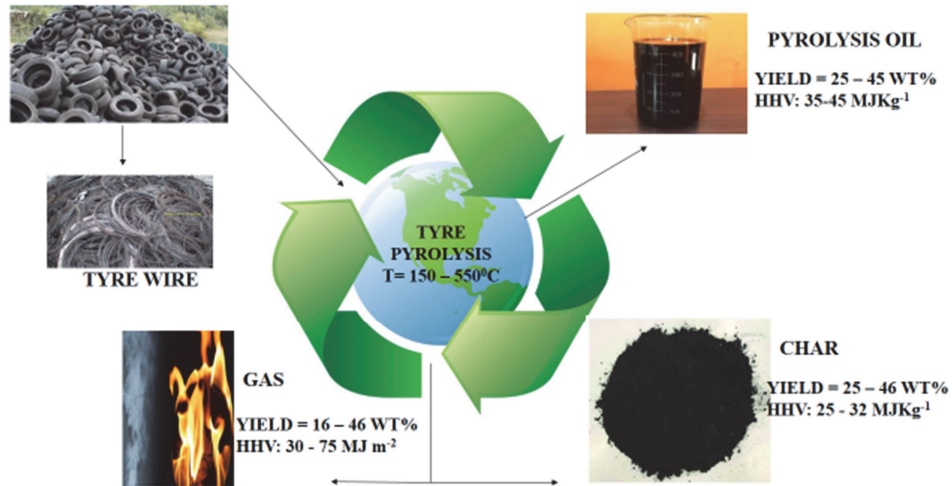


Fig. 1: The pyrolysis product of waste tyres

Thus, it is possible to utilize fewer conventional fossil fuels when waste tyres are converted to alternative fuels. For this reason, waste tyre pyrolysis has been shown to be a practical method of indirectly reducing greenhouse gas emissions [9]. Furthermore, the tyre's steel reinforcing can be extracted from the leftover char and recycled back into the iron and steel sector [10].

1.1 Pyrolysis Tyre Char

One of the primary byproducts of pyrolysis made from used tyres is tyre char, whose marketability is essential to the ongoing growth of waste tyre pyrolysis commerce [11]. Tyre pyro-char is a carbon-rich solid material that is produced during pyrolysis. It is a black porous substance that contains high amounts of carbon, and low amounts of volatiles and ash [12,13]. It is a solid residue obtained from pyrolysis that can be used as a soil amendment, carbon sequestration, or fuel. It has high carbon content water retention, and reduce greenhouse gas emissions [14]. It can also be used as a fuel, as it has a high calorific value and burns cleanly [12,13]. (Fig: 2)

So many reviewed work have been focusing on pyrolysis oil been one of the product obtained during the process, but in this paper will focus on pyrolysis char as one of the important product obtained during pyrolysis so as to highlight its characteristics, application and further possible modification of the char.



Fig. 2: Pyrolysis char from waste tyres

2. STRUCTURAL CHARACTERISTICS OF TYRE PYROLYSIS CHAR

The physical and chemical characteristics of the waste tyre char have been reported in many research articles [15,16]. It is of great interest to understand the structural characteristics of tyre char for its further application. The modification scheme of tyre char could be determined by its structural characteristics.

2.1 Physical Structure Characteristics

The primary physical properties of tyre char are its composition, specific surface area, pore volume, and pore diameter. Elemental analysis, proximate

analysis, SEM, EDS, TGA, XRF, BET, and Raman spectroscopy are examples of common physical characteristic detection procedures [17]. The fixed carbon content, ash content, element analysis, and proximate analysis are used to further characterize tyre char. TGA in an air atmosphere could potentially be used to determine the ash concentration [18]. Tyre char is a high-carbon substance, typically more than 85%, that is mostly derived from the carbon black that is injected during the tyre formulation process. In addition, during the pyrolysis process, subsequent condensation and depolymerization events generated by the pyrolysis volatiles result in the production of carbonaceous deposits across the tyre char surface. Process circumstances have a major impact on the amount of these reactions [19,20].

The heating value of tyre char is associated with high carbon content. The HHV of tyre char is reported in the literature to range between 25 and 32 MJ·kg⁻¹, [21-23]. However, the interest in tyre char as a solid fuel is hindered by the high sulfur content.

Tyre char's stability could be examined using TGA analysis in an environment with inert gas. The low-temperature tyre char's qualities are more erratic than those of the high-temperature tyre char because the discarded tyre doesn't undergo complete thermal degradation. The breakdown of inorganic chemicals on the tyre char's surface at high temperatures could be the cause of this [24]. The presence of disorder in carbon and graphene 2D hexagonal lattice in the tyre char with Raman spectra has been reported [24]. In the meantime, the char generated from the pyrolysis of the tyre tread and the char created from the pyrolysis of the tyre side wall have completely distinct elemental and proximate analysis results. Compared to the tread rubber char, the side wall rubber char has less ash in it [2]. At -196°C, N₂ adsorption-desorption (BET) analysis might be used to measure the specific surface area and pore diameter. Numerous reports have demonstrated that tyre char has a specific surface area of less than 140 m²·g⁻¹ [22,25], in addition, there are more mesopores and few micropores in tyre char [2,24]. Various tyres produce tyre char with highly varied physical structures. It should be highlighted that these characteristics are very dependent on the type of carbon black utilized in tyre formulation as well as the pyrolysis conditions, particularly pressure, temperature, and residence time. The char formed during the pyrolysis of the tyre tread rubber and side wall rubber differs significantly [19].

2.2 Chemical structure characteristics.

Tyre char's chemical properties mostly consist of its calorific value and surface functional groups. Tyre char's chemical properties could be ascertained using FT-IR, XRD, and HHV [26]. FT-IR provides a good picture of the kind and strength of the surface functional groups associated with tyre char. The surface functional groups of tyre char often consist of alcohols, carboxylic acids, phenols, and C-O/C-O-C chemical structures, according to published research [27]. Additionally, it has been reported that tyre char surface sulfur retention is higher at low temperatures than at high ones, this is thought to be caused by some stable metallic sulfides that persist in the tyre char as well as the relatively high sulfur volatility at high temperatures [28]. The surface nature of activated char from the waste tyre was reported to be hydrophobic [29].

3 COMPARISON OF PROPERTIES OF TYRE CHAR WITH COMMERCIAL CARBON BLACK

Tyre char's primary ingredient, carbon, makes up more than 80% of the material. Tyre char has a particular surface area of about 90 m²·g⁻¹ and contains a certain amount of ash [21, 30]. Zn, Si, Al, Na, Ca, and Fe are among the inorganic components in ash, according to EDS and XRF examinations of tyre char. Ash has a comparatively greater Si concentration than other elements—up to 3.47% [24]. In tyre char, certain nanoparticles combine to form microparticles. The tyre char has fewer pores, a rough surface, an uneven form, and an uneven size distribution. However, tyre char has fewer particles than commercial carbon black [31]. Commercial carbon's main particles typically have a mean size in the nanometer range (8–100 nm), and they frequently aggregate into grape-like clusters up to 500 nm in size. Tyre char has a well-developed porous structure, with more mesopores than micropores and an average pore diameter of 25–30 nm [31].

4. UPGRADING OF TYRE PYRO CHAR

According to some researcher, untreated tyre char has the potential to be useful for recycling and could replace commercial carbon black in rubber additives [32]. The ash content in tyre char can limit the end-use application of tyre char [19]. The high sulfur content of tyre char also represents a major drawback for its utilization [15]. The possi-

bility for ash and volatile oily materials to adhere to tyre char's surface during the pyrolysis process, clogging pores and acting as agglomerating particles, is another disadvantage of tyre char. Because tyre char's quality has been demonstrated to be lower than that of commercial carbon black, it must be treated and filtered before to use [19]. It is important to remember that the minerals added during the tyre manufacturing process are primarily responsible for the high ash concentration of tyre char [33,34].

Various methods have been suggested to demineralize tyre char and increase its market value. Ash leaching, for instance, can be done either before or after tyre pyrolysis. The chemical pathway and selectivity of the pyrolysis reactions can be altered by the ashes found in tyre rubber. Furthermore, pyrolysis can result in the generation of harmful species and less corrosion on process equipment when the feedstock is demineralized [35].

The main constituent of waste tyres ashes is ZnO, moreover, other metallic species commonly present are Fe, Al, Ca, and Mg [16, 36, 37]. Leaching is the method of choice for demineralizing tyres. A number of variables affect how well this liquid-solid extraction process works, most notably the feedstock's characteristics (particle size or starting porosity) and the operating environment (temperature,

contact time, leaching rate, or agitation). The solubility and composition of the ashes [38].

Various leaching reagents have been utilized in tyre or tyre char demineralization; solvents are categorized into three classes based on pH: alkaline, acidic, and water. Of them, acid leaching—using HCl, H₂SO₄, or HNO₃ is employed more frequently in earlier literature reports [27, 39, 40]. Since tyre char is porous, leaching is easier than it would be with original rubber; in fact, effective ash removal only happens on the rubber's surface [41].

Tyre char demineralization is an intriguing pre-activation process; hence, the removal of minerals encourages the formation of new mesopores and micropores, which serve as active sites in the activation stage that follows [42,43]. Additionally, this technique is intriguing because it prevents the substantial burn-off carbon losses during activation from leading to a rise in ash content [19,44]. Additionally, acid treatment has been shown to have a good impact on tyre char's sulfur concentration. For instance, Gao *et al.*, [19] leached tyre char using a mixture of HCl and HNO₃, which produced extremely efficient desulfurization of tyre char (95.3%). Nevertheless, the demineralization of tyre char using H₂SO₄ may encourage the addition of further residual sulfur. Certain types of sulfur in carbonaceous materials can also be removed more effectively by applying alkaline reagents [28].

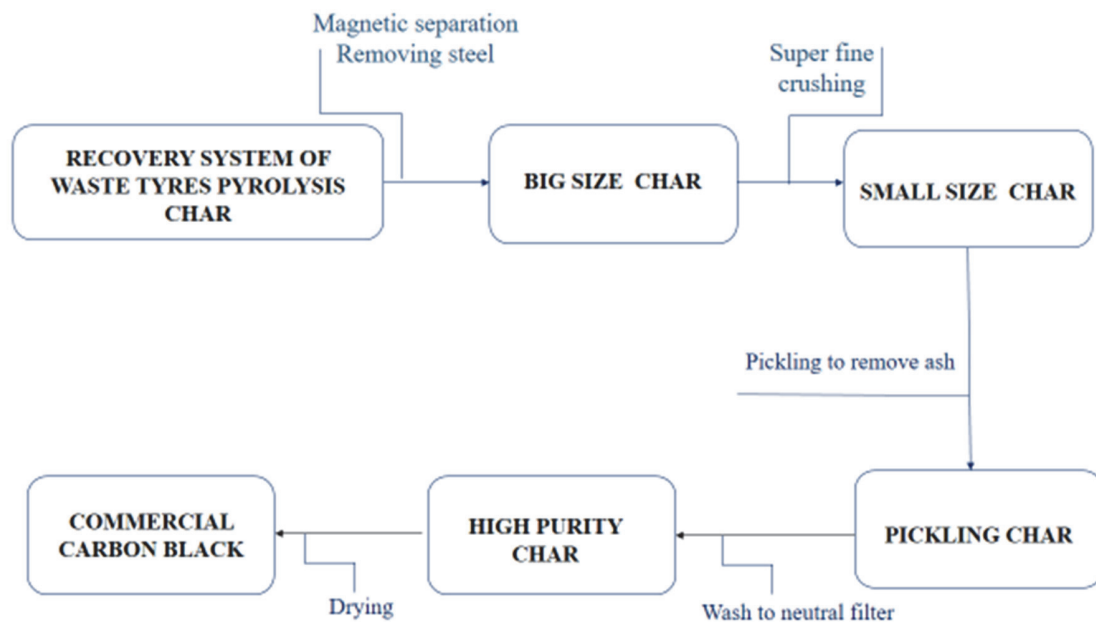


Fig.3: Flow chart of char from waste tyre via pyrolysis modified to carbon black

Tyre char is partially gasified during the physical activation process utilizing a variety of oxidizing chemicals, primarily carbon dioxide and steam. Particle size, temperature, activation agent, and activation time are the typical operational variables that are taken into account [19]. Different alteration procedures are required based on the purposes. Fig. 3 depicts the typical tyre char alteration procedures. After being ultra-finely ground, the tyre char's particle size dramatically shrank in comparison to the original, and the powdered result was tightly packed. Particle agglomeration is easier with finer particle sizes. The process of creating activated carbon from used tyres usually consists of two stages: (i) Waste tyres are pyrolyzed in an inert gas atmosphere to create gas, pyrolysis oil, and carbon compounds that can be used as fuel. (ii) Chemical or physical means are used to activate the tyre char [19]. However, the drawbacks of conventional activation techniques are their intricate procedures and poor effectiveness. The procedure of modifying tyre char must be altered in accordance with the application requirement in order to meet the standard criteria needed for commercial carbon black [19].

5. APPLICATIONS OF TYRE CHAR

The primary driver of the tyre char market's explosive growth is the annual increase in the global supply of discarded tyres, which has very low or even negative costs as a process feedstock. As a result, the cost of generating tyre char is reduced. Tyre char, with an ash level of roughly 7.0–15%, makes up 30-37 weight percent of the results of tyre pyrolysis,

as a result of the various sources and pyrolysis processes of discarded tyres. The usage of tyre char has been proposed for numerous purposes. Tyre char, for instance, can be used as the pigment added to printing ink, which is a colloid dispersive system made up of filler, connecting material, pigment, and auxiliary agent [19,23,24]. For example, the performance of tyre char as a pigment in offset printing ink has been reported [28].

The application of tyre char as solid fuel has also been reported in the literature [24,26]. It was also suggested that tyre char could be used as filler in modifying asphalt [28,42]. The specific surface area, pore diameter, and surface properties of tyre char are also different when obtained under different tyre pyrolysis conditions [4,19].

Small pore widths and developed pores are features of tyre char. It cannot, however, match the application requirements of commercial carbon black due to its low specific surface area. Its economic worth is therefore minimal [23,24,26]. As a result, efforts are concentrated on finding efficient ways to raise tyre char's added value. Tyre char now has a wide range of applications; Fig. 4 illustrates these potential uses. The primary uses of activated carbon are as adsorbents made from modified tyre char [28], as well as asphalt additives, battery materials, commercial carbon black, rubber reinforcing materials, and catalyst support materials. Additional applications include gasification of fuel gas, adsorbent (activated carbon) as a catalyst and supporting material, reinforcement of tyre rubber as a material for batteries and capacitors, and materials for construction [19].



Fig. 4: The main high added value application of tyre char

6. CONCLUSION

Many different fields employ tyre char extensively. Tyre char that hasn't been altered can be utilized straight away as a solid fuel and tyre rubber reinforcement agent. Additionally, tyre char could be utilized directly as a catalyst material to lower operating costs and enhance the quality of the oil and gas produced during pyrolysis. To increase its economic value, the modified tyre char with its increased specific surface area and decreased ash content might be employed as a capacitor electrode, catalyst and catalytic support, and an adsorbent material for activated carbon.

The majority of tyre char applications are still in the early stages of laboratory research. Comprehensive technical and economic analyses of tyre char activation technology and waste tyre pyrolysis are lacking. However, as waste tyre pyrolysis technology develops and becomes more industrialized, the standards for pyrolysis product quality will rise. It is recommended that tyre char recycling applications be developed, since this might lead to a high degree of potential economic opportunities for the waste tyre pyrolysis business. Even with the advancements in waste tyre pyrolysis technology and the use of pyrolysis products, numerous problems still need to be fixed in order to satisfy various industrial demands.

REFERENCES

- [1] S. Farzad, M. Mandegari, J.F. Görgens (2021) A novel approach for valorization of waste tires into chemical and fuel (limonene and diesel) through pyrolysis: Process development and techno economic analysis, *Fuel Process Technol.* 224, 107006. <https://doi.org/10.1016/j.fuproc.2021.107006>
- [2] F. Wang, N. Gao, C. Quan (2020) Investigation of hot char catalytic role in the pyrolysis of waste tires in a two-step process, *J Anal Appl Pyrolysis.* 146, 104770. <https://doi.org/10.1016/j.apenergy.2019.113678>
- [3] N. Antoniou, A. Zabaniotou (2013) Features of an efficient and environmentally attractive used tyres pyrolysis with energy and material recovery, *Renew Sustain Energy Rev.* 20, 539–558. <https://doi.org/10.1016/j.rser.2014.07.143>
- [4] S. Singh, W. Nimmo, B.M. Gibbs (2009) Waste tyre rubber as a secondary fuel for power plants, *Fuel.*, 88, 2473–2480. <https://doi.org/10.1016/j.fuel.2009.02.026>
- [5] A. Uyumaz, B. Aydogan, H. Solmaz (2019) Production of waste tyre oil and experimental investigation on combustion, engine performance and exhaust emissions, *J Energy Inst.* 92, 1406–1418. <https://doi.org/10.1016/j.joei.2018.09.001>
- [6] S.S. Narani, M. Abbaspour, S.M. M. Hosseini (2020) Sustainable reuse of waste tire textile fibers (WTFs) as reinforcement materials for expansive soils: With a special focus on landfill liners/covers, *J Cleaner Prod.*, 247, 119151. <https://doi.org/10.1016/j.jclepro.2019.119151>
- [7] W. Li, C. F. Huang, D.P. Li (2016) Derived oil production by catalytic pyrolysis of scrap tires, *Chin J Catal.*, 37, 526–532. [https://doi.org/10.1016/S1872-2067\(15\)60998-6](https://doi.org/10.1016/S1872-2067(15)60998-6)
- [8] P.T. Williams (2013) Pyrolysis of waste tyres: A review, *Waste Manage (Oxford).*, 33, 1714–1728. [https://doi.org/10.1016/0016-2361\(94\)00005-C](https://doi.org/10.1016/0016-2361(94)00005-C)
- [9] H. Yaqoob, Y. H. Teoh, F. Sher (2021) Current status and potential of tire pyrolysis oil production as an alternative fuel in developing countries, *Sustainability.*, 13, 3214–3224. <https://doi.org/10.3390/su13063214>
- [10] Y.P. Wang, L.L. Dai, L.L. Fan (2017) Microwave-assisted catalytic fast co-pyrolysis of bamboo sawdust and waste tire for bio-oil production, *J Anal Appl Pyrolysis.*, 23, 224–228. <https://doi.org/10.1016/j.jaap.2016.11.025>
- [11] A. Donatelli, P. Iovane, A. Molino (2010) High energy syngas production by waste tyres steam gasification in a rotary kiln pilot plant. Experimental and numerical investigations, *Fuel.* 89, 2721–2728. <https://doi.org/10.1016/j.fuel.2010.03.040>
- [12] P.T. Williams (2013) Pyrolysis of waste tyres: a review. *Waste Management*; 33, 1714-1728. <http://dx.doi.org/10.1016/j.wasman.2013.05.003>.
- [13] S.E. Hosseini, M. A. Wahid, J. R. Seay, K.A. Schimmel (2018) A review on the pyrolysis of waste tyres: Effect of pyrolysis conditions pathways and methods, *Journal of Analytical and Applied Pyrolysis.*, 130, 142–179. <https://doi.org/10.1016/j.jclepro.2019.119151>
- [14] P. Straka, A. Miloš, V. Dan, K. Hugo, S. Pavel, V. Petr (2023) Production of transportation fuels via hydrotreating of scrap tyres pyrolysis oil, *Chemical Engineering Journal.*, 460, 141764 <https://doi.org/10.1016/j.cej.2023.141764>
- [15] N. Antoniou, A. Zabaniotou (2013) Features of an efficient and environmentally attractive used tyres pyrolysis with energy and material recovery, *Renew Sustain Energy Rev.* 20, 539–558. <https://doi.org/10.1016/j.rser.2012.12.005>
- [16] G. San Miguel, G.D. Fowler, C. Sollars (2002) The leaching of inorganic species from activated carbons produced from waste tyre rubber, *Water Res.*, 36, 1939–1946. <https://doi.org/10.1021/ie970728x>
- [17] Q.Q. Zhou, A. Zarei, A. De-Girolamo (2019) Catalytic performance of scrap tyre char for the upgrading of eucalyptus pyrolysis derived bio-oil via cracking and deoxygenation, *J Anal Appl Pyrolysis.*, 139, 167–176. <https://doi.org/10.1016/j.jaap.2019.02.001>
- [18] A.M. Mocanu, C. Moldoveanu, L. Odochian (2012) Study on the thermal behavior of casein under nitrogen and air atmosphere by means of the TG-FTIR technique, *Thermochim Acta.*, 546, 120–126. <https://doi.org/10.1016/j.tca.2012.07.031>
- [19] N. Gao, W. Fengchao, Q. Cui, S. Laura, L. Gartzten, T.W. Paul (2022) Tire pyrolysis char: Processes, properties, upgrading and applications. *Progress in*

- Energy and Combustion Science, 93, 101022 <https://doi.org/10.1016/j.pecs.2022.101022>
- [20] G. Lopez, M. Olazar, R. Aguado (2010) Vacuum pyrolysis of waste tires by continuously feeding into a conical spouted bed reactor. *Ind Eng Chem Res.*, 49, 8990–8997. <https://doi.org/10.1016/j.wasman.2009.06.005>
- [21] R. J. Chen, L.Y. Lun, K. L. Cong (2019) Insights into pyrolysis and co-pyrolysis of tobacco stalk and scrap tire: thermochemical behaviors, kinetics, and evolved gas analysis, *Energy.*, 183, 25–34. <https://doi.org/10.1016/j.energy.2019.06.127>
- [22] P. Hadi, K. Y. Yeung, J. X Guo (2016) Sustainable development of tyre char-based activated carbons with different textural properties for value-added applications, *J Environ Manage.*, 170, 1–7. <https://doi.org/10.1016/j.jenvman.2016.01.005>
- [23] A. M Cunliffe, P.T. Williams (1998) Properties of chars and activated carbons derived from the pyrolysis of used tyres, *Environ Technol.*, 19, 1177–1190. <https://doi.org/10.1080/09593331908616778>
- [24] M.Y. Wang, L. Zhang, A.M. Li (2019) Comparative pyrolysis behaviors of tire tread and side wall from waste tire and characterization of the resulting chars, *J Environ Manage.*, 232, 364–371. <https://doi.org/10.1016/j.wasman.2007.10.009>
- [25] J.F. Gonzalez, J.M. Encinar, J.L. Canito, J.J. Rodriguez (2001) Pyrolysis of automobile tyre waste. Influence of operating variables and kinetics study, *J Anal Appl Pyrolysis*, 58, 667–683. [http://dx.doi.org/10.1016/S0165-2370\(00\)00201-1](http://dx.doi.org/10.1016/S0165-2370(00)00201-1).
- [26] J. Pastor-Villegas, C.J. Duran-Valle (2001) Pore structure of chars and activated carbons prepared using carbon dioxide at different temperatures from extracted rockrose, *J Anal Appl Pyrolysis.*, 57, 1–13. [https://doi.org/10.1016/S0165-2370\(00\)00097-8](https://doi.org/10.1016/S0165-2370(00)00097-8)
- [27] T.A. Saleh, G.I. Danmaliki (2016) Adsorptive desulfurization of dibenzothiophene from fuels by rubber tyres-derived carbons: kinetics and isotherms evaluation, *Process Saf Environ Prot.*, 102, 9–19. <https://doi.org/10.1016/j.psep.2016.02.005>
- [28] H. Darmstadt, C. Roy, S. Kaliaguine (1995) Characterization of pyrolytic carbon-blacks from commercial tire pyrolysis plants, *Carbon.*, 33, 1449–14455. [https://doi.org/10.1016/0008-6223\(95\)00096-V](https://doi.org/10.1016/0008-6223(95)00096-V)
- [29] W. Tanthapanichakoon, P. Ariyadejwanich, P. Japthong (2005) Adsorption-desorption characteristics of phenol and reactive dyes from aqueous solution on mesoporous activated carbon prepared from waste tires, *Water Res.*, 39, 1347–1353. <https://doi.org/10.1016/j.watres.2004.12.044>
- [30] A. Undri, B. Sacchi, E. Cantisani (2013) Carbon from microwave assisted pyrolysis of waste tires, *J Anal Appl Pyrolysis.* 104:396–404. <https://doi.org/10.1016/j.jaap.2013.06.006>
- [31] M. Sagar, K. Nibedita, N. Manohar (2018) A potential utilization of end-of-life tyres as recycled carbon black in EPDM rubber, *Waste Manage (Oxford).*, 74, 110–122. <https://doi.org/10.1016/j.wasman.2018.01.003>
- [32] D. Pantea, H. Darmstadt, S. Kaliaguine (2003) Heat-treatment of carbon blacks obtained by pyrolysis of used tires. Effect on the surface chemistry, porosity and electrical conductivity, *J Anal Appl Pyrolysis.*, 67, 55–76. [https://doi.org/10.1016/S0165-2370\(02\)00017-7](https://doi.org/10.1016/S0165-2370(02)00017-7)
- [33] J.O Ighalo, K.O Iwuozor, L.A. Ogunfowora (2021) Regenerative desulphurisation of pyrolysis oil: a paradigm for the circular economy initiative, *J Environ Chem Eng.* 9:106864. <https://doi.org/10.1016/j.jece.2021.106864>
- [34] R. Helleur, N. Popovic, M. Ikura (2001) Characterization and potential applications of pyrolytic char from ablative pyrolysis of used tires, *J Anal Appl Pyrolysis.*, 58, 813–824. [https://doi.org/10.1016/S0165-2370\(00\)00207-2](https://doi.org/10.1016/S0165-2370(00)00207-2)
- [35] C.Yu, P. Thy, L. Wang (2014) Influence of leaching pretreatment on fuel properties of biomass, *Fuel Process Technol.*, 128, 43–53. <https://doi.org/10.1016/j.fuproc.2014.06.030>
- [36] A. Quek, R. Balasubramanian (2011) Preparation and characterization of low energy post-pyrolysis oxygenated tire char, *Chem Eng J.*, 170, 194–201. <https://doi.org/10.1016/j.cej.2011.03.053>
- [37] M. Selbes, O. Yilmaz, A.A. Khan (2015) Leaching of DOC, DN, and inorganic constituents from scrap tires. *Chemosphere.*, 139, 617–623. <https://doi.org/10.1016/j.chemosphere.2015.01.042>
- [38] I. Iraola-Arregui, P. Van Der Gryp, J.F. G'orgens (2018) A review on the demineralisation of pre- and post-pyrolysis biomass and tyre wastes, *Waste Manage (Oxford).*, 79, 667–688. <https://doi.org/10.1016/j.wasman.2018.08.034>
- [39] S. Manocha, G. Prasad, P. Joshi (2013) Preparation and characterization of activated carbon from demineralized tyre char, *AIP Conf Proc.*, 1538, 109–112. <https://doi.org/10.1063/1.4810039>
- [40] F.A L'opez, T.A. Centeno, O. Rodriguez (2013) Preparation and characterization of activated carbon from the char produced in the thermolysis of granulated scrap tyres, *J Air Waste Manage Assoc.*, 63, 534–544. <https://doi.org/10.1016/j.wasman.2011.08.006>
- [41] K.J. Collins, A. Jensen, J. Mallinson (2002) Environmental impact assessment of a scrap tyre artificial reef, *ICES J Mar Sci.*, 59, 243–249. <https://doi.org/10.1006/jmsc.2002.1297>
- [42] J. Shah, M.R. Jan, F. Mabood (2006) Conversion of waste tyres into carbon black and their utilization as adsorbent, *J Chin Chem Soc.*, 53, 1085–1089. <https://doi.org/10.1007/s10924-007-0062-7>
- [43] P. Ariyadejwanich, W. Tanthapanichakoon, K. Nakagawa (2003) Preparation and characterization of mesoporous activated carb on from waste tires, *Carbon.*, 41, 157–64. [https://doi.org/10.1016/S0008-6223\(02\)00267-1](https://doi.org/10.1016/S0008-6223(02)00267-1)
- [44] S. Doja, L.K. Pillari, L. Bichler (2021) Processing and activation of tire-derived char: a review, *Renew Sustain Energy Rev.*, 155, 111860. <https://doi.org/10.1016/j.rser.2021.111860>

IZVOD

KARAKTERISTIKE PIROLIZE IZ OTPADNIH GUMA, NADOGRADNJA I PRIMENA

Piroliza otpadnih guma može da reciklira energiju i proizvede proizvode za višekratnu upotrebu (ulje, ugljen i gas). Iako u literaturi ima mnogo pregleda u vezi sa piroliznim karakteristikama otpadnih guma, ovaj rad je kritički pogledao kao pirolizni ugljen kao jedan od korisnih proizvoda. Njegove fizičke karakteristike uključuju prečnik pora, zapreminu pora, specifičnu površinu i sastav. Uobičajene tehnike detekcije fizičkih karakteristika uključuju elementarnu analizu, proksimnu analizu, SEM, EDS, TGA, KSRF, BET i Raman spektroskopiju. Hemijske karakteristike ugljenisane gume uglavnom uključuju kalorijsku vrednost, površinske funkcionalne grupe (tj. fenole, alkohole, karboksilnu kiselinu i hemijske strukture C-O/C-O-C) koje se mogu odrediti pomoću FT-IR, XRD. Veće zadržavanje sumpora na površini ugljenisane gume postiže se na niskoj temperaturi u poređenju sa onim dobijenim na visokoj temperaturi. Ugljenost guma se takođe može direktno koristiti kao katalizatorski materijal za smanjenje operativnih troškova i poboljšanje kvaliteta piroliznog ulja i gasa. Modifikovano ugljenisanje pneumatika sa visokom specifičnom površinom i nižim sadržajem pepela može se koristiti kao adsorbujući materijal sa aktivnim ugljem, nosač katalizatora i katalizatora, elektroda kondenzatora za stvaranje veće komercijalne vrednosti, kao adsorbent, u baterijama i tako dalje. Predlaže se da se razvijaju aplikacije za reciklažu ugljenih guma, što može stvoriti visok nivo potencijalnih ekonomskih izgleda za industriju pirolize otpadnih guma.

Ključne reči: *Piroliza, otpadne gume, ugljen, modifikacija, čađ.*

Naučni rad

Rad primljen: 31.03.2024.

Rad korigovan: 1.06.2024.

Rad prihvaćen: 15.06.2024.

The ORCID Ids of all the authors are as follows:

1. Nura Alhaji Yaro: <https://orcid.org/0000-0002-7780-9620>

2. Pramod Kumar Singh: <https://orcid.org/0000-0002-3155-6621>

3. Bashir Abdu Muzakkari: <https://orcid.org/0000-0001-9432-5313>

4. Umar Muhammad Jibreel: <https://orcid.org/0009-0003-0664-4878>

Anna Stepashkina*, Khurram Shehzad

Zhejiang Lab, Kechuang Avenue, Zhongtai Sub-District, Yuhang District, Hangzhou, Zhejiang Province, P.R. China.

Scientific paper

ISSN 0351-9465, E-ISSN 2466-2585

<https://doi.org/10.62638/ZasMat1110>



Zastita Materijala 65 (4)
756 – 764 (2024)

Examining the Impact of Anisotropic Particle Orientation in a Polymer Matrix on the Electrical Properties of Composite Materials

ABSTRACT

A number of works have experimentally shown the significant influence of mechanical stretching on the electrically conductive properties of composite polymer materials. Thus, stretching polymer composite films and filaments can lead to deterioration in electrical conductivity properties which can significantly affect the characteristics of products made from such materials. The research conducted in this study focuses on simulation the impact of anisotropic particle orientation within a polymer matrix and mechanical stretching on the electrical properties of composite materials. Based on the Boltzmann statistics, an expression was obtained that allows predicting the change in electrical conductivity during the stretching of polymer composite samples. The Monte Carlo method was used to simulate the destruction of a percolation chain of conductive particles during stretching.

Keywords: Polymer composite materials, anisotropic fillers, electrical conductivity, stretching, Monte Carlo simulation

1. INTRODUCTION

Adding electrically conductive fillers, such as carbon nanoparticles, is a common method used to reduce the resistance of polymer materials [1-15]. These fillers enhance the conductivity of the polymer matrix, allowing for improved electrical performance.

In addition to high conductivity, such composites also exhibit superior mechanical properties compared to metals, are resistant to corrosion. Electrically conductive polymer structures can be used as shielding or antistatic parts of the equipment [7, 14, 16-19]. In modern additive technologies, new polymer composites are used for producing filaments with special properties [20-22]. The relationship between the electrical resistivity of composites and filler concentration exhibits a threshold characteristic [3, 8, 9, 23, 24]. At certain filler concentrations, called critical concentration, filler particles form conducting clusters. These clusters allow electrical cur-

rent to flow efficiently through the material, reducing the overall resistance of composites compared to the initial resistance of the insulating matrix.

Previous studies [3, 8, 9, 23, 24] have introduced methods for predicting the concentration of fillers in a polymer matrix to identify the threshold concentration required for achieving the desired conductive properties of materials. To describe the percolation process, the researchers used a model of a composite material in the form of a regular cubic lattice [9, 23-25]; the basic algorithm for forming an infinite conducting cluster was the Monte Carlo method. The fillers randomly occupied a position in the cubic lattice, and the geometry of the filler was not taken into account [8, 9, 23, 24]. Next, conditions are applied to identify percolation clusters that can arise as a result of interactions on edges, surfaces or vertices in the three-dimensional case [8, 9]. Samples with high electrical conductivity can even allow the formation of a percolation cluster through one cell [9]. Such modelling is implemented using Monte Carlo simulation; the simulation result well describes the formation of a percolation cluster for isotropic large particles and agglomerates of filler particles. Additionally, the impact of the size of isotropic copper particles on the electrically

* Corresponding author: Anna Stepashkina
E-mail: anna_step@zhejianglab.com
Paper received: 22.04.2024.
Paper accepted: 20.05.2024.

conductive properties of a composite material based on an epoxy binder is also investigated [26]. Several researchers [14, 27-33] have also reported modelling of electrically conductive cluster forming for anisotropic particles like carbon nanofibers and nanotubes. These studies pay attention to the aspect ratio of the fillers. It has been established that a higher aspect ratio significantly increases the likelihood of percolation cluster formation, with simulation results closely aligning with experimental outcomes [30, 31].

However, despite advancements, challenges persist in accurately predicting the electrical conductivity properties in practical, real-world operational scenarios. Experimental works [34-41] have reported the influence of mechanical stretching on the electrically conductive properties of polymer composite materials, where an increase in electrical resistance even by 1 order can lead to a loss of the electrically conductive properties on many orders of magnitude. Thus, in the applications of conductive composites in applications such as protective clothing or covers, where composites experience strong mechanical influence can lead to loss of shielding properties which entail to equipment failure and the negative impact of electromagnetic radiation on humans.

In summary, while modelling the formation of percolation chains has seen significant development, including the study of filler geometry and size, the influence of mechanical deformations on the electrically conductive properties of composite materials remains an open question. There are some experimental results but it is necessary to build the approach for prediction the behaviour of composite conductivity during stretching. This work is dedicated to the examination and modelling of anisotropic filler orientation and its impact on the electrical conductivity and shielding properties of composite materials.

EXPERIMENTAL

The researches [34-39] demonstrated the impact of stretching on the electrically conductive properties of composites with carbon nanofillers. Specifically, when subjected to an elongation value of 5%, the electrical resistance of the fillers increased by 3 times [35-37]. In certain cases, the increase in the electrical resistance was even greater, exceeding an order of magnitude [34, 36, 37]. These experimental results highlight the significant influence of mechanical factors, such as stretching, on the electrical conductive properties of composites.

The influence of orientation stretching on the electrically conductive properties of composite materials is also significant [42, 43]. For the study, in [43] composite filaments based on polypropylene (PP) matrix and carbon nanofibers (CNF) were obtained. The electrical resistivity was measured for two types of samples: without orientation stretching $\lambda=1$ and with orientation stretching in 8 times $\lambda=8$. The change in orientation stretching is shown on Figure 1 (right) in range of mass fraction. During orientation stretching of polypropylene filament, the polymer molecules are oriented along the stretching axis (Fig. 1, left). Thus, anisotropic particles tend to assume a more energetically favorable state according to the oriented structure of polymer [43].

Based on the experimental results of the composite PP/CNF described above [43], for the experimental study, composite materials based on PP matrix and CNF as a filler were obtained. The mass fraction of CNF was chosen to be 8% due to an electrical resistivity value of less than $120 \Omega \cdot \text{cm}$. Properties of both PP and CNF are provided in Table 1.

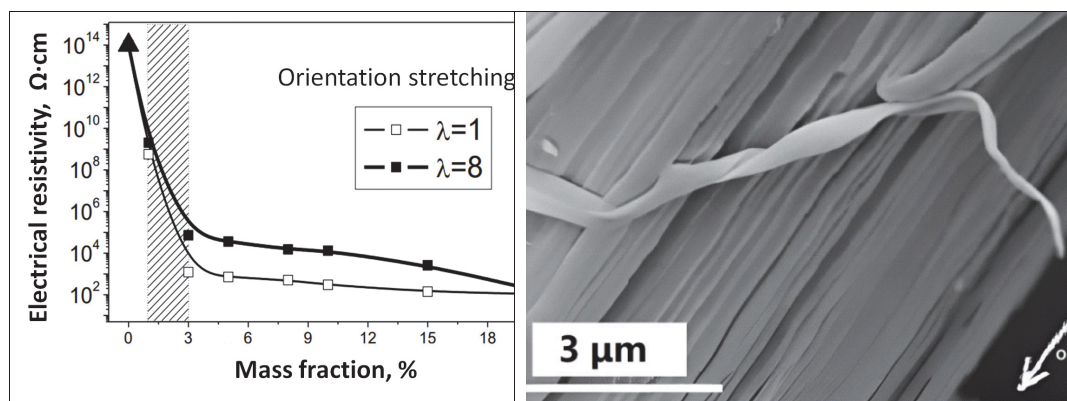


Figure 1. The dependence of electrical resistivity on the filler mass fraction for polymeric filaments in not orientated and orientated conditions (left); the oriented polypropylene filament structure (right) [43].

Table 1. Component characteristics

Material	Characteristics, units of measurement	Value
PP	Melt fluidity index, gr/min	22-30
	Volume electrical resistance of compressed powder, $\Omega \cdot m$	1014
	Poisson ration	0.38
	Melting point, $^{\circ}C$	170-176
CNF	Fiber diameter, nm	150
	Fiber length, μm	10-20
	Density, g/cm^3	2
	Content of volatile impurities, %	0,1
	Volume electrical resistance of compressed powder, $\Omega \cdot m$	10-4

The samples were obtained using melt technology. CNF as a filler was dispersed in a PP melt within a microcompounder. Mixing was conducted at a temperature of 180 $^{\circ}C$ for 2 minutes, and then the samples were formed. The samples were obtained in three geometrical forms: blocks, films and filaments. Block-shaped samples were formed by cooling the melt within molds. Film-shaped composites were obtained by rapidly cooling the melt as it exited the slot die. For filament formation, a round die was used. The film and filaments were promptly cooled using compressed air, and then wound onto reels at a constant speed. The films had a width of 25 mm and a thickness ranging from 100 to 200 microns, the filaments had a diameter of 400 μm .

The electrical resistivity of samples with different geometries was measured at room temperature using the four-contact method, and the results are presented in Table 2. At an equal CNF concentration the electrical conductivity of filaments and films is higher than for blocks. This effect can be explained by the difference in the technology of obtaining samples. For the fabrication of the block samples, the composite material was molded in a special form. For films and fibers, a forming dies were installed at the exit of the microcompounder. As it mentioned before, after that films and fibers wound on the reels of the receiving device, $\lambda=1$. Thus, the internal structure of composite films and filaments (Fig. 1) have a nominally oriented structure [43].

Table 2. Electrical resistivity of composites with different shape.

Material	Blocks: PP/CNF	Films: PP/CNF	Filaments: PP/CNF
Electrical resistivity	185 \pm 12 $\Omega \cdot m$	4.2 \pm 0.4 $\Omega \cdot m$	0.20 \pm 0.06 $\Omega \cdot m$

This study focuses on investigating the impact of stretching on the electrical conductivity properties of previously obtained samples in form of films and filaments. To conduct the experimental research, a tensile testing machine was upgraded with an electrical circuit to measure current and voltage. The material being studied is subjected to tension. Initially, the mechanical stress (strain) and electrical resistivity values are determined. The films and filaments are then slowly stretched, and the electrical resistivity is measured at control points.

The results show a significant increase in electrical resistivity, with a 1 order of magnitude increase observed at 5% strain (as shown in Figure 2).

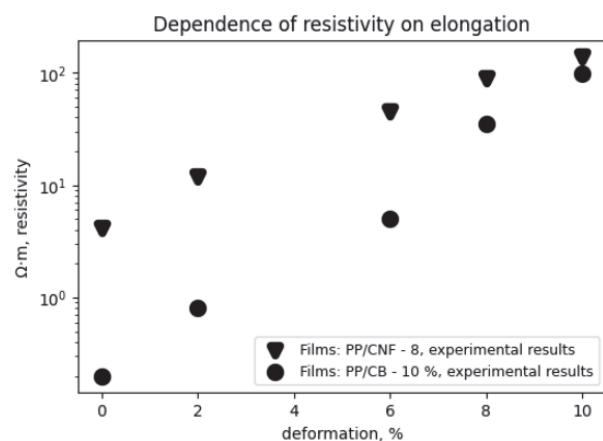


Figure 2. Influence of stretching on the electrically conductive properties of composite materials.

Increase in electrical resistance can be attributed to the reorganizing of the polypropylene structure, specifically the stretching of polymer chains along the direction of mechanical force, resulting in a change in the position of carbon nanofibers. The carbon nanofiber particles tend to align themselves in a more favourable energy state, causing a decrease in the angle relative to the stretching axis and ultimately breaking the percolation chains. The experimental findings suggest that there exists an optimal angle of orientation for the anisotropic filler particles within the matrix, which can lead to the best electrically conductive properties of the composite at a given filler concentration.

RESULTS AND DISCUSSIONS

As a first approximation, we assume that fillers do not agglomerate in order to reveal the dependence of electrical conductivity on the orientation of anisotropic filler particles. A change in filler orientation can occur due to stretching of the composite. In this case, a change in the structure of the polymer matrix molecule occurs, which may entail a change in the orientation of the filler particles and destruction of the percolation cluster, which will entail a deterioration in electrical conductivity properties. To find the optimal angle of orientation, a model using the Monte Carlo method to study the formation of a percolation cluster was developed. The model is implemented in the Python programming language. The primary goal of the model is to examine how the orientation of anisotropic carbon nanoparticles affects the overall structure. However, it is important to note that, for simplicity, the model doesn't take into account the ability of CNF particles to agglomerate in this initial approximation.

The composite material is treated as a two-dimensional square with a side length of " m ". The anisotropic CNF particles can be represented as linear functions, specifically $y = k \cdot x + b$. The orientation of the fibers will be set relative to the OX axis, where the value of " k " will determine the angle of orientation of the anisotropic particles in the composite material. The parameter " b " will represent the initial and final coordinates of the segment along the abscissa axis and will be randomly set within the range from 0 to " m ". The following parameters will be provided as input for the program:

- " n ": mass fraction of filler in percent
- " m ": dimension of space (a natural number)

- " α ": maximum orientation angle of carbon nanofiber in degrees, ranging from 0° to 90°
- particle aspect ratio.

Firstly, filler particles are randomly generated as segments based on input data. Then, a search is conducted to identify interacting particles, which are determined by the presence of at least one point of intersection between the segments. In the third stage, a percolation cluster is determined using a breadth-first search algorithm. The output of the model is an image that visually represents the distribution of carbon nanofibers in the polymer material. Figure 3 illustrates the distribution model of carbon nanofiber particles with a mass fraction of 8% in a polymer matrix, considering an orientation angle of anisotropic particles up to 40° . The influence of the orientation of carbon nanofibers on the electrical conductive properties of the composite material is examined at a filler concentration of 8%. The simulation is conducted for the maximum orientation angle of carbon nanofibers (α) ranging from 0° to 90° with a step of 5° . Figure 4 presents the results of modeling the formation of a percolation cluster or long chains for five different types of angles.

The probability of the percolation cluster formation is calculated as the proportion of successful formation attempts for all simulations. The program performs the simulation 100 times, in each case the algorithm searches for a percolation chain. If a percolation chain has been formed, then the algorithm considers the attempt successful. All successful attempts are summed up.

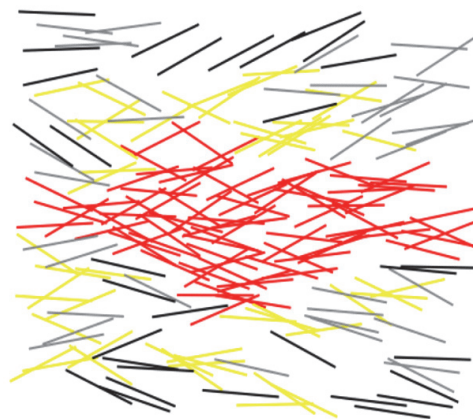


Figure 3. Distribution of carbon nanofibers in the polymer matrix (the filler concentration is 8%): red – the percolation cluster, yellow – long chains of interacting particles in the absence of a percolation cluster, gray – interacting particles not included in long chains, black – non-interacting particles.

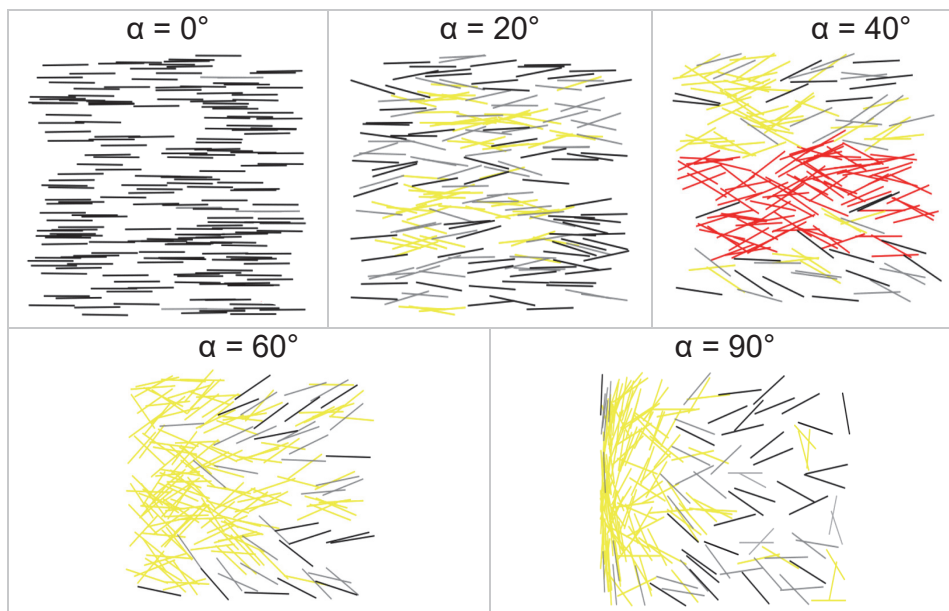


Figure 4. Results of modelling the orientation of carbon nanofibers in a composite material at a filler concentration of 8%.

In the absence of orientation along the abscissa axis (in this case, we take the maximum orientation angle $\alpha = 90^\circ$), the percolation cluster is not formed. A similar result is confirmed experimentally for samples in the form of blocks, the formation of which is carried out by rapid cooling of the solidification of the melt in the mold. The probability of formation of a percolation chain is zero. During the formation of block samples, the particles of carbon nanofibers are randomly distributed in the volume, and the electrical resistivity is 2 orders of magnitude higher than for film samples, in which orientation is present due to the method of obtaining samples. As the maximum angle decreases to 60° , the probability of the formation of a percolation cluster greatly increases and reaches 70%.

The maximum probability of formation of a percolation cluster 97-100% is achieved at the maximum value of the orientation angle in the range from 35° to 55° . This practically corresponds to the formation of unoriented film materials. With a further decrease in the maximum orientation angle of nanofibers in the material, the probability of the formation of a percolation cluster decreases, and at a value of $\alpha = 0^\circ$, it is unlikely that one segment will intersect two. Such a deterioration in the electrically conductive properties is described by the orientational stretching of film composite materials.

Thus, we can conclude that the highest probability of the formation of a percolation cluster in a

composite material based on a polymer matrix and carbon fillers can be achieved by orienting carbon nanofibers along some axis. Anisotropic carbon nanoparticles are considered as dipoles, thus, carbon nanofiber particles have some orientation relative to the film drawing axis, which is confirmed by micrographs of samples [26, 41].

As the strain increases, the orientation angle of the anisotropic particles decreases. Thus, in structures which there is no orientation (the maximum angle between the axis of the orientation stretching and the axis of the anisotropic particle is 90°), the orientation angle decreases upon stretching, and the probability of the formation of a percolation cluster increases until a certain value is reached. The simulation results make it possible to predict that the maximum angle between the axis of the orientation stretch and the axis of the anisotropic particle is in the range of 35° - 55° . Thus, orientation upon stretching can improve the properties of composite materials. So, at equal concentrations, block and film materials have different values of electrical resistance block materials have a greater value. This is an agreement with the Monte Carlo simulation however it is worth noting the limits of reliability of modelling. A similar scenario takes place only at filler concentrations close to the threshold value.

In oriented structures, there is a loss of electrically conductive properties, which is confirmed experimentally. In this case, the orientation angle continues

to decrease and, at a certain value, the conductive chains are destroyed. Modelling suggests that at a maximum angle between the axis of the orientation stretching and the axis of the anisotropic particle of 35° or less, the probability of destruction of the percolation cluster increases.

In this section, a model is constructed that allows one to predict the value of the electrical resistance of a composite material depending on stretching. Electrons are considered as carriers of electric charge in composite materials. It is assumed that electrons are a classical non-degenerate gas, taking into account the amorphous structure of the matrix and the random distribution of the filler. If the electron gas is in thermodynamic equilibrium, such a system obeys Boltzmann-Maxwell statistics. The charge transfer from one conducting particle to another is carried out due to the electron-phonon interaction. Under mechanical action on the sample and a change in the orientation of the filler in the matrix, a change in the internal energy occurs, which in turn leads to an increase in the thermal vibrations of the lattice. An electron under the action of thermal vibrations of the lattice performs a transition from state 1 to state 2, overcoming some energy barrier, height H and width δ. The width and height of the barrier are linearly related to the mechanical effects on the system.

In accordance with Boltzmann-Maxwell statistics, we write the probability of overcoming the energy barrier from state 1 to state 2 in the case of a material transition from a non-conductive to a conductive state

$$W_{12} = \omega_{12} e^{\frac{-H-eE}{k_b T}}, \tag{1}$$

where e is the electron charge, E is the field strength, k_b is the Boltzmann constant, T is the temperature, ω₁₂ is the fraction of particles that have passed from state 1 to state 2. The barrier value H is a function inversely proportional to two variables: filler concentration ϑ and deformation ε (orientation angle α):

$$H = H(\vartheta, \varepsilon(\alpha))$$

Such a process will be considered reversible, i.e. a transition from state 2 to state 1 is possible, with probability

$$W_{21} = -\omega_{21} e^{\frac{H-eE}{k_b T}}, \tag{2}$$

where ω₂₁ is the fraction of particles that have passed from state 2 to state 1. The difference in ex-

pressions (1) and (2) gives us the dependence of the resistivity change on the height of the potential barrier, i.e. on deformation, concentration of fillers, and orientation angle of anisotropic particles:

$$\delta\rho = \rho_0 \varepsilon \cosh(\gamma H) \tag{3}$$

- electrical resistance in the absence of mechanical influences. T

As objects of study, in addition to the experimental results shown in Figure 1, we will consider the experimental dependencies presented in works [35, 36]. In [35], PEO (polyethylene oxides) was used as a polymer matrix, carbon nanotubes were used as fillers, the filler concentration was 3%. In [36], materials based on rubber filled with carbon black were experimentally studied. We believe that conductivity is related to the deformation and mechanical properties of the matrix, thus taking into account the Poisson's ratio.

$$\rho = \rho_0(1 + \varepsilon \cdot \cosh(\varepsilon \cdot \gamma)) \tag{4}$$

Figure 5 shows good agreement between the obtained mathematical expression and the experimental results, thus the expression for resistance can be used to predict the properties of polymer composite materials.

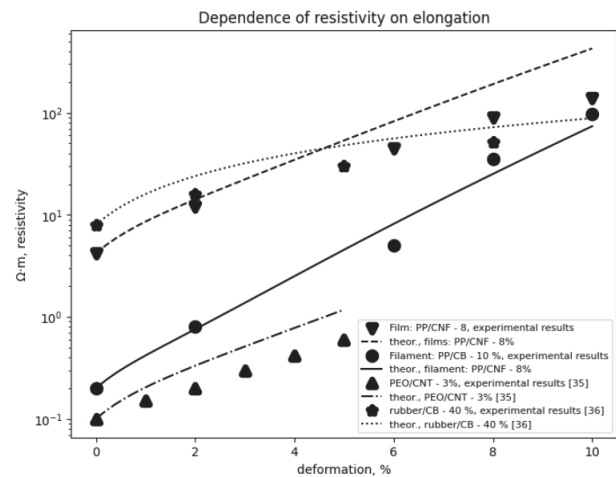


Figure 5. Theoretical and experimental dependences of stretching deformation on the electrically conductive properties of composite materials

CONCLUSIONS

This study investigates how mechanical stretching and the resulting alignment of anisotropic particles within composite materials affect their electrical conductivity. Our findings reveal that orienting fillers, such as carbon nanofibers, between 35° to 55° relative to

a specific axis significantly enhances the likelihood of percolation cluster formation. Our simulations closely align with experimental results. By strategically orienting these particles without altering filler concentration, we can markedly enhance electrical conductivity, achieving the necessary electrical resistivity for shielding properties in composite polymer materials and their derived products. Notably, materials exposed to high mechanical stress risk losing their electrical conductivity and subsequent shielding properties, posing safety hazards in composite material-based products. One viable solution to counteract the decline in electrical conductivity during operation is by increasing filler concentration. Moreover, our work derives an expression rooted in Boltzmann statistics, offering insight into predicting the rise in electrical resistance when film samples undergo stretching. This expression holds promise in forecasting the performance of composite polymers, particularly in film and textile formats utilized for shielding against electric fields.

REFERENCES

- S.Zhou, A.Hrymak, M.Kamal (2017) *Electrical and morphological properties of microinjection molded polypropylene/carbon nanocomposites*. Journal of Applied Polymer Science, **134**(43) 45462. doi: 10.1002/app.45462.
- D.Youngá Lim (2016) *Fabrication of a stretchable electromagnetic interference shielding silver nanoparticle/elastomeric polymer composite*. RSC advances, **6**(57), 52250-52254. doi:10.1039/C6RA04765C.
- L.d.S. Vieira, E.G.E.d Anjos, G.E.A. Verginio, I.C.Oyama, N.F. Braga, T.F.d.Silva, L.S. Montagna, F.R. Passador (2022) *A review concerning the main factors that interfere in the electrical percolation threshold content of polymeric antistatic packaging with carbon fillers as antistatic agent*. Nano Select, **3**(2), 248-260. doi: 10/1002/nano.202100073.
- A. Tarhini, A.R. Tehrani-Bagha (2023) *Advances in preparation methods and conductivity properties of graphene-based polymer composites*. Applied Composite Materials, **30**(6), 1737-1762. doi: 10.1007/s10443-023-101455-5.
- Y.Yao, X.Zheng, G.Pan, J.Sun, J.Hu, Y.Huang, R.Sun, J.-B. Xu, C.-P. Wong (2016) *Interfacial engineering of silicon carbide nanowire/cellulose microcrystal paper toward high thermal conductivity*. ACS applied materials & interfaces, **8**(45), 31248-31255. doi: 10.1021/acsami.6b10935.
- D.Xiang, E.Harkin-Jones, D.Linton, P.Martin (2015) *Structure, mechanical, and electrical properties of high-density polyethylene/multi-walled carbon nanotube composites processed by compression molding and blown film extrusion*. Journal of Applied Polymer Science, **132**(42), 42665. doi: 10.1002/app.42665.
- N.Ucar, B.K.Kayaoglu, A.Bilge, G.Gurel, P.Sencandan, S. Parker (2018) *Electromagnetic shielding effectiveness of carbon fabric/epoxy composite with continuous graphene oxide fiber and multiwalled carbon nanotube*. Journal of Composite Materials, **52**(24), 3341-3350. doi: 10.1177/0021998318765273.
- R. Taherian (2016) *Experimental and analytical model for the electrical conductivity of polymer-based nanocomposites*. Composites Science and Technology, **123**, 17-31. doi: 10.1016/j.compscitech.2015.11.029.
- A. Stepashkina, E. Tsobkallo, A. Alyoshin (2014) *Electrical conductivity modeling and research of polypropylene composites filled with carbon black*. Journal of Physics: Conference Series, **572**, 012032. doi: 10.1088/1742-6596/572/1/012032.
- S.Maiti, S.Suin, N.K. Shrivastava, B.B. Khatua (2014) *A strategy to achieve high electromagnetic interference shielding and ultra low percolation in multiwall carbon nanotube-polycarbonate composites through selective localization of carbon nanotubes*. RSC Advances, **4**(16), 7979-7990. doi: 10.1039/C3RA46480F.
- L.Li, D.Chung (1994) *Electrical and mechanical properties of electrically conductive polyethersulfone composites*. Composites, **25**(3), 215-224. doi: 10.1016/0010-4361(94)90019-1.
- M.Fogel, P.Parlevliet, M.Geistbeck, P.Olivier, E.Dantaras (2015) *Thermal, rheological and electrical analysis of MWCNTs/epoxy matrices*. Composites Science and Technology, **110**, 118-125. doi: 10.1016/j.compscitech.2015.02.002.
- K. Bhaskaran, R.K. Bheema, K.C. Etika (2020) *The influence of Fe₃O₄@ GNP hybrids on enhancing the EMI shielding effectiveness of epoxy composites in the X-band*. Synthetic Metals, **265**, 116374. doi: 10.1016/j.synthmet.2020.116374.
- P. Bhardwaj, A.N. Grace (2020) *Antistatic and microwave shielding performance of polythiophene-graphene grafted 3-dimensional carbon fibre composite*. Diamond and Related Materials, **106**, 107871. doi: 10/1016/j.diamond.2020.107871.
- M.H. Al-Saleh, U. Sundararaj (2009) *A review of vapor grown carbon nanofiber/polymer conductive composites*. Carbon, **47**(1), 2-22. doi: 10.1016/j.carbon.2008.09.039.
- S.P Pradhan, L.Shubhadarshinee, P. Mohapatra, P. Mohanty, B.R. Jali, P. Mohapatra, A.K. Barick (2022) *Conducting polymer composites for antistatic application in aerospace*. Aerospace Polymeric Materials, **7**, 155-187. doi: 10.1002/978119905264.ch7.
- R. Yadav, M. Tirumali, X. Wang, M. Naebe, B. Kandasubramanian (2020) *Polymer composite for antistatic application in aerospace*. Defence Technology, **16**(1), 107-118. doi: 10.1016/j.dt.2019.04.008.
- K.Tian, D.Hu, Q.Weil, Q.Fu, H.Deng (2023) *Recent progress on multifunctional electromagnetic interference shielding polymer composites*. Journal of Materials Science & Technology, **134**, 106-131. doi: 10.1016/j.jmst.2022.06.031.

19. Y.Gao, C.Xie, Z.Zheng (2021) *Textile composite electrodes for flexible batteries and supercapacitors: opportunities and challenges*. *Advanced Energy Materials*, **11**(3), 2002838. doi: 10.1002/aenm.202002838.
20. O.S. Saran, A.P.Reddy, L. Chaturya, M. Pavan Kumar (2022) *3D printing of composite materials: A short review*. *Materials Today: Proceedings*, **64**, 615-619. doi: 10.1016/j.matpr.2022.05.144.
21. M. Ateeq, M. Shafique, A. Azam, M. Rafiq (2023) *A review of 3D printing of the recycled carbon fiber reinforced polymer composites: Processing, potential, and perspectives*. *Journal of Materials Research and Technology*, **26**, 2291-2309. doi: 10.1016/j.jmrt.2023.07.171
22. P. Jagadeesh, M. Puttegowda, S.M. Rangappa, A. Karfidov, S. Gorbatyuk, A. Khan, M.Doddamani, S. Siengchin (2022) *A comprehensive review on 3D printing advancements in polymer composites: technologies, materials, and applications*. *The International Journal of Advanced Manufacturing Technology*, **121**(1-2), 127-169. doi: 10.1007/s00170-022-094606-7.
23. S.Y. Kim, Y.J. Noh, J. Yu (2015) *Prediction and experimental validation of electrical percolation by applying a modified micromechanics model considering multiple heterogeneous inclusions*. *Composites Science and Technology* **106**, 156-162. doi: 10.1016/j.comp-scitech.2014.11.015.
24. A. Manta, M. Gresil, C. Soutis (2016) *Multi-scale finite element analysis of graphene/polymer nanocomposites: Electrical performance*. in *European Congress on Computational Methods in Applied Sciences and Engineering*. National Technical University of Athens. 1984-2022.
25. D. Budač, V. Milos, M. Carda, M. Paida, J. Fuhrmann, K. Bouzek (2023) *Prediction of Electrical Conductivity of Porous Composites Using a Simplified Monte Carlo 3D Equivalent Electronic Circuit Network Model: LSMYSZ Case Study*. *Electrochimica Acta*, **457**, 142512. doi: 10.1016/j.electacta.2023.142512.
26. R. Araújo, M.C. Paiva, M.F. Proenca, C.J.R. Silva (2007) *Functionalization of carbon nanofibres by 1, 3-dipolar cycloaddition reactions and its effect on composite properties*. *Composites science and technology*, **67**(5), 806-810. doi: 10.1016/j.comp-scitech.2006.01.040.
27. R. Yadav, M. Tirumali, X. Wang, M. NB. Kandasubramanian (2020) *Polymer composite for antistatic application in aerospace*. *Defence Technology*, **16**(1), 107-118. doi: 10.1016/j.dt.2019.04.008.
28. S. Rana, R. Figueiro (2016) *Advanced composites in aerospace engineering*, in *Advanced composite materials for aerospace engineering*. *Advanced Composite Materials for Aerospace Engineering*. Processing, Properties and Applications, p. 1-15. doi: 10.1016/B978-0-08-100037-3.00001-8.
29. Z.-H. Tang, D.-Y. Wang, Y.-Q. Li, P.Huang, S.-Y. Fu (2022) *Modeling the synergistic electrical percolation effect of carbon nanotube/graphene/polymer composites*. *Composites Science and Technology*, **225**, 109496. doi: 10.1016/j.comp-scitech.2022.109496.
30. F.Nilsson, J. Kruckel, D.W. Schubert, F. Chen, M. Unge, U.W. Gedde, M.S. Hedenqvist (2016) *Simulating the effective electric conductivity of polymer composites with high aspect ratio fillers*. *Composites Science and Technology*, **132**, 16-23. doi: 10.1016/j.comp-scitech.2016.06.008.
31. E.S. Tsobkallo, O.A. Moskalyuk, V.E. Yudin, A.N. Aleshin (2020) *Influence of particle aspect ratio and ability to aggregate on electrical conductivity of fiber-forming polymer composites*. *Physics of Complex Systems*, **1**(3), 99-107. doi: 10.33910/2687-153X-2020-1-3-99-107.
32. N. Zhao, Y. Kim, J.H. Koo (2018) *3D Monte Carlo simulation modeling for the electrical conductivity of carbon nanotube-incorporated polymer nanocomposite using resistance network formation*. *Materials Science: Advanced Composite Materials*, **2**(2). doi: 10.18063/msacm.v2i2.672.
33. D.-K. Lee, J. Yoo, H. Kim, B.-H. Kang, S.-H. Park (2022) *Electrical and Thermal Properties of Carbon Nanotube Polymer Composites with Various Aspect Ratios*. *Materials*, **15**(4), 1356. doi: 10.3390/ma15041356.
34. L. Abell, P. Adams, A. Monkman (1996) *Electrical conductivity enhancement of predoped polyaniline by stretch orientation*. *Polymer*, **37**(26), 5927-5931. doi: 10.1016/S0032-3861(96)00580-0.
35. C. Feng, L. Jiang (2015) *Micromechanics modeling of bi-axial stretching effects on the electrical conductivity of CNT-polymer composites*. *International Journal of Applied Mechanics*, **7**(01), 1550005. doi: 10.1142/S1758825115400050.
36. N.C. Das, T.K. Chaki, D. Khastgir (2002) *Effect of axial stretching on electrical resistivity of short carbon fibre and carbon black filled conductive rubber composites*. *Polymer International*, **51**(2), 156-163. doi:10.1002/pi.811.
37. C. Feng, L.Y. Jiang (2014) *Investigation of uniaxial stretching effects on the electrical conductivity of CNT-polymer nanocomposites*. *Journal of Physics D: Applied Physics*, **47**(40), 405103. doi: 10.1088/0022-3727/47/40/405103.
38. B. Zhang, Z.-g. Zhang, L. Wei (2015) *Mechanical properties, electrical conductivity and microstructure of CuCrZr alloys treated with thermal stretch process*. *Transactions of Nonferrous Metals Society of China*, **25**(7), 2285-2292. doi: 10.1016/S1003-6326(15)63843-2.
39. R.R. de Sousa Jr, D.A. Heinze, J.B. Sacramento, A. J.C. Lanfredi, D.J Carastan (2023) *Electrical Conductivity and In Situ SAXS Probing of Block Copolymer Nanocomposites Under Mechanical Stretching*. *ACS Applied Materials & Interfaces*, **15**(22), 27156-27165. doi: 10.1021/acsami.3c03573.
40. J. Aneli, G.E. Zaikov, L.M. Khananashvili (1999) *Effects of mechanical deformations on the structuriza-*

- tion and electric conductivity of electric conducting polymer composites. *Journal of Applied Polymer Science*, **74**(3), 601-621. doi: 10.1002/(SICI)1097-4628(19991017)74:3<601::AID-APP14>3.0.CO;2-K.
41. T. Prasse, J.-Y. Cavaille, W. Bauhofer (2003) *Electric anisotropy of carbon nanofibre/epoxy resin composites due to electric field induced alignment*. *Composites Science and Technology*, **63**(13), 1835-1841. doi:10.1016/S0266-3538(03)00019-8.
42. E.S. Tsobkhalo, A.S. Balanov, V.E. Yudin, O.A. Moskaluyk (2010) *The influence of orientation drawing on the physical and mechanical properties of polypropylene film filaments filled with carbon black nanoparticles*. *Izvestiya Vuzov. Tekhnologiya Legkoy Promishlennosti*, **10**(4), 25-29.
43. E. Tsobkhalo, O. Moskaluyk, A. Stepashkina, V. Yudin (2020) *Functional composite polymer materials for electrical purpose*. in AIP Conference Proceedings, **2308**, 030002. doi: 10.1063/5.0033667.

IZVOD

ISPITIVANJE UTICAJA ANISOTROPNE ORIJENTACIJE ČESTICA U POLIMERNOJ MATRICI NA ELEKTRIČNA SVOJSTVA KOMPOZITNIH MATERIJALA

Veliki broj radova je eksperimentalno pokazao značajan uticaj mehaničkog istezanja na elektroprovodna svojstva kompozitnih polimernih materijala. Dakle, istezanje polimernih kompozitnih filmova i filamenata može dovesti do pogoršanja svojstava električne provodljivosti što može značajno uticati na karakteristike proizvoda napravljenih od takvih materijala. Istraživanje sprovedeno u ovoj studiji se fokusira na simulaciju uticaja anizotropne orijentacije čestica unutar polimerne matrice i mehaničkog istezanja na električna svojstva kompozitnih materijala. Na osnovu Bolcmanove statistike dobijen je izraz koji omogućava predviđanje promene električne provodljivosti tokom istezanja uzoraka polimernih kompozita. Monte Karlo metoda je korišćena za simulaciju uništavanja perkolacionog lanca provodnih čestica tokom istezanja.

Ključne reči. Polimerni kompozitni materijali, anizotropna punila, električna provodljivost, istezanje, Monte Karlo simulacija

Naučni rad

Rad primljen: 16.03.2024.

Rad prihvaćen: 3.06.2024.-

The ORCID Ids of all the authors are as follows:

Anna Stepashkina: <https://orcid.org/0000-0003-3326-0776>

Khurram Shehzad: <https://orcid.org/0000-0002-1374-4987>

Thangarajan Umamathi¹, Venkatachalam Prathipa², Arockiam Roslin³, Arockiaraj Little Jewelcy³, Micheal Velankanni Jeevithe Clara³, Nilavan Anitha³, Mohamed Ibrahim Nasrin Sahana³, Susai Rajendran^{3,4}, Arjunan Krishnaveni⁵

¹Department of Chemistry, Sri Meenakshi Government Arts College for Women(A), Madurai, India; ²Department of Chemistry, PSNA College of Engineering and Technology, Dindigul, Tamil Nadu, India; ³Corrosion Research Centre, Department of Chemistry, St Antony's College of Arts and Sciences for Women, Dindigul, Tamil Nadu, India (Affiliated to Mother Teresa Women's University, Kodaikanal), Tamil Nadu, India; ⁴Centre for Nanoscience and Technology, Pondicherry University, Chinna Kalapet, Kalapet, Puducherry, India; ⁵PG Department of Chemistry, Yadava College, Natham Road, Tiruppalai, Madurai, Tamil Nadu, India

Scientific paper

ISSN 0351-9465, E-ISSN 2466-2585

<https://doi.org/10.10.62638/ZasMat1173>



Zastita Materijala 65 (4)

765 - 777 (2024)

Influence of sodium chloride on corrosion resistance of ever silver vessels in the presence of curd rice

ABSTRACT

The present work is undertaken to investigate the corrosion resistance of ever silver in the presence of water, water+curd system, water+curd+rice system, water+curd+rice+Salt system. The corrosion resistance has been evaluated by AC impedance spectra. AC impedance spectra have been employed to investigate the corrosion resistance of ever silver electrode when it is immersed in various test solutions like water, curd, curd rice recipe, curd rice recipe with salt (sodium chloride 500 ppm). The corrosion resistance of ever silver electrode when it is immersed in various test solutions like water, water+curd, water+curd+rice and water+curd+rice+salt have been evaluated by AC impedance spectroscopy. If a protective film is formed, the charge transfer resistance increases, impedance value increases, phase angle value increases and double layer capacitance (C_{dl}) value decreases. When Ever silver electrode is immersed in water + curd rice system + 500ppm sodium chloride system, the corrosion resistance of ever silver electrode decreases. This is due to the presence of chloride ion introduced into the curd rice system. It implies that when curd rice is packed in vessels made of ever silver, we should avoid adding salt to the curd rice. It is better to keep the salt and curd rice separately. It is to be noted that this corrosion resistance is better than the corrosion resistance in water alone.

The corrosion resistance decreases in the following order:

Water + Curd + Rice system > Water + Curd + Rice + Salt system (sodium chloride 500ppm) > Water + Curd system > Water

Keywords: corrosion resistance, ever silver, curd rice, sodium chloride, electrochemical studies

1. INTRODUCTION

Corrosion of food cans is influenced by various factors. They are content of certain compounds in corrosive food products such as sulfur compounds, chloride, nitrates, etc., which are derived from canned materials or from additive compounds; acidity or pH of food products.

For corrosion protection of metal cans used as food and beverage packaging, coatings based on epoxy phenolics and epoxy esters are the most common. Plastic coating offers several benefits to metal objects. It acts as a barrier against moisture, preventing rust and corrosion. It also provides insulation, electrical resistance, and impact resistance, enhancing the durability and lifespan of the metal. Several research works have been published dealing with alloys and metals used in food package process and the corrosion behavior of these materials [1-10]. The main findings are summarized in Table 1.

*Corresponding author: Susai Rajendran

E-mail: susairajendran@gmail.com

Paper received: 15.05.2024.

Paper accepted: 05.06.2024.

Table 1. Corrosion behavior of metals and alloys used in food packaging processes

SNo/ Ref	Title	Methods employed and findings
1	Electrochemical and AFM study of inhibitory properties of thin film formed by tartrazine food additive on 304L stainless steel in saline solution	Trisodium (4E)-5-oxo-1-(4-sulfonatophenyl)-4-[(4-sulfonatophenyl) hydrazono]-3-pyrazolecarboxylate, effect on the corrosion rate of 304L stainless steel used as canned food packaging has been studied by estimating the inhibitory properties of the organic film formed on the alloy surface during the electrochemical measurements performed in saline solution containing 0.9 % NaCl, without and with tartrazine inhibitor. AFM technique revealed the main surface changes of steel corroded in saline blank solution as well as in saline solution containing tartrazine food additive compared to standard stainless steel sample.
2	An update on the innovative surgical double-glove hole puncture indication systems: Reliability and performance	During operative procedures, operating room personnel wear sterile surgical gloves designed to protect them and their patients against transmissible infections. The Food and Drug Administration (FDA) has set compliance policy guides for manufacturers of gloves. The FDA allows surgeons' gloves whose leakage defect rates do not exceed 1.5 acceptable quality level (AQL) to be used in operating rooms. The implications of this policy are potentially enormous to operating room personnel and patients. This unacceptable risk to the personnel and patient could be significantly reduced by the use of sterile double surgical gloves.
3	Testing the corrosion resistance of stainless steels during the fermentation of probiotic drink	Over recent years, food producers have devoted much attention to the production of safe foods. Simultaneously, using advanced process technologies, it has been necessary to carefully select materials for use in process equipment. Milk and its products are exposed to metal surfaces from the time they are processed, through the various stages of handling and manufacture, to the packaging of the finished products for market. The selection of suitable materials for daily use in the dairy industry cannot be governed solely by their price and mechanical properties but must also take into consideration their influence on the quality of milk products. The results indicated that Nb played the most protective role against corrosion during kefir fermentation, since the steel containing Nb but no Mo showed the lowest corrosion rate.
4	The 04Kh19AFT nickel-free stainless sheet steel	Ferrite steel 04Kh19AFT has been developed. It may be obtained by integrated alloying chrome steel by Ti and V at the controlled content of interstitial impurities. Control on the Ti and V carbonitrides precipitates of most suitable sizes enhances the ductility and deformability and makes the stamping of products of any size and forms easier. Field tests show that this corrosion-resistant steel is well welded, stamped, polished and liable to deep drawing when producing welded constructions. It is attractive for food engineering industry, automobile industry, household appliances, etc.
5	Internal corrosion in domestic drinking-water installations	Domestic drinking-water installations involve the use of a variety of plumbing materials. This paper describes the correlation between material quality, plumbing and operational conditions and water quality. Specific attention is paid to galvanized steel, copper and lead but the new plumbing materials stainless steel and plastic are also mentioned.
6	Superhydrophobic systems in food science and technology: Concepts, trends, challenges, and technological innovations	The natural phenomenon of superhydrophobicity that occurs in plants and animals has been a current topic for research and development with the goal of widening its applications. However, a more complete understanding of such surfaces is necessary to assess the effects of morphology, chemical structure, and surface roughness. In the food sector, such investigations tend to be at an early stage, although superhydrophobic surfaces (SHS) are known to hold promise for food packaging, processing, safety, and preservation. A review of the phenomenon of superhydrophobicity, the parameters to be evaluated for producing superhydrophobic surfaces, and the main impact factors is presented.
7	Effective electrodeposition of poly(3,4-ethylenedioxythiophene)-based organic coating on metallic food packaging for active corrosion protection	Modern technologies continuously need special materials with specific properties to adopt the desired application. Recently, numerous researches have been dedicated to the development of new food packaging materials that can ensure optimum protection of the packaged product. In this context, conducting polymers-based coatings were considered promising materials to be used as contact compounds in the packaging industries. Poly(3, 4-ethylenedioxythiophene) (PEDOT) films were electrochemically synthesized on two different metallic food packaging substrates, namely, tinplate and aluminum.

8	Passivation and Chemical Conversion Combined Multi-Elements Coating on Low Sn-Coated Steel for Corrosion Protection	In this work, the tinplate with 0.5 g·m ⁻² tin coating mass was prepared in order to improve the economic benefit for food packaging field. We studied this low Sn-coated steel surface state and developed a process combined Mo-Mn-Al-P coating based on its special structure.
9	Corrosion of aluminum for beverage packaging in acidic media containing chlorides and copper ions	Corrosion of aluminum packaging plays an important role concerning economic and health issues. The effect of aggressive ions on the behavior of the AA3104-H19 alloy provides knowledge to the food and packaging industries to improve materials and also minimizes losses associated with the corrosion. This study evaluated the interaction of the AA3104-H19 alloy and beverage using model solutions containing chloride and copper at levels close to those found in soft drinks. Information about the corrosion electrochemical behavior of aluminum alloys used for food and beverage is very scarce.
10	Corrosion protection of metallic archaeological artefacts using parylene based removable barrier coating	Barrier films are used in wide range of industrial fields such as microelectronics, food packaging or anticorrosion layers to protect material against external environmental influences. Using of barrier films may be an alternative way of anticorrosion protection and conservation of metallic archaeological objects and it is the aim of this study. Based on our previous work, polymer parylene (poly-p-xylylene) was chosen for preparation of thin films for this purpose thanks to its desirable properties such as excellent barrier properties, transparency and formation of conformal coating without defects.

A case study has been undertaken in this area.

CASE STUDY

2. EXPERIMENTAL

Ever silver Composition

Ever silver is an alloy of silver that consists of 92.5% pure silver and 7.5% other metal, usually copper [Figure 1]. The other metals in the alloy increase hardness, so the material will be durable.



Figure 1. Ever silver vessel containing curd rice

Curd

Curd is made by bacterial fermentation of milk. In this process, lactose in milk is converted into lactic acid by several probiotic microorganisms. The species involved in the fermentation depends on the temperature and humidity of the environment and may include *Lactococcus lactis*, *Streptococcus diacetylactis*, *Streptococcus cremoris*, *Lactobacillus delbrueckii* subsp. *bulgaricus* and *Streptococcus thermophilus* [11].

Boiled rice

Plain boiled rice is cooked using rice and water. Rice and water are the raw materials required to make boiled rice hence are called ingredients [12].

Preparation of Curd Rice Recipe

Curd rice is also known as thayir sadam, dahi chawal and daddo janam. A very simple dish made using the most basic ingredients, curd and rice with an authentic south-indian tempering does not take more than 15 minutes to cook.

Easy to make, the curd rice is made by mixing rice with tempering it with mustard and green chillies. Allow the rice to cool slightly before adding the curd, to avoid the curds from splitting. Many people consider South Indian curd rice to be the best dish to carry along to school, work or travel.

We have taken the following combinations for investigation.

Water system, (Water + Curd system), (Water + Curd + Rice system) and (Water + Curd + Rice + Salt system).

Surface characterization study

The ever silver specimens were immersed in various test solutions for a period of one day. After one day the specimens were taken out and dried. The nature of the film formed on the metal surface was analyzed by surface characterization studies such as SEM, contact angle and Vickers hardness.

Scanning electron microscopy (SEM)

The mild steel specimens immersed in various test solutions for one day were taken out, dried and subjected to the surface examination. The surface morphology measurements of the mild steel surface were carried out by scanning electron microscopy (SEM) using CAREL ZEISS make model EVO-18.

Contact angle

The contact angle measurements on the surface were performed on a VCA Optima instrument equipped with a CCD camera for imaging. The deionized water under static conditions with a drop volume of 5 μ l was employed to determine the contact angle. VCA Optima XC software provided with instruments was used for fitting the drop shapes to find the contact angle of water on the surface. This measurement was repeated three times for each sample, the average values with standard deviations ± 2 are reported.

Vickers hardness

The ever silver specimens immersed in various test solutions for one day were taken out, rinsed with double distilled water, dried and subjected to Vicker hardness. The Vicker hardness measurements of the mild steel surface were carried out by Shimadzu make model HMV-2T.

AC impedance spectra

AC impedance spectral studies were carried out on a CHI – Electrochemical workstation with impedance. The corrosion resistance of ever silver electrode immersed in various test solutions has been measured. A three – electrode cell assembly

was used. The working electrode was Ever silver electrode. A saturated calomel electrode (SCE) was the reference electrode and platinum was the counter electrode.

The real part (Z') and imaginary part ($-Z''$) of the cell impedance were measured in Ohms at various frequencies. Values of the charge transfer resistance (R_t) and the double layer capacitance (C_{dl}) were calculated from Nyquist plots and Bode plots.

3. RESULTS AND DISCUSSION

Ever silver is popularly used for cookware, kitchen utensils and cutlery. This is because it is hard-wearing, corrosion resistant and it doesn't affect the flavour of the food when used for food storage or production. Due to the resistance levels, foods with high acidity won't cause damage. Usually, students take much variety rice in stainless steel. In this project we have taken water, water+curd, water+curd+rice and water+curd+rice+salt (sodium chloride) systems, in a stainless steel. To identify whether ever silver has undergone corrosion or not, we have undertaken AC impedance spectra.

Analysis of results of AC impedance Spectra [Electrochemical Impedance Spectra (EIS)]

AC impedance spectra have been used to detect the formation of the film on the metal surface [13-17]. If a protective film is formed, the charge transfer resistance (R_t) increases, impedance value increases, phase angle value increases and double layer capacitance (C_{dl}) value decreases (Figure 2).

The AC Impedance spectra of ever silver electrode immersed in various solutions are shown in Figures 3 to 6 (Nyquist plots) and Figures 7 to 10 (Bode plots). The interactive 3D plots are shown in Figures 11 to 14.

The AC Impedance parameters, namely, charge transfer resistance (R_t), impedance value, phase angle value and double layer capacitance (C_{dl}) are given in Table 2.

Let us recollect the principles of AC impedance spectra and corrosion inhibition study.

"If a protective film is formed, the charge transfer resistance (R_t) increases, impedance value increases, phase angle value increases and double layer capacitance (C_{dl}) value decreases" (Figure 2).

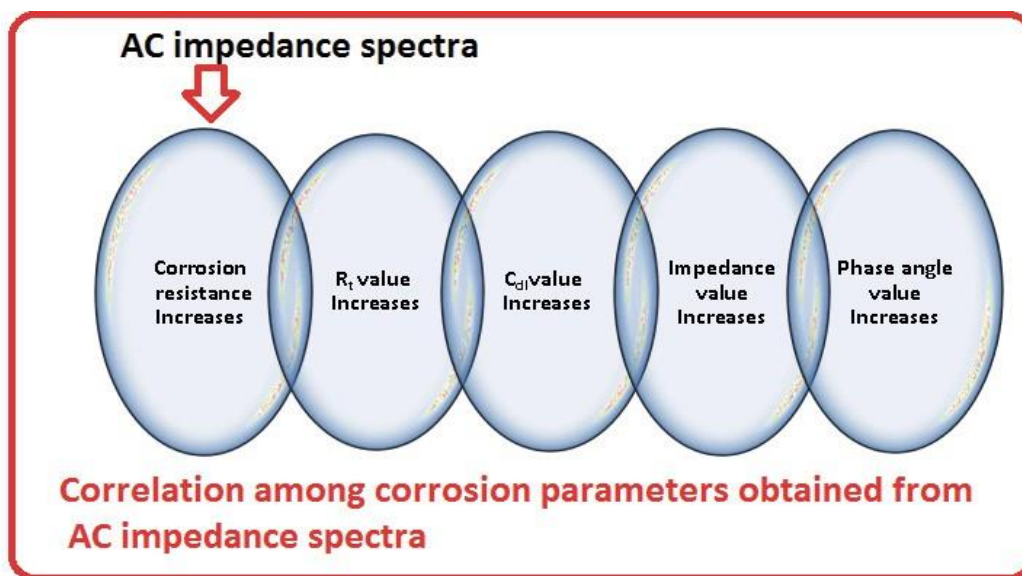


Figure 2. Correlation among corrosion parameters obtained from AC impedance spectra

Table 2. Corrosion parameters of Ever silver electrode immersed in various test solutions, obtained from AC Impedance spectra

System	R_t , Ohm.cm ²	C_{dl} , F/cm ²	Impedance Log(Z/Ohm)	Phase Angle ^o
water	24.63	482.94×10^{-4}	1.675	0.0033
water+Curd	25.56	501.176×10^{-4}	2.047	0.100
Water+Curd+Rice	504	9882.35×10^{-4}	3.217	5.678
Water+Curd+Rice+Salt	32.99	646.86×10^{-4}	1.934	1.240

Interesting conclusions are derived from Table 1.

Water system

When Ever silver electrode is immersed in water the charge transfer resistance (R_t) is 24.63 Ohm.cm². Double layer capacitance (C_{dl}) value is 482.94×10^{-4} F/cm².

Water+curd system

When ever silver electrode is immersed in water+curd system, the corrosion resistance of ever silver electrode increases. This is due to the adsorption of molecules of the ingredients present in curd. When ever silver is electrode immersed in water+curd system the charge transfer resistance (R_t) is 25.56 Ohm.cm². Double layer capacitance (C_{dl}) value is 501.176×10^{-4} F/cm².

Water +curd+rice system

When ever silver electrode is immersed in water+curd+rice system, the corrosion resistance of Ever silver electrode further increases. This is due to the adsorption of molecules of the ingredients present in curd and boiled rice. When ever silver electrode is immersed in water+

curd+rice system the charge transfer resistance (R_t) is 504 Ohm.cm². Double layer capacitance (C_{dl}) value is 9882.35×10^{-4} F/cm².

Water+curd+rice+salt system

When Ever silver electrode is immersed in water+curd+rice+salt system, the corrosion resistance of ever silver electrode decreases.

When ever silver electrode is immersed in water+curd+rice+salt system the charge transfer resistance (R_t) is 32.99 Ohm.cm². Double layer capacitance (C_{dl}) value is 646.86×10^{-4} F/cm².

When ever silver electrode is immersed in water + curd rice system + 500 ppm sodium chloride system, the corrosion resistance of ever silver electrode decreases. This is due to the presence of chloride ion introduced into the curd rice system. It implies that when curd rice is packed in vessels made of ever silver, we should avoid adding salt to the curd rice. It is better to keep the salt and curd rice separately. It is to be noted that this corrosion resistance is better than the corrosion resistance in water alone.

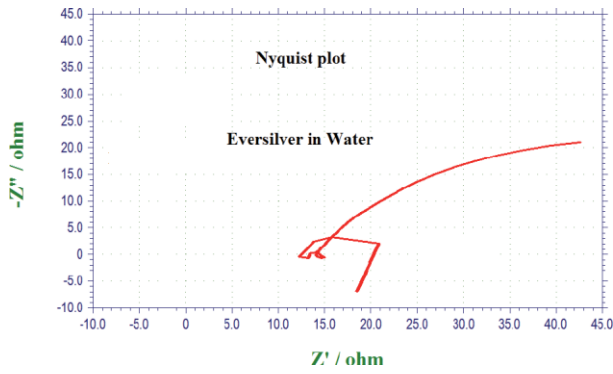


Figure 3. Nyquist plot of Ever silver electrode immersed in Water

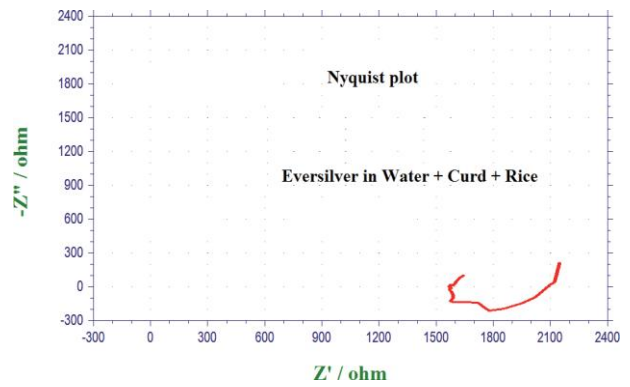


Figure 5. Nyquist plot of Ever silver electrode immersed in Water+Curd + Rice system

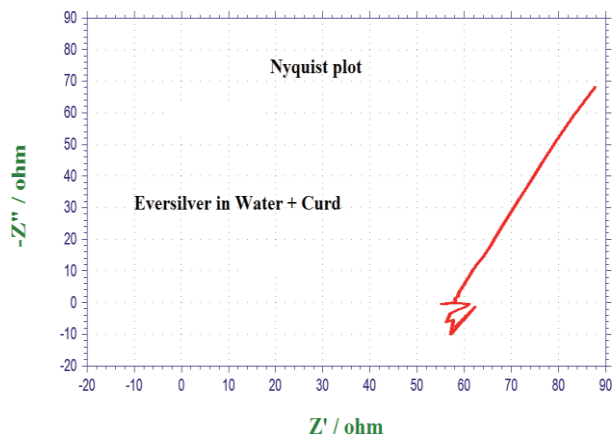


Figure 4. Nyquist plot of Ever silver electrode immersed in Water+ Curd system

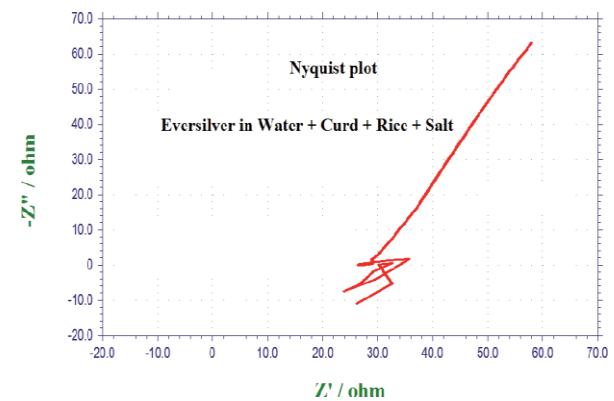


Figure 6. Nyquist plot of Ever silver electrode immersed in Water+ Curd+ Rice+ Salt system

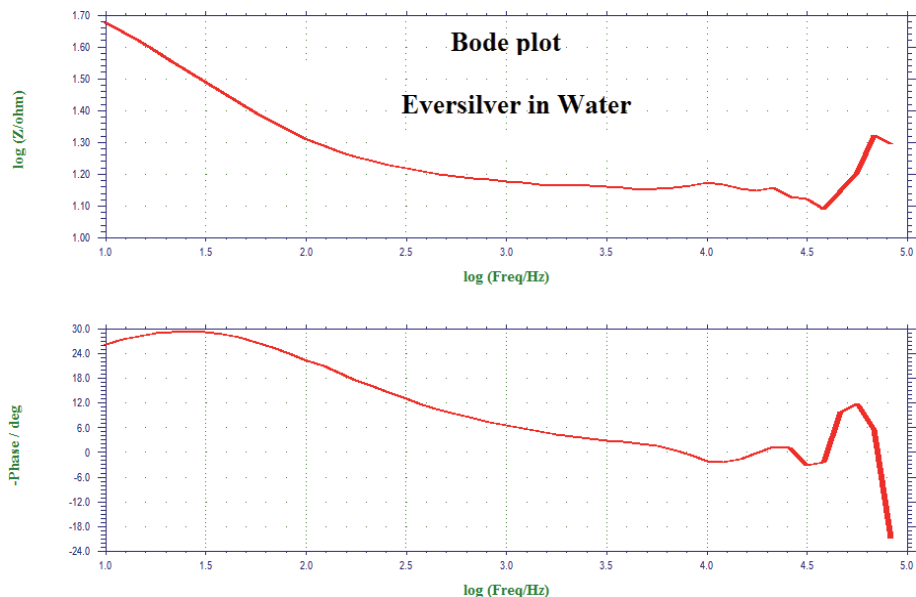


Figure 7. Bode plot of Ever silver electrode immersed in Water

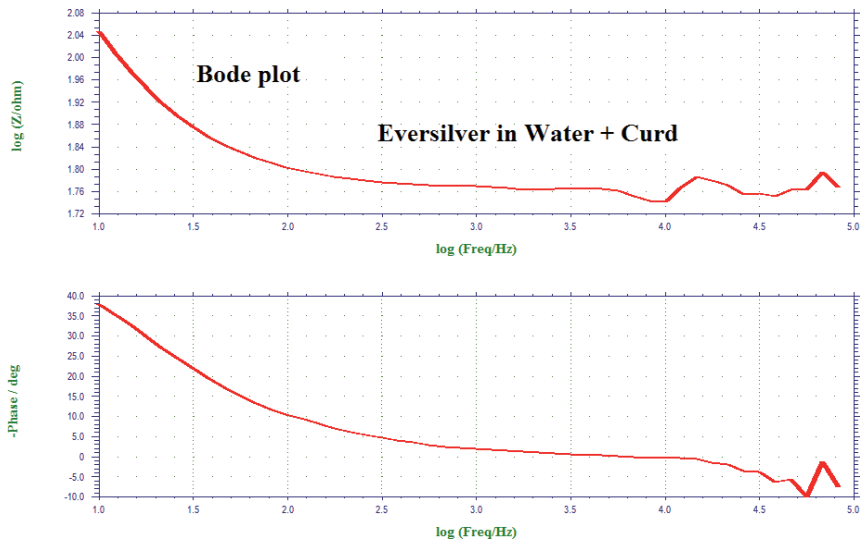


Figure 8. Bode plot of Ever silver electrode immersed in Water+ Curd system

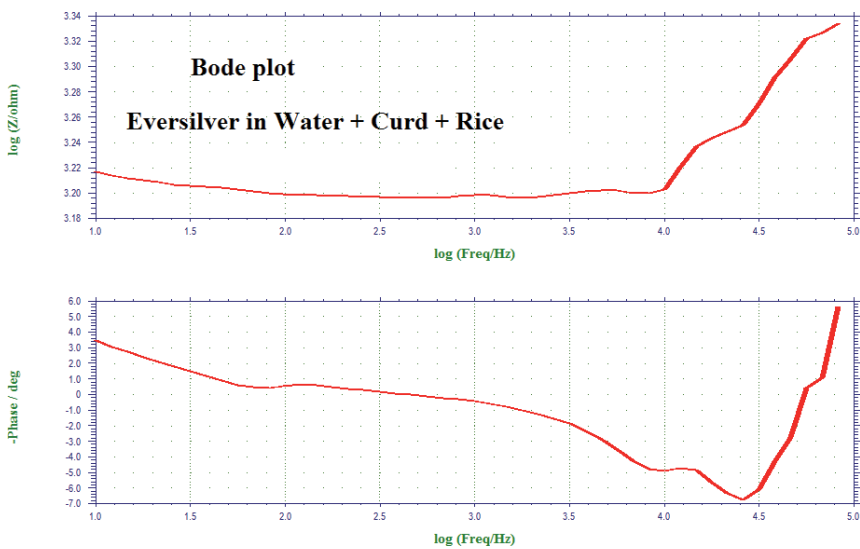


Figure 9. Bode plot of Ever silver electrode immersed in Water+Curd+ Rice system

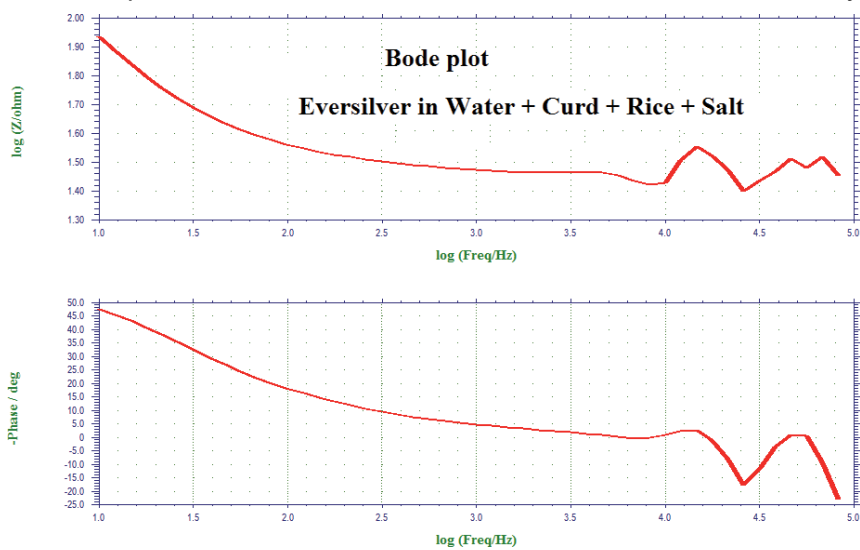


Figure 10. Bode plot of Ever silver electrode immersed in Water+Curd+Rice+Salt system

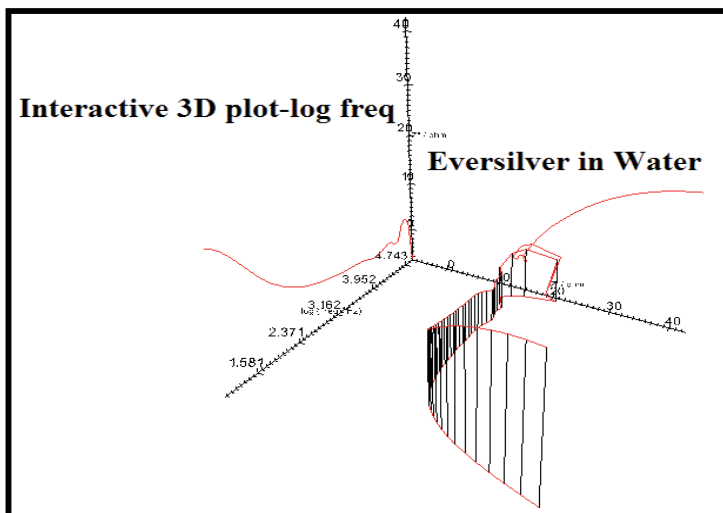


Figure 11. Interactive 3D plot-log freq of Ever silver electrode immersed in Water system

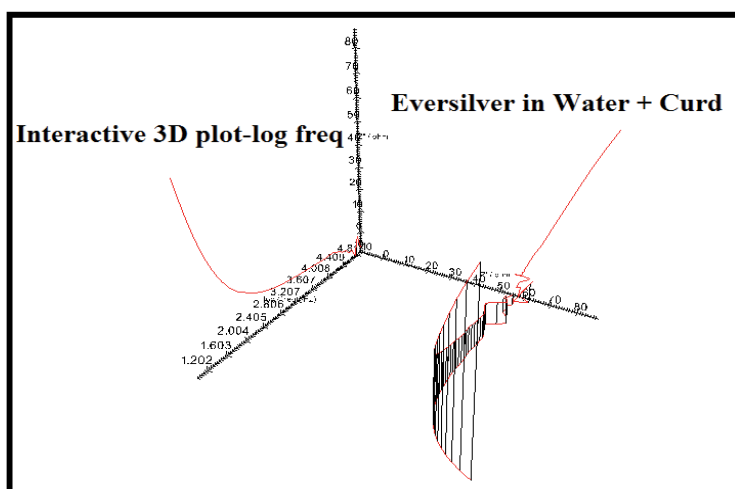


Figure 12. Interactive 3D plot-log freq of Ever silver electrode immersed in Water + Curd system

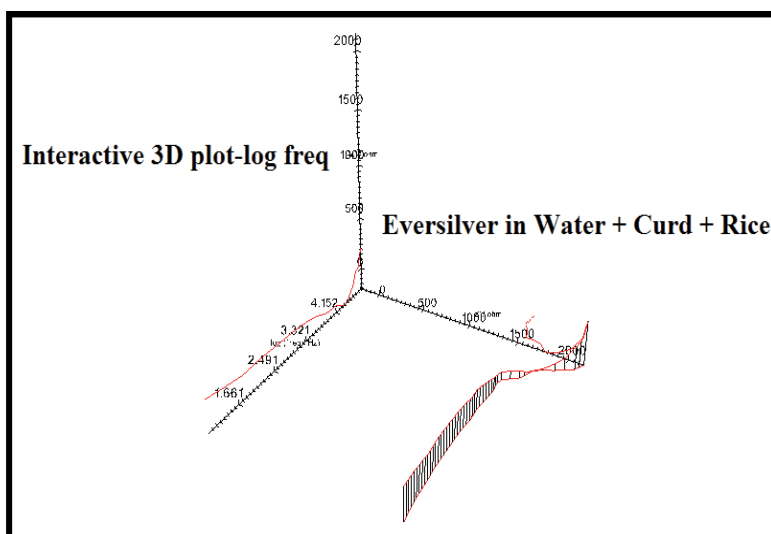


Figure 13. Interactive 3D plot-log freq of Ever silver electrode immersed in Water + Curd + Rice system

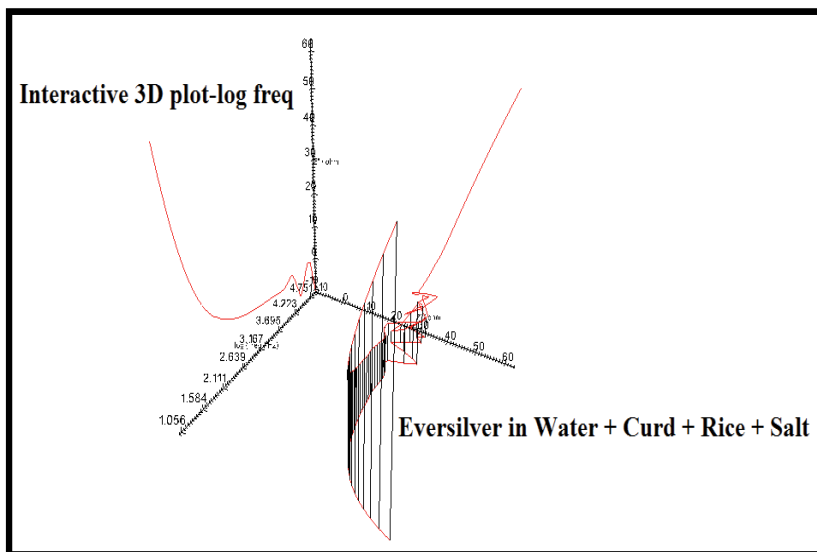


Figure 14. Interactive 3D plot-log freq of Eversilver electrode immersed in Water + Curd + Rice + Salt system

Analysis of surface morphology

Polarization study revealed that for ever silver + water + curd rice system the Charge transfer resistance value was higher (504 Ohmcm²) than that for the ever silver + water + curd rice + salt (sodium chloride 500 ppm) system (32.99 Ohmcm²). For these two systems surface morphology was analysed using Vickers hardness measurement, SEM and contact angle measurement.

Vickers hardness (HV)

Vickers hardness (HV) has been used to measure hardness of metal surfaces before corrosion and after corrosion process [18-22].

In the present study the Vickers hardness (HV) of ever silver in Water+Curd+Rice system and Water+Curd+Rice+Salt system have been calculated. This is due to the following reasons. In the first system ever silver has a LPR value of 504 Ohmcm². But in the second system the LPR value decreases due to corrosion process induced by chloride ions introduced into the first system (Table 3, Figure 15).

Table 3. Vickers hardness of various surfaces

System	Load	L1	L2	HV
Water+Curd+Rice	50 g	35.14	36.02	73.2
Water+Curd+Rice+Salt	50 g	49.41	51.79	36.2

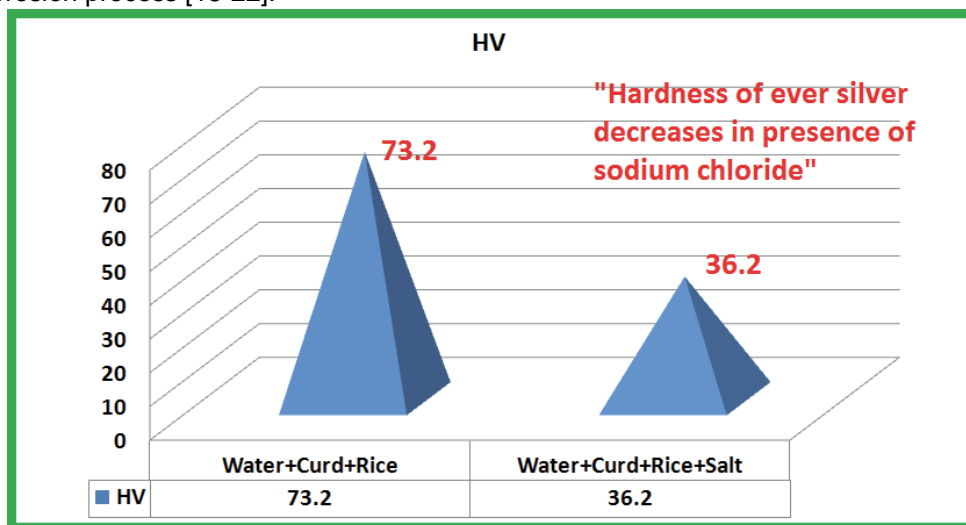


Figure 15. Comparison of Vickers Hardness values

Contact angle measurement

Contact angle measurements have been widely used in corrosion study [23-27]. The contact angles have been measured for ever silver immersed in Water+Curd+Rice system and Water+Curd+Rice+Salt system (Figure 16). This is due to the following reasons. In the first system ever silver has a R_c (charge transfer resistance) value of 504 Ohmcm. In the second system the R_c (charge transfer resistance) value in AC impedance spectral study.

for first system is higher (112.3°) than that for second system (99.1°). This indicates that the first system is hydrophobic (contact angle $> 90^\circ$) and the later is less hydrophobic in nature. So in the first case water molecules could not reach the metal surface and so higher R_c (charge transfer resistance) value of 504 Ohmcm. But in the second system the R_c (charge transfer resistance) value in AC impedance spectral study.



Figure 16. Comparison of contact angle values

ANALYSIS OF SEM IMAGES

SEM images have been used in corrosion inhibition studies [28-32]. When the metal surface is in a corrosive medium corrosion resistance decreases and pits are noticed. The surface becomes rough. On the other hand in a corrosion protected system the metal surface is smooth. The

SEM images of the surface of ever silver immersed in water + curd rice system and water + curd rice + sodium chloride (salt 500 ppm) are shown in Figure 17. It is evident that ever silver has undergone corrosion when it is immersed in water + curd rice + sodium chloride (salt 500 ppm) system. Pits are noticed on the metal surface (Figure 17).

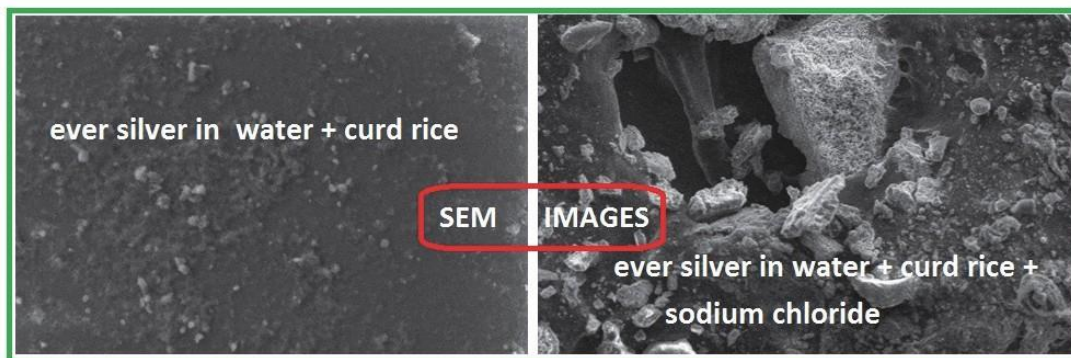


Figure 17. SEM images

CONCLUSION

- This project is undertaken to know if Eversilver vessels undergo corrosion or not, when they come in contact with some food items (recipes)
- AC impedance spectra have been employed to investigate the corrosion resistance of ever silver electrode when it is immersed in various test solutions like water, curd, curd rice recipe, curd rice recipe with salt (sodium chloride 500 ppm).
- The corrosion resistance of ever silver electrode when it is immersed in various test solutions like water, water+curd, water+curd+rice and water+curd+rice+salt have been evaluated by AC impedance spectroscopy.
- If a protective film is formed, the charge transfer resistance increases, impedance value increases, phase angle value increases and double layer capacitance (Cdl) value decreases.

- When Ever silver electrode is immersed in water + curd rice system + 500ppm sodium chloride system, the corrosion resistance of ever silver electrode decreases. This is due to the presence of chloride ion introduced into the curd rice system. It implies that when curd rice is packed in vessels made of ever silver, we should avoid adding salt to the curd rice. It is better to keep the salt and curd rice separately. It is to be noted that this corrosion resistance is better than the corrosion resistance in water alone.

- The corrosion resistance decreases in the following order:

Water + Curd + Rice system > Water + Curd + Rice + Salt system (sodium chloride 500ppm) > Water + Curd system > Water

SCOPE FOR FURTHER STUDIES

The present work is undertaken to investigate the corrosion inhibition of ever silver in the presence of water, water+curd system, water+curd+rice system, water+curd+rice+salt system.

The corrosion resistance has been evaluated by AC impedance spectra .

In future the following study can be undertaken

- Instead of curd other food item can be used.
- Instead of ever silver other metals can be used.
- Surface analysis such as AFM, FTIR, EDAX., can be employed.

Acknowledgements

The authors are thank ful to their respective man-agements for their help and support

REFERENCES

- [1] A.Samide, G.E.Iacobescu, B.Tutunaru, C.Tigae (2017) Electrochemical and AFM study of inhibitory properties of thin film formed by tartrazine food additive on 304L stainless steel in saline solution, International Journal of Electrochemical Science, 12(3), 2088–2101.
- [2] R.F.Edlich, T.C.Wind, C.L.Heather, J.G.Thacker (2017) An update on the innovative surgical double-glove hole puncture indication systems: Reliability and performance, Journal of Long-Term Effects of Medical Implants, 27(2-4), 339–353.
- [3] D.Pečar, M.Slemnik, A.Goršek (2011) Testing the corrosion resistance of stainless steels during the fermentation of probiotic drink, Journal of the Science of Food and Agriculture, 91(7), 1293–1297. Doi: <https://doi.org/10.1002/jsfa.4315>
- [4] K.A.Yushchenko, R.I.Morozova, Yu.N.Kakhovskij, G.F.Nastenko, E.V.Mokrov (1992) The 04Kh19AFT nickel-free stainless sheet steel, Stal', 4, 69–70.
- [5] I.Wagner (1992) Internal corrosion in domestic drinking-water installations, J. Water supply research & Technology-aqua, 41(4), 219–223.
- [6] M.M.Frota, A.L.A.Mattos, K.W.E.Miranda, H.N.Cheng, A.Biswas, M.D.S.R.Bastos (2022) Superhydrophobic systems in food science and technology: Concepts, trends, challenges, and technological innovations, Applied Food Research, 2(2), 100213. Doi: <https://doi.org/10.1016/j.afres.2022.100213>
- [7] A.El Guerraf, S.Ben Jadi, Z.Aouzal, M.Bouabdallaoui, N.K. Bakirhan, S.A.Ozkan, M.Bazzaoui, E.A.Bazzaoui, (2022) Effective electrodeposition of poly(3,4-ethylenedioxythiophene)-based organic coating on metallic food packaging for active corrosion protection, Journal of Applied Electrochemistry, 52(9), 1383–1407.
- [8] Y.Zhao, X.Yin, P.Shen, N.Li, Y.Xu (2022) Passivation and Chemical Conversion Combined Multi-Elements Coating on Low Sn-Coated Steel for Corrosion Protection, Journal of the Electrochemical Society, 169(8), 082501. Doi: [10.1149/1945-7111/ac7efa](https://doi.org/10.1149/1945-7111/ac7efa)
- [9] B.M.C.Soaes, S.T.Dantas, C.A.R.Anjos (2017) Corrosion of aluminum for beverage packaging in acidic media containing chlorides and copper ions, Journal of Food Process Engineering, 40(6), e12571. Doi: <https://doi.org/10.1111/jfpe.12571>
- [10] L.Blahova, J.Horak, R.Prikryl, F.Krcma (2016) Corrosion protection of metallic archaeological artefacts using parylene based removable barrier coating, European Corrosion Congress, EUROCORR 2016, 3, 1723–1731.
- [11] [https://en.wikipedia.org/wiki/Dahi_\(curd\)](https://en.wikipedia.org/wiki/Dahi_(curd))
- [12] https://www.google.com/search?q=boiled+rice+ingredients&source=lmns&bih=612&biw=1366&prmd=isvnmvtz&hl=en&sa=X&ved=2ahUKEwi-kqTGn-MuFAxWmGMGHZ_mB-UQ0pQJKAB6BAGBEAI
- [13] A.Krishnaveni, N.Anitha, V.Velkannan, D.Sarmina, T.Shanthi, G.Singh, H.Abdulhameed, S.Rajendran, C.Lacnjevac (2022) Inhibition of corrosion of L 80 alloy pipeline carrying simulated oil well water by succinic acid | Inhibicija korozije cevovoda od legure l 80, koji nosi simuliranu vodu iz bunara, ćilibarnom kiselinom, Materials Protection, 63(4), 454–462. Doi: <https://doi.org/10.5937/zasmat2204454K>
- [14] P.Shanthy, K.Kavipriya, A.Santhiya Brintha, G.Priyanka, K.Vigneswari, V.Velkannan, G.Singh, A.Al Hashem, A.Nilavan, S.Rajendran, C.Lacnjevac (2022) Influence of thiourea on the corrosion resistance of mild steel immersed in simulated concrete pore solution, Materials Protection, 63(4), 447–453.
- [15] A.Nilavan, L.Jewelcy Arockiaraj, A.A.Thomas Antony, C.M.Velankanni Jeevitha, R.Jeyalakshmi, A.Roslin, P.Muruges, V.Velkannan, G.Singh, A.Al Hashem, S.Rajendran, A.Krishnaveni (2023) Corrosion resistance of mild steel immersed in simulated concrete pore solution in the presence of sodium potassium tartrate, Materials Protection, 64(2), 170–176. Doi: <https://doi.org/10.5937/zasmat2302170N>

- [16] R.S.S.Kumar, R.S.S.Kumar, S.Ramalingam, S.S.Swe-tha, A.S.Ra. Mariya Selastina, F.X.Punitha Pricilla, S.J.Ramesh, M.Sathya Priya, S.Hema Dharshini, R.Yuva Sri, A.Nilavan, S.Rajendran (2023) Inhibition of corrosion of L 80 alloy in sodium hydroxide solution (pH=12) by succinic acid, *Materials Protection*, 64(1), 78–85. Doi: <https://doi.org/10.5937/zasmat2301078K>
- [17] S.Rajendran, A.Al-Hashem, A.Krishnaveni, L.J.Arockiaraj, G.Singh, C.Lacnjevac, M.N.Jothi, P.Shanthy (2024) Corrosion inhibition by fruit extracts-Inhibition of corrosion of mild steel in simulated concrete pore solution prepared in sea water by an aqueous extract of apple juice-A Case study, *Materials Protection*, 65(1), 22–34. Doi: <https://doi.org/10.62638/ZasMat1040>
- [18] V.Jeslina, S.J.Kirubavathy, A.Al-Hashem, S.Rajendran, R.M.Joany, C.Lacnjevac (2023) Mild Steel Corrosion Inhibition in 1 M HCl by an Alcoholic Extract of *Sargassum Muticum*, *Portugalica Electrochimica Acta*, 41(2), 151–165.
- [19] J.J.M.Praveena, J.A.Clara, S.S.Rajendran, A.J.Amal-raj (2021) Inhibition of corrosion of mild steel in well water by an aqueous extract of soapnut (*Sapindus Trifoliatum*) *Materials Protection*, 62(4), 277–290. Doi: <https://doi.org/10.5937/zasmat2104277P>
- [20] R.Dorothy, T.Sasilatha, S.Rajendran (2021) Corrosion resistance of mild steel (Hull plate) in sea water in the presence of a coating of an oil extract of plant materials, *International Journal of Corrosion and Scale Inhibition*, 10(2), 676–699. Doi: [doi: 10.17675/2305-6894-2021-10-2-13](https://doi.org/10.17675/2305-6894-2021-10-2-13)
- [21] A.S.Prabha, K.Kavitha, H.B.Shrine, S.Rajendran (2020) Inhibition of corrosion of mild steel in simulated oil well water by an aqueous extract of *Andrographis paniculata*, *Indian Journal of Chemical Technology*, 27(6), 452–460. Doi: [10.56042/ijct.v27i6.33654](https://doi.org/10.56042/ijct.v27i6.33654)
- [22] A.Casaroli, M.V.Boniardi, B.Rivolta, R.Gerosa, F.Iacoviello (2023) Metallurgical Failure Analysis of Closed Water Circuit Containing Molybdate-Based Inhibitor, *Metals*, 13(4), 723. Doi: <https://doi.org/10.3390/met13040723>
- [23] X.Luo, B.Chen, J.Li, C.Zhou, M.Guo, K. Peng, H.Dai, B.Lan, W.Xiong, Y.Liu (2024) Zwitterion modified chitosan as a high-performance corrosion inhibitor for mild steel in hydrochloric acid solution, *International Journal of Biological Macromolecules*, 267, 131429. Doi: <https://doi.org/10.1016/j.ijbiomac.2024.131429>
- [24] G.D.Pai, M.R.Rathod, R.S.K, A.A.Kittur (2024) Effect of *tabebuia heterophylla* plant leaves extract on corrosion protection of low carbon steel in 1M HCl medium: Electrochemical, quantum chemical and surface characterization studies, *Results in Surfaces and Interfaces*, 15, 100203. Doi: <https://doi.org/10.1016/j.rsurfi.2024.100203>
- [25] M.A.Abd El-Ghaffar, N.M.Nooredeen, E.A.Youssef, A.-R.M.Mousa (2024) Alkyd coating containing metal phosphomolybdate/cobalt ferrite nanocomposites as efficient corrosion inhibitor for stainless steel 316L in saline solution, *Journal of Industrial and Engineering Chemistry*, 132, 86–110. Doi: <https://doi.org/10.1016/j.jiec.2023.10.044>
- [26] O.Kharbouch, K.Dahmani, N.Errahmany, A. Belkheiri, M.Galai, F.El Hajri, A.A.Alobaid, I. Warad, S.Boukhris, M.Ebn Touhami, H.Nassali (2024) Enhancing Corrosion Resistance of Mild Steel in 1M HCl: Investigation of New Benzoxazepine Derivatives Through Synthesis, Electrochemical Analysis, Surface Analysis, XPS, DFT, and Molecular Dynamics Simulation, *Chemistry Select*, 9(15), e202303045. Doi: <https://doi.org/10.1002/slct.202303045>
- [27] X.Gao, Y.Gao, H.Cao, J.Zhang (2024) Eco-Friendly Sustainable and Responsive High-Performance Benzotriazole-Metal Organic Frameworks/Silica Composite Coating with Active/Passive Corrosion Protection on Copper, *Langmuir*, 40(14), 7639–7652. Doi: <https://doi.org/10.1021/acs.langmuir.4c00328>
- [28] A.Elsamman, K.F.Khaled, S.A.Halim, N.S. Abdelshafi (2024) Gravimetric and electrochemical evaluation of environmentally novel nanopyrzole derivatives for 304 SS in acidic solution: AFM, SEM/EDX, contact angle, and DFT/MDs simulations, *Journal of Molecular Structure*, 1309, 138157. Doi: <https://doi.org/10.1016/j.molstruc.2024.138157>
- [29] S.Alami, O.Moumouche, H.E.Harmouchi, M.Ouakki, R.Khaoulaf, K.Brouzi, N.Dkhireche, M.Harcharras (2024) Enhancing steel corrosion resistance in 1.0 M HCl medium through the synthesized and characterized mixed pyrophosphates BMnP₂O₇ (B = Ni, Co, and Cd), *Journal of Molecular Structure*, 1309, 138182. Doi: <https://doi.org/10.1016/j.molstruc.2024.138182>
- [30] A.Mohammadkhani, F.Mohammadkhani, N.Farhad-yar, M.S.Sadjadi, E.Kianfar (2024) Novel nanocomposite zinc phosphate/ polyvinyl alcohol / carboxymethyl cellulose: Synthesis, characterization and investigation of antibacterial and anticorrosive properties, *Case Studies in Chemical and Environmental Engineering*, 9, 100591. Doi: <https://doi.org/10.1016/j.csee.2023.100591>
- [31] G.Wei, S.Deng, D.Xu, J.Xu, D.Shao, X.Li (2024) Invasive weed of *Eupatorium Adenophora Spreng* leaves extract as a novel efficient inhibitor for the corrosion of cold rolled steel in chloroacetic acid solution, *Journal of Molecular Liquids*, 400, 124501. Doi: <https://doi.org/10.1016/j.molliq.2024.124501>
- [32] H.M.K.Sheit, S.M.Kani, M.A.Sathiq, K.S.Mohan, S.S.S.Abuthahir (2024) Anti-corrosive Efficiency of Expired Propranolol Drug as a Corrosion Inhibitor on Mild Steel in Acid Medium, *High Temperature Corrosion of Materials*, 101(2), 351–367. DOI: [10.1007/s11085-024-10227-0](https://doi.org/10.1007/s11085-024-10227-0)

IZVOD

UTICAJ NATRIJUM HLORIDA NA OTPORNOST NA KOROZIJU SREBRNIH POSUDA U PRISUSTVU PIRINČA

Ovaj rad je napisan kako bi se istražila otpornost na koroziju srebra u prisustvu vode, sistema voda+gruša, sistema voda+skuta+pirinač, voda+sir+pirinač+so. Otpornost na koroziju je procenjena spek-trima impedanse naizmjenične struje. Spektri impedanse naizmjenične struje su korišćeni da se ispita otpornost na koroziju srebrne elektrode kada je uronjena u različite test rastvore kao što su voda, skuta, recept za sirni pirinač, recept za sirni pirinač sa solju (natrijum hlorid 500 ppm). Otpornostna koroziju srebrne elektrode kada je uronjena u različite test rastvore kao što su voda, voda+sir, voda+skuta+pirinač i voda+suta+pirinač+sol procenjena je spektroskopijom AC impedanse. Ako se formira zaštitni film, otpor prenosa naelektrisanja se povećava, povećava se vrednost impedanse, povećava se vrednost faznog ugla i smanjuje se vrednost kapacitivnosti dvostrukog sloja (Cdl). Kada se srebrna elektroda uroni u vodu + sistem pirinča + 500ppms sistem natrijum hlorida, otpornost na koroziju svake srebrne elektrode se smanjuje. Ovo je zbog prisustva hloridnog jona unešenog u sistem skute pirinča. To implicira da kada se pirinač pakuje u posude napravljene od srebra, treba izbegavati dodavanje soli u skutu. Bolje je držati so i skutu odvojeno. Treba napomenuti da je ova otpornost na koroziju bolja od otpornosti na koroziju samo u vodi. Otpornost na koroziju se smanjuje sledećim redosledom: sistem voda + skuta + pirinač > voda + skuta + pirinač + so sistem (natrijum hlorid 500ppm) > sistem voda + skuta > voda

Ključne reči: otpornost na koroziju, srebro, skuta, natrijum hlorid, elektrohemijska ispitivanja
ORCID Numbers of all the authors

Naučni rad

Rad primljen: 15.05.2024.

Rad prihvaćen: 05.06.2024.

Paulcy Rani Palayyan Raja Bai¹, Sivakala Sarojam², Anju Krishna Salimkumar Shailaja¹, Anu Mini Aravind³, Xavier Thankappan Suryabai³

¹ Department of Chemistry, Government College for Women, Thiruvananthapuram 14, Kerala; ² Department of Chemistry, Sree Narayana College, Chempazhanthy, Thiruvananthapuram, Kerala; ³ Centre for advanced materials research, Department of Physics, Government College for Women, Thiruvananthapuram 14, Kerala

Scientific Paper

ISSN 0351-9465, E-ISSN 2466-2585

<https://doi.org/10.62638/ZasMat1175>



Zastita Materijala 65 (4)
778 – 785 (2024)

The Electrochemical Performance of Perovskite LaMnO_3

ABSTRACT

Perovskite oxides have attracted as promising electrode materials for supercapacitors because of their unique structure, compositional flexibility, and inherent oxygen vacancy. In the present work, LaMnO_3 (LMO) perovskites are synthesised by microwave assisted chemical coprecipitation and followed by calcination at 750 °C. The crystal structure and the presence of functional groups in LaMnO_3 were studied through X-ray diffraction (XRD) and Fourier transform infrared spectroscopy (FT-IR). The surface morphology was characterized by field emission scanning electron microscopy (FESEM). Electrochemical performance of LMO electrodes is evaluated in 3M KOH and 3M NaOH electrolytes. The specific capacitance of the LMO electrode in 3M NaOH and 3M KOH electrolyte were calculated to be 557.76F/g and 290.63F/g at scan rate of 5mV/s. The enhancement in the specific capacitance of the LMO electrode in 3M NaOH can be attributed to the effective charge storage mechanism.

Keywords: Microwave, LaMnO_3 perovskite, electrochemical performance, specific capacitance

1. INTRODUCTION

Constantly increasing energy demands and environmental pollution have compelled us to seek environment friendly and renewable energy resources. Energy-storage technologies such as batteries, supercapacitors, and fuel cells are important for sustaining renewable energy resources [1]. Electrochemical supercapacitors gain prime importance as electrochemical energy storage due to their high-power densities at reasonably high energy densities and significantly long cycle life so that they can be used in heavy electric vehicles and consumer electronic devices, industrial power management, and military devices [2-4]. Supercapacitor is a device that have higher specific capacitance and minimum internal resistance, which is composed of two electrodes separated by a separator and an electrolyte. The performance of a supercapacitor mainly depends upon the selection of the electrode material. Based on the charge storage mechanism, SCs can

be classified into two categories as electrochemical double layer capacitors (EDLCs) and pseudo capacitors (PCs) [5]. EDLCs store charge through charge accumulation at the interface between the electrolyte and the electrode's surface. EDLCs store charge through non faradic process in which charge separation and accumulation take place at the active material and electrolyte interface. Because of their high specific surface area and desirable conductivity, carbon-based materials such as carbon nanotubes, activated carbon, graphene, graphene oxide and reduced graphene oxide are the most attractive active material for EDLCs [6,7]. Where as in pseudo capacitance type of mechanism the oxidation and reduction reactions take place between electrode and electrolyte that results in the charge transportation. Since the electrochemical reactions occur both on the surface and in the bulk near the solid electrode surface, PCs often show far higher capacitance values and energy densities than EDLCs [8]. Conducting Polymers and transition metal oxides such as MnO_2 , NiO, Fe_2O_3 and Co_3O_4 can act as electrode material for pseudo capacitors.

Perovskite oxides with ABO_3 formula have been widely investigated for their applications in catalysis [9], water splitting [10], supercapacitance [11], bat-

* Corresponding author: Paulcy Rani P R
E-mail: pr.paulcyrani@gmail.com
Paper received: 22.04.2024.
Paper accepted: 20.05.2024.

teries [12], optical [13], superconductivity [14], etc., and are considered to be a replacement for single oxides in the stipulated application. The ABO_3 perovskites are promising for supercapacitance owing to the presence of multiple transition- metal ions in their crystal structure and therefore, perovskite oxides have the potential to enhance the performance of the supercapacitor through different charge storing mechanisms [15,16], by controlling the ratio of metallic ions used during the synthesis [17]. Moreover, perovskite oxides are capable of accommodating a large number of inherent oxygen vacancies [18].

In the present work, perovskite nano LaMnO_3 (LMO) was prepared by microwave assisted co-precipitation. The electrochemical performance of the LMO electrodes is examined in electrolytes such as 3M KOH and 3M NaOH.

2. EXPERIMENTAL DETAILS

LaMnO_3 perovskites were synthesised by microwave assisted chemical coprecipitation. A mixture of 0.5 molar solutions Lanthanum (III)chloride and Manganese (II)chloride in the molar ratio of 1:1 is taken and stirred in a magnetic stirrer. Then 1M NaOH is added to the solution with stirring and then heated in a microwave oven for 10 minutes. Finally, the precipitate was filtered, washed with distilled water, dried in air oven at 80°C for 24 hours and calcinated in a muffle furnace at 750°C for 12 h at a heating rate 2°C per minute.

2.2 Characterizations

The functional groups present in the material are analysed using FT-IR spectroscopy, performed in Perkin-Elmer 'Spectrum Two' FT-IR Spectrometer. The structural properties of the material are analysed by X-ray diffraction (XRD) Rigaku Miniflex-600 benchtop diffractometer with a $\text{Cu K}\alpha$ radiation source ($\lambda = 1.542 \text{ \AA}$) in the range $10\text{--}90^\circ$. The morphology of the sample was analysed using FES-EM with EDX (CARL ZEISS USA, resolution 1.5nm). BET (Brunauer-Emmett-Teller) analysis (Altamira Instruments, Inc) was carried out to examine surface area and pore size distribution using nitrogen adsorption-desorption isotherms. All Electrochemical investigations were carried out in BioLogic VSP electrochemical workstation with three electrode system. Nickel foam casted with an active electrode material act as working electrode, Platinum wire acts coun-

ter electrode and Ag/AgCl electrode act as reference electrode.

2.3 Preparation of working electrode and electrochemical study

Before the preparation of electrode, the Ni-foam (1 cm X 1 cm) was cleaned with detergent, ethanol, concentrated hydrochloric acid and washed several times with DI water to eliminate the impurities and surface oxidant contents. To prepare the working electrodes, the electrode material (80%), polyvinylidene fluoride binder (10%) and carbon black (10%) were first mixed together using a mortar-pestle to make slurry using N-methyl-2-pyrrolidinone solvent. This slurry was drop casted into Ni-foam (1 cm X 1 cm) and dried at 120°C for 5h. The prepared electrodes were used for electrochemical characterizations.

The electrochemical performance of the prepared electrode material was tested through CV techniques. The electrochemical tests are performed in BioLogic VSP electrochemical workstation with three electrode system. Nickel foam casted with an active electrode material, Platinum wire and Ag/AgCl electrode are used as working, counter and reference electrodes respectively. The CV measurements were carried over a potential range of -0.4 to 0.6V at scan rate from 5 mV/s to 100 mV/s . Various aqueous electrolytes such as 3M NaOH and 3M KOH were used in the electrochemical measurements.

3 RESULTS AND DISCUSSION

3.1 FT-IR

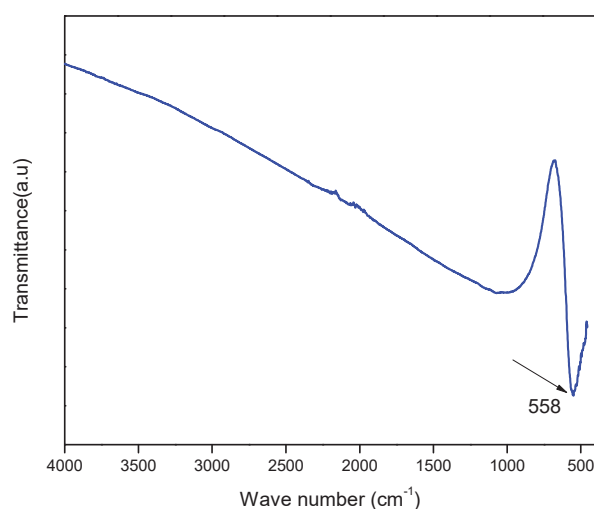


Fig. 1 FT IR Spectrum of LMO

FTIR analysis is performed to study the vibrational spectrum of perovskite LaMnO_3 as shown in Fig.1. The strong absorption peak at 558 cm^{-1} is corresponding to Mn-O vibrations. The presence of this vibrational peak is the characteristic of the ABO_3 type perovskite which confirms the successful synthesis of perovskite LaMnO_3 [19].

3.2 XRD Analysis

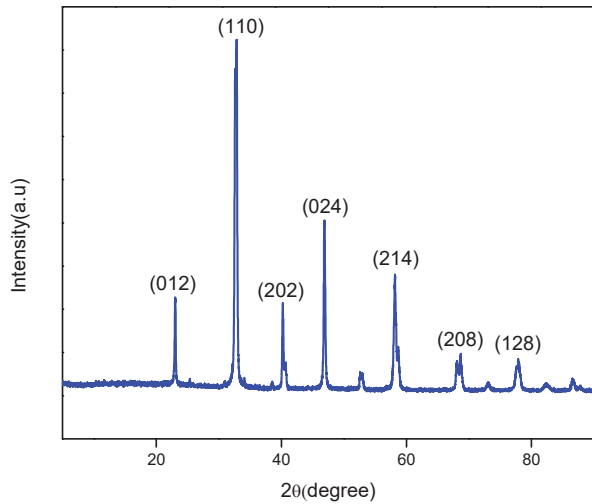


Fig. 2. XRD pattern of LMO

The XRD pattern of the synthesised compound is well matched with JCPDS 89-8775, which cor-

responds to rhombohedral perovskite structure of LaMnO_3 with R-3c group. The peaks at 2θ values 23.2° , 32.9° , 40.3° , 46.86° , 58.3° , 68.6° and 78.05° are corresponding to (012), (110), (202), (024), (214), (208), (128) planes. The strongest diffraction peak occurs at 2θ value 32.7° which is the characteristic diffraction peak of LaMnO_3 . The highly crystalline nature of the synthesised material is confirmed by the narrow and strong diffraction peaks.

3.3 Brunauer-Emmett-Teller (BET) surface area analysis

The surface area of the synthesised LMO is analysed by N_2 adsorption-desorption at 77K. The nitrogen adsorption-desorption isotherm for LMO is displayed in Fig 3. (a). From the BET analysis surface area was evaluated to be $2.703\text{m}^2\text{g}^{-1}$. The BJH (Barrett, Joyner, and Halenda) pore size distribution diagrams of LMO electrode material are displayed in figure 3. (b). From the figure it is examined that the material shows broad distribution curves. The average pore diameter of LMO was evaluated as 9.027nm in the mesoporous region of LMO. The mesoporous nature of the electrode material determines charge transport across the electrode-electrolyte interface.

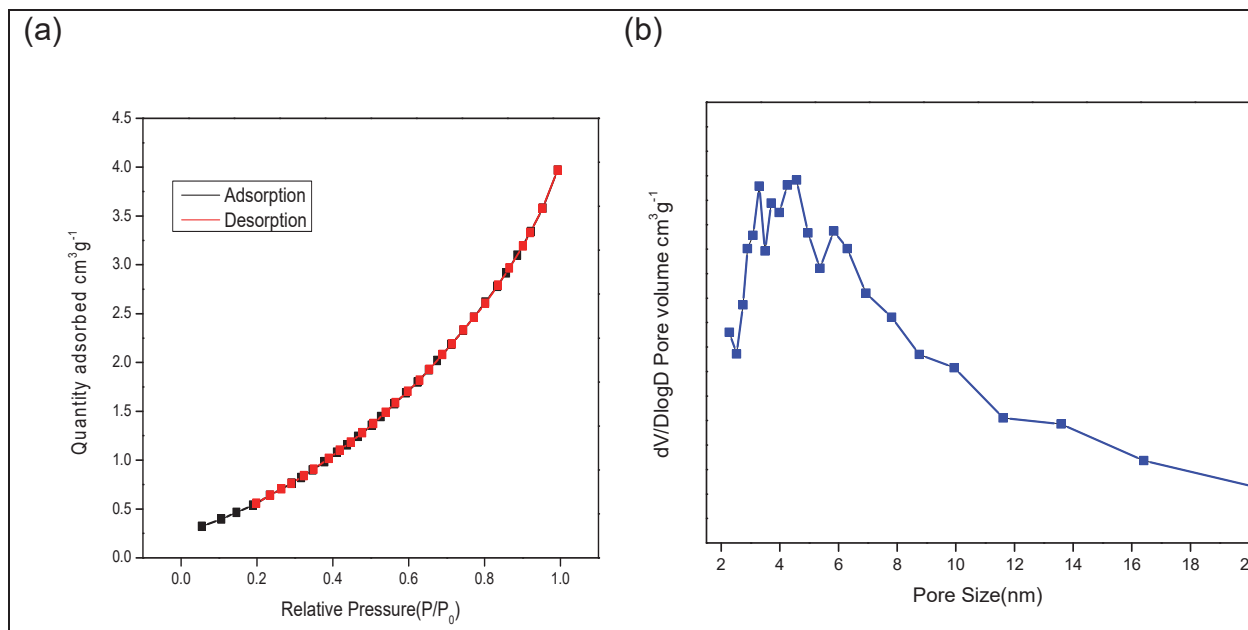


Fig 3 (a) BET Nitrogen adsorption-desorption isotherms of LMO
(b) Pore size distribution curve of LMO.

3.4 Morphological study

Surface morphology of the prepared material is examined through FESEM analysis, micrograph demonstrate there is agglomeration of nano particles and reveals the presence three-dimensional

nano crystalline nature of the material. (Figure 4.). The X-ray energy dispersive spectrum (EDAX) (Fig. 4(d)) shows that La, Mn and O elements are in a molar ratio of 1: 1: 3 in the synthesised material, which confirms that the obtained product is LaMnO_3 .

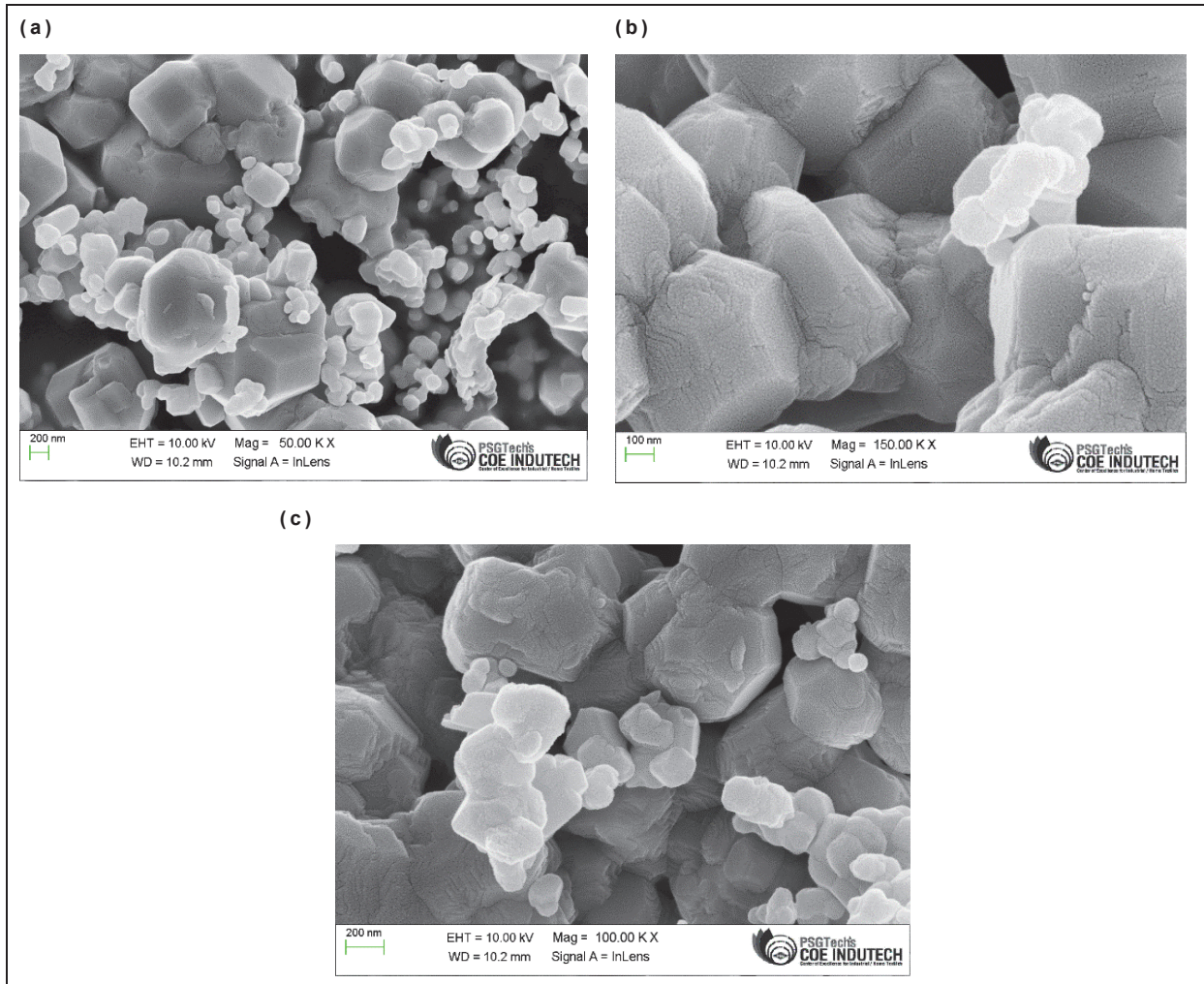


Fig 4. FE-SEM micrographs of the LMO at different magnification(a) (b)and (c)

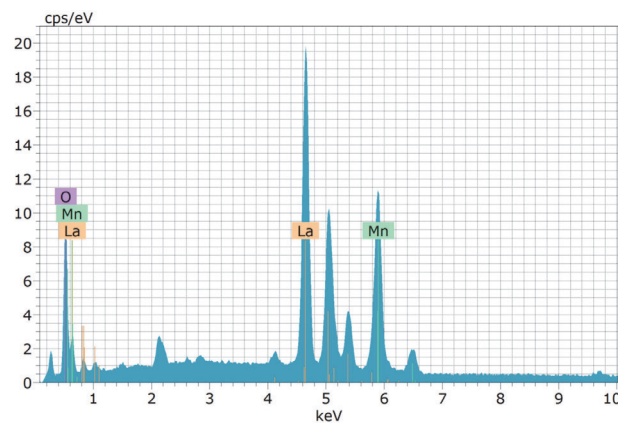


Fig.4(d) EDAX spectrum of LMO.

3.5 Electrochemical study

The electrochemical performances of the synthesised LMO material as electrode materials for supercapacitors were examined by Cyclic voltammetry (CV), and Electrochemical impedance spectroscopy (EIS). The electrochemical tests are performed in Biologic VSP electrochemical workstation with three electrode system. Nickel foam casted with an active

electrode material, platinum wire and Ag/AgCl electrode are used as working, counter and reference electrodes respectively. The CV measurements were carried over a potential range of -0.4 to 0.6V in aqueous electrolytes such as 3M KOH and 3M NaOH at scan rate from 5 mV/s to 100 mV/s. EIS measurement was carried over wide frequency range of 200KHz to 100mHz applying an AC voltage of 1 mV.

3.5.1 Cyclic voltammetry (CV)

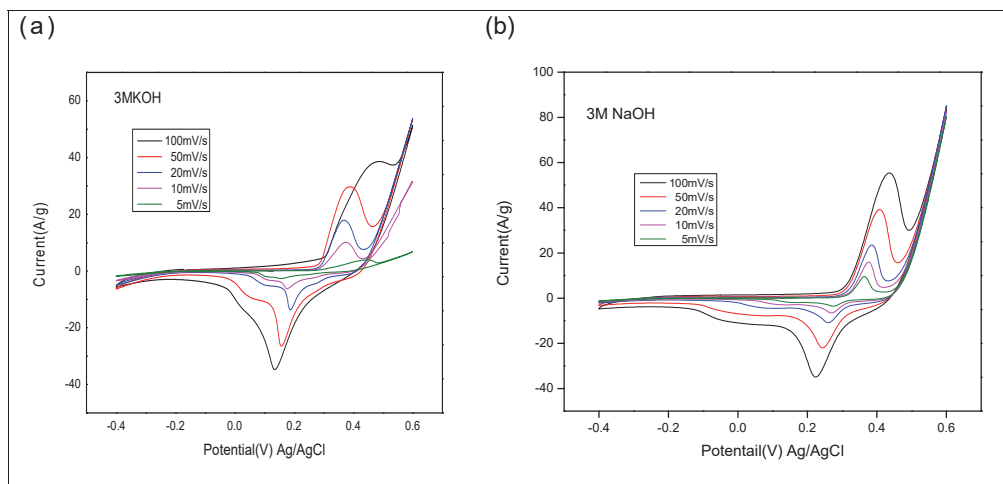


Fig. 5. CV plot of LMO in (a) 3M KOH and (b) 3M NaOH electrolyte.

The electrochemical performance of the as-prepared LMO electrode was analysed by cyclic voltammetry in 3M KOH and 3M NaOH electrolytes at different scan rates, as shown in Fig. 5. The redox peaks are clearly observed in the CV curve for both the electrolytes, this confirms the pseudocapacitive nature of the LMO electrodes. These redox peaks are mainly due to the fast reversible process of ionic intercalations on the electrode material. The change in oxidation state of manganese as $\text{Mn}^{+2} \leftrightarrow \text{Mn}^{+3}$ and $\text{Mn}^{+3} \leftrightarrow \text{Mn}^{+4}$ favours the ionic intercalation/deintercalation in the electrode material.

The Specific capacitance of LMO electrodes is calculated by Equation (1)

$$C_s = \frac{\int_{v_1}^{v_2} i(v) dv}{(v_2 - v_1)ms} \quad (1)$$

where the numerator indicated the total charge enclosed by the CV curve, $(v_2 - v_1)$ is the working potential window, m is the mass, and s is the scan rate. The area under the CV curve is directly proportional to the specific capacitance of the electrode material. The specific capacitance of the LMO electrodes in 3

M KOH electrolyte is determined as 290.63, 184.76, 157.14, 84.33 and 52.19 F/g for 5, 10, 20, 50 and 100 mV/s. LMO electrodes have achieved higher specific capacitance at lower scan rate. This is because at lower scan rate, the electrolyte ions get access to the entire active sites of the electrode material. However, at the higher scan rates, the electrolyte ions get insufficient time for diffusion [20].

From CV curve it is appeared that area of the CV curve of the LMO electrode in 3 M NaOH is larger than that of 3 M KOH. Table:1 summarizes the specific capacitance values of the LMO electrode material determined from the CV plots at different scan rates in 3M KOH and 3M NaOH electrolyte. The specific capacitance of the LMO electrode in 3M NaOH and 3M KOH electrolyte were found to be 557.76F/g and 290.63F/g at scan rate of 5mV/s. This is enhanced electrochemical performance in NaOH is due to the increased ionic mobility and diffusivity of Na^+ ions are compared the K^+ ions, that leads to better diffusion of Na^+ and thus facilitates the fast charge transport across the electrolyte–electrode interface. Therefore, LMO electrodes exhibit better electrochemical performance in NaOH than KOH electrolyte [21].

Table 1. The specific capacitance values of the LMO electrode material calculated from the CV plots at different scan rates in 3M KOH and 3M NaOH electrolyte.

Scan rate(mV/s)	Specific Capacitance F/g	
	3M KOH	3M NaOH
5	290.63	557.76
10	184.76	317.38
20	157.14	190.00
50	84.33	97.67
100	52.19	65.02

3.5.2 Electrochemical impedance spectroscopy (EIS)

EIS study has been performed for analysing resistance that occurs due to charge transportation

and diffusion of active material. The Nyquist plot for LMO electrodes obtained in 3M KOH and 3M NaOH are shown in Fig.6. This EIS spectrum shows straight line in lower frequency and a semi-circle in high frequency. The internal resistance (R_s) of the cell consists of intrinsic resistance of the electrode material, contact resistance between current collector and electrode, and resistance offered by an electrolyte. R_{ct} is the charge transfer resistance resulting from the faradic reactions at the electrode–electrolyte boundary [22]. The internal resistance and charge transfer resistance are calculated by using Zfit of the EC lab software. The values of R_s and R_{ct} determined from EIS analysis are 0.97Ω and 2.50Ω in 3M KOH, 0.67Ω and 0.86Ω in 3M NaOH electrolyte. The lower values of R_s and R_{ct} is obtained for electrode material in 3M NaOH and LMO electrodes exhibit enhanced electrochemical performance in 3M NaOH over 3M KOH.

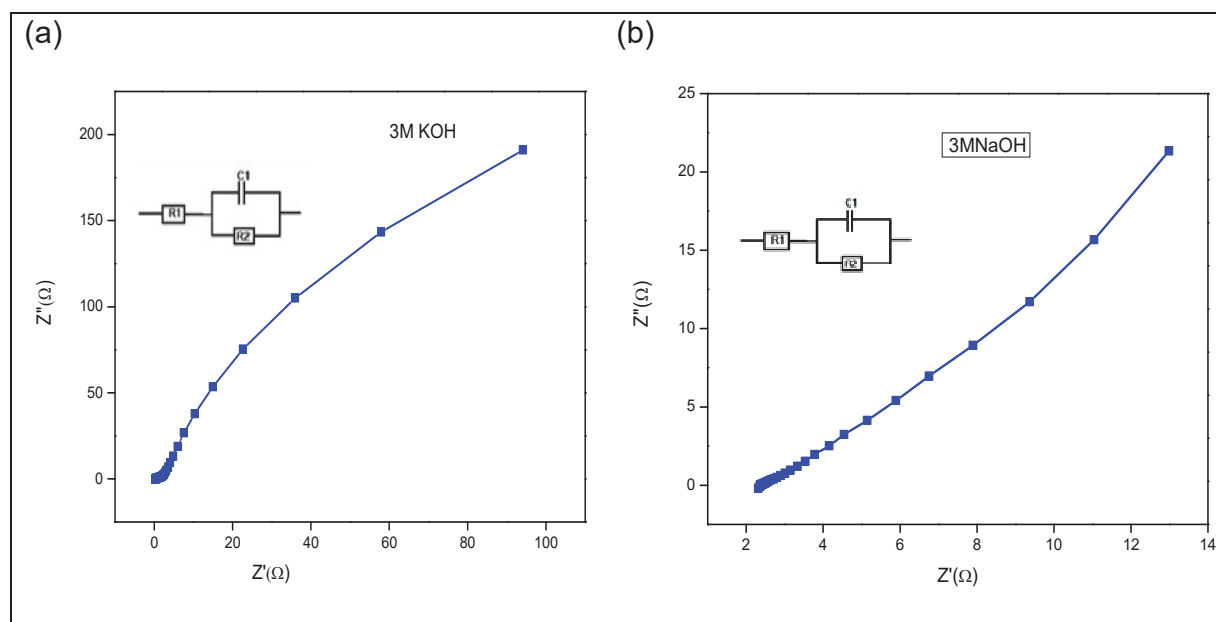


Fig.6 EIS plot of LMO(a) 3M KOH and (b) 3M NaOH

4 CONCLUSIONS

Perovskite LaMnO_3 nanoparticles was successfully synthesized by facile microwave assisted co-precipitation. The XRD analysis confirms the highly crystalline nature of the synthesised perovskite LaMnO_3 by the narrow and strong diffraction peaks. The mesoporous nature of the LMO electrode material was confirmed through BET analysis with a specific surface area of $2.703\text{m}^2\text{g}^{-1}$ and an average pore diameter of 9.08nm . The specific capacitance

of the LMO electrode in 3M NaOH and 3M KOH electrolyte was found to be 557.76F/g and 290.63F/g at scan rate of 5mV/s . Therefore, LMO electrodes exhibit better electrochemical performance in NaOH than KOH electrolyte. The lower values of R_s and R_{ct} is obtained for electrode material in 3M NaOH and LMO electrodes exhibit enhanced electrochemical performance in 3M NaOH. These results suggest that the perovskite LaMnO_3 electrode material are prominent candidates for fabricating efficient electrochemical capacitors.

Acknowledgements

For analytical support, the authors acknowledge the Centralized Common Instrumentation Facility (CCIF), Government College for Women, Thiruvananthapuram.

REFERENCES

- [1] Zh. Sanliang, Y. Li, N. Pan (2012) Graphene based supercapacitor fabricated by vacuum filtration deposition, *Journal of Power Sources.*, 206, 476–482. doi:10.1016/j.jpowsour.2012.01.124.
- [2] S. Zheng, H. Xue, H. Pang (2018) Supercapacitors based on metal coordination materials, *Co-ordination chemistry Reviews.*, 373, 2–21. doi.org/10.1016/j.ccr.2017.07.002.
- [3] Y. Yang, D. Cheng, S. Chen, Y. Guan, J. Xiong (2016) Construction of hierarchical NiCo₂S₄@Ni(OH)₂ core-shell hybrid nanosheet arrays on Ni foam for high-performance aqueous hybrid supercapacitors, *Electrochimica Acta.*, 193, 116–127. doi: 10.1016/j.electacta.2016.02.053.
- [4] S. Bose, T. Kuila, A. Mishra, R. Rajasekar N. Kim, J. Lee (2012) Carbon-based nanostructured materials and their composites as supercapacitor electrodes, *Journal Materials Chemistry.*, 22, 767–784. doi. 10.1039/c1jm14468e.
- [5] J. Yan, S. i Li, B. Lan, Y. Wu (2019) Rational design of nanostructured electrode materials toward multifunctional supercapacitors, *Advanced functional materials reviews.*, 1902564, 1-35. doi.10.1002/adfm.201902564.
- [6] L. Candelaria, L. Stephanie, Y. Shao, W. Zhou, X. Li, J. Xiao, J. Guang Zhang, Y. Wang, J. Liu, J. Li, G. Cao (2012) Nanostructured carbon for energy storage and conversion, *Nano Energy.*, 1, 195–220. Doi.10.1016/j.nanoen.2011.11.006.
- [7] Y. Wang, L. Zhang, H. Hou, W. Xu, G. Duan, S. He, K. Liu, S. Jiang (2021) Recent progress in carbon-based materials for supercapacitor electrodes: a review, *Journal of Material Science.*, 56, 173–200. doi.10.1007/s10853-020-05157-6.
- [8] Y. Liu, Z. Wang, Y. Zhong, X. Xu, J.-P. M. Veder, M. R. Rowles, M. Saunders, R. Ran, Z. Shao (2020) Activation-free supercapacitor electrode based on surface-modified Sr₂CoMo_{1-x}Ni_xO_{6-δ} perovskite, *Chemical Engineering Journal.*, 390, 124645, 1-10. doi.org/10.1016/j.cej.2020.124645.
- [9] A.H. McDaniel, A. Ambrosini, E.N. Coker, J.E. Miller, W.C. Chueh, R. O Hayre, J. Tong (2014) Nonstoichiometric perovskite oxides for solar thermochemical H₂ and CO production, *Energy Procedia.*, 49, 2009–2018. doi.org/10.1016/j.egypro.2014.03.213
- [10] J. Wang, Y. Gao, D. Chen, J. Liu, Z. Zhang, Z. Shao, F. Ciucci (2017) Water splitting with an enhanced bifunctional double perovskite, *ACS Catalysis.*, 8, 1, 364–371. doi.org/10.1021/acscatal.7b02650.
- [11] Y. Liu, J. Dinh, M.O. Tade, Z. Shao (2016) Design of perovskite oxides as anion-intercalation-type electrodes for supercapacitors: cation leaching effect, *ACS Applied Materials and Interfaces.*, 8(36), 23774–23783. doi.org/10.1021/acscami.6b08634.
- [12] P. Tan, M. Liu, Z. Shao (2017) Recent advances in perovskite oxides as electrode materials for nonaqueous lithium–oxygen batteries, *Advanced Energy Materials.*, 7, 1602674, 1-23. doi.10.1002/aenm.201602674.
- [13] Y. Yamada, Y. Kanemitsu (2013) Photoluminescence spectra of perovskite oxide semiconductors, *Journal of Luminescence.*, 133, 30–34, doi: 10.1016/j.jlumin.2011.12.037.
- [14] C.N.R.Rao (1990) Perovskite oxides and high-temperature superconductivity, *Ferroelectrics.*, 102, 297–308. Doi.10.1080/00150199008221489.
- [15] N. Arjun, G.-T. Pan, T.C.K. Yang (2017) The exploration of lanthanum-based perovskites and their complementary electrolytes for the supercapacitor applications, *Results in Physics.*, 7, 920–926. doi.org/10.1016/j.rinp.2017.02.013.
- [16] J.T. Mefford, W.G. Hardin, S. Dai, K.P. Johnston, K. J. Stevenson (2014) Anion charge storage through oxygen intercalation in LaMnO₃ perovskite pseudo capacitor electrodes, *Nature Materials.*, 13, 726–732. doi.10.1038/NMAT4000.
- [17] J. Zhu, H. Li, L. Zhong, P. Xiao, X. Xu, X. Yang, Z. Zhao, J. Li (2014) Perovskite oxides: preparation, characterizations, and applications in heterogeneous catalysis, *ACS Catalysis.*, 4, 2917–2940. doi.org/10.1021/cs500606g.
- [18] F. Galasso (1990) *Perovskites and High Tc Superconductors* Routledge, New York.
- [19] J. Hu, J. Ma, L. Wang, H. Huang, L. Ma (2014) Preparation, characterization and photocatalytic activity of co-doped LaMnO₃/graphene composites, *Powder Technology.*, 254, 556-562. doi.org/10.1016/j.powtec.2014.01.071.
- [20] N. Maheswari, G. Muralidharan (2015) Supercapacitor behaviour of cerium oxide nanoparticles in neutral aqueous electrolytes, *Energy and Fuels.*, 29(12), 8246–8253. doi. 10.1021/acs.energyfuels.5b02144.
- [21] D. Lundberg, D. Warmińska, A. Fuchs, I. Persson (2018) On the relationship between the structural and volumetric properties of solvated metal ions in O-donor solvents using new structural data in amide solvents, *Physical Chemistry Chemical Physics.*, 20, 14525-14536. Doi.10.1039/x0xx00000x.
- [22] P. Gao, P. Metz, T. Hey, Y. Gong, D. Liu, D.D. Edwards, J.Y. Howe, R. Huang, S. T. Misture (2017) The critical role of point defects in improving the specific capacitance of δ-MnO₂ nanosheets, *Nature Communications.*, 8, 14559. doi: 10.1038/ncomms14559.

IZVOD

ELEKTROHEMIJSKE PERFORMANSE PEROVSKITA LaMnO_3

Perovskit oksidi su se privukli kao obećavajući elektrodni materijali za superkondenzatore zbog svoje jedinstvene strukture, fleksibilnosti kompozicije i inherentne praznine za kiseonik. U ovom radu, LaMnO_3 (LMO) perovskiti se sintetišu hemijskom koprecipitacijom uz pomoć mikrotalasne pećnice, a zatim kalcinacijom na $750\text{ }^\circ\text{C}$. Kristalna struktura i prisustvo funkcionalnih grupa u LaMnO_3 proučavani su difrakcijom rendgenskih zraka (XRD) i infracrvenom spektroskopijom Furijeove transformacije (FT-IR). Morfologija površine je okarakterisana pomoću polja emisije skenirajuće elektronske mikroskopije (FESEM). Elektrohemijske performanse LMO elektroda se procenjuju u 3M KOH i 3M NaOH elektrolitima. Specifični kapacitet LMO elektrode u 3M NaOH i 3M KOH elektrolitu je izračunat na 557,76F/g i 290,63F/g pri brzini skeniranja od 5mV/s. Povećanje specifične kapacitivnosti LMO elektrode u 3M NaOH može se pripisati efikasnom mehanizmu skladištenja naelektrisanja.

Cljučne reči: mikrotalasna pećnica, LaMnO_3 , perovskit, elektrohemijske performanse, specifična kapacitivnost

ORCID Numbers of all the authors

Paulcy Rani Palayyan Raja Bai: <https://orcid.org/0009-0003-4200-1474>

Anju Krishna Salimkumar Shailaja: <https://orcid.org/0009-0005-1453-3021>

Sivakala Sarojam: <https://orcid.org/0000-0002-2126-1790>

Anu Mini Aravind: <https://orcid.org/0000-0002-2941-208X>

Xavier Thankappan Suryabai: <https://orcid.org/0000-0001-8955-0743>

Naučni rad

Rad primljen 23.02.2024.

Rad korigovan 23.05.2024.

Rad prihvaćen 3.06.2024

Sonia Yadav¹, Nadeem Sharma^{1*}

¹Department of Chemistry, Maharishi Markandeshwar Engineering College, Maharishi Markandeshwar (Deemed to be University), Mullana, Ambala, Haryana, India-133207

Scientific paper

ISSN 0351-9465, E-ISSN 2466-2585

<https://doi.org/10.62638/ZasMat1067>Zastita Materijala 65 (4)
786 – 796 (2024)

Cerium(III) Phosphotungstate: an Efficient Catalyst in Esterification of Fatty Acids

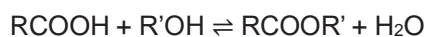
ABSTRACT

In this report, a known heteropolyacid salt (HPAs) cerium (III) phosphotungstate was synthesized in a volume ratio 2:1:2 with a molar ratio 1:1:1 of each ingredient. These HPAs are further utilized in form of a catalyst to generate biodiesel through the esterification of variable carbon chain length alcohols (methanol, ethanol, n-propanol, isopropanol, n-butanol) and stearic acid at different conditions of reaction. FTIR of the produced biodiesel was also done for the assurance of ester peaks in it. Analysis of some important biodiesel properties such as density, dynamic viscosity, acid value, aniline point, cloud, pour point, flash and fire point etc., done to differentiate and validate the results. A large surface area of the catalyst i.e. 121.427 m²/g determined using the BET surface area analyser, supports the fact of outrageous catalytic action in the esterification reaction. The effect of additives was also studied on the properties of resultant biodiesel. The calorific value of the samples was measured as 7320 Kcal/kg without additive and 7512 Kcal/kg after adding toluene (as an additive) in the biodiesel generated in the study. The pour point temperature of the biodiesel with additives was observed even < 20°C.

Keywords: Cerium(III) Phosphotungstate, Biodiesel, butyl stearate, fuel value, additives

1. INTRODUCTION

Catalysts may be of different varieties but the one that gives the best outputs with a higher reaction rate is the heteropolyacid salts [1] which have been many times used in the reactions based upon amended lipids, esters with some additional features, and free fatty acids which has characteristics like; emulsification, and aroma [2,3]. Given below is a general form of esterification reaction:



The present study investigates the esterification of stearic acid with different alcohols, such as; n-butanol, iso-propanol, n-propanol, ethanol, and methanol, using cerium (III) phosphotungstate as a catalyst. The literature is rich in studies where heteropolyacid salts as catalysts were used in biodiesel production.

Researchers have developed various methods to produce pure and degradable fuel using transesterification and esterification processes. For instance, Sahu et al. carried out the study related to the kinetic aspects of homogeneously catalysed esterification of a sequence of aliphatic acids with different types of alcohols [4]. In another study, de Lima and his team immobilized six lipases sustained on a styrene-divinylbenzene and estimated the batch esterification reaction parameters of stearic acid with fusel oil, which resulted in a high conversion rate of 90-93% [5]. Ibrahim et al. used Tin zirconium oxide catalysts (Sn-supported TMOs) to obtain a 74% quantitative result of methyl stearate under various conditions as mentioned [6]. Additionally, Ahmed et al. used interlinked amidoximated polyacrylonitrile ion-swapping web protonated by sulfuric acid as a catalyst for the conversion of stearic acid to methyl stearate (biodiesel) and achieved a conversion rate of 94.1%, which is almost equivalent to the yield achieved with 1wt% H₂SO₄ [7]. Mahmoud et al. produced biodiesel through the esterification of C₁₈H₃₆O₂ (stearic acid) with C₂H₅OH catalyzed

*Corresponding author: Nadeem Sharma

E-mail: sameeksha20002@gmail.com

Paper received: 22.04.2024.

Paper accepted: 20.05.2024.

by mesoporous material (ZrO_2/SiO_2). The catalysts displayed the maximum conversion of 69.2% at 120°C following 3 hrs of reaction time [8]. In another study, biodiesel was produced by the reaction of fatty acid (stearic acid) with ethanol, where organophosphonic acid supported on NaY molecular sieve, having Arrhenius coefficient and activation energy of 6.394×10^3 and 70.51 kJ/mol, respectively [9]. Vinod and team performed the steps for the synthesis of alkyl stearates from stearic acid within a closed batch reactor by means of heteropolyacid catalysts, available in the market [10]. Saravanan et. al demonstrated that an increase in the ratio of Zr:Si from 1:2 to 2:1 leads to the increase in yield of methyl stearate from 71% to 91% keeping a constant temperature of 60°C for 7 hrs, due to an elevation in acid spot concentration [11]. In another study, an environment-friendly carbon-based catalyst developed from extracted bagasse lignin was exploited in the esterification of stearic acid and methanol under most favourable conditions, i.e. 260 °C temperature for 5 min with a 9:1 methanol:stearic acid molar proportion, 5% wt catalyst, and 10% v/v toluene yielding 91.1% methyl stearate [12]. Kastratovic et al. were able to secure a maximum yield of

99% with H_2SO_4 as a catalyst while reacting stearic acid and 1-butanol with an acid/alcohol/catalyst in a mole ratio of 1/15/0.75 at 65°C. The observed order of reactivity of different alcohols was: 1-butanol ($CH_3CH_2CH_2CH_2OH$) > 1-propanol ($(CH_3CH_2CH_2OH)$) > 2-methyl-1-propanol ($CH_3CH(CH_3)CH_2OH$) > ethanol (CH_3CH_2OH) > 2-butanol ($CH_3CH_2CH(OH)CH_3$) > 2-propanol ($(CH_3)_2CH_2OH$) > 2-methyl-2-propanol ($CH_3C(CH_3)_2OH$) [13]. A detail of efficiency of different catalysts is shown in table 1. Han and his team synthesised ethyl palmitate using tungstophosphoric acid ($H_3PW_{12}O_{40}$; HPW) with keggin geometry incorporated with ionic liquids having SO_3H as functional units, and the observed yield was 97.2%. This report indicates that heteropolyacid salts can be useful in obtaining a high yield of biodiesels. In this study, cerium (III) phosphotungstate is used for the first time to produce biodiesel from stearic acid with different alcohols. Several studies were conducted to optimize different parameters of the biodiesel, resulting in high calorific value, pour and cloud point, etc. This report's centre of attraction is the comparison between the properties of pure biodiesel obtained and the blended form of this biodiesel with additive (toluene) in 2:8, 1:9 ratios.

Table 1. Esterification of stearic acid using a variety of catalysts to obtain diverse yield.

Sr. no.	Reaction conditions/ Reactants	Catalyst	Biodiesel produced	yield	Reference no.
1.	Lipases which were assayed on a packed-bed system	Sulfuric acid	Isoamyl stearate	90-93 %	5
2.	T=120°C Time=60 minutes, Methanol: stearic 150 M: 1	Tin zirconium oxide (TMOs) 0.2 g	Methyl stearates	74 %	6
3.	Methanol: stearic acid 35.5:1 T=90°C	Protonated and crosslinked amidoximated polyacrylonitrile	Methyl stearate	94 %	7
4.	Time=3hr T=120 °C Ethanol: stearic acid 120:1	Protonated mesoporous ZrO_2/SiO_2 (0.4 g)	Ethyl stearate	76.9 %	8
5.	Time=4hour Alcohol: acid. 4:1, T=95°C and 100°C.	organophosphonic acid with Na exchanged zeolite (2.0 g)	Ethyl stearate	69.10 %	9
6.	Time=4 hours T= 110°C Slight excess of alcohols	Heteropoly acid; phosphotungstic acid (PTA) as catalyst (1 mol%)	Alkyl stearates	>95 %	10
7.	T= 60°C Time=7 hours Stearic acid: methanol	Aerogel-sulfated ZrO_2-SiO_2 blended with oxide solid acid catalyst	Methyl stearate	91%	11

8.	Stearic acid: methanol 1:9, T=240°C Time=10 minutes	sulfonated carbon derived catalysts from organosolv- lignin with methane sulfonic acid 5 wt%	Methyl stearate	89.2%	12
9.	Acid/alcohol/H ₂ SO ₄ 1/15/0.75, T=65°C	Sulfuric acid	Alkyl stearates	99%	13
10.	EtOH/PA = 7.7 mol/mol, catalyst % = 4.4 wt%, Time = 2.5 h, T = 363 K,	Keggin tungstophosphoric acid with ionic liquids having SO ₃ H functional unit	Ethyl palmitate	97.2%	14
11.	Stearic acid: Methanol 1:10, T. = 90°C, Time = 2.5 hours	Cerium (III) Phosphotungstate	Butyl Stearate	98.7%	Proposed work

2. EXPERIMENTAL PROCEDURE

Required materials

Cerium nitrate (CDH), Orthophosphoric acid (HI media), and sodium tungstate (CDH), methanol, ethanol, iso-propanol, n-propanol, n-butanol, and stearic acid (Qualikems), Ostwald's viscometer, Pensky Martin's closed cup flash point apparatus with standard: IP 34, ASTM D 93, IS 1448 (P-21), ISO 2719, Bomb calorimeter (ASTM-D5865-98a), Pour point analyser (IS 1448, P:10), BET surface area analyser (AutosorbiQ Station 1).

Procedure followed

Synthesis of catalyst (HPAs)

A known catalyst, cerium (III) phosphotungstate as reported by Raj et al [15] was prepared in the present report in different chemical proportions. Cerium nitrate, Orthophosphoric acid, and sodium tungstate were the compounds used in the preparation of this catalyst. All these compounds were mixed in their respective volumetric ratios 2:1:2 and their respective concentrations were 108.6 gm/dm³, 24.5 gm/dm³, 82.5 gm/dm³. The molar ratio was Ce:P:W::1:1:1. The resultant solution was heated at a temperature of 60°C after adjusting its pH at 1.08, by pouring an appropriate quantitative volume of dilute HCl/NaOH in the solution. Hence, mixture obtained was refluxed for 3 hours, keeping the reaction temperature at 40-45°C. The product obtained after this reaction have been filtered and, washed multiple times with de-ionized water. After drying the compound at room temperature in a desiccator, it was further immersed into distilled water to absorb the water molecule in the channel of the structure. Then, it was activated with dilute HCl acid in volume 25 ml.

Then, again washing, and drying at room temperature bestowed the desired heteropolyacid salt cerium (III) Phosphotungstate as a which appears as a greyish-white compound; the same was further used in form of a catalyst during the esterification reaction for synthesis of biodiesel.

Esterification reaction

Stearic acid is mixed with five different types of alcohols; methanol, ethanol, iso-propanol, n-propanol, and n-butanol followed by an esterification reaction using a catalyst cerium (III) phosphotungstate. A generalized form of esterification reaction is as mentioned below;

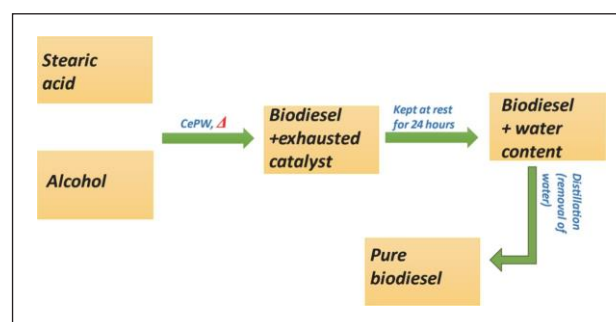
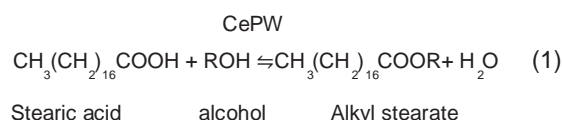


Figure 1. Generalised experimental procedure followed to produce biodiesel.

By following this procedure, varieties of biodiesels were produced through the esterification of stearic acid with varieties of alcohols (methanol, ethanol, isopropanol, n-propanol, n-butanol) keeping constant value for catalyst loading 3% (w/v), reaction temperature (90°C) and reaction time (1.5 hours).

The %yield of produced biodiesel was measured in every half an hour by titrating a liquefied reaction mixture against standardised NaOH.

To identify the sample with the most optimal results, the following conditions were implemented during the study:

Effect of variable reaction parameter

Effect of different alcohols

In this study, different types of alcohol were tried during esterification of stearic acid. Following reaction was preceded for 1.5 hours. Catalyst quantity was kept 3% w.r.t to stearic acid. The whole setup was subjected to a reaction temperature of 90°C. After half an hour the reaction mixture has been filtered for separation of the heterogeneous catalyst. At this stage, this resultant mixture contains only the ester product, and water as by-product, and, also the alcohol, which was used as a solvent. The mixture obtained in this way, was reserved in a separating funnel and then both fractions were collected separately.

Effect of reaction temperature

In this case, n-butanol was selected for further analysis, as already investigated in the previous study, and the reaction time was performed for 1 hour, while the temperature acted as a variable factor, i.e. from 60°C to 90°C. This study analysed the impact of reaction temperature by determining physicochemical properties.

Effect of reaction time

The present study helped to optimize the contact time of ingredients to get a quantitative yield of the esterification reaction. In this study, the reaction temperature was fixed at 90°C. Different reaction times ranging from one hour, 1.5 hours and 2.5 hours were tried and tested to conclude the most optimal reaction temperature and most optimal time for the reaction to proceed to its maximum.

Biodiesel properties over adding additive

We have tried to enhance the fuel value and other parameters of synthesized biofuel by mixing the resultant product with the additives in different ratios and optimizing the physicochemical properties. So, the addition of an additive enhanced these properties in a very good manner. In the present study, Toluene is used as an additive in different volumetric ra-

tios with the biodiesel (butyl stearate). Studies were done to standardize conditions to produce good quality biodiesel in recognizable yield.

Properties discussed in this study

Density, dynamic viscosity, acid value, aniline point, flash point, fuel point, cloud and pour point, were measured to compare biodiesel characteristics while using different alcohols (methanol, ethanol, isopropanol, n-propanol, and n-butanol) during esterification.

During measurement of all the physicochemical properties, the room temperature was noted to be approximately 13°C. The following properties were measured for the biodiesel samples:

- Density: The density of each sample was assessed using a Pycnometer. The density was calculated in terms of g/cm^3 .
- Dynamic viscosity: The Ostwald's viscometer was used to measure the dynamic viscosity of the biodiesel samples. The viscosity was calculated using the formula provided by Anzueto and his team [16]. The units are mPa. s.
- Acid value: This parameter of the biodiesel samples was determined by titration with a standard NaOH solution. The formula utilized for this property was the same as used by Bashiri et al [17] and was used to calculate the acid value in terms of mg NaOH/g stearic acid.
- Aniline point: The aniline point of the samples is determined as the temperature at which there is uniformity in the mixture of aniline and oil [18]. The aniline point of any fuel indicates its aromatic content.
- Cloud and pour point: These characteristics of the fuel determine its stability in very cold weather. Pour point indicates the temperature at which the liquid stops flowing, while the cloud point indicates the presence of cloudiness at a particular temperature [19]. A lower value of these properties indicates better quality of the fuel.
- Flash and fuel point: This value of a fuel is the temperature required to catch fire by a fuel, while the fire point represents the temperature needed to burn the sample [20]. The Pensky Marten's flash point instrument was used to determine these properties.

3. RESULT AND DISCUSSION

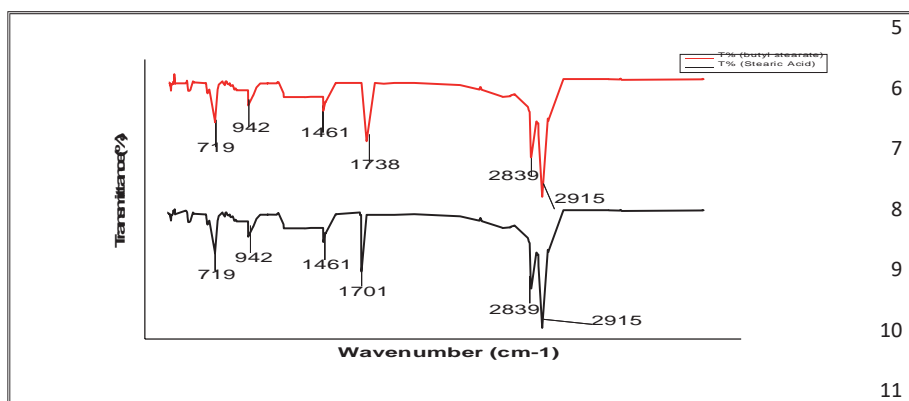


Figure 2. FTIR of butyl stearate and stearic acid.

FTIR analysis: Although the progress of this reaction was monitored via titration with a standardized alkaline solution but, the final confirmation of the product formation was done with the help of IR study of the desired product after separation.

FTIR peak analysis was conducted on butyl stearate and stearic acid. The peak at 1738 cm^{-1} denotes the formation of ester. Figure 2 compares the FTIR spectra of butyl stearate (1738 cm^{-1}) and stearic acid (1701 cm^{-1}) and it confirms the formation of biodiesel (ester formed).

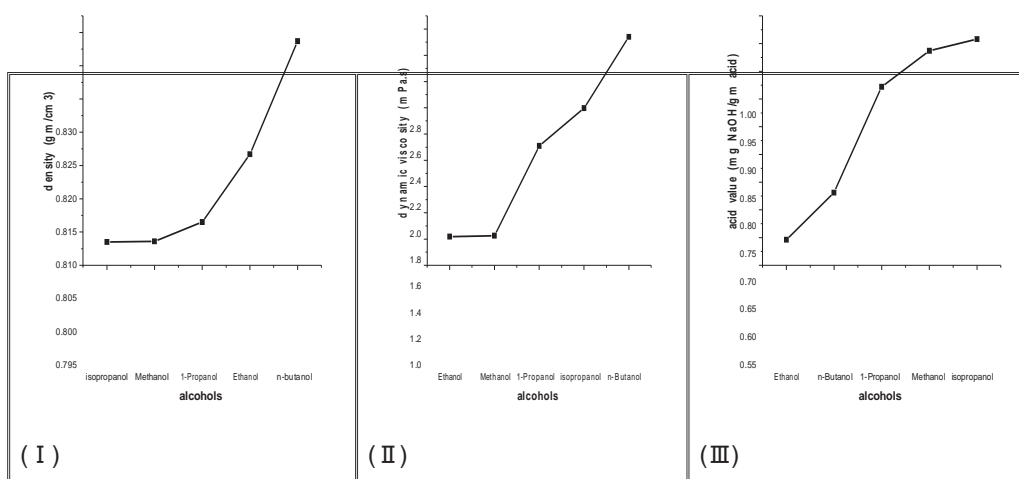


Figure 3. Properties of synthesized biodiesel using different carbon chain length of alcohols (I) density, (II) dynamic viscosity, (III) acid value.

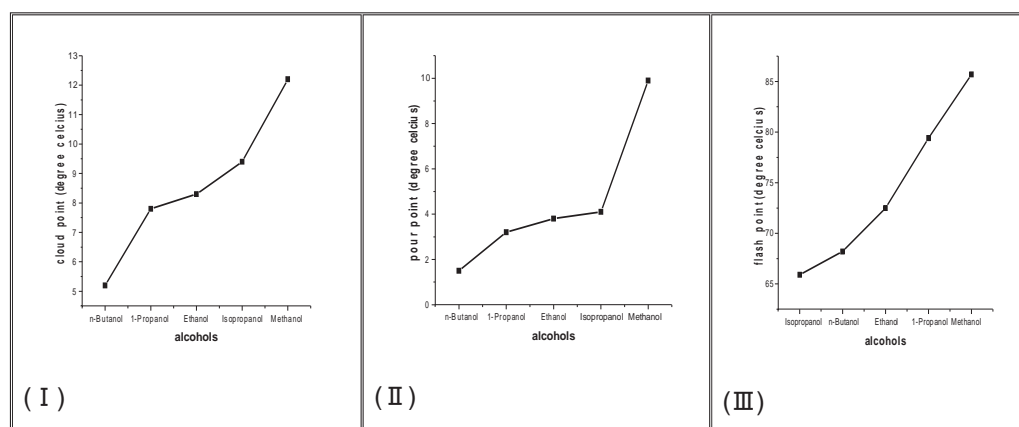


Figure 4. Properties of synthesized biodiesel using different carbon chain length of alcohols (I) pour point, (II) cloud point, (III) flash point.

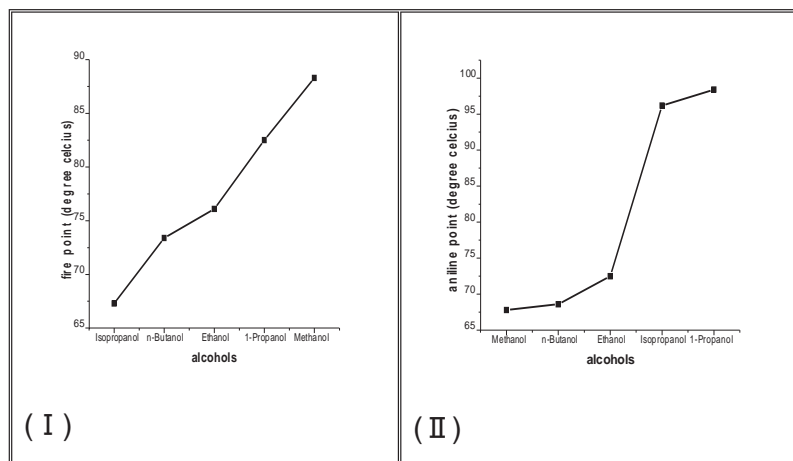


Figure 5. Properties of synthesized biodiesel using different carbon chain length of alcohols (I) fire point, (II) aniline point.

Study of several physicochemical properties with variation of types of alcohols

Effect of alcohol carbon chain length: From the above results mentioned in Figure (3-5), it was concluded that n-butanol gave the best results like; a low acid value, low but above room temperature flash and fire point, and very low temperature values for cloud and pour points which is considered as one of the best features for a fuel. So, all these factors favour the suitability of biodiesel obtained via esterification of stearic acid with butanol and hence chosen for further studies.

Therefore, n-butanol is mixed with stearic acid in vicinity of catalyst cerium (III) phosphotungstate to produce the required biodiesel through an esterification reaction. In the present section, the varying factors were as; reaction temperature (90°C), reaction time (1.5 hours), and effect of additive (toluene), etc. The % yield, we obtained in the case of alcohols methanol, ethanol, 1-propanol, isopropanol, and n-butanol was calculated as 86.2, 88.5, 90.3, 92.8, and 96.5 % respectively at 90°C with reaction time 1.5 hours.

Effect of reaction temperature

Evolved from the results of this study, it was culminated that n-butanol produced the highest percentage yield compared to other alcohols. Therefore, this subsequent study used n-butanol as the alcohol in the esterification process. The discussion of the results obtained under the variable reaction temperature condition (60°C, 70°C, 80°C, 90°C) for reaction time 1.5 hours. Percentage yield, we obtained in

case of butyl stearate (biodiesel) was calculated at different reaction temperatures 60°C, 70°C, 80°C and 90°C as 74.8, 76.2, 88.3, and 96.5 % respectively.

Effect of reaction time

Now the maximum %yield we obtained at reaction temperature 90°C (kept fixed) during this study. The percentage yield in the case of n-butanol was calculated at different reaction times 1, 1.5, 2.5 hours as 94.2, 96.5, and 98.7 % respectively.

Analysis of biodiesel properties over adding additive (Toluene)

Additives are chosen based upon their various physicochemical characteristics like; density, dynamic viscosity, flash and fire point, acid value, aniline point, cloud and pour point, % yield, and calorific values etc [21-24]. By using additives, the lifetime of a machine/engine can be increased as additives prevent machines from many kinds of technological issues. The trend shown by the physicochemical properties of butyl stearate are expressed in terms of their successive plots in Figure (6-9). All these results obtained, in case of different blends of biodiesel and toluene (used as an additive here) viz; pure biodiesel, toluene: biodiesel::1:9, and toluene: biodiesel::2:8 are arranged in the ascending values as mentioned in these graphs.

Conclusively, it can be expressed here that the incorporation of toluene as an additive brought excellent changes in all these properties as compared to the pure biodiesel that have been clearly expressed below in these respective plots.

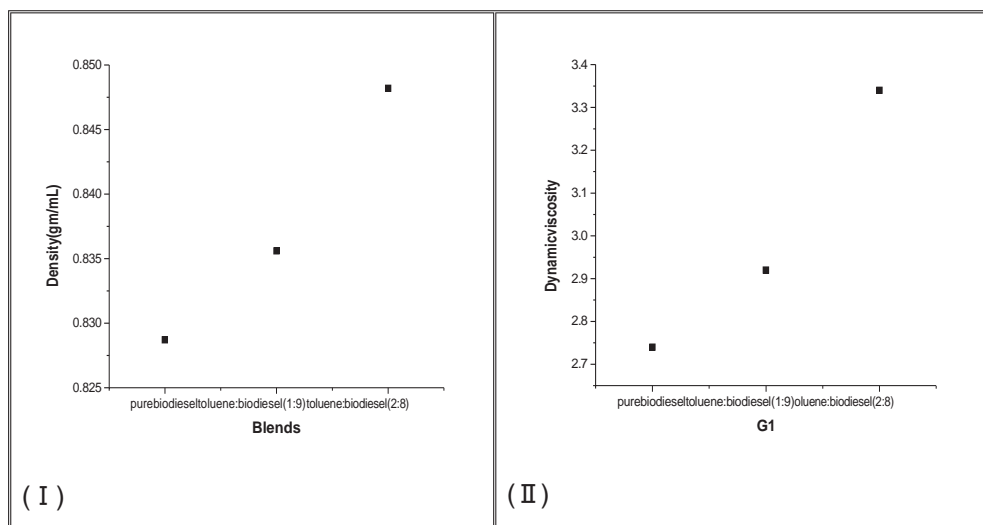


Figure 6. Observations of results: density (I) and dynamic viscosity (II)for pure biodiesel and additive: biodiesel: 1:9 and 2:8 with different alcohols.

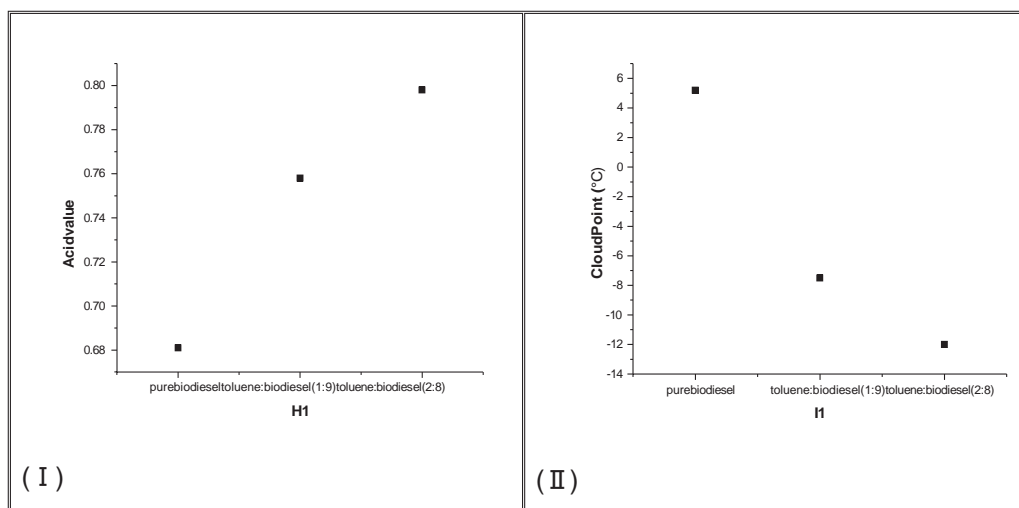


Figure 7. Observations of results: acidvalue (I) and cloudpoint (II) for pure biodiesel and additive: biodiesel: 1:9 and 2:8 with different alcohols.

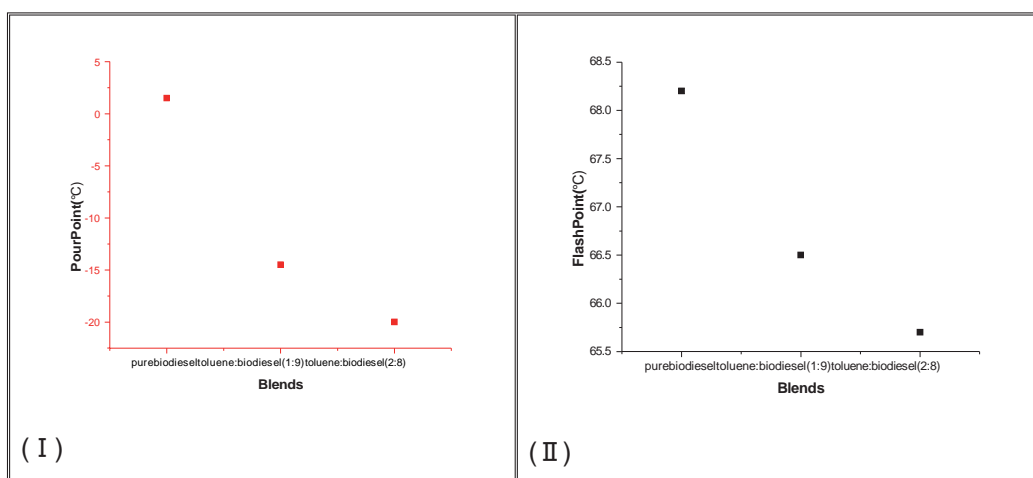


Figure 8. Observations of results: pour point (I) and flash point (II) for pure biodiesel and additive: biodiesel: 1:9 and 2:8 with different alcohols.

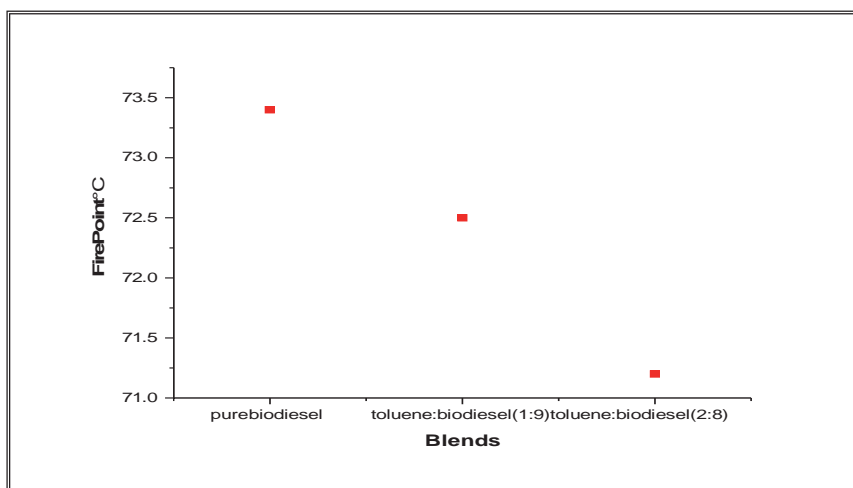


Figure 9. Observations of results: Fire point for pure biodiesel and additive: biodiesel::1:9 and 2:8 with different alcohols.

Calorific value & surface area

The test method ASTM-D5865-98a was used to measure calorific values of selected pure biodiesel and biodiesel with additive, i.e. butyl stearate and butyl stearate with toluene (additive). 7320 Kcal/kg without additive (pure biodiesel) and 7512 Kcal/kg with additive were observed through the technique as mentioned. These results showed the enhancement in fuel calorific value which further supports the

applicability of the fuel. Higher values point towards the better efficiency of biodiesel.

BET surface area analyzer (AutosorbIQ Station 1) [25] was utilized to find the surface region of the catalyst which helps in measurement of adsorption rate of the catalyst. The surface area of the catalyst cerium (III) phosphotungstate was determined as 121.427 m²/g, the original plots obtained for this property are mentioned in Figure 10.

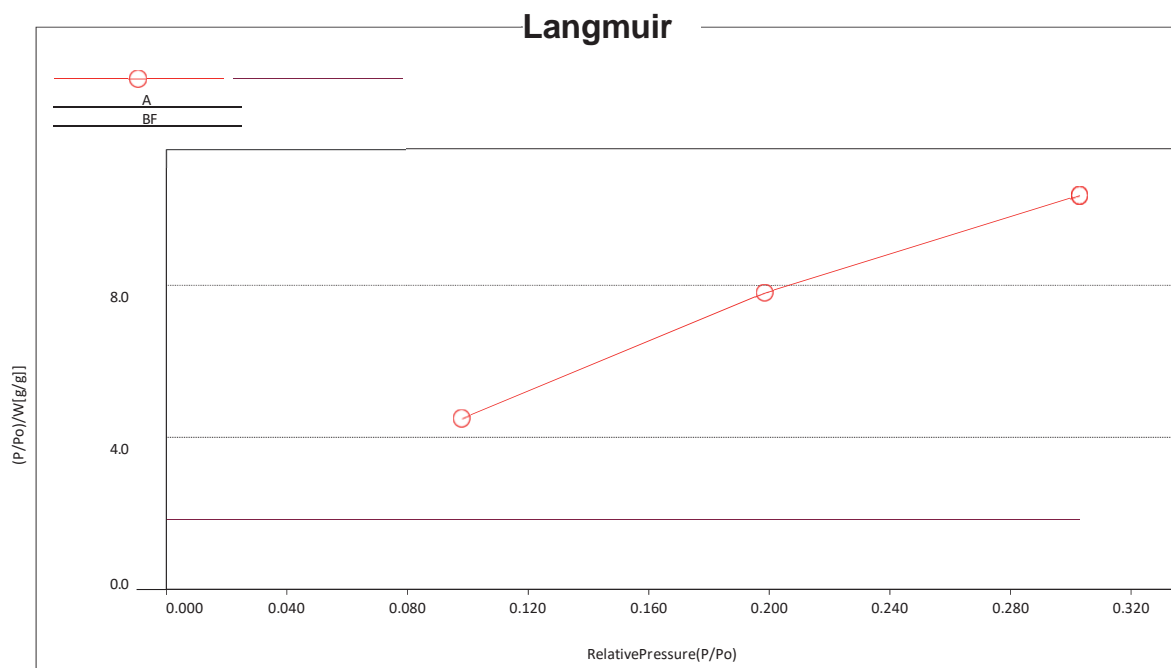


Figure 10. Langmuir plot for surface area of catalyst.

% yield of biodiesel

The values for percentage yield point the total biodiesel we obtained from its starting material per hundred; following formula applied for required calculations [26]:

Biodiesel % yield = (weight of biodiesel/weight of initial stearic acid) × 100

Different % values correspond to all these alcohols with stearic acid and CePW as the catalyst. A graphical comparison of the % yield obtained is given in Figure 11, and Table 2 depicts optimised reaction conditions. Based upon this observation, n-butanol-derived biodiesel was prioritized over other alcohols.

Table 2. % age yield obtained in esterification reaction with the variation of carbon chain length of alcohol

Alcohol	% age yield	Reaction Temperature	Reaction Time
Methanol	89.2%	90°C	2.5 hours
Ethanol	90.8%		
n-Propanol	92.5%		
Isopropanol	94.3%		
n-Butanol	98.7%		

Figure 11. Variation of % yield with different alcohols used during esterification process.

Rejuvenation of catalyst

On completion of this reaction, the catalyst was separated from the reaction mixture and was washed properly with de-ionized water before drying to make it suitable for reuse. The catalyst was used three times for the same procedure, and the percentage yields of biodiesel obtained were measured each time. A small decrease in yield percentage was observed, and by the third cycle of catalyst use, the final decrease was approximately 92.6%.

4. CONCLUSION

The synthesis of catalyst cerium (III) phosphotungstate was done in a volumetric ratio of 2:1:2 and their corresponding molar ratio was 1:1:1 for the respective ingredients. The colour of the catalyst was recognized as greyish-white. This catalyst was utilized during esterification of stearic acid with variable carbon chain length alcohols. Using the same catalyst, we have found that the properties of n-butanol-derived biodiesel were best suited than other alcohols. So, n-butanol was selected for further studies in which the addition of toluene as an additive was done which resulted in remarkable changes in the properties of biodiesel

than its pure form without an additive. Maximum % yield of biodiesel was found to be ~98.7% in the case of butyl stearate (biodiesel) which was reduced to 92.6% by 3rd cycle of its use. Hence, butyl stearate is a competent biodiesel obtained through esterification using stearic acid, n-butanol and cerium (III) phosphotungstate (HPAs) as catalyst.

Acknowledgement

The authors are highly thankful to MM(DU), Mul-lana (Ambala) for various physical facilities and moral support during the work.

5. REFERENCES

- [1] A.Gaurav, S.Dumas, C.Mai, F.T.Ng (2019) A kinetic model for a single step biodiesel production from a high free fatty acid (FFA) biodiesel feedstock over a solid heteropolyacid catalyst, *Green Energy & Environment*, 4(3), 328-341. <https://doi.org/10.1016/j.gee.2019.03.004>.
- [2] P.Chandra, R.Enespa, R.Singh, P.Arora (2020) Micro-bial lipases and their industrial applications: a comprehensive review. *Microbial cell factories*, 19, 1-42. <https://doi.org/10.1080/10408398.2022.2038076>.
- [3] W.Lee, Z.Zhang, O.Lai, C.Tan, Y.Wang (2020) Diacylglycerol in food industry: Synthesis methods, functionalities, health benefits, potential risks, and drawbacks. *Trends in Food Science & Technology*, 97, 114-125. <https://doi.org/10.1016/j.tifs.2019.12.032>.
- [4] A.Sahu, A.Pandit (2019) Kinetic study of homogeneous catalyzed esterification of a series of aliphatic acids with different alcohols. *Industrial & Engineering Chemistry Research*, 58(8), 2672-2682. <https://doi.org/10.1021/acs.iecr.8b04781>.
- [5] R.De Lima, H.Bento, C.Reis, R.N.Bôas, L. de Freitas, A.Carvalho, H. de Castro (2022) Biolubricant production from stearic acid and residual secondary alcohols: system and reaction design for lipase-catalyzed batch and continuous processes. *Catalysis Letters*, 152(2), 547-558. <https://doi.org/10.1007/s10562-021-03663-z>.
- [6] S.Ibrahim (2021) Preparation, characterization, and application of novel surface-modified ZrSnO₄ as Sn-based TMOs catalysts for the stearic acid esterification with methanol to biodiesel. *Renewable Energy*, 173, 151-163. <https://doi.org/10.1016/j.renene.2021.03.134>.
- [7] R.Ahmed, S.Rashid, K.Huddersman (2023) Esterification of stearic acid using novel protonated and crosslinked amidoximated polyacrylonitrile ion exchange fibres. *Journal of Industrial and Engineering Chemistry*, 119, 550-573. <https://doi.org/10.1016/j.jiec.2022.12.001>.
- [8] H.Mahmoud, S.El-Molla, M.Ibrahim (2020) Biodiesel production via stearic acid esterification over mesoporous ZrO₂/SiO₂ catalysts synthesized by sur-

- factant-assisted Sol-gel auto-combustion route. *Renewable Energy*, 160, 42-51. <https://doi.org/10.1016/j.renene.2020.06.005>.
- [9] W.Liu, P.Yin, X.Liu, S.Zhang, R.Qu (2015) Biodiesel production from the esterification of fatty acid over organophosphonic acid. *Journal of Industrial and Engineering Chemistry*, 21, 893-899. <https://doi.org/10.1016/j.jiec.2014.04.029>.
- [10] N.Vinod, R.Tiwari, N.Bhat, S.S.Mal, S.Dutta (2020) High-yielding synthesis of alkyl stearates from stearic acid within a closed batch reactor using heteropolyacids as efficient and recyclable catalyst. In *AIP Conference Proceedings*, vol. 2225, No. 1. AIP Publishing. <https://doi.org/10.1063/5.0005580>.
- [11] K.Saravanan, B.Tyagi, H.Bajaj (2016) Esterification of stearic acid with methanol over mesoporous ordered sulfated $\text{ZrO}_2\text{-SiO}_2$ mixed oxide aerogel catalyst. *Journal of Porous Materials*, 23(4), 937-946. <https://doi.org/10.1007/s10934-016-0151-x>.
- [12] P.Sangsiri, N.Laosiripojana, W.Laosiripojana, P.Daorattanachai (2022) Activity of a Sulfonated Carbon-Based Catalyst Derived from Organosolv Lignin toward Esterification of Stearic Acid under Near-Critical Alcohol Conditions. *ACS Omega*, 7(44), 40025-40033. <https://doi.org/10.1021/acsomega.2c04693>.
- [13] V.Kastratovic, M.Bigovic (2018) Esterification of stearic acid with lower monohydroxylic alcohols. *Chemical Industry and Chemical Engineering Quarterly*, 24(3), 283-291. <https://doi.org/10.2298/ciceq170327040k>.
- [14] X.Han, S.Jiang, Z.Chen, Z.Zeng, Q.Chen, F.Niu, S.Liu (2023) Highly active sulfonic ionic liquid modified heteropoly acid composite catalysts for efficient production of ethyl palmitate. *Renewable Energy*, Article ID 118918. <https://doi.org/10.1016/j.renene.2023.118918>.
- [15] P.Raj (2011) Synthesis, and Ion Exchange Characteristics of Cerium (IV) Phosphotungstate. *Orient. J.Chem.*, 27(3), 1257-1260. <https://doi.org/10.1007/bf02517309>.
- [16] J.Camas-Anzueto, J.Gómez-Pérez, R.Meza-Gordillo, G.Anzueto-Sánchez, M.Pérez-Patricio, F.López-Estrada, C.Ríos-Rojas (2017) Measurement of the viscosity of biodiesel by using an optical viscometer. *Flow Meas. Instrum.*, 54, 82-87. <https://doi.org/10.1016/j.flowmeasinst.2016.12.004>.
- [17] S.Bashiri, B.Ghobadian, M.Dehghani Soufi, S.Gorjian (2021) Chemical modification of sunflower waste cooking oil for biolubricant production through epoxidation reaction. *Mater. Sci. Energy Technol.*, 4, 119-127. <https://doi.org/10.1016/j.mset.2021.03.001>.
- [18] S.Esso, Z.Xiong, W.Chaiwat, M.Kamara, X.Longfei, J.Xu, J.Xiang (2022) Review on synergistic effects during co-pyrolysis of biomass and plastic waste: Significance of operating conditions and interaction mechanism. *Biomass and Bioenergy*, 159, 106415. <https://doi.org/10.1016/j.biombioe.2022.106415>.
- [19] A.Folayan, P.A.Anawe, A.Aladejare, A.Ayeni (2019) Experimental investigation of the effect of fatty acids configuration, chain length, branching and degree of unsaturation on biodiesel fuel properties obtained from lauric oils, high-oleic and high-linoleic vegetable oil biomass. *Energy Reports*, 5, 793-806. <https://doi.org/10.1016/j.egy.2019.06.013>.
- [20] S.Sehar, F.Sher, S.Zhang, U.Khalid, J.Sulejmanović, E.Lima (2020) Thermodynamic and kinetic study of synthesised graphene oxide-CuO nanocomposites: A way forward to fuel additive and photocatalytic potentials. *Journal of Molecular Liquids*, 313, 113494. <https://doi.org/10.1016/j.molliq.2020.113494>.
- [21] P.Ghodke, A.Sharma, K.Moorthy, W.Chen, A.Patel, L.Matsakas (2022) Experimental investigation on pyrolysis of domestic plastic wastes for fuel grade hydrocarbons. *Processes*, 11(1), 71-77. <https://doi.org/10.3390/pr11010071>.
- [22] M.E.Soudagar, N.Nik-Ghazali, M.Kalam, I.Badruddin, N.Banapurmath, N.Akram (2018) The effect of nano-additives in diesel-biodiesel fuel blends: A comprehensive review on stability, engine performance and emission characteristics. *Energy Conversion and Management*, 178, 146-177. <https://doi.org/10.1016/j.enconman.2018.10.019>.
- [23] S.Madiwale, A.Karthikeyan, V.Bhojwani (2017) A comprehensive review of effect of biodiesel additives on properties, performance, and emission. *IOP Conference Series: Materials Science and Engineering*, 197, 012015. <https://doi.org/10.1088/1757-899x/197/1/012015>.
- [24] A.Agarwal, L.Da (2001) Biodiesel development and characterization for use as a fuel in compression ignition engines. *J.Eng.Gas Turbines Power*, 123(2), 440-447. <https://doi.org/10.1115/1.1364522>.
- [25] M.Ba-Abbad, A.Kadhum, A.B.Mohamad, M.Takriff, K.Sopian (2012) Synthesis and catalytic activity of TiO_2 nanoparticles for photochemical oxidation of concentrated chlorophenols under direct solar radiation. *Int. J. Electrochem. Sci*, 7(6), 4871-4888. [https://doi.org/10.1016/s1452-3981\(23\)19588-5](https://doi.org/10.1016/s1452-3981(23)19588-5).
- [26] T.Mohammed (2022) Biodiesel Yield and Conversion Percentage from Waste Frying Oil Using Fish Shell at Elmina as a Heterogeneous Catalyst and the Kinetics of the Reaction", *International Journal of Chemical Engineering*, Article ID 8718638, p.9. <https://doi.org/10.1155/2022/8718638>.

IZVOD

CERIJUM(III) FOSFOTUNGSTAT: EFIKASAN KATALIZATOR U ESTERIFIKACIJI MASNIH KISELINA

U ovom radu, poznati fosfotungstat cerijuma(III) soli heteropoli kiseline (HPAs) sintetizovan je u zapreminskom odnosu 2:1:2 sa molarnim odnosom 1:1:1 svakog sastojka. Ovi HPA se dalje koriste u obliku katalizatora za generisanje biodizela kroz esterifikaciju alkohola promjenljive dužine ugljeničnog lanca (metanol, etanol, n-propanol, izopropanol, n-butanol) i stearinske kiseline u različitim uslovima reakcije. FTIR proizvedenog biodizela je, takođe, urađen za osiguranje estarskih pikova unjemu. Analiza nekih važnih svojstava biodizela kao što su gustina, dinamički viskozitet, kiselinska vrednost, tačka anilina, oblak, tačka stinjanja, tačka paljenja i plamena itd., urađena su da bi se razlikovali i potvrdili rezultati. Velika površina katalizatora, tj. 121.427 m²/g, određena korišćenjem BET površinskog analizatora, podržava činjenicu nečuvanog katalitičkog delovanja u reakciji esterifikacije. Takođe je proučavan uticaj aditiva na svojstva dobijenog biodizela. Izmerena je kalorijska vrednost uzoraka na 7320 Kcal/kg bez aditiva i 7512 Kcal/kg nakon dodavanja toluena (kao aditiva) u biodizel generisan u studiji. Temperatura tečenja biodizela sa aditivima je primećena čak i < 20°C.

Ključne reči: cerijum(III) fosfovolframat, biodizel, butil stearat, vrednost goriva, aditivi.

Naučni rad

Rad primljen: 22.04.2024.

Rad prihvaćen: 20.05.2024.

The ORCID Ids of all the authors are as follows:

1. Sonia Yadav: <https://orcid.org/0000-0002-5080-7959>

2. Nadeem Sharma: <https://orcid.org/0000-0001-7191-0333>

Vladimir D. Jović

Institute for Multidisciplinary Research University of Belgrade, Belgrade, Serbia

Short communication

ISSN 0351-9465, E-ISSN 2466-2585

<https://doi.org/10.62638/ZasMat1308>



Zastita Materijala 65 (4)
797 - 800 (2024)

The long time performance of catalysts usually used in the literature

ABSTRACT

This communication discusses the “long time operation” in characterizing catalysts for the hydrogen evolution reaction (HER). It has been explained that the commonly used procedure in practically all published papers is useless and that it is necessary to define the “accelerated service life test” (ASLT) to predict the behavior of electrodes under industrial conditions. At the same time, one example of ASLT for cathodes in chlor-alkali electrolysis, obtained in our previously published papers is presented.

Keywords: Long time operation, industrial electrolysis, accelerated service life tests

During the last decade in almost each paper describing the behavior of certain catalyst for certain electrochemical reaction, mostly the HER the “long time operation” was practically mandatory in order to predict their behavior (stability) during the application in industrial plant for water splitting, or chlor-alkali electrolysis. If the authors did not present such test, reviewers recommended such test. This test assumed at least 24 h of potential measurements at a current density and temperature of electrolyte used in the industrial electrolysis. If the potential of catalysts didn't change for more than 5 % - 10 % of the initial value the test was satisfactory and the reviewers gave positive review and accordingly the paper has been published. Since the number of these publications is extremely large, none of them will be listed in the references.

It is important to note that such tests are useless for several reasons: (1) tests are usually performed in a stationary electrolyte, while in industrial application circulating electrolyte is used; (2) often, used current density is much lower than that in industrial plants; (3) process of industrial electrolysis is never continuous and is always interrupted due to different reasons (explained in a further text).

*Corresponding author: Vladimir D. Jović

E-mail: vladajovic@imsi.bg.ac.rs

Paper received: 22. 10. 2024.

Paper accepted: 24. 11. 2024.

CHLOR-ALKALI ELECTROLYSIS

In order to predict stability of commercial cathodes for the HER in industrial chlor-alkali electrolysis in zero-gap membrane cell configuration, ASLT for commercial cathodes has been designed and partially disclosed in the literature [1]. The efficiency of cathodes is a result of combination of certain activity and stability at the high cathodic current densities ($> - 300 \text{ mA cm}^{-2}$) used in industrial applications. The loss of activity and stability of cathodes during long term operation is a consequence of the so-called polarity inversion of the electrodes. This is happening during the replacement of old electrodes of an electrolyzer with new ones in the zero-gap membrane configuration cells, when anodes and cathodes in the rest of cells in the industrial plant are short-circuited, causing a reverse current flow.

Although the replacement of electrodes lasts for some time (depending on the number of electrolyzers in the industrial plant), reverse current flow may damage the cathodes and negatively affect their activity for the HER [2]. The manufacturers can predict how often in a certain period of time such operation should be performed and, in accordance with that, design appropriate ASLT for cathodes. Such approach is missing in the literature and there are only few papers dealing with the ASLT of electrode materials promising for use in industrial electrolysis [1,3,4] which was designed by De Nora Industries [1]. The procedure is based on a sequence of galvanostatic

polarizations in the HER range and cyclic voltammetry (CV) in a wide potential range, from hydrogen evolution as negative limit, to oxygen evolution as positive limit (simulating the conditions of polarity inversion). According to Ref. [1] ASLT procedure should simulate 5 years of cathode operation in the industrial cells (32 wt.% NaOH, 90 °C, $j = -300 \text{ mA cm}^{-2}$) and is composed of following sequences: (1) Galvanostatic electrolysis for 30 min. at $j = -300 \text{ mA cm}^{-2}$; (2) pseudo-steady-state current-potential curve (corrected for ohmic drop) recorded at 0.5 mV s^{-1} in order to determine Tafel plots, followed with EIS measurements at various potentials in the HER region; (3) A series of five cyclic voltammograms (CVs) from $-1.05 \text{ V vs. Hg/HgO}$ to $0.70 \text{ V vs. Hg/HgO}$ (sweep rate 10 mV s^{-1}); (4) Galvanostatic electrolysis for 30 min. at $j = -300 \text{ mA cm}^{-2}$; (5) Pseudo-steady-state current-potential curve and EIS, as in sequence 2; (6) Repeating sequences 1 - 5 with 10 CVs five times.

In the work of Antozzi et al. [1] procedure for ASLT is slightly modified in comparison with that used in the industry (see Ref. [4]).

These procedures are designed by the industry and could be completely different. Some industries are using ASLT designed by application of much higher current density than normally used in industrial plant for certain period of time, followed by zero current for shorter time and repeating this sequence for several times. Once the sequence is finished polarization curve is recorded in a defined current density region. Such procedure should be repeated for several times in order to predict stability of catalyst for a long time period (mainly 5 years).

In this communication the most important results of ASLT for electrodeposited NiSn alloys are presented as an example for simulation of industrial process of chlor-alkali electrolysis.

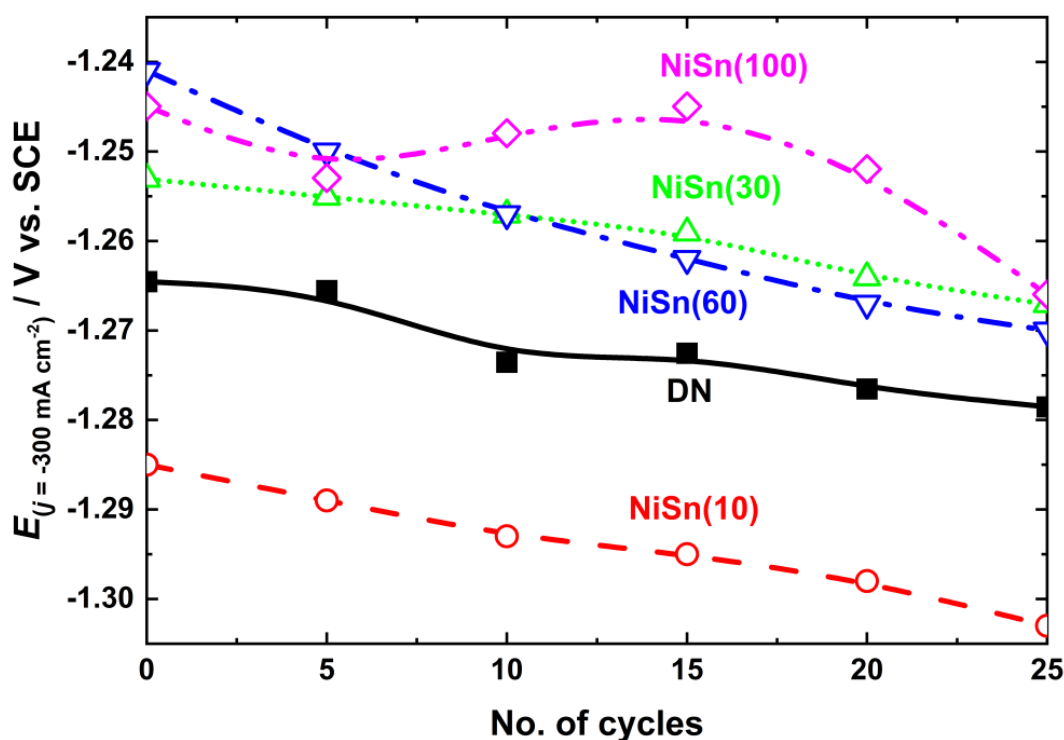


Figure 1. Dependence of E (corrected for IR drop) at $j = -300 \text{ mA cm}^{-2}$ vs. no. of cycles. (Reprinted from Ref. [6] with the permission of the Engineers Society of Corrosion, Belgrade, Serbia)

Four samples of Ni-Sn alloys were electrodeposited to a constant charge of -70 C cm^{-2} on Ni mesh 40 at constant current densities of -10 mA cm^{-2} (NiSn 10), -30 mA cm^{-2} (NiSn30), -60 mA cm^{-2} (NiSn60) and -100 mA cm^{-2} (NiSn 100) from

the solution containing Ni^{2+} , Sn^{2+} , pyrophosphate and glycine [5,6]. All samples, together with the commercial De Nora (Ni-RuO_2) cathode, were submitted to the ASLT [5,6] in a stationary electrolyte under the conditions of industrial

electrolysis (32 wt. % NaOH, 90 °C). Potentials recorded at $j = -300 \text{ mA cm}^{-2}$ for all investigated electrodes are presented in Figure 1 as a function of number of CVs (set of 5 CVs represent 1 year of operation in industrial cell). Hence, after 25 CVs 5 years of operation in industrial cell is simulated.

Presented results clearly show better performance of samples NiSn(30, 60 and 100) in comparison with that for the commercial De Nora cathode (DN). As it could be expected after reverse polarization (CVs) potential of all electrodes become more negative, but those for samples NiSn(30, 60 and 100) are more positive than DN for approximately 20 mV. Although this test was not performed in a circulating electrolyte, all samples were tested by the same procedure under the same conditions.

In Figure 2 are presented SEMs of NiSn(100) sample before the ASLT (a) and after the ASLT (b). As can be seen certain amounts of the NiSn coating were dissolved after the ASLT and these coatings are mainly on the convex part of the Ni mesh 40, where the cathodic and anodic current densities are higher due to different current distribution at different positions of the Ni mesh 40.

Considering presented results it could be concluded that when performing "long time performance" of catalysts it is necessary to apply the ASLT procedure in order to predict their performance in the industrial cell.

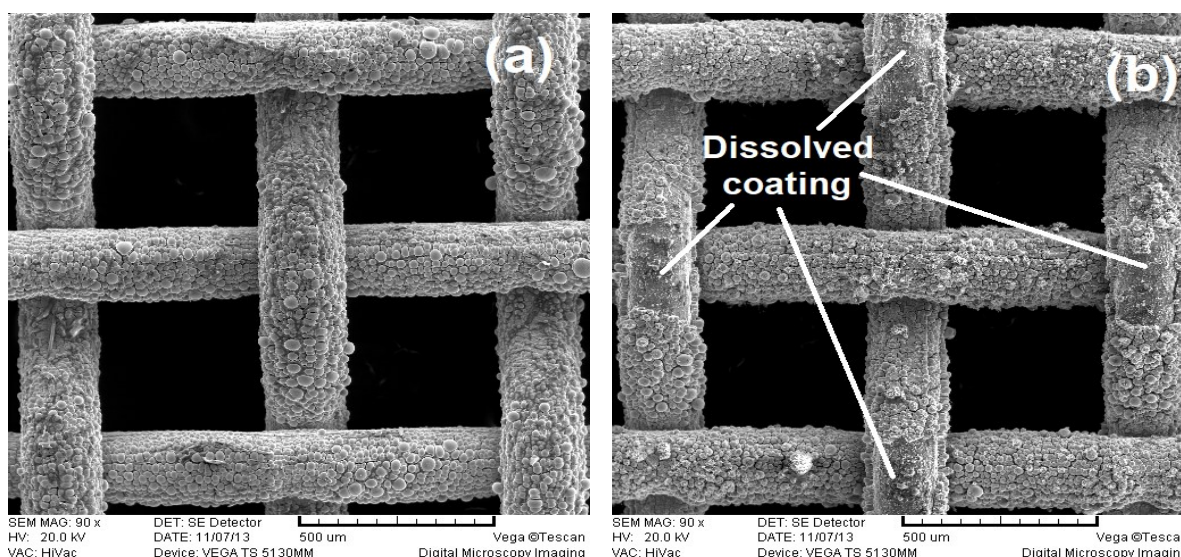


Figure 2. Appearance of the NiSn(100) coating before ASLT (a) and after the ASLT (b)

REFERENCES

- [1] A.L. Antozzi, C. Bargioni, L. Iacopetti, M. Musiani, L. Vazquez-Gomez (2008) EIS study of the service life of activated cathodes for the hydrogen evolution reaction in the chlor-alkali membrane cell process, *Electrochim. Acta*, 53, 7410-7416.
- [2] C. Iwakura, M. Tanaka, S. Nakamatsu, H. Noue, M. Matsuoka, N. Furukawa (1995) Electrochemical properties of Ni/(Ni+RuO₂) active cathodes for hydrogen evolution in chlor-alkali electrolysis, *Electrochim. Acta*, 40, 977-982.
- [3] V.D. Jović, U. Lačnjevac, B.M. Jović, N.V. Krstajić (2012) Service life test of non-noble metal composite cathodes for hydrogen evolution in sodium hydroxide solution, *Electrochim. Acta*, 63, 124-130.
- [4] V.D. Jović, U.Č. Lačnjevac, B.M. Jović, Lj.M. Gajić-Krstajić, N.V. Krstajić (2013) Ni-MoO₂ composite cathodes for hydrogen evolution in alkaline solution. Effect of aging of the electrolyte for their electrodeposition, *J. Serb. Chem. Soc.*, 78, 689-700.
- [5] B.M. Jović, U.Č. Lačnjevac, N.V. Krstajić, V.D. Jović (2014) Service life test of the Ni-Sn coatings as cathodes for hydrogen evolution in chlor-alkali electrolysis, *Int. J. Hydrogen Energy*, 39, 8947-8958.
- [6] V. D. Jović, U. Č. Lačnjevac, B. M. Jović, N. V. Krstajić (2014) Electrodeposited, Ni-based, non-noble metal coatings as cathodes for hydrogen evolution in chlor-alkali electrolysis, *Zaštita Materijala*, 55, 111-125.

IZVOD

PONAŠANJE KATALIZATORA PRI DUGOTRAJNOM ISPITIVANJU KOJE SE OBIČNO KORISTI U NAUČNIM RADOVIMA

U poslednjih 10-ak godina u skoro svakom naučnom radu koji opisuje ponašanje određenog katalizatora u određenoj elektrohemijskoj reakciji, najčešće izdvajanje vodonika i kiseonika, tzv. "dugotrajno ispitivanje" koje traje više od 24 sata je postalo obavezno, kako bi se predvidelo ponašanje (stabilnost) katalizatora pri primeni u industrijskom postrojenju za elektrolizu vode, ili hloralkalnu elektrolizu. U ovoj komunikaciji se govori o „dugotrajnoj operaciji“ u karakterizaciji katalizatora za reakciju evolucije vodonika (HER). Objasnjeno je da je uobičajena procedura u skoro svim objavljenim radovima beskorisna i da je neophodno definisati „test ubrzanog radnog veka“ (ASLT) kako bi se predvidelo ponašanje elektroda u industrijskim uslovima. Istovremeno je prikazan jedan primer za ASLT za katode u hlor-alkalnoj elektrolizi, dobijen u našim prethodno objavljenim radovima.

Ključne reči: dugotrajno ispitivanje, ubrzani test, industrijska elektroliza

Short communication

Rad primljen: 22.10.2024.

Rad prihvaćen: 24.11.2024.

Rad je dostupan na sajtu: <https://www.zastita-materijala.org/>